

Clemson University

TigerPrints

All Dissertations

Dissertations

December 2019

Typhoon Wind Modeling and Flutter Fragility Analysis of Long-Span Bridges in Coastal Regions of China

Genshen Fang

Clemson University, fgs_root@163.com

Follow this and additional works at: https://tigerprints.clemson.edu/all_dissertations

Recommended Citation

Fang, Genshen, "Typhoon Wind Modeling and Flutter Fragility Analysis of Long-Span Bridges in Coastal Regions of China" (2019). *All Dissertations*. 2529.

https://tigerprints.clemson.edu/all_dissertations/2529

This Dissertation is brought to you for free and open access by the Dissertations at TigerPrints. It has been accepted for inclusion in All Dissertations by an authorized administrator of TigerPrints. For more information, please contact kokeefe@clemson.edu.

TYPHOON WIND MODELING AND FLUTTER FRAGILITY ANALYSIS
OF LONG-SPAN BRIDGES IN COASTAL REGIONS OF CHINA

A Dissertation
Presented to
the Graduate School of
Clemson University

In Partial Fulfillment
of the Requirements for the Degree
Doctor of Philosophy
Civil Engineering

By
Genshen Fang
December 2019

Accepted by:
Dr. Weichiang Pang, Committee Chair
Dr. Yaojun Ge, Co-Chair
Dr. Thomas E. Cousins
Dr. Nigel B. Kaye

ABSTRACT

Typhoon or hurricane or tropical cyclone, which is a large-scale air rotating system around a low atmospheric pressure center, frequently causing devastating economic loss and human casualties along coastal regions due to violent winds, heavy rainfall, massive storm surges, flash flooding or even landslides in mountainous areas. The coastal region of China, which is characterized by high population densities and well-developed cities, is always exposed to typhoon threats with 7~8 landfall typhoons every year since Western Pacific Basin is the most active typhoon basin on earth, accounting for almost one-third of global annual storms. With more long-span bridges are being constructed along this coastal area, it is of great importance to perform the risk assessments on these flexible or wind-sensitive structures subjected to typhoon winds.

To reconstruct the mean typhoon wind speed field, a semi-analytical height-resolving typhoon boundary layer wind field model, including a parametric pressure model and an analytical wind model was first developed in Chapter 2 using a scale analysis technique. Some basic characteristics of the inner structure of typhoon wind field, such as the logarithmic vertical wind profile near the ground and super-gradient winds were reproduced. Then, Chapter 3 develops a dataset of two wind field parameters, i.e. the radius to maximum wind speed, $R_{max,s}$ and the Holland pressure profile parameter, B_s in Western Pacific Ocean using the wind data information from best track dataset archived by the Japan Meteorological Agency (JMA) coupled with

the present wind field model. The proposed dataset of $R_{max,s}$ and B_s is able to reproduce the JMA wind observations as closely as possible, which allows performing more accurate typhoon wind hazard estimation. On this basis, the maximum wind hazard footprints for over-water, roughness only and roughness and topography combined conditions of 184 observed landed or offshore typhoon-scale storms are generated and archived for risk assessment. Moreover, this supplementary dataset of $R_{max,s}$ and B_s enables the development of recursive models to facilitate both sub-region typhoon simulations and full track simulations.

Since the present wind field model can only generate long-time-duration speed, say 10-min mean wind speed, Chapter 4 develops an algorithm to compute the gust factor curve by taking the non-stationary and non-Gaussian characteristics of typhoon winds into account. The real wind data of nine typhoons captured by the structural health monitoring system (SHMS) installed in Xihoumen Bridge were utilized to validate the proposed model. Then, the probability distributions of gust factor associated with any gust time duration of interest can be readily achieved after introducing the statistical models of skewness and kurtosis of typhoon winds.

To predict the typhoon wind hazard along the coastal region of China, a geographically-weighted-regression (GWR) -based subregion model was proposed in Chapter 5. The storm genesis model was first applied to a circular boundary around the site of interest. Then, the typhoon forward model including the tracking model, intensity model, and wind field parameter model was developed utilizing the GWR method. A series of performance assessments were performed on the present

subregion model before it was employed to predict the typhoon wind hazards around the coastal regions of China.

Chapter 6 develops a framework to investigate the probabilistic solutions of flutter instability in terms of critical wind speed accounting for multiple resources of uncertainty to facilitate the development of the fragility curve of flutter issue of long-span bridges. The quantifications of structural uncertainties, as well as aerodynamic uncertainties or the randomness of flutter derivatives, were conducted using both literature survey and experimental methods. A number of probabilistic solutions of flutter critical wind speed for two bridges, say a simply supported beam bridge and the Jianguyin Suspension Bridge were achieved by introducing different sources of uncertainty utilizing both 2D step-by-step analysis and 3D multimode techniques.

To examine the flutter failure probability of long-span bridge due to typhoon winds, a case study of a 1666-m-main-span suspension bridge located in the typhoon-prone region was performed. The fragility curves of this bridge in terms of critical wind speed and the typhoon wind hazards curves of the bridge site as the probability of occurrence with respect to any years of interest were developed, respectively by exploiting the techniques achieved in previous chapters. Then a limit state function accounting for the bridge-specific flutter capacity and the site-specific mean typhoon wind hazard as well as the gust factor effects was employed to determine the flutter failure probabilities utilizing Monte Carlo simulation approach.

DEDICATION

Dedicated to my beloved parents, Rongmei Fang (方荣梅) and Chunliang Cheng (程春亮), and my supportive grandmother, Zixiang Fang (方子香) and to loving memory of my grandfather, Chunsheng Fang (方春胜).

Also, I dedicate this study to my beloved wife, Yuanyuan Fang (方媛媛).

ACKNOWLEDGMENTS

I would like to express my gratitude to my advisors and committee chairs, Dr. Weichiang Pang in Clemson University and Dr. Yaojun Ge in Tongji University for their generous guidance, kind help and continued encouragement throughout my doctoral study. I also would like to thank my committee members, Dr. Thomas E. Cousins and Dr. Nigel Kaye for their comments and supports.

Special thanks are due to all my family members for their unconditional love, patience, and unwavering support.

My sincere thanks also go to Dr. Lin Zhao and Dr. Shuyang Cao at Tongji University for their insightful comments and precious supports. In particular, I am grateful to Dr. Jingquan Wang at Southeast University for enlightening me the first glance of research.

I would take this opportunity to thank all the faculty and staff of the Glenn Department of Civil Engineering for their help and supports. I would like to thank my friends, Fanfu Fan, Wenxin Liu, Zhengshou Lai, Weiwei Zhan, Yuting Cheng, Pufeng Wang, Weiqi Wang and Feiyang Chen who helped me a lot in my Ph.D. life in Clemson. I would also like to appreciate research group members, Prashant Rawal, Sri Harshitha Polamuri, Samiuddin Fazil and Amir Safiey, who helped me overcome difficulties and kept me progressing.

I would like to give my appreciation to Dual-PhD Degree Program between Clemson University and Tongji University. I am grateful to the China Scholarship Council and

the teacher assistant funding at Clemson University for supporting my study at Clemson.

TABLE OF CONTENTS

	Page
TITLE PAGE	i
ABSTRACT	ii
DEDICATION	v
ACKNOWLEDGMENTS	vi
TABLE OF CONTENTS	viii
LIST OF TABLES	xii
LIST OF FIGURES.....	xiv
CHAPTER 1 INTRODUCTION	1
1.1 Typhoon-related hazards	1
1.2 Typhoon wind observations.....	5
1.3 Typhoon wind modeling.....	12
1.4 Flutter risks of long-span bridges	15
1.5 Objectives and scope of research.....	17
1.6 References	21
CHAPTER 2 A SEMI-ANALYTICAL TYPHOON BOUNDARY LAYER WIND FIELD MODEL.....	25
2.1 Background	25
2.2 Height-resolving parametric pressure field	27
2.3 Height-resolving wind speed field	31
2.4 Typhoon boundary layer wind model	36
2.5 Model validation with observed typhoons	47

	Page
2.6	Conclusion 51
2.7	Reference 53
CHAPTER 3 TOWARD A REFINED ESTIMATION OF TYPHOON WIND: PARAMETRIC MODELLING AND UPSTREAM TERRAIN EFFECTS..... 57	
3.1	Background 57
3.2	Typhoon parametric modelling 60
3.3	Estimation of model parameters 64
3.4	Upstream terrain effects 84
3.5	Reconstruction of typhoon wind hazard 92
3.6	Conclusion 98
3.7	Reference 99
CHAPTER 4 OBSERVATION-BASED GUST CHARACTERISTICS OF NEAR- GROUND TYPHOON WINDS: A NON-GAUSSIAN PERSPECTIVE 104	
4.1	Background 104
4.2	Typhoon winds dataset 108
4.3	Gust characteristics 111
4.4	Peak factor estimation with PSD-based theory 118
4.5	Results comparison and discussion 126
4.6	Conclusion 135
4.7	Reference 136
CHAPTER 5 A GEOGRAPHICALLY WEIGHTED REGRESSION SUBREGION MODEL FOR TYPHOON WIND simulation 141	
5.1	Background 141
5.2	Statistical characteristics of typhoon tracks 145

	Page
5.3	GWR-based track forward model.....154
5.4	Wind hazard prediction171
5.5	Conclusion187
5.6	Reference187
CHAPTER 6 PROBABILISTIC FLUTTER ANALYSIS OF LONG-SPAN BRIDGES: A MONTE-CARLO SIMULATION FRAMEWORK.....193	
6.1	Background193
6.2	Models for flutter analysis.....198
6.3	Structural parameters.....205
6.4	Aerodynamic parameters212
6.5	Probabilistic solutions223
6.6	Conclusion236
6.7	Reference237
CHAPTER 7 FLUTTER FRAGILITY ANALYSIS OF LONG-SPAN BRIDGES SUBJECTED TO TYPHOON WINDS.....249	
7.1	Background249
7.2	Linear flutter model.....251
7.3	Structural and aerodynamic randomness.....255
7.4	Fragility curve of flutter instability.....264
7.5	Hazard curves of typhoon wind266
7.6	Flutter failure probability.....273
7.7	Conclusion279
7.8	Reference279

	Page
CHAPTER 8 CONCLUSIONS AND RECOMMENDATIONS.....	284
8.1 Conclusions and summary.....	284
8.2 Recommendations for future study.....	286
APPENDIX A. COEFFICIENTS OF TRACKING MODEL	288
APPENDIX B. PERFORMANCE ASSESSMENT OF THE TRACKING MODEL.....	293
APPENDIX C. COEFFICIENTS OF INTENSITY MODEL	296
APPENDIX D. COEFFICIENTS OF $R_{max,s}$ AND B_s MODEL.....	300
APPENDIX E. PERFORMANCE ASSESSMENT OF SUBREGION MODEL: TIME HISTORIES OF PARAMETERS.....	305
APPENDIX F. PERFORMANCE ASSESSMENT OF SUBREGION MODEL: PDFs OF PARAMETERS	315
APPENDIX G. CDFs OF GENESIS PARAMETERS OF NINE COASTAL CITIES	322
APPENDIX H. FLUTTER ANALYSIS MODELS	325
APPENDIX I. FLUTTER ANALYSIS OF A SIMPLY SUPPORTED BEAM WITH AN IDEAL PLATE FLATE SECTION	336
APPENDIX J. FLUTTER ANALYSIS OF JIANGYIN SUSPENSION BRIDGE WITH AN IDEAL FLAT PLATE SECTION GIRDER.....	341
APPENDIX K. WIND TUNNEL TEST OF A QUASI-FLAT PLATE MODEL.....	345
APPENDIX L. WIND TUNNEL TEST OF A PK SECTION MODEL.....	349
APPENDIX M. CORRELATION COEFFICIENT MATRIX OF FLUTTER DERIVATIVES.....	350
APPENDIX N. LITERATURE SURVEY RESULTS OF FLUTTER DERIVATIVES OF QUASI-FLAT PLATE SECTIONS	352
CURRICULUM VITAE	354

LIST OF TABLES

Table	Page
Table 1.1 Tropical cyclone classification of NHC and JMA	3
Table 1.2 Dvorak current intensity chart	3
Table 1.3 Coefficients of vertical wind profiles of major building codes/standards	8
Table 3.1 Land-cover-based classification for the surface roughness length	88
Table 4.1 Statistics of skewness and kurtosis of 10-m typhoon winds (Li et al. 2015).....	130
Table 5.1 Distribution models and coefficients for TC track genesis parameters	151
Table 5.2 Coefficients of PDFs for track genesis parameters	174
Table 5.3 Comparison of typhoon design wind speed at selected cities (MRI = 100 year; T = 10 min; z = 10 m, z ₀ = 0.05m, m/s)	177
Table 5.4 Classification of tropical cyclones by JMA.....	178
Table 6.1 Flutter critical wind speed of a simply supported beam with the section of ideal flat plate	205
Table 6.2 Probabilistic models for mass and stiffness parameters of the bridge structure	208
Table 6.3 Arrangement of uncertainty quantification for flutter derivatives.....	215
Table 6.4 Quasi-steady approximations for FDs.....	223
Table 6.5 Static coefficients for three sections.....	223
Table 6.6 Calculation cases for probabilistic solutions.....	224
Table 6.7 Statistics of probabilistic flutter solutions for the simply supported beam.....	228
Table 7.1 Design parameters of the sectional model.....	260
Table 7.2 Statistics of probabilistic flutter solutions.....	265
Table 7.3 Flutter failure probability (Fragility curves: SBSA solutions using σ_{exp} for FDs; Wind hazard curves: all winds no considerations of wind direction).....	275

Table	Page
Table 7.4 Flutter failure probability (Fragility curves: SBSA solutions using σ_{exp} for FDs; Wind hazard curves: only wind components that are perpendicular to the bridge orientation)	275
Table 7.5 Flutter failure probability (Fragility curves: SBSA solutions using $1.5\sigma_{exp}$ for FDs; Wind hazard curves: all winds no considerations of wind direction).....	276
Table 7.6 Flutter failure probability (Fragility curves: SBSA solutions using $1.5\sigma_{exp}$ for FDs; Wind hazard curves: only wind components that are perpendicular to the bridge orientation)	276
Table 7.7 Flutter failure probability (Fragility curves: multimode solutions using σ_{exp} for FDs; Wind hazard curves: all winds no considerations of wind direction)	276
Table 7.8 Flutter failure probability (Fragility curves: multimode solutions using σ_{exp} for FDs; Wind hazard curves: only wind components that are perpendicular to the bridge orientation)	277
Table 7.9 Flutter failure probability (Fragility curves: multimode solutions using $1.5\sigma_{exp}$ for FDs; Wind hazard curves: all winds no considerations of wind direction)	277
Table 7.10 Flutter failure probability (Fragility curves: multimode solutions using $1.5\sigma_{exp}$ for FDs; Wind hazard curves: only wind components that are perpendicular to the bridge orientation)	277
Table 7.11 Target reliability (Annual probability of failure, P_f) and associated reliability indices (β) for load conditions that do not include earthquake, tsunami, or extraordinary events (ASCE/SEI, 2016).....	278

LIST OF FIGURES

Figure	Page
Fig. 1.1 Total economic loss percentage for different windstorms	2
Fig. 1.2 Number of typhoons observed per year in the Western Pacific.....	7
Fig. 1.3 1700 tracks documented by JMA best track dataset (1951-2015)	7
Fig. 1.4 A sketch summary of mean vertical wind profile for a typical tropical cyclone (Giammanco et al., 2013).....	9
Fig. 1.5 Vertical wind profiles of observed mean typhoon boundary layer and specified by major building codes	9
Fig. 1.6 High-rise buildings located at coastal regions of China (Legend of wind profiles is same to Fig. 1.5)	10
Fig. 1.7 Observed winds of Typhoon Hagupit (0814) at the height of 60 m (Grey curve: 0.1 s winds; Black line: 10-min averaged winds).....	11
Fig. 1.8 Design wind speed map of China ($z = 10$ m, $T = 10$ min, $z_0 = 0.05$, $RP = 100$ years) (JTG/T D60-01-2004).....	12
Fig. 1.9 Probability plot of 1912-1948 annual largest speeds at Corpus Christi, Texas (Simiu E and Filliben J J, 1975; Simiu and Scanlan, 1996).....	13
Fig. 1.10 Aerodynamic flutter and collapse of Tacoma Narrows Bridge (1940).....	16
Fig. 1.11 Threats that strong typhoons pose to long-span bridges along coastal regions of China	17
Fig. 1.12 Demand versus capacity for risk assessment of structures.....	17
Fig. 2.1 Relative humidity and temperature profiles of hurricanes Cristobal, Erika, and Hermine corresponding to dropsondes data at three moments: (a) Relative humidity profile, (b) Temperature profile	30

Figure	Page
Fig. 2.2 Comparison of vertical pressure profiles (hollow points: observation, solid points: model): (a) Pressure profile, (b) Observed and modeled pressures	31
Fig. 2.3 Height-resolving parametric pressure difference ΔP profiles	31
Fig. 2.4 Vertical wind profiles with some constant K ($\Delta P_s = 80hPa, z_0 = 0.05 m$)	39
Fig. 2.5 Flowchart for typhoon wind field numerical solutions	40
Fig. 2.6 Vertical wind field (Eastern slice) of a synthetic typhoon ($\Delta P_s = 80hPa, B_s = 1.5, R_{max,s} = 50km, z_0 = 0.0002m, c = 5m/s, \theta_0 = 120^\circ$): (a) Radial decay wind speed u_d (m/s); (b) Tangential decay wind speed v_d (m/s); (c) Eddy viscosity K (m^2/s); (d) Velocity difference between gradient height and other heights $V_z - V_{GH}$ (m/s) ; (e) Wind direction α ($^\circ$); (f) Wind speed V_z (m/s). The black dash line is the gradient height.	44
Fig. 2.7 Horizontal wind field of a synthetic typhoon ($\Delta P_s = 80hPa, B_s = 1.5, R_{max,s} = 50km, z_0 = 0.0002m, c = 5m/s, \theta_0 = 120^\circ$): (a) Eddy viscosity K (m^2/s); (b) Radial decay wind speed u_d (m/s); (c) Tangential decay wind speed v_d (m/s); (e) Wind speed V_z (m/s). White arrows in wind speed contours indicate wind direction.	45
Fig. 2.8 Comparison of vertical profiles between the synthetic typhoon and observations.....	46
Fig. 2.9 Comparison of surface wind speed snapshots with MTCSWA : (a) Hagupit (JMA: $P_{cs} = 935 hPa, \theta_T = 76.26^\circ$ (CCW from N), $B_s = 1.72, R_{max,s} = 88 km$ (47.52 nmi), $V_{max} = 90 kt$; (b) Haiyan (JMA: $P_{cs} = 895 hPa, \theta_T = 78.83^\circ$ (CCW from N), $B_s = 1.60, R_{max,s} = 40 km$ (21.60 nmi), $V_{max} = 125 kt$) ; (c) Rammasun (JMA: $P_{cs} = 940 hPa, \theta_T = 48.85^\circ$ (CCW from N), $B_s = 1.28, R_{max,s} = 47 km$ (25.38 nmi), $V_{max} = 85 kt$)	48
Fig. 2.10 Vertical wind field (Eastern profiles, m/s): (a)Hagupit; (b)Haiyan;(c)Rammasun.....	49
Fig. 2.11 Vertical wind profiles: (a)Locations; (b)Near eyewall;(c) Outer vortex	51
Fig. 3.1 A selection of the JMA best track dataset.....	66

Figure	Page
Fig. 3.2 Storm locations from JMA with radii to 30 knots and 50 knots winds (Both R_{30} and R_{50} : 13347 points; Only R_{30} : 10168 points).....	67
Fig. 3.3 A sketch of parametric typhoon wind field.....	67
Fig. 3.4 Extraction of $R_{max,s}$ and B_s with JMA wind data: (a) Algorithm flowchart; (b) A diagrammatic sketch.....	69
Fig. 3.5 Results of $R_{max,s}$ and B_s extracted from JMA wind data	72
Fig. 3.6 Reproduced radial wind profiles of some extreme cases	73
Fig. 3.7 Reproduced radial wind profiles of four typhoons: (a) Yancy (199313); (b) Bilis (200010); (Numbers at each time step from top to bottom or left to right: P_{cs} , $R_{max,s}$ and B_s)	75
Fig. 3.7 (Cont.) Reproduced radial wind profiles of four typhoons: (c) Saomai (200608); (d) Rammasun (201409) (Numbers at each time step from top to bottom or left to right: P_{cs} , $R_{max,s}$ and B_s)	76
Fig. 3.8 Correlations among parameters (Black and red numbers in each panel are correlation coefficients for oversea and overland cases).....	78
Fig. 3.9 Correlations of $R_{max,s}$ and B_s with previous steps: (a) $\ln R_{max,s}(i)$ and $\ln R_{max,s}(i + 1)$; (b) $\ln R_{max,s}(i - 1)$ and $\ln R_{max,s}(i + 1)$; (c) $B_s(i)$ and $B_s(i + 1)$; (d) $B_s(i - 1)$ and $B_s(i + 1)$;	82
Fig. 3.10 Model errors of $R_{max,s}$ and B_s : (a) scatter plot $\varepsilon_{\ln R_{max,s}}$; (b) CDF $\varepsilon_{\ln R_{max,s}}$; (c) scatter plot ε_{B_s} ; (d) CDF ε_{B_s} ;	82
Fig. 3.11 Comparison of $\ln R_{max,s}$ between model and observations: (a)-(d) relations between $\ln R_{max,s}(i)$, $\ln R_{max,s}(i - 1)$, $\Delta P_s(i + 1)$ and $\ln R_{max,s}(i + 1)$ without errors; (e)-(h) relations between $\ln R_{max,s}(i)$, $\ln R_{max,s}(i - 1)$, $\Delta P_s(i + 1)$ and $\ln R_{max,s}(i + 1)$ with errors	83

Figure	Page
Fig. 3.12 Comparison of B_s between model and observations: (a)-(d) relations between $B_s(i), B_s(i+1), \Delta P_s(i+1)$ and $B_s(i+1)$ without errors; (e)-(h) relations between $B_s(i), B_s(i+1), \Delta P_s(i+1)$ and $B_s(i+1)$ with errors	83
Fig. 3.13 Grid points along the coastal region of China (EEZ: Exclusive economic zone)	86
Fig. 3.14 Determination of the equivalent roughness length at the site in question	88
Fig. 3.15 Directional equivalent roughness length: (a) Coastal region of China; (b) Hainan island	89
Fig. 3.16 Directional speed-up factor for Yangjiang meteorological station (111.9793°E, 21.8458°N)	91
Fig. 3.17 Directional topographic speed-up factor: a) Coastal region of China; b) Hainan island	91
Fig. 3.18 Wind field of strong typhoon Rammasun at 06:00 UTC, 07/18, 2014 (10 m): (a) Wind field with a uniform z_0 (m/s); (b) Directional z_0 (m); (c) Wind field with directional z_0 (m/s); (d) Elevation map (m); (e) Directional K_t ; (f) Wind field with directional z_0 and K_t (m/s);	93
Fig. 3.19 184 historical typhoon tracks from 1977 to 2015 reached 200 km off China coastline area	95
Fig. 3.20 Maximum wind speed footprints of typhoon events (m/s): (a) Rammasun (201409); (b) Wayne (198614); 1~3 are open water, directional roughness only and roughness and topography combined conditions, respectively.....	95
Fig. 3.21 Comparison of observed and modeled 10-min wind speed (m/s): a) Khanun (200515); b) Hagupit (201408);	96

Figure	Page
Fig. 4.1 Typhoon winds observation in Xihoumen Bridge: (a) Arrangement of bridge and anemometers, (b) Typhoon tracks (map images from Google Map, (TD: Tropical depression (10.8~17.1 m/s), TS: Tropical storm (17.2~24.4 m/s), STS: Strong Tropical storm (24.5~32.6 m/s), TY: Typhoon (32.7~41.4 m/s), STY: strong typhoon (41.5~50.9 m/s), Super TY: Super typhoon (≥ 51 m/s))	110
Fig. 4.2 Wind speed decomposition and probability density of fluctuating component: a) Stationary record; b) Weak non-stationary record; c) Strong non-stationary record; (u and u^* are the fluctuating components of wind speed for the stationary and non-stationary models)	114
Fig. 4.3 Skewness and kurtosis distributions of stationary fluctuating winds: a) skewness ($\tau=0.25s$), b) kurtosis ($\tau=0.25s$), c) skewness ($\tau=3s$), d) kurtosis ($\tau=3s$)	116
Fig. 4.4 Correlations among first four-order statistics and gust characteristics (The number in each figure is correlation coefficient ρ , red: strongly correlated ($\rho \geq 0.5$); dark blue: moderately correlated ($0.5 > \rho \geq 0.3$); green: weak correlated ($0.3 > \rho \geq 0.1$); light blue: uncorrelated ($\rho < 0.1$). $\tau = 3s$, $T = 600s$)	118
Fig. 4.5 Observed and fitted von Kármán PSD (From left to right: $\bar{U}^* \in 5, 10, 10, 15, 15, 20, [20, 25]$)	120
Fig. 4.6 Skewness vs kurtosis of records and monotonic limits of Hermite model	124
Fig. 4.7 Non-Gaussian effects on gust factor: a) $\gamma_3 = -0.4$; b) $\gamma_3 = 0$; c) $\gamma_3 = 0.4$; d) $\gamma_4 = 2$; e) $\gamma_4 = 3$; f) $\gamma_4 = 4$	125
Fig. 4.8 Non-Gaussian effects $g(3s, 600s)$ and $G_u(3s, 600s)$: a) $g(3s, 600s)$ vs γ_3 and γ_4 ; b) $G_u(3s, 600s)$ vs γ_3 and γ_4	126

Figure	Page
Fig. 4.9 Comparisons of peak factor : a) $\tau = 0.03s$; b) $\tau = 0.13s$; c) $\tau = 0.25s$; d) $\tau = 0.5s$; e) $\tau = 1s$; f) $\tau = 3s$; (ρ : correlation coefficient; $\varepsilon_{\text{mean}}$: mean value of relative errors; The dash line: $y = x$; same as below.)	127
Fig. 4.10 Comparisons of gust factor: a) $\tau = 0.03s$; b) $\tau = 0.13s$; c) $\tau = 0.25s$; d) $\tau = 0.5s$; e) $\tau = 1s$; f) $\tau = 3s$	127
Fig. 4.11 Simulation results for open exposure: (a) Skewness vs kurtosis; (b) Gust factor curve; (c) Probability distribution ($\tau = 0.25s$); (d) Probability distribution ($\tau = 3s$).....	131
Fig.4.12 Development of wind boundary layer from sea to land (subscript 1 and 2 denote values at heights z_1 and z_2 , respectively; subscript 0 stands for the over-sea profile; x_1 and x_2 represent upstream fetch).....	134
Fig. 5.1 Overview of circular sub-region method used in this study.....	145
Fig. 5.2 Track segments within a circular region centered on Hong Kong with a radius of 500 km	150
Fig. 5.3 CDF of annual storm rate (λ_a).....	150
Fig. 5.4 Radial wind speed profiles (a) Saomai(2006-08-09, 15:00UTC); (b) Parma (2009-10-01, 06:00UTC); (c) Rammasun(2014-07-18, 12:00UTC).....	151
Fig. 5.5 CDFs of genesis parameters: (a) α_0 ; (b) ΔP_0 ; (c) θ_{T0} ; (d) V_{T0} ; (e) $R_{\text{max},s0}$; (f) B_{s0}	152
Fig. 5.6 Simulated and observed genesis parameters (Red triangles: observations; Grey dots: simulations; Upper numbers: ρ_{sim} ; Lower numbers in parenthesis: ρ_{obs}).....	154
Fig. 5.7 Exponential kernel with various bandwidths.....	156
Fig. 5.8 GWR with adaptive exponential kernels.....	157
Fig. 5.9 Optimal bandwidths for heading direction model: (a) Easterly headed storms; (b) Westerly headed storms.....	158

Figure	Page
Fig. 5.10 Contour plots of coefficients of heading direction model for easterly headed storms: (a) h_1 ; (b) h_2 ; (c) h_3 ; (d) h_4	160
Fig. 5.11 Contour plots of errors of heading direction model for easterly headed storms: (a) Error mean; (b) Error standard deviation	160
Fig. 5.12 Tracking model error for the grid point of (116°E, 20°N): (a) $\varepsilon_{\Delta\theta_T}$ for easterly headed storms; (b) $\varepsilon_{\Delta\theta_T}$ for westerly headed storms; (c) $\varepsilon_{\Delta\ln V_T}$ for easterly headed storms; (d) $\varepsilon_{\Delta\ln V_T}$ for westerly headed storms; (k is the K-S test values)	161
Fig. 5.13 Typhoon Khanun: 2-day simulation from 2005-09-10 09:00 UTC.....	162
Fig. 5.14 Decay model in circular sub-region around Hong Kong:(a) Curve fitting of decay model; (b) Decay rate versus ΔP_0	165
Fig. 5.15 Typhoon Gerald: simulation from 1984-08-16 00:00 UTC: (a) 2-Day track simulation; (b) Central pressure P_{CS} ; (c) Radius to maximum winds $R_{max,s}$; (d) Pressure shape parameter B_s	168
Fig. 5.16 Comparison between real and simulated storms in Hong Kong: (a) Real tracks from 2006 to 2015; (b) Simulated 10-year storms 1; (c) Real tracks from 1991 to 2000; (d) Simulated 10-year storms 2	169
Fig. 5.17 Comparison of PDF for real and simulated parameters within the domain of Hong Kong (1,0000-year simulations): (a) Central pressure deficit ΔP_s ; (b) Heading direction θ_T ; (c) Forward speed V_T ; (d) Radius to maximum winds $R_{max,s}$; (e) Pressure shape parameter B_s	169
Fig. 5.18 Typhoon wind hazard curves in Hong Kong: (a) Mean wind speed versus return period; (b) Annual probability of exceedance for mean wind speed	173
Fig. 5.18 Locations 10 selected coastal cities in China.....	174

Figure	Page
Fig. 5.19 Strong typhoon tracks affect Ningbo, Wenzhou, Hong Kong and Zhanjiang: (a) Violent typhoons; (b) Strong typhoons.....	178
Fig. 5.20 Annual storm rates of 10 coastal cities (R = 500 km)	178
Fig. 5.21 Predicted and code-suggested typhoon design wind speed versus return period of nine coastal cities in China.....	180
Fig. 5.22 Design wind speed map (MRI = 100 year; T = 10 min; z = 10 m, z ₀ = 0.01m, m/s): (a) CSM; (b) FTM.....	183
Fig. 5.23 Design wind speed map (MRI = 100 year; T = 10 min; z = 10 m, z ₀ = 0.05m, m/s): (a) CSM; (b) FTM.....	184
Fig. 5.24 Design wind speed map (MRI = 50 year; T = 10 min; z = 10 m, z ₀ = 0.01m, m/s): (a) CSM; (b) FTM.....	185
Fig. 5.25 Design wind speed map (MRI = 50 year; T = 10 min; z = 10 m, z ₀ = 0.05m, m/s): (a) CSM; (b) FTM.....	186
Fig. 6.1 Potential uncertainties of flutter analysis for long-span bridges.....	197
Fig. 6.2 Flutter derivatives of the ideal flat plate.....	204
Fig. 6.3 Simulated frequencies of a simply supported beam (10,000 runs) : (a) First 10 modes; (b) 2nd mode (1st symmetric torsional mode).....	209
Fig. 6.4 Simulated frequencies of Jiangyin Suspension Bridge (10,000 runs): (a) First 20 modes; (b) 14th mode (1st symmetric torsional mode)	209
Fig. 6.5 CDF of damping ratios for cable-supported bridges: (a) Vertical bending mode; (b) Torsional mode. (k is the statistic of K-S test)	212
Fig. 6.6 Quasi-flat plate section models (unit: mm)	215
Fig. 6.7 A Pasco-Kennewick (P-K) section model (unit: mm).....	215
Fig. 6.8 A closed-box section model (Jiangyin bridge, unit: m, Gu et al. (2000))	215

Figure	Page
Fig. 6.9 Flutter derivatives of a quasi-flat section model	217
Fig. 6.10 Flutter derivatives of the P-K section model	220
Fig. 6.11 Flutter derivatives of the closed-box section model adopted by the Jiangyin Bridge	221
Fig. 6.12 Comparisons of simulated and experimental FDs (quasi-flat plate section model, 10% turbulence intensity)	222
Fig. 6.13 Effects of MC simulation runs on the probabilistic solution of critical wind speed: (a) CoV for SBSA method; (b) γ_3 and γ_4 for SBSA method; (c) CoV for multimode method; (d) γ_3 and γ_4 for multimode method	225
Fig. 6.14 Empirical PDFs and CDFs of probabilistic flutter solutions for the simply supported beam: (a)~(e) Cases #2~#6.....	229
Fig. 6.14 (cont.) Empirical PDFs and CDFs of probabilistic flutter solutions for the simply supported beam: (f)~(j) Case #7~#11.....	230
Fig. 6.14 (cont.) Empirical PDFs and CDFs of probabilistic flutter solutions for the simply supported beam: (k)~(n) Case #12~#15	231
Table 6.8 Statistics of probabilistic flutter solutions for the Jiangyin Suspension Bridge.....	232
Fig. 6.15 Empirical PDFs and CDFs of probabilistic flutter solutions for the Jiangyin Suspension Bridge: (a)~(e) Cases #2~#6	233
Fig. 6.15 (cont.) Empirical PDFs and CDFs of probabilistic flutter solutions for the Jiangyin Suspension Bridge: (f)~(j) Case #7~#11	234
Fig. 6.15 (cont.) Empirical PDFs and CDFs of probabilistic flutter solutions for the Jiangyin Suspension Bridge: (k)~(n) Case #12~#15.....	235
Fig. 7.1 Threats of strong typhoons on long-span bridges along coastal regions of China	250
Fig. 7.2 Layout of the Lingdingyang suspension bridge	251
Fig. 7.3 The finite element model of the Lingdingyang Suspension Bridge	256

Figure	Page
Fig. 7.4 Simulated frequencies of Lingdingyang Suspension Bridge (10,000 runs): (a) First 20 modes; (b) 14th mode (1st symmetric torsional mode).....	257
Fig. 7.5 CDF of damping ratios for cable-supported bridges: (a) Vertical bending mode; (b) Torsional mode. (k is the statistic of K-S test)	258
Fig. 7.6 Cross-section of the sectional model (Unit: mm).....	260
Fig. 7.7 Wind tunnel test: (a) The TJ-1 open-jet wind tunnel; (b) Sectional model.....	260
Fig. 7.8 Flutter derivatives from 30-time repeated tests.....	261
Fig. 7.9 Correlation coefficients between flutter derivatives.....	263
Fig. 7.10 Comparisons of simulated and experimental FDs (1000 runs).....	264
Fig. 7.11 Empirically probabilistic distribution of flutter critical wind speed: (a) σ_{exp} of FDs; (b) $1.5\sigma_{exp}$ of FDs;.....	266
Fig. 7.12 Comparison between real and simulated 15-year storms around the bridge site: (a) Real observation from 2001 to 2015; (b) 15-year simulations.....	267
Fig. 7.13 Comparison of empirical PDFs for real and simulated parameters within the circular subregion centered in bridge site (10,000-year simulations): (a) Central pressure deficit ΔP_s ; (b) Heading direction θ_T ; (c) Forward speed V_T ; (d) Radius to maximum winds $R_{max,s}$; (e) Pressure shape parameter B_s	267
Fig. 7.14 Predicted typhoon design wind speed versus return period of the bridge site at height of bridge deck ($z = 91.5$ m, CSM: circular subregion model, FTM: full track model)...	268
Fig. 7.15 Probability of exceedance at any given T years of maximum typhoon winds ($z = 91.5$ m): (a) $z_0 = 0.01$ m; (b) $z_0 = 0.0002$ m.....	270
Fig. 7.16 Wind rose of maximum wind for 100,000-year simulated storms ($z = 91.5$ m, $z_0 = 0.0002$ m).....	271

Figure	Page
Fig. 7.17 Probability of exceedance at any given T years of maximum typhoon winds that are perpendicular to the bridge deck ($z = 91.5$ m): (a) $z_0 = 0.01$ m; (b) $z_0 = 0.0002$ m...	272
Fig. 7.18 Empirical probability density functions of gust factor (10,000 simulations, $z = 91.5$ m): (a) Gust duration $\tau = 3$ s; (b) Gust duration $\tau = 1$ min.....	273
Fig. A1 The optimal bandwidths for tracking model: (a) V_T for easterly headed storms; (b) V_T for westerly headed storms; (c) θ_T for easterly headed storms; (d) θ_T for westerly headed storms.....	288
Fig. A2 Contour plots of coefficients for forward speed model: (a)~(d) $v_1 \sim v_4$; left column corresponds to easterly headed storms, right column corresponds to westerly headed storms.....	289
Fig. A3 Contour plots of error term for forward speed model: (a) error mean; (b) error standard deviation; the left column corresponds to easterly headed storms, right column corresponds to westerly headed storms.....	290
Fig. A4 Contour plots of coefficients for heading direction model: (a)~(d) $h_1 \sim h_4$; left column corresponds to easterly headed storms, right column corresponds to westerly headed storms.....	291
Fig. A5 Contour plots of error term for heading direction model: (a) error mean; (b) error standard deviation; the left column corresponds to easterly headed storms, right column corresponds to westerly headed storms.....	292
Fig. B1 Typhoon Matsa: 2-day simulation from 2005-08-04 15:00 UTC.....	293
Fig. B2 Typhoon Hagupit: 2-day simulation from 2008-09-23 00:00 UTC.....	293
Fig. B3 Typhoon Rammasun: 2-day simulation from 2014-07-17 00:00 UTC.....	293
Fig. B4 Typhoon Tembin: 2-day simulation from 2012-08-23 06:00 UTC.....	294
Fig. B5 Typhoon Soudelor: 2-day simulation from 2015-08-07 15:00 UTC.....	294

Figure	Page
Fig. B6 Typhoon Goni: 2-day simulation from 2015-08-21 00:00 UTC.....	294
Fig. B7 Typhoon Wayne: 2-day simulation from 1986-08-22 12:00 UTC.....	295
Fig. B8 Typhoon Wayne: 2-day simulation from 1986-08-30 12:00 UTC.....	295
Fig. C1 The optimal bandwidths for intensity model: (a) Easterly headed storms; (b) Westerly headed storms;	296
Fig. C2 Contour plots of coefficients for relative intensity model: (a)~(d) $a_1 \sim a_4$; left column corresponds to easterly headed storms, right column corresponds to westerly headed storms	297
Fig. C2 (cont.) Contour plots of coefficients for relative intensity model: (e)~(f) $a_5 \sim a_6$; left column corresponds to easterly headed storms, right column corresponds to westerly headed storms.....	298
Fig. C3 Contour plots of error term for relative intensity model: (a) error mean; (b) error standard deviation; left column corresponds to easterly headed storms, right column corresponds to westerly headed storms	299
Fig. D1 The optimal bandwidths for $R_{max,s}$ and B_s models: (a) $R_{max,s}$ for easterly headed storms; (b) $R_{max,s}$ for westerly headed storms; (c) B_s for easterly headed storms; (d) B_s for westerly headed storms.....	300
Fig. D2 Contour plots of coefficients for $R_{max,s}$ model: (a)~(d) $r_1 \sim r_4$; left column corresponds to easterly headed storms, right column corresponds to westerly headed storms.....	301
Fig. D3 Contour plots of error term for $R_{max,s}$ model: (a) error mean; (b) error standard deviation; left column corresponds to easterly headed storms, right column corresponds to westerly headed storms	302
Fig. D4 Contour plots of coefficients for B_s model: (a)~(d) $b_1 \sim b_4$; left column corresponds to easterly headed storms, right column corresponds to westerly headed storms.....	303

Figure	Page
Fig. D5 Contour plots of error term for B_s model: (a) error mean; (b) error standard deviation; left column corresponds to easterly headed storms, right column corresponds to westerly headed storms.....	304
Fig. E1 Typhoon Utor: simulation from 2013-08-12 18:00 UTC: (a) 2-Day track simulation; (b) central pressure; (c) $R_{max,s}$; (d) B_s	305
Fig. E2 Typhoon Megi: simulation from 2010-10-20 18:00 UTC: (a) 2-Day track simulation; (b) central pressure; (c) $R_{max,s}$; (d) B_s	306
Fig. E3 Typhoon Vicente: simulation from 2012-07-21 06:00 UTC: (a) 2-Day track simulation; (b) central pressure; (c) $R_{max,s}$; (d) B_s	307
Fig. E4 Typhoon York: simulation from 1999-09-13 12:00 UTC: (a) 2-Day track simulation; (b) central pressure; (c) $R_{max,s}$; (d) B_s	308
Fig. E5 Typhoon Linfa: simulation from 2009-06-19 06:00 UTC: (a) 2-Day track simulation; (b) central pressure; (c) $R_{max,s}$; (d) B_s	309
Fig. E6 Typhoon Haikui: simulation from 2012-08-07 00:00 UTC: (a) 2-Day track simulation; (b) central pressure; (c) $R_{max,s}$; (d) B_s	310
Fig. E7 Typhoon Matsa: simulation from 2005-08-05 06:00 UTC: (a) 2-Day track simulation; (b) central pressure; (c) $R_{max,s}$; (d) B_s	311
Fig. E8 Typhoon Jelawat: simulation from 2000-08-09 00:00 UTC: (a) 2-Day track simulation; (b) central pressure; (c) $R_{max,s}$; (d) B_s	312
Fig. E9 Typhoon Doug: simulation from 1994-08-08 06:00 UTC: (a) 2-Day track simulation; (b) central pressure; (c) $R_{max,s}$; (d) B_s	313
Fig. E10 Typhoon Mamie: simulation from 1985-08-16 18:00 UTC: (a) 2-Day track simulation; (b) central pressure; (c) $R_{max,s}$; (d) B_s	314

Figure	Page
Fig. F1 Comparison between real and simulated storms around Shanghai (121.483°E, 31.233°N): (a) Real tracks from 2006 to 2015; (b) Simulated 10-year storms 1; (c) Real tracks from 1991 to 2000; (d) Simulated 10-year storms 2.....	315
Fig. F2 Comparison of PDF for real and simulated parameters within the circular subregion centered in Shanghai (10,000-year simulations): (a) Central pressure deficit ΔP_s ; (b) Heading direction θ_T ; (c) Forward speed V_T ; (d) Radius to maximum winds $R_{max,s}$; (e) Pressure shape parameter B_s	315
Fig. F3 Comparison between real and simulated storms around Ningbo (121.517°E, 29.867°N): (a) Real tracks from 2006 to 2015; (b) Simulated 10-year storms 1; (c) Real tracks from 1991 to 2000; (d) Simulated 10-year storms 2.....	316
Fig. F4 Comparison of PDF for real and simulated parameters within the circular subregion centered in Ningbo (10,000-year simulations): (a) Central pressure deficit ΔP_s ; (b) Heading direction θ_T ; (c) Forward speed V_T ; (d) Radius to maximum winds $R_{max,s}$; (e) Pressure shape parameter B_s	316
Fig. F5 Comparison between real and simulated storms around Taipei (121.593°E, 25.041°N): (a) Real tracks from 2006 to 2015; (b) Simulated 10-year storms 1; (c) Real tracks from 1991 to 2000; (d) Simulated 10-year storms 2.....	317
Fig. F6 Comparison of PDF for real and simulated parameters within the circular subregion centered in Taipei (10,000-year simulations): (a) Central pressure deficit ΔP_s ; (b) Heading direction θ_T ; (c) Forward speed V_T ; (d) Radius to maximum winds $R_{max,s}$; (e) Pressure shape parameter B_s	317
Fig. F7 Comparison between real and simulated storms around Wenzhou (120.650°E, 28.017°N): (a) Real tracks from 2006 to 2015; (b) Simulated 10-year storms 1; (c) Real tracks from 1991 to 2000; (d) Simulated 10-year storms 2.....	318

Figure	Page
Fig. F8 Comparison of PDF for real and simulated parameters within the circular subregion centered in Wenzhou (10,000-year simulations): (a) Central pressure deficit ΔP_s ; (b) Heading direction θ_T ; (c) Forward speed V_T ; (d) Radius to maximum winds $R_{max,s}$; (e) Pressure shape parameter B_s	318
Fig. F9 Comparison between real and simulated storms around Fuzhou (119.300°E, 26.083°N): (a) Real tracks from 2006 to 2015; (b) Simulated 10-year storms 1; (c) Real tracks from 1991 to 2000; (d) Simulated 10-year storms 2.....	319
Fig. F10 Comparison of PDF for real and simulated parameters within the circular subregion centered in Fuzhou (10,000-year simulations): (a) Central pressure deficit ΔP_s ; (b) Heading direction θ_T ; (c) Forward speed V_T ; (d) Radius to maximum winds $R_{max,s}$; (e) Pressure shape parameter B_s	319
Fig. F11 Comparison between real and simulated storms around Xiamen (118.100°E, 24.483°N): (a) Real tracks from 2006 to 2015; (b) Simulated 10-year storms 1; (c) Real tracks from 1991 to 2000; (d) Simulated 10-year storms 2.....	320
Fig. F12 Comparison of PDF for real and simulated parameters within the circular subregion centered in Xiamen (10,000-year simulations): (a) Central pressure deficit ΔP_s ; (b) Heading direction θ_T ; (c) Forward speed V_T ; (d) Radius to maximum winds $R_{max,s}$; (e) Pressure shape parameter B_s	320
Fig. F13 Comparison between real and simulated storms around Haikou (110.333°E, 20.367°N): (a) Real tracks from 2006 to 2015; (b) Simulated 10-year storms 1; (c) Real tracks from 1991 to 2000; (d) Simulated 10-year storms 2.....	321

Fig. F14	Comparison of PDF for real and simulated parameters within the circular subregion centered in Haikou (10,000-year simulations): (a) Central pressure deficit ΔP_s ; (b) Heading direction θ_T ; (c) Forward speed V_T ; (d) Radius to maximum winds $R_{max,s}$; (e) Pressure shape parameter B_s	321
Fig. G1	CDFs of genesis parameters for Shanghai: (a) α_0 ; (b) ΔP_0 ; (c) θ_{T0} ; (d) V_{T0} ; (e) $R_{max,s0}$; (f) B_{s0}	322
Fig. G2	CDFs of genesis parameters for Ningbo: (a) α_0 ; (b) ΔP_0 ; (c) θ_{T0} ; (d) V_{T0} ; (e) $R_{max,s0}$; (f) B_{s0}	322
Fig. G3	CDFs of genesis parameters for Wenzhou: (a) α_0 ; (b) ΔP_0 ; (c) θ_{T0} ; (d) V_{T0} ; (e) $R_{max,s0}$; (f) B_{s0}	322
Fig. G4	CDFs of genesis parameters for Fuzhou: (a) α_0 ; (b) ΔP_0 ; (c) θ_{T0} ; (d) V_{T0} ; (e) $R_{max,s0}$; (f) B_{s0}	323
Fig. G5	CDFs of genesis parameters for Xiamen: (a) α_0 ; (b) ΔP_0 ; (c) θ_{T0} ; (d) V_{T0} ; (e) $R_{max,s0}$; (f) B_{s0}	323
Fig. G6	CDFs of genesis parameters for Guangzhou: (a) α_0 ; (b) ΔP_0 ; (c) θ_{T0} ; (d) V_{T0} ; (e) $R_{max,s0}$; (f) B_{s0}	323
Fig. G7	CDFs of genesis parameters for Shenzhen: (a) α_0 ; (b) ΔP_0 ; (c) θ_{T0} ; (d) V_{T0} ; (e) $R_{max,s0}$; (f) B_{s0}	324
Fig. G8	CDFs of genesis parameters for Zhanjiang: (a) α_0 ; (b) ΔP_0 ; (c) θ_{T0} ; (d) V_{T0} ; (e) $R_{max,s0}$; (f) B_{s0}	324
Fig. G9	CDFs of genesis parameters for Haikou: (a) α_0 ; (b) ΔP_0 ; (c) θ_{T0} ; (d) V_{T0} ; (e) $R_{max,s0}$; (f) B_{s0}	324
Fig. H1	The flowchart of multimode flutter analysis.....	335
Fig. I1	FEM model of a simply supported beam.....	336

Figure	Page
Fig. I2 Frequencies and mode shapes of the first ten modes	336
Fig. I3 Flutter solution using CEVA.....	337
Fig. I4 Flutter solution using SBSA	337
Fig. I5 Flutter solution using Roger-function-based state space method: (a) Frequency vs. wind speed; (b) Damping ratio vs. wind speed.....	338
Fig. I6 Flutter solution using multi-mode method: (a) Real part vs. imaginary part of eigen values; (b) Frequency vs. wind speed; (c) Damping ratio vs. wind speed	339
Fig. I7 Flutter motion in terms of the structural modal participation ($U = 139.7$ m/s)	340
Fig. J1 Jiangyin suspension bridge	341
Fig. J2 ANSYS FEM model of Jiangyin suspension bridge	341
Fig. J3 Mode shapes of first two fundamental modes: (a) Symmetric lateral bending; (b) Antisymmetric vertical bending; (c) Antisymmetric lateral bending; (d) Symmetric vertical bending; (e) Antisymmetric torsion; (f) Symmetric torsion;	342
Fig. J4 Flutter solution using SBSA	343
Fig. J5 Flutter solution using the multi-mode method: (a) Real part vs. imaginary part of eigenvalues; (b) Frequency vs. wind speed; (c) Damping ratio vs. wind speed	343
Fig. J6 Flutter motion in terms of the structural modal participation ($U = 70.9$ m/s).....	344
Fig. K1 Wind tunnel test of a quasi-flat plate: (a) Sectional model and Cobra probe; (b) Grid I ($I_u = 5\%$); (c) Grid II ($I_u = 10\%$); (d) Grid III ($I_u = 14\%$).....	345
Fig. K2 Mean and standard deviations for flutter derivatives of the quasi-flat section model	346
Fig. K3 Standard deviations for flutter derivatives of the quasi-flat section model.....	347
Fig. K4 Surface plots of the coefficient of variation of flutter derivatives for the quasi-flat section model	348
Fig. L1 Wind tunnel setup of a PK section model.....	349

Figure	Page
Fig. L2 Standard deviations of flutter derivatives of the P-K section model	349
Fig. N1 Flutter derivatives of quasi-flat plates	352
Fig. N2 Comparison of standard deviations of flutter derivatives for quasi-flat plates between the literature survey and present study	353

CHAPTER 1 INTRODUCTION

Wind, which is caused by the difference of atmospheric pressure on the surface of Earth, plays a significant role during human civilization process. In particular, the wind near the planetary boundary layer, which is always featured with fluctuation or turbulence due to the friction effects by obstruction of ground objects, is closely related to human life and productive activities. Accordingly, its potential applications as a power source, impact on structures as well as the effects on inhabitation environment and air pollution have received intensive attention over several centuries, which drive the development of wind engineering as a separate discipline. In civil engineering, the prime objective is to quantitatively describe the wind effects on structures or wind loads and minimize the damages and losses, especially for these strong and extreme winds, such as tornado, typhoon (hurricane) or heavy storm (Simiu and Scanlan, 1996). Moreover, with rapid advancements in construction materials and techniques in recent years, there has been an upward trend in the long-span bridges (Xiang and Ge, 2007) and high-rise buildings (Tanaka et al., 2012) being proposed, which are usually wind-sensitive as they are more flexible and their aerodynamic performance will dominate the design process.

1.1 Typhoon-related hazards

Typhoon (same to tropical cyclone here), which is a strong rotating storm system (typically between 100 and 2,000 km in diameter) as a result of the conservation of angular momentum imparted by the Earth's rotation, is always characterized with a low-pressure center, strong winds, and heavy rain. Meanwhile, it usually drives some secondary disasters,

including storm surge, inland flooding, currents, wind-borne debris, and even tornadoes. As a result, the typhoon-related hazard is one of severest natural disaster that causes significant casualties and huge financial losses every year. In the past two centuries, it was reported that typhoon has been responsible for the deaths of about 1.9 million people around the whole world. It was estimated that 10, 000 people perish on average due to typhoons per year (Adler, 2005). For example, the deadliest strong typhoon on record, Haiyan (2013) killed at least 6,300 people in the Philippines and caused more than US\$10.8 billion damages. The strong typhoon Meranti (2016) impacted the Philippines and China, caused US\$4.8 billion in damage and killed 47 people. Another extremely destructive typhoon in the Atlantic Ocean, known as Katrina (2005) resulted in 1,836 deaths and US\$ 125 billion property damage. According to the statistics of Emergency Events Database (EM-DAT) maintained by the Centre for Research on the Epidemiology of Disaster (CRED) (2016), the typhoon is the most destructive wind climate, as shown in Fig. 1.1. Western Pacific Basin is vulnerable to typhoon genesis throughout the whole year, which is the most active typhoon basin globally with 30 typhoons on average every year, accounting for nearly one-third of annual tropical cyclones

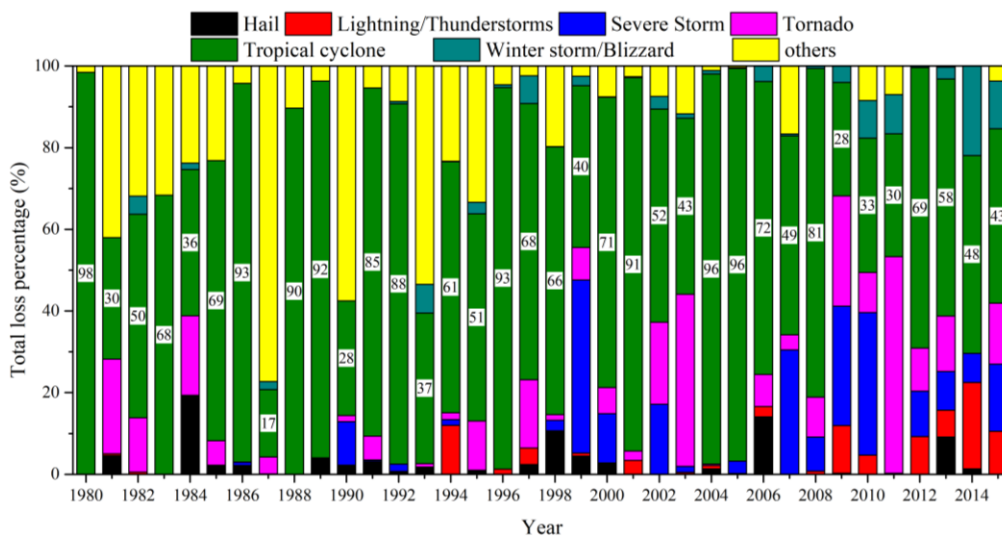


Fig. 1.1 Total economic loss percentage for different windstorms

Table 1.1 Tropical cyclone classification of NHC and JMA

Beaufort scale	1-min MSW (NHC) knots (km/h)	10-min MSW (JMA) knots (km/h)	NHC	JMA
0-7	<34 (63)	<30 (56)	TD	TD
8	34-37(63-69)	30-33 (56-61)	TS	TS
9-10	38-54 (70-100)	34-47 (63-87)		TS
11	55-63 (102-117)	48-55 (89-102)	Category I	STS
	64-71 (119-131)	56-63 (104-117)		STS
12+	72-82 (133-152)	64-72 (119-133)	Category II	TY(118-156 km/h)
	83-95 (154-176)	73-83 (135-154)	Category III	TY(118-156 km/h)
	96-112 (178-207)	84-98 (156-181)	Category III	STY(157-193 km/h)
	113-122 (209-226)	99-107 (183-198)	Category IV	STY(157-193 km/h)
	123-136 (228-252)	108-119 (200-220)	Category IV	STY(157-193 km/h)
	>137 (>254)	>120 (>220)	Category V	VTY(>193 km/h)

Note: TD: Tropical Depression; TS: Tropical Storm; STS: Severe Tropical Storm; TY: Typhoon; STY: Strong typhoon; VTY: Violent typhoon

Table 1.2 Dvorak current intensity chart

CI number	MSW (knots)	MSW (MPH)	MSW (km/h)	MSLP (NHC) (mb)	MSLP (JMA) (mb)	Scale (NHC/JMA)
1	25	29	46			TD
1.5	25	29	46			TD
2	30	35	55	1009	1000	TD
2.5	35	40	65	1005	997	TS
3	45	52	83	1000	991	TS
3.5	55	63	102	994	984	STS
4	65	75	120	987	976	I (TY)
4.5	77	89	143	979	966	I - II (TY)
5	90	104	167	970	954	II -III(STY)
5.5	102	117	189	960	941	III(STY)
6	115	132	213	948	927	IV (VTY)
6.5	127	146	235	935	914	IV (VTY)
7	140	161	259	921	898	V (VTY)
7.5	155	178	287	906	879	V (VTY)
8	170	196	315	890	858	V (VTY)

around the world (Knapp et al., 2010). Moreover, along with a high storm frequency, this basin also features the most globally intense storms on record with 5 violent typhoons (10 min maximum sustained winds at surface level is larger than 105 knots or 54 m/s) on average every year, causing severe property damages to China, Philippines, Vietnam, and Japan. China's coastline covers approximately 14,500 km, which is a typhoon-prone region with 6~8 landfall typhoons on average. A half of the population (about 700 million) in China is concentrated in this region, where is feature with well-developed economic zones as well as many wind-sensitive structures, including more than 10 skyscrapers higher than 400 m and 9 long-span bridges with main span longer than 1,000m (6 suspension bridges: Xihoumen-1650 m, East Humen 2nd-1688 m, West Humen 2nd-1200 m, Lingding-1666 m, Shuangyumen-1708 m and Tsing Ma-1377 m; 3 cable-stayed bridges: Sutong-1088 m, Stonecutters-1018 m, Hutong-1092 m). Accordingly, it is essentially important to perform typhoon hazard assessment in coastal regions of China for risk prediction and engineering applications.

Generally, the tropical cyclone is ranked into several intensity scales according to their maximum sustained winds (MSW) near the surface and which basins they are located in. A summary of the classification of tropical cyclones adopted by National Hurricane Center (NHC) and Japan Meteorological Agency (JMA) is listed in Table 1.1. Tropical cyclones that occur in Atlantic, Eastern, and Central Pacific, are officially monitored by NHC. It classifies tropical cyclone scales based on 1-min averaged MSW while 10 min is used by JMA, which is responsible to monitor and documented the tropical cyclone tracks in Western Pacific. Since the difference of time-duration, the minimum sea-level pressure (MSLP) estimated from the Dvorak current intensity (CI) number (Dvorak, 1975), which is determined by the patterns

of cloud images observed by satellite, would be different as well. The CI number and corresponding MSW together with MSLP employed by NHC and JMA are shown in Table 1.2.

1.2 Typhoon wind observations

Field observation of typhoons is great of use for not only compiling the track dataset archive but also for better understanding the inner structure of typhoon vortex and numerically modeling the wind field for engineering applications and risk assessments. In the past several decades, except for the land-based observations by meteorological stations, advances in technology have included using upper-level aircraft to traverse through the typhoon, satellites to monitor the atmospheric circulation from outer space, radars to remotely detect typhoon's progress near the coastline, and recently the introduction of unmanned drones to penetrate storms.

Track dataset, which usually consists of storm names, date and time, storm eye location in terms of latitude and longitude, minimum central pressure, heading direction and speed is the fundamental information for typhoon activity study as well as typhoon-related hazard assessments. As compiled by IBTrACS (International Best Track Archive for Climate Stewardship) project ([Knapp et al., 2010](#)), there are four major agencies issue typhoon best track datasets for Western Pacific basin, including the World Meteorological Organization (WMO) Regional Specified Meteorological Center (RSMC) in Tokyo or JMA, China Meteorological Administration's Shanghai Typhoon Institute (CMA/STI), U.S. Department of Defense Joint Typhoon Warning Center (JTWC) and the Hong Kong Observatory (HKO). Fig. 1.2 illustrates the number of typhoons observed in Western Pacific documented in IBTrACS ($0^{\circ}\text{N}\sim 90^{\circ}\text{N}$, $100^{\circ}\text{E}\sim 180^{\circ}\text{E}$) maintained by National Ocean and Atmospheric Administration (NOAA) and JMA best track data ($0^{\circ}\text{N}\sim 60^{\circ}\text{N}$, $100^{\circ}\text{E}\sim 180^{\circ}\text{E}$). IBTrACS.v03r10 dataset was

achieved by working directly with all the Regional Specialized Meteorological Centers and other international centers and individuals to create a global best track dataset, merging storm information from multiple centers into one product and archiving the data for public use. The former dataset is higher than the later one, which is possible because that the IBTrACS.v03r10 merges storm information from multiple centers, the agency-specified diagnosis strategy for tropical cyclone varies from one agency to another due to the differences in wind averaging time, Dvorak parameters, etc. Taking the year of 1971 as an example, except for the typhoons observed and named by the JMA (JMA also contains several unnamed typhoons), there are some tropical disturbances recorded by CMA, JTWC and National Climatic Data Center (NCDC) are also archived. Moreover, when two storms merge into one circulation, the path in IBTrACS of a single storm ends at the merge point while the other track continues until the storm dissipates. Generally, the typhoon numbers in these two datasets are approaching to be the same in recent years. Moreover, JMA also provides the additional data of maximum sustained wind speed, the longest and shortest radii of 50 knots and 30 knots winds with the time duration of 10 min, and the corresponding directions determined mainly by surface observation, ASCAT (the Advanced Scatterometer) observation and low-level cloud motion winds derived from satellite images (JMA). Accordingly, the best track information provided by JMA will be adopted in this study. More details are shown in Fig. 1.3, 1700 typhoons in total are observed in Western Pacific from 1951-2015.

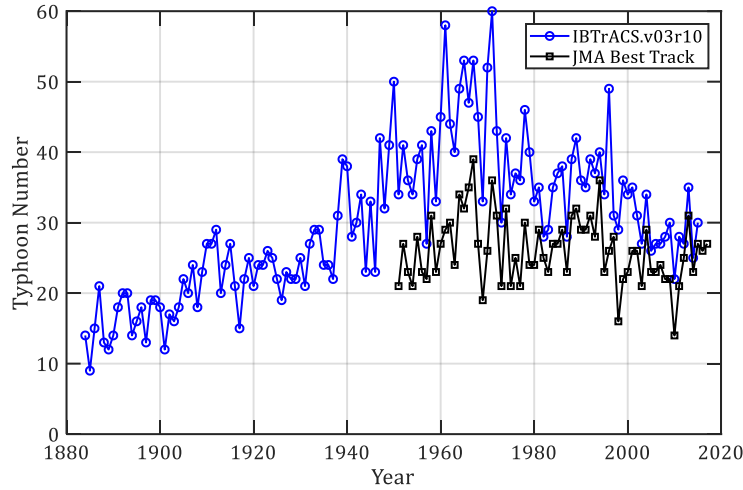


Fig. 1.2 Number of typhoons observed per year in the Western Pacific

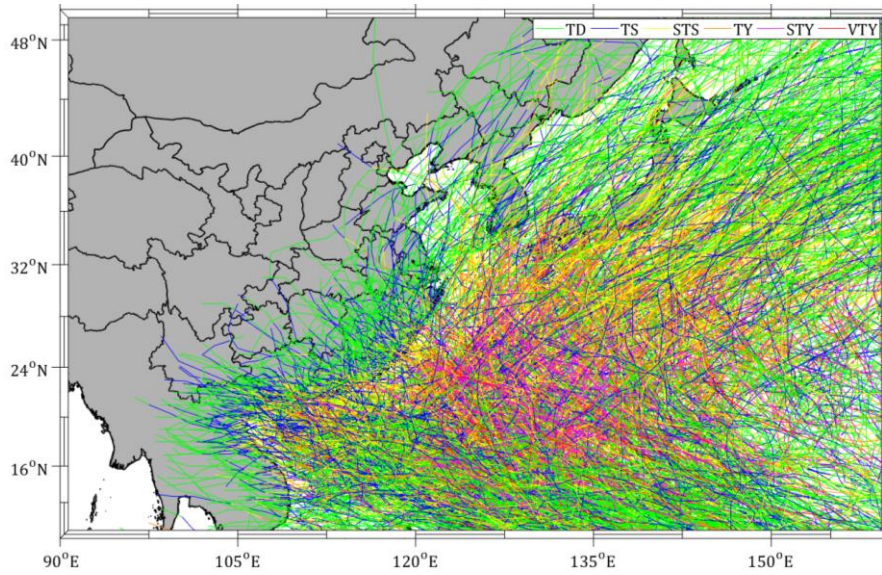


Fig. 1.3 1700 tracks documented by JMA best track dataset (1951-2015)

In addition to the basic information of tracks, observation of typhoon inner wind structures and wind speed characteristics is essential for supporting the wind field modeling. Commonly, observed natural wind speed with a short time duration is mathematically decomposed into a mean wind speed over a relatively long reference period T (10 min or 1 hour) and a zero-mean fluctuating component. As a result, wind characteristics with respect to design mean wind speed, mean wind vertical profile, turbulence intensity, turbulence integral scale length, turbulence power spectrum density as well as gust factor, are

comprehensively investigated and discussed to facilitate the flexible structure design, such as high-rise buildings and long-span bridges and therefore enhance their safety and serviceability. Recent year, more accurate observations have been conducted, which provide an effective supplement to clearly reveal the wind characteristics of typhoon winds, including strong non-stationary and non-Gaussian features, radial distance-dependent vertical profiles with a prominent jet structure at near 0.5~1.0 km above ground level etc.. For example, the commonly used vertical wind profile specified by major building codes are expressed as power and logarithmic laws with the forms of

$$\frac{U_z}{U_{10}} = \left(\frac{z}{10}\right)^\alpha \quad (1.1)$$

$$U_z = \frac{u^*}{0.4} \ln\left(\frac{z}{z_0}\right) \quad (1.2)$$

in which U_z and U_{10} are wind speeds at height of z m and 10 m, α is the terrain-dependent power coefficient, z_0 is the equivalent roughness length (in m) and u^* is the friction velocity (m/s). As listed in Table 1.3, the vertical profile coefficients as well as the gradient heights (δ) with the open terrain or over water underlying exposure specified by different codes or standards are compared (Ge et al., 2013; Kwon et al., 2013).

Table 1.3 Coefficients of vertical wind profiles of major building codes/standards

Terrain category	Power law	ASCE	AIJ	CNS	IWC	Log law	AS/NZ*	EU	ISO
Open and flat terrain, sea, lake	$T(\min)$	60	10	10	60	$T(\min)$	10	10	10
	$z_0(m)$	-	-	0.01	-	$z_0(m)$	0.002	0.01	0.003
	$\delta(m)$	210	250	300	250	$\delta(m)$	300	-	-
	α	0.11	0.10	0.12	0.10	$u^*(m/s)$	0.055~0.061	0.068	0.059~0.064

Note: AS/NZ obtained from fitting results by Zhou et al (2002); IWC profile is valid above 100m height; δ is the gradient height; α is the exponent of power-law-based vertical wind profile; u^* is the friction wind speed.

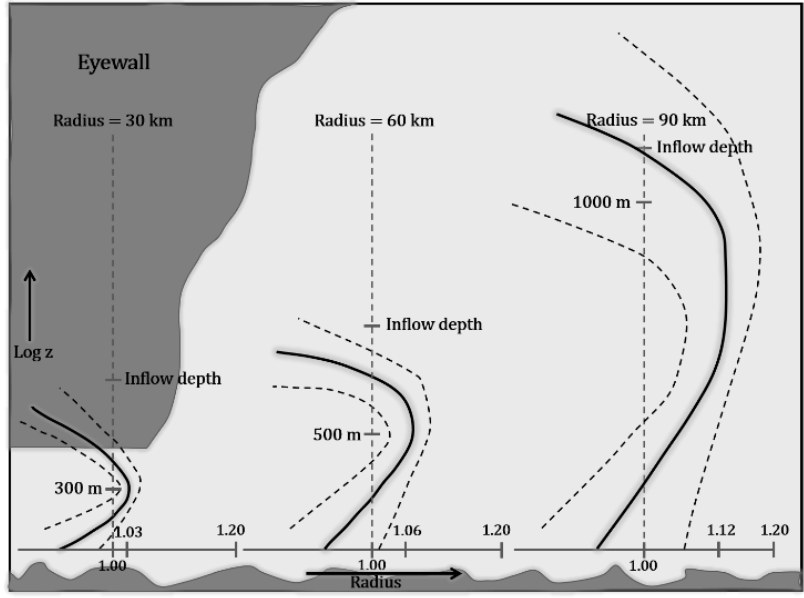


Fig. 1.4 A sketch summary of mean vertical wind profile for a typical tropical cyclone (Giammanco et al., 2013)

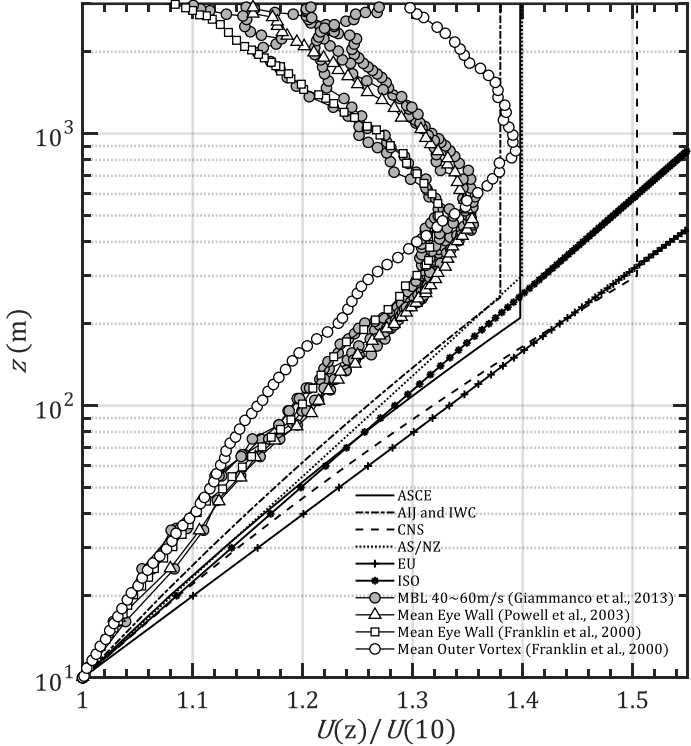


Fig. 1.5 Vertical wind profiles of observed mean typhoon boundary layer and specified by major building codes



Fig. 1.6 High-rise buildings located at coastal regions of China (Legend of wind profiles is same to Fig. 1.5)

Fig. 1.4 illustrates a sketch of mean vertical wind profile for a typical tropical cyclone summarized by Giammanco et al. (2013). The gradient height of vertical profiles was observed to increase from the eyewall to the outer region of a storm. Correspondingly, the code-specified wind profiles together with some observed mean typhoon boundary layer profiles recorded by dropsondes are illustrated in Fig. 1.5. It can be noted that the code-specified profiles are able to envelop the observed typhoon winds. However, the gradient height of typhoon wind, which is dependent on the radius from typhoon center is higher than the provisions of codes. Moreover, current profiles in codes fail to describe the characteristics of jet-induced front and decrease of wind speed at upper free layer of typhoon winds. Fig. 1.6 shows seven high-rise buildings located at coastal regions of China that subjected to typhoon threats. The highest building has reached the super-gradient level of typhoon storms, i.e. 500~700 m as plotted in Figs. 1.4~1.5. The typhoon-wind-resistant design of these buildings could require an independent criterion or standard.

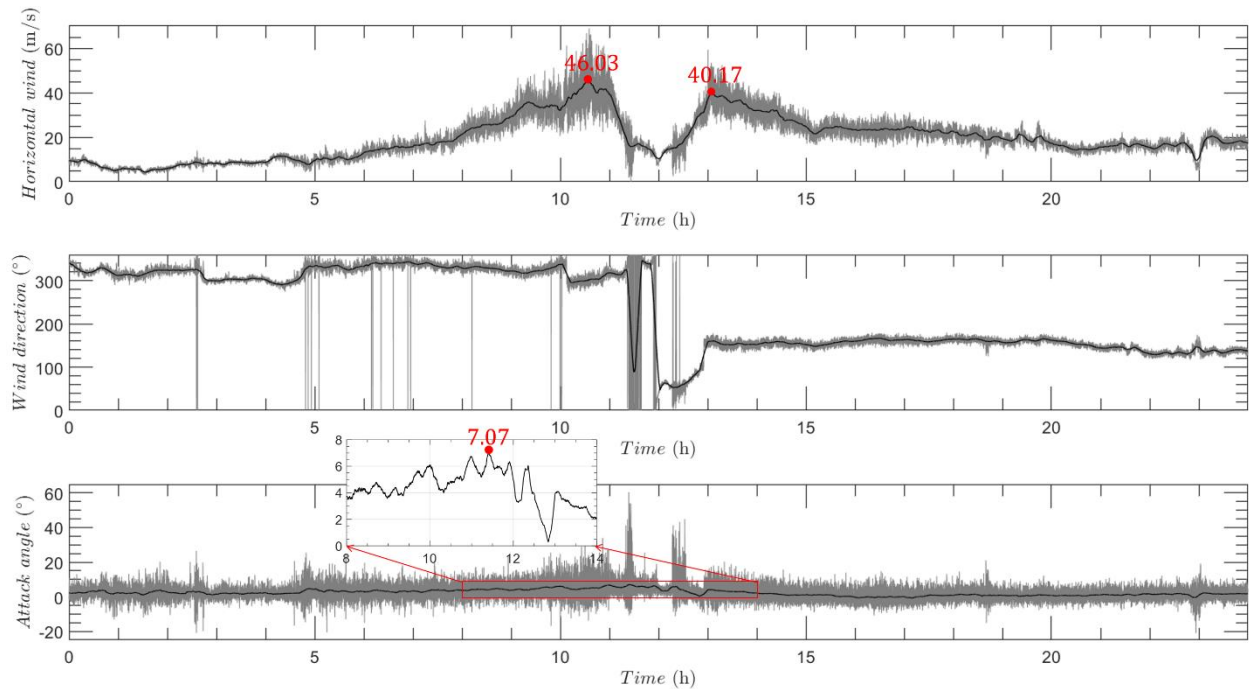


Fig. 1.7 Observed winds of Typhoon Hagupit (0814) at the height of 60 m (Grey curve: 0.1 s winds; Black line: 10-min averaged winds)

Furthermore, typhoon winds always exhibit strong non-stationary and non-Gaussian characteristics due to the effects of thermodynamic interaction (Li et al., 2015) and its rotating storm system, which has been proved in many recent field observations (Chen et al., 2007; Balderrama et al., 2012). Fig. 1.7 illustrates the observed winds of strong typhoon Hagupit (0814) at a height of 60 m, which shows an obvious non-stationary characteristic. Accordingly, more and more studies try to examine the non-stationary and non-Gaussian characteristics of typhoon winds (Chen et al., 2007; Balderrama et al., 2012) and reveal their potential effects on structure dynamic behaviors.

1.3 Typhoon wind modeling

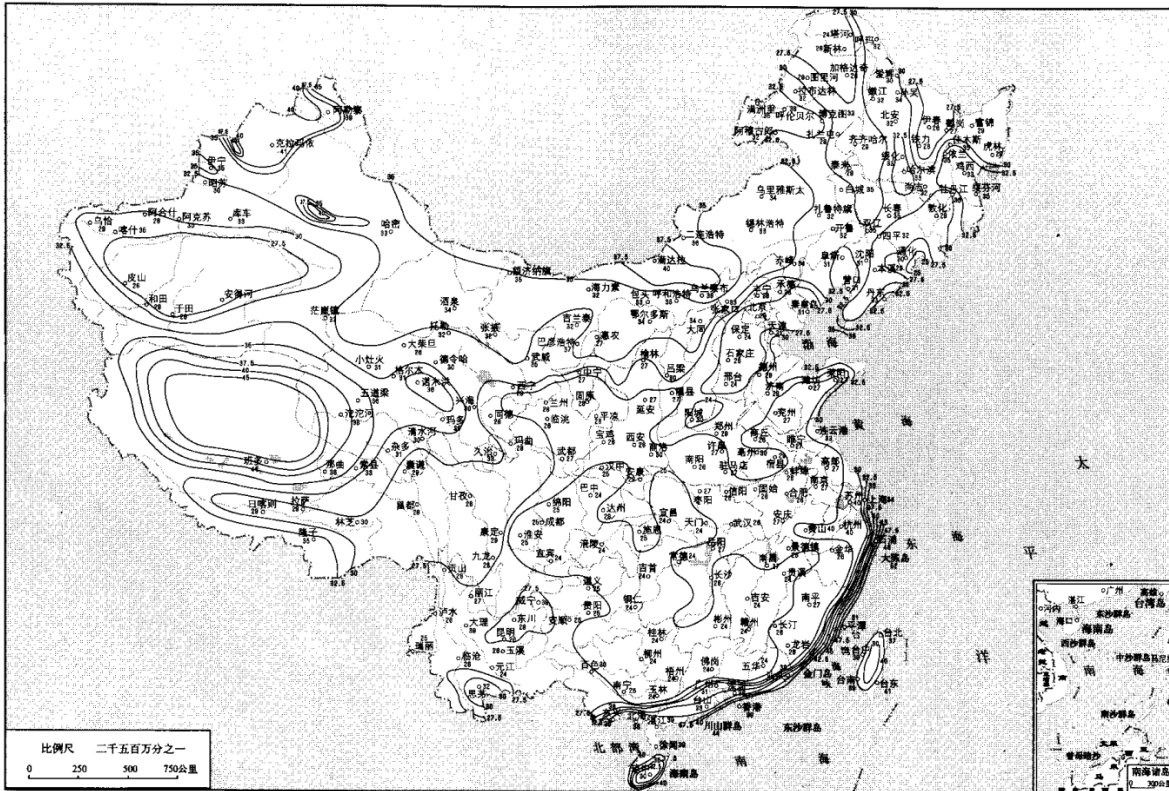


Fig. 1.8 Design wind speed map of China ($z = 10 \text{ m}$, $T = 10 \text{ min}$, $z_0 = 0.05$, $RP = 100 \text{ years}$) (JTG/T D60-01-2004)

The well-developed design wind maps in ASCE 7-10 “Minimum Design Loads for Building and Other Structures” (ASCE 2010) consists of two sets of wind speeds, say typhoon (hurricane) and non-typhoon (non-hurricane) winds. The non-typhoon design wind speeds are derived from a statistical model (extreme value distributions) by using the observation data provided by the National Climate Data Center (NCDC) weather monitoring stations. And typhoon wind speed is developed by a stochastic typhoon simulation model present by Vickery et al. (2009, 2010). Comparatively, the design wind speed in coastal regions of China still employs the statistical model-determined results, as shown in Fig. 1.8. That is, all design wind speeds in the coastal region are developed by both typhoon and non-typhoon winds recorded by meteorological stations over 35~40 years. However, typhoon winds observed

by meteorological stations are not enough and non-homogeneous, which makes them inappropriate to be used for the estimation of extreme wind speed with a certain return period by adopting the traditional extreme value probability distributions by stage extremum sampling method. Fig. 1.9 is an example employed by Simiu and Scanlan (1996), which is the annual largest 5-min speeds recorded at Corpus Christi, Texas with two records of strong hurricane winds. Type II extreme value distribution would result in a ridiculous value of 1950 mph related to the 1000-year return period. And mixed Fréchet probability distribution would yield only 76 mph associated with the 50-year return period, which is severely low than the real case. Moreover, wind anemometers are vulnerable to damage during strong typhoon events so that some high winds information always fails to be captured. Consequently, it is essential to independently map the design wind speed of typhoon climate in coastal regions of China.

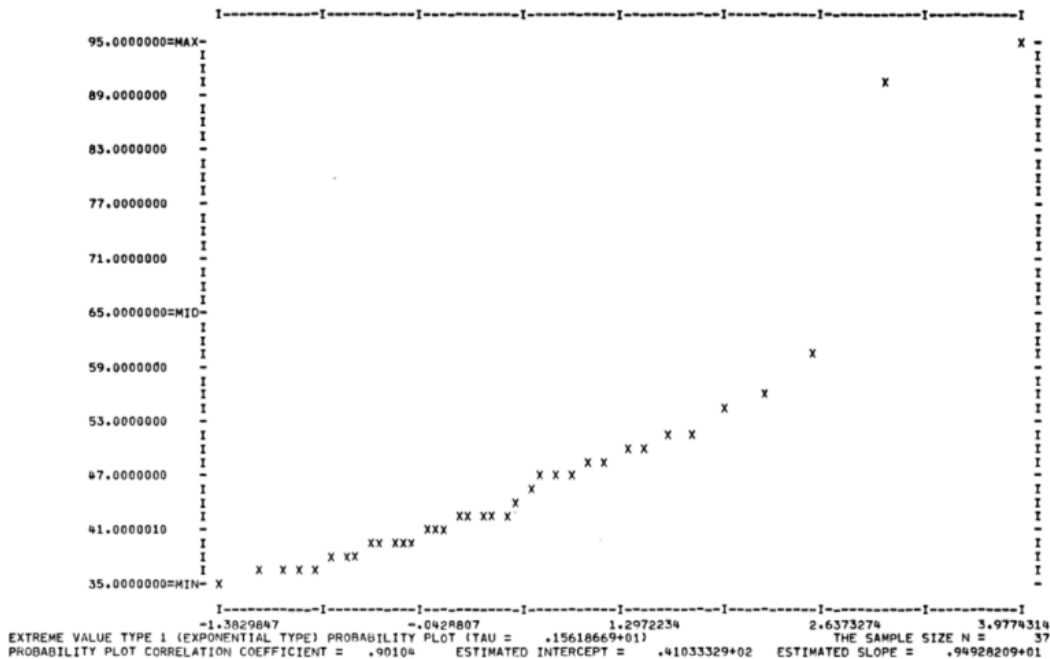


Fig. 1.9 Probability plot of 1912-1948 annual largest speeds at Corpus Christi, Texas (Simiu E and Filliben JJ, 1975; Simiu and Scanlan, 1996)

In the past several decades, some observation-based parametric typhoon models have been developed and being continuously improved for typhoon modeling as well as typhoon-induced hazard assessments. Unlike some advanced meteorological models, such as the Weather Research and Forecasting (WRF) system, parametric typhoon models are practical for Monte Carlo simulation by generating a large number of scenarios. Moreover, these parametric models, which are able to be easily updated and improved using the constant supplement of observation data, even have higher precision than some meteorological models to some extent.

By following the pioneer study performed by [Russell \(1971\)](#), the statistical modeling approach of typhoon hazard has developed significantly both in wind field model and track simulations. Currently, the most commonly used wind field model is a gradient wind speed model solved by the atmospheric balance equation coupled with a depth-averaged ([Vickery et al., 2000](#)) or a semi-empirically determined boundary layer vertical profile model ([Vickery et al., 2009a](#)). Another more sophisticated physical model is called height-resolving model by semi-analytically solving the boundary layer wind field based on 3D Navier-Stokes equations ([Meng et al., 1995](#); [Kepert, 2010](#); [Snaiki et al., 2017](#)), which is of great help in facilitating the interpretation of underlying physics for the typhoon boundary layer.

As for typhoon track simulations, which usually consist of genesis model, translation (track) model, intensity (central pressure) model, central pressure filling rate (decay) model after landfall, there are two approaches commonly adopted. One is called circular sub-region method or site-specific probabilistic method ([Vickery et al., 1995](#); [Li et al., 2015](#)), which only considers the statistical characteristics of track segments within a circle centered at the specific site. The other method is known as full track or empirical track model developed by

Vickery et al. (2000), which is able to simulate the typhoon track from its genesis to final dissipation by using the regressive models of heading direction and speed as well as the relative intensity in terms of central pressure and sea surface temperature.

Recently, some studies have tried to map the design typhoon wind speed in the coastal region of China by circular sub-region method (Xiao et al., 2011; Li et al., 2015; Hong et al., 2016) or full track model (Li et al., 2016; Chen et al., 2018). Two typical wind parameters, say radius to maximum wind speed (R_{\max}) and Holland pressure profile coefficient (B), which directly determine the size and distribution of typhoon wind field are always statistically modeled as the functions of central pressure and latitude within the whole region of interest. And those parameter models in different ocean basins are usually cross adopted, which is unable to unveil the real characteristics of the typhoon wind field in the Western Pacific basin.

1.4 Flutter risks of long-span bridges

As shown in Fig. 1.10, the collapse of Tacoma Narrows Bridge due to 40 mph (18 m/s) wind action in 1940 has received intense attention, which was considered as a significant landmark in wind engineering and boosted studies into aerodynamic effects on bridges. When the bridge structures are immersed in the wind flow, apart from the static wind loads, two kinds of aerodynamic load generated by the mean and fluctuating wind components would determine its aerodynamic performance. Commonly, these two dynamics loads are called self-excited force, which is a function of motion variables (displacement, velocity or acceleration), and buffeting force, which is aroused by the wind gusty. Among them, the static divergence and aerodynamic flutter could cause catastrophic failure of the structure, which is the top priority during the wind-resistant design of long-span bridges. After that, vortex-induced and buffeting vibrations, which would cause discomfort in users and fatigue

problems of the structure, will be checked by conducting wind tunnel tests or numerical simulations.

Nowadays, with the advancements of light and high-performance materials, more long-span bridge schemes are being proposed, such as Strait of Messina suspension bridge with main span of 3,300 m, Canakkale 1915 cable-suspension bridge with main span of 2023 m (under construction) and Hutong Yangtze River cable-stayed bridge with main span of 1092 m (under construction). Fig. 1.11 illustrates the distribution of long-span bridges along the coastal region of China and observed strong typhoons ($P_c < 960$ or $V_{max} > 83$ knots, V_{max} only available from 1977 for JMA best track dataset) surrounding these bridges (within 300 km) from 1951 to 2015, it can be noted that all these long-span bridges are subjected to threats of strong typhoons. Consequently, assessment of aerodynamic performance for long-span bridges under the action of strong typhoons is critically important, which can also be extended to guide the design of longer span bridges in the future.

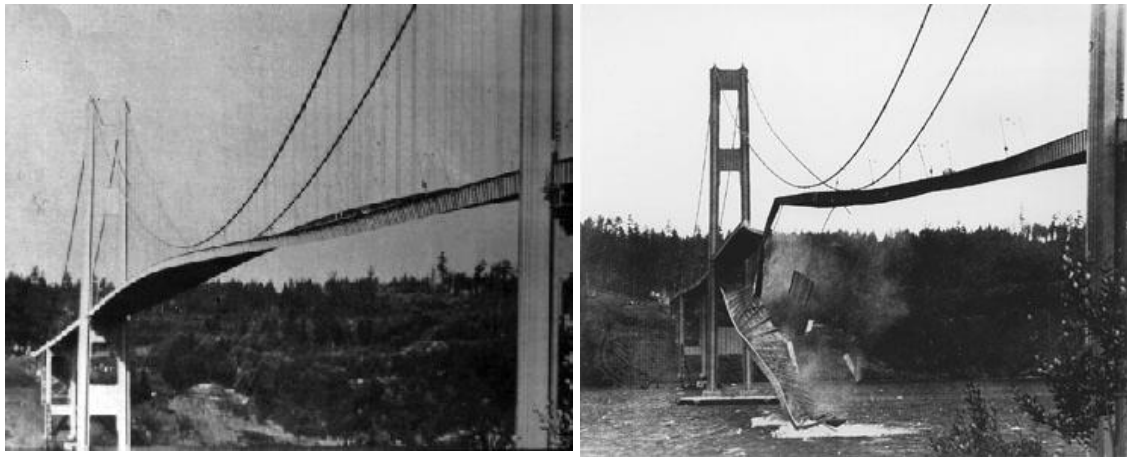


Fig. 1.10 Aerodynamic flutter and collapse of Tacoma Narrows Bridge (1940)

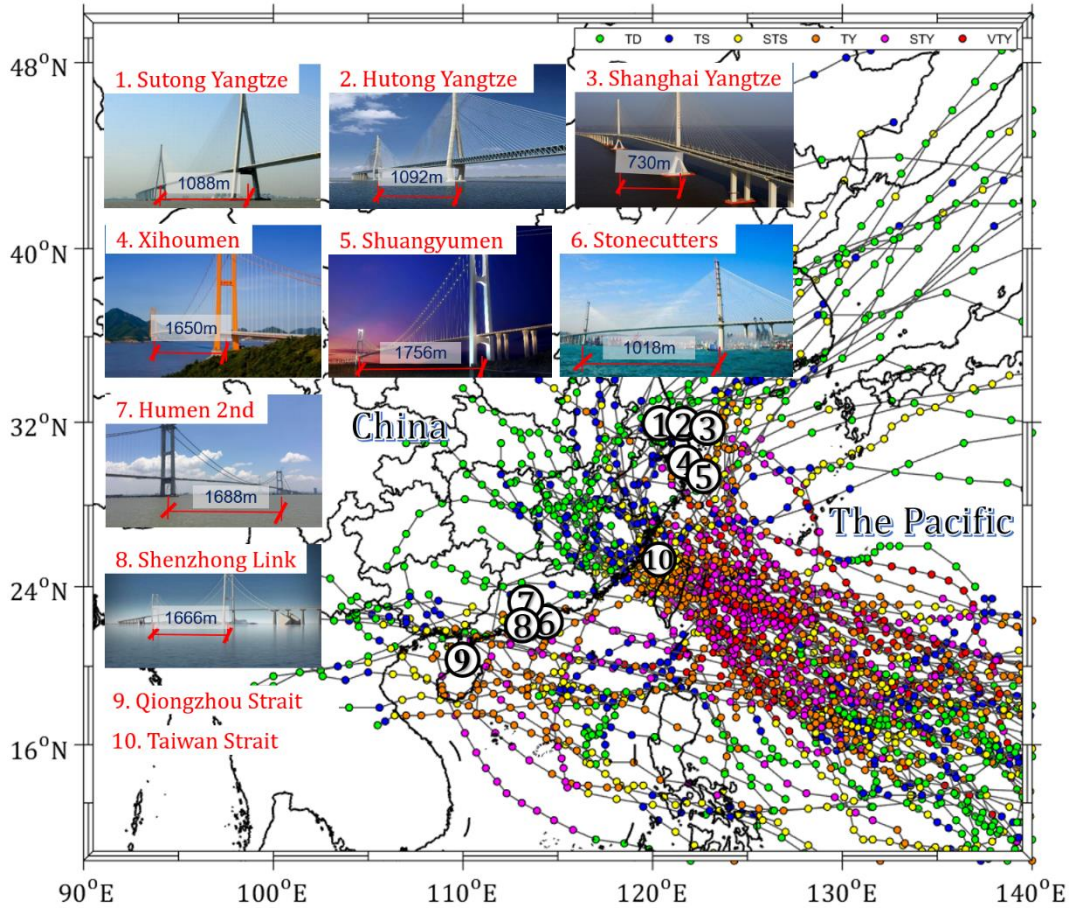


Fig. 1.11 Threats that strong typhoons pose to long-span bridges along coastal regions of China

1.5 Objectives and scope of research

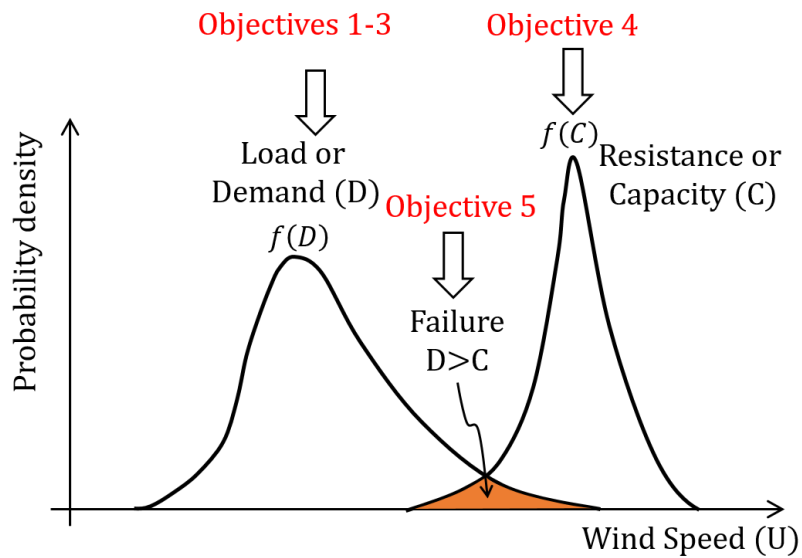


Fig. 1.12 Demand versus capacity for risk assessment of structures

As shown in Fig. 1.12, the overall objective of this dissertation is to map the design typhoon wind speed in coastal regions of China (objectives 1-3 for demand developments) and conduct the risk assessment for the aerodynamic performance of long-span bridges under typhoon winds (objective 4 for capacity developments). A case study on determining the flutter failure probability of a long-span suspension bridge due to typhoon winds will also be performed (Objective 5). The research findings would provide guidance for the wind-resistant design of structure around coastal regions of China as well as typhoon-related hazards assessments. Five sub-objectives were divided as

(1) Mean Wind Model: Development of a semi-analytical typhoon boundary layer wind field model

To physically figure out the inner structure of the typhoon wind field, a semi-analytical typhoon boundary layer wind field model would be developed by simplifying the three-dimensional Navier-Stokes equations coupled with a height-resolving parametric pressure model. The present model allows us to generate a three-dimensional wind speed field and enables the estimation of typhoon-induced wind hazard at any heights of interest within the boundary layer, such as the height of the bridge deck. It will also be adopted to optimally fit two key parameters of the typhoon wind field at surface level, say radius to maximum wind speed ($R_{max,s}$) and Holland pressure profile parameter (B_s) by employing the JMA best track dataset during years of 1977-2015 before reproducing the historical typhoon surface wind field and comparing with some observations. This parameter information would be documented into the typhoon track dataset to facilitate the stochastic simulation of typhoon tracks as well as hazard assessments.

(2) Gust Factor Model: Quantification of gust characteristics for strong typhoon winds based on observations

Typhoon winds within the atmospheric boundary layer are always featured with gust or fluctuation due to the frictional effects caused by obstruction of ground objects as well as the effects of deep convection. The quantification of gust characteristics in terms of turbulence intensity, turbulence integral scale length, power spectrum density function as well as gust factor is always a fundamental work to better understand the turbulence structure and provide enough information for the wind-resistant design of structures. Based on the field measurement data of typhoons captured by several meteorological stations along coastal regions of China as well as the structure health monitor systems in two long-span bridges, the gust characteristics of typhoons would be analyzed. A probabilistic gust factor model will be developed accounting for the non-stationary and non-Gaussian effects typhoon winds, aiming at the consideration of typhoon wind gust effects on risk assessment of flutter issues for long-span bridges.

(3) Typhoon Wind Hazard: Mapping the typhoon design wind speed for coastal regions of China

The current design wind speed maps provided by the Code were developed utilizing the extreme-value-distribution-based model by mixing both typhoon and non-typhoon wind data over 35~40 years. And the station records always fail to capture some violent typhoon winds due to the sensor or tower damages. To achieve the typhoon wind hazard assessments, a great number of synthetic typhoon tracks will be simulated using a geographically-weighted-regression (GWR)-based circular sub-region model. It allows attaining the typhoon design wind speeds with various return periods for any typhoon-prone sites of

interest. Moreover, a stochastic full-track model in Western Pacific would be adopted to couple with the present wind field model to compare with the sub-region model and optimally map the design wind speeds in coastal regions of China. The site-specific typhoon wind hazard information provided by this map would be of great help for performing the typhoon-resistant design of building structures and bridges.

It would also provide the load or demand for reliability design and risk assessment of long-span bridges in the next objectives.

(4) Flutter Capacity of Bridges: Development of a framework for probabilistic flutter analysis of long-span bridges

As a divergent motion that would lead to the catastrophic failure of bridges, flutter is always the top priority issue during the wind-resistant design process. A framework for determining the probabilistic flutter solutions of long-span bridges will be developed by taking the structural uncertainties and aerodynamic uncertainties into account. The structural uncertainties in terms of the variability of structural modal information and damping ratios will be quantified by the stochastic finite element technique and literature surveys. The uncertainties of aerodynamic parameters, i.e. flutter derivatives will be estimated using repeated wind tunnel tests. The flutter probabilistic solutions of bridges facilitate the development of fragility curves and risk assessment of flutter issues.

(5) A Case Application: Flutter risk assessment of a long-span bridge subjected to typhoon winds

To examine potential risks of typhoon wind hazards on the flutter problem of long-span bridges, a case study was performed on a 1666-m-main-span suspension bridge located at the typhoon-prone region. The use of typhoon wind hazard curves generated by Objectives

(1) ~ (3) and fragility curves developed in Objective (4) enables the flutter risk assessments of the present long-span bridge subjected to typhoon winds. The flutter-induced failure probability of the target bridge will be calculated under various combinations of design years and gust durations.

1.6 References

- Adler R F, (2005). Estimating the benefit of TRMM tropical cyclone data in saving lives. American meteorological society, 15th Conference on Applied Climatology, Savannah.
- Balderrama J A, Masters F J, Gurley K R, (2012). Peak factor estimation in hurricane surface winds. *Journal of Wind Engineering & Industrial Aerodynamics*, 102(3):1-13.
- Chen J, Hui M C H, Xu Y L, (2007). A Comparative Study of Stationary and Non-stationary Wind Models Using Field Measurements. *Boundary-Layer Meteorology*, 122(1):105-121.
- Chen Y, Duan Z, (2018). A statistical dynamics track model of tropical cyclones for assessing typhoon wind hazard in the coast of southeast China. *Journal of Wind Engineering & Industrial Aerodynamics*, 172:325-340.
- China's State Communication Ministry Standard, Wind-Resistant Design Specification for Highway Bridges (JTG/T D60-01-2004), People's Communication Press, Beijing, 2004 (in Chinese).
- Dvorak V F, (1975). Tropical Cyclone Intensity Analysis and Forecasting from Satellite Imagery. *Monthly Weather Review*, 103(5):420-430.
- Ge Y, Cao S, Jin X, (2013). Comparison and harmonization of building wind loading codes among the Asia-Pacific Economies. *Frontiers of Structural & Civil Engineering*, 7(4):402-410.

Hong H P, Li S H, Duan Z D, (2016). Typhoon Wind Hazard Estimation and Mapping for Coastal Region in Mainland China. *Natural Hazards Review*, 17(2):04016001.

Giammanco I M, Schroeder J L, & Powell M D, (2013). GPS dropwindsonde and WSR-88D observations of tropical cyclone vertical wind profiles and their characteristics. *Weather and Forecasting*, 28(1), 77-99.

Japan Meteorological Agency (JMA), RSMC Tokyo-Typhoon Center, Best Track Data (1951~2015). <<https://www.jma.go.jp/jma/jma-eng/jma-center/rsmc-hp-pub-eg/besttrack.html>> (2016-05-20).

Keprt J D, (2010). Slab- and height-resolving models of the tropical cyclone boundary layer. Part I: Comparing the simulations. *Quarterly Journal of the Royal Meteorological Society*, 136(652):1700-1711.

Knapp K R, Kruk M C, Levinson D H, et al, (2010). The International Best Track Archive for Climate Stewardship (IBTrACS): unifying tropical cyclone data. *Bulletin of the American Meteorological Society*, 91(3):363-376.

Kwon D K, Kareem A, (2013) Comparative study of major international wind codes and standards for wind effects on tall buildings. *Engineering Structures*, 51(2):23-35.

Li L, Kareem A, Hunt J, et al, (2015) Turbulence Spectra for Boundary-Layer Winds in Tropical Cyclones: A Conceptual Framework and Field Measurements at Coastlines. *Boundary-Layer Meteorology*, 154(2):243-263.

Li S H, Hong H P, (2015). Use of historical best track data to estimate typhoon wind hazard at selected sites in China. *Natural Hazards*, 76(2):1395-1414.

Li S H, Hong H P, (2016). Typhoon wind hazard estimation for China using an empirical track model. *Natural Hazards*, 82(2): 1009-1029.

Meng Y, Matsui M, Hibi K, (1995). An analytical model for simulation of the wind field in a typhoon boundary layer. *Journal of Wind Engineering and Industrial Aerodynamics*, 56(2-3):291-310.

Russell L R, (1971). Probability distributions for hurricane effects. *Journal of Waterways, Harbors, and Coastal Engineering Division*, 97: 139–154.

Snaiki R and Wu T, (2017). Modeling tropical cyclone boundary layer: Height-resolving pressure and wind fields. *Journal of Wind Engineering & Industrial Aerodynamics*, 170:18-27.

Simiu E and Filliben J J, (1975). Statistical analysis of extreme winds, Technical Note No. 868, National Bureau of Standards, Washington, DC.

Simiu E, Scanlan R H, (1996). *Wind Effects on Structures: Fundamentals and Applications to Design*. J. Wiley and Sons, New York, Chichester, Brisbane, 3rd edition.

Tanaka H, Tamura Y, Ohtake K, et al, (2012). Experimental investigation of aerodynamic forces and wind pressures acting on tall buildings with various unconventional configurations. *Journal of Wind Engineering & Industrial Aerodynamics*, 107-108(8):179-191.

The International Disaster Database (EM-DAT) [G/OL], (2016). <<http://www.emdat.be/>> (2016-08-23).

Vickery P J, Twisdale L A, (1995). Prediction of Hurricane Wind Speeds in the United States. *Journal of Structural Engineering*, 121(11):1691-1699.

Vickery P J, Skerlj P F, Twisdale L A, (2000). Simulation of hurricane risk in the U.S. using empirical track model. *Journal of Structural Engineering*, 126: 1222-1237.

Vickery P J, Wadhera D, Powell M D, et al, (2009a). A Hurricane Boundary Layer and Wind Field Model for Use in Engineering Applications. *Journal of Applied Meteorology & Climatology*, 48(2):381-405.

Vickery P J, Masters F J, Powell M D, et al, (2009b). Hurricane hazard modeling: The past, present, and future. *Journal of Wind Engineering & Industrial Aerodynamics*, 97(7):392-405.

Vickery P J, Wadhera D, Galsworthy J, et al, (2010) Ultimate Wind Load Design Gust Wind Speeds in the United States for Use in ASCE-7. *Journal of Structural Engineering*, 136(5):613-625.

Xiang H, Ge Y, (2007). Aerodynamic challenges in span length of suspension bridges. *Frontiers of Architecture & Civil Engineering in China*, 1(2):153-162.

Xiao Y F, Duan Z D, Xiao Y Q, et al, (2011). Typhoon wind hazard analysis for southeast China coastal regions. *Structural Safety*, 33(4):286-295.

Zhou Y, Kareem A, (2002). Definition of Wind Profiles in ASCE 7. *Journal of Structural Engineering*, 128(8):1082-1086.

CHAPTER 2 A SEMI-ANALYTICAL TYPHOON BOUNDARY LAYER

WIND FIELD MODEL

2.1 Background

Typhoon-related natural hazards pose serious threats to people's life and productive activities. The safety and reliability of flexible structures in typhoon-prone regions, including long-span bridges and high-rise buildings, need to be estimated during landfalls of the moving strong typhoons. However, typhoon-resistant design and typhoon-related risk prediction, i.e. design wind speed maps, storm surge simulation, and disaster early warning, are mainly based on numerically derived typhoon wind fields because of the limited amount of field observation data (Vickery et al., 2009). Currently, advanced meteorological models, such as the Weather Research and Forecasting (WRF) system, have continuously improved the accuracy and efficiency of typhoon numerical simulation for meteorological applications. However, using these models is still time-consuming and not practical for hazard risk prediction in typhoon-prone regions. Alternatively, parametric typhoon engineering models provide a fundamental methodology for Monte Carlo simulation by generating a large number of samples for typhoon-related natural-hazard assessments, was first introduced by Russell et al. (1974) and improved significantly in some other pioneering studies (Batts et al., 1980; Vickery et al., 1995, 2000). For engineering applications, the wind field model should be accurate, efficient and timesaving, so as not the simulation algorithm be too complex. Moreover, these models, which can be easily updated and improved using the observation data, even have higher precision than WRF model.

The most common option for typhoon field modeling in engineering applications is the slab or depth-averaged model ([Batts et al., 1980](#); [Vickery et al., 1995, 2000, 2009](#)), in which the momentum equation is averaged vertically. In this model, the typhoon boundary layer height is usually defined as a constant value and the surface wind speed is estimated by an empirically based reduction relationship between the gradient and the near ground wind velocity. As a result, a series of studies have been carried out to determine the values of V_{10}/V_G involving average wind speeds at 10m high and gradient height, sea-land transition and gust factors ([Vickery et al., 2009](#)). However, the accuracy of the slab model, especially for simulating the typhoon boundary layer, is not well-behaved because it relies heavily on modification from observation data and empirical analysis. Furthermore, the spatial velocity distribution in the typhoon boundary layer and the terrain effects are ignored to some extent. The height-resolving model is an improved method for directly solving the Navier-Stokes equation and is based on several simplified semi-analytical algorithms ([Meng et al., 1995](#); [Kepert, 2001](#)). The features of the wind field can be described approximately and the terrain types, treated as roughness-related parameters, are included in the updated wind field model. Some studies ([Kepert, 2010](#)) have compared these two kinds of models and demonstrated the inherent superiorities of the height-resolving model.

In light of Meng's model, Huang et al ([2012](#)) developed the height-varying pressure model, taking into account the influence of temperature. Moreover, Snaiki et al ([2016](#)) introduced temperature and moisture effects into the pressure field, which can be helpful for predicting wind speed by considering global climate change effects. Besides, some evidence ([Vickery et al., 2008](#); [Xiao et al., 2011](#); [Zhao et al., 2013](#)) suggests that the features of typhoons in the Northwest Pacific Ocean (NPO) and hurricanes in the Northwest Atlantic Ocean (NAO) are

quite different, which means statistical models of field parameters in the NAO cannot be easily applied to the NPO directly. It is essential to develop an improved typhoon model suitable for regions in the NPO, especially on the southeast coastlines of China.

In this study, by introducing a height-resolving pressure field model based on Holland parametric pressure profile (Holland, 1980), a semi-analytical typhoon boundary layer wind field model was developed by directly solving the three-dimensional Navier-Stokes equation using scale analysis. An iteration algorithm was proposed to model the eddy viscosity in typhoon boundary layer. It would be of great help to explicitly illustrate the inner structure of the typhoon boundary layer wind field. A couple of validation by comparing with observation data, including dropsondes vertical profile data, near-ground typhoon winds, and surface wind field re-analysis results, would be conducted.

2.2 Height-resolving parametric pressure field

The typhoon's surface pressure profile along the radial direction from storm center is always prescribed before solving the pressure term of Navier-Stokes equations in an analytical wind field model, which is of great importance for determining the wind field distributions. By combining gradient wind equations with empirically determined maximum winds obtained by Dvorak (1975) and Atkinson & Holliday (1977), Holland (1980, hereafter H80) proposed a commonly used parametric model illustrating radial axisymmetric wind and pressure profiles at sea surface with a nominal height of 10 m. The H80 model contains only two undetermined parameters, i.e. the radius to maximum wind speed (R_{max}) and the Holland radial pressure profile parameter (B_s) with the form of

$$P_{rz} = P_{cs} + \Delta P_s \cdot \exp \left[- \left(\frac{R_{max,s}}{r} \right)^{B_s} \right] \quad (2.1)$$

in which subscripts r, z and s denote values at the radius of r , height of z and surface, respectively, P_{rs} = surface air pressure at the radius of r from the typhoon's axis (hPa), P_{cs} = central pressure (hPa), $\Delta P_s = P_{ns} - P_{cs}$ is the central pressure difference (hPa). Although this two-parameter model is unable to produce the azimuthal and radial variation of the pressure field and sometimes fails to simulate the highly-asymmetric traits of a typhoon (Vickery and Wadhera, 2008), it is still shown to perform exceptionally well in most cases and its operational convenience enables the rapid estimation of typhoon hazard by generating many statistical scenarios with Monte Carlo algorithm. Besides, the statistical central pressure deficit-based functions of B_s and $R_{max,s}$ provide a more acceptable verification for this parametric model since the center location and central pressure information are readily available in most historical best-track datasets. In order to explicitly reveal the height-varying characteristics of typhoon pressures and quantify the pressure distribution above the typhoon gradient layer to facilitate the construction of a height-resolving wind model, the Holland surface pressure model would be extended to vertical direction with the gas state equation accounting for the effects of temperature and moisture (Satoh, 2014). Thus, a height-resolving parametric typhoon pressure field model is developed as

$$P_{rz} = \left\{ P_{cs} + \Delta P_s \cdot \exp \left[- \left(\frac{R_{max,s}}{r} \right)^{B_s} \right] \right\} \cdot \left(1 - \frac{gkz}{R_d \theta_v} \right)^{\frac{1}{k}} \quad (2.2)$$

$$\theta_v = T_v (P_s / P_z)^k \approx (1 + 0.61q)(T_z + 273.15) + \frac{kgz}{R_d} \quad (2.3)$$

$$T_z = T_s - \tau \cdot z \quad (2.4)$$

$$k = \frac{R}{c_p} = \frac{R_d(1 + 0.61q)}{c_{pd}(1 + 0.86q)} = \frac{2(1 + 0.61q)}{7(1 + 0.86q)} \quad (2.5)$$

$$q = RH \cdot \frac{3.802}{100P_z} \cdot \exp\left(\frac{17.67T_z}{T_z + 243.5}\right) \quad (2.6)$$

$$T_s = SST - 1 \text{ or } T_s = 28 - 3(\phi - 10)/20 \quad (2.7)$$

in which $g = 9.8 \text{ N/kg}$ is the gravitational acceleration, $R_d = 287 \text{ J/kg/K}$ is the specific gas constant of dry air, $\theta_v =$ virtual potential temperature (K), $q =$ specific humidity (kg/kg), $\tau =$ temperature lapse rate (0.0065K/m), $z =$ elevation (m), $RH =$ relative humidity (%), $R =$ specific gas constant of moist air (J/K/kg), $c_p =$ specific heat at constant pressure, $T_s =$ surface air temperature (K), $SST =$ sea surface temperature ($^{\circ}\text{C}$), and $\phi =$ latitude ($^{\circ}$).

In order to determine the value of RH and validate the accuracy of the proposed model, dropsondes measurement data collected by the Hurricane Research Division (HRD) of the United States National Oceanic and Atmospheric Administration (NOAA) were analyzed. Dropsondes data of three hurricanes, Cristobal (2014), Erika (2015) and Hermine (2016), at three moments: August 25, 2014, observed by NOAA 42 (17 dropsondes data); August 27, 2015, observed by NOAA 43 (13 dropsondes data); and August 25, 2016, observed by NOAA 43 (6 dropsondes data), respectively, were selected. Fig. 2.1 illustrates the relative humidity (RH) and temperature profiles of a totally 36 dropsondes data. RH basically fluctuates between 70% and 100% below 2km elevation. And RH here is defined as a constant 90% which is consistent with Holland's suggestion (Holland, 2008). The temperature lapse rate of the observations is approximately equal to 4.8K/km which is obviously less than the dry adiabatic lapse rate of 9.8K/km. Although Snaiki et al. (2017) suggested a Holland-like radial profile of temperature lapse rate, it is still an observation-based model. The value of 6.5 K/km for the adiabatic lapse rate was selected in this paper, although this may vary from 4 K/km to 9 K/km. As shown in Fig. 2.2, pressure profiles of totally 36 dropsondes data and

modeled results are compared. The present model almost perfectly reproduces the pressure vertical profiles. Besides, the introduction of SST could potentially play a role in analyzing climate change effects on typhoon fields and corresponding prediction of future hazards. Conventionally, Eq. (2.1) is directly employed to obtain the analytical solution of the radial pressure gradient in the equation of gradient balance velocity (Holland 1980; Meng et al., 1995). However, as shown in Fig. 2.3, the pressure drop ΔP at gradient height is obviously smaller than that at surface level, which also has been proved by observed data (He et al., 2018). Besides, the air density is closely correlated with the atmospheric pressure, which has been highlighted by Holland et al. (2008, 2010). Accordingly, it is more reasonable to solve the gradient wind field at different heights above the boundary layer coupled with the height-resolving pressure field.

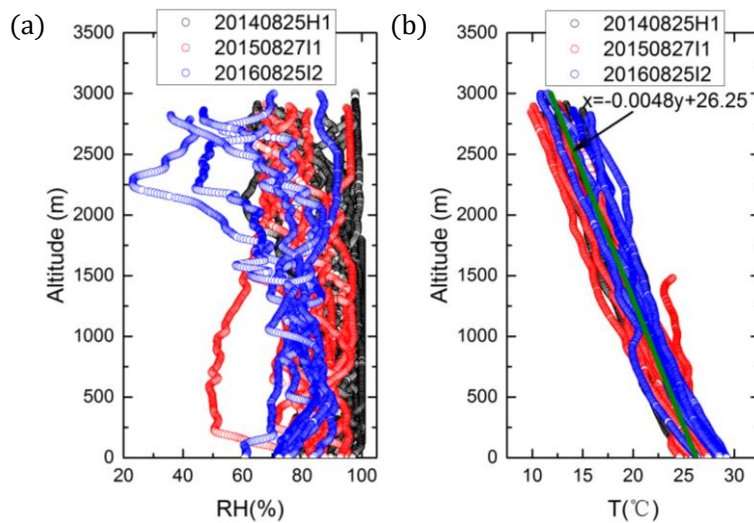


Fig. 2.1 Relative humidity and temperature profiles of hurricanes Cristobal, Erika, and Hermine corresponding to dropsondes data at three moments: (a) Relative humidity profile, (b) Temperature profile

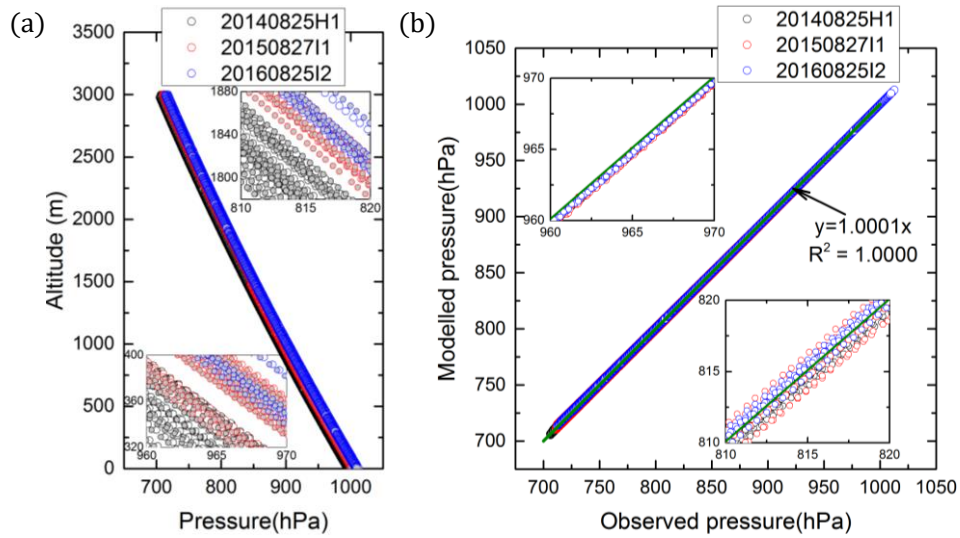


Fig. 2.2 Comparison of vertical pressure profiles (hollow points: observation, solid points: model): (a) Pressure profile, (b) Observed and modeled pressures

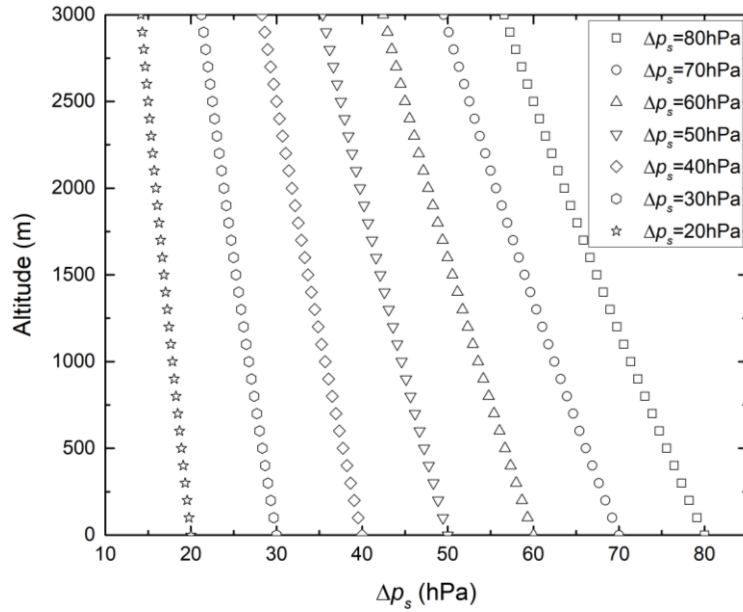


Fig. 2.3 Height-resolving parametric pressure difference (ΔP) profiles

2.3 Height-resolving wind speed field

2.3.1 Dynamics of mature typhoons

Forces per unit mass acting on a tiny atmosphere element in the boundary layer under typhoon conditions include the pressure gradient force, gravitational force, viscous force and

Coriolis force. On the basis of Newton's second law, the balance of momentum equation (Holton et al. 2004) is

$$\frac{D\mathbf{V}}{Dt} = \frac{\partial \mathbf{V}}{\partial t} + \mathbf{V} \cdot \nabla \mathbf{V} = -\frac{1}{\rho_a} \nabla P - f \cdot (\mathbf{k} \times \mathbf{V}) + \mathbf{g} + \mathbf{F}_d \quad (2.8)$$

where \mathbf{V} is typhoon-induced wind velocity vector and ρ_a is air density. $f = 2\Omega \sin\phi$ is the Coriolis coefficient, in which Ω (radian/s) is the earth's rotational speed and ϕ is the latitude of the location of interest. \mathbf{k} is the unit vector in the vertical direction. \mathbf{g} is the gravitational acceleration vector. \mathbf{F}_d represents the frictional force in the boundary layer. ∇ is the Hamilton operator.

According to the turbulence gradient theory or K theory (Holton et al. 2004), the frictional force can be expressed as the product of eddy viscosity and wind speed gradient. In a typhoon-centered cylindrical coordinate system (r, θ, z) , the motion equation can be decomposed into three components as

Radial direction:

$$\frac{\partial u}{\partial t} + u \frac{\partial u}{\partial r} + \frac{v}{r} \frac{\partial u}{\partial \theta} + w \frac{\partial u}{\partial z} - \frac{v^2}{r} = -\frac{1}{\rho_a} \frac{\partial p}{\partial r} + fv + K_u \left[\nabla^2 u - \frac{1}{r^2} \left(u + 2 \frac{\partial v}{\partial \theta} \right) \right] \quad (2.9)$$

Tangential direction:

$$\frac{\partial v}{\partial t} + u \frac{\partial v}{\partial r} + \frac{v}{r} \frac{\partial v}{\partial \theta} + w \frac{\partial v}{\partial z} + \frac{uv}{r} = -\frac{1}{r\rho_a} \frac{\partial p}{\partial \theta} - fu + K_v \left[\nabla^2 v - \frac{1}{r^2} \left(v - 2 \frac{\partial u}{\partial \theta} \right) \right] \quad (2.10)$$

Vertical direction:

$$\frac{\partial w}{\partial t} + u \frac{\partial w}{\partial r} + \frac{v}{r} \frac{\partial w}{\partial \theta} + w \frac{\partial w}{\partial z} = -\frac{1}{\rho_a} \frac{\partial p}{\partial z} - g + K_w \nabla^2 w \quad (2.11)$$

in which u, v and w are the radial, tangential and vertical wind components, respectively. ∇^2 is the Laplace operator. K_u, K_v and K_w are the eddy viscosities (m^2/s) in three directions and a constant is set such that $K_u = K_v = K_w = K$.

2.3.2 Scale analysis

Scale analysis is a convenient and effective technique for simplifying the strongly nonlinear differential equations (Holton et al. 2004). By estimating and comparing the magnitudes of various terms in the equations, the primary factors are highlighted but the accuracy of the results is little influenced. In typhoon wind field, the speed scales U, V, W for the wind components u, v, w and space scales R, Z for radius r and height z are introduced. The time scale $T = R/U$ is defined by the radial flow of the atmosphere, and the perturbation scales of pressure in three directions are $\delta_r P, \delta_\theta P, \delta_z P$. After that, several dimensionless parameters, such as a swirl parameter $S = U/V$; Rossby number $R_o = V/fR$; Reynolds number $R_e = VZ/K$ and aspect ratio $A = Z/R$, are introduced. It is acceptable to assume that the horizontal wind speeds U and V have the same magnitude in the typhoon boundary layer, i.e. swirl parameter $S = 1$. Accordingly, it is easy to find that the magnitudes of U/R and V/R are the same as that of W/Z according to the continuity equation, as given by the Eq. (2.12), i.e. $U/R \sim V/R \sim W/Z$. This can be applied to simplify the scale analysis and to obtain the magnitudes of each term of the momentum equations as expressed by Eqs. (2.13)-(2.15). The first rows below every equation are the scales of each term and the second ones are the corresponding dimensionless scales divided by V^2/R for Eqs. (2.13)~(2.14) and V^2/Z for Eq. (2.15).

Continuity equation:

$$\frac{1}{r} \frac{\partial ru}{\partial r} + \frac{1}{r} \frac{\partial v}{\partial \theta} + \frac{\partial w}{\partial z} = 0 \quad (2.12)$$

$$\frac{U}{R} \quad \frac{V}{R} \quad \frac{W}{Z}$$

Radial direction:

$$\begin{array}{cccccccc}
\frac{\partial u}{\partial t} + u \frac{\partial u}{\partial r} + \frac{v}{r} \frac{\partial u}{\partial \theta} + w \frac{\partial u}{\partial z} - \frac{v^2}{r} - fv & = & - \frac{1}{\rho_a} \frac{\partial P}{\partial r} & + K[\nabla^2 u - \frac{1}{r^2}(u + 2\frac{\partial v}{\partial \theta})] \\
\frac{U}{T} \quad \frac{U^2}{R} \quad \frac{UV}{R} \quad \frac{UW}{Z} \quad \frac{V^2}{R} \quad fV & & \frac{\delta_r P}{\rho R} & \quad K \frac{U}{R^2} \quad K \frac{U}{Z^2} \quad K \frac{2V}{R^2} \\
S^2 \quad S^2 \quad S \quad S^2 \quad 1 \quad \frac{1}{R_o} & & \frac{\delta_r P}{\rho V^2} & \quad \frac{SA}{R_e} \quad \frac{S}{AR_e} \quad \frac{2A}{R_e} \\
1 \quad 1 \quad 1 \quad 1 \quad 1 \quad 2.2 & & \frac{\delta_r P}{100} & \quad 1.5 \times 10^{-5} \quad 1.7 \quad 3 \times 10^{-5}
\end{array} \quad (2.13)$$

Tangential direction:

$$\begin{array}{cccccccc}
\frac{\partial v}{\partial t} + u \frac{\partial v}{\partial r} + \frac{v}{r} \frac{\partial v}{\partial \theta} + w \frac{\partial v}{\partial z} + \frac{uv}{r} + fu & = & - \frac{1}{r\rho_a} \frac{\partial P}{\partial \theta} & + K[\nabla^2 v - \frac{1}{r^2}(v - 2\frac{\partial u}{\partial \theta})] \\
\frac{V}{T} \quad \frac{UV}{R} \quad \frac{V^2}{R} \quad \frac{VW}{Z} \quad \frac{UV}{R} \quad fU & & \frac{\delta_\theta P}{\rho R} & \quad K \frac{V}{R^2} \quad K \frac{V}{Z^2} \quad K \frac{2U}{R^2} \\
S \quad S \quad 1 \quad S \quad S \quad \frac{S}{R_o} & & \frac{\delta_\theta P}{\rho V^2} & \quad \frac{A}{R_e} \quad \frac{1}{AR_e} \quad \frac{2AS}{R_e} \\
1 \quad 1 \quad 1 \quad 1 \quad 1 \quad 2.2 & & \frac{\delta_r P}{100} & \quad 1.5 \times 10^{-5} \quad 1.7 \quad 3 \times 10^{-5}
\end{array} \quad (2.14)$$

Vertical direction:

$$\begin{array}{cccccccc}
\frac{\partial w}{\partial t} + u \frac{\partial w}{\partial r} + \frac{v}{r} \frac{\partial w}{\partial \theta} + w \frac{\partial w}{\partial z} + g & = & - \frac{1}{\rho_a} \frac{\partial P}{\partial z} & + K\nabla_h^2 w + K \frac{\partial^2 w}{\partial z^2} \\
\frac{W}{T} \quad \frac{UW}{R} \quad \frac{VW}{R} \quad \frac{W^2}{Z} \quad G & & \frac{\delta_z P}{\rho Z} & \quad K \frac{W}{R^2} \quad K \frac{W}{Z^2} \\
S^2 A^2 \quad S^2 A^2 \quad SA^2 \quad S^2 A^2 \quad \frac{GZ}{V^2} & & \frac{\delta_z P}{\rho V^2} & \quad \frac{SA^3}{R_e} \quad \frac{SA}{R_e} \\
10^{-5} \quad 10^{-5} \quad 10^{-5} \quad 10^{-5} \quad 10^2 & & \frac{\delta_z P}{100} & \quad 1.35 \times 10^{-10} \quad 1.5 \times 10^{-5}
\end{array} \quad (2.15)$$

Given that a typhoon is a mesoscale vortex system and the depth of the boundary layer is typically slim compared to the radial scale, the vertical space scale Z can be set as at 10^3 m and the horizontal scale R is $3 \times 10^5 \text{ m}$. Horizontal wind speeds U and V have the same magnitude as 10 m/s . The eddy viscosity K is in the order of $50 \text{ m}^2/\text{s}$, as estimated from some previous studies (Meng et al. 1995). And it is reasonable to set the Coriolis coefficient as $f = 2\Omega \sin\phi \approx 2 \times 2\pi/(3600 \times 24) \times \sin 30^\circ = 7.27 \times 10^{-5}$. The scales of gravitational acceleration G and air density ρ are set at 10 m/s^2 and 1 kg/m^3 , respectively. As a result,

the orders for the dimensionless scales are $S = U/V \sim 1$, $R_o = V/fR \sim 0.46$, $R_e = VZ/K \sim 200$ and $A = Z/R \sim 0.3 \times 10^{-2}$. The third rows under Eqs. (2.13)~(2.15) are corresponding values of magnitude for each term. Based on the above analyses and neglecting the perturbation term of pressure in the azimuthal direction, the 3-D momentum equations of typhoon boundary layer can be simplified as

$$\frac{\partial u}{\partial t} + u \frac{\partial u}{\partial r} + \frac{v}{r} \frac{\partial u}{\partial \theta} + w \frac{\partial u}{\partial z} - \frac{v^2}{r} - fv = -\frac{1}{\rho_a} \frac{\partial p_r}{\partial r} + K \frac{\partial^2 u}{\partial z^2} \quad (2.16)$$

$$\frac{\partial v}{\partial t} + u \frac{\partial v}{\partial r} + \frac{v}{r} \frac{\partial v}{\partial \theta} + w \frac{\partial v}{\partial z} + \frac{uv}{r} + fu = K \frac{\partial^2 v}{\partial z^2} \quad (2.17)$$

$$g = -\frac{1}{\rho_a} \frac{\partial p_z}{\partial z} \quad (2.18)$$

2.3.3 Gradient wind speed at the free atmosphere

At the top of the boundary layer and in the free atmosphere, the frictional effects in the typhoons are ignored. The wind speeds in cylindrical coordinates are u_g , v_g and w_g . And the assumption that horizontal wind speeds in the gradient layer move at the translation velocity of the typhoon is followed, which means the unsteady term can be expressed as

$$\frac{\partial \mathbf{V}_{hg}}{\partial t} = -\mathbf{c} \cdot \nabla \mathbf{V}_{hg} = -\left(c_r \frac{\partial u_g}{\partial r} + \frac{c_\theta}{r} \frac{\partial u_g}{\partial \theta} - \frac{c_\theta v_g}{r} \right) \mathbf{e}_r - \left(c_r \frac{\partial v_g}{\partial r} + \frac{c_\theta}{r} \frac{\partial v_g}{\partial \theta} - \frac{c_\theta u_g}{r} \right) \mathbf{e}_\theta \quad (2.19)$$

where subscripts h and g represent the horizontal speed at gradient height, \mathbf{c} is the typhoon's translation velocity vector, and $c_r = c \cdot \cos(\theta - \theta_0)$ and $c_\theta = -c \cdot \sin(\theta - \theta_0)$, in which θ_0 is the approach counterclockwise positive angle from the east. \mathbf{e}_r and \mathbf{e}_θ are unit vectors.

By substituting Eq. (2.19) into Eq. (2.16) and considering that the tangential wind speed is larger than the radial and vertical ones, the first and second convection terms in Eq. (2.16) are disregarded. The gradient balance equation is obtained as

$$\frac{v_g^2}{r} + \left(f - \frac{c_\theta}{r}\right) v_g - \frac{1}{\rho_g} \frac{\partial p_g}{\partial r} = 0 \quad (2.20)$$

Then the gradient wind speed is solved as

$$v_g = \frac{c_\theta - fr}{2} + \sqrt{\left(\frac{c_\theta - fr}{2}\right)^2 + \frac{r}{\rho_g} \frac{\partial p_g}{\partial r}} \quad (2.21)$$

2.4 Typhoon boundary layer wind model

2.4.1 Axisymmetric height-resolving boundary layer model

Using the decomposition method, wind speeds in the typhoon boundary layer are expressed as the addition of gradient wind speeds and the decay wind speeds caused by frictional effects: $u = u_g + u_d \approx u_d$, $v = v_g + v_d$. The radial pressure gradients at different heights are regarded as essentially unchanged. From Eqs. (2.16)~(2.17), the axisymmetric ($\partial V/\partial \theta = 0$) linear dynamic equations for a stationary typhoon ($\partial V/\partial t = 0$) are expressed as

$$\xi_g v_d = K \frac{\partial^2 u_d}{\partial z^2} \quad (2.22)$$

$$\xi_{ag} u_d = K \frac{\partial^2 v_d}{\partial z^2} \quad (2.23)$$

in which $\xi_g = 2v_g/r + f$ and $\xi_{ag} = \partial v_g/\partial r + v_g/r + f$ are the absolute angular velocity and the vertical component of absolute vorticity in the gradient layer, respectively. Given that u_d and v_d remain finite as height increases, these two equations can be solved analytically (Meng et al. 1995) with the form of

$$u_d = e^{-\lambda z'} \eta [D_1 \sin(\lambda z') - D_2 \cos(\lambda z')] \quad (2.24)$$

$$v_d = e^{-\lambda z'} [D_1 \cos(\lambda z') + D_2 \sin(\lambda z')] \quad (2.25)$$

in which $\lambda = \sqrt[4]{\xi_g \xi_{ag}} / \sqrt{2K}$, $\eta = \sqrt{\xi_g / \xi_{ag}}$ and parameters D_1 and D_2 can be determined by the slip boundary condition:

$$\rho_a K \left. \frac{\partial V_h}{\partial z} \right|_{z'=0} = \rho_a C_d |V_h| V_h \Big|_{z'=0} \quad (2.26)$$

in which C_d is the drag coefficient, which refers to the assumption of a logarithmic law near the ground surface as

$$C_d = \frac{\kappa^2}{\left\{ \ln \left[\frac{(h + z_{10} - d)}{z_0} \right] \right\}^2} \quad (2.27)$$

in which κ is the von Kármán constant, empirically determined to be about 0.4. h is the mean height of roughness elements (m), expressed as a function of equivalent roughness length $z_0(m)$: $h = 11.4z_0^{0.86}$ (Meng et al. 1995). z_{10} is set at 10 m height above h and the base of computation domain $z' = 0$ is at $h + z_{10}$. $d = 0.75h$ denotes the zero-plane displacement. By substituting Eqs. (2.22)~(2.23) into the boundary condition, Eq. (2.26), D_1 and D_2 can be solved by the following formulas

$$K\lambda(D_2 - D_1) = C_d \sqrt{(D_2\eta)^2 + (v_g + D_1)^2} (v_g + D_1) \quad (2.28)$$

$$K\lambda(D_1 + D_2) = -C_d \sqrt{(D_2\eta)^2 + (v_g + D_1)^2} D_2 \quad (2.29)$$

It can be found that D_1 and D_2 are on a circle with center at $(-v_g/2, v_g/2)$ and radius of $v_g/\sqrt{2}$:

$$D_1 = \frac{(\sqrt{2}v_g \cos \alpha - v_g)}{2} \quad (2.30)$$

$$D_2 = \frac{(\sqrt{2}v_g \sin \alpha - v_g)}{2} \quad (2.31)$$

in which α is an undetermined parameter that can be obtained by solving Eq. (2.28) or Eq. (2.29) using a dichotomy method in the domain of $(\pi/4, 3\pi/4)$.

2.4.2 Eddy viscosity within the boundary layer

It is generally assumed that the atmospheric boundary layer is subdivided into three parts (Holton et al. 2004). The lowest one is the ground layer within 2 meters of the ground surface, in which the molecular viscosity stress is larger than the turbulent stress. The middle one is the Prandtl layer or the constant flux layer from 10m to about 100m above the ground surface, where turbulent viscosity stress is dominant, and a logarithmic velocity profile is adopted. The outer region is the so-called Ekman layer, whose top is usually below 1.5km, in which the turbulent viscosity stress, Coriolis force, and pressure gradient force are equally important, and the motion of the atmosphere has quasi-steady characteristics. The above analytical solutions of the wind field are all based on the assumption of a constant value of eddy viscosity K . Meng et al. (1995) fixed the value of K at $100 \text{ m}^2/\text{s}$ based on several observation results. However, some literature has shown a larger range of K values. For example, Kepert et al. (2001) set $K = 5 \text{ m}^2/\text{s}$ while Montgomery et al. (2001) used a value of $K = 50 \text{ m}^2/\text{s}$. Meng et al. (1997) also pointed out that K could not be a constant value at typhoon boundary layer and he used a turbulence closure model to get the value of K by an iterative solution.

As shown in Fig. 2.4, the presented model yields vertical wind speed profiles with different values of K . The value of K has a great influence on the boundary layer wind speed profiles, which directly impact civil engineering structures nearby the surface ground. It is evident that the wind speeds in the Prandtl layer (below about 100m) do not follow a logarithmic law when a constant of K is adopted. Actually, eddy viscosity is a representation of

momentum transfer caused by turbulent eddies which analogous to the molecular viscosity.

It depends on the fluid density and distance from the underlying surface. Basically, it can be

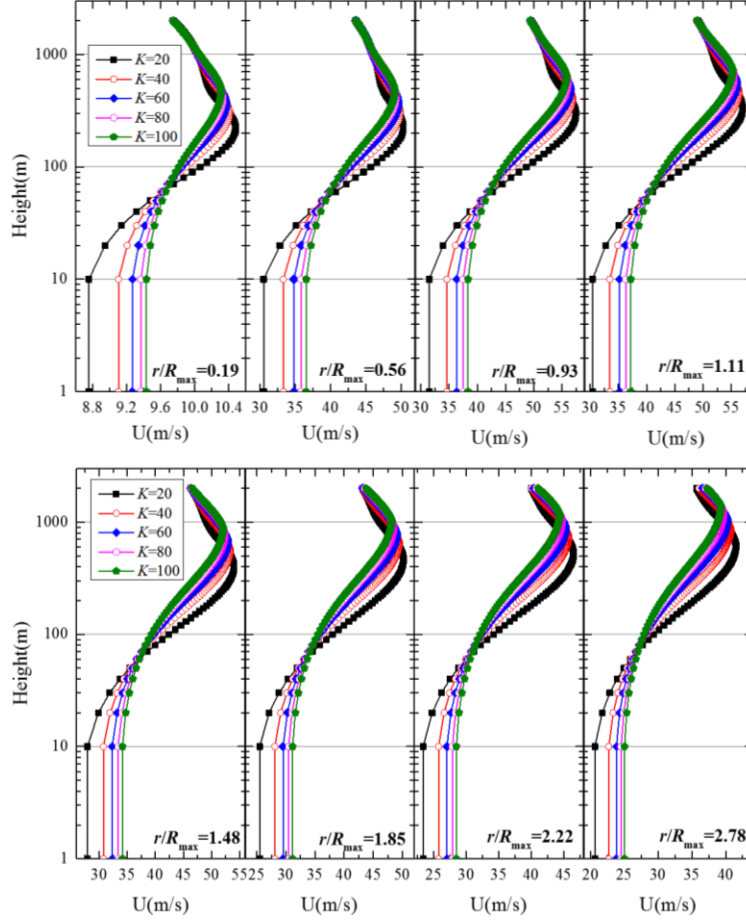


Fig. 2.4 Vertical wind profiles with some constant K ($\Delta P_s = 80hPa$, $z_0 = 0.05 m$)

determined from the local vertical deformation or shear absolute magnitude (S_v) and moist Brunt-Vaisala frequency (N_m) by considering mixing length hypothesis as

$$K = l_v^2 (S_v^2 - N_m^2)^{1/2} \quad (2.32)$$

$$S_v^2 = \left(\frac{\partial u}{\partial z} \right)^2 + \left(\frac{\partial v}{\partial z} \right)^2 \quad (2.33)$$

$$N_m^2 = \frac{g \partial \theta_v}{\theta_v \partial z} \quad (2.34)$$

The vertical mixing length l_v is formulated with an upper bound of l_∞ ($\sim 1/3$ boundary layer depth in a neutral atmospheric condition as suggested by Apsley (1995)) as

$$l_v = \left(\frac{1}{\kappa(z + z_0)} + \frac{1}{l_\infty} \right)^{-1} \quad (2.35)$$

Instead of substituting Eq. (2.32) into Eqs. (2.22)-(2.23), which is unable to attain the analytical solutions, an iterative loop is employed during the calculation of typhoon wind speed to achieve a convergent result of eddy viscosity and wind speed.

2.4.3 Numerical typhoon wind solutions

Based on the aforementioned equations, the typhoon wind field can be numerically solved by following the procedures as shown in Fig. 2.5. The boundary layer depth defined as the height of gradient wind speed equal to the solved boundary layer wind speed would be first determined with an iteration loop. After that, the eddy viscosity at different locations (both in radial and vertical directions) would be calculated before the wind speed field is solved.

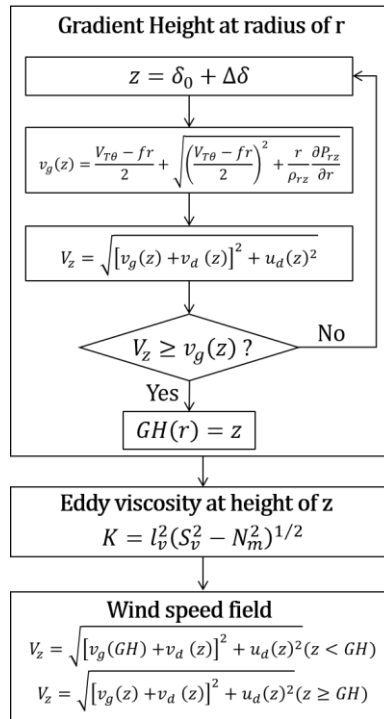


Fig. 2.5 Flowchart for typhoon wind field numerical solutions

A synthetic typhoon over the Western Pacific with the eye location of ($120^{\circ}E, 20^{\circ}N$) is solved using the present boundary layer model. Several input parameters are defined as the central pressure difference $\Delta P_s = 80hPa$, $z_0 = 0.0002m$, $c = 5 m/s$, $\theta_0 = 120^{\circ}$ shape parameter of Holland pressure profile $B_s = 1.5$; radius to maximum wind speed $R_{max,s} = 50km$; translation speed $c = 5 m/s$; translation direction $\theta_0 = 120^{\circ}$ (positive from east counterclockwise); surface roughness length $z_0 = 0.0002 m$ which is the over-water value used in Moderate Resolution Imaging Spectroradiometer (MODIS) -based global land cover product (Broxton et al., 2014). Fig. 6 illustrates the contour plots of the vertical field of several parameters for eastern slice. The black dash line is the gradient height above which the drag effects caused by planetary surface obstruction would be ignored. It is different from the code-defined winds, which assumed a simple shear vertical velocity profile and a constant gradient height associated with a specific surface roughness length. Comparatively, a gradual increase trend of gradient height from center to outer area can be observed for a typhoon storm. This has been proved by a number of observations, either the used of remote sensing techniques, such as Radar (Li et al., 2013; He et al., 2013, 2016; Shu et al., 2017), Lidar (Zhao et al., 2019; Tsai et al., 2019), etc. or GPS dropsondes (Franklin et al., 2003; Powell et al., 2003; Giammanco et al., 2012, 2013; Snaiki and Wu, 2018).

Fig. 2.6 (a)~(b) show the contours of radial decay wind speed u_d and tangential decay wind speed v_d . u_d is equal to the radial wind speed representing the distribution of inflow ($u_d \leq 0$) and outflow ($u_d > 0$). The maximum inflow is found near the surface layer (10 m) at the location of about twice of $R_{max,s}$. A slanting cap level of inflow region ($u_d = 0$) occurs from the storm center to the radius of about twice of $R_{max,s}$ below 2 km. A weak outflow can also be noticed near the storm core. Similarly, the maximum tangential decay wind speed v_d

occurs at the radius of about 1.5 times of $R_{max,s}$. And a horn-shaped domain of positive v_d can be observed, which is considered as a supergradient region with maximum of 1.4 m/s located at radius of $R_{max,s}$ and height of about 650 m. More specifically, the contour plot of velocity difference between gradient height and other heights, i.e. $V_z - V_{GH}$ is shown in Fig. 2.6(d). Accordingly, three sub-regions, say boundary layer decay region, supergradient region, and gradient decay region are divided by the zero contours $V_z - V_{GH} = 0$. V_z in the boundary layer decay region is smaller than V_{GH} due to the effects of underlying roughness effects while gradient decay region results from the variation of pressure and moisture fields along the height. The middle supergradient region accounting for the effects of both u_d and v_d is different from that defined only by v_d (Fig. 2.6(b)).

Fig. 2.6(c) shows the distribution of eddy viscosity K . Because eddy viscosity K has an insignificant influence on the wind profiles above the gradient height as illustrated in Fig. 4, K values above the gradient height in the present model is assumed to same as that at gradient height. Within the boundary layer, the eddy viscosity increases with height, as discussed by Bryan et al. (2017). The maximum eddy viscosity $111 \text{ m}^2/\text{s}$ occurs at the gradient height of about 610 m and radius of about 3 times of $R_{max,s}$. And a lower bound of $0.1 \text{ m}^2/\text{s}$ is set when the calculated eddy viscosity is not a real number.

Fig. 2.6(e)-(f) are the wind direction and wind speed. The wind direction is defined as the angle between geographical true north and the incoming wind with positive clockwise. Because the synthetic typhoon rotates counterclockwise in the Northern Hemisphere, the wind directions in the eastern slice are most likely within 90° - 180° . Directions in Fig. 2.6 (e) are between 137° and 180° , encountering a slight decrease along the radial direction from the storm center and an increase along the vertical direction. This is consistent with the

dropsonde observations analyzed by Giammanco et al. (2012) with about 40° wind direction increase from surface to 2-km height. The maximum wind speed in Fig. 2.6 (f) occurs at radius of $R_{max,s}$ and height of 400 m~600 m with a maximum of 61.35 m/s. And the winds near the eye center region is close to zero.

Furthermore, Fig. 2.7 shows horizontal fields of eddy viscosity, radial decay wind speed, tangential decay wind speed and wind speed at three heights, say 10m, 110m, and 510m. the distribution of eddy viscosity illustrated in Fig. 2.7(a) and follows a similar pattern of wind speed, increasing from storm center to the radius of $R_{max,s}$ before decreasing gradually to the outer region. And an obvious rise trend of eddy viscosity can be noticed with the increase of height. The maximum eddy viscosity at 10 m is $12.23 \text{ m}^2/\text{s}$. As expected, 10-m results in Fig. 2.7(b)-(c) have maximum radial and tangential decay wind speeds. And tangential decay wind speeds suffer a more rapid decrease with height than radial decay wind speeds which is consistent with Fig. 2.6(a)-(b). The wind directions in Fig. 2.7(d) turn toward the low-pressure center and suffer a slight increase with height.

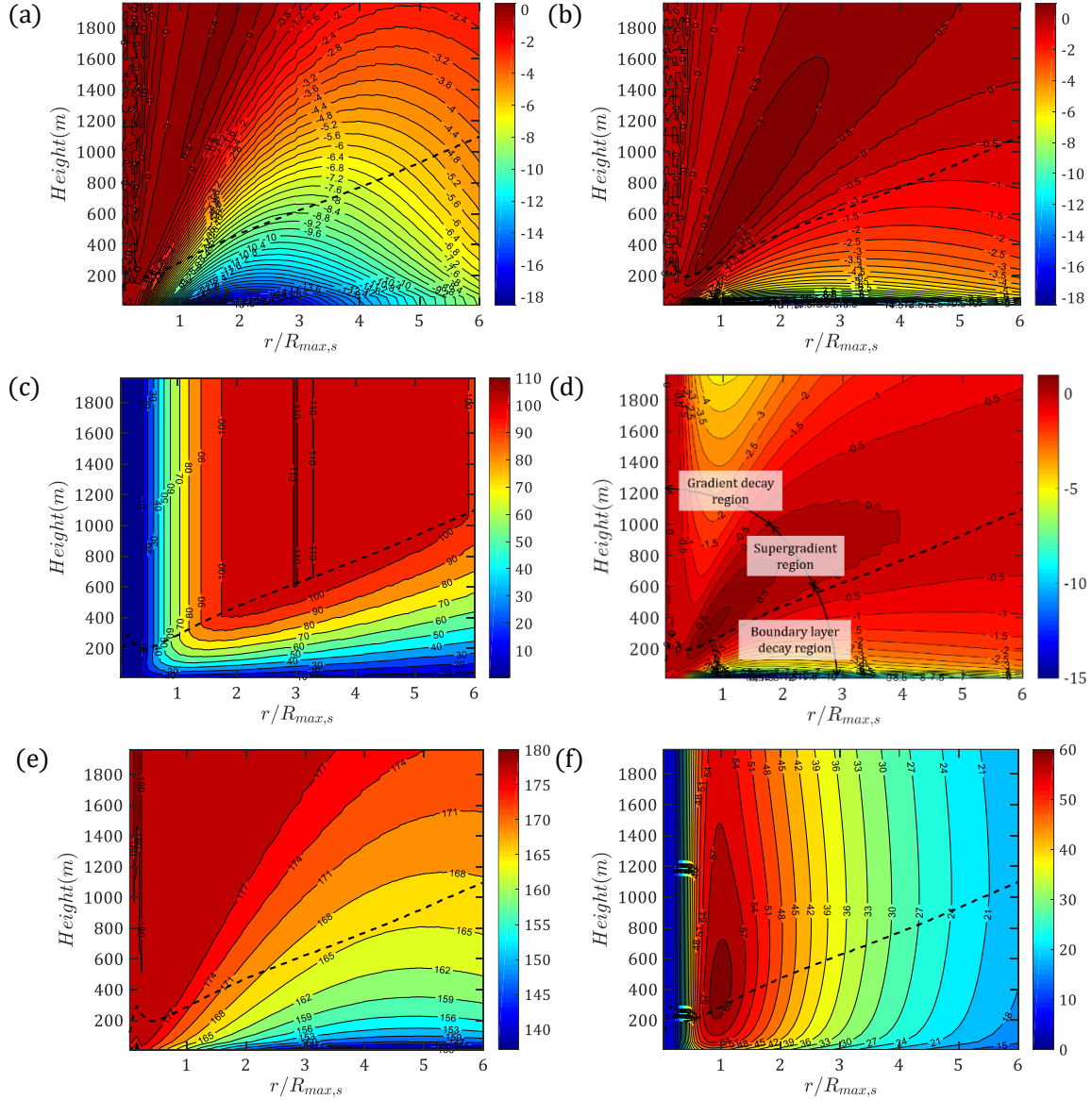


Fig. 2.6 Vertical wind field (Eastern slice) of a synthetic typhoon ($\Delta P_s = 80hPa, B_s = 1.5, R_{max,s} = 50km, z_0 = 0.0002m, c = 5 m/s, \theta_0 = 120^\circ$): (a) Radial decay wind speed u_d (m/s); (b) Tangential decay wind speed v_d (m/s); (c) Eddy viscosity K (m^2/s); (d) Velocity difference between gradient height and other heights $V_z - V_{GH}$ (m/s); (e) Wind direction α ($^\circ$); (f) Wind speed V_z (m/s). The black dash line is the gradient height.

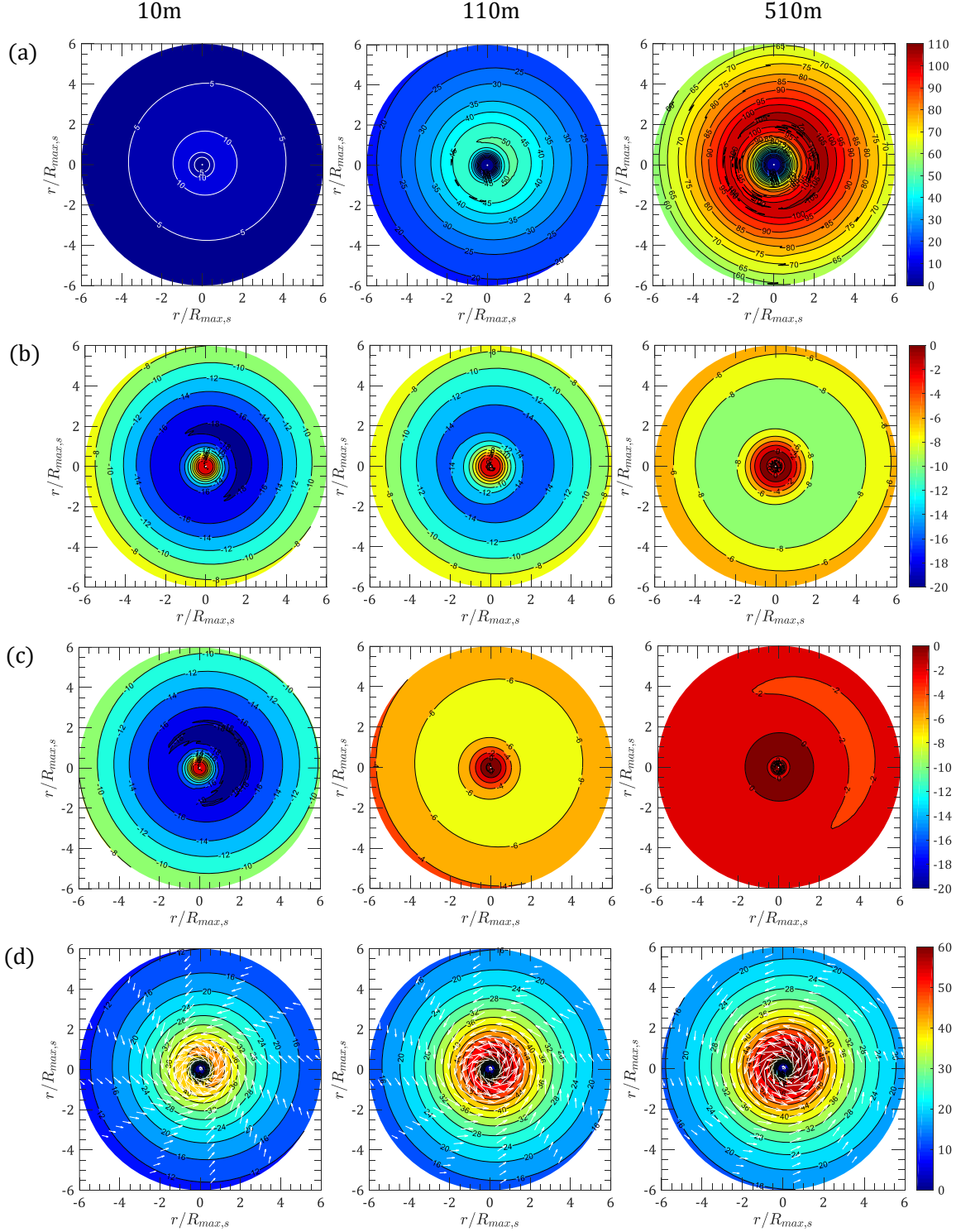


Fig. 2.7 Horizontal wind field of a synthetic typhoon ($\Delta P_s = 80hPa$, $B_s = 1.5$, $R_{max,s} = 50km$, $z_0 = 0.01m$, $c = 5 m/s$, $\theta_0 = 120^\circ$): (a) Eddy viscosity K (m^2/s); (b) Radial decay wind speed u_d (m/s); (c) Tangential decay wind speed v_d (m/s); (e) Wind speed V_z (m/s). White arrows in wind speed contours indicate wind direction.

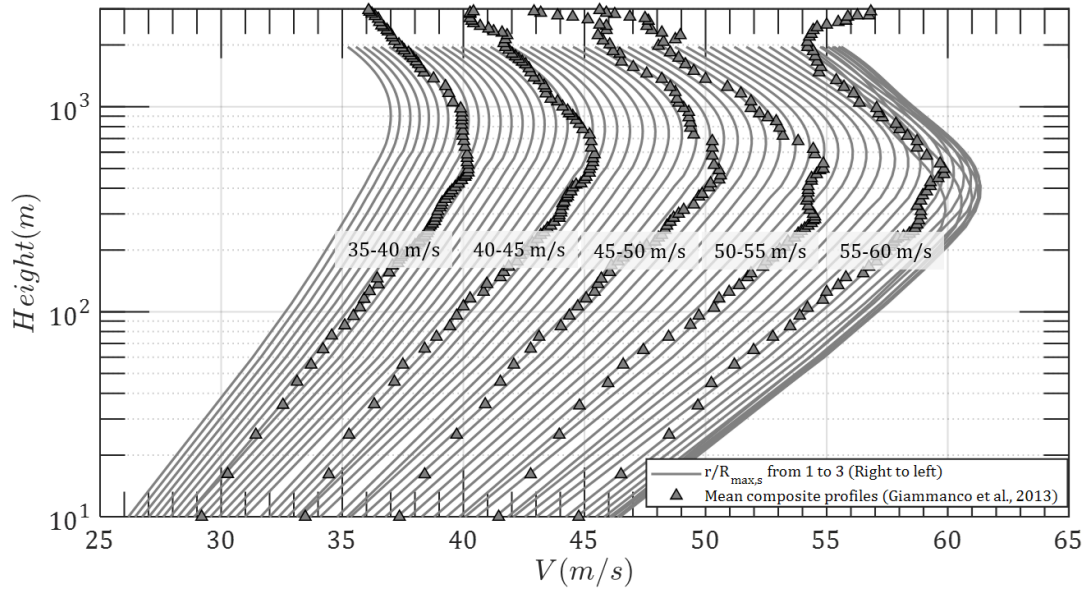


Fig. 2.8 Comparison of vertical profiles between the synthetic typhoon and observations

The vertical profiles in the eastern direction within the radius range of $r/R_{max,s} = 1\sim 3$ of the synthetic typhoon are illustrated in Fig. 2.8, which are compared with the five mean composite wind profiles for various mean boundary layer (MBL) groups analyzed by Giammanco et al. (2013). Owing to the rotation of the typhoon storm, it is difficult to capture the vertical wind profile at a specific location of a real typhoon. An alternative widely employed approach was proposed by Powell et al. (2003), using a composite sense to obtain a normalized profile, i.e. mean boundary layer (MBL). The composite wind profiles in Giammanco's study were developed using a large number of GPS dropsondes profiles and radar-derived profiles through velocity–azimuth display (VAD) technique. They were stratified by the MBL wind speed with 5 m/s bin size for dropsondes data and 10 m/s bin size for VAD profiles. It can be noted that the present wind field model well reproduces the vertical profiles. The location of maximum wind increases from about 400 m to 1,000m from radius of $R_{max,s}$ to $3R_{max,s}$. Since the composite profile is a representation of a group of observed wind profiles with a similar MBL wind speed, which is almost impossible to be

completely matched by the vertical profile of a synthetic typhoon. And the fluctuations of composite profiles are not taken into account in Fig. 2.8. Generally, the proposed wind field model has good performance on the reconstruction of typhoon inner wind structures.

2.5 Model validation with observed typhoons

Specifically, three strong typhoons, Hagupit in 2008, Haiyan in 2013 and Rammasun in 2014, are selected as examples to figure out their inner structure and compare them with some observations. The parameters of B and R_{max} are estimated from JMA surface wind observations, more details will be present in next chapter. As illustrates in Fig. 2.9, three surface wind speed snapshots are simulated together with satellite-based six-hourly multi-platform tropical cyclone surface wind analysis (MTCSWA, 2018) products developed by NOAA (Knaff and Demaria, 2006). This product combines information from five data sources (the ASCAT scatterometer, feature track winds from the operational satellite centers, 2-d flight-level winds estimated from infrared imagery and 2-d winds created from Advanced Microwave Sounding Unit and the QuickSCAT scatterometer) to create a mid-level (near 700 hPa) wind analysis using a variational approach described in Knaff and DeMaria (2006) before the surface winds were generated applying a very simple single column approach. Over the ocean an adjustment factor is applied, which is a function of radius from the center ranging from 0.9 to 0.7, and the winds are turned 20 degrees toward low pressure. Overland, the oceanic winds are reduced by an additional 20% and turned an additional 20 degrees toward low pressure. Since the MTCSWA surface winds are defined with the time duration of 1 min while JMA provides 10-min-time-averaging track information, a converting factor of 1.24 (Vickery et al., 2005; Cao et al., 2015) is employed to adjust wind speeds from 10 min

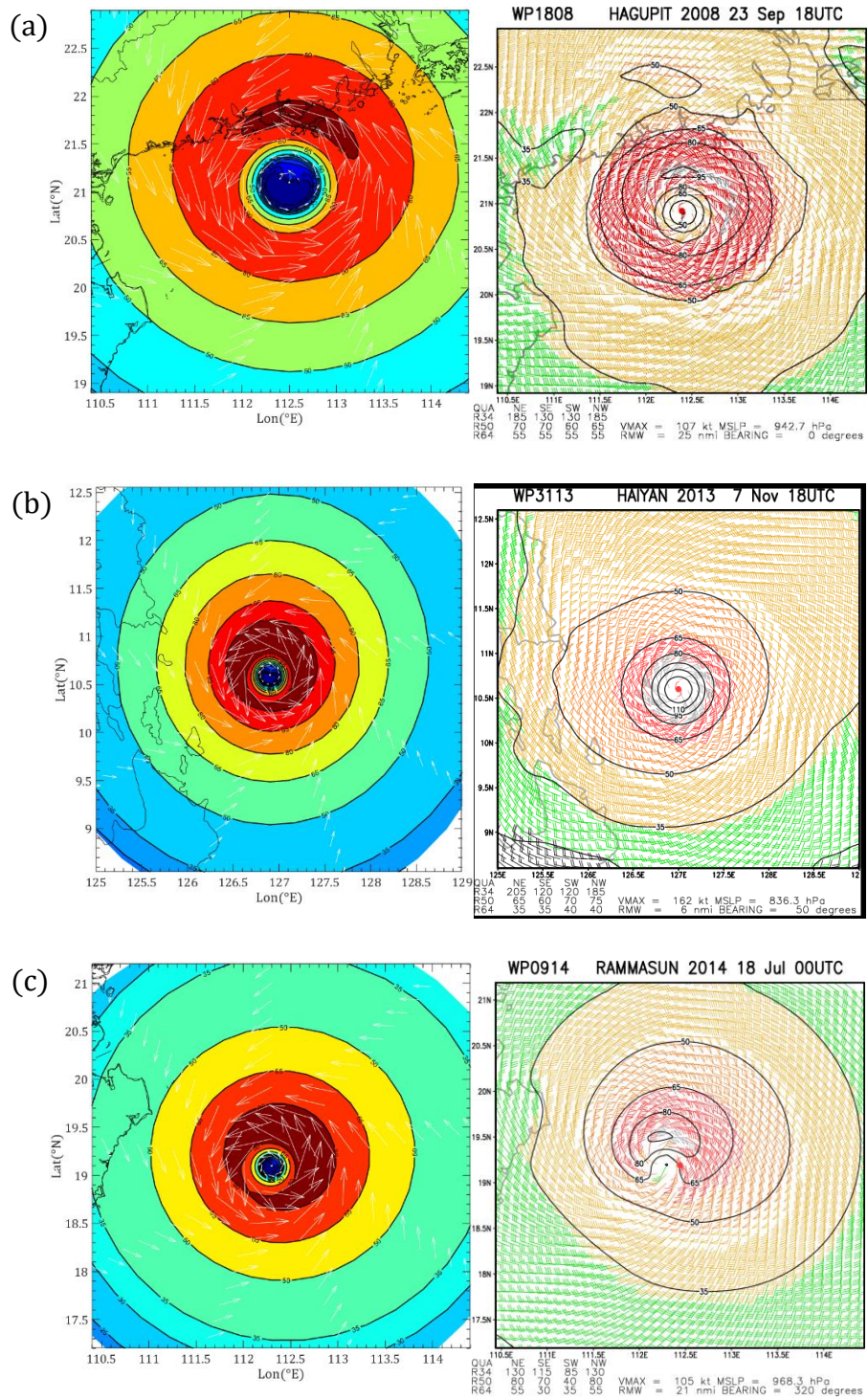


Fig. 2.9 Comparison of surface wind speed snapshots with MTCSWA : (a) Hagupit (JMA: $P_{cs} = 935$ hPa, $\theta_T = 76.26^\circ$ (CCW from N), $B_s = 1.72$, $R_{max,s} = 88$ km (47.52 nmi), $V_{max} = 90$ kt); (b) Haiyan (JMA: $P_{cs} = 895$ hPa, $\theta_T = 78.83^\circ$ (CCW from N), $B_s = 1.60$, $R_{max,s} = 40$ km (21.60 nmi), $V_{max} = 125$ kt) ; (c) Rammasun (JMA: $P_{cs} = 940$ hPa, $\theta_T = 48.85^\circ$ (CCW from N), $B_s = 1.28$, $R_{max,s} = 47$ km (25.38 nmi), $V_{max} = 85$ kt)

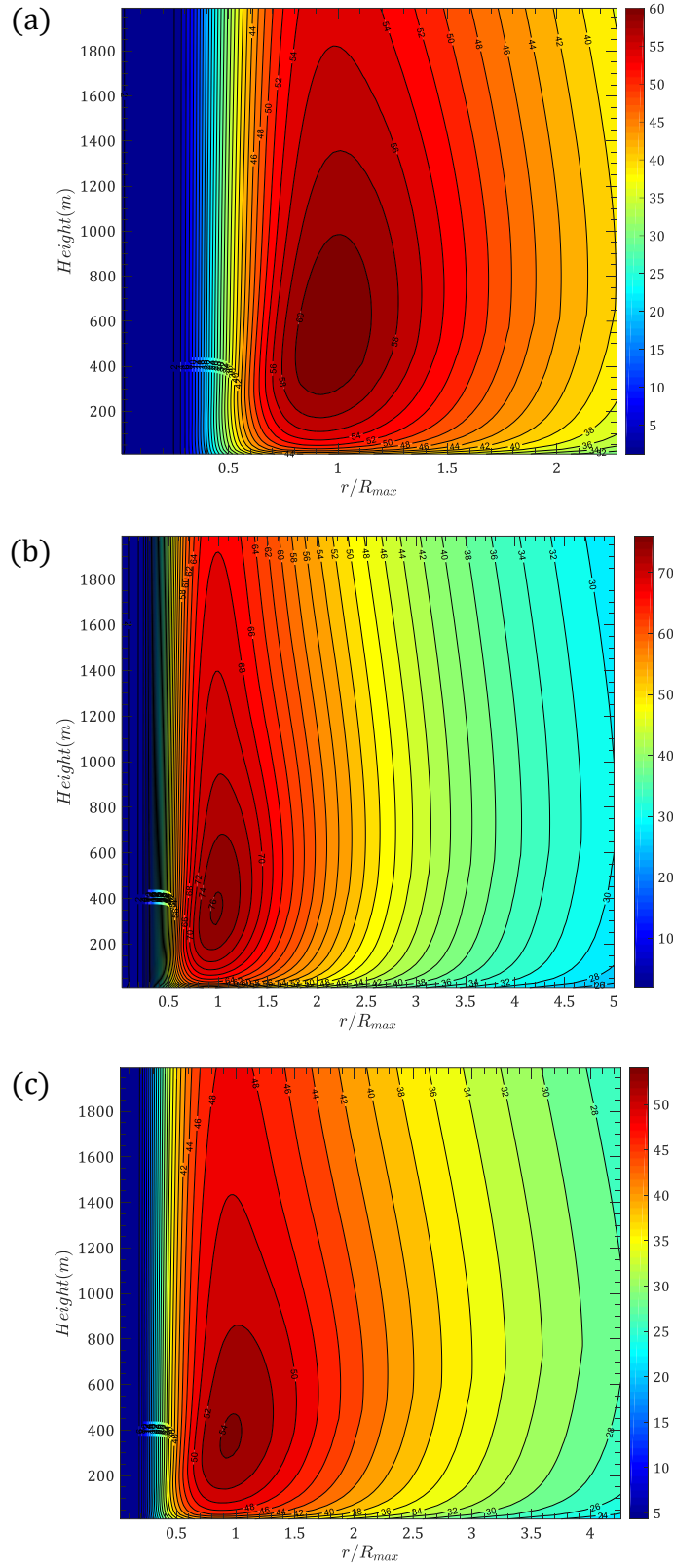


Fig. 2.10 Vertical wind field (Eastern profiles, m/s): (a)Hagupit; (b)Haiyan;(c)Rammasun

to 1 min. Coincidentally, the mean ratio of surface sustained maximum wind speeds V_{max} between MTCSWA and JMA data in Fig. 2.9 are also 1.24. It can be noted that the R_{max} estimated from JMA data are slightly larger than that of MTCSWA, but the surface wind speed fields match well.

Furthermore, the vertical wind speed fields in the eastern direction of these three typhoons are also illustrated in Fig. 2.10. The maximum wind speed region occurs at the radius of R_{max} and height of 200 m~800 m while the eye center region is close to no winds. An obvious super-gradient height region can be observed at which the wind speeds reach the maximum, which is a transition area between boundary layer and upper free atmosphere. Moreover, the vertical wind speed profiles at different locations are extracted to facilitate the interpretation of vertical wind distributions, as shown in Fig 2.11. Two sub-regions, near the eyewall ($r/R_{max} = 0.8\sim 1.2$) and outer vortex ($r/R_{max} = 2.0\sim 3.0$) are divided and vertical wind profiles in 12 directions (black dots in Fig 2.11a) are extracted for previous three wind speed snapshots. As illustrated in Fig 11b~c, the normalized mean boundary layers analyzed from flight-level dropsonde data by Powell et al. (2003), Franklin et al. (2003) and Giammanco et al. (2013) are adopted to compare with the simulated results. A pronounced super-gradient region characterized by a wind maximum can be observed both in the eyewall and outer vortex. The wind speeds increase logarithmically from surface to the super-gradient height, whereas a decrease can be noted above the super-gradient region due to the decrease of central pressure difference as well as the radial pressure gradient. And the height of super-gradient winds or maximum winds increases from the typhoon center to outer region. Generally, the simulated vertical wind profiles are well in agreement with the observed mean boundary layer winds.

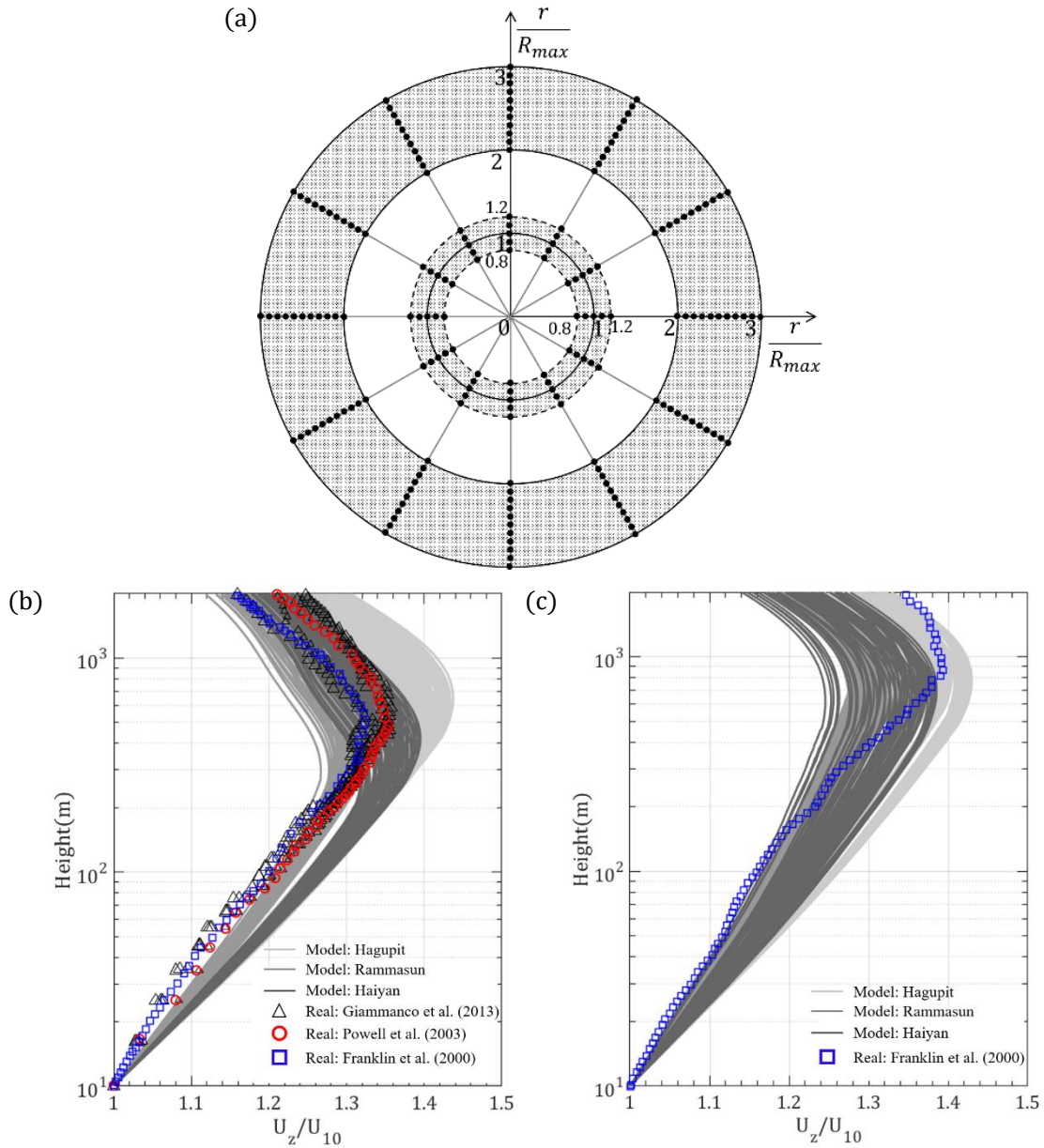


Fig. 2.11 Vertical wind profiles: (a)Locations; (b)Near eyewall;(c) Outer vortex

2.6 Conclusion

A height-resolving typhoon boundary layer model, including a parametric pressure model and an analytical wind model, was developed using a scale analysis technique. And an algorithm for solving the wind field at gradient and boundary layers was proposed. The spatial distribution characteristics of the eddy viscosity as well as various wind components,

i.e. wind speed along radial and tangential directions are analyzed. A couple validations with respect to surface wind speed field and vertical wind profiles are conducted. Several conclusions can be drawn as follows:

(1) The variation of pressures at different heights has a significant influence on the decrease of pressure deficit of a typhoon storm, which would directly affect the wind distribution at different height, i.e. vertical wind profiles. The height-resolving pressure model well reproduces the pressure field of the storm, facilitating the solution of the wind field at free atmosphere above the boundary layer.

(2) The eddy viscosity plays an essential role in determining the distribution of the wind field in typhoon boundary layer. A constant eddy viscosity would result in unreal wind predictions at low-level boundary layers. The use of mixing length hypothesis to model the eddy viscosity is able to overcome this shortcoming, providing a good estimation of typhoon winds at boundary layer.

(3) Three sub-regions can be observed from typhoon vertical wind field according to the difference between calculated wind speed at different heights and gradient wind speed, say boundary layer decay region, supergradient region and gradient decay region. The wind speed in the boundary layer decay region is smaller than gradient wind speed due to the effects of underlying roughness effects whereas the gradient decay region results from the variation of pressure and moisture fields along the height. The wind speeds at middle supergradient region are higher than that of at gradient height. And gradient height is observed to gradually increase from the storm's center to outer region.

(4) The present typhoon wind field is able to reproduce the typhoon wind field at different heights, providing a reliable and rapid estimation of typhoon vertical wind profiles. The

satellite-based surface wind analysis results, as well as dropsonde-based composite vertical profiles, are compared with the reconstruction winds of three typhoons using present model, showing good agreements with each other. It can thus be helpful in hazard modelling for typhoon-prone areas, especially for engineering applications in the low-level boundary layer.

2.7 Reference

Broxton, P. D., Zeng, X., Sulla-Menashe, D., & Troch, P. A., (2014). A global land cover climatology using MODIS data. *Journal of Applied Meteorology and Climatology*, 53(6), 1593-1605.

Bryan, G. H., Worsnop, R. P., Lundquist, J. K., & Zhang, J. A., (2017). A simple method for simulating wind profiles in the boundary layer of tropical cyclones. *Boundary-Layer Meteorology*, 162(3), 475-502.

Batts, M. E., Russell, L. R., & Simiu, E., (1980). Hurricane wind speeds in the United States. *Journal of the Structural Division*, 106(10):2001-2016.

China Meteorological Administration, (1949-2015). *Tropical Cyclone Annuals*. Beijing: China Meteorological Press (in Chinese).

Franklin, J. L., Black, M. L., & Valde, K., (2003). GPS dropwindsonde wind profiles in hurricanes and their operational implications. *Weather and Forecasting*, 18(1), 32-44.

Giammanco, I. M., Schroeder, J. L., & Powell, M. D., (2012). Observed characteristics of tropical cyclone vertical wind profiles. *Wind and Structures: An International Journal*, 15 (1), 65-86.

Giammanco, I. M., Schroeder, J. L., & Powell, M. D., (2013). GPS dropwindsonde and WSR-88D observations of tropical cyclone vertical wind profiles and their characteristics. *Weather and Forecasting*, 28(1), 77-99.

He, Y. C., Chan, P. W., & Li, Q. S., (2013). Wind profiles of tropical cyclones as observed by doppler wind profiler and anemometer. *Wind and Structures: An International Journal*, 17(4).

He, Y. C., Chan, P. W., & Li, Q. S., (2016). Observations of vertical wind profiles of tropical cyclones at coastal areas. *Journal of Wind Engineering and Industrial Aerodynamics*, 152, 1-14.

Holland, G. J., (1980). An analytic model of the wind and pressure profiles in hurricanes. *Mon. Weather Rev.*, 108(8), 1980, 1212-1218.

Holton, J. R., & Staley, D. O., (2004), *An Introduction to Dynamic Meteorology*, fourth edition. Academic Press.

Huang, W., Xu, Y., (2012), A refined model for typhoon wind field simulation in boundary layer. *Advances in Structural Engineering*, 15(1):77-89.

Keper, J., (2001), The dynamics of boundary layer jets within the tropical cyclone core. Part I: linear theory. *J. Atmos. Sci.*, 58(58), 2469-2484.

Keper, J. D., (2010) Slab- and height-resolving models of the tropical cyclone boundary layer. Part I: comparing the simulations. *Q. J. Roy. Meteor. Soc.*, 136(136), 1686-1699.

Li, L., Kareem, A., Xiao, Y., Song, L., & Qin, P., (2012). Wind Profile and Spectra in Typhoon-Prone Regions in South China. *ATC & SEI Conference on Advances in Hurricane Engineering*.

Meng, Y., Matsui, M., & Hibi, K., (1995), An analytical model for simulation of the wind field in a typhoon boundary layer. *J. Wind Eng. & Ind. Aerodyn.*, 56(2-3), 291-310.

Meng, Y., Matsui, M., & Hibi, K., (1997), A numerical study of the wind field in a typhoon boundary layer. *J. Wind Eng. & Ind. Aerodyn.*, 67-68(97), 437-448.

Montgomery, M. T., Snell, H. D., & Yang, Z., (2001). Axisymmetric spindown dynamics of hurricane-like vortices. *Journal of the Atmospheric Sciences*, 58(5), 421-435.

Powell, M. D., Vickery, P. J., & Reinhold, T. A., (2003). Reduced drag coefficient for high wind speeds in tropical cyclones. *Nature*, 422(6929), 279-283.

Russell, L., & Schueller, G., (1974), Probabilistic Models for Texas Gulf Coast Hurricane Occurrences. *Journal of Petroleum Technology*, 26(26):279-288.

Satoh M, (2014), *Atmospheric Circulation Dynamics and General Circulation Models (Second Edition)*. New York: Springer.

Shu, Z. R., Li, Q. S., He, Y. C., & Chan, P. W., (2017). Vertical wind profiles for typhoon, monsoon and thunderstorm winds. *Journal of Wind Engineering and Industrial Aerodynamics*, 168, 190-199.

Snaiki R., & Wu T., (2016). Temperature and moisture effects on the tropical cyclone boundary layer: Pressure and wind field. 8th International Colloquium on Bluff Body Aerodynamics and Applications, Boston, Massachusetts, USA.

Snaiki R., & Wu T., (2018). A semi-empirical model for mean wind velocity profile of landfalling hurricane boundary layers. *Journal of Wind Engineering and Industrial Aerodynamics*, 180, 249-261.

Tsai, Y. S., Miao, J. J., Yu, C. M., & Chang, W. T., (2019). Lidar observations of the typhoon boundary layer within the outer rainbands. *Boundary-Layer Meteorology*.

Vickery, P. J., & Twisdale, L. A., (1995). Wind-Field and Filling Models for Hurricane Wind-Speed Predictions. *Journal of Structural Engineering*, 121(11):1700-1709.

Vickery, P. J., Skerlj, P. F., & Twisdale, L. A., (2000). Simulation of Hurricane Risk in the U.S. Using Empirical Track Model. *Journal of Structural Engineering*, 126(10):1222-1237.

- Vickery, P. J., Skerlj, P. F., Steckley, A. C., & Twisdale, L. A., (2000). Hurricane wind field model for use in hurricane simulations. *J. Struct. Eng.*, 126(10), 1203-1221.
- Vickery, P. J., & Wadhera, D., (2008). Statistical Models of Holland Pressure Profile Parameter and Radius to Maximum Winds of Hurricanes from Flight-Level Pressure and H*Wind Data. *Journal of Applied Meteorology & Climatology*, 47(10):2497-2517.
- Vickery, P. J., Masters, F. J., Powell, M. D., & Wadhera, D., (2009). Hurricane hazard modeling: the past, present, and future. *J. Wind Eng. & Ind. Aerodyn.*, 97(7), 392-405.
- Xiao, Y. F., Duan, Z. D., Xiao, Y. Q., Ou, J. P., Chang, L., & Li, Q. S., (2011). Typhoon wind hazard analysis for southeast china coastal regions. *Struct. Saf.*, 33(4-5), 286-295.
- Zhao, L., Lu, A., Zhu, L., Cao, S., & Ge, Y., (2013). Radial pressure profile of typhoon field near ground surface observed by distributed meteorologic stations. *J. Wind Eng. & Ind. Aerodyn.*, 122(11), 105-112.
- Zhao, L., Pan, J. J., Liang, X. D., Song, L. L., Zhu, L. D. & Ge, Y. J., (2016). Characteristics of mean wind profile near flat ground at and inside the periphery of strong typhoons during landfall. *China Civil Engineering Journal*, 49(8), 46-51. (in Chinese)
- Zhao, L., Yang, X. N., Fang, G. S., Cui, W., Song, L. L., & Ge, Y. J., (2019). Observation-based study for the evolution of vertical wind profiles in the boundary layer during super typhoon Mangkhut. *Acta Aerodynamica Sinica*, 37(1): 43-54 (in Chinese).

CHAPTER 3 TOWARD A REFINED ESTIMATION OF TYPHOON WIND: PARAMETRIC MODELLING AND UPSTREAM TERRAIN EFFECTS

3.1 Background

Typhoon or hurricane (typhoon hereafter is a general representation of tropical cyclone unless otherwise stated), which is a large-scale air rotating system around a low atmospheric pressure center, frequently causing devastating economic loss and human casualties along coastal regions due to violent winds, heavy rainfall, massive storm surges, flash flooding or even landslides in mountainous areas. The coastal region of China, which is characterized by high population densities and highly developed cities, is always exposed to typhoon threats with 7~8 landfall typhoons every year since Northern Pacific Basin is the most active typhoon basin on earth, accounting for almost one-third of global annual storms. It was estimated that averaged 472 people lost their lives and annual direct economic loss reached 28.7 billion RMB as a result of landfall typhoons from year 1983 to 2016 in China ([Zhang et al., 2009](#)), which are expected to rise because of growing population and increasing wealth in coastal regions as well as the potential increase of typhoon frequency and intensity due to climate change. Consequently, it is of great importance to investigate the characteristics of typhoon wind field and predict the potential typhoon-induced hazards to facilitate the disaster prevention and mitigation.

The quantification of typhoon boundary layer with the depth about 2~3 km, within which we live and carry out most human activities, has received intensive attention in past several decades ([Batts et al., 1980](#); [Meng et al., 1995](#); [Vickery et al., 2000, 2009](#); [Kepert, 2010](#); [Snaiki and Wu, 2017](#); [Fang et al., 2018](#)) for the uses of engineering applications and wind hazard

estimations. And parametric typhoon boundary layer model was commonly adopted for its high efficiency on Monte Carlo simulations by generating a large number of scenarios as well as its continuous updates and improvements with the help of the abundance of measurement data. Recent years, the ever-increasing observation data have enabled a further investigation on typhoon inner structures. Taking the advantages of flight-level aircraft and dropsondes measurements in Atlantic Basin, a series of pioneering studies have been conducted to examine the characteristics of two typical typhoon field parameters, say the radius to maximum wind speed (R_{max}) and radial pressure profile shape parameter (B), and model them with some statistically-based equations for the convenience of stochastic simulations (Powell et al., 2005; Vickery and Wadhera, 2008). Recently, several parameter models have also been successively developed in Western Pacific region using observation data (Xiao et al., 2011; Zhao et al., 2013; Fang et al., 2018).

However, several issues remain to be discussed about these two parameters with respect to their height-variation, region-dependent and time duration characteristics. Conventionally, both the upper-level reconnaissance and surface observation data were applied to the wind speed formula derived from the cyclostrophic balance of the free atmosphere to estimate R_{max} and B , which are neither suitable to be employed in height-resolving typhoon wind model (Snaiki and Wu, 2017; Fang et al., 2018) nor useful for understanding wind distribution within the boundary layer. Moreover, as discussed by Willoughby et al. (2004), it showed that the mean value of R_{max} would increase slightly with height while B witnessed a 45% increase from the altitude about 750 m to 2500 m based on a flight-level database. Holland et al. (2010) also tried to revise the pressure-wind model by addressing the differences between surface and gradient layers. In addition, these typhoon field parameters

are usually region-dependent due to the difference of atmospheric circulation features, which means the cross-adoption of these parameter models could result in some unreasonable predictions. Furthermore, the agency-specified wind speed averaging period varies considerably (from 1 min to 10 min), resulting in the difference of central pressure estimation based on Dvorak method (Dvorak, 1984; Velden et al., 2006), which could be extended to the misunderstanding of R_{max} and B during their extractions and applications. Another issue is that the previous statistical models of R_{max} and B were always formulated as the function of central pressure deficit, typhoon center latitude and sea surface temperature T_s , the autocorrelations between different time steps were not fully taken into account which are usually propagated from the central pressure deficit, and sea surface temperature T_s during empirical full track simulations. This could result in the storm size and distribution of wind speed fluctuate notably with time steps, which is inconsistent with the real cases.

It is noteworthy that most present parametric wind field models are simplified from Navier-Stokes equations, i.e. several nonlinear terms and non-symmetric characteristics are customarily eliminated. If the Holland parametric pressure model described by R_{max} and B is derived from real pressure observations, the pressure field would be well reconstructed. But it could lead to unreal wind field due to the use of simplified model solutions. Alternatively, if R_{max} and B are extracted from the fitting results of real winds, the modeled wind field would be as close to the reality as possible regardless of whether the pressure field is real or unreal. This can be achieved using the archived wind information in some best track dataset, such as HURDAT2 in Atlantic Basin and RSMC Best Track Data in Northwestern Pacific Ocean provided by Japan Meteorological Agency. It also allows the consideration of

autocorrelations R_{max} and B between different time steps to better conduct the stochastic simulations of wind hazard. Moreover, the evolutions of wind speed for each historical typhoon event could be reconstructed to facilitate the typhoon hazard assessment and mitigation.

In this study, R_{max} and B at surface level would be optimally fitted with a high-resolving typhoon boundary layer wind field model by employing the JMA best track dataset to better estimate typhoon wind hazards over coastal regions. The correlations between multiple typhoon field parameters would be investigated before the development of recursive models for R_{max} and B accounting for the autocorrelations with previous time steps. After that, the wind hazards of historical typhoon events were reconstructed. The upstream roughness and topographic effects for sites of interest would be quantitatively estimated with a directional equivalent roughness length and a topographic speed-up factor.

3.2 Typhoon parametric modelling

3.2.1 Parametric pressure modelling

The typhoon's surface pressure profile along the radial direction from storm center is always prescribed before solving the pressure term of Navier-Stokes equations in an analytical wind field model, which is of great importance for determining the wind field distributions. Holland (1980) described the radial surface pressure of a typhoon with two typical parameters, i.e. the radius to maximum wind speed ($R_{max,s}$) and a shape parameter of pressure profile (B_s) with the form of

$$P_{rz} = P_{cs} + \Delta P_s \cdot \exp \left[- \left(\frac{R_{max,s}}{r} \right)^{B_s} \right] \quad (3.1)$$

in which subscripts r, z and s denote values at the radius of r , height of z and surface, respectively, P_{rs} = surface air pressure at radius of r from the typhoon's axis (hPa), P_{cs} = central pressure (hPa), $\Delta P_s = P_{ns} - P_{cs}$ is the central pressure difference (hPa). Although this two-parameter model is unable to produce the azimuthal and radial variation of the pressure field and sometimes fails to simulate the highly-asymmetric traits of a typhoon (Vickery and Wadhwa, 2008), it is still shown to perform exceptionally well in most cases and its operational convenience enables the rapid estimation of typhoon hazard by generating many statistical scenarios with Monte Carlo algorithm. In order to explicitly reveal the height-varying characteristics of typhoon pressures and quantify the pressure distribution above the typhoon gradient layer to facilitate the construction of height-resolving wind model, the Holland surface pressure model would be extended to vertical direction with the gas state equation accounting for the effects of temperature and moisture. Thus, a height-resolving parametric typhoon pressure field model is developed as

$$P_{rz} = \left\{ P_{cs} + \Delta P_s \cdot \exp \left[- \left(\frac{R_{max,s}}{r} \right)^{B_s} \right] \right\} \cdot \left(1 - \frac{gkz}{R_d \theta_v} \right)^{\frac{1}{k}} \quad (3.2)$$

$$T_z = T_s - \tau \cdot z \quad (3.3)$$

$$\theta_v = T_v (P_s / P_z)^k \approx (1 + 0.61q)(T_z + 273.15) + \frac{kgz}{R_d} \quad (3.4)$$

$$k = \frac{R}{c_p} = \frac{R_d(1 + 0.61q)}{c_{pd}(1 + 0.86q)} = \frac{2(1 + 0.61q)}{7(1 + 0.86q)} \quad (3.5)$$

$$q = RH \cdot \frac{3.802}{100P_z} \cdot \exp \left(\frac{17.67T_z}{T_z + 243.5} \right) \quad (3.6)$$

$$T_s = SST - 1 \text{ or } T_s = 28 - \frac{3(\phi - 10)}{20} \quad (3.7)$$

in which $g = 9.8$ N/kg is the gravitational acceleration, $R_d = 287$ J/kg/K is the specific gas constant of dry air, θ_v = virtual potential temperature (K), q = specific humidity (kg/kg), τ

= temperature lapse rate (0.0065K/m), z = elevation (m), RH = relative humidity (90%), R = specific gas constant of moist air (J/K/kg), c_p = specific heat at constant pressure, T_s = surface air temperature (°C), SST = sea surface temperature (°C), and ϕ = latitude (°).

3.2.2 Height-resolving wind speed modelling

Wind speeds in the typhoon boundary layer are decomposed into radial and tangential winds as u and v , which are treated as the sum of gradient winds ($U_g = 0, V_g$) and decay winds (u_d, v_d) caused by the frictional effects

$$u = u_d \quad (3.8)$$

$$v = V_g + v_d \quad (3.9)$$

The gradient wind is solved as

$$V_g = \frac{V_{T\theta} - fr}{2} + \sqrt{\left(\frac{V_{T\theta} - fr}{2}\right)^2 + \frac{r}{\rho_g} \frac{\partial P_g}{\partial r}} \quad (3.10)$$

The decay winds in the boundary layer are expressed as

$$u_d = e^{-\lambda z'} \eta [D_1 \sin(\lambda z') - D_2 \cos(\lambda z')] \quad (3.11)$$

$$v_d = e^{-\lambda z'} [D_1 \cos(\lambda z') + D_2 \sin(\lambda z')] \quad (3.12)$$

$$\lambda = \sqrt[4]{\xi_g \xi_{ag} / \sqrt{2K}} \quad (3.13)$$

$$\eta = \sqrt{\xi_g / \xi_{ag}} \quad (3.14)$$

$$\xi_g = 2V_g / r + f \quad (3.15)$$

$$\xi_{ag} = V_g / r + f \quad (3.16)$$

in which K is the eddy viscosity (m^2/s) determined from the local vertical deformation or shear absolute magnitude (S_v) by considering mixing length hypothesis as

$$K = l_v^2 S_v \quad (3.17)$$

$$S_v^2 = \left(\frac{\partial u}{\partial z}\right)^2 + \left(\frac{\partial v}{\partial z}\right)^2 \quad (3.18)$$

The vertical mixing length l_v is formulated with an upper bound of l_∞ ($\sim 1/3$ boundary layer depth in a neutral atmospheric condition as suggested by Apsley (1995)) as

$$l_v = \left(\frac{1}{\kappa(z + z_0)} + \frac{1}{l_\infty}\right)^{-1} \quad (3.19)$$

in which κ is the von Kármán constant, empirically determined to be about 0.4. Coefficients D_1 and D_2 are determined by the slip boundary condition as

$$\rho_s K \frac{\partial \mathbf{V}_h}{\partial z} \Big|_{z'=0} = \rho_s C_d |\mathbf{V}_h| \mathbf{V}_h \Big|_{z'=0} \quad (3.20)$$

$$C_d = \kappa^2 / \{\ln[(h + z_{10} - d)/z_0]\}^2 \quad (3.21)$$

$$h = 11.4z_0^{0.86} \quad (3.22)$$

$$d = 0.75h \quad (3.23)$$

Coefficients D_1 and D_2 are solved by the formulas

$$D_1 = (V_g \cos \alpha - V_T / \sqrt{2}) / \sqrt{2} \quad (3.24)$$

$$D_2 = (V_g \sin \alpha - V_T / \sqrt{2}) / \sqrt{2} \quad (3.25)$$

in which $V_{T\theta} = -V_T \cdot \sin(\theta - \theta_T)$, V_T is the translation speed (m/s), θ_T and θ are the translation direction and the direction of interest (counterclockwise positive from the east, °), f is the Coriolis force, ρ_g (kg/m^3) and P_g (hPa) are the air density and pressure at the gradient layer, K is the turbulence exchange coefficient, $\rho_s = 1.2 kg/m^3$ is the surface air density, C_d is the drag coefficient, h indicates the mean height of roughness elements (m), z_0 is the equivalent roughness length accounting for upstream terrain effects (m), d denotes the zero-plane displacement, α is an undetermined parameter by solving Eq. (3.19) by a dichotomy method in the domain of $(\pi/4, 3\pi/4)$. It is noteworthy that the wind gradient

term $\partial V_g / \partial r$ used in ξ_{ag} (Eq. (3.15)) by Fang et al. (2018) is removed here. This is because $\partial V_g / \partial r$ would be negative in the rapid decay region when some large B_s are used to reproduce the surface winds. Then ξ_{ag} could be negative and η (Eq. (3.13)) would be a complex number. In fact, the omission of $\partial V_g / \partial r$ have an insignificant effect on the wind speed field. Moreover, the optimally fitted pairs of $R_{max,s}$ and B_s are able to cover the errors induced by the simplification of wind field model to well reproduce the observed wind field. This will be discussed in the following section. The typhoon wind field is solved in a cylindrical coordinate (r, θ, z) , and the base of the computation domain $z' = 0$ is set at $h + z_{10}$, in which z_{10} is 10 m height above h .

3.3 Estimation of model parameters

3.3.1 Description of JMA best-track dataset

In western North Pacific and the South China Sea ($0^\circ \sim 60^\circ \text{N}$, $100^\circ \sim 180^\circ \text{E}$), the Japan Meteorological Agency (JMA) was designated by the World Meteorological Organization (WMO) as the responsible agency to provide information on typhoons to support disaster mitigation activities. JMA publicly releases the best track dataset of typhoons in its responsible area from the year of 1951 to date (JMA, 1951-2017), which contains the following information recorded at a 6- 3- or 1-hour interval for each storm: (1) storm time step and location, expressed in terms of latitude and longitude of the storm eye; (2) minimum sea level pressure (central pressure, P_{cs}); (3) estimated 10-minute-averaged maximum sustained wind speed (V_{max}); (4) direction and distance of the longest radius of 50 knots winds or greater (R_{50}); (5) direction and distance of the longest radius of 30 knots winds or greater (R_{30}), as shown in Fig. 1. The central pressure as well as the maximum

sustained wind speed in the vicinity of the center are mainly determined by the current intensity (CI) number, which is derived from the satellite imagery using the Dvorak method (Dvorak, 1984; Velden et al., 2006). The radii with the wind speeds larger than 30 and 50 knots are reproduced from the surface observation, ASCAT observation and low-level cloud motion satellite images. Before 1970s, the typhoon location and intensity are primarily estimated by aircraft reconnaissance coupled with some radar observations due to the immature satellite technology for detecting the typhoon-related information. After 1971, the satellite-derived typhoon reconnaissance data were becoming used operationally to locate the typhoon center and determine the intensity with the advancement of Dvorak technique. Since 1977, the wind information including V_{max} together with R_{50} and R_{30} have been recorded with Dvorak technique and supplemented into best track dataset by JMA.

Some other agencies, including the China Meteorological Administration (CMA), Joint Typhoon Warning Center (JTWC) and the Hong Kong Observatory (HKO) also issue the best-track dataset of TCs for Western Pacific Basin (Ying et al., 2014). And they have been consolidated and documented by the International Best Track Archive for Climate Stewardship (IBTrACS) project (Knapp et al., 2010). However, some inconsistencies among these datasets should be carefully considered. In addition to the differences of storm track information (eye location) and annual frequencies, the storm intensity in term of V_{max} or P_{CS} show discrepancies due to the use of different averaging period during the wind speed estimation. The US agencies (NOAA and JTWC) use the 1-min time direction while CMA and JMA adopt 2 min and 10 min, respectively. But it was found that there was no simple global conversion between these wind speeds (Knapp et al., 2010; Song et al. 2010). Generally, trends of $V_{max}(\text{JTWC}) > V_{max}(\text{CMA}) > V_{max}(\text{JMA})$ and $P_{CS}(\text{JTWC}) < P_{CS}(\text{CMA}) \leq P_{CS}(\text{JMA})$

were found for typhoon- or stronger level storms. For weak storms, i.e. tropical depressions, $V_{max}(JTWC) < V_{max}(CMA)$, $V_{max}(JTWC) < V_{max}(JMA)$ and $P_{cs}(JTWC) > P_{cs}(CMA)$, $P_{cs}(JTWC) > P_{cs}(JMA)$ were found, but the difference is insignificant (Song et al. 2010). The difference of techniques and algorithms for determining the V_{max} and P_{cs} based on Dvorak technique (Dvorak, 1984; Velden et al., 2006) with satellite cloud images could also contribute to this inconsistency. However, 10 min time duration employed by JMA is consistent with most design codes or standards, which is also suggested by WMO. And the 50-knot or 30-knot radii information provided by JMA dataset from 1977 is a supplement of great importance to facilitate the estimation of typhoon wind field parameters. Accordingly, $R_{max,s}$ and B_s would be estimated based on JMA wind field information from 1977 using the present boundary layer wind model before assessing the typhoon wind hazards.

Indicator	International number ID	Number of data line	TC number ID	International number ID	Last data line flag	Time difference between last data and final analysis	Name of storm	Data of the latest revision		
66666	1422	048	0024	1422	0	6	HAGUPIT	20150109		
14113012	002	2	026	1560	1006	000				
14113018	002	2	036	1548	1004	000				
14120100	002	3	041	1534	1000	035	00000	0000	90120	0120
14120106	002	3	049	1522	998	035	00000	0000	90120	0120
14120112	002	3	055	1507	994	040	00000	0000	90120	0120
14120118	002	3	059	1489	990	045	00000	0000	90120	0120
14120200	002	4	059	1469	985	050	00000	0000	90180	0180
14120206	002	4	061	1451	980	055	90050	0050	90180	0180
14120212	002	4	062	1435	975	060	90050	0050	90180	0180
14120218	002	5	066	1421	965	070	90050	0050	90180	0180
14120300	002	5	075	1405	955	075	90060	0060	90180	0180
14120306	002	5	082	1386	950	080	90060	0060	90180	0180
14120312	002	5	087	1368	945	085	90070	0070	90210	0210
14120318	002	5	092	1353	935	095	90070	0070	90210	0210
14120400	002	5	098	1338	915	105	90080	0080	90210	0210
14120406	002	5	104	1324	905	115	90080	0080	90210	0210

Fig. 3.1 A selection of the JMA best track dataset

3.3.2 Estimation of $R_{max,s}$ and B_s

As shown in Fig. 3.2, 23515 wind data points including 13347 points for both R_{30} and R_{50} and 10168 points for R_{30} only are available in JMA best track dataset from 1977 to 2015. And

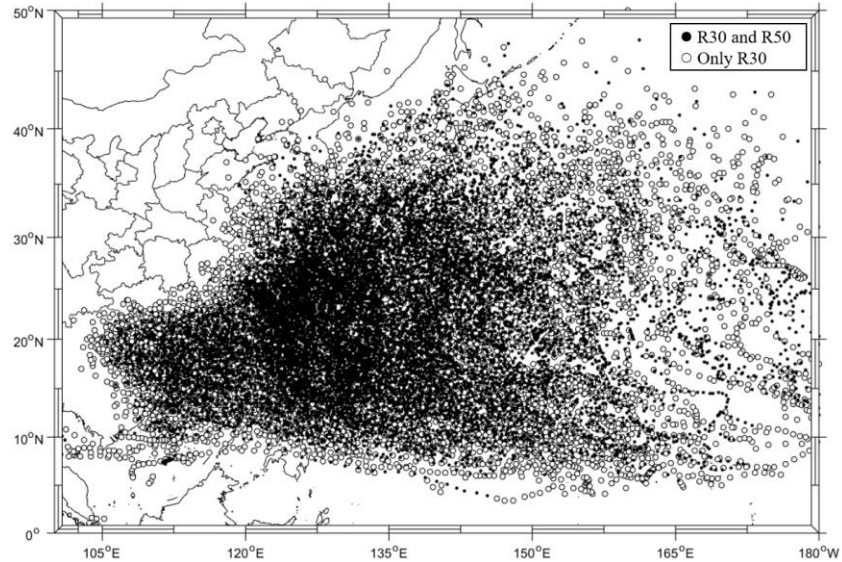


Fig. 3.2 Storm locations from JMA with radii to 30 knots and 50 knots winds (Both R30 and R50: 13347 points; Only R30: 10168 points)

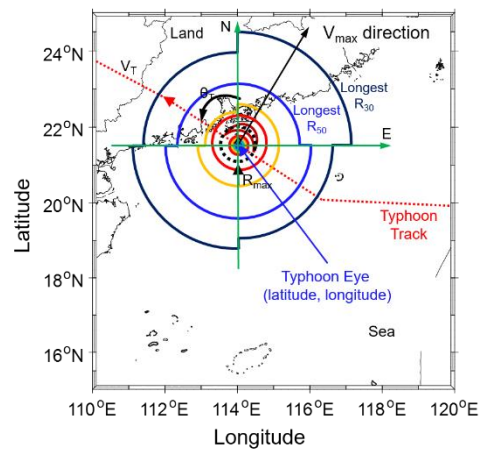


Fig. 3.3 A sketch of parametric typhoon wind field

the V_{max} information is also available for these storms. Tropical cyclones in the northern hemisphere are characterized with the counterclockwise rotation because of the Coriolis effect and the motion of the storm would contribute to its swirling winds, resulting in the maximum winds on the right side of the storm with respect to the its heading direction. That is, the maximum wind speed always occurs at the right side of the storm, or more accurately, in the perpendicular direction to the heading angle, as shown in Fig. 3.3. Accordingly, 3 pairs

of radius and wind speed, (R_{30}, V_{30}) , (R_{50}, V_{50}) and $(R_{max,s}, V_{max})$ except the undetermined $R_{max,s}$ in the direction of $\theta_T - 90^\circ$ can be employed to extract $R_{max,s}$ and B_s (Sometimes, only two pairs of data point are available, i.e. (R_{30}, V_{30}) , $(R_{max,s}, V_{max})$).

The flowchart in Fig. 3.4(a) illustrates the general algorithm for extracting $R_{max,s}$ and B_s . The sea surface temperature (SST) data provided by NOAA Optimum Interpolation 1/4 Degree Daily Sea Surface Temperature (OISST) Analysis project (NOAA, 2018), which uses Advanced Very High Resolution Radiometer (AVHRR) satellite data from September 1981 through December 2005 together with the operational Navy AVHRR Multi-Channel SST data for 2006 to the present day, are introduced. In addition, the HadISST1 month averaged Data through 1977 to August 1981 are adopted to match the time period of JMA dataset. The underlying exposure in term of surface roughness length z_0 needs to be predefined before solving the surface wind speed field. When the typhoon is over sea, the surface roughness can be estimated using the logarithmic wind profile law within the lowest portion of the planetary boundary layer in the form (Vickery and Skerlj, 2005)

$$z_0 = 10.0 \cdot \exp(-\kappa/\sqrt{C_{D10}}) \quad (3.26)$$

in which C_{D10} is the surface drag coefficient formulated as a linear function of the mean wind speed at 10 m in the form

$$C_{D10} = (0.49 + 0.065U_{10}) \times 10^{-3}, C_{D10} \leq C_{Dmax} \quad (3.27)$$

in which U_{10} is the mean wind speed at a height of 10 m, and the maximum value of C_{D10} is modeled as a function of radius from storm center with the following expression

$$C_{Dmax} = (0.0881r + 17.66) \times 10^{-4}, 0.0019 \leq C_{Dmax} \leq 0.0025 \quad (3.28)$$

in which r is the radial distance from the typhoon center (km). After the storm landfall, a smooth and flat open land without obstructions terrain category is employed with $z_0 = 0.01$

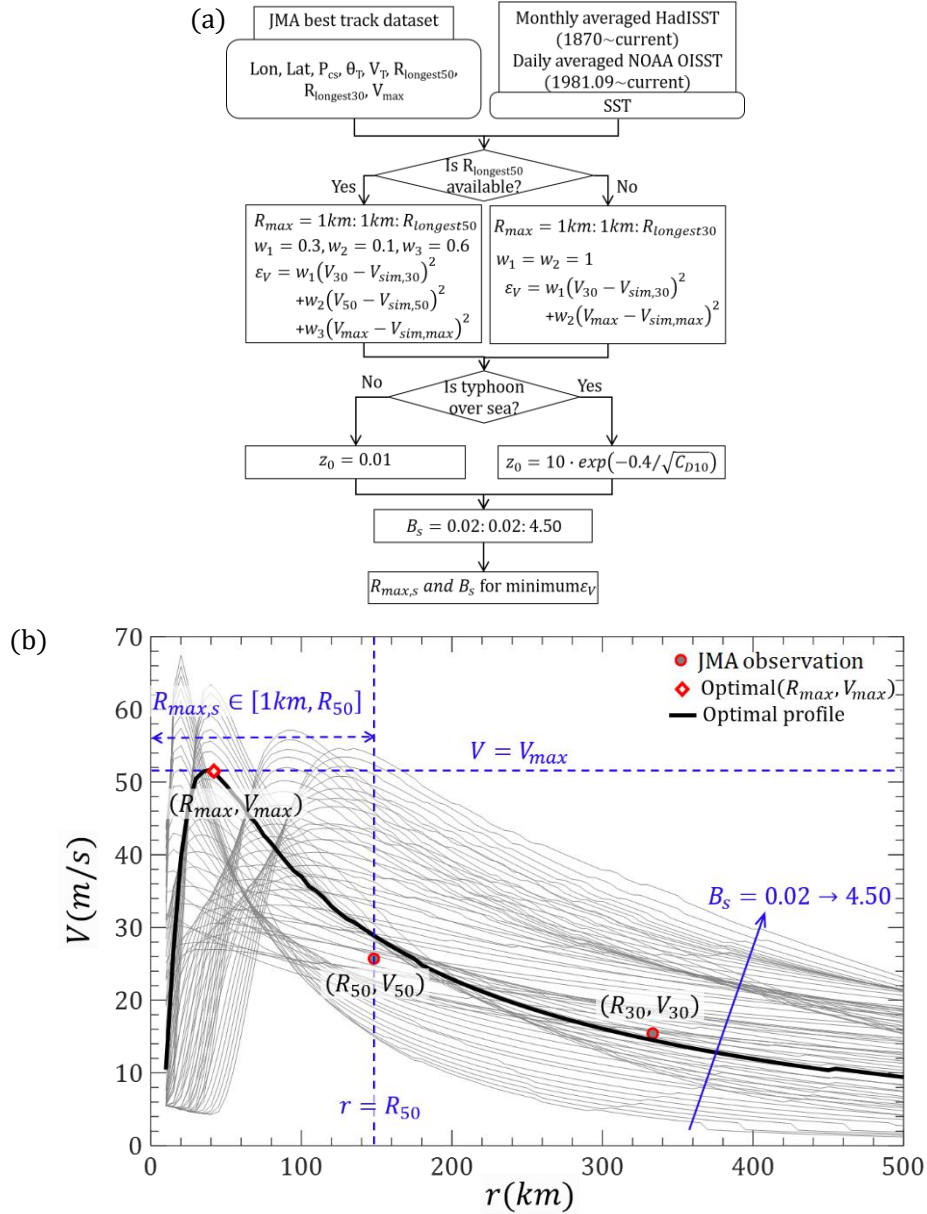


Fig. 3.4 Extraction of $R_{max,s}$ and B_s with JMA wind data: (a) Algorithm flowchart; (b) A diagrammatic sketch

as specified in the load code for design of building structures of China ([GB 50009-2012](#)). This is reasonable when we consider that JMA dataset provides the longest radii with the wind speeds larger than 30 and 50 knots by reanalyzing the surface observation, ASCAT observation and low-level cloud motion satellite images. The outermost 30- and 50-knot wind speed in radial direction are most likely to be recorded at a site with an open and flat

upstream terrain since the wind speed is supposed to decrease along the radial direction from $R_{max,s}$. And this should always be the case along the coastal areas at which most of them are featured with open and flat underlying terrain. Correspondingly, as shown in Fig. 3.4(b), a series of a series of combinations for $R_{max,s}(1km \rightarrow R_{50})$ and $B_s(0.04 \rightarrow 4.50)$ are used to simulate the radial wind speed profiles and compare with the JMA observations to achieve an optimal pair of $R_{max,s}$ and B_s by minimizing the weighted residual.

The results of $R_{max,s}$ and B_s extracted from JMA wind data are illustrated in Fig. 3.5 ($R_{max,s}$ is shown with logarithmic scale to clearly illustrate the small $R_{max,s}$), including 23175 over-sea and 336 over-land samples. The maximum and minimum $R_{max,s}$ are 1116 km and 2 km, respectively while B_s ranges from 0.16 to 4.4. Conventionally, as highlighted by Holland (1980,2008), Vickery et al. (2000, 2008) and Fang et al. (2018), the shape parameter of radial pressure profile was thought to be less than 2.5. This is mainly attributed to the use of different wind field models and data sources. Two approaches were commonly employed to estimate $R_{max,s}$ and B_s based on the use of data sources, say atmospheric pressure data and wind speed data. The pressure data can be directly applied to Eq. (3.1) to obtain $R_{max,s}$ and B_s , which is considered as the most physically reasonable method. Vickery et al. (2000, 2008) utilized the surface pressures converted from flight-level reconnaissance data to optimally obtain a pair of $R_{max,s}$ and B_s for each traverse observation through the storm. Fang et al. (2018) fitted the surface pressure data of landing typhoons observed by distributed meteorological stations in the mainland of China. However, when this equation is applied to model the wind speed field using Eq. (3.10) as used by most wind field models (Vickery et al., 2008), some inconsistencies could be introduced since the pressure distribution at free atmosphere is somewhat different from that at the surface. This can be approved from the

results obtained by Willoughby et al (2004) and Vickery et al. (2000). Vickery et al. (2000) estimated Holland's profile parameter from upper-level wind speed data using Eq. (3.1) and Eq. (3.10), which were about 20%~30% higher than that estimated from surface pressures. That means if Eq. (3.1) is estimated from the surface pressures, it cannot be directly applied to Eq. (3.10) due to the height-resolving characteristics of air density and pressures. And Eq. (3.10) is actually an approximate formula by neglecting the radial and vertical wind components. Moreover, even the pressure observation-based $R_{max,s}$ and B_s were employed in the present wind field model, some inevitable errors on the estimations of wind speed would be introduced due to the simplification and linearization of the Navier-Stokes equations as discussed by Kepert and Wang (2001).

The other method is the use of wind speed observations. Vickery et al. (2008) used a boundary layer model to match the H* Wind surface wind field. The Holland pressure model, say Eq. (3.1) was also directly applied to Eq. (3.10) for calculating the gradient wind speed before converting to surface level. In fact, if Holland pressure model is considered to be valid at gradient level and substituted into Eq. (3.10), which is commonly used (Vickery et al., 2000; Jakobsen et al., 2004), it is acceptable and self-consistent. That means R_{max} and B are estimated from gradient wind. And real wind field at gradient or surface level can be well captured although the real pressure field has a large deviation from Holland's model. The only problem is how to predetermine a gradient height since it is a variable and generally believed to increase from the storm center to peripheral area. Comparatively, the present wind field model uses the surface level, say 10 m above the ground as a standard height. It converts the surface pressures to gradient layer before calculating the surface wind speed using an analytical solution. Similarly, the surface pressures modeled by Eq. (3.1) using an

optimal pair of $R_{max,s}$ and B_s could have a remarkable difference from the real pressures, but the surface wind speeds are perfectly reproduced. Because of the decrease of central pressure difference from the surface to gradient layer and the use of an analytical boundary layer model, which disregards some nonlinear terms and neglects the non-axisymmetric effects, a larger B_s is required to reproduce the observed surface wind.

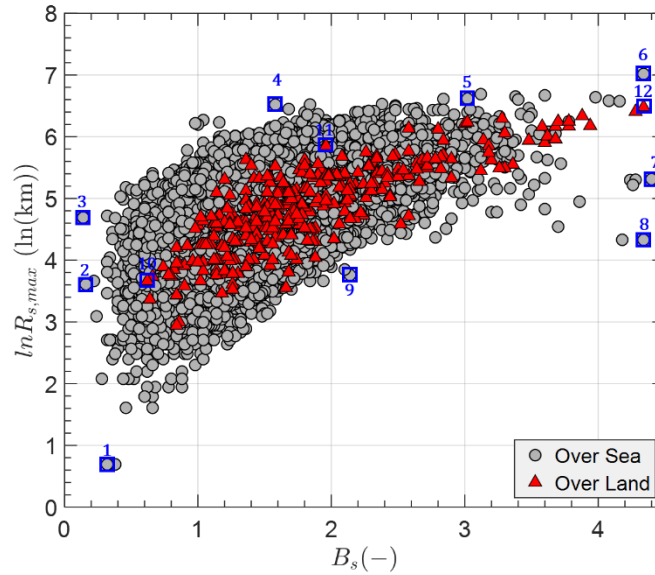


Fig. 3.5 Results of $R_{max,s}$ and B_s extracted from JMA wind data

12 reproduced radial wind profiles associated with the extreme cases labeled in Fig. 3.5 are illustrated in Fig. 3.6. Almost all of them are fitted with the information of (R_{30}, V_{30}) and V_{max} . Generally, the reproduced wind profiles are able to well capture the observed data. Some fluctuations of the wind curves can be observed which are attributed to the effects of the eddy viscosity (K in Eq. (3.17)) and over-sea roughness length (z_0 in Eq. (3.26)). An iteration algorithm is required when solving the eddy viscosity, which would introduce some numerical errors. The upper and lower bounds as formulated by Eqs. (3.27)~(3.28) for over-sea roughness length would also result in a sudden decrease of wind speed at the outer

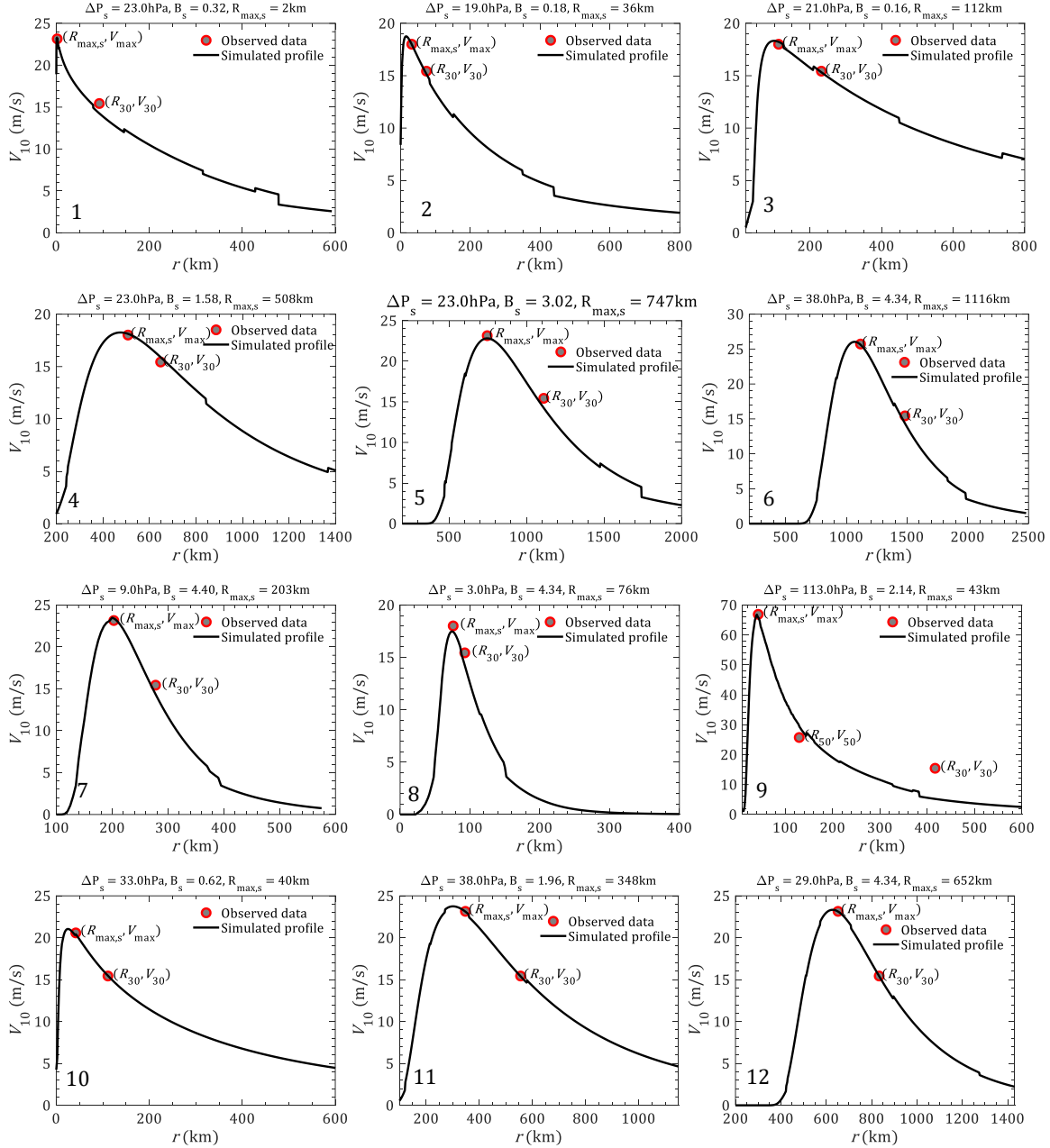


Fig. 3.6 Reproduced radial wind profiles of some extreme cases

region. Comparatively, the wind profiles of over-land cases (10~12 in Fig. 3.6) with a uniform roughness length are smoother. In short, the algorithm present above has a good performance on reproducing the wind field. Furthermore, Fig. 3.7 shows the central pressures as well as fitted $R_{max,s}$ and B_s at each time step of four typhoons. It can be noted that the reproduced radial wind profiles agree well with observed data points. And $R_{max,s}$

and B_s show a gradual variation with the development and dissipation of typhoons. It is noteworthy that the fitted $R_{max,s}$ and B_s do not always increase or decrease with the variation of central pressures. More details regarding the correlations among these parameters will be discussed in next section.

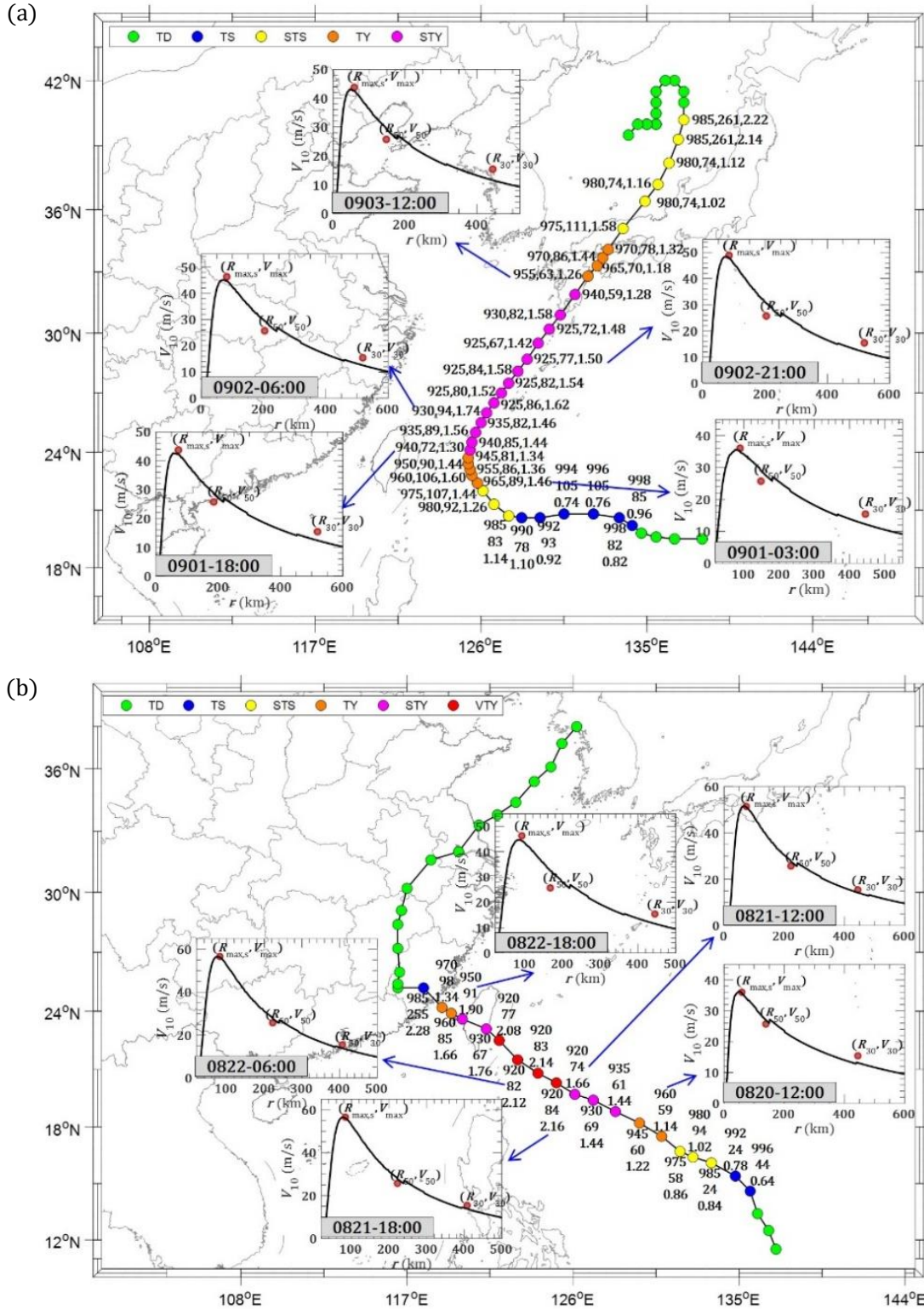


Fig. 3.7 Reproduced radial wind profiles of four typhoons: (a) Yancy (199313); (b) Bilis (200010); (Numbers at each time step from top to bottom or left to right: $P_{CS}, R_{max,s}$ and B_s)

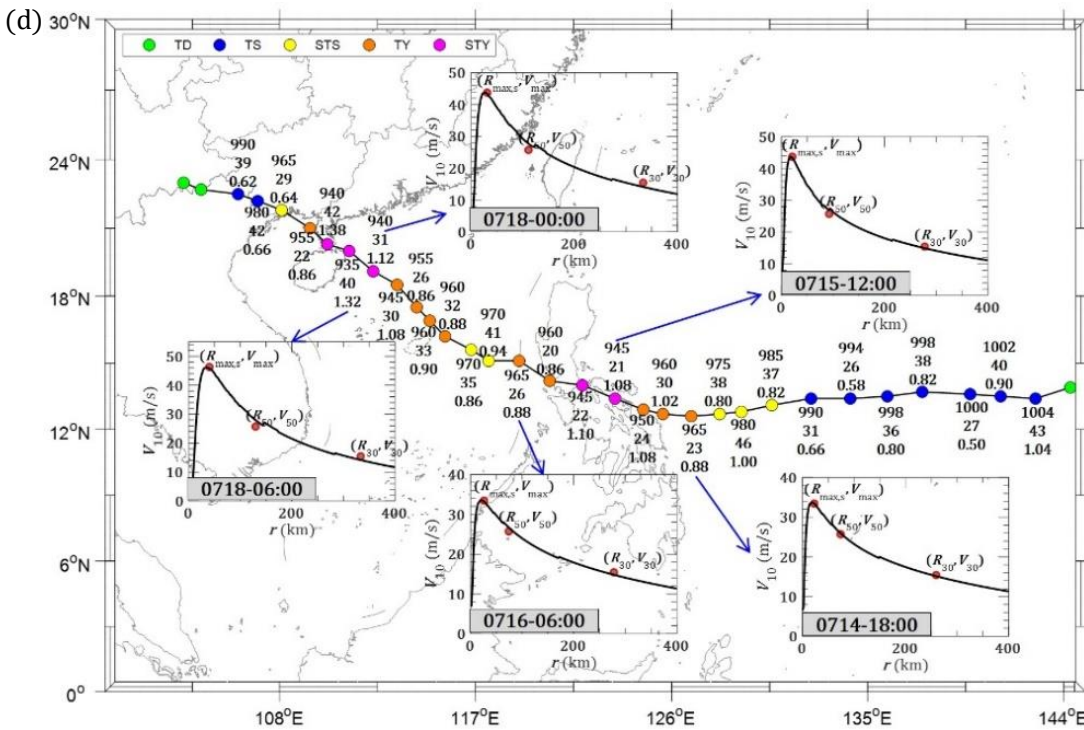
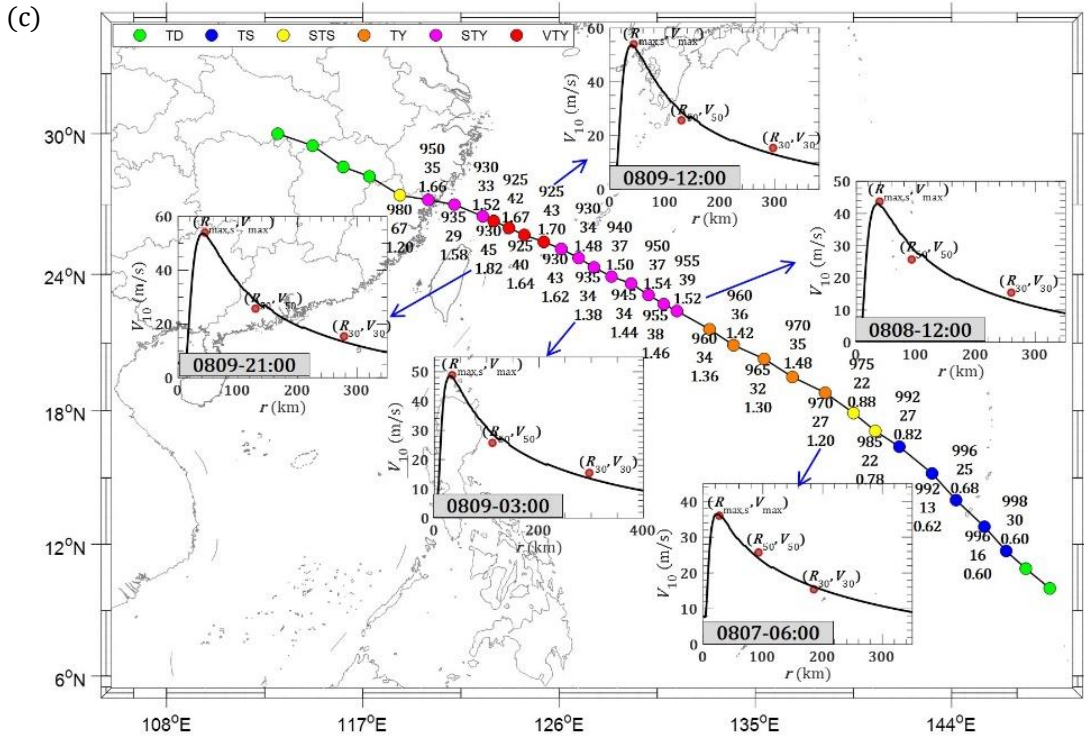


Fig. 3.7 (Cont.) Reproduced radial wind profiles of four typhoons: (c) Saomai (200608); (d) Rammasun (201409) (Numbers at each time step from top to bottom or left to right: P_{cs} , $R_{max,s}$ and B_s)

3.3.3 Statistical correlations

Traditionally, the typhoon wind field parameters, i.e. $R_{max,s}$ and B_s are commonly estimated with observation-based statistically correlated formulas (Vickery et al., 2008; Fang et al., 2018). However, the correlations are not very strong as studied by Vickery et al. (2008) with all coefficients of determination less than 0.3. As shown in Fig. 3.8, correlation analyses were conducted between latitude (Lat), ΔP_s , B_s , $\ln R_{max,s}$ and surface sea temperature (SST). The strongest correlation is between $\ln R_{max,s}$ and B_s with the correlation coefficients $\rho = 0.605$ and $\rho = 0.856$ for oversea and overland scenarios, respectively, which is consistent with Vickery's results (Vickery et al., 2008). Undoubtedly, SST and Lat have a strong correlation, but it seems to be nonlinear. $\ln R_{max,s}$ has weak correlations with SST and Lat, but almost no correlation with ΔP_s . Weak correlation can also be observed between B_s and Lat as well as ΔP_s . Correlation coefficients between other parameters are smaller than 0.2. These correlations provide some basic information for the statistical model of $R_{max,s}$ and B_s . Customarily, $R_{max,s}$ is first formulated as the function of ΔP_s and Lat based on statistical correlation analyses. Then B_s will be statistically modeled as the function of $R_{max,s}$, ΔP_s , Lat and SST. However, $R_{max,s}$ appears weak correlations with ΔP_s and Lat. And the errors between the regression model of $R_{max,s}$ and observation data usually show some biases as demonstrated by Vickery et al. (2008). Same problems would happen to B_s as well. It is noteworthy that no obvious decay trend was observed for B_s after the landfall of the storm which was adopted by Vickery et al. (2009) to estimate the over-land B_s . In some cases, B_s was even observed to increase after the storm's landfall. This can also be found in Fig. 3.8, in which B_s and ΔP_s almost have no correlation and some large B_s associated with weak storms (low ΔP_s) were obtained. The potential reason is the use of wind field fitting method in this

study which requires some numerical adjustment for $R_{max,s}$ and B_s to match the historical wind information.

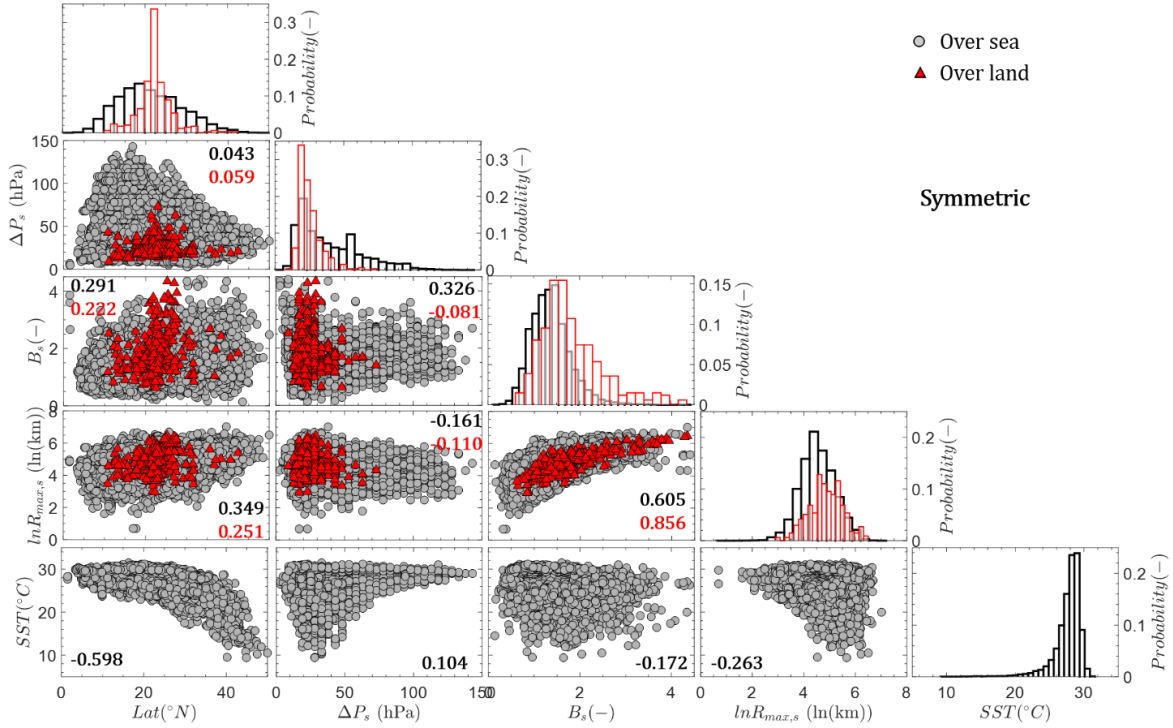


Fig. 3.8 Correlations among parameters (Black and red numbers in each panel are correlation coefficients for oversea and overland cases)

3.3.4 Recursive models of $R_{max,s}$ and B_s

As discussed before, the traditional statistical models of $R_{max,s}$ and B_s has some inherent shortcomings. The $R_{max,s}$ and B_s of each storm are estimated in every time steps in this study, which facilitates the development of recursive models. Similar to the idea of full track model for typhoon simulation (Vickery et al., 2000), it is feasible to model $R_{max,s}$ and B_s by considering their autocorrelations of adjacent time steps. Fig. 3.9 presents the variation of all $R_{max,s}$ and B_s as separate linear functions of previous two steps. It is obvious that $R_{max,s}(i + 1)$ and $B_s(i + 1)$ (values at next step) are strongly correlated with previous steps i and $i - 1$. And $R_{max,s}$ has a higher dependence on previous steps than B_s . By combining

with the correlation analyses in Fig. 8, the linearly weighted progressive equations of $R_{max,s}$ and B_s can be modeled as

$$\ln R_{max,s}(i+1) = r_1 + r_2 \cdot \ln R_{max,s}(i) + r_3 \cdot \ln R_{max,s}(i-1) + r_4 \cdot \Delta p_s(i+1) + r_5 \cdot \psi(i+1) + \varepsilon_{\ln R_{max,s}} \quad (29)$$

$$B_s(i+1) = b_1 + b_2 \cdot B_s(i) + b_3 \cdot B_s(i-1) + b_4 \cdot \Delta p_s(i+1) + b_5 \cdot \sqrt{\ln R_{max,s}(i+1)} + \varepsilon_{B_s} \quad (30)$$

in which $r_j (j = 1 \sim 5)$ are the coefficients of logarithmic $R_{max,s}$ regression model, $b_j (j = 1 \sim 5)$ are the coefficients of B_s regression model, ψ is the latitude of the storm eye. $\ln R_{max,s}(i)$ and $B_s(i)$ are the values at time step i , $\varepsilon_{\ln R_{max,s}}$ and ε_{B_s} are error terms accounting for modeling differences between models and observations. Vickery et al. (2008) introduce a nondimensional parameter A to incorporate the effects of R_{max} , Δp_s , ψ and SST to model Holland B as a linear function of \sqrt{A} . It was found that the over-sea (SST is available) B_s in this study only has a medium correlation with \sqrt{A} with the correlation coefficient of 0.5017. It noteworthy that the correlation between B_s and \sqrt{A} is positive, which is unexpectedly opposite to Vickery's (Vickery et al., 2008) results. This is because our study shows a positive correlation between B_s and $R_{max,s}$ (Fig. 3.8) while Vickery et al. (2008) found a negative relationship. As for the reason leading to this difference is still not clear. It is possible the use of different fitting approaches. As mentioned before, the pressure equation (Eq. (3.1)) using our B_s and $R_{max,s}$ could have a remarkable difference from the real pressure field with the emphasis on the reproduction of wind field using a simplified boundary layer model. Vickery et al. (2009) also suggested a decay model for Holland B after storm's landfall, but no trend was observed for B_s in present study as mentioned before. Accordingly, a unified model of Eq. (29) can be adopted for both over-sea and over-land B_s , which ignores the effects of ψ and SST .

The regression coefficients of r_j and $b_j(j = 1\sim 5)$ are fitted as 0.3838, 0.8480, 0.0484, -4.1937 $\times 10^{-4}$, 5.5425 $\times 10^{-3}$ and -1.8013 $\times 10^{-3}$, 0.6005, 0.0159, 3.0431 $\times 10^{-3}$, 0.0413, respectively if all data points in Western Pacific are employed. The error scatter plots of $\ln R_{max,s}$ and B_s , i.e. $\varepsilon_{\ln R_{max,s}}$ and ε_{B_s} are illustrated in Fig. 3.10. There is no obvious bias or potential trend for errors with the means (μ) and standard derivations (σ) of 0, 0 and 0.27, 0.22, respectively. Three candidate probability distribution models, i.e. normal, t location-scale and unbound Johnson system distributions are employed to fit the errors. The probability density functions of normal and t location-scale distributions are

$$f(x; \mu, \sigma) = \frac{1}{\sigma\sqrt{2\pi}} \exp\left\{-\frac{(x - \mu)^2}{2\sigma^2}\right\} \quad (31)$$

$$f(x; \mu, \sigma, \nu) = \frac{\Gamma\left(\frac{\nu + 1}{2}\right)}{\sigma\sqrt{\nu\pi}\Gamma\left(\frac{\nu}{2}\right)} \left[\frac{\nu + \left(\frac{x - \mu}{\sigma}\right)^2}{\nu}\right]^{-\frac{\nu+1}{2}} \quad (32)$$

in which μ , σ and ν are location, scale and shape parameters. $\Gamma(\cdot)$ is the Gamma function. The Johnson system distribution (Johnson, 1949) refers to a family of transformations that enables the flexible translation of a number of data populations into the normal distribution. The identity, exponential, logistic and hyperbolic sine transformations are utilized to generate normal (SN), lognormal (SL), bounded (SB) and unbounded (SU) distributions, respectively. Generally, the SL, SB and SU transformations can be expressed as

$$z = \gamma + \delta \cdot f\left(\frac{x - \xi}{\lambda}\right) \quad (33)$$

in which x is the input data population, z is the standard normally distributed variate, $f(\cdot)$ is transformation function, γ , δ , ξ and λ are four undetermined coefficients. In order to solve these four coefficients, four quantiles of empirical distribution for x associated with four

quantiles [-1.5 -0.5 0.5 1.5] of the normal distribution that correspond to the cumulative probabilities [0.067 0.309 0.691 0.993] will be first estimated. Then by substituting the quantiles of x and quantiles [-1.5 -0.5 0.5 1.5] of normal distribution into Eq. (3.33), four equations will be obtained to determine four coefficients. It was found that Johnson SU transformation is preferable to model the $\varepsilon_{lnR_{max,s}}$ and ε_{B_s} with the form of

$$z = \gamma + \delta \cdot \sinh^{-1} \left(\frac{x - \xi}{\lambda} \right) \quad (3.34)$$

Then, x can be randomly generated using the inverse function of Eq. (3.34) after normally sampling z . The fitting results are shown in Fig. 3.10 using maximum likelihood method. k in the figure represents the one-sample Kolmogorov–Smirnov (K-S) test statistic for each distribution model at the 5% significance level. The corresponding critical value is 0.0093 (sample size = 21485). It can be noted that Johnson SU distribution has the best performance with a smallest K-S test statistic. And t location-scale distribution model is also a good candidate while normal model has a relatively worst fitting.

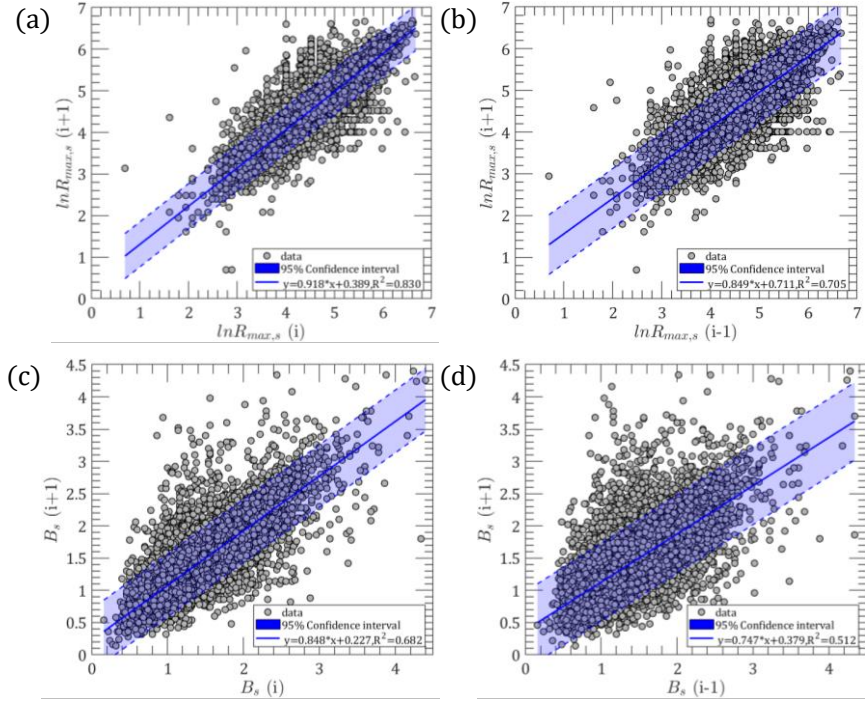


Fig. 3.9 Correlations of $R_{max,s}$ and B_s with previous steps: (a) $\ln R_{max,s}(i)$ and $\ln R_{max,s}(i+1)$; (b) $\ln R_{max,s}(i-1)$ and $\ln R_{max,s}(i+1)$; (c) $B_s(i)$ and $B_s(i+1)$; (d) $B_s(i-1)$ and $B_s(i+1)$;

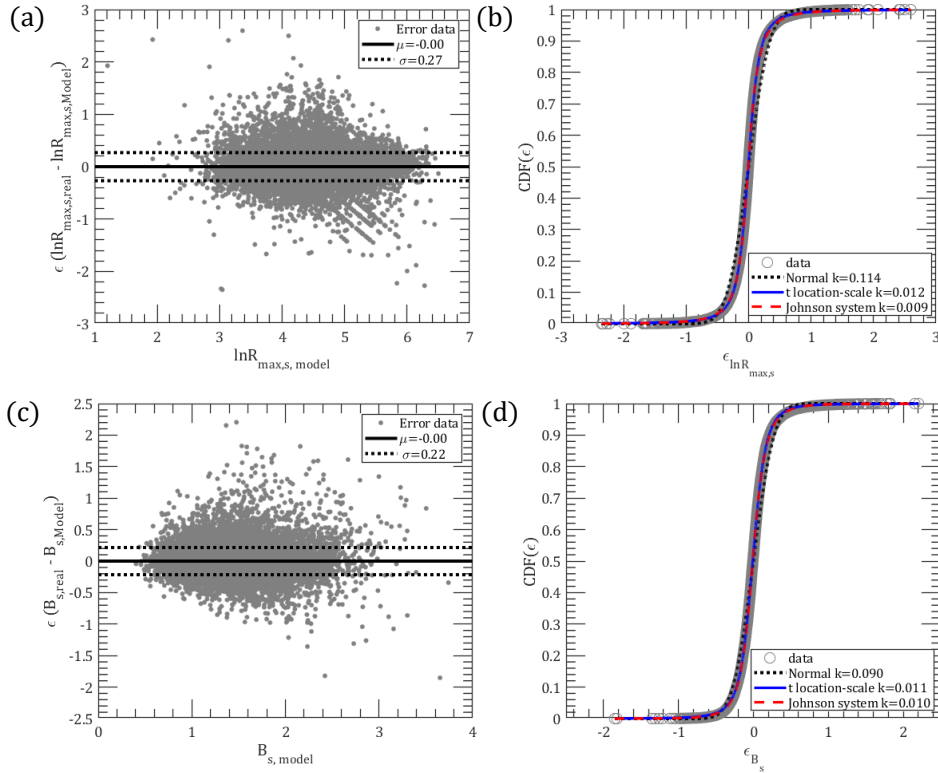


Fig. 3.10 Model errors of $R_{max,s}$ and B_s : (a) scatter plot ($\epsilon_{\ln R_{max,s}}$); (b) CDF ($\epsilon_{\ln R_{max,s}}$); (c) scatter plot (ϵ_{B_s}); (d) CDF (ϵ_{B_s});

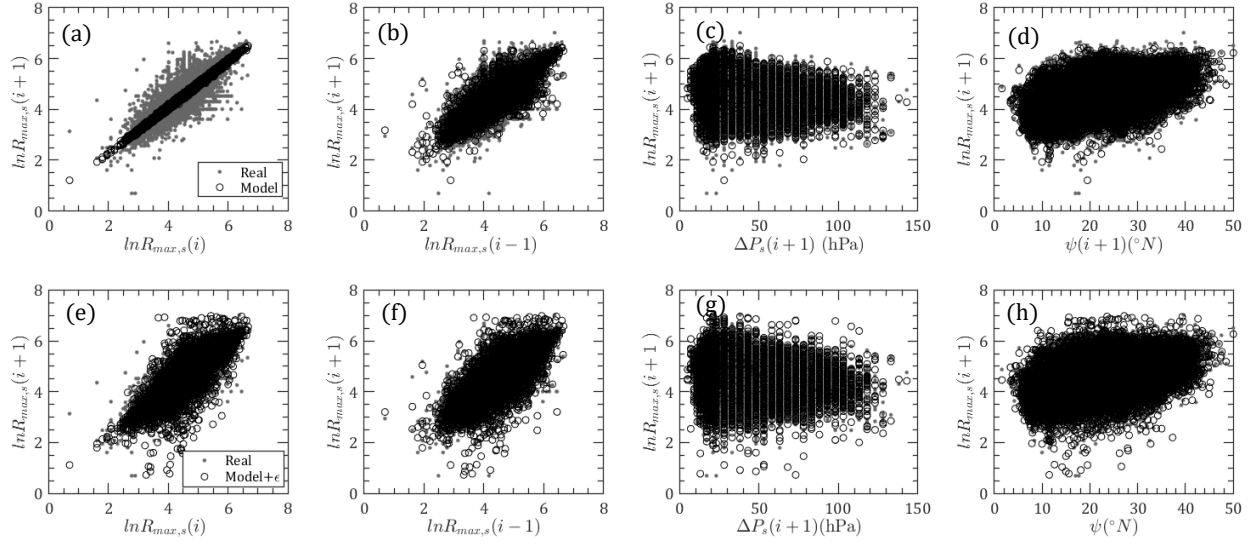


Fig. 3.11 Comparison of $\ln R_{max,s}$ between model and observations: (a)-(d) relations between $\ln R_{max,s}(i)$, $\ln R_{max,s}(i-1)$, $\Delta P_s(i+1)$ and $\ln R_{max,s}(i+1)$ without errors; (e)-(h) relations between $\ln R_{max,s}(i)$, $\ln R_{max,s}(i-1)$, ΔP and $\ln R_{max,s}(i+1)$ with errors

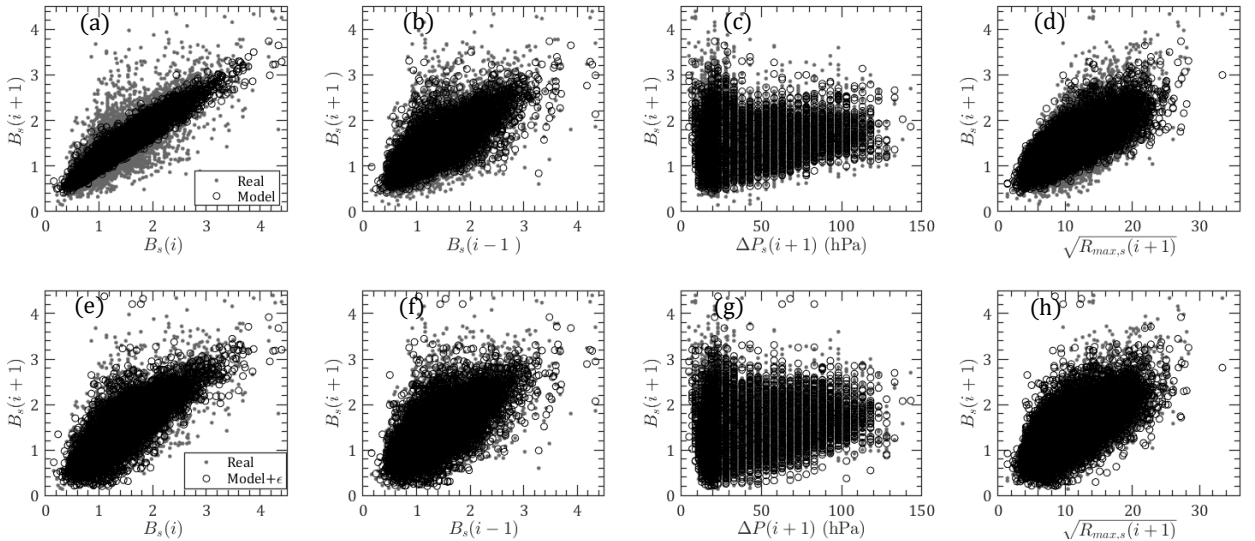


Fig. 3.12 Comparison of B_s between model and observations: (a)-(d) relations between $B_s(i)$, $B_s(i-1)$, $\Delta P_s(i+1)$ and $B_s(i+1)$ without errors; (e)-(h) relations between $B_s(i)$, $B_s(i-1)$, $\Delta P_s(i+1)$ and $B_s(i+1)$ with errors

As illustrated in Figs. 3.11~3.12, $\ln R_{max,s}$ and B_s at next steps are estimated by introducing the historical track information using Eqs. (3.29)-(3.30) and compared with real observations. The first rows of these two figures (Fig. 3.11(a)~(d) and Fig. 3.12(a)~(d)) only consider the mean terms of Eqs. (3.29)-(3.30), which indicates that $\ln R_{max,s}$ and B_s

significantly depends on the previous steps with linearly concentrated modeled mean values. The mode mean values are more scattered with the variation of $\ln R_{max,s}$ and B_s at the previous second step and other parameters (Δp_s and ψ for $\ln R_{max,s}$, Δp_s and $\sqrt{R_{max,s}}$ for B_s), but they are still within the scatter range of historical data. The second rows, i.e. Fig. 3.11(e)~(h) and Fig.3.12(e)~(h), introduce the error terms ($\varepsilon_{\ln R_{max,s}}$ and ε_{B_s}) utilizing Johnson SU distribution, which show good agreements with real observations. That is, $\ln R_{max,s}$ and B_s can be well randomly sampled using the recursive models formulated by Eqs. (3.29)-(3.30).

It is noteworthy that the present recursive models are developed based on global regression of all data within the Western Pacific region. However, the same models can also be applied to any subregions using the site-specific regressive coefficients (r_j and b_j). The recursive models of $\ln R_{max,s}$ and B_s can also be added into full track modeling using the similar simulation algorithm of tracks and intensity, either cell-by-cell regression or site-by-site geographically weighted regression (GWR).

3.4 Upstream terrain effects

After the extraction of $R_{max,s}$ and B_s , the wind speed field of a typhoon at each time step can be reproduced using the present boundary layer model to facilitate the estimation of wind hazards of historical typhoons. As shown in Fig. 3.13, a set of grid points for the provinces along the coastal region of China is generated. The resolution for coastline area within the range of about 50 km is 0.02° (or about 2.2 km) while the 400-km inland region and exclusive economic zone (EEZ) are divided by a coarser resolution, say 0.05° (or about 5.6

km). The rest of the grids have a 0.1° (or about 11.1 km) resolution. In total, 172812 grid points were generated.

Although open flat areas along the coastline are usually treated as the same exposure in wind engineering applications, local terrain roughness and topographic features as well as surrounding obstacles would determine the development of a boundary layer and evolution of turbulence. In reality, a sudden change of elevation or topography would have an obvious impact on surface wind speed over a very short distance ([Miller et al., 2013](#)), especially the speeds near the crests of ridges and hills, which show marked increases when compared with the wind speed measured at same height above the flat terrain. Some studies ([Lemelin et al., 1988](#); [Weng et al., 2000](#)) found that the wind speed at top of the hill could even double the speed that over flat terrain due to topographic effects, which represents a structure on top of hill would experience an increase of 300% in the wind load than that in flat area. Accordingly, quantification of directional roughness and topographic effects is essentially important for typhoon wind hazards assessments. The equivalent roughness length and speed-up effect at each site are first evaluated before the construction of wind hazard footprints.

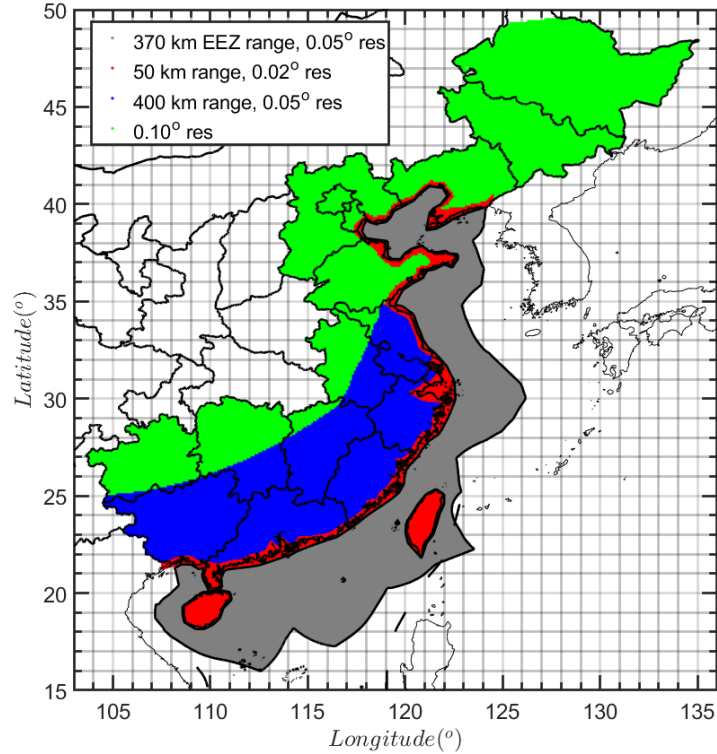


Fig. 3.13 Grid points along the coastal region of China (EEZ: Exclusive economic zone)

3.4.1 Directional equivalent roughness length

As an important input parameter, the equivalent surface roughness length (z_0) accounting for the local and upstream terrain exposures would directly determine the wind behavior within the neutral boundary layer (lower than about 50 m) (Vickery et al., 2005). The 10-year-based (2001-2010) collection 5.1 Moderate Resolution Imaging Spectroradiometer (MODIS) Land Cover Type (MCD12Q1) (Broxton et al., 2014) product provides a database to roughly estimate the global surface roughness length based on the classification of land covers, as shown in Table 3.1 It can be seen that z_0 is not a determined value for most land-cover classifications. This is mainly because of the evolution of surface cover with time such that z_0 cannot be defined as a constant. Correspondingly, in order to check the classification and show the variability of z_0 , the values of z_0 recommended by the US Geological Survey (USGS) are also listed in Table 3.1. The lower bound of z_0 for each category would be adopted

to develop the directional equivalent roughness length. The ESDU document (82026) suggested that a fetch of at least 100 km of uniform terrain is needed before the boundary layer is in equilibrium. However, a sufficiently long upwind fetch of uniform terrain is always unlikely while several changes of upstream roughness within a few kilometers are more common. Since our consideration about typhoon hazards is at the reference height of 10 m, whose wind speed is typically affected by the ground obstacles within a short unwind fetch. Accordingly, the z_0 within 20-km upstream fetch around the site in question would be taken into account. They are categorized into 16 parts at 22.5° increments according to upwind directions, i.e. N, NNE, NE, ENE, E, ESE, SE, SSE, S, SSW, SW, WSW, W, WNW, NW, WNW to achieve an equivalent z_0 at each direction. An improved algorithm present in Fig. 3.14 was employed by following the simplifying assumptions suggested by ESDU (82026). Correspondingly, the equivalent roughness lengths in four upwind directions (N, E, S, W) are illustrated in Fig. 3.15. Most sites feature with $z_0 < 0.20\text{ m}$, which is consistent with the classifications in Table 3.1. The highest z_0 occurs in urban and built-up areas, such as the Shanghai city. In practice the variation of land cover or surface roughness would be gradual, resulting in a distinct region-by-region distribution of roughness lengths. Fig. 3.15 (b) shows the enlarged view of Hainan island which mainly includes four categories of z_0 . And an obvious difference can be observed between off-land and off-sea wind along the coastline. The off-land winds more likely keep the characteristics of overland before blowing a sufficiently long distance oversea, and vice versa.

Table 3.1 Land-cover-based classification for the surface roughness length

Class	Category	z_0 (m)		Class	Category	z_0 (m)	
		MODIS	USGS			MODIS	USGS
0	Water	0.0002	0.0001	11	Permanent wetlands	0.30	0.20~0.40
	Evergreen/ Deciduous/ Mixed forest	0.20~0.50	0.20~0.50	12	Croplands	0.05~0.15	0.02~0.15
6	Closed scrublands	0.01~0.05	0.01~0.06	13	Urban and built-up	0.50~0.80	0.50
7	Open scrublands	0.01~0.06		14	Cropland/Natural vegetation mosaic	0.05~0.14	0.05~0.20
8	Woody savannas	0.17	0.15	15	Snow and ice	0.001	0.001
9	Savannas	0.15		16	Barren or sparsely vegetated	0.01	0.01
10	Grasslands	0.10~0.12	0.10~0.12	254	Unclassified	-	-

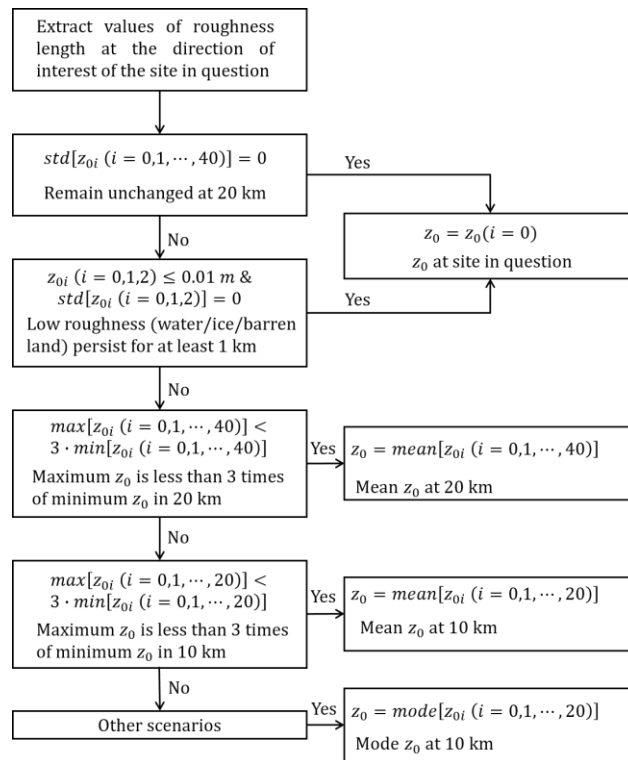


Fig. 3.14 Determination of the equivalent roughness length at the site in question

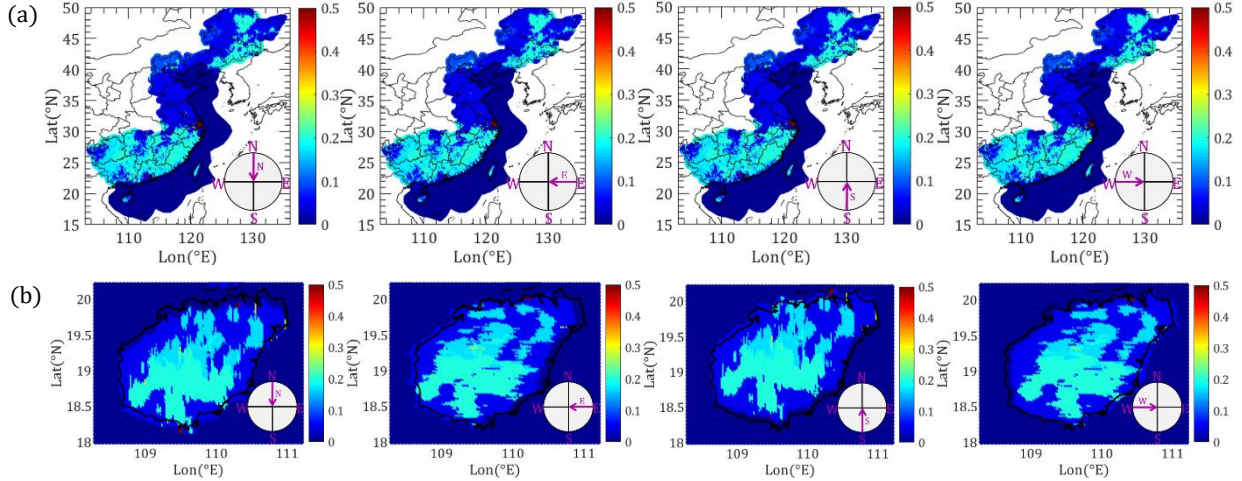


Fig. 3.15 Directional equivalent roughness length: (a) Coastal region of China; (b) Hainan island

3.4.2 Topographic speed up

Traditionally, a uniformly underlying flat topography was assumed for the estimation of wind hazards. However, as discussed by [Miller et al., \(2013\)](#), surface wind speeds would be significantly affected by the small-scale topography, especially a marked increase near the crests of ridges and hills. The near-surface wind speed perturbation caused by the presence of hill or ridge is usually quantitatively expressed in term of a speed-up factor K_t defined as

$$K_t(x, z) = \frac{u(x, z)}{u_0(z)} \quad (3.35)$$

in which $u_0(z)$ is an upstream unperturbed reference wind speed at height z above the ground, $u(x, z)$ is the velocity at the same height z above the local hill or ridge surface with the horizontal coordinate x . The speed-up factor is mainly governed by the slope of the hill and weakly dependent on the amount of shear in the upwind boundary layer. Some pioneer studies ([Jackson and Hunt, 1975](#); [Taylor et al., 1983](#); [Hunt et al., 1988](#)) have well developed the theory of boundary layer flow over low-slope topography. [Miller et al., \(2013\)](#) employed the Fourier-transform-based linearized model ([Taylor et al., 1983](#)) to quantitatively estimate the effects of underlying topography on the hurricane winds over the Bermuda

island. These methods provide a good estimation of topography effects for low-slop hills, but the computational time could be huge if they are applied to a large area. And nonlinear effects of wind flow over high-slop hills would be significant due to flow separation. Alternatively, some design codes (Eurocode, 1991) or technical specifications (ESDU, 91043) have provided several simple methods based on some published and unpublished studies, either theoretical solutions or wind tunnel tests, which enables a rapid and programmed estimation of topographic speed-up factors. Similar to Tan and Fang (2018), the recommendations of the Eurocode (1991) were adopted in this study, which categorizes topographies into hills or ridges, cliffs or escarpments and valleys. The topography digital data were obtained from the 1 arc-second horizontal grid resolution (approximately 30 meters at the equator) ASTGTM (Advanced Spaceborne Thermal Emission and Reflection Radiometer (ASTER) Global Digital Elevation Model) Version 3 dataset, which is publicly available on the website of <https://asterweb.jpl.nasa.gov/gdem.asp>.

For each grid point as shown in Fig. 3.13, the elevation information within 1 km in 16 upstream directions is extracted. Then the directional topographic speed-up factors will be determined by following the algorithm in Eurocode (1991). The critical slope is set as 0.05, suggesting the isolated hill is featured with both upwind and downwind slopes smaller than 0.05 while upwind cliff or escarpment is defined with upwind slope larger than 0.05 and downwind slope smaller than 0.05. For other cases, i.e. both slopes smaller 0.05 (quasi flat terrain) or upwind slope less than 0.05 and downwind slope higher than 0.05 (valley), no speed up are to be considered (the potential funneling effects in valleys are ignored). Fig. 3.16 illustrates an example of 16 directional speed-up factors for the site of Yangjiang meteorological station with a maximum of 1.2361 from NNW to SSE and minimum of 1.1047

from ENE to WSW. Correspondingly, the directional speed-up factors in 16 directions of all grid points (Fig. 3.13) are determined. Fig. 3.17 shows the results in 4 directions of whole coastal region of China as well as Hainan Island. The maximum K_t reaches to 1.6. A slight speed reduction can be noted in some sites, which are usually located at downwind side of the hill.

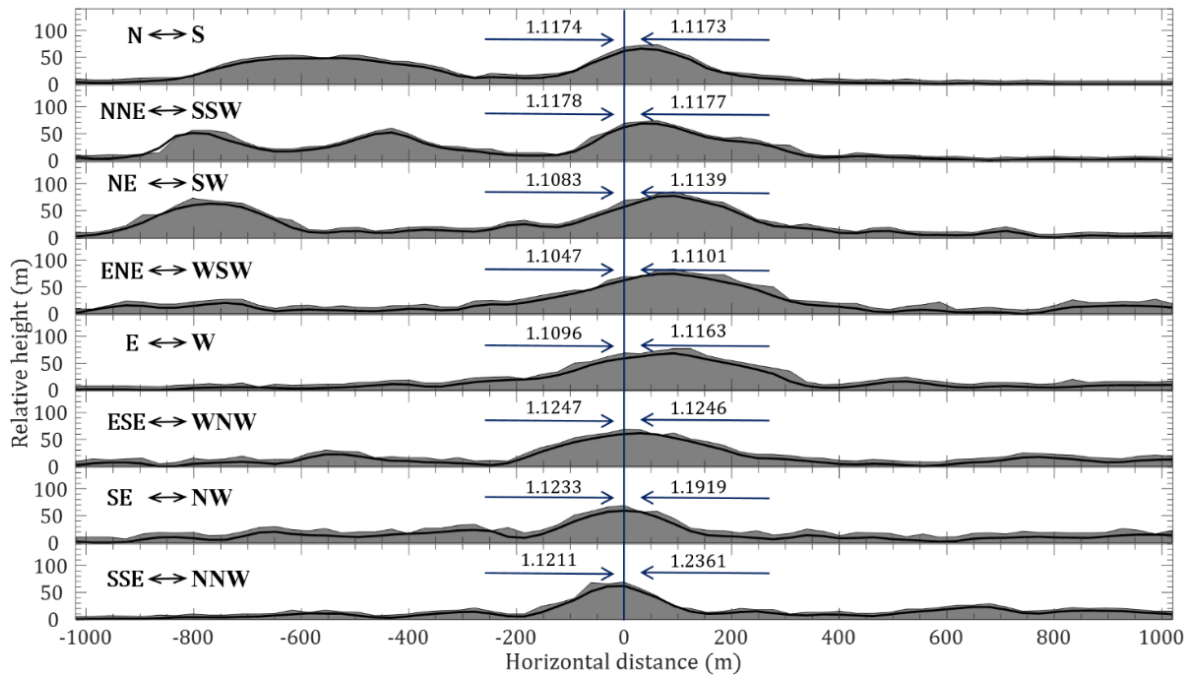


Fig. 3.16 Directional speed-up factor for Yangjiang meteorological station (111.9793°E, 21.8458°N)

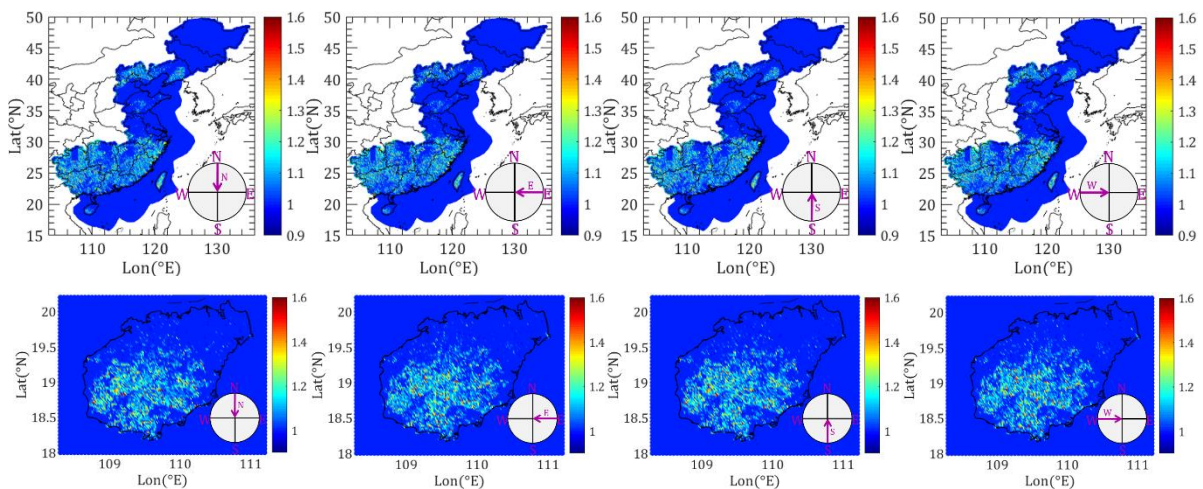


Fig. 3.17 Directional topographic speed-up factor: a) Coastal region of China; b) Hainan island

3.5 Reconstruction of typhoon wind hazard

3.5.1 Surface wind field

To show the effects of surface roughness and topography on the surface wind speed, Fig. 18 illustrates the calculated wind field speeds of the typhoon Rammasun at 06:00 UTC, 07/18, 2014 at a height of 10 m above the ground as well as the adjustment factors in terms of z_0 and K_t . At this moment, typhoon Rammasun was about to land on Hainan island. Fig. 18a is the rebuilt 10-min mean wind speed field using the parameters identified in section 3 (JMA: $P_c = 935 \text{ hPa}$, $\theta_T = 72.11^\circ$ (counter clockwise from north), $B_s = 1.00$, $R_{max,s} = 32 \text{ km}$ (59.26 nmi), $V_{max} = 90 \text{ kt}$) with a uniform underlying roughness length $z_0 = 0.0002\text{m}$, which is the suggested value for over-water condition by MODIS. The over-water typhoon wind fields have also been commonly adopted to reconstruct the real-time wind hazards using multi-platform observation data, such as H*Wind (Powell, et al., 1998). Fig. 18c is the wind velocity field by introducing the directional roughness length (z_0) present in Fig. 18b. The over-water z_0 is given as the function of wind velocity (Eqs. (3.26) - (3.28)). The in-land wind speeds show a pronounced decrease due to the effects of underlying roughness. The coastal off-sea winds remain the velocities as high as that of over-sea winds while off-land winds are featured with the wind characteristics of in-land winds as a result of obstruction of ground objects, suggesting the wind direction play a significant role on typhoon wind hazards. Fig. 3.18(e) is the speed-up factor estimated from the digital elevation data shown in Fig. 3.18(d). After inclusion of speed-up effects, the wind speeds in some inland sites can be observed to be significantly enhanced due to topographic effects (Fig. 3.18(f)). However, it noteworthy that the highest elevation in this example is larger than 1600 m, the typhoon structure around this mountainous area would be greatly

destroyed. The present model is unable to account for the obstruction effects of underlying huge mountains on the elevation of typhoon structures, but to provide a more accurate estimation of typhoon wind hazards using some simple approaches. This issue would be of extreme importance for Taiwan island, which is characterized by largest number and density of high mountains in the world.

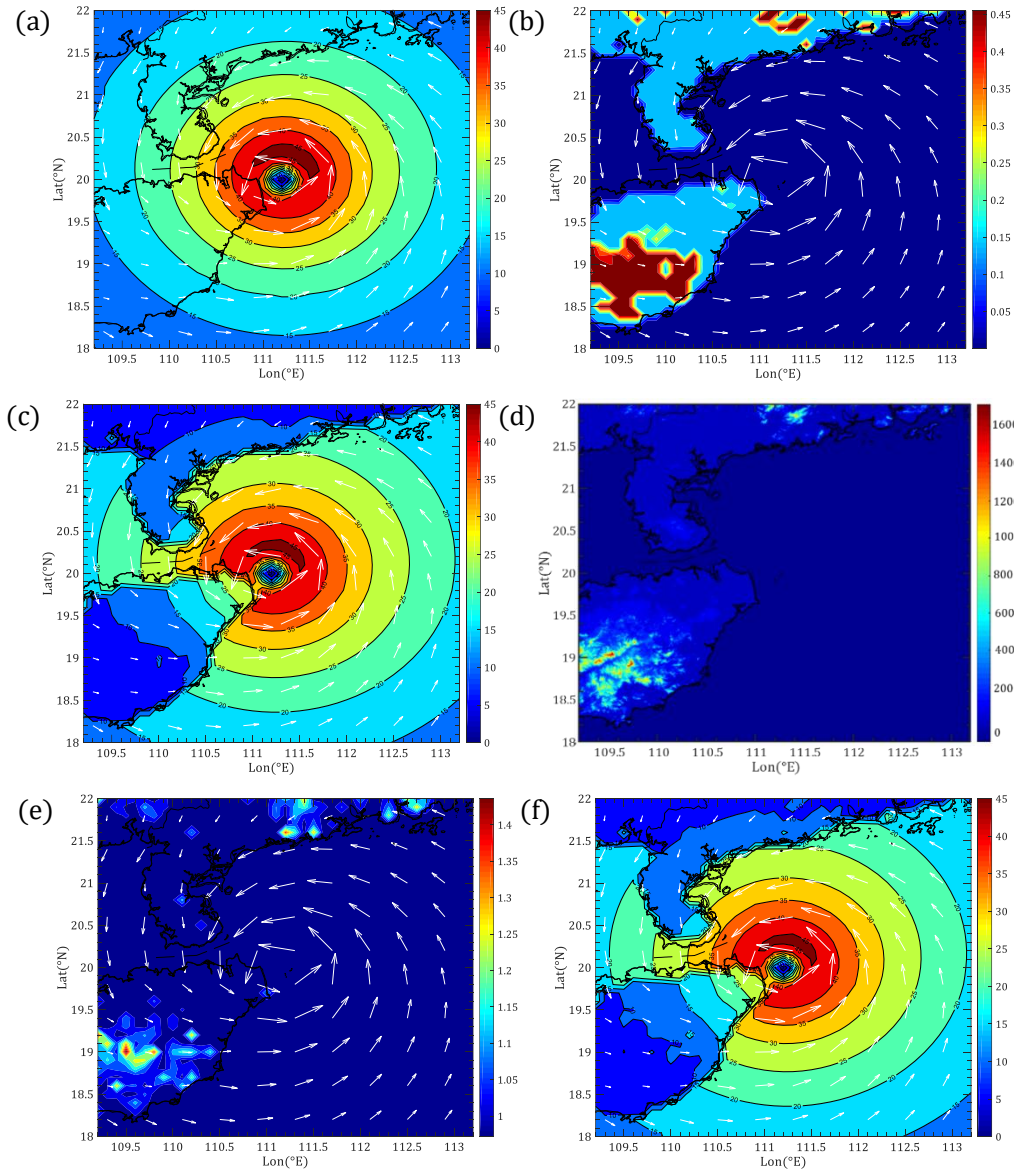


Fig. 3.18 Wind field of strong typhoon Rammasun at 06:00 UTC, 07/18, 2014 (10 m): (a) Wind field with a uniform z_0 (m/s); (b) Directional z_0 (m); (c) Wind field with directional z_0 (m/s); (d) Elevation map (m); (e) Directional K_t ; (f) Wind field with directional z_0 and K_t (m/s);

3.5.2 Maximum wind speed footprints

To reconstruct the wind hazards of historical typhoon events to facilitate the risk assessment and disaster mitigation, the track information of 184 observed typhoon-scale storms from 1977 to 2015 that reached 200 km off China coastline area is extracted, as shown in Fig. 3.19. For each typhoon event, the influence region is first determined with a radius of 350 km centered in observed eye locations. The historical 6-h typhoon track information is interpolated into 15 min to capture the maximum wind speed as accurately as possible. Then, the wind speeds for open water, directional roughness only and roughness and topography combined conditions of each site within the influence region are calculated. The maximum wind speed footprint for each storm event would be readily generated. A database including all this wind information of 184 typhoons has been archived.

Fig. 3.20 presents two examples of maximum wind speed footprints for typhoons Rammasun (201409) and Wayne (198614). Typhoons Rammasun was one of the only two Category 5 super typhoons on record in the South China Sea with maximum 10-min sustained surface wind speed $V_{max} = 90$ knots (46.3 m/s) and lowest central pressure $P_{c,s} = 935$ hPa. Wayne was one of the longest-lasting typhoons on record in the north-western Pacific Ocean with an unusual track meandering for 3 weeks. The recorded $V_{max} = 90$ knots (38.58 m/s) and $P_{c,s} = 955$ hPa. As expected, the over-sea wind speeds almost remain unchanged whereas a significant decrease happens to over-land winds after introducing the roughness. And topographic effects are observed to enhance the over-land wind speed, which is particularly notable to the Taiwan island. The modeled maximum wind speed for typhoon Wayne is up to 47.6 m/s after the introduction of topographic speed-up effects, which is about 23% higher than that of recorded V_{max} and reaches the same storm scale of Rammasun.

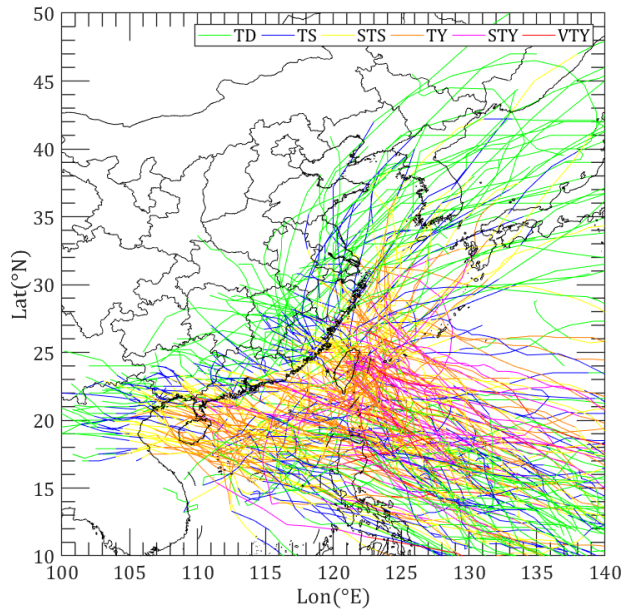


Fig. 3.19 184 historical typhoon tracks from 1977 to 2015 reached 200 km off China coastline area

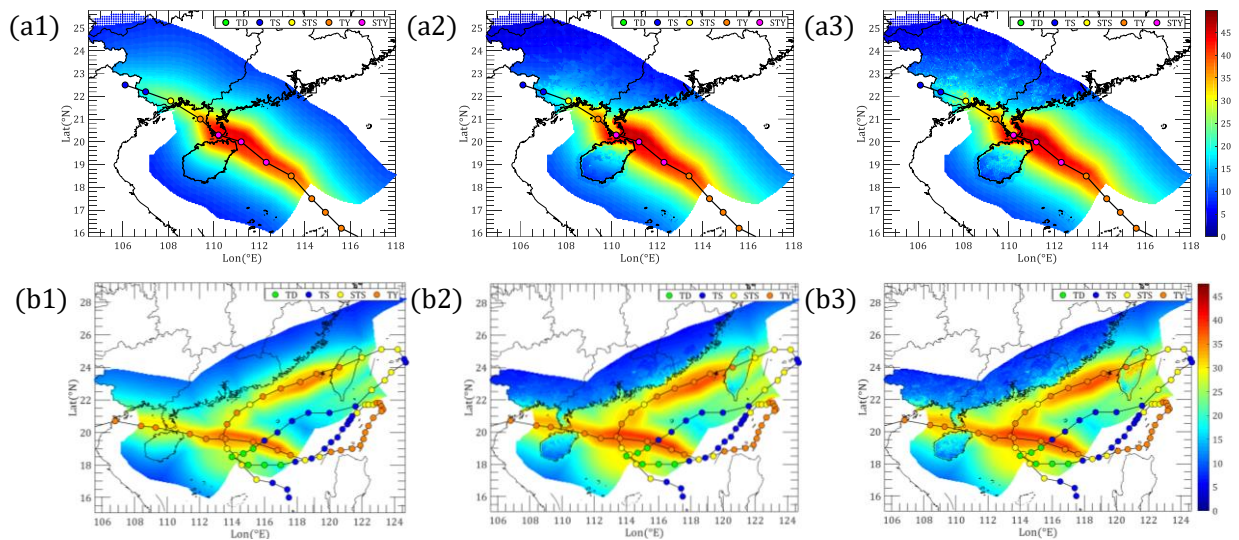


Fig. 3.20 Maximum wind speed footprints of typhoon events (m/s): (a) Rammasun (201409); (b) Wayne (198614); 1~3 are open water, directional roughness only and roughness and topography combined conditions, respectively

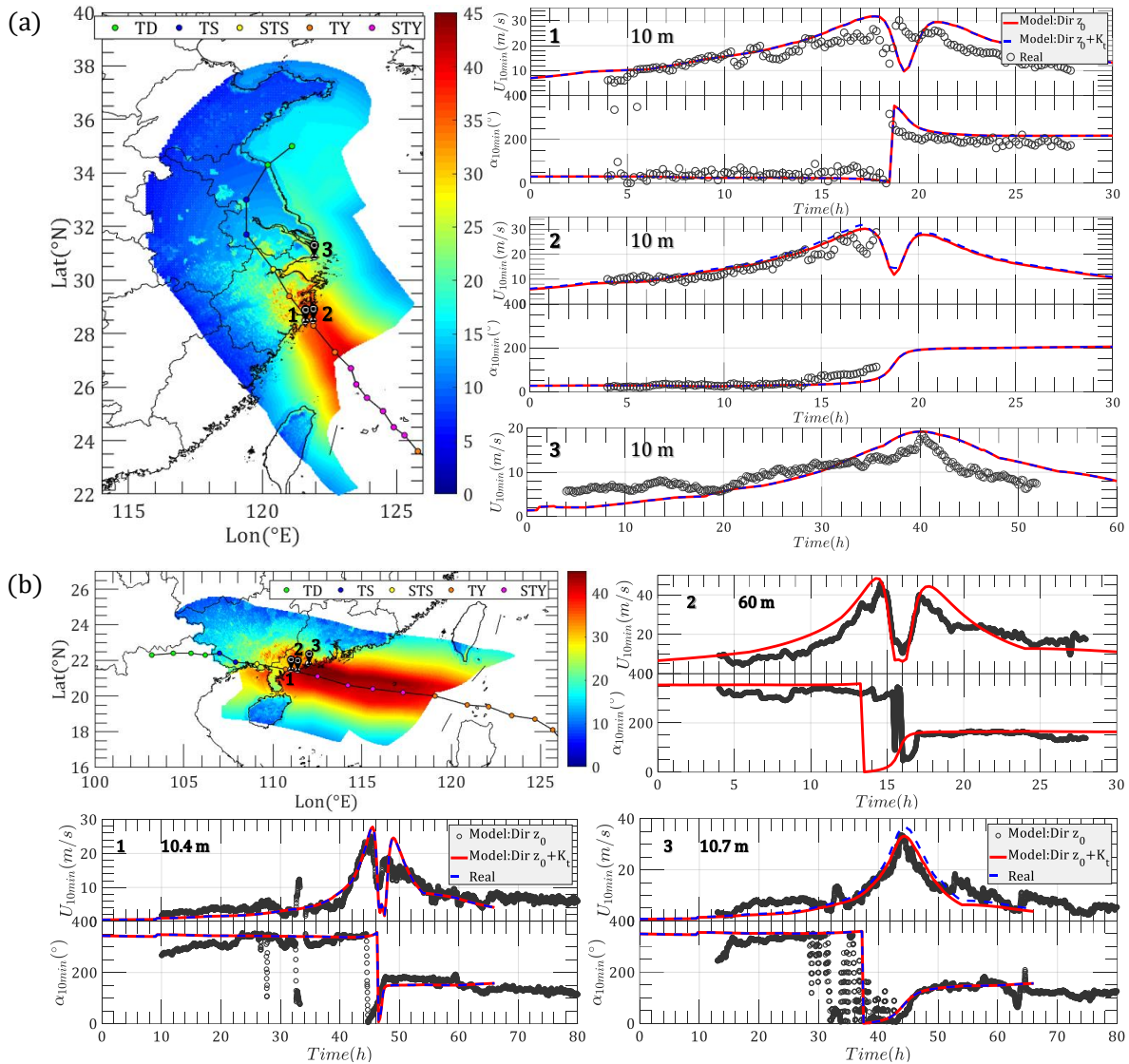


Fig. 3.21 Comparison of observed and modeled 10-min wind speed (m/s): a) Khanun (200515); b) Hagupit (201408);

Two more typhoon events, i.e. Khanun (200515) and Hagupit (200814) are utilized to validate the modeled surface wind speeds, as shown in Fig. 3.21. Khanun is a strong typhoon, which is formed in 2005 and made landfall in Taizhou, Zhejiang Province. During the passage of the typhoon, the wind speeds were captured by three meteorological towers, say (1) Donghaitang (121.6000°E, 28.4642°N), (2) Shangdachen Island (121.8830°E, 28.4952°N) and (3) Luchaogang (121.9305°E, 30.8684°N). Donghaitang and Luchaogang stations locate at open flat areas with speed-up factors equal to 1.0 while the offshore Shangdachen Island

has a maximum speed-up factor of 1.24 from SE to NW. The wind information after the landfall of the typhoon in Shangdachen Island was not recorded due to the sensor damage. And the wind direction information was missing in Luchaogang station. Hagupit was a strong typhoon in 2008, striking Guangdong Province with the $V_{max} = 90$ knots (46.3 m/s) and $P_{c,s} = 935$ hPa. Three stations, i.e. (1) Dianbai (110.9978°E, 21.4982°N), (2) Zhizai Island (111.3795°E, 21.4512°N) and (3) Yangjiang (111.9793°E, 21.8458°N) successfully captured the wind speed time series. The 10-min real wind speeds in Dianbai and Yangjiang showed in Fig. 3.21(b) are moving averaged from 1-min time interval data while 0.1s fluctuating winds are averaged in Zhizai Island. Dianbai has insignificant effects of topography while Yangjiang featured with moderate topographic speed up as shown Fig. 3.16. Zhizai Island is very small that locates about 4.5 km off the coastline (Song et al., 2016) with almost no effects of topography. The wind speeds observed at Dianbai and Yangjiang stations are at 10.4 m and 10.7 m above the ground, respectively, which are considered as 10 m for topography effects. And Zhizai Island recorded wind speeds at height of 60 m. Generally, both the modeled 10-min wind velocities and directions show reasonable agreements with the observed mean results. The topography has slight influence of wind speed in the stations of Shangdachen Island and Yangjiang. Modeled wind time series still fail to reproduce the fluctuations of observed values. These fluctuations could result from a number of sources, such as the vibration and tilt of meteorological tower, the transient terrain effects due to the nonstationary wind direction, rain effects, etc., which are greatly challenging to be ascertained and quantified. The nonstationary characteristics of 10-min mean wind directions can also be observed from Fig. 3.21, which is significantly responsible for the fluctuations of wind speed. The double peaks of an eyewall passage over the station can be

well reconstructed. However, the proximity of the second peak between model and observation is worse than the first peak. [Miller et al., \(2013\)](#) also found a similar issue and discussed two possibilities, i.e. a sudden transition of underlying terrain and imperfections H*WIND model. Similar reasons can also be utilized to explain the present results. From the perspective of wind hazard predictions, the present parametric model has a good estimation of maximum wind speed of each typhoon event that provides us enough confidence for the development of wind hazard curves by running a large number of scenarios.

3.6 Conclusion

The present study developed a dataset of wind parameters, i.e. $R_{max,s}$ and B_s in the Western Pacific Ocean using the wind data information from JMA best track dataset coupled with a semi-analytical typhoon wind field model. Although the parametric pressure model using present $R_{max,s}$ and B_s would result in significant difference from the real pressure field, the modeled wind field is forced to match the observations as closely as possible to increase the accuracy of wind hazards estimation. Each time step of historical tracks from 1977 to 2015 has been allocated an optimal pair of $R_{max,s}$ and B_s that allows the development of recursive models to account for the autocorrelations of parameters between different time steps. Instead of using a single statistical model for the whole domain of interest during the stochastic simulations of wind hazard, the recursive model can be site-specific and can be applied to both sub-region typhoon simulations and full track simulations. This kind of concept is similar to the empirical track and intensity model ([Vickery et al., 2000](#)).

The extraction of $R_{max,s}$ and B_s for each typhoon event also facilitates the reconstruction of wind hazard footprints. The directional upstream terrain effects on wind speed in terms of

an equivalent roughness length z_0 and topographic speed-up factor K_t were investigated. A remarkable decrease can be observed when the roughness effects are considered. And a gradual transition can be noted for both the off-sea and off-land winds. A map including 172812 grid points along the coastal region of China was generated to analyze the typhoon wind hazards during landfall. The wind hazard footprints for over-water, roughness only and roughness and topography combined conditions of 184 observed landed or offshore typhoon-scale storms are generated and archived for risk assessment. The comparison of wind speeds and directions of two typhoons between model and observations shows a reasonable agreement. The good capture of peak wind speeds provides us enough confidence for the present model to conduct the wind hazard simulations by running a large number of scenarios.

3.7 Reference

Batts M E, Russell L R, Simiu E. Hurricane wind speeds in the United States[J]. Journal of the Structural Division, 1980, 106(10):2001-2016.

Broxton, P. D. , Zeng, X. , Sulla-Menashe, D. , & Troch, P. A. . (2014). A global land cover climatology using MODIS data. Journal of Applied Meteorology and Climatology, 53(6), 1593-1605.

Dvorak V F. Tropical cyclone intensity analysis using satellite data[J]. Noaa Tech Rept, 1984, 11.

ESDU, 2011. Mean wind speeds over hills and other topography. Engineering Sciences Data Unit 91043.

European Committee for Standardization (CEN), 2010. Eurocode 1: Actions on Structures Part 1-4: General Actions -Wind Actions. EN 1991 -1-4:2005/AC:2010 (E). European Standard (Eurocode), European Committee for Standardization (CEN), Europe.

Fang G, Zhao L, Cao S, et al. A novel analytical model for wind field simulation under typhoon boundary layer considering multi-field correlation and height-dependency[J]. Journal of Wind Engineering and Industrial Aerodynamics, 2018, 175:77-89.

Fang G, Zhao L, Song L, et al. Reconstruction of radial parametric pressure field near ground surface of landing typhoons in Northwest Pacific Ocean[J]. Journal of Wind Engineering and Industrial Aerodynamics, 2018, 183:223-234.

Holland G J . An analytic model of the wind and pressure profiles in hurricanes[J]. Monthly Weather Review, 1980, 108(8):1212-1218.

Holland G. A Revised Hurricane Pressure-Wind Model[J]. Monthly Weather Review, 2008, 136(9):3432-3445.

Jackson, P. S. , & Hunt, J. C. R. . (1975). Turbulent wind flow over a low hill. Quarterly Journal of the Royal Meteorological Society, 101(430), 929-955.

Jakobsen F, Madsen H. Comparison and further development of parametric tropical cyclone models for storm surge modelling. Journal of wind engineering and industrial aerodynamics, 2004, 92: 375-391.

Hunt, J. C. R. , Leibovich, S. , & Richards, K. J. . (1988). Turbulent shear flows over low hills. Quarterly Journal of the Royal Meteorological Society, 114(484), 1435-1470.

Japan Meteorological Agency (JMA), RSMC Tokyo-Typhoon Center, Best Track Data (1951~2017).

<https://www.jma.go.jp/jma/jma-eng/jma-center/rsmc-hp-pub-eg/besttrack.html>.

Johnson, N. L. . (1949). Systems of frequency curves generated by methods of translation. *Biometrika*, 36(1-2), 149-176.

Kepert J D. Slab- and height-resolving models of the tropical cyclone boundary layer. Part I: Comparing the simulations[J]. *Quarterly Journal of the Royal Meteorological Society*, 2010, 136(652):1700-1711.

Kepert J, Wang Y. The dynamics of boundary layer jets within the tropical cyclone core. Part II: Nonlinear enhancement. *Journal of the atmospheric sciences*, 2001, 58 (17), 2485-2501

Knapp K R , Kruk M C , Levinson D H , et al. THE INTERNATIONAL BEST TRACK ARCHIVE FOR CLIMATE STEWARDSHIP (IBTrACS)[J]. *Bulletin of the American Meteorological Society*, 2010, 91(3):363-376.

Lemelin D R , Surry D , Davenport A G . Simple approximations for wind speed-up over hills[J]. *Journal of Wind Engineering & Industrial Aerodynamics*, 1988, 28(1):117-127.

Miller C , Gibbons M , Beatty K , et al. Topographic Speed-Up Effects and Observed Roof Damage on Bermuda following Hurricane Fabian (2003)[J]. *Weather and Forecasting*, 2013, 28(1):159-174.

National Standards Committee. Load code for the design of building structures, China National Standard (CNS) [S]. GB 50009-2012, National Standards Committee, Beijing, China; 2012.

NOAA Optimum Interpolation 1/4 Degree Daily Sea Surface Temperature (OISST) Analysis, Version 2: Sea Surface Temperature - Optimum Interpolation, <https://www.ncdc.noaa.gov/oisst>, NOAA National Centers for Environmental Information, 2018.

Powell, M. D. , Houston, S. H. , Amat, L. R. , & Morisseauleroy, N. . (1998). The HRD real-time hurricane wind analysis system. *J. Wind Eng. Ind. Aerodyn.*, 77(5), 53–64.

Powell M, Soukup G, Cocke S, et al. State of Florida hurricane loss projection model: Atmospheric science component. *Journal of Wind Engineering & Industrial Aerodynamics*, 2005, 93(8):651-674.

Snaiki R, Wu T. Modeling tropical cyclone boundary layer: Height-resolving pressure and wind fields[J]. *Journal of Wind Engineering & Industrial Aerodynamics*, 2017, 170:18-27.

Song, L. , Chen, W. , Wang, B. , Zhi, S. , & Liu, A. . (2016). Characteristics of wind profiles in the landfalling typhoon boundary layer. *Journal of Wind Engineering & Industrial Aerodynamics*, 149, 77-88.

Tan, C. , & Fang, W. . (2018). Mapping the wind hazard of global tropical cyclones with parametric wind field models by considering the effects of local factors. *International Journal of Disaster Risk Science*, 9(1), 86-99.

Taylor, P. A. , Walmsley, J. L. , & Salmon, J. R. . (1983). A simple model of neutrally stratified boundary-layer flow over real terrain incorporating wavenumber-dependent scaling. *Boundary-Layer Meteorology*, 26(2), 169-189.

Velden C, Harper B, Wells F, et al. The Dvorak Tropical Cyclone Intensity Estimation Technique: A Satellite-Based Method that Has Endured for over 30 Years[J]. *Bull.amer.meteor.soc*, 2006, 87(9):6.

Vickery P J, Skerlj P F, Steckley A C, et al. Hurricane Wind Field Model for Use in Hurricane Simulations[J]. *Journal of Structural Engineering*, 2000, 126(10):1203-1221.

Vickery P J , Skerlj P F , Twisdale L A . Simulation of Hurricane Risk in the U.S. Using Empirical Track Model[J]. *Journal of Structural Engineering*, 2000, 126(10):1222-1237.

Vickery P J , Skerlj P F . Hurricane Gust Factors Revisited[J]. Journal of Structural Engineering, 2005, 131(5):825-832.

Vickery P J , Wadhera D . Statistical Models of Holland Pressure Profile Parameter and Radius to Maximum Winds of Hurricanes from Flight-Level Pressure and H*Wind Data[J]. Journal of Applied Meteorology and Climatology, 2008, 47(10):2497-2517.

Vickery P J , Wadhera D , Powell M D , et al. A Hurricane Boundary Layer and Wind Field Model for Use in Engineering Applications[J]. Journal of Applied Meteorology & Climatology, 2009, 48(2):381-405.

Vickery, P. J. , Wadhera, D. , Twisdale, L. A. , & Lavelle, F. M. . (2009). U.S. hurricane wind speed risk and uncertainty. Journal of Structural Engineering, 135(3), 301-320.

Weng W , Taylor P A , Walmsley J L . Guidelines for airflow over complex terrain: model developments[J]. Journal of Wind Engineering & Industrial Aerodynamics the Journal of the International Association for Wind Engineering, 2000, 86(2):169-186.

Xiao Y F , Duan Z D , Xiao Y Q , et al. Typhoon wind hazard analysis for southeast China coastal regions[J]. Structural Safety, 2011, 33(4):286-295.

Yan Meng , Masahiro Matsui , Kazuki Hibi . An analytical model for simulation of the wind field in a typhoon boundary layer[J]. Journal of Wind Engineering and Industrial Aerodynamics, 1995, 56(2-3):291-310.

Zhang Q , Liu Q , Wu L . Tropical Cyclone Damages in China 1983–2006[J]. Bulletin of the American Meteorological Society, 2009, 90(4):489-495.

Zhao L , Lu A , Zhu L , et al. Radial pressure profile of typhoon field near ground surface observed by distributed meteorologic stations[J]. Journal of Wind Engineering and Industrial Aerodynamics, 2013, 122:105-112.

CHAPTER 4 OBSERVATION-BASED GUST CHARACTERISTICS OF NEAR-GROUND TYPHOON WINDS: A NON-GAUSSIAN PERSPECTIVE

4.1 Background

Wind in the atmospheric boundary layer is always featured with gust or fluctuation due to the friction effects caused by obstruction of ground objects as well as the deep convection process. The quantification of gust characteristics, i.e. gust factor, turbulence intensity and power spectrum density (PSD), is always a fundamental work to better understand the turbulence structure and provide enough information for the wind-resistant design of structures. Among them, gust factor, which is defined as the ratio of maximum gust wind speed (averaged over a short time period τ in wind engineering) at height z to mean wind speed over a relatively long reference period T , can be formulated as

$$G_u(\tau, T, z, z_0) = \frac{\hat{U}(\tau, z, z_0)_{max}}{\bar{U}(T, z, z_0)} \quad (4.1)$$

where z_0 is the roughness length approximately accounting for the underlying terrain exposure effects on wind fluctuations. $\hat{U}(\tau, z, z_0)$ and $\bar{U}(T, z, z_0)$ are peak gust value and mean wind speed over a given reference period T , in which, $\tau = 3$ s and $T = 600$ s or 3600 s are widely adopted. Gust factor serves as a medium to convert mean wind speeds to peak gusts and vice versa, and is commonly-used in wind engineering applications, e.g. typhoon gust wind prediction (Vickery et al., 2005, 2009a; Masters et al., 2010), potential extreme wind load in engineering applications (ESDU, 1983; Vickery et al., 2009; ASCE, 2014) and standardization of observation metadata from different stations (Masters et al., 2010, He et al., 2014, 2017). Moreover, in the field of climatology and forecasting, the agency-specified

wind speed averaging period varies considerably which could result in the misunderstanding of forecasting results and misuse of observation data. For example, the tropical cyclone intensity scale, which is officially ranked by its maximum surface sustained wind speed, suffers remarkable difference due to the averaging-time inconsistency, such as the National Hurricane Center (NHC) and Joint Typhoon Warning Center (JTWC) use 1 min, Japan Meteorological Agency (JMA) employs 10 min while 2 min is adopted by the China Meteorological Administration (CMA). More importantly, the code-specified gust durations in different countries also exhibit some differences, i.e. 3 s (WMO, 2010; ASCE 7-10, 2014; Kwon et al., 2013) and 0.2s (Holmes et al., 2012). Thus, a great deal of wind observations, especially for strong typhoon winds (Vickery et al., 2005; Yu et al., 2008; WMO, 2010; Balderrama et al., 2012; Cao et al., 2015; Shu et al., 2015), are conducted in the past several decades with the emphasis on recommending a reasonable value of gust factor. The most widely used model is the Krayner and Marshall (1992) gust factor curve for converting between averaging times which was also adopted by ASCE 7-95.

Theoretically, based on the assumption that wind-speed fluctuations are mutually independent and follow a Gaussian distribution, the gust factor can be alternatively estimated in the light of the peak factor theory (Durst 1960) as

$$G_u(\tau, T, z, z_0) = 1 + g(\tau, T) \frac{\sigma_u(\tau, T, z, z_0)}{\bar{U}(T, z, z_0)} = 1 + g(\tau, T) SD_u(\tau, T, z, z_0) \quad (4.2)$$

where $\sigma_u(\tau, T, z, z_0)$ is the standard deviation of the gust fluctuations filtered with a cut-off low-frequency $1/T$ and a high frequency of $1/\tau$ Hz. $g(\tau, T)$ is called the peak factor. $SD_u(\tau, T, z, z_0)$ is the normalized standard deviation. If gust period τ is the same as the sampling duration of instantaneous wind, usually 0.25s~3s depending on the specific

requirement from various codes, $SD_u(\tau, T, z, z_0)$ is equal to the turbulence intensity I_u . Eq. (4.2) provides an alternative approach for rapid estimation of gust factor, which has also been studied in a great deal of work (Davenport, 1964; Kareem et al., 1994; Balderrama et al., 2012). Balderrama et al. (2012) analyzed the peak factors in hurricane winds stratified by wind speed and turbulence intensity regime, and this work showed that the non-Gaussian effects cannot be neglected in the estimation of peak factors. Many more studies have investigated the relationship between gust factor and turbulence intensity of typhoon winds and extended the expression of Eq. (4.2) to several more complex formulas (Choi, 1983; Ishizaki, 1983; Cao et al., 2009).

Conventionally, wind speed is usually considered as a stationary and Gaussian random process which has been accepted by various codes and standards during the wind-resistant design. And the peak factor as described in Eq. (4.2) is customarily estimated based on an underlying stationary and Gaussian process with peaks over threshold approach suggested by some pioneer studies (Davenport, 1964). However, unlike normal winds, typhoon winds always exhibit strong non-stationary and non-Gaussian characteristics due to the effects of thermodynamic interaction (Li et al., 2015) and its rotating storm system, which has been proved in many recent field observations (Chen et al., 2007; Balderrama et al., 2012). Accordingly, more and more studies try to examine the non-stationary and non-Gaussian characteristics of typhoon winds (Chen et al., 2007; Balderrama et al., 2012; Tao et al., 2017) and reveal their potential effects on structure dynamic behaviors (Chen, 2008; Hu et al., 2017). Although a non-stationary wind record could suffer various transient characteristics in both frequency and time domains, the time-varying mean wind speed is the most concerned non-stationary feature in wind engineering applications. Thus, most studies

decomposed the non-stationary wind speed with a time-varying mean trend and a stationary fluctuating component with different numerical techniques, such as discrete wavelet transform (DWT) (Tao et al., 2017) and empirical mode decomposition (EMD) (Chen et al., 2007). And some researches highlighted that if the non-stationarity of typhoon winds is inadequately considered, the gust factors could be overestimated (Wieringa, 1973; Tao et al., 2017). Non-Gaussian characteristic of fluctuating typhoon winds in terms of skewness $\neq 0$ or kurtosis $\neq 3$ is an inherently essential due to the complex effects of atmospheric convection coupled with mechanical interaction with near-ground roughness elements in the boundary layer (Balderrama et al., 2012; Li et al., 2015). A number of field measurements also demonstrated that these non-Gaussian features would disperse the values of peak factor as well as the gust factor (Balderrama et al., 2012; Li et al., 2015) which can also be extended to explain the non-Gaussian wind pressure and dynamic response of structures subjected to tropical cyclones (Xu et al., 2001; Li et al., 2004). Consequently, the traditional model based on stationary and Gaussian assumption is unable to reproduce the observed gust characteristics and the extreme wind loads could be underestimated.

Moreover, as summarized by the World Meteorological Organization (WMO, 2010), the observed and some theoretical typhoon gust factor curves that are used for wind speed conversions between various periods show many inconsistencies. Although a series of near-surface (10m) convention factors were recommended for four categories of terrain exposures, there are still significant gaps in our understanding of near-ground turbulence characteristics for strong typhoon winds.

In this study, the non-stationary characteristics of typhoon winds, which are featured as the time-varying mean, and the non-Gaussian characteristics in terms of skewness and kurtosis

are first examined based on field observations during 9 typhoons. Then the first four-order statistics of each 10 min segments together with the gust representations, i.e. turbulence intensity, gust factor, and peak factor are determined by the non-stationary model. The correlation analyses among these measures are conducted to reveal the potential effects of non-Gaussian features on peak factor as well as gust factor. After that, a non-Gaussian theoretical model for peak factor estimation is developed with a PSD-based Gaussian solution coupled with a moment-based translation model, followed by a discussion of variation tendencies of peak and gust factors with the change of skewness and kurtosis. A comparison is conducted with respect to peak and gust factors for various gust durations obtained from theoretical solutions and observations to validate the accuracy of the model. Finally, a standardization scheme for site-specific gust factor curve is developed by using a commonly used standard deviation equation of typhoon winds. With the introduction of the distributions of skewness and kurtosis, a cluster of gust factor curves is generated by Monte Carlo simulation. Moreover, a discussion regarding the effects of model and aleatory uncertainties on gust characteristics of near-ground typhoon winds is performed.

4.2 Typhoon winds dataset

4.2.1 Description of the observation site

The Xihoumen bridge (121°54'E, 30°03'N), which connects the Jintang and Cezi islands in Zhejiang Province of China with the main span of 1650m, is the longest-span box-girder suspension bridge around the world built in 2009. The bridge axis is located at 45° north by east. The bridge site is located right in the eastern coastal region of China, which is a typhoon-prone area with an average of 2~3 typhoons each year. Thus, an advanced structural health

monitoring system (SHMS) was implemented to monitor the real-time dynamic response as well as the wind field characteristics. As shown in Fig. 4.1a, six Young Model 8100 3D ultrasonic anemometers (UA1 ~UA6) were installed on the lighting columns at the 1/4, 1/2 and 3/4 main spans with 6 m height above the bridge deck to capture the transient wind speeds. And the mid-span anemometer at an elevation of about 76.5m above the sea level. The 3D ultrasonic anemometer is able to record the wind speeds ranging from 0 to 40m/s (0 to 90 mph) with a resolution of 0.01m/s and the horizontal wind direction from 0° to 360° with a resolution of 0.1°. The sampling frequency was set as 32 Hz during the typhoon measurements. North is defined as 0° for wind direction with the positive direction clockwise. Three directions (x , y , and z) of the body axis of the anemometer are orientated to north, west and vertical directions, respectively while the corresponding recorded wind speeds are denoted as u_x , u_y and u_z . Before analyzing the wind characteristics, all measured wind speeds are decomposed into three orthogonal components, i.e. longitudinal, lateral and vertical wind speeds, by the vector decomposition method. The study for the longitudinal component, especially for gust characteristics is always an issue of priority in engineering applications which is also the main concern in the present study.

From years of 2011 to 2015, wind data during 9 typhoons were successfully captured by the anemometers, as shown in Fig.1b, including 1109 Muifa, 1115 Roke, 1215 Bolaven, 1216 Sanba, 1307 Soulik, 1408 Neoguri, 1416 Fung-Wong, 1509 Chan-Hom, and 1515 Goni. In Total, 624-hour wind speeds for each anemometer were measured. It can be noted at the latitude of about 30°N, only a few of typhoons would land and pass through the bridge site directly due to the effects of Coriolis force. Most typhoons would turn their directions or proceed northward as they approach the bridge site, which results in a great many directions

of high-speed wind are approximately parallel to the bridge axis and would be excluded from final results. This is the primary cause that the highest 10-min mean longitudinal wind speed adopted in this study is only 25m/s.

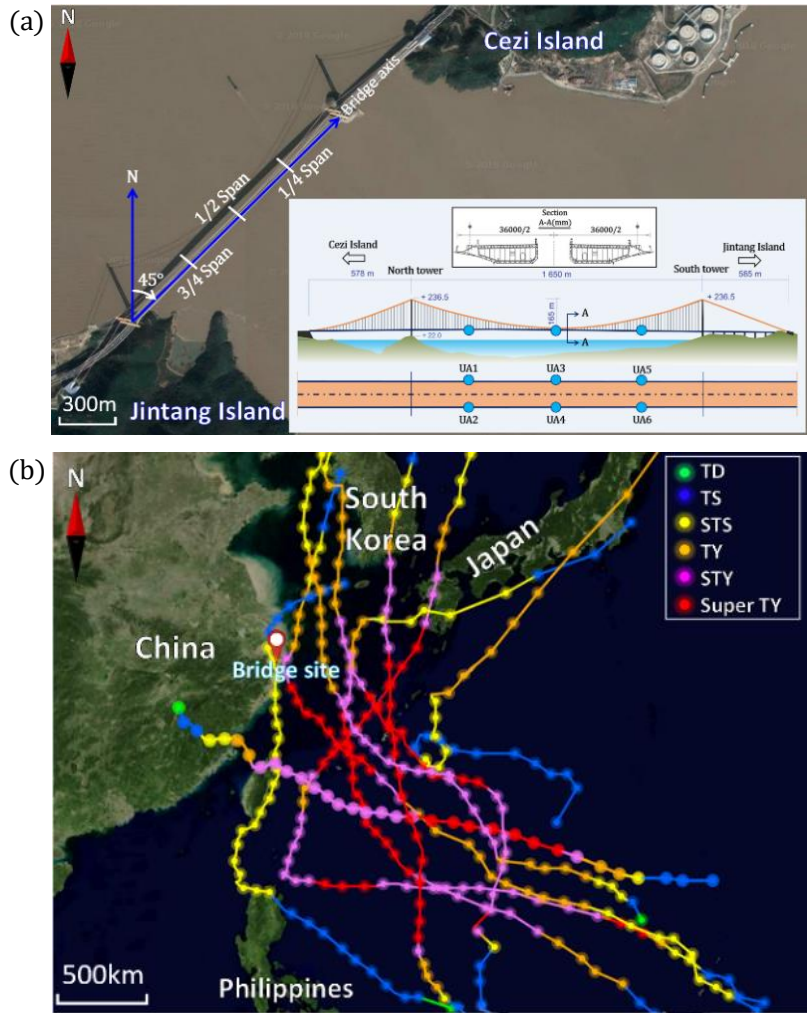


Fig. 4.1 Typhoon winds observation in Xihoumen Bridge: (a) Arrangement of bridge and anemometers, (b) Typhoon tracks (map images from Google Map, (TD: Tropical depression (10.8~17.1 m/s), TS: Tropical storm (17.2~24.4 m/s), STS: Strong Tropical storm (24.5~32.6 m/s), TY: Typhoon (32.7~41.4 m/s), STY: strong typhoon (41.5~50.9 m/s), Super TY: Super typhoon (≥ 51 m/s))

4.2.2 Data quality control

To guarantee the data quality, all records are preprocessed to remove the data affected by the bridge structure and malfunctioning or damaged sensors. Data quality control is conducted by following several criteria as: (1) Given that typhoon is a typically strong vortex

structure whose wind directions will continuously vary in a specific site during its translation, only the winds with their horizontal directions within $60^{\circ}\sim 210^{\circ}$ north by east for anemometers of UA1, UA3, UA5 and $-120^{\circ}\sim 30^{\circ}$ for UA2, UA4, UA6 are considered to minimize the effects of bridge structure on wind filed. (2) 10-min mean wind velocity is constrained to be higher than 5m/s which is a reasonable and practical criterion to meet the neutral stability condition of the boundary layer (Masters et al., 2010). (3) The maximum 3s-gust wind speed in the 10-min record should not be beyond 5 times the standard deviations away from the mean wind speed (Masters et al., 2010; He et al., 2013). As thus, the effects of noise or anomalous gust values caused by the anemometer's own defects as well as several environmental factors can be basically eliminated. (4) All power spectral densities in the frequency domain are also examined to detect the energy peaks at high-frequency region ($>2\text{Hz}$). It could be caused by the resonant response of the lighting columns that support the anemometers since their natural frequencies are almost higher than 2Hz (Caracoglia et al., 2007). After that, 4007 sets of 10-min record wind speed have remained.

4.3 Gust characteristics

4.3.1 Non-stationarity

As mentioned before, a non-stationary process is theoretically considered as a stochastic process whose unconditional joint probability distribution would change when shifted in time. Consequently, the statistics, such as mean value and standard deviation, as well as frequency components would change over time. For engineering applications, the time-varying mean wind speed is always characterized the most concerned feature in typhoon events which is also the most common cause of violation of stationarity. To accurately depict

non-stationary characteristics of typhoon winds, the extraction of the time-varying mean value is one of the critical steps before calculating the gust parameters, say, turbulence intensity and gust factor. Furthermore, the averaging time or segment time of mean wind speed always largely control the value of design wind velocity as well as characteristics of the fluctuating component. As highlighted by [Cao et al. \(2015\)](#) and [Tao et al. \(2017\)](#), the stationarity portion of typhoon winds would first increase and then drop with the increase of averaging time from 1 min to 1 hour and would reach the maximum when segment duration is set as about 10min to 30min. However, a same number of sub-segments was selected in their studies for different averaging durations during run tests, i.e. $N = 30$ in [Cao et al. \(2015\)](#), which would have immediate impacts on stationary tests. In present study, 10-min segment duration is adopted in order to be consistent with the most design codes as well as previous studies ([Cao et al., 2015](#); [Tao et al., 2017](#)), which is also a commonly used averaging duration in typhoon numerical simulation and hazard prediction ([Vickery et al., 2009](#); [Fang et al., 2018](#)).

First, the run tests ([Cao et al., 2015](#)) are conducted for 4007 sets of 10-min records. Each 10-min record is divided into $N = 60$ sub-segments to count the number of runs with the confidence level of 5% by considering the sampling frequency is 32 Hz. That is, each 10-s sub-segments is roughly considered as a stationary process. The test results show that there is about 92.5% portion (46.99 % when $N = 30$) of records reject the null hypothesis at the 5% significance level, say non-stationary wind speed records. After that, the time-varying trend of each sample would be extracted by a self-adaptive DWT-based method as introduced by [Tao et al. \(2017\)](#) with the db10 wavelet if the run test suggests a non-stationary result. Otherwise, a constant mean would be adopted. The maximum decomposed

level for DWT is $n_0 = \log_2(T \cdot f_{sampling}) = 14$. Finally, the non-stationary model (Tao et al., 2017) is employed to calculate the gust parameters, including turbulence intensity I_u , gust factor G_u and peak factor g with the form of

$$I_u^*(\tau, T) = \frac{\sigma_u^*(\tau, T)}{\bar{U}^*(T)} \quad (4.3)$$

$$G_u^*(\tau, T) = \max \left[\frac{U(\tau, T)}{\tilde{U}^*(\tau, T)} \right] \quad (4.4)$$

$$g^*(\tau, T) = \frac{\max[u^*(\tau, T)]}{\sigma_u^*(\tau, T)} \quad (4.5)$$

in which the asterisk (*) indicates the non-stationary model, $U(\tau, T)$ is the longitudinal wind speed record, $u^*(\tau, T)$ is the fluctuating component after removing the underlying trend of wind speed $\tilde{U}^*(\tau, T)$ expressed as

$$u^*(\tau, T) = U(\tau, T) - \tilde{U}^*(\tau, T) \quad (4.6)$$

$\bar{U}^*(T)$ is an equivalent mean wind speed defined as

$$\bar{U}^*(T) = \frac{1}{T} \int_0^T \tilde{U}^*(\tau, T) d\tau \quad (4.7)$$

Fig. 4.2 illustrates three typical cases of stationary and non-stationary records as well as the corresponding probability density of the fluctuating component of wind speed. It can be noted that the time-varying mean wind speed obtained by DWT-based method for those stationary records that pass the run test is close to the constant mean (Fig. 4.2a). But for non-stationary cases, as shown in Fig. 4.2b~c, a remarkably obvious difference can be observed between time-varying and constant mean wind speeds. Moreover, the probability density of fluctuating wind components after removing the constant and time-varying means as shown in Fig.2 also exhibits a significant difference. And it seems that the probability density of

fluctuating wind speed after extracting underlying trend is closer to Gaussian distribution in which the skewness (γ_3) and kurtosis (γ_4) are closer to 0 and 3.0, respectively when compared to the stationary assumption-based model. More details regarding non-Gaussian characteristics will be discussed in the next section. Given that several gust characteristics, including gust factor, turbulence intensity and PSD identified by stationary and non-stationary models have been comparatively investigated by [Tao et al., \(2017\)](#), a similar comparison study is omitted herein for brevity. The non-stationary model, which is considered to more accurately reveal the wind field features in essence, will be adopted to study the gust factor characteristics.

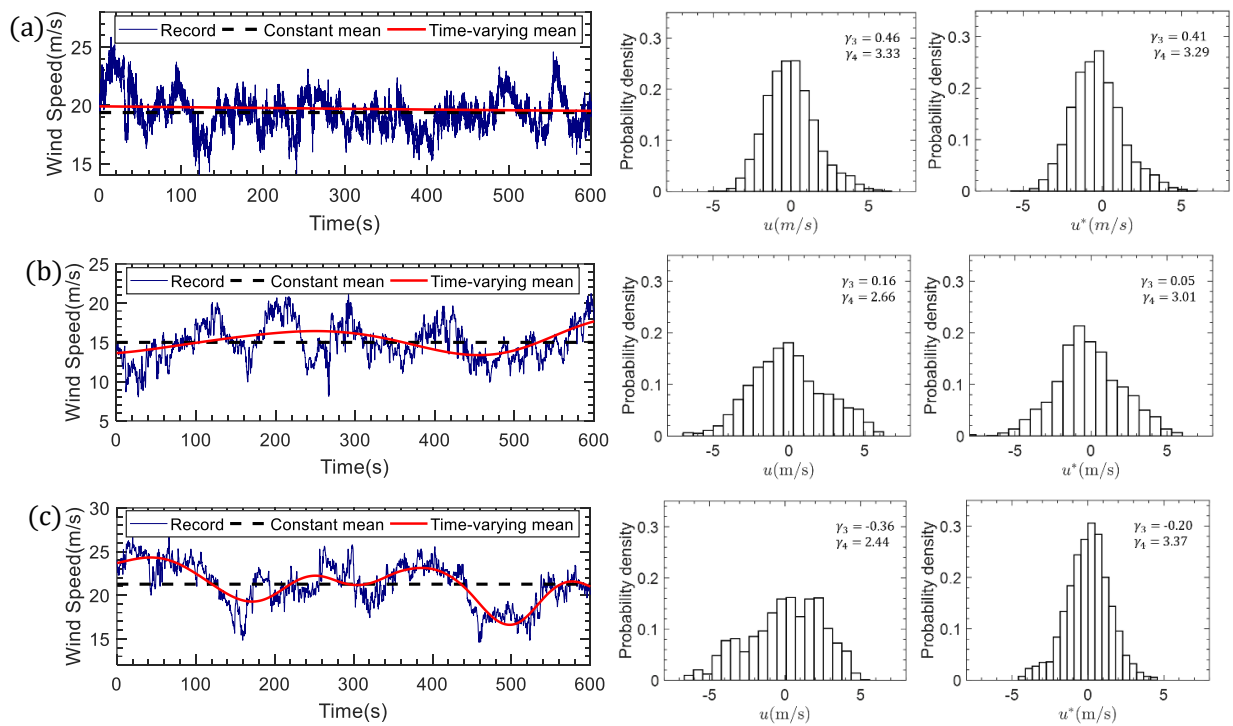


Fig. 4.2 Wind speed decomposition and probability density of fluctuating component: a) Stationary record; b) Weak non-stationary record; c) Strong non-stationary record; (u and u^* are the fluctuating components of wind speed for the stationary and non-stationary models)

4.3.2 Non-Gaussian characteristics

A random variable with a Gaussian or normal distribution is usually said to be Gaussian distributed and is called a Gaussian time series which can be characterized in terms of its 3rd and 4th moments, say, skewness $\gamma_3 = 0$ and kurtosis $\gamma_4 = 3$ for a normalized Gaussian history. It is also a fundamental assumption for wind time series ([Davenport, 1964](#)). In reality, non-Gaussian features of wind speed are the primary cause why observed statistics are likely to scatter during actual events. As shown in Fig. 4.3, the skewness and kurtosis of all stationary fluctuating winds u^* with gust durations of 0.25 s ([Holmes et al., 2012](#)) and 3 s ([WMO, 2010](#); [ASCE 7-10, 2014](#)) are illustrated in term of cumulative probability. The values of skewness fluctuates at the range of $-2 \sim 1$ and approximately follow the normal distribution with the means of -0.09 ($\tau = 0.25\text{s}$) and -0.13 ($\tau = 3\text{s}$), and the standard deviations of 0.31 ($\tau = 0.25\text{s}$) and 0.29 ($\tau = 3\text{s}$), which means most distributions of fluctuating winds are left-skewed or left-tailed. As for kurtosis, its value varies from 2 to about 10 which indicates that the majority of fluctuating winds distributions are leptokurtic and more peaked than a normal distribution with longer tails. And a lognormal distribution is adopted to describe the variation of kurtosis with logarithmic means of 1.17 ($\tau = 0.25\text{s}$) and 1.22 ($\tau = 3\text{s}$), and logarithmic standard deviations of 0.18 ($\tau = 0.25\text{s}$) and 0.17 ($\tau = 3\text{s}$). Thus, Gaussian distribution always fails to describe the fluctuating characteristics of winds. In particular, the peak factor as well as gust factor, which are two typically representations for the magnitude of maximum winds cannot be accurately estimated by following the Gaussian distribution, sometimes even are underestimated.

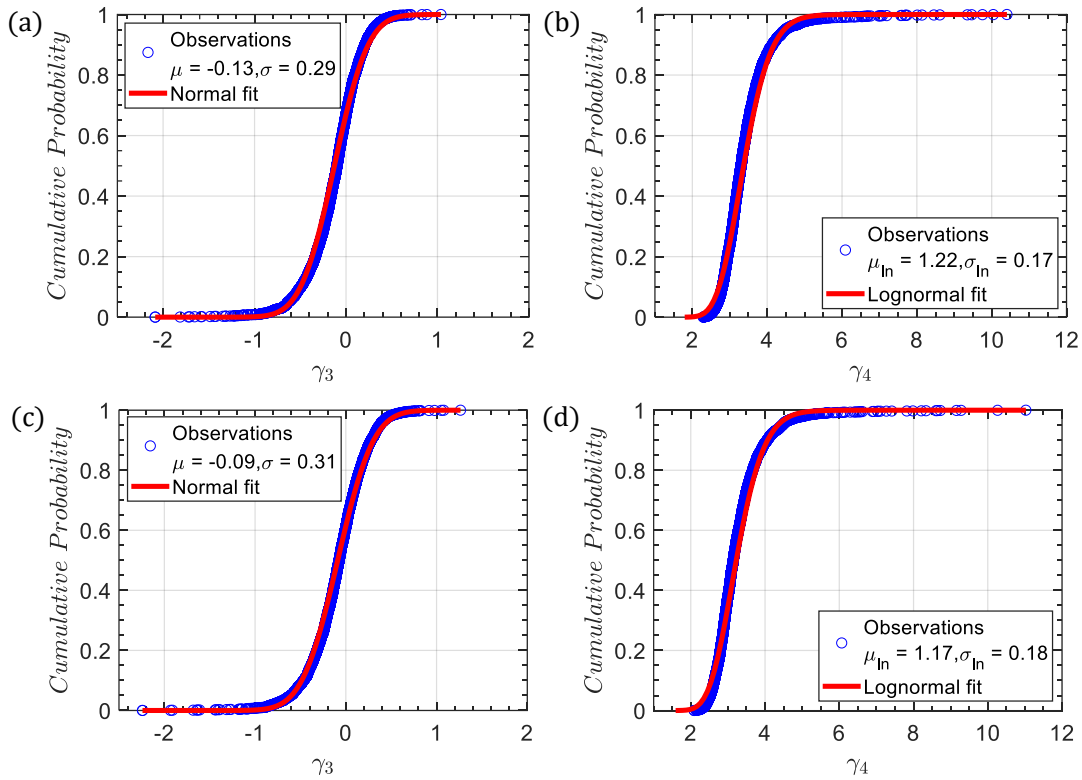


Fig. 4.3 Skewness and kurtosis distributions of stationary fluctuating winds: a) skewness ($\tau=0.25s$), b) kurtosis ($\tau=0.25s$), c) skewness ($\tau=3s$), d) kurtosis ($\tau=3s$)

4.3.3 Gust statistics and correlations

To better understand the correlations between each statistic as well as gust characteristics, the dependence analysis of first four-order statistics of wind speeds coupled with turbulence intensity, gust factor and peak factor calculated by Eqs. (4.3)~(4.7) are conducted ($\tau = 3 s$). As shown in Fig. 4.4, the turbulence intensity and gust factor are negatively correlated with mean wind speed to some extent which has been proved in many observations (Vickery et al., 2005; Yu et al., 2008; Cao et al., 2015; Shu et al., 2015). Two high-order statistical attributes of non-Gaussian characteristics, say, skewness (γ_3) and kurtosis (γ_4) almost has no relation with mean wind speed. Peak factor is also independent of wind speed with a

mean of 2.93. This is a little higher than the estimated value based on the Gaussian assumption with $\tau = 3$ s and $T = 600$ s which is approximately 2.575 from the standard normal deviate for $1-3/600=0.995$. Moreover, the peak factor has a wide range of scattering from 1 to 6. Standard deviation and mean wind speed are always characterized by a non-dimensional turbulence intensity, which shows a remarkably strong relation with gust factor and a weak relation with peak factor. As suggested by [Ishizaki et al. \(1983\)](#) and [Choi \(1983\)](#), this strong relationship can be mathematically formulated with

$$G_u^*(T, \tau) = 1 + k_1 \cdot I_u^{*k_2} \cdot \ln \frac{T}{\tau} \quad (4.8)$$

in which k_1 and k_2 are two undetermined coefficients. Ishizaki and Choi suggested $k_1 = 0.5$, $k_2 = 1.0$ and $k_1 = 0.62$, $k_2 = 1.27$. The fitting results in the present study are $k_1 = 0.45$, $k_2 = 0.92$ when $\tau = 3$ s and $T = 600$ s, which has a better agreement with Ishizaki's recommendation and is consistent with the conclusion reached by [Li et al. \(2015\)](#). More simply, G_u^* and I_u^* can also be connected with Eq. (4.2) with a constant peak factor of 3.02 which is higher than the Gaussian estimation as well. Besides, turbulence intensity also exhibits a weak relation with γ_3 and γ_4 which could propagate from the weak relations with standard deviation.

Furthermore, Skewness (γ_3) and kurtosis (γ_4) are moderately independent with each other with the correlation coefficient $\rho = -0.315$. And these two statistics have weak or even no correlations with turbulence intensity and gust factor. However, a relatively strong correlation can be readily noted between γ_3 and peak factor while γ_4 also has a moderate relation with peak factor. This suggests that the peak factor can be potentially modeled with γ_3 and γ_4 to account for the non-Gaussian effects. Unsurprisingly, the peak factor is

independent of gust factor which can be explained from Eq.(4.2) and previous analyses, the fitting result for the peak factor is always a constant.

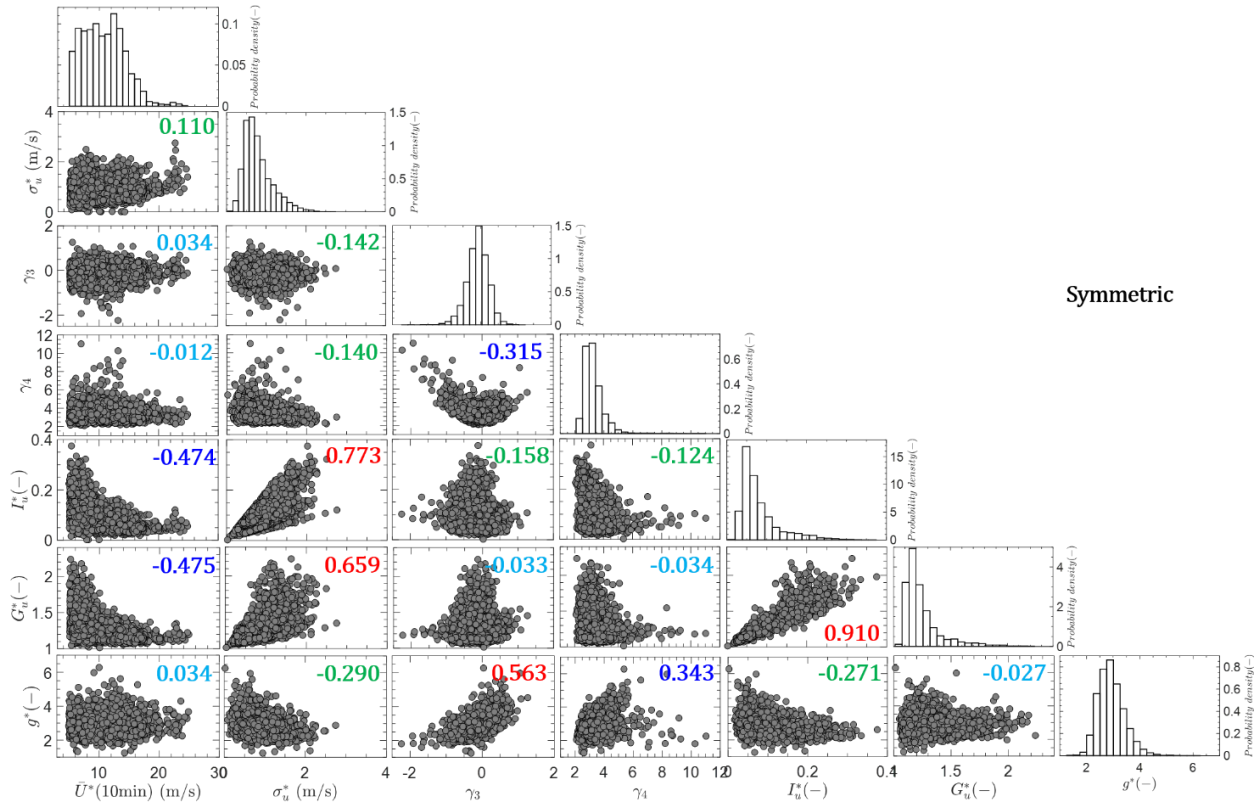


Fig. 4.4 Correlations among first four-order statistics and gust characteristics (The number in each figure is correlation coefficient ρ , red: strongly correlated ($\rho \geq 0.5$); dark blue: moderately correlated ($0.5 > \rho \geq 0.3$); green: weak correlated ($0.3 > \rho \geq 0.1$); light blue: uncorrelated ($\rho < 0.1$). $\tau = 3s$, $T = 600s$)

4.4 Peak factor estimation with PSD-based theory

4.4.1 Stationary and Gaussian solutions

As suggested by Davenport (1964) and extended by ESDU (83045), if the fluctuations of a stationary sequence of wind speed are mutually independent and normally distributed about the mean value, the peak factor can be estimated by

$$g(\tau, T) = \left[\sqrt{2 \ln(vT)} + \frac{\gamma}{\sqrt{2 \ln(vT)}} \right] \frac{\sigma_u(\tau, T)}{\sigma_u(\tau \rightarrow 0, T \geq 1h)} \quad (4.9)$$

where $\gamma =$ Euler's constant, 0.5772, $\nu =$ zero up-crossing rate (crossings/time) can be estimated as

$$\nu^2(\tau, T) = \frac{\int_0^\infty f^2 S_u^*(f) |H_{TA}(f, \tau, T)|^2 df}{\int_0^\infty S_u^*(f) |H_{TA}(f, \tau, T)|^2 df} \quad (4.10)$$

in which $S_u^* = S_u/\sigma_u^2$, S_u is the power spectrum density (PSD) function of longitudinal fluctuating winds, $f =$ frequency, $H_{TA}(f, \tau, T)$ is a time-averaging filter which considers the truncation effects of wind PSD caused by the gust average τ (cutoff of high frequency) and the high-pass filtering effects associated with the record duration T , which can be expressed as

$$|H_{TA}(f, \tau, T)|^2 = \left[\frac{\sin(f\pi\tau)}{f\pi\tau} \right]^2 - \left[\frac{\sin(f\pi T)}{f\pi T} \right]^2 \quad (4.11)$$

This filter has no consideration of the mechanical filtering of the measurement device since the ultrasonic anemometer is used in the present study. The second term on the right side of the Eq. (4.9) is a reduction factor which accounts for the reduced variance of the truncated spectrum with the form of

$$\frac{\sigma_u^2(\tau, T)}{\sigma_u^2(\tau \rightarrow 0, T \geq 1h)} = \int_0^\infty S_u^*(f) |H_{TA}(f, \tau, T)|^2 df \quad (4.12)$$

And von Kármán PSD is routinely the first choice for the longitudinal winds which was widely recommended by pioneer studies ([ESDU 83045](#); [Master et al., 2010](#); [Balderrama et al., 2012](#)) as

$$f S_u^*(f) = \frac{f S_u(f)}{\sigma_u^2} = \frac{4\hat{f}}{[1 + 70.8(\hat{f})^2]^{5/6}} \quad (4.13)$$

in which $\hat{f} = f\Lambda/\bar{U}$ is the reduced frequency and Λ is a length scale usually replaced by height z above the ground or integral length scale L . ESDU (83045) introduces an integral time scale parameter of turbulence:

$$T_u = \Lambda/\bar{U} = 3.13z^{0.2} \quad (4.14)$$

Similar to Balderrama et al., (2012), a comparison between observed and Von Kármán PSDs are conducted. All observed PSDs are calculated from 10-min records by Welch’s method and stratified by equivalent mean wind speed. Each observed PSDs is fitted with von Kármán PSD, and Fig. 4.5 shows all observed PSDs as well as the mean observed and fitted results. The captured highest frequency of PSD reaches 16 Hz (sampling frequency is 32 Hz) in this study. Generally, von Kármán PSD is a reasonable choice for modeling the PSD of fluctuating winds. However, an obvious inconsistency can be noted both in low and high-frequency regions between modeled and empirical PSD functions, especially at lower wind speed regimes, which agrees well with Balderrama’s conclusion (Balderrama et al., 2012). Moreover, von Kármán PSD still fails to capture the energy in a fraction of high-frequency region, such as $f > 5\text{Hz}$ when mean wind speed higher than 20m/s, which would result in the underestimate of the up-crossing rate for small gust duration cases.

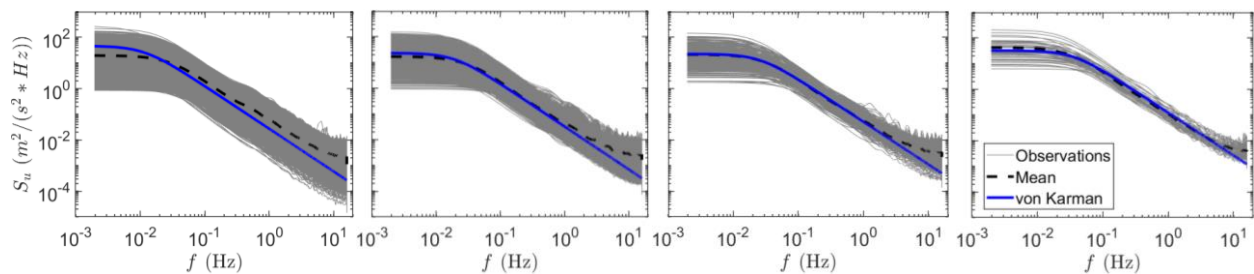


Fig. 4.5 Observed and fitted von Kármán PSD (From left to right: $\bar{U}^* \in [5,10), [10,15), [15,20), [20,25)$)

4.4.2 Non-Gaussian solutions

Theoretically, an arbitrary normalized non-Gaussian sequence can be expressed as the monotonic function of a standard Gaussian process. Similar to the widely used approach on

evaluating the non-Gaussian fluctuating wind pressure of structures, the moment-based Hermite polynomials model (Kwon et al., 2011; Yang et al., 2015; Ding et al., 2016) is adopted to translate the non-Gaussian winds into Gaussian histories. Hermite polynomials, which provide a basis for modeling the translation function, are a classical orthogonal polynomial sequence with the form of

$$H_n(x) = (-1)^n \cdot e^{\frac{x^2}{2}} \cdot \frac{d^n}{dx^n} e^{-\frac{x^2}{2}} \quad (4.15)$$

in which e = exponential constant. Generally, the non-Gaussian sequence can be roughly divided into three types based on the value of kurtosis, namely, hardening (kurtosis < 3), softening (kurtosis > 3) and skewed non-Gaussian (kurtosis = 3) processes. Winterstein (1987) suggested that a normalized softening non-Gaussian process, $Z(t)$ can be approximately substituted by the first four-term Hermite polynomials expansion of the standard Gaussian process $U(t)$ as:

$$Z(t) = \frac{X(t) - \mu_x}{\sigma_x} = k\{H_1[U(t)] + h_3 \cdot H_2[U(t)] + h_4 \cdot H_3[U(t)]\} \quad (4.16)$$

in which $X(t)$ is a softening non-Gaussian time history, μ_x and σ_x are the mean and standard deviation of $X(t)$. k , h_3 , and h_4 are model coefficients which can be determined by the first four-order statistical moments of the non-Gaussian process. In order to work out the model coefficients, a basis that the moments between two sides of Eq. (4.16) are automatically equal to each other is adopted, followed by the Taylor expansion of $H_n[U(t)]$ (Winterstein, 1987). By employing the first-order Taylor expansion and considering the orthogonality of Hermite polynomials, the shape parameters can be produced as

$$k = 1, h_3 = \frac{\gamma_3}{6}, h_4 = \frac{\gamma_4 - 3}{24} \quad (4.17)$$

In which γ_3 , and γ_4 are the skewness and kurtosis of $Z(t)$. To ensure the one-one translation function is always monotonically increasing, a limited boundary condition should be followed as (Winterstein, 1987)

$$\frac{h_3^2}{(1/2)^2} + \frac{(h_4 - 1/6)^2}{(1/6)^2} \leq 1 \quad (4.18)$$

And the peak factor of non-Gaussian time series can be translated from the Gaussian history based on their one-to-one mapping relationship as

$$g_{NG} = k[g + h_3 \cdot (g^2 - 1) + h_4 \cdot (g^3 - 3g)] \quad (4.19)$$

In which g is the peak factor obtained from Gaussian history as expressed in Eq. (4.9). Similarly, for hardening non-Gaussian sequence, Winterstein (1987) also proposed a translation formula for modeling a standardized hardening non-Gaussian process $Z(t)$ through an underlying standard Gaussian process $U(t)$:

$$U(t) = k \cdot Z(t) - h_3 \cdot [Z^2(t) - 1] - h_4 \cdot [Z^3(t) - 3Z(t)] \quad (4.20)$$

In which k , h_3 and h_4 can be determined by the same equations as described in Eq. (4.17).

And the monotonic limits and peak factor for hardening process have been derived as

$$\frac{h_3^2}{(1/2)^2} + \frac{(h_4 + 1/6)^2}{(1/6)^2} \leq 1 \quad (4.21)$$

$$g = k[g_{NG} - h_3 \cdot (g_{NG}^2 - 1) - h_4 \cdot (g_{NG}^3 - 3g_{NG})] \quad (4.22)$$

As for the skewed Non-Gaussian process (skewness $\neq 0$, kurtosis=3), Yang et al., (2015)

suggested that the kurtosis within a range of $[3 - \sqrt{24 \cdot \chi^2(p, 2)/n}, 3 + \sqrt{24 \cdot \chi^2(p, 2)/n}]$, in which $\chi^2(p, 2)$ is the Chi-square distribution with two degrees of freedom and the occurrence probability p , n is the number of data in $U(t)$, can be approximately regarded as the skewed model. The peak factor can be estimated by

$$g_{NG} = k \cdot [g + h_3 \cdot (g^2 - 1)] \quad (4.23)$$

in which the shape parameters can be solved by

$$\begin{cases} 1 = k^2(1 + 2h_3^2) \\ \gamma_3 = k^3(6h_3 + 8h_3^3) \end{cases} \quad (4.24)$$

As shown in Fig. 4.6, the skewness and kurtosis of all records ($\tau = 3s$) are illustrated together with the monotonic boundary conditions for three types of non-Gaussian models. Although the above models only adopt the first-order Taylor expansion of Hermite polynomials, only 5 points, whose values of kurtosis are higher than 14, are beyond the limited boundaries for $\tau = 3s$ case. Other cases are also checked which shows that all data are within the monotonic boundaries for $\tau = 1/32 s$ case and only very few points are outside the boundaries for other gust durations. Thus, Fig. 4.6 indicates that almost all data can be simulated by the above non-Gaussian model except for 5 anomalous points. And the upper and lower limits of the skewed model in this figure are 3.15 and 2.85 by assigning $p = 0.95$ for Chi-square distribution and $n = 6000$. However, the results turn out that no points in this study locate on the skewed model region. And there are 80.61% of samples are softening histories while 19.39% of them are hardening histories.

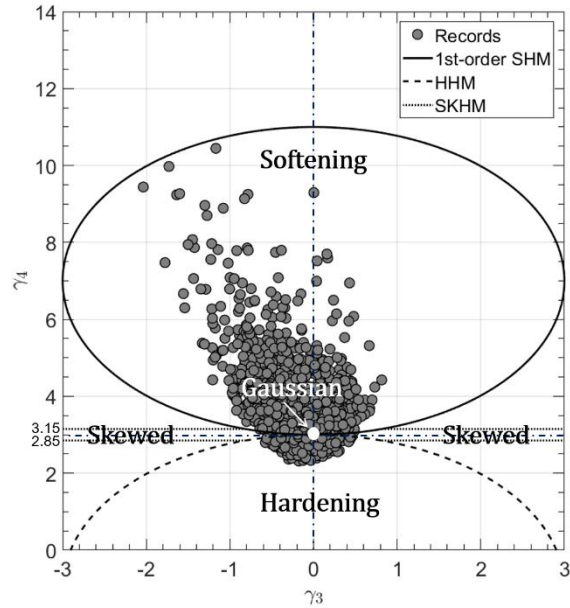


Fig. 4.6 Skewness vs kurtosis of records and monotonic limits of Hermite model

4.4.3 Non-Gaussian effects on peak and gust factors

Several peak and factor curves versus gust durations are developed in this section by adopting the above-mentioned theoretical solutions to intuitively highlight the non-Gaussian effects. As shown in Fig. 4.7, various combinations of skewness ($\gamma_3 = -0.4 \sim 0.4$) and kurtosis ($\gamma_4 = 2 \sim 5$) are employed to develop the peak factor curves. In this case, height $z = 10 \text{ m}$, record duration $T = 600 \text{ s}$ and turbulence intensity is set as 0.15. It can be noted that all curves nearly intersect at the same point $\tau = 20 \text{ s}$ when γ_3 is set as a constant (Fig. 4.7a~c), and peak factor remains almost no change when $\tau > 20 \text{ s}$. But for constant kurtosis cases (Fig. 4.7d~f), the point of intersection is located around at $\tau = 30 \text{ s}$ or 0.5 min. This means the peak factor is approximately independent of skewness and kurtosis when the gust duration is higher than 30 s ($T = 10 \text{ min}$). In other words, non-Gaussian characteristics can be neglected when $\tau > 30 \text{ s}$ and the Gaussian theory is able to estimate peak or gust factors accurately. In addition, when skewness is a constant, peak factor would increase with kurtosis at the range of $\tau < 20 \text{ s}$. And the same trends can be observed when skewness

increases from -0.4 to 0.4. That is, higher skewness and kurtosis would produce higher peak factor. Moreover, in most cases, the Gaussian theory fails to reproduce the expected peak factors. Especially when skewness and kurtosis are both high values, the actual peak factor is almost twice as the value of the Gaussian estimation.

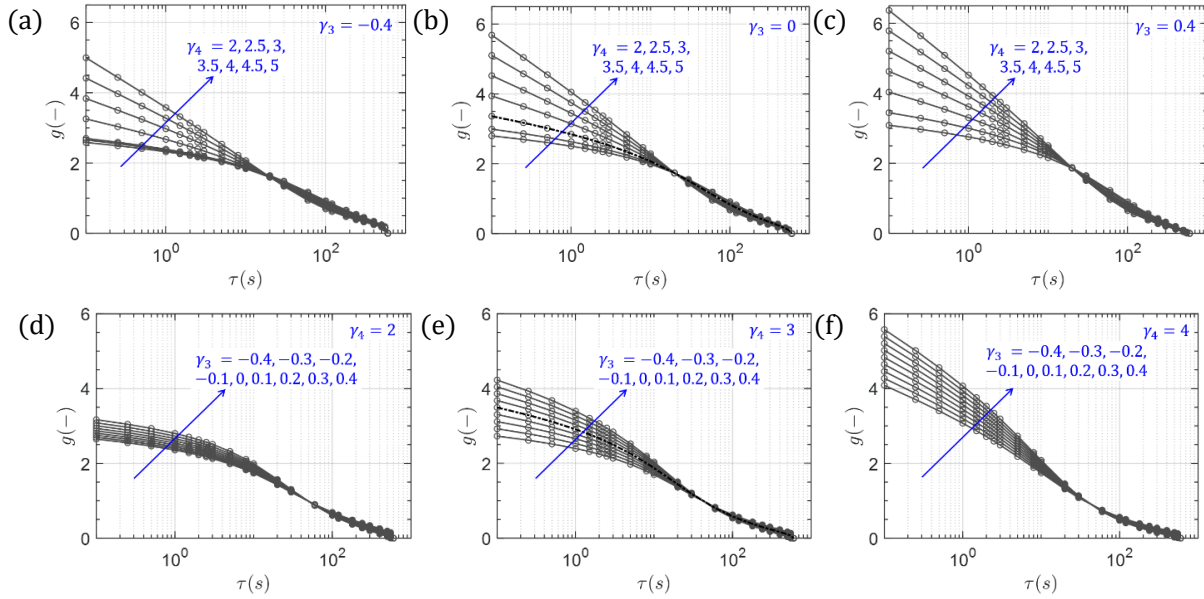


Fig. 4.7 Non-Gaussian effects on gust factor: a) $\gamma_3 = -0.4$; b) $\gamma_3 = 0$; c) $\gamma_3 = 0.4$; d) $\gamma_4 = 2$; e) $\gamma_4 = 3$; f) $\gamma_4 = 4$

To better understand the variation pattern of peak factor as the result of non-Gaussian effects, $\tau = 3$ s and $T = 600$ s are selected to model the values of the peak factor versus skewness and kurtosis. As shown in Fig. 8a, peak factors are denoted with a curved surface which increase with the increase of γ_3 and γ_4 . The sudden changes around the locations of $\gamma_3 < -0.2$ or $\gamma_3 > 0.2$ and $\gamma_4 = 3$ are largely due to the imperfection of skewed model at high skewness region. Compared with Gaussian result, there is a huge part of peak factors at non-Gaussian region would be underestimated. Besides, given that turbulence intensity almost has no correlation with skewness and kurtosis (Fig. 4.4), this non-Gaussian feature can be translated to gust factors by adopting Eq.(4.2). Fig. 4.8b illustrates the corresponding

variation of gust factor by setting turbulence intensity as a constant of 0.15, which witnesses a same pattern as peak factor.

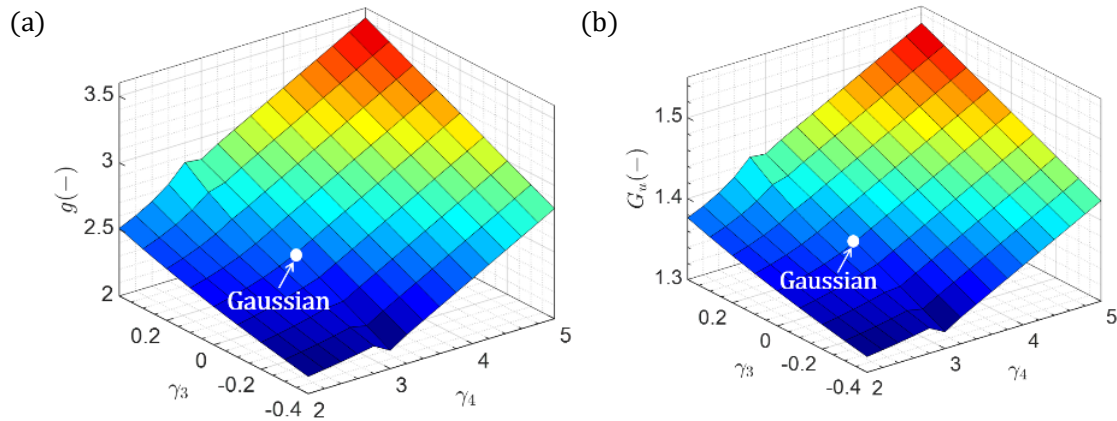


Fig. 4.8 Non-Gaussian effects $g(3s,600s)$ and $G_u(3s,600s)$: a) $g(3s,600s)$ vs γ_3 and γ_4 ; b) $G_u(3s,600s)$ vs γ_3 and γ_4

4.5 Results comparison and discussion

4.5.1 Results comparison

By employing the above-mentioned non-Gaussian translation model coupled with the first four-order statistics of each segment, peak and gust factors are estimated and compared with observations, as shown in Figs. 4.9~4.10. It can be noted that the correlation coefficient ρ between modeled and observed peak as well as gust factors shows an increasing tendency with the increase of gust duration ($\tau = 0.03s, 0.13s, 0.25s, 0.5s, 1s, 3s$). And the mean value of relative error varies from positive to negative with the minimum of -0.84% for peak factor ($\tau = 0.5s$). This indicates that the peak factors estimated by the non-Gaussian translation model are slightly larger than the field measurements when the gust duration is less than about 0.5 s and an opposite tendency can be witnessed when $\tau > 0.5$ s. As for gust factors, all of them are slightly underestimated with mean relative errors are positive. However, it is noteworthy that the relative errors for gust factors are pretty small with the largest value of

2.1 % for $\tau = 3$ s, which means that the non-Gaussian translation model present in this study is proved to be accurate enough to estimate the gust factor in engineering applications. In

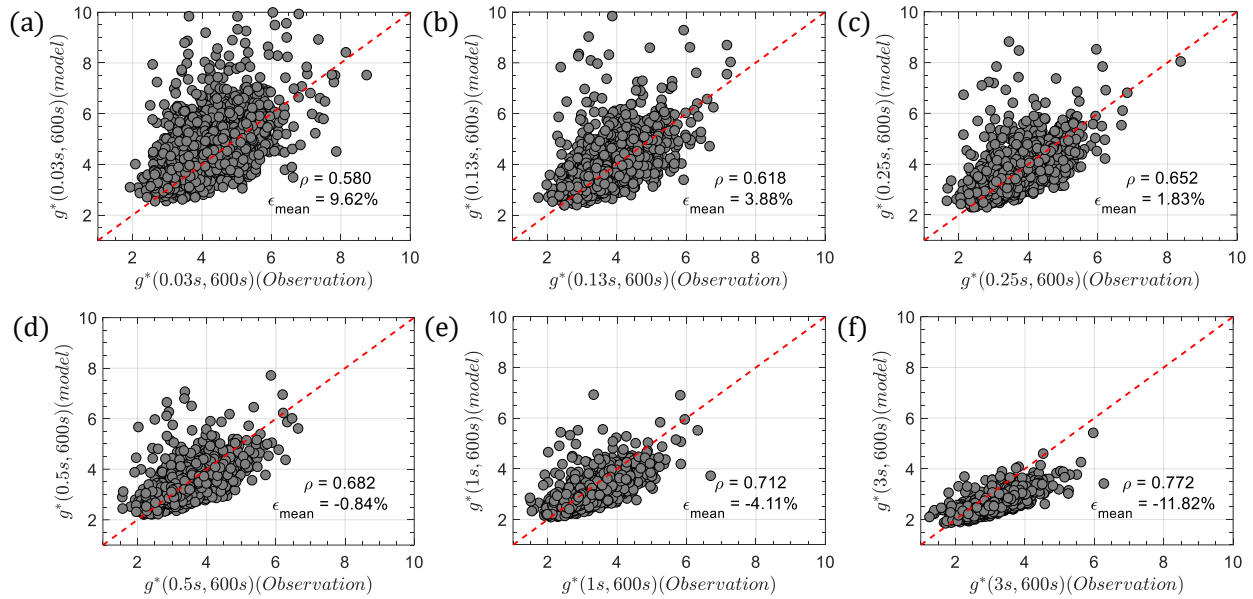


Fig. 4.9 Comparisons of peak factor : a) $\tau = 0.03$ s; b) $\tau = 0.13$ s; c) $\tau = 0.25$ s; d) $\tau = 0.5$ s; e) $\tau = 1$ s; f) $\tau = 3$ s; (ρ : correlation coefficient; ϵ_{mean} : mean value of relative errors; The dash line: $y = x$; same as below.)

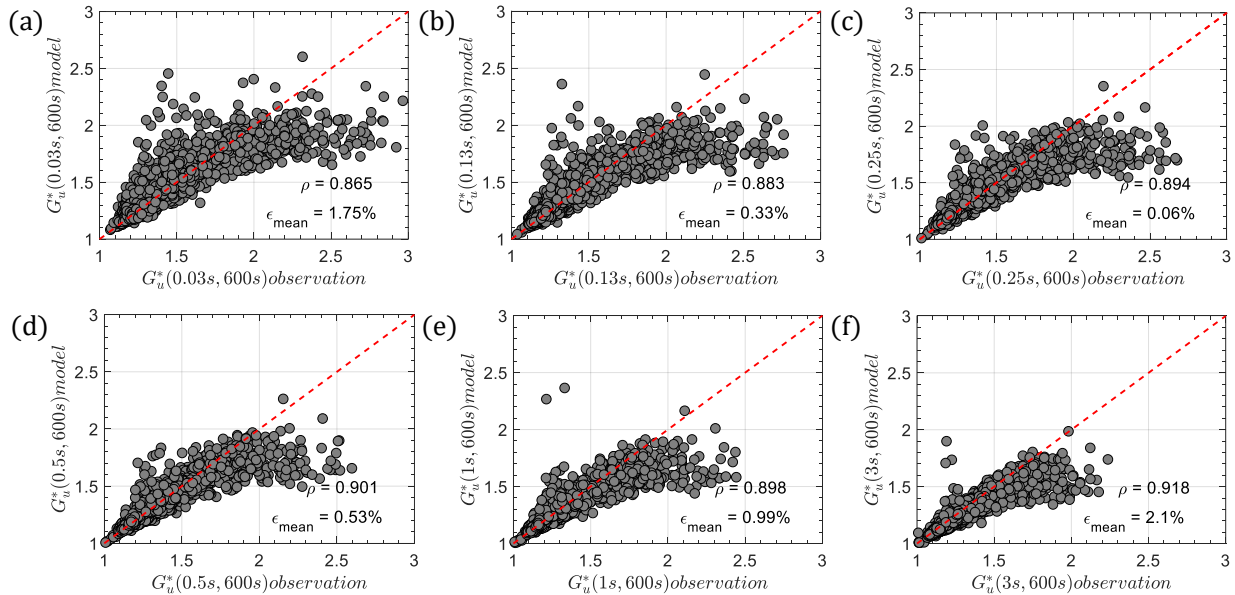


Fig. 4.10 Comparisons of gust factor: a) $\tau = 0.03$ s; b) $\tau = 0.13$ s; c) $\tau = 0.25$ s; d) $\tau = 0.5$ s; e) $\tau = 1$ s; f) $\tau = 3$ s.

Fig. 4.10, the higher correlation coefficients for modeled and observed gust factors can be observed than Fig. 4.9, which are mainly because of the introduction of the same turbulence intensities (Eq. (4.2)). More discussions regarding the effects of model imperfection and potential uncertainties on simulation results will be presented in section 4.5.3.

4.5.2 Standardization of gust factor curve

As described above, a general model was developed to estimate the peak factor of non-Gaussian winds. Then, it can be routinely used to predict the gust factor of typhoon winds by introducing a site-specific standard deviation of fluctuating winds or turbulence intensity model as shown in Eq. (4.2). Turbulence intensity profile, which is usually defined as an underlying terrain dependent curve, can be obtained from different codes or standards as summarized by [Kwon et al. \(2013\)](#). More specifically, as suggested by [ESDU \(83045\)](#), if the boundary layer at a local site follows the equilibrium condition with the upwind uniform terrain over 30km, the standard deviation of fluctuating winds can be directly modeled with

$$\sigma_u = \frac{u_* 7.5 \eta [0.538 + 0.09 \ln(z/z_0)]^{\eta^{16}}}{1 + 0.156 \ln(u_* / |f_c| z_0)} \quad (4.25)$$

$$\eta = 1 - \frac{6|f_c|z}{u_*} \quad (4.26)$$

in which f_c is the Coriolis parameter. u_* is the frictional wind speed which can be determined by calculating the ground surface Reynolds stress or fitting with a logarithmic profile as

$$u_* = \frac{\kappa \bar{U}(T, z, z_0)}{\ln(z/z_0)} \quad (4.27)$$

in which $\kappa = 0.4$ is the von Kármán constant.

As thus, the site-specific gust factor curve is able to be modeled with arbitrary mean wind speed and an equivalent roughness length coupled with the distributions of skewness and

kurtosis. However, the data used in this study are observed at the height of the bridge deck (roughly 76.5m above the sea level), which cannot be applied directly to the wind engineering applications with a standard height of 10 m. Meanwhile, there are few data available for skewness and kurtosis of fluctuating winds at height of 10m. As a reference, the observation results studied by [Li et al. \(2015\)](#) were adopted, as listed in Table 4.1, in which the statistics of skewness and kurtosis of typhoon winds at a 10-m height above the ground surface were obtained. Three categories of exposure are defined with different ranges of z_0 . However, there are no studies regarding the distributions of skewness and kurtosis as well as their correlations. Accordingly, in order to develop a standardization method and approximately study the variation pattern of gust factor curve for 10-m winds, the normal and lognormal distributions are still employed for skewness and kurtosis with the correlation coefficient of -0.315, as presented in sections 3.2~3.3. Correspondingly, the logarithmic mean and standard deviation for the kurtosis can be calculated by

$$\mu_{ln} = 2 \times \ln(\mu) - \frac{1}{2} \ln(\mu^2 + \sigma^2) \quad (4.28)$$

$$\sigma_{ln}^2 = -2 \times \ln(\mu) + \ln(\mu^2 + \sigma^2) \quad (4.29)$$

in which μ and σ are the mean and standard deviation of original data, respectively.

Taking the open exposure as an example, which is close to the basic terrain category in several codes ([Kwon et al. 2013](#)), the Monte Carlo simulation is conducted to generate 10^4 samples of skewness and kurtosis based on above-mentioned distributions and correlation coefficient. The roughness length $z_0 = 0.05m$ and mean wind speed is set as 30m/s. Fig.4.11a illustrates the scatter plots of simulated γ_3 and γ_4 with the correlation coefficient of -0.314 which is almost identical to the input value. Then, a cluster of gust factor curves is developed together with the [Durst \(1960\)](#) and [Kramer and Marshall \(1992\)](#) (KM curve) gust

factor curves as shown in Fig.11b. It can be noted that the mean curve is higher than the Gaussian distribution-based result, which is close to the curve of Mean–Std. And Durst curve is in close proximity to the curve of Mean–2Std. Moreover, the KM curve is roughly consistent with the mean value of present model at small gust duration region but higher than the model values for gust durations in the range of 10s~200s, which has also been highlighted by Vickery et al. (2005). Fig.4.11c~d show the probability density of simulated gust factors for $\tau = 0.25s$ and $3s$, which are fitted with general extreme value (GEV) distribution by maximum likelihood estimates with 95% confidence intervals with the form of

$$f(x; \mu, \sigma, \gamma) = \frac{1}{\sigma} \exp \left[- \left(1 + \gamma \cdot \frac{x - \mu}{\sigma} \right)^{-\frac{1}{\gamma}} \right] \left(1 + \gamma \cdot \frac{x - \mu}{\sigma} \right)^{-1 - \frac{1}{\gamma}}, \gamma \neq 0 \quad (4.30)$$

$$f(x; \mu, \sigma, 0) = \frac{1}{\sigma} \exp \left[- \exp \left(- \frac{x - \mu}{\sigma} \right) - \frac{x - \mu}{\sigma} \right], \gamma = 0 \quad (4.31)$$

in which γ , σ and μ are called shape, scale and location parameters, respectively, and $1 + \gamma \cdot (x - \mu)/\sigma > 0$. Correspondingly, for $\gamma = 0$, $\gamma > 0$ and $\gamma < 0$ conditions, GEV distributions can be reduced to types I (Gumbel), II (Fréchet) and III(Weibull) extreme value distributions. It can be observed that the shape parameters are less than 0 but very close to zero, which means the gust factor can be described by the Weibull distribution, or Gumbel distribution. It is consistent with several observation results presented by Bardal et al. (2016).

Table 4.1 Statistics of skewness and kurtosis of 10-m typhoon winds (Li et al. 2015)

Exposure	z_0 (m)	Skewness (γ_3)				Kurtosis (γ_4)					
		μ	Max.	Min.	σ	μ	Max.	Min.	σ	μ_{ln}	σ_{ln}
Sea	(0,0.005)	-0.28	0.29	-1.15	0.30	3.10	5.44	2.23	0.64	1.11	0.20
Smooth	[0.005,0.02)	0.02	0.59	-1.21	0.36	2.88	4.76	2.27	0.47	1.05	0.16
Open	[0.02,0.05)	0.21	0.56	-0.19	0.23	2.87	3.77	2.39	0.31	1.05	0.11

Note: μ : mean, σ : standard deviation

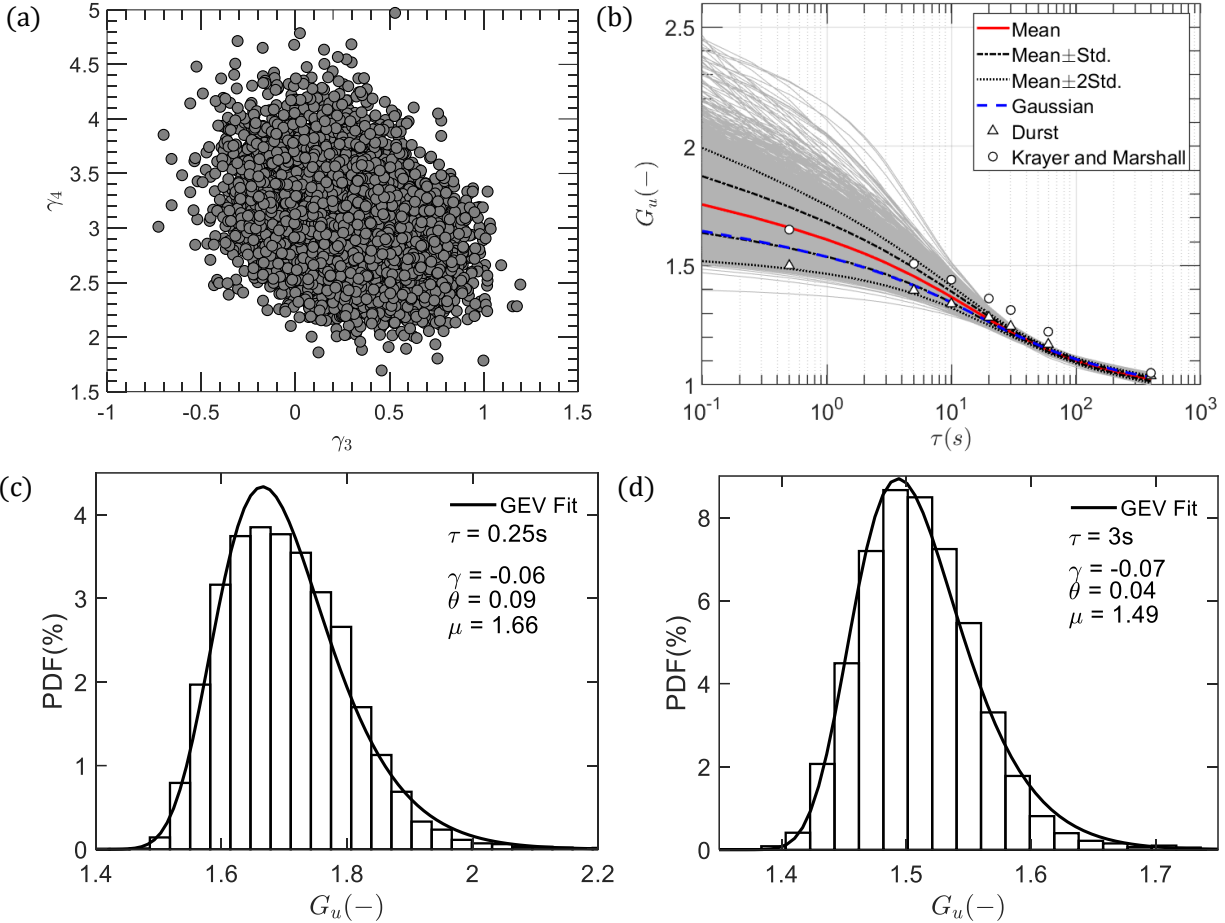


Fig. 4.11 Simulation results for open exposure: (a) Skewness vs kurtosis; (b) Gust factor curve; (c) Probability distribution ($\tau = 0.25s$); (d) Probability distribution ($\tau = 3s$)

4.5.3 Uncertainty discussion

Although this study attempts to develop a standardization scheme for site-specific gust factor curve by considering the effects of non-stationary and non-Gaussian characteristics of typhoon winds, there are multiple uncertainties that would immediately affect the accuracy of the model. Generally, there are two types of uncertainty: epistemic uncertainty due to the lake of knowledge and data which may be reduced as better models are developed, and aleatory uncertainty due to the inherent randomness or error which is usually irreducible. As a result, except for the lack of data, the model imperfection and several potential aleatory uncertainties are discussed as follows,

(1) Model imperfection. First, the Gaussian solutions in section 4.4.1 for the peak factor is developed from a specified PSD model. Although the von Kármán spectrum has been examined and validated by many observations (Cao et al., 2009; Balderrama et al., 2012; Li et al., 2015), it fails to capture the high frequency energy for typhoon winds, especially around the typhoon wall region, caused by the transition between complex convection and sheared eddies generated by low-level jet (Li et al., 2015). It can also be proved by Fig. 4.5. Moreover, the time scale parameter as expressed by Eq. (4.14), as well as the standard deviation of fluctuating winds (Eq. (4.25)) are both empirically-determined models. Second, the equivalent roughness length z_0 , which is used to approximately account for the underlying terrain exposure effects on wind fluctuations, is usually roughly estimated by observational survey and classification assessment. Actually, there are few sites providing a uniform upstream terrain with a long distance. This means the equivalent z_0 at the local site is a direction- and upstream terrain evolution-dependent value, which makes it difficult to give a definitive value. Third, the logarithmic vertical profile of wind speed described by Eq. (4.26) is also a semi-empirical relationship and only valid when the neutral atmospheric stability assumption is met. Besides, the wind profiles under typhoon boundary layer exhibit radius-dependent characteristics (Vickery et al. 2009; Fang et al., 2018), which means typhoon boundary layer is not only dominated by the terrain exposure, but also by its internal convective circulation. Last but not least, a stationary time series is only valid from the mathematical perspective, it does not exist in reality. An underlying assumption that the 10 s sub-segments of wind speed are stationary is adopted in this study during the extraction of the time-varying mean. Furthermore, the non-stationary features of variance or even

higher-order statistics are eliminated which are considered to have little impacts on gust factor.

(2) Aleatory uncertainties. First, as mentioned before, it is almost impossible, at least for now, to quantitatively evaluate the effects of the evolution of upstream terrain roughness and topography on wind turbulence. Although open flat areas along the coastline are usually treated as the same exposure in wind engineering applications, local terrain roughness and topographic features, as well as surrounding obstacles, would determine the development of a boundary layer and evolution of turbulence. Theoretically, a desired equilibrium boundary would be developed if there a harsh condition, which is wind has blown over a fetch of 100 km of uniform terrain (ESDU 82026) is met. In reality, few places have an ideal uniform terrain over a long distance, even over the sea, which is influenced by wave, tide and current. As shown in Fig.4.12, an expected boundary layer in equilibrium with the underlying sea surface is blowing to the land and a new internal layer begins toward developing with the variation of roughness and topography. In coastline areas, a sudden change of elevation or topography would have an obvious impact on surface wind speeds over a very short distance (Miller et al., 2013). Besides, the turbulence intensity could decrease due to changing mean strain rates as the turbulence is converted over a small-scale topography. As studied by Britter et al. (1981), the gust factor on top of a two-dimensional ridge can be expressed as

$$G_u = 1 + g(t, T) \cdot I_u \cdot \left(\frac{9}{5} - \frac{4}{5} S \right)^{0.5} \quad (4.32)$$

in which S is the speed-up factor. After wind landfall, the internal boundary layer continues to develop, coupled with rapidly-growing strong turbulence. Outside the internal layer, it is

assumed that the wind profile is the same as the immediately upwind profile at the same level. This can explain why the observed gust factor of off-land winds is smaller than that of off-sea winds at a height of 10 m, while values at other heights are almost the same as discussed by [Cao et al. \(2015\)](#). Because of the insufficient development of an internal boundary layer, the gust factor at low level is relatively small due to the effects of topography and roughness compared with off-sea winds, which still retain the characteristics of the over-sea profile.

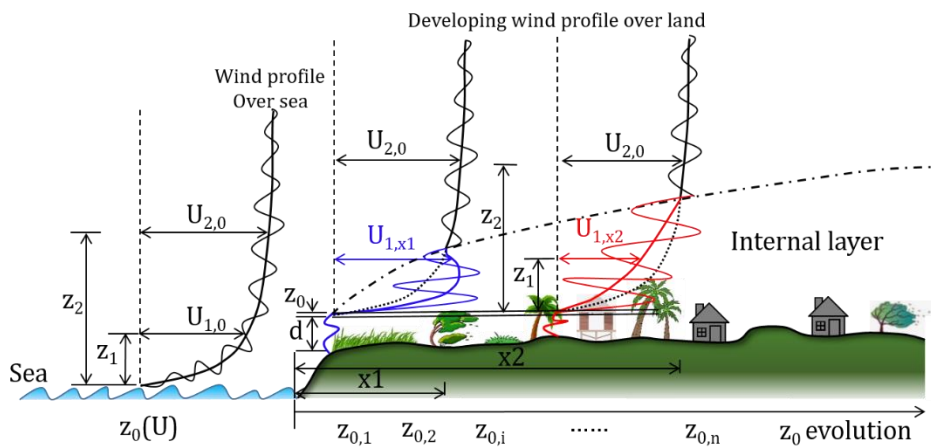


Fig.4.12 Development of wind boundary layer from sea to land (subscript 1 and 2 denote values at heights z_1 and z_2 , respectively; subscript 0 stands for the over-sea profile; x_1 and x_2 represent upstream fetch)

Besides, as suggested by [Sharma et al. \(2009\)](#) and [Sparks et al. \(2001\)](#), the convective instability in tropical cyclone winds coupled with the thermodynamic effects such as temperature and moisture would potential impacts on the turbulence structure. Thus, the statistical characteristics of near-ground typhoon winds, including turbulence intensity, skewness and kurtosis inevitably exhibit high randomness. Second, although several criteria are employed to minimize the effects of the surrounding unnatural environment on observations, some extremely rare events might also be remained. Meanwhile, the imperfection of anemometers as well the effects of temperature and moisture during strong

typhoons would also influence the accuracy of observation results. [WMO \(2010\)](#) also demonstrated that the accurate measurements of wind speed, especially for strong typhoon winds, is always a difficult and demanding task that will inevitably result in the scatter from even the most elaborate analyses.

4.6 Conclusion

Based on the 4007 sets of 10-min segments of near-ground typhoon winds observed by the anemometers that are installed at Xihoumen Bridge during 9 typhoons, the non-stationary and non-Gaussian characteristics were carefully examined. The turbulence intensity as well as gust and peak factors of non-stationary winds were extracted to study their correlations. A non-Gaussian translation model was developed to estimate the peak factor of strong typhoon winds and compared with the field observation results. Several conclusions are summarized as below:

- (1) Most typhoon wind records are featured with non-stationary characteristics with an obvious time-varying mean trend, which would directly affect the statistics as well as the probability distribution of fluctuating winds.
- (2) The skewness and kurtosis of typhoon wind records show a remarkable departure from the Gaussian distribution. Some correlations between the peak factor and skewness as well as kurtosis are observed, which reveals the non-Gaussian effects of fluctuating winds on peak factor. The negatively strong correlation between gust factor and turbulence intensity was verified and it is suggested that Ishizaki's recommendation is preferable.
- (3) Higher skewness and kurtosis would produce higher peak factor. The Gaussian theory always fails to reproduce the expected peak factors, especially when skewness and kurtosis

are both high values. The non-Gaussian effects can be eliminated when gust duration is higher than the 30s.

(4) Present non-Gaussian PSD- and moment-based translation model is accurate enough to reproduce the peak factor as well as the gust factor in engineering applications. By comparing with the non-Gaussian solutions, a large portion of gust factors would be underestimated if the non-Gaussian effects were ignored.

4.7 Reference

ASCE. Minimum Design Loads for Buildings and Other Structures (ASCE 7-10)[S]. American Society of Civil Engineers, 2014.

Bardal L M, Sætran L R. Wind Gust Factors in a Coastal Wind Climate [J]. Energy Procedia, 2016, 94:417-424.

Caracoglia L, Jones N P. Numerical and experimental study of vibration mitigation for highway light poles[J]. Engineering Structures, 2007, 29(5):821-831.

Cao S, Tamura Y, Kikuchi N, et al. Wind characteristics of a strong typhoon[J]. Journal of Wind Engineering & Industrial Aerodynamics, 2009, 97(1):11-21.

Cao S, Tamura Y, Kikuchi N, et al. A case study of gust factor of a strong typhoon[J]. Journal of Wind Engineering & Industrial Aerodynamics, 2015, 138:52-60.

Chen J, Hui M C H, Xu Y L. A Comparative Study of Stationary and Non-stationary Wind Models Using Field Measurements[J]. Boundary-Layer Meteorology, 2007, 122(1):105-121.

Chen X. Analysis of Alongwind Tall Building Response to Transient Nonstationary Winds[J]. Journal of Structural Engineering, 2008, 134(5):782-791.

Choi, E.C.C., 1983. Wind Loading in Hong Kong —Commentary on the Code of Practice on Wind Effects Hong Kong[R]. Hong Kong Institute of Engineers, Hong Kong.

Davenport A G. Note on the Distribution of the Largest Value of a Random Function with Application to Gust Loading[J]. Proceedings of the Institution of Civil Engineers, 1964, 28(2):187-196.

Durst, C. S. 1960. Wind speeds over short periods of time[J], Meteorol. Mag., 89, 181–186.

Ding J, Chen X. Moment-Based Translation Model for Hardening Non-Gaussian Response Processes[J]. Journal of Engineering Mechanics, 2016, 142(2).

ESDU, 1983: Strong winds in the atmospheric boundary layer. Part 2: Discrete gust speeds[R], Engineering Sciences Data Unit 83045.

Fang G, Zhao L, Cao S, et al. A novel analytical model for wind field simulation under typhoon boundary layer considering multi-field correlation and height-dependency[J]. Journal of Wind Engineering & Industrial Aerodynamics, 2018, 175:77-89.

He Y C, Chan P W, Li Q S. Wind characteristics over different terrains[J]. Journal of Wind Engineering & Industrial Aerodynamics, 2013, 120(3):51-69.

He Y C, Chan P W, Li Q S. Standardization of raw wind speed data under complex terrain conditions: A data-driven scheme[J]. Journal of Wind Engineering & Industrial Aerodynamics, 2014, 131:12-30.

Hu L, Xu Y L, Zhu Q, et al. Tropical Storm–Induced Buffeting Response of Long-Span Bridges: Enhanced Nonstationary Buffeting Force Model[J]. Journal of Structural Engineering, 2017, 143(6):04017027.

Holmes, J. D., and Ginger, J. D.. The gust wind speed duration in AS/NZS 1170.2[J]. Australian Journal of Structural Engineering, 2012, 13(3), 207 –218.

Ishizaki H. Wind profiles, turbulence intensities and gust factors for design in typhoon-prone regions[J]. *Journal of Wind Engineering & Industrial Aerodynamics*, 1983, 13(1):55-66.

Masters F J, Vickery P J, Bacon P, et al. Toward Objective, Standardized Intensity Estimates from Surface Wind Speed Observations[J]. *Bulletin of the American Meteorological Society*, 2010, 91(12):1665-1681.

Krayer W R, Marshall R D. Gust Factors Applied to Hurricane Winds.[J]. *Bulletin of the American Meteorological Society*, 1992, 73(5):613-618.

Kwon D K, Kareem A. Peak Factor for Non-Gaussian Load Effects Revisited[J]. *Journal of Structural Engineering*, 2011, 137(12):1611-1619.

Kwon D K, Kareem A. Comparative study of major international wind codes and standards for wind effects on tall buildings[J]. *Engineering Structures*, 2013, 51(2):23-35.

Li L, Kareem A, Xiao Y, et al. A comparative study of field measurements of the turbulence characteristics of typhoon and hurricane winds[J]. *Journal of Wind Engineering & Industrial Aerodynamics*, 2015, 140:49-66.

Li L, Kareem A, Hunt J, et al. Turbulence Spectra for Boundary-Layer Winds in Tropical Cyclones: A Conceptual Framework and Field Measurements at Coastlines [J]. *Boundary-Layer Meteorology*, 2015, 154(2):243-263.

Li Q S, Xiao Y Q, Wong C K, et al. Field measurements of typhoon effects on a super tall building[J]. *Engineering Structures*, 2004, 26(2):233-244.

Sharma R N, Richards P J. A re-examination of the characteristics of tropical cyclone winds[J]. *Journal of Wind Engineering & Industrial Aerodynamics*, 1999, 83(1-3):21-33.

Shu Z R, Li Q S, He Y C, et al. Gust factors for tropical cyclone, monsoon and thunderstorm winds[J]. *Journal of Wind Engineering & Industrial Aerodynamics*, 2015, 142:1-14.

Sparks P R, Huang Z. Gust factors and surface-to-gradient wind-speed ratios in tropical cyclones[J]. *Journal of Wind Engineering & Industrial Aerodynamics*, 2001, 89(11–12):1047-1058.

Tao T, Wang H, Wu T. Comparative Study of the Wind Characteristics of a Strong Wind Event Based on Stationary and Nonstationary Models[J]. *Journal of Structural Engineering*, 2016, 143(5):04016230.

Vickery P J, Skerlj P F. Hurricane Gust Factors Revisited[J]. *Journal of Structural Engineering*, 2005, 131(5):825-832.

Vickery P J, Masters F J, Powell M D, et al. Hurricane hazard modeling: The past, present, and future[J]. *Journal of Wind Engineering & Industrial Aerodynamics*, 2009, 97(7):392-405.

Wieringa J. Gust factors over open water and built-up country[J]. *Boundary-Layer Meteorology*, 1973, 3(4):424-441.

Winterstein, S. R. and Kashef, T.. Moment-based Hermite model of random vibration. Report No. 219, Dept. of Structural Engineering, Technical University of Denmark, Lyngby, Denmark, 1987.

Winterstein, S.R., Kashef, T.. Moment-based load and response models with wind engineering applications. *Journal of Solar Energy Engineering*, 2000, 122 (3), 122–128.

WMO 2010: Guidelines for Converting between Various Wind Averaging Periods in Tropical Cyclone Conditions[R]. World Meteorological Organization, WMO/TDNo.1555, Geneva.

Xu Y L, Zhan S. Field measurements of Di Wang Tower during Typhoon York[J]. *Journal of Wind Engineering & Industrial Aerodynamics*, 2001, 89(1):73-93.

Yang Q, Tian Y. A model of probability density function of non-Gaussian wind pressure with multiple samples[J]. Journal of Wind Engineering & Industrial Aerodynamics, 2015, 140:67-78.

Yu B, Chowdhury A G. Gust Factors and Turbulence Intensities for the Tropical Cyclone Environment[J]. Journal of Applied Meteorology & Climatology, 2007, 48(3):534-552.

CHAPTER 5 A GEOGRAPHICALLY WEIGHTED REGRESSION SUBREGION MODEL FOR TYPHOON WIND SIMULATION

5.1 Background

Tropical cyclones (TCs) or typhoons are rapidly rotating storms characterized by strong winds, heavy rain, high storm surges and even devastating tornadoes. They inflict tremendous damage on property and considerable loss of human life and pose threats to flexible structures in coastal areas. In the Western Pacific Basin, TCs form throughout the year. It is the most active TC basin in the world, producing more than 30 storms annually, accounting for almost one-third of the global total ([Knapp et al., 2010](#)). The Southeast China coastal area has long coastlines and numerous islands, which is featured with high population densities as well as many wind-sensitive structures including high-rise buildings and long-span bridges. It is a TC-prone region, with an average of 6~8 TC landfalls per year. It has been estimated that more than 1,600 fatalities and 80 billion RMB of direct economic loss can be attributed to TCs and subsequent floods in 2006 alone in coastal regions of China ([Liu et al., 2009](#)), demonstrating that this area is extremely vulnerable to TC damage. Accordingly, it is an issue of great importance to analyze TC wind hazards to support wind-resistant design as well as disaster mitigation and insurance-related risk assessment.

Unlike synoptic winds such as monsoons, TCs are moving rotating storms with a small occurrence rate at a specific location. Moreover, wind anemometers are usually vulnerable to damage during strong typhoon events, making the record of historically observed winds an unreliable predictor for design wind speed based on statistical distribution models. The largest yearly wind speed dataset derived from both synoptic and TC winds is considered to be not well-behaved because the contribution of each wind speed to describe the

probabilistic behavior of the extreme winds is inhomogeneous (Simiu and Scanlan, 1996). An alternative approach, called stochastic simulation or Monte Carlo simulation, introduced in the 1970s by some pioneering studies (e.g. Russell and Schueller, 1971; Batts et al., 1980), has been widely adopted to stochastically generate a large number of wind speed samples using historical data-based probability distributions of several key field parameters. In order to achieve TC-hazard assessment by Monte Carlo simulation, the circular sub-region method (CSM) was developed by Georgiou (1985) and later employed by Vickery and Twisdale (1995), Xiao et al. (2011) and Li and Hong (2015). CSM uses the circled historical track information centered on the site of interest to characterize the statistics of some TC parameters before conducting storm simulation and wind speed prediction. This is a site-specific approach. The state-of-the-art empirical full track technique was first developed by Vickery et al. (2000) and followed by FEMA (2015) as well as ASCE 7-16 loads standard (2017) and Li et al. (2016), which simulate the TC tracks as well as the intensity in terms of a relative intensity index from genesis to lysis, facilitating the TC risk assessments for the whole coastal region. Although the full track model is preferable for modeling the TC hazards along the whole coastline, CSM is widely used for some site-specific TC risk studies and can be easily updated and improved by supplementary observations.

However, there are some limitations in conventional CSM approach. First, all synthetic tracks are assumed to be straight lines that intersect the circular subregion modeled with forward wind speeds and a minimum approaching distance. It is not consistent with real conditions, especially a relatively large size of subregion is selected. Second, the central pressure is always treated as unchanged before the storm's landfall for the simplicity in the simulation. More storms tend to weaken when they are close to the coastline. Sometimes, the storm

could intensify just before its landfall, such as the violent typhoon Rammasun (Year 2014, No. 9), which was the only two Category 5 super typhoons on record in the South China Sea. Typhoon Rammasun was degraded after passing the Philippine, but rapidly deepened and was upgraded to a devastating typhoon before making landfall over Hainan Province at peak intensity. Typhoon Hato (Year 2017, No. 13) is the other example, which is one of the strongest typhoons to impact Macau and Hong Kong in the past 50 years. It reached peak intensity just about 50-km away from its landfall site. Third, same statistical models of wind field parameters, i.e. the radius to maximum wind speed R_{max} and shape parameter of radial pressure profile B are applied to different sites of interest. They were statistically modeled as functions of surface central pressure deficit, TC eye center latitude and sea surface temperature (Vickery et al., 2000, 2008; Xiao et al., 2011; Zhao et al., 2013; FEMA, 2015; Fang et al., 2018). However, the correlations between these parameters were not very strong, as shown by Vickery et al. (2000), with all coefficients of determination less than 0.30. And the cross-adoption of these parameter models in different basins and sites could cause some undesired results since they are always region-dependent due to differences among macroscopic atmospheric thermodynamic environments. Last but not least, the correlations among different parameters are not fully examined and considered (Huang and Sun, 2018). These issues could result in the erroneous predictions of wind hazard curve. And sometimes, they would mislead the design of structures as well as the risk assessments.

During TC wind estimation, the parametric TC wind field model has been commonly adopted and has been continuously improved over the past several decades based on the ever-increasing amount of observation data. This model is considered to be more economical with time and even more accurate in predicting TC wind velocity compared with some

meteorological models. Some pioneering studies on parametric TC wind field modeling have been performed since the 1980s (Batts et al., 1980; Georgiou, 1985; Vickery et al., 2000, 2009). These studies employed a gradient wind speed model solved by the atmospheric balance equation of a stationary storm coupled with a depth-averaged (Vickery et al., 2000) or a semi-empirical observation-based boundary layer vertical profile model (Vickery et al., 2009). In recent years, with advances in computing capacity, another more sophisticated physical model has received intensive attention. This is the so-called height-resolving model, in which the boundary layer wind field is solved semi-analytically based on 3D Navier-Stokes equations (Meng et al., 1995; Kepert, 2010; Snaiki et al., 2017; Fang et al., 2018). This is of great help in interpreting the underlying physics of the TC boundary layer.

In this study, the graphically weighted regression technique was introduced to achieve the site-specific simulations of typhon hazards. As shown in Fig. 5.1, based on the historical track information extracted from the JMA dataset within a circular subregion centered at the site of interest, the genesis parameter model and storm forward models was developed. The genesis parameters, including the annual storm rate, the position of the first track dot, heading direction, central pressure difference, translation speed, radius to maximum wind speed and pressure profile shape parameter at first time step would be determined with several preferable probability distributions and correlation analyses. The storm forward models, which consist of tracking model, intensity model and wind field parameter model would be developed utilizing GWR technique. A series of performance assessments of the present subregion model were conducted. Finally, the site-specific simulations were performed to investigate the TC wind hazard of coastal cities of China.

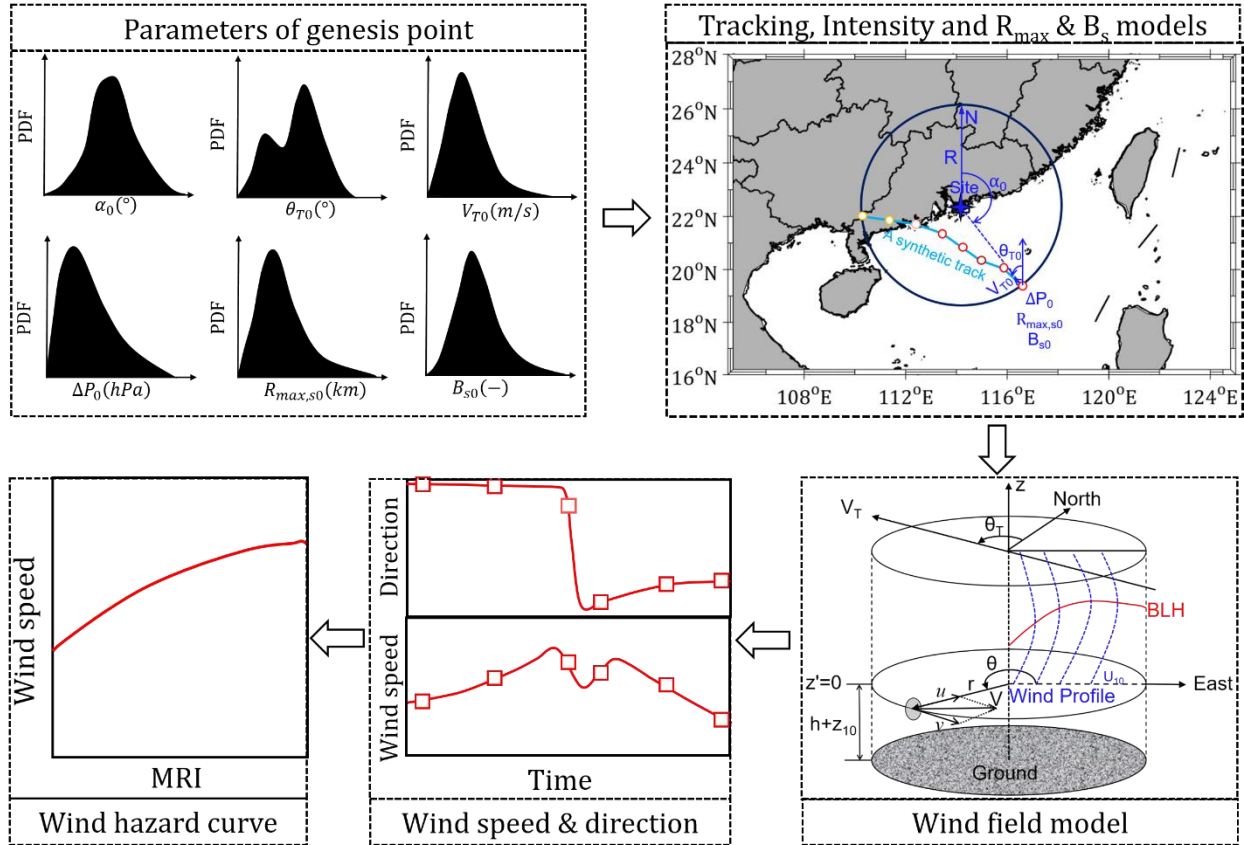


Fig. 5.1 Overview of circular sub-region method used in this study

5.2 Statistical characteristics of typhoon tracks

5.2.1 JMA best track dataset

In the Western Pacific Basin ($0^{\circ}\sim 60^{\circ}\text{N}$, $100^{\circ}\sim 180^{\circ}\text{E}$), the Japan Meteorological Agency (JMA) serves as the Regional Specified Meteorological Center (RSMC, 2018), as specified by the World Meteorological Organization (WMO). As such, it is responsible for forecasting, naming, tracking, distributing warnings and issuing advisories of TCs. Accordingly, JMA has been publicly releasing best track datasets of TCs in the Western Pacific Basin since 1951. These datasets contain not only some basic track information of TCs in terms of latitude and longitude of TC eye centers as well as dates and times, but also some wind speed information including minimum surface central pressure (P_{cs}), maximum sustained surface wind speed

($V_{max,s}$) and 50-knot or 30-knot winds radii estimated from surface observation, ASCAT observation and low-level cloud motion satellite images. Although some other organizations issue their own track dataset of TCs for the Western Pacific Basin (Ying et al., 2014), such as the China Meteorological Administration (CMA), Joint Typhoon Warning Center (JTWC), the Hong Kong Observatory (HKO) and the International Best Track Archive for Climate Stewardship (IBTrACS) project, there are some inconsistencies among these datasets that should be carefully considered. In addition to differences of TC track information and annual TC frequencies, two typical TC intensity representations, i.e. P_{cs} and $V_{max,s}$, show inconsistency from agency to agency, as discussed by Song et al. (2010). Generally, a remarkable difference was found, i.e., that $V_{max,s}(\text{JTWC}) > V_{max,s}(\text{CMA}) > V_{max,s}(\text{JMA})$ and $P_c(\text{JTWC}) < P_c(\text{CMA}) < P_c(\text{JMA})$, when TCs reach typhoon level, and this trend becomes apparent along with storm intensification (Song et al. 2010). It could attribute to time interval differences since JMA uses 10 min, CMA uses 2 min while JTWC uses 1 min is adopted by JTWC. The differences among estimation techniques and algorithms for determining $V_{max,s}$ and P_{cs} based on the Dvorak technique (Dvorak, 1984; Velden et al., 2006) with satellite cloud images could also contribute to this inconsistency. However, the 10-min time duration employed by JMA is consistent with most design codes or standards, and is also suggested by WMO (Fang et al., 2019). Furthermore, the 50-knot or 30-knot radii information provided by the JMA dataset is a supplement of great importance in facilitating the estimation of TC wind field parameters. As a result, the JMA best track dataset was selected as the basic information for the following TC hazards studies in the Southeast China region.

5.2.1 Statistical models of genesis parameters

In order to examine the statistical characteristics of historical track information around a site of interest, track segments that intersect and are within a circular sub-region centered at the target location are usually extracted from the best track dataset. The size of the subregion directly affects the data sampling as well as final design wind speed prediction (Georgiou, 1985; Xiao et al., 2011; Li and Hong, 2015). A suitable circle size should enable the TC tracks and wind field parameters to be least sensitive and to cover as many high wind speed samples as possible. Three radii, 500 km, 1000 km and 250 km were employed by Vickery and Twisdale (1995), Xiao et al. (2011) and Li and Hong (2015), respectively. A reasonable size of subregion should allow as many high wind speeds as possible to be considered and avoids the overuse of some extremely violent typhoons. Meanwhile, it cannot remarkably increase the computation cost. The use of 1000 km could overestimate the effects of high winds on a site of interest since some extremely violent typhoons over distant sea would be circled and used to model the central pressure before landfall. However, these typhoons have little chance of maintaining an extremely high intensity until landfall on mainland China. Based on the JMA dataset from 1951 to 2015, only seven violent typhoons ($P_{cs} \leq 935 \text{ hPa}$ or $V_{\max,s} \geq 54 \text{ m/s}$ (105 knots)), Nina (195307), Wanda (195606), Grace (195819), Saomai (200608), Hagupit (200814), Usagi (201319) and Rammasun (2014) directly landed on mainland China. Moreover, the largest $R_{\max,s0}$, illustrated in Figs. 8 and 16, range from 500 km to 600 km if the size of subregion $R = 500 \text{ km}$ is employed. And as mentioned by Yuan et al. (2007), about 50% of the radii of historical storms associated with a wind speed of 15.4 m/s range from 222 km to 463 km and only 10% are larger than 555 km. In fact, we can show experimentally that at the outer regions of a typhoon, 500 km or

larger away from storm center would have only a slight influence on the specific region. More details regarding the effects of size of the subregion will be investigated in the following discussion. $R = 500$ km, which is consistent with Vickery and Twisdale (1995) and will be used first.

Taking the example of the Hong Kong region (centered in 114.1678°E , 22.3186°N), which is severely affected by TCs, 412 segments of track data within a circle of $R = 500$ km were captured from the JMA dataset (1951-2015), as shown in Fig. 5.2. Although few TCs originate in this circular region, they only reach the strongest level of a severe tropical storm with P_{CS} larger than 980 hPa belonging to a normal-intensity storm. Their genesis locations are also close to the circular boundary. Accordingly, all simulated tracks can be assumed to originate from the circular boundary by considering the location distribution of historical tracks in term of origin angle α_0 , which is the direction relative to the site of interest and clockwise positive from the north.

The annual storm rate (storms/year) is usually modeled by negative binomial (Li et al., 2016) or Poisson distributions (Xiao et al., 2011; Li and Hong, 2015). However, the mean of the storm genesis within the circular region around Hong Kong is 6.339, which is larger than the variance of 2.280. It does not satisfy the prerequisite of the negative binomial distribution. The Poisson distribution was employed to model the annual storm rate (λ_a), as shown in Fig. 5.3. Based on the circular sub-region method, the position of first track dot (α_0) and its heading direction (θ_{T0}) determines the location of the simulated track line while the translation speed (V_{T0}) is used to estimate the TC center location at each time step. First values of the central pressure difference (ΔP_0) for each segment are applied for the TC intensity modeling before landfall.

Two wind field parameters, $R_{max,s}$ and B_s , are always predefined to model the surface pressure field before solving the wind speed. The JMA best track dataset is a preferable option for TC hazard assessments in the Western Pacific as discussed before. Its wind speed information in terms of maximum sustained surface wind speed ($V_{max,s}$) and 50-knot or 30-knot winds radii is of great help in extracting $R_{max,s}$ and B_s . Although JTWC also provides information of $V_{max,s}$ as well as the wind radii with respect to 34 knot, 50 knot and 64 knot and radius of maximum winds, the inconsistency of time-averaging issue should be carefully considered. Moreover, the wind information in the JTWC dataset is only available from 2001 while JMA documents extend over a longer record from 1977. So JMA dataset is more reliable for developing the parent distribution for use in Monte Carlo simulation. Accordingly, $R_{max,s}$ and B_s used in this study were extracted from the JMA best track dataset (from 1977 to present) by using 50-knot- or 30-knot-radii information as well as the maximum sustained surface wind speeds. For example, in Fig. 5.4, three radial wind profiles modeled by the optimally fitted $R_{max,s}$ and B_s closely match the JMA observation winds. It is noteworthy that the fitted values of B_s are slightly higher than traditional results, i.e. [Vickery et al. \(2000, 2008\)](#) while $R_{max,s}$ are almost unchanged. This is mainly attributed to the wind field model used in this study, which transfers the surface pressure field to the gradient layer before working out the surface wind speed using a height-resolving boundary model. As a result, a higher B_s needs to be employed to achieve a strong enough gradient wind field before it is converted to surface level.

Based on the statistical characteristics of historical data, the probabilistic distributions of these six parameters ($\alpha_0, \theta_{T0}, V_{T0}, \Delta P_0, R_{max,s0}, B_{s0}$) are fitted with several commonly used models using a maximum likelihood method before achieving the most suitable choices by

the Kolmogorov–Smirnov distribution test (K-S test). The preferable distribution models, i.e. Weibull, lognormal and bimodal normal for all genesis parameters and their probability density functions (PDFs) together with fitted coefficients are listed in Table 5.1. Correspondingly, Fig.5.5 compares the observed and modeled cumulative distribution functions (CDF) for these parameters. The critical value of K-S test for the historical data samples of α_0 , θ_{T0} , V_{T0} and ΔP_0 with the degrees of freedom $n = 409$ is 0.0667 at a 5% significance level while $R_{max,s0}$ and B_{s0} have the critical value of 0.1056 with $n = 162$. As can be seen, all modeled K-S values (values of k in Fig. 5.5) are smaller than critical statistics, which fails to reject the null hypothesis and proves that we have enough evidence to simulate the virtual TC tracks by adopting these distribution models.

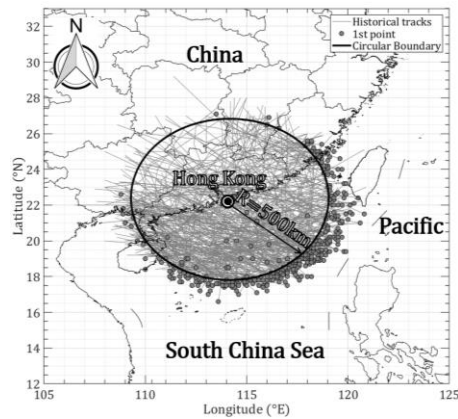


Fig. 5.2 Track segments within a circular region centered on Hong Kong with a radius of 500 km

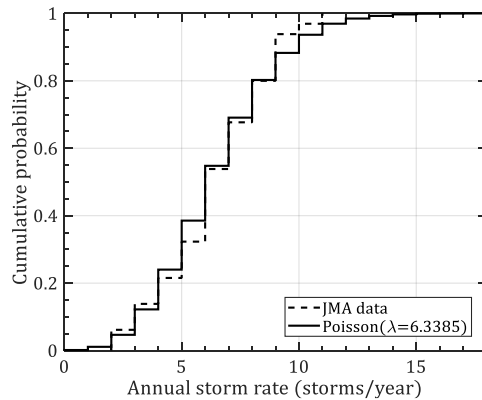


Fig. 5.3 CDF of annual storm rate (λ_a)

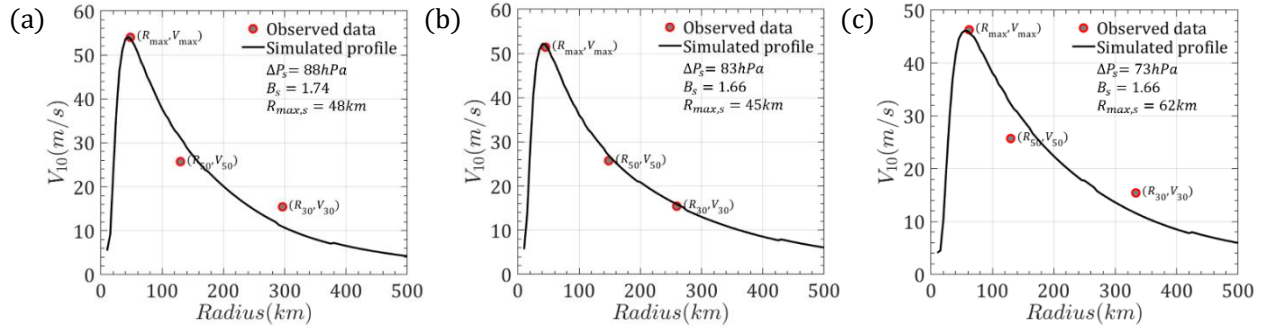


Fig. 5.4 Radial wind speed profiles (a) Saomai(2006-08-09, 15:00UTC); (b) Parma (2009-10-01, 06:00UTC); (c) Rammasun(2014-07-18, 12:00UTC)

Table 5.1 Distribution models and coefficients for TC track genesis parameters

Parameter	Distribution model	Probability density function (PDF)	Coefficients (Hong Kong)
λ_a	Poisson	$f(x; \lambda) = \frac{\lambda^x}{x!} e^{-\lambda}, \quad x = 0, 1, 2, \dots, \infty$	$\lambda = 6.34$
α_0	Weibull	$f(x; k, \gamma) = \frac{k}{\gamma} \left(\frac{x}{\gamma}\right)^{k-1} e^{-(x/\gamma)^k}, \quad x \geq 0$	$k = 3.14; \gamma = 157.03$
θ_{T0}	Bimodal normal	$f(x; p, \mu_1, \sigma_1, \mu_2, \sigma_2)$ $= p \frac{1}{\sigma_1 \sqrt{2\pi}} \exp\left\{-\frac{(x - \mu_1)^2}{2\sigma_1^2}\right\}$ $+ (1 - p) \frac{1}{\sigma_2 \sqrt{2\pi}} \exp\left\{-\frac{(x - \mu_2)^2}{2\sigma_2^2}\right\}$	$p = 0.59; \mu_1 = -66.36; \sigma_1 = 19.88; \mu_2 = -7.99; \sigma_2 = 64.55;$
V_{T0}	Lognormal	$f(x; \mu, \sigma) = \frac{1}{x\sigma\sqrt{2\pi}} \exp\left\{-\frac{(\ln x - \mu)^2}{2\sigma^2}\right\},$ $x > 0$	$\mu = 1.50; \sigma = 0.50$
ΔP_0			$\mu = 3.14; \sigma = 0.58$
$R_{max,s0}$			$\mu = 4.54; \sigma = 0.64$
B_{s0}			$\mu = 0.23; \sigma = 0.33$

Note: x denotes the argument or the input of the function.

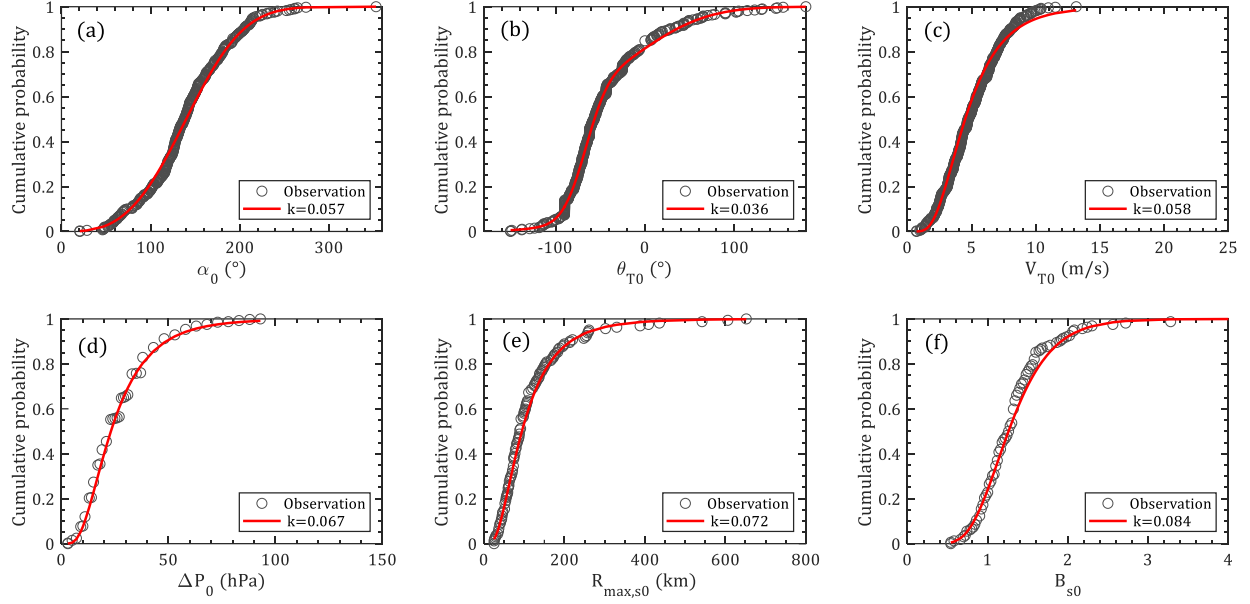


Fig. 5.5 CDFs of genesis parameters: (a) α_0 ; (b) ΔP_0 ; (c) θ_{T0} ; (d) V_{T0} ; (e) $R_{max,s0}$; (f) B_{s0}

5.2.1 Parameter correlations

As shown by the scatter plots in Fig. 5.6, the observed (red triangles) genesis (at first time step) parameters show some correlations, especially between θ_0 and α_0 , $R_{max,s0}$ and B_{s0} with correlation coefficients larger than 0.5. This means that the heading direction at the first time step is dependent on genesis location and two wind field parameters are strongly correlated with each other. Accordingly, the correlations between these genesis parameters, i.e. α_0 , ΔP_0 , θ_0 , V_{T0} , $R_{max,s0}$ and B_{s0} , would be considered utilizing the Cholesky decomposition method, which is a distribution-free approach introduced by [Iman and Conover \(1982\)](#). The randomly generated independent variables can be written into a matrix of size $N \times 6$ (N is the number of simulation samples) as

$$\mathbf{X} = [\alpha_0, \Delta P_0, \theta_0, V_{T0}, R_{max,s0}, B_{s0}] \quad (5.1)$$

The correlation coefficient matrix is \mathbf{C} and is derived from historical data of size 6×6 , which is positive definite and symmetric and can be alternatively expressed as $\mathbf{C} = \mathbf{A}\mathbf{A}^T$ using the

Cholesky decomposition method, in which \mathbf{A} is a lower triangular matrix. If the correlation matrix of \mathbf{X} is \mathbf{Q} , it can also be decomposed into the product of a lower triangular matrix \mathbf{P} and its transpose \mathbf{P}^T , i.e. $\mathbf{Q} = \mathbf{P}\mathbf{P}^T$. A matrix $\mathbf{S} = \mathbf{A}\mathbf{P}^{-1}$ can be determined such that $\mathbf{S}\mathbf{Q}\mathbf{S}^T = \mathbf{C}$. After that, the final transformed correlated matrix $\mathbf{X}_c = \mathbf{X}\mathbf{S}^T$ can be obtained, which has the desired correlation matrix \mathbf{C} . It is noteworthy that the values in each column of the input $N \times 6$ matrix \mathbf{X} can be rearranged to have the same rank-order as the target matrix.

The correlated genesis samples for 100 years for Hong Kong are generated by Monte Carlo simulations coupled with parameter correlation analysis, as shown in Fig. 5.6. As can be seen, the observed JMA data points are scattered around the simulated results. And the correlation coefficients of the simulated variables (ρ_{sim}) are almost identical to those of the original observations (ρ_{obs}). It is worth mentioning that the historical data for α_0 , ΔP_0 , θ_0 , V_{T0} are more than those for $R_{max,s0}$ and B_{s0} since the wind speed information is only available from 1977 and the wind data estimations are usually not provided during the first and last several time steps of a TC track due to its weak intensity. As a result, the scatter plots for historical observations in Fig. 5.6 associated with $R_{max,s0}$ and B_{s0} contain fewer data than others. Correspondingly, the correlation coefficients associated with these two parameters would also be derived from fewer data.

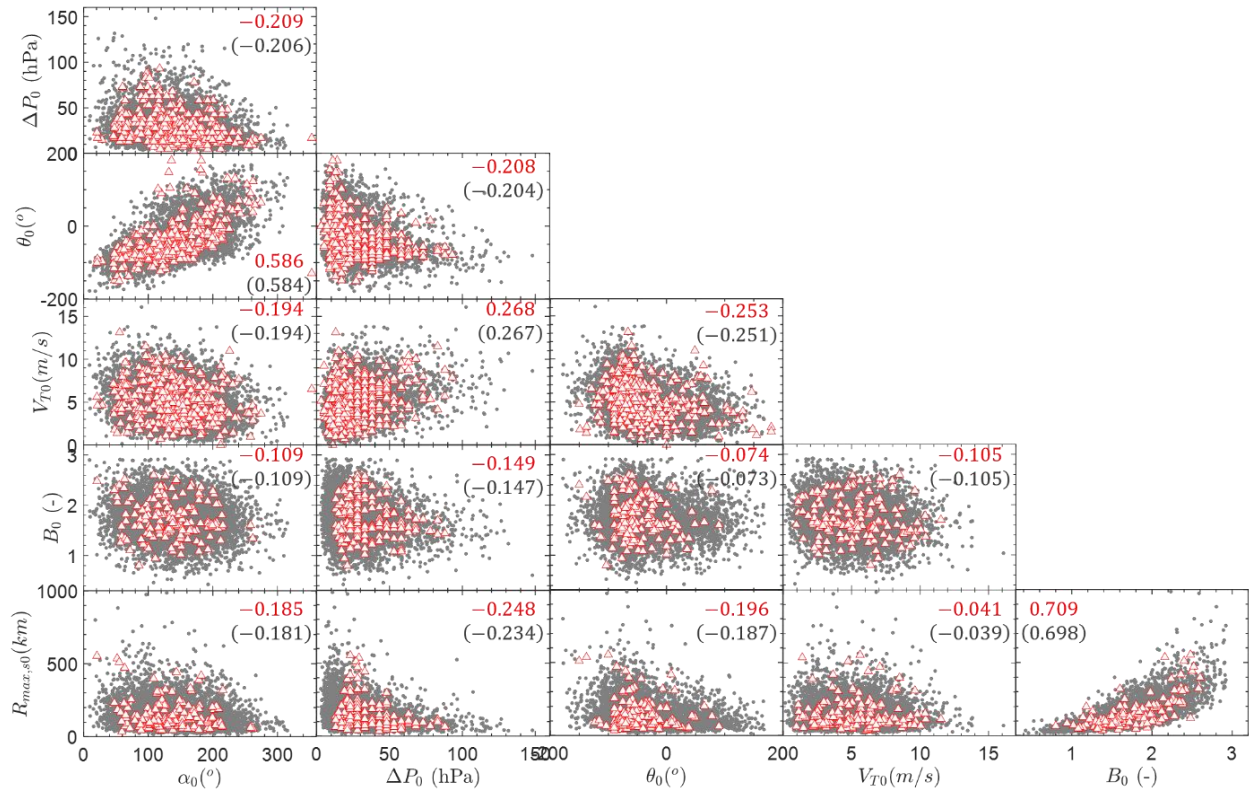


Fig. 5.6 Simulated and observed genesis parameters (Red triangles: observations; Grey dots: simulations; Upper numbers: ρ_{sim} ; Lower numbers in parenthesis: ρ_{obs} ;

5.3 GWR-based track forward model

5.3.1 GWR method

Geographically weighted regression (GWR) is a spatial data analysis technique that utilizes distance-weighted variables to model local relationship between predictors and an outcome of interest (Fotheringham, 1998; 2002). GWR utilizes the site-specific sub-samples of data information from nearby observations to produce estimates, which enables the estimation of local parameters rather than the global parameters. It is able to capture the spatial heterogeneity by allowing the relationships between the inputs and outputs to vary by locality. If there are n data points observed in the space that makes up an $n \times 1$ vector of dependent variable denoted \mathbf{Y} . A set of m explanatory or independent variables X_k , ($k =$

1,2, ..., m) was assumed. And the location or position information of n observations in a suitable coordinate system should be available. Then, the GWR model associated with point i can be expressed as

$$\mathbf{W}_{n \times n} \mathbf{Y}_{n \times 1} = \mathbf{W}_{n \times n} \mathbf{X}_{n \times m} \boldsymbol{\beta}_{m \times 1} + \mathbf{W}_{n \times n} \boldsymbol{\varepsilon}_{n \times 1} \quad (5.2)$$

in which $\mathbf{W} = \text{diag}[w_{1i}, w_{2i}, \dots, w_{ni}]$ is an $n \times n$ diagonal distance-weighted matrix, \mathbf{X} represents n observations of m explanatory variables, $\boldsymbol{\beta}$ are fitted m parameters related to each explanatory variable, $\boldsymbol{\varepsilon}$ is an $n \times 1$ vector of error term. The parameter estimates can be given as

$$\hat{\boldsymbol{\beta}}_{m \times 1} = (\mathbf{X}_{n \times m}^T \mathbf{W}_{n \times n} \mathbf{X}_{n \times m})^{-1} \cdot (\mathbf{X}_{n \times m}^T \mathbf{W}_{n \times n} \mathbf{Y}_{n \times 1}) \quad (5.3)$$

The distance-based weights w_{ji} ($j = 1, 2, \dots, n$) in \mathbf{W} are defined as a decay function of distance or kernel between objective point i and j th observations. A number of weighted functions have been adopted in recent studies, such as exponential function, Gaussian function and tri-cube function (LeSage, 1999). The exponential kernel, which will be adopted in this study is given with the form of

$$w_{ji} = \sqrt{\exp(-d_{ji}^2/\theta_i^2)} \quad (5.4)$$

in which d_{ji} is the distance between the objective point i and j th observations, θ_i is a decay parameter termed "bandwidth". Fig. 5.7 illustrates the exponential kernel curves with various bandwidths. The distance weight decays more slowly with the increase of bandwidth. That is, for a selected datapoint, greater weight will be employed if a larger bandwidth is used. It worth mentioning that the exponential kernels would retain non-zero weights to all observations, regardless how far they are from the regression point. It leads to the weights assigned to most observations are close to zero, which have insignificant effects on the

regression. In order to improve the calculation speed and reduce memory requirements, only these non-negligible weighted elements will be retained with a lower bound of 0.01. Moreover, a cross-validation estimation for bandwidth for each regression point was performed. The optimal bandwidth was determined by searching the minimum standard deviation of errors between real observations and regressions. Figure 5.7 shows that if the bandwidth is equal to 1, the observations within a circular region centered at the regression point with the radius about three-unit distances will be covered. Since our estimation for the coefficients of typhoon tracking and intensity model will be performed in each latitude and longitude grid point with the resolution of 1° , the maximum potential bandwidth is set as 1 in this study. Then, the optimal bandwidth for each objective regression point will be determined from the range of $[0.1, 1]$ based on the cross-validation. That means we will utilize adaptive exponential kernels at different regression points, as shown in Fig. 5.8.

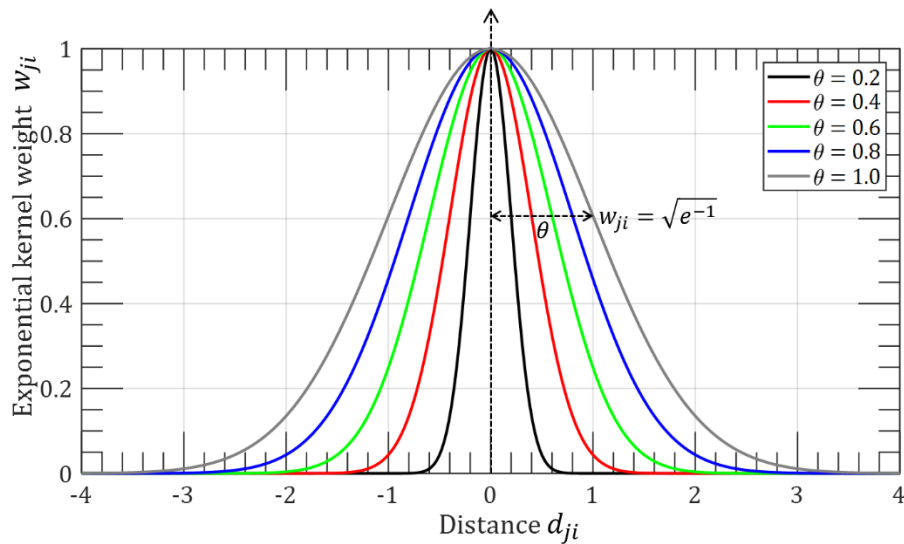


Fig. 5.7 Exponential kernel with various bandwidths

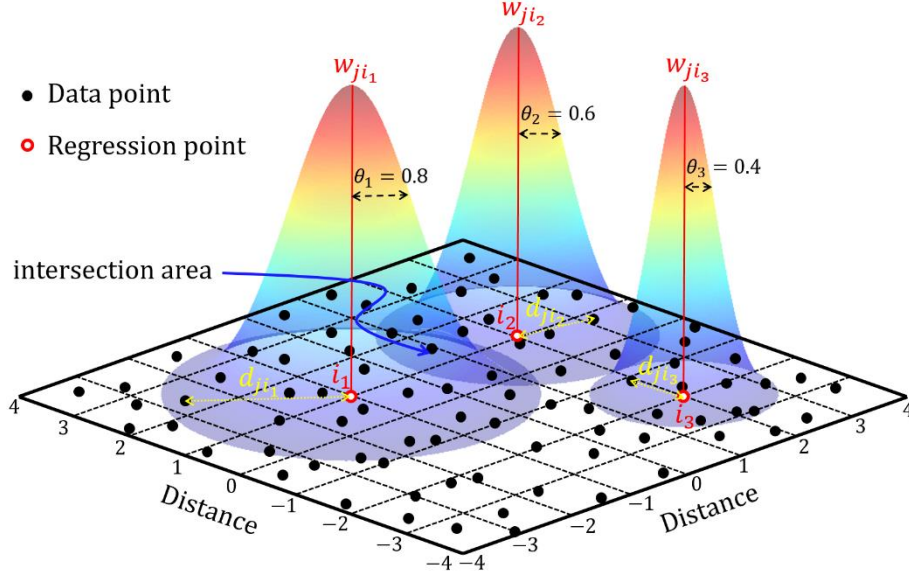


Fig. 5.8 GWR with adaptive exponential kernels

5.3.2 Tracking model

The tracking model, which consists of two progressive formulas of the change in translation speed V_T and heading direction θ_T , is used for determining the TC eye locations at every time step and contributes slightly to the TC wind speed field. Conventionally, it was randomly sampled from a historical-data-based probability distribution (Xiao et al., 2011; Li and Hong, 2015). In reality, V_T and θ_T at next step should be correlated with previous steps which is also the statistical basis for empirical full track modeling (Vickery et al., 2000; Li et al., 2016). Accordingly, given the initial storm forward speed and heading direction, the updated speed and direction for next steps can be modeled as two recursive formulas

$$\Delta \ln V_T = \ln V_T(i+1) - \ln V_T(i) = v_1 + v_2 \cdot \ln V_T(i) + v_3 \cdot \ln V_T(i-1) + v_4 \cdot \theta_T(i) + \varepsilon_{\Delta \ln V_T} \quad (5.5)$$

$$\Delta \theta_T = \theta_T(i+1) - \theta_T(i) = h_1 + h_2 \cdot \theta_T(i) + h_3 \cdot \theta_T(i-1) + h_4 \cdot V_T(i) + \varepsilon_{\Delta \theta_T} \quad (5.6)$$

in which v_j and h_j ($j = 1 \sim 4$) are model coefficients obtained from the GWR analysis for historical data, $V_T(i)$ and $\theta_T(i)$ are the forward speed and heading direction at time step i ,

$\varepsilon_{\Delta \ln v_T}$ and $\varepsilon_{\Delta \theta_T}$ are the error terms accounting for modeling differences between the regression models and the real observations.

For each grid point in Northwestern Pacific area at geographic coordinate system with the resolution of 1° , the GWR was performed for tracking model, say Eqs. (5.5)-(5.6). Fig. 5.9 illustrates the optimal bandwidths for heading direction model by minimizing the residuals between model and real observations. In order to obtain reliable estimation of model coefficients using least squares regression, only those regression points cover ten or more observation data points are employed. And for those grid points without sufficient data, the coefficients and distribution parameters of modeling errors are borrowed from adjacent grid points. Accordingly, some grid points in Fig. 5.10 have same optimal bandwidth. They are not optimally determined from their neighborhood observations, but just copied from adjacent grid points.

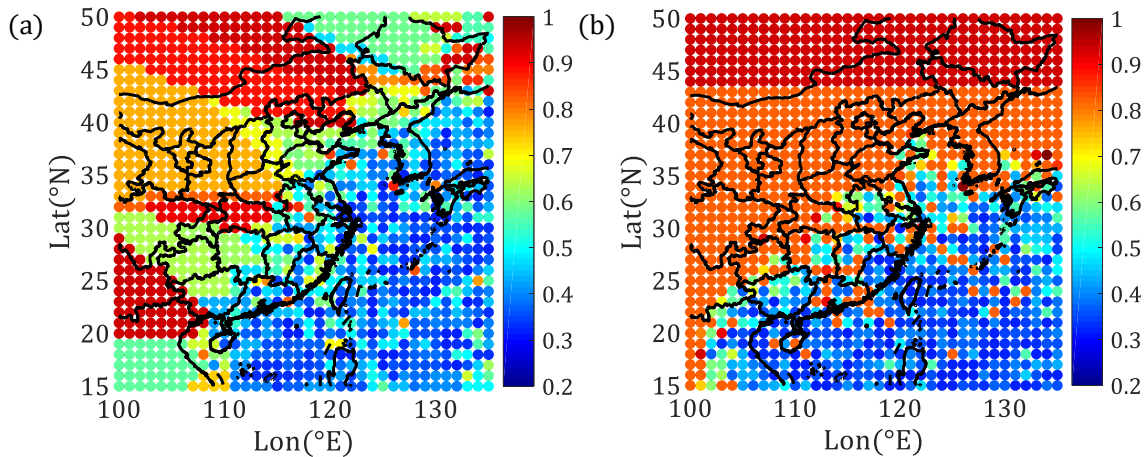


Fig. 5.9 Optimal bandwidths for heading direction model: (a) Easterly headed storms; (b) Westerly headed storms

Once the coefficients $v_1 \sim v_4$ and $h_1 \sim h_4$ at each grid point are determined, the 2-D interpolation of these scattered data is adopted to fill in the whole domain of interest. It allows the generation of a number of coefficient maps. Fig. 5.10 shows the contour plots of

coefficients ($h_1 \sim h_4$) of heading direction model for easterly headed storms. Note that the coefficients at those grid points with insufficient observations (less than 10 data points) would be copied from the closest coefficients-available neighbouring point. Most coefficients of inland grid points are obtained using this algorithm, resulting in the same coefficient in some over-land areas, as shown in Fig. 5.10.

Since the GWR technique can only guarantee that the difference between weighted explanatory variables and dependent variables (weighted errors) approximately follows the zero-mean normal distribution (Eq. 5.3). Hence, the unweighted errors usually have non-zero mean and do not well match the normal distribution. In Fig. 5. 11, the contour plots of errors of heading direction model for easterly headed storms are illustrated. It can be noticed that most areas are featured with non-zero means. Furthermore, Fig. 5.12 shows the cumulative distribution functions (CDFs) of modelling errors for $\Delta\theta_T$ and ΔV_T for the grid point of (116°E, 20°N). As can be seen, the weighted errors are scattered around zero and approximately follow the normal distribution. That indicates the GWR approach provides unbiased estimation. However, the means of unweighted errors are not always zero. And more fluctuations can be observed than weighted errors since all weights are less than 1. In Fig. 5.12, the normal distribution and unbounded Johnson distribution (Liu, 2014) models are used to fit the errors. Generally, both of them match the empirical CDFs well. But the unbounded Johnson distribution is preferable with smaller Kolmogorov-Smirnov test (K-S test) statistics. Accordingly, the unbounded Johnson distribution was employed for modeling the errors.

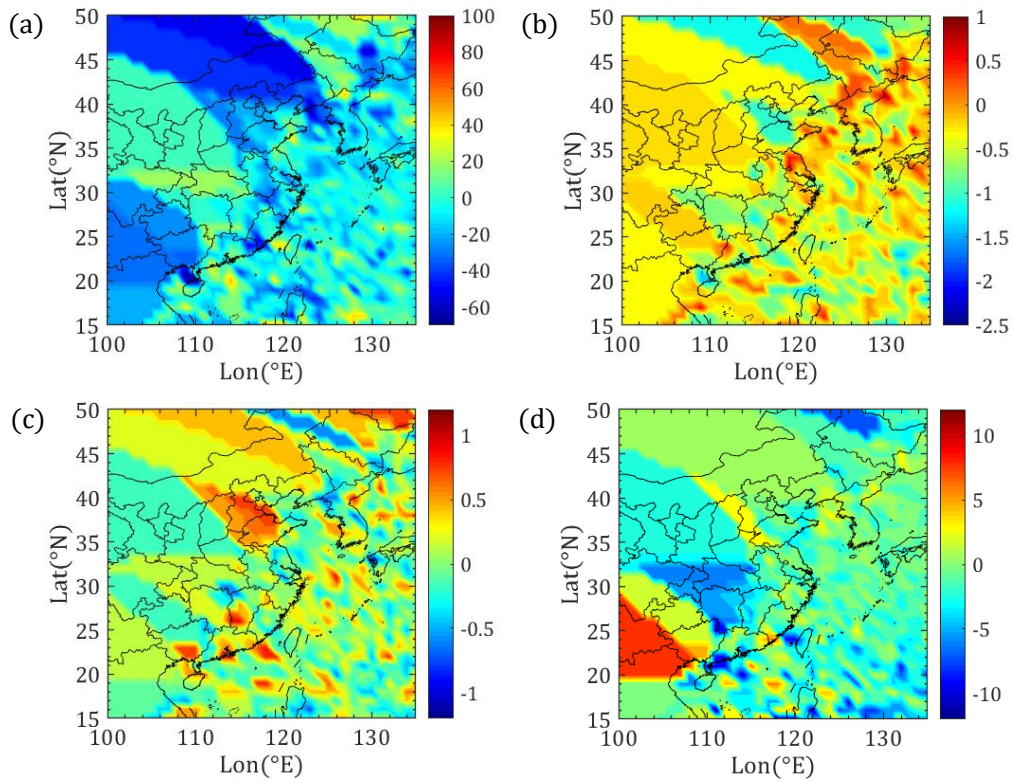


Fig. 5.10 Contour plots of coefficients of heading direction model for easterly headed storms: (a) h_1 ; (b) h_2 ; (c) h_3 ; (d) h_4

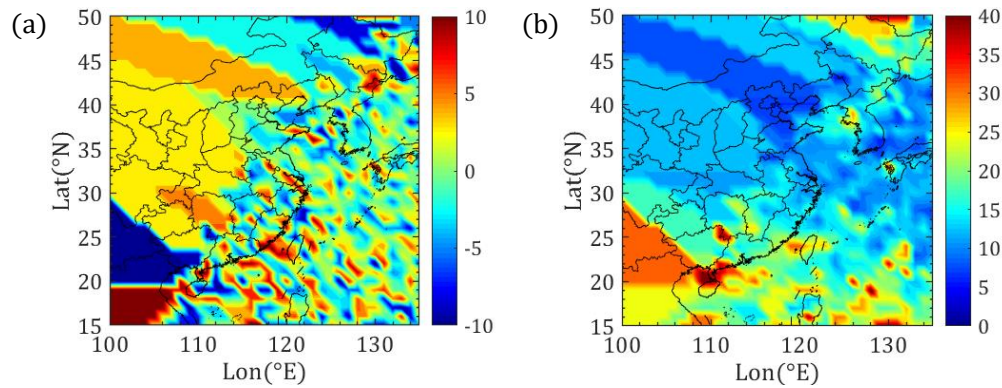


Fig. 5.11 Contour plots of errors of heading direction model for easterly headed storms: (a) Error mean; (b) Error standard deviation

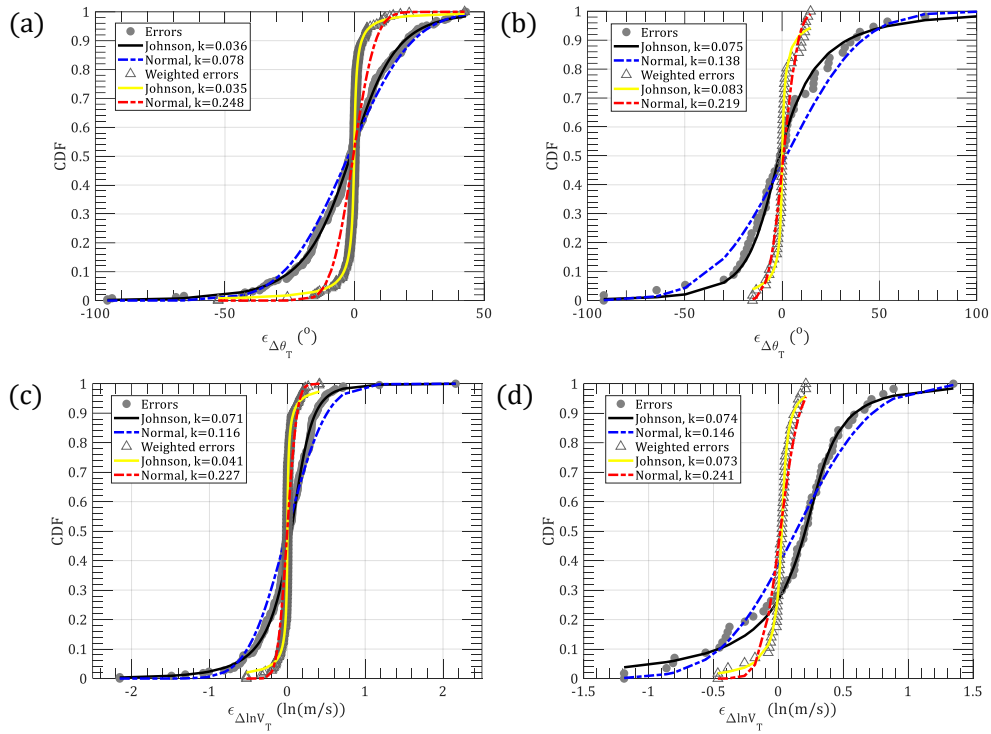


Fig. 5.12 Tracking model error for the grid point of (116°E, 20°N): (a) $\epsilon_{\Delta\theta_T}$ for easterly headed storms; (b) $\epsilon_{\Delta\theta_T}$ for westerly headed storms; (c) $\epsilon_{\Delta\ln v_T}$ for easterly headed storms; (d) $\epsilon_{\Delta\ln v_T}$ for westerly headed storms; (k is the K-S test values)

In order to examine the performance of the tracking model, track simulation was conducted using the initial conditions of typhoon Khanun at 09:00 UTC and 12:00 UTC on September 10th, 2005 as first two steps, including the locations of typhoon center, heading directions and forward speeds. As shown in Fig. 5.13, 1,000 synthetic tracks were generated for next two days (48 hours). And a cone of spatial standard deviation in terms of the standard deviations of heading directions and forward speeds was calculated using 1,000 simulated tracks. It can be noted that the real historical track falls inside the standard deviation cone of synthetic tracks.

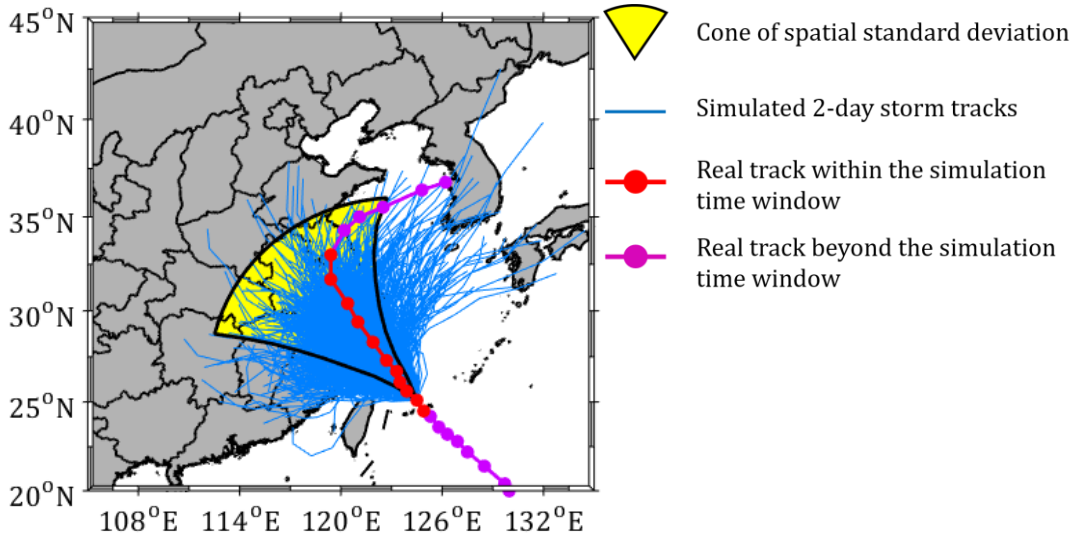


Fig. 5.13 Typhoon Khanun: 2-day simulation from 2005-09-10 09:00 UTC

5.3.3 Intensity model

The intensity model or central pressure model is customarily divided into two part, say relative intensity model for over-sea storms and decay model (or filling-rate model) for over-land storms.

(1) Relative intensity model for over-sea storms

For over-sea storms, the central pressure is alternatively modeled with the relative intensity (Darling, 1991) accounting for the effects of sea surface temperature and air moisture with the form of

$$I = \frac{p_{da} - (p_{cs} - e_s)}{p_{da} - p_{dc}} = \frac{1013 - p_{cs} + (1 - RH_a)e_s}{(1 - x)[1013 - RH_a \cdot e_s]} \quad (5.7)$$

in which e_s is the saturation vapor pressure expressed as

$$e_s = 6.122 \cdot e^{\frac{17.67(T_s - 273.16)}{T_s - 29.66}} \quad (5.8)$$

RH_a is the relative humidity of ambient air, approximately taken as 0.75, $p_{da} = 1013 - RH_a \cdot e_s$ is the surface value of the partial pressure of ambient dry air, p_{dc} is the minimum

sustainable surface central pressure of dry air, T_s is the sea surface temperature, $x = p_{dc}/p_{da}$ is solved from the equation as

$$\ln x = -A \left(\frac{1}{x} - B \right) \quad (5.9)$$

in which

$$A = \frac{\varepsilon L_v e_s}{(1 - \varepsilon) R_v T_s P_{da}} \quad (5.10)$$

$$B = RH_a \cdot \left[1 + \frac{e_s \ln(RH_a)}{A \cdot P_{da}} \right] \quad (5.11)$$

$$L_v = 2.5 \times 10^6 - 2320(T_s - 273.16) \quad (5.12)$$

$$\varepsilon = \frac{T_s - T_0}{T_s} \quad (5.13)$$

T_0 is the troposphere (assume at height of 100mb pressure) temperature at typhoon center, R_v is the specific gas constant of water vapor, taken to be $461 \text{ J}/(\text{kg} \cdot \text{K})$.

Then the relative intensity model for an over-sea storm can be modeled by the following recursive formula as (Vickery et al. 2000)

$$\begin{aligned} \ln[I(i+1)] = & c_1 + c_2 \cdot \ln[I(i)] + c_3 \cdot \ln[I(i-1)] + c_4 \cdot \ln[I(i-2)] + c_5 \cdot T_s(i+1) + c_6 \\ & \cdot [T_s(i+1) - T_s(i)] + \varepsilon_{\ln(I)} \end{aligned} \quad (5.14)$$

in which c_j ($j = 1 \sim 6$) are model coefficients obtained from the GWR analysis for historical data, $I(i)$ and $T_s(i)$ are the relative intensity and sea surface temperature at time step i , $\varepsilon_{\ln(I)}$ is the error terms accounting for modeling differences between the regression models and the real observations.

Since the relative intensity is a function of sea surface temperature (T_s), the T_s dataset of HadISST (Hadley Centre sea Ice and Sea Surface Temperature) monthly averaged T_s from 1951 to August 1981 (Hadley Centre for Climate Prediction and Research, 2006) and NOAA

Optimum Interpolation 1/4 Degree Daily Sea Surface Temperature (OISST) (Richard W et al., 2008) from the September 1981 to present were used. To transform the central pressure in JMA best track dataset to relative intensity, the historical T_s grid data closest to the location of storm eye will be assigned. Then, similar to tracking model, the coefficients of relative intensity model of Eq. (5.14) will be determined using GWR method at each $1^\circ \times 1^\circ$ grid point. The contour plots each coefficient are shown in Appendix C.

It noteworthy that the storm intensity should be constrained under a certain climatic condition. Hence, a lower limit was imposed on the surface central pressure (p_{cs}) during the simulation to prevent unrealistically values. Since the surface air at the storm center is saturated (the relative humidity is 100%), the potential minimum surface central pressure can be defined as

$$p_{cs,min} = p_{dc} + e_s \quad (5.15)$$

Then, during the simulation, a $p_{cs,min}$ will be used under a certain climatic condition (mainly sea surface temperature here) if the program yields a p_{cs} lower than $p_{cs,min}$ at that time step.

(2) Decay model after landfall

Once the storm makes landfall, the central pressure deficit will witness a sudden decrease due to the cutoff of warm and moist air from the underlying oceanic environment, after which the TC intensity decay model or filling-rate model is adopted. The modeling of storm decay is of great importance for accurately estimating the TC design wind speed at the site of interest since the maximum winds normally occur during storm landfall in most cases. Georgious (1985) modeled the decay of central pressure as a function of distance after landfall for four regions of the United States based on historical data. The other commonly

used filling-rate model assumes that the central pressure deficit decays exponentially with time after landfall in the form of (Vickery, 2005)

$$\Delta P(t) = \Delta P_0 \cdot \exp(-at) \quad (5.16)$$

in which t is the time after landfall (hour), ΔP_0 is the central pressure difference at landfall (hPa), and a is called the decay rate, which is correlated with ΔP_0 and modeled as

$$a = a_1 + a_2 \Delta P_0 + \varepsilon_a \quad (5.17)$$

where a_1 and a_2 are two region- and topographic-dependent coefficients, and ε_a is a zero-mean normally-distributed error term. As shown in Fig. 5.14a, the decay information of the ratio of central pressure deficit was extracted from the landfall TCs in the circular region around Hong Kong (Fig. 5.2) and fitted with the decay model of Eq. (5.16) using a least squares analysis. Generally, the decay model is well-behaved although it is unable to capture the unchanged central pressures with time after landfall. This is also discussed in detail by Vickery (2005). Furthermore, the correlation between decay rate and central pressure difference at landfall is plotted in Fig. 5.14b with the correlation coefficient $\rho = 0.3019$, which is also modeled by the linear function of Eq. (5.17). Then the residual error is unbiased and can be modeled by a normal distribution with mean and standard deviation of 0 and 0.0227, respectively.

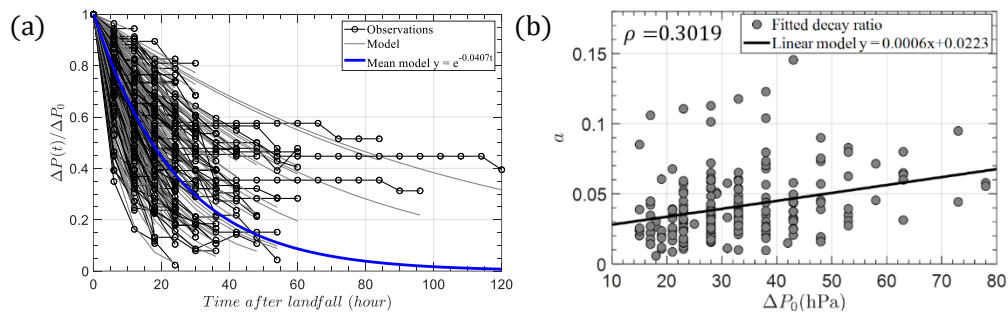


Fig. 5.14 Decay model in circular sub-region around Hong Kong:(a) Curve fitting of decay model; (b) Decay rate versus ΔP_0

5.3.4 $R_{max,s}$ and B_s model

Similar to tracking and intensity models, the supplemental data information of $R_{max,s}$ and B_s extracted from the JMA dataset for storms from years 1977 to present facilitates the development their recursive models. The successive values of $R_{max,s}$ and B_s for each storm allows the analyses of their autocorrelations of adjacent time steps. It was found that $R_{max,s}(i + 1)$ and $B_s(i + 1)$ (values at next step) are strongly correlated with previous steps i and $i - 1$. By conducting the correlation analyses, the linearly weighted progressive equations of $R_{max,s}$ and B_s were modeled as

$$\ln R_{max,s}(i + 1) = r_1 + r_2 \cdot \ln R_{max,s}(i) + r_3 \cdot \ln R_{max,s}(i - 1) + r_4 \cdot \Delta P_s(i + 1) + \varepsilon_{\ln R_{max,s}} \quad (5.17)$$

$$B_s(i + 1) = b_1 + b_2 \cdot \sqrt{R_{max,s}(i + 1)} + b_3 \cdot B_s(i) + b_4 \cdot B_s(i - 1) + \varepsilon_{B_s} \quad (5.18)$$

in which $r_j(j = 1 \sim 4)$ and $b_j(j = 1 \sim 4)$ are model coefficients that can be fitted with the GWR method, $\ln R_{max,s}(i)$ and $B_s(i)$ are values at time step i , and $\varepsilon_{\ln R_{max}}$ and ε_{B_s} are error terms accounting for modeling differences between the models and observations. Similar to tracking and intensity models, the coefficients of $R_{max,s}$ and B_s models will be determined using GWR method at each $1^\circ \times 1^\circ$ grid point. The contour plots each coefficients are shown in the Appendix D.

5.3.5 Model assessment

To evaluate the performance of tracking, intensity and wind field parameter models, simulations were performed on each model module independently. The initial conditions of a circled historical track, i.e. typhoon Gerald (Year 1984, No. 08) at 00:00 UTC and 06:00 UTC on August 16th, 1984, including the locations of storm eye in terms of longitudes and latitudes, heading directions, forward speeds, central pressures, radii to maximum wind speed and

pressure profile shape parameters were utilized. As shown in Fig. 5.15, 1,000 simulations on tracking model, intensity model and wind field parameter model were performed and compared with real observations, respectively. The synthetic tracks were only generated for next two days (48 hours) (Fig. 5.15(a)). And a cone of spatial standard deviation in terms of the standard deviations of heading directions and forward speeds was calculated using 1,000 simulated tracks. It can be noted that the real historical track does not always lie inside the standard deviation cone of synthetic tracks but covered by synthetic tracks. It indicates the present tracking model not only has a good performance on simulating the site-specific general forward trend of storm tracks, but also allows the generation of some wired paths as observed in history.

Similarly, 1,000 simulations on central pressured were also performed using the intensity model and initial conditions of a same real track, i.e. typhoon Gerald (Year 1984, No. 08) at 00:00 UTC and 06:00 UTC on August 16th, 1984. The track information of historical real observations was employed. The relative intensity model (Eq. (5.14)) was adopted to calculate the central pressure when the storm eye is over the sea surface. And the filling-rate model (Eqs. (5.16) ~ (5.17)) was applied to simulate the pressure decay after its landfall. As illustrated in Fig. 5.15b, 1,000 simulated central pressure time histories were compared with real observations. It shows that the real central pressures of typhoon Gerald are close to the mean values of simulation and within bounds of standard deviation. The lowest central pressure of typhoon Gerald during this time period was 980 hPa. That implies at least half of simulations only reach the level of strong tropical storm (STS). But the simulations also show the chance for this storm to become a violent strong typhoon.

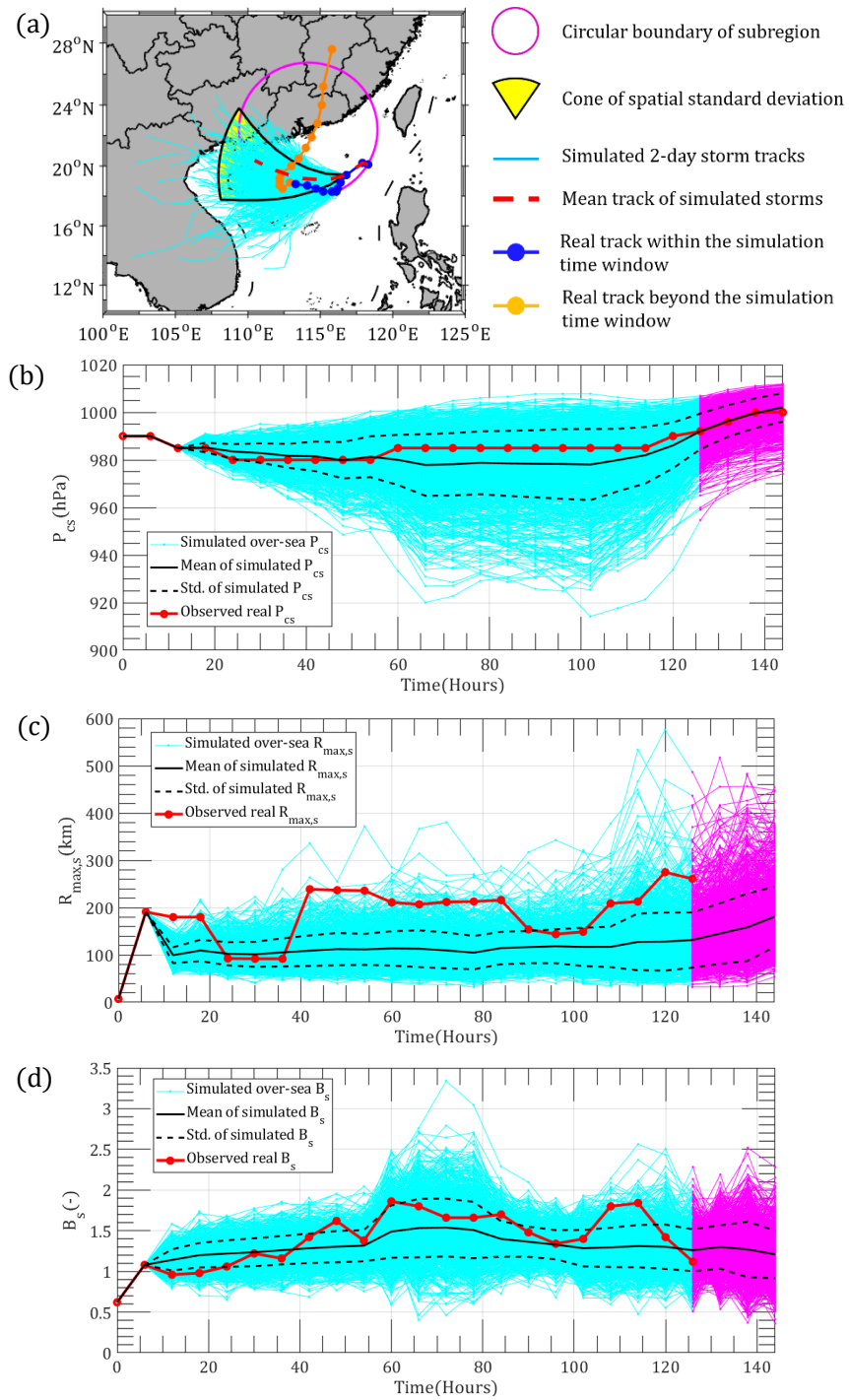


Fig. 5.15 Typhoon Gerald: simulation from 1984-08-16 00:00 UTC: (a) 2-Day track simulation; (b) Central pressure P_{cs} ; (c) Radius to maximum winds $R_{max,s}$; (d) Pressure shape parameter B_s

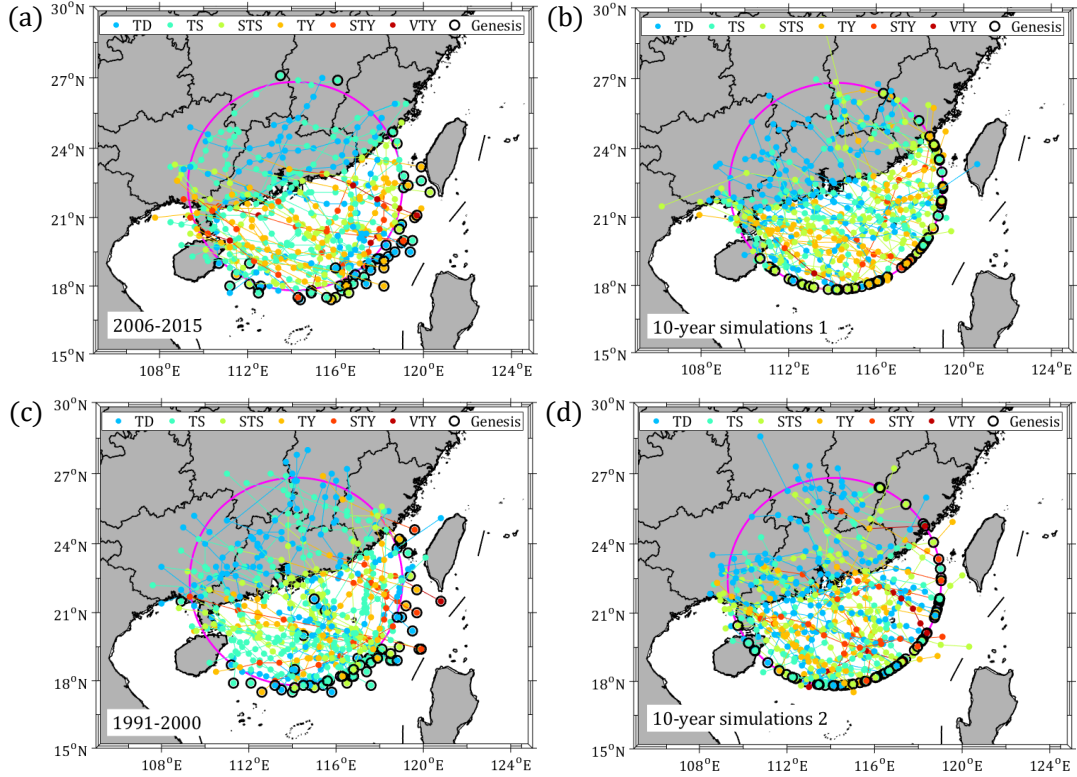


Fig. 5.16 Comparison between real and simulated storms in Hong Kong: (a) Real tracks from 2006 to 2015; (b) Simulated 10-year storms 1; (c) Real tracks from 1991 to 2000; (d) Simulated 10-year storms 2

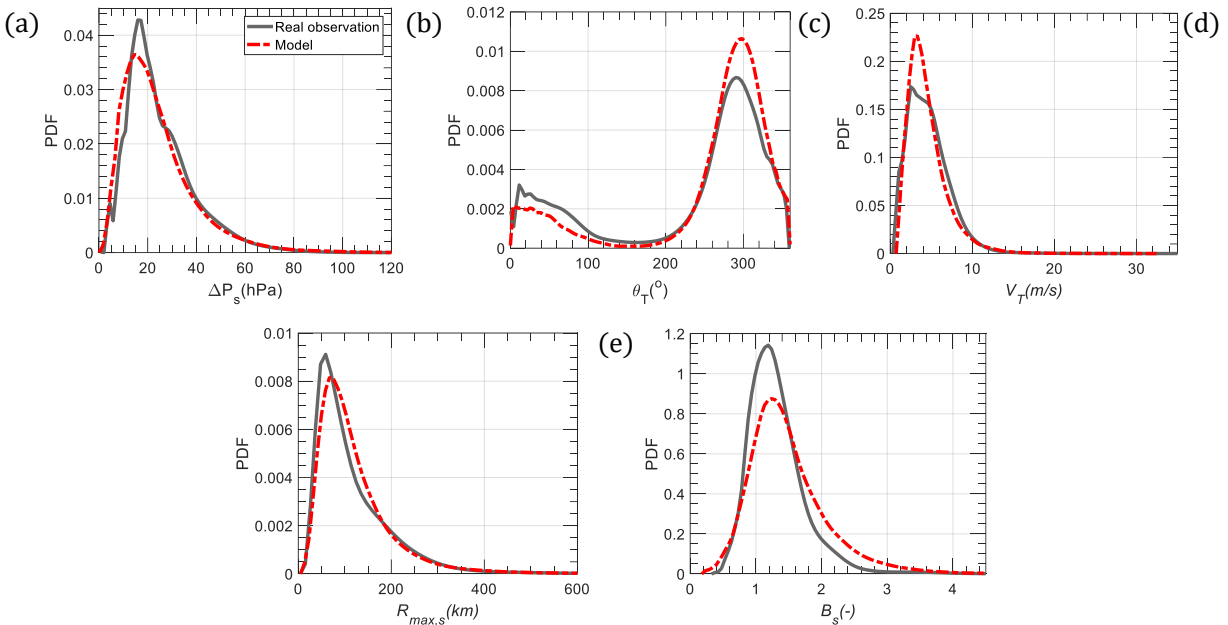


Fig. 5.17 Comparison of PDF for real and simulated parameters within the domain of Hong Kong (1,000-year simulations): (a) Central pressure deficit ΔP_s ; (b) Heading direction θ_T ; (c) Forward speed V_T ; (d) Radius to maximum winds $R_{max,s}$; (e) Pressure shape parameter B_s

Furthermore, similar simulations were also performed on $R_{max,s}$ and B_s models using Eqs. (5.17) ~ (5.18), as shown in Fig. 5.15(c)~(d). Since JMA did not provide the wind speed information, i.e. the maximum sustained surface wind speed ($V_{max,s}$) and 50-knot or 30-knot winds radii after the landfall of typhoon Gerald, $R_{max,s}$ and B_s were not estimated after its landfall. But their models enable the simulation using site-specific coefficients estimated from GWR. It can be noted that 1,000 simulations can cover the real observations. A large part of the time history of real $R_{max,s}$ lies outside of the upper standard deviation bound of simulations while B_s observations are mostly enclosed in the bounds of the standard deviations. More examples are shown in Appendix E.

More performance assessments of present model were conducted on the whole circular subregion of interest. Fig. 5.16(a) and Fig. 5.16(c) show the real tracks within the 500km-radius-circle centered in Hong Kong from years 2006 to 2015 and 1991 to 2000, respectively. In comparison, two 10-year simulations were randomly sampled from 10,000 simulated database and plotted in Fig. 5.16(b) and Fig. 5.16(d). As can be seen, genesis locations for both simulated and real tracks are concentrated on the right rear quadrant. And a number of violent typhoons, will could be dominant for the wind hazard curve can be noted in 10-year simulations. Meanwhile, the obvious inland decay when the storm moves to land can be observed. In addition, Fig. 5.17 illustrates the comparison of PDFs for real and simulated parameters within the domain of interest, including central pressure deficit ΔP_s , heading direction θ_T , forward speed V_T , radius to maximum winds $R_{max,s}$ and pressure shape parameter B_s . It shows reasonable agreements between observations and simulations. More comparisons are performed as illustrated in Appendix F.

5.4 Wind hazard prediction

5.4.1 Design wind speed prediction

After generating the virtual tracks as well as the wind field parameters, the TC wind speed at the site of interest can be readily solved using the wind speed field model. Then, our final objective is to investigate the design wind speeds with various return intervals or TC wind hazard curves for the site of interest. 10,000-year simulations would be conducted for each site to achieve adequate TC samples. The underlying terrain exposure is assumed to be consistent with the standard condition specified by Load Code for the Design of Building Structures (GB-50009 2012), i.e. flat open and low-density residential area of terrain category B with equivalent roughness length $z_0 = 0.05$ m. Meanwhile, a smaller $z_0 = 0.01$ m, which is associated with the terrain category A in the Code is also employed for comparison. These simulated tracks can also be employed to estimate the wind speed with respect to other underlying exposures by simply using a desired input of z_0 . And all simulated tracks can be interpolated into 15 min so as to capture every potential maximum wind speed.

By assuming that number of typhoons occurring in a given season is independent of any other season such that the occurrence probability $P_T(n)$ of n TCs over the time period T can be assumed to follow the Poisson distribution. Then, the probability that the extreme wind speed v_i is larger than a certain wind speed V within a time period T can be determined as

$$P_T(v_i > V) = 1 - \sum_{n=0}^{\infty} P(v_i \leq V|n)P_T(n) = 1 - \exp\left(-\frac{N}{Y}T\right) \quad (5.19)$$

in which $P(v_i \leq V|n)$ is the probability that the peak wind speed v_i of a given TC is less than or equal to V , N is the total number of TCs that each of them has a peak wind v_i larger than

V , and Y is total simulation years. Defining $T=1$ year, the annual probability of exceeding a given wind speed V is

$$P_{T=1yr}(v_i > V) = 1 - \exp[-\lambda P(v_i > V)] = 1 - \exp\left(-\frac{N}{Y}\right) \quad (5.20)$$

in which λ is the annual storm occurrence rate within the region of interest. The mean recurrence interval (MRI) or return period (RP) of a given wind speed V at a specific site can be estimated using the inverse of the result of Eq. (12) with the form

$$RP(v_i > V) = \frac{1}{\lambda P(v_i > V)} = \frac{Y}{N} \quad (5.21)$$

Fig. 5.18 illustrates the typhoon wind hazard curves in Hong Kong in terms of return period and annual probability of exceedance for typhoon mean wind speeds (10-min duration at 10-m height). Fig. 5.18(a) compares the predicted design mean wind speeds with the recommended values in Wind-resistant Design Specification for Highway Bridges ([JTG/T D60-01-204, code hereafter](#)) for different return periods. It can be noted that the code's values are larger than those obtained in this study and the difference seems to decrease with increase in return period. This is because the values recommended in the code are developed by statistical approaches based on both TC and non-TC observations over 30~40 years. Some strong non-TC winds captured by meteorological stations could dominate the design values for short return periods while strong TC winds would control the higher design wind speed corresponding to longer return periods.

As mentioned in the explanatory materials to the Hong Kong Code ([2004](#)), the 50-year-MRI hourly mean wind speed of 46.9m/s at 90 m above mean sea level with the underlying exposure of open sea was selected as the reference. In this case, the 10-m wind speed is estimated as 36.83 m/s using the power wind profile with the suggested exponent of 0.11

(0.12 for terrain exposure A in Chinese code, 1/9 for terrain exposure D in ASCE 7-16). The estimated 10-min mean wind speed is roughly 39.04 m/s if the conversion factor is 1.06 from 1 hour to 10 min. The predicted design wind speed associated with return period of 50 years is 33.27 m/s when $z_0 = 0.01$ m. Since the underlying terrain is over sea for the recommended wind speeds by Hong Kong Code, which should have a smaller z_0 than 0.01 m.

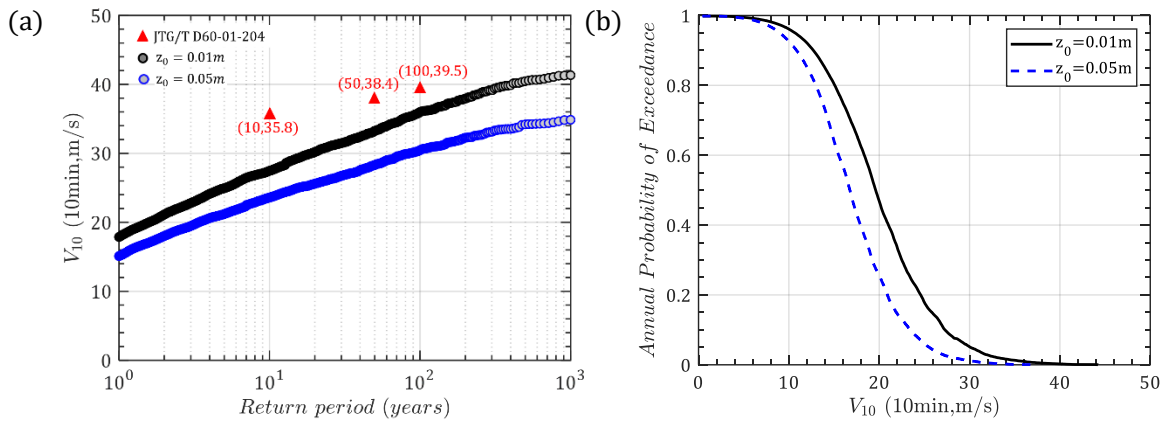


Fig. 5.18 Typhoon wind hazard curves in Hong Kong: (a) Mean wind speed versus return period; (b) Annual probability of exceedance for mean wind speed

5.4.2 Wind hazard curves at selected coastal cities

For comparison with other studies (Xiao et al., 2011; Li and Hong, 2015), nine other coastal cities (Fig. 5.18), i.e. Shanghai, Ningbo, Wenzhou, Fuzhou, Xiamen, Guangzhou, Shenzhen, Zhanjiang, and Haikou were selected for Monte Carlo simulations following the aforementioned algorithm. As shown in Table 2, coefficients of each distribution for various input parameters in another nine coastal cities of China were estimated using a maximum likelihood method based on historical observation around the site of interest within a radius of 500 km. The annual storm rate was observed to gradually increase from north to south. Correspondingly, the empirical and fitted preferred CDFs for each parameter in nine cities are illustrated in Appendix G together with the K-S test statistics. It can be seen that the distribution models successfully matched the empirical historical samples.

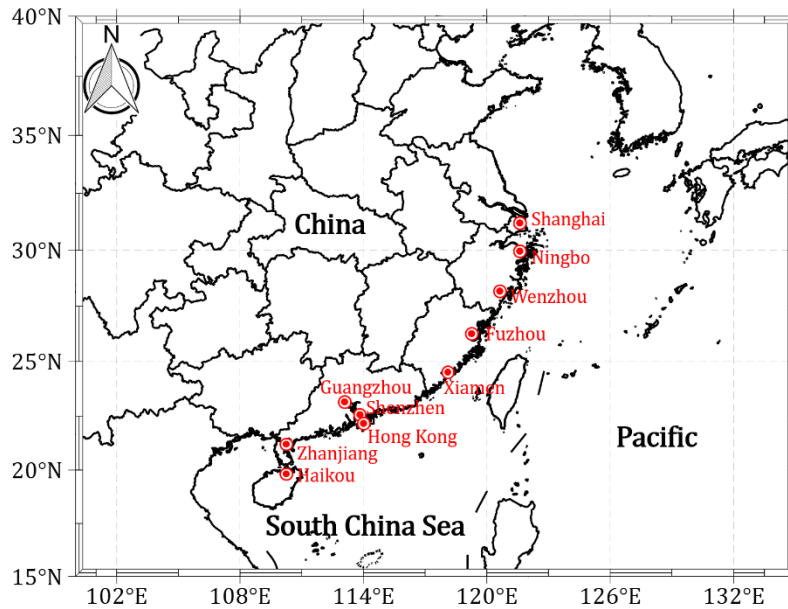


Fig. 5.18 Locations 10 selected coastal cities in China

Table 5.2 Coefficients of PDFs for track genesis parameters

City	Lat (°N)	Lon (°E)	λ_a		α_0			ΔP_{z_0}			θ_{T0}				V_{T0}		$R_{max,s0}$		B_{s0}	
			λ	k	γ	μ	σ	p	μ_1	σ_1	μ_2	σ_2	μ	σ	μ	σ	μ	σ		
Shanghai	31.23	121.48	3.15	4.16	182.97	3.31	0.68	0.76	-22.38	35.86	34.30	23.30	1.80	0.48	4.85	0.71	0.40	0.34		
Ningbo	29.86	121.51	3.66	3.90	180.39	3.37	0.71	0.12	-43.06	7.55	-12.11	45.00	1.76	0.43	4.81	0.68	0.36	0.33		
Wenzhou	28.01	120.65	4.60	3.70	176.54	3.47	0.76	0.28	-50.21	21.56	-5.39	50.57	1.76	0.44	4.61	0.67	0.33	0.32		
Fuzhou	26.08	119.30	4.92	3.12	172.85	3.48	0.73	0.42	-48.63	24.64	4.60	55.36	1.65	0.44	4.56	0.60	0.29	0.29		
Xiamen	24.48	118.10	5.62	3.30	170.40	3.41	0.72	0.42	-58.29	21.42	0.23	56.82	1.58	0.46	4.55	0.62	0.29	0.28		
Guangzhou	23.00	113.22	5.68	3.34	155.82	3.20	0.53	0.58	-67.12	22.39	-11.25	59.10	1.53	0.48	4.53	0.65	0.23	0.31		
Shenzhen	22.55	114.12	6.15	3.22	157.99	3.17	0.58	0.54	-67.06	18.18	-12.44	61.51	1.51	0.50	4.53	0.70	0.24	0.34		
Zhanjiang	21.27	110.36	5.57	3.32	139.07	3.20	0.53	0.87	-65.65	26.58	18.65	67.85	1.55	0.46	4.51	0.60	0.17	0.27		
Haikou	20.37	110.33	5.86	3.29	132.45	3.16	0.55	0.85	-67.65	24.76	7.56	76.38	1.55	0.48	4.49	0.62	0.17	0.26		

Similar to Hong Kong, the 10-min mean design wind speeds at height 10 m above the ground with a surface roughness of 0.05 m with respect to various return periods were developed based on 10,000-year Monte Carlo simulations. Table 5.3 lists the simulation results for TC design wind speed at selected cities with an MRI of 100 years and compared them with two Chinese codes (JTG/T D60-01-2004; GB 50009-2012) as well as other pioneering studies. The design wind speeds in the two codes are consistent with each other, except for a 2.5 m/s difference in Shanghai. It can be seen that the predicted wind speeds ($z_0 = 0.05$ m) in this study are smaller than the code-recommended values, except for Ningbo and Wenzhou,

which are both about 1.5 m/s higher than codes. In Xiamen, Shenzhen, Hong Kong, Zhanjiang and Haikou, about 10 m/s lower than code values can be observed. This is mainly attributed to the limitations of the statistically short-term data-based method used in the code development. As mentioned before, the design wind speeds in the Chinese codes are developed from short-term observations utilizing both TC and non-TC winds (30~40 years). However, the series of largest annual wind speeds are, in most cases, not well-behaved (Simiu and Scanlan, 1996) when used for modeling the probabilistic behavior of the extreme winds since most of the largest annual winds are remarkably smaller than the extreme winds associated with TCs. That is, the contribution of each group of data used for characterizing the probabilistic behavior of the largest annual winds is uneven, resulting in some unrealistically high or low predictions (Simiu and Scanlan, 1996). Although some alternative approaches can be adopted to better consider TC winds, such as the use of maximum average monthly speed or mixed distributions of TC and non-TC winds, to the authors' knowledge, no published literature clearly discusses the development of design wind speed in the Chinese codes. Furthermore, correction of averaging time, height, station migration and surrounding roughness to make the wind speed records meteorologically homogeneous would introduce some unpredictable errors. As listed in Table. 5.3, the predicted wind speeds associated with $z_0 = 0.01$ m are greater than that of $z_0 = 0.05$ m with 4.5~5.5 m/s. That means the underlying terrain would have significant effects on the observed wind speeds in the meteorological stations.

Moreover, the annual storm rate for these 10 coastal cities are compared with respect to six scales of tropical cyclones, as listed in Table 5.4. This classification based on $V_{\max,s}$ is provided by JMA. To classify the scale of tropical cyclones before 1977, the other measure

listed in Table 5.4, say P_{CS} was approximately estimated using Dvorak current intensity chart. As shown in Fig. 5.19, violent typhoons ($P_{CS} < 935 \text{ hPa}$ or $V_{\max,s} > 55 \text{ m/s}$ (107 knots)) as well as strong typhoons ($P_{CS} < 960 \text{ hPa}$ or $V_{\max,s} > 43 \text{ m/s}$ (83 knots)) that affect Zhanjiang (close to Haikou), Hong Kong (close to Shenzhen), Wenzhou and Ningbo within 500 km are extracted from the 65-year JMA dataset. It turns out that only two TCs (200814 Hagupit and 201409 Rammasun) around Zhanjiang (or Haikou) and six TCs (195408 Ida, 197909 Hope, 200814 Hagupit, 201013 Megi, 201319 Usagi and 1409 Rammasun) around Hong Kong (or Shenzhen) reached the violent level. Comparatively, 25 and 13 violent typhoons were observed around Wenzhou and Ningbo, respectively. Moreover, 40 and 52 strong typhoons affected Zhanjiang and Hong Kong, respectively, while Wenzhou and Ningbo suffered 89 and 55 strong typhoons over the past half a century. Furthermore, the annual storm rate of each city is illustrated in Fig. 5.20. An obvious difference can be noted between the northern and southern regions of Xiamen. The rates of weak tropical cyclones say tropical storm (TS) and severe tropical storm (STS) in southern cities almost double that of northern cities. However, strong winds caused by strong typhoons (STY) and violent typhoons (VTY) have much higher chance to occur in northern regions of Xiamen. That is, Xiamen, Fuzhou and Wenzhou are prone to be swept by strong and violent typhoons while Guangzhou, Shenzhen, Hong Kong, Zhanjiang and Haikou have higher rate of weak storms, but much smaller probabilities to be hit by strong typhoons. This is thanks to the obstacle effects of several high mountains in the Philippines so that the violent typhoons making landfall in Hainan and Guangdong provinces usually need to re-intensify in the South China Sea or directly pass through the Bashi Channel between Taiwan and the Philippines, so not many violent typhoons were observed to affect these two provinces. In addition, the maximum wind of the rotating storm

in the northern hemisphere always occurs on its right side with respect to the heading direction due to the Coriolis effect. Thus, westward-heading violent typhoons seldom occur in Zhanjiang and Haikou before their intensities decay due to the effect of Hainan island. Instead, Wenzhou or Ningbo has greater chances of being swept by a storm's maximum wind. Meanwhile, the lower annual rates of strong tropical cyclones would result in smaller sample sizes of high typhoon winds in the records of meteorological stations. The conventional extreme-value-distribution-based statistical model, which assembles both typhoon wind non-typhoon winds could have higher chance to overestimate the design wind speeds. Accordingly, the prediction results should be reasonable with higher design wind speeds in Wenzhou and Ningbo than that in Zhanjiang and Haikou.

Table 5.3 Comparison of typhoon design wind speed at selected cities (MRI = 100 year; T = 10 min; z = 10 m, z₀ = 0.05m, m/s)

City	JTG/T D60- 01- 2004	GB 5009- 2012	Xiao et al. (2011)	Li and Hong (2016)		Chen and Duan (2017)	This study		GWR-FTM	
				CSM	FTM		z ₀ =0.01m	z ₀ =0.05m	z ₀ =0.01m	z ₀ =0.05m
Shanghai	33.8	31.30	48.27	32.2	31.7	31.7	34.94	29.51	32.84	27.58
Ningbo	31.3	31.30	44.93	33.3	33.0	34.5	38.10	32.76	37.24	31.31
Wenzhou	33.8	33.81	48.75	36.1	36.5	34.9	40.96	35.07	38.32	32.26
Fuzhou	37.4	37.25	48.47	37.8	35.1	33.6	38.12	32.42	34.96	29.45
Xiamen	39.7	39.38	46.70	39.1	38.9	37.7	36.19	30.59	34.28	29.00
Guangzhou	31.3	31.30	41.57	30.5	31.4	–	33.45	28.27	32.16	27.22
Shenzhen	38.4	38.33	43.79	36.4	36.8	36.4	34.74	29.60	34.19	29.19
Hong Kong	39.5	39.38	45.03	37.6	37.7	–	36.03	30.52	34.85	29.81
Zhanjiang	39.4	39.38	42.86	40.9	37.4	37.5	32.52	27.73	31.25	26.74
Haikou	38.4	38.33	42.94	–	–	38.5	32.53	28.07	31.72	27.25

Note: CSM and FTM represent the circular sub-region and full track methods, respectively. The wind speeds estimated only by preferred distributions of ΔP in Li and Hong (2016) are listed in the table.

Table 5.4 Classification of tropical cyclones by JMA

Measure	Tropical Depression (TD)	Tropical Storm (TS)	Severe Tropical Storm (STS)	Typhoon (TY)	Strong Typhoon (STY)	Violent Typhoon (VTY)
10-min $V_{max,s}$ (knots)	≤ 33	(33,47]	(47,63]	(63,83]	(83,107]	> 107
P_{cs} (hPa)	≥ 998	[989,998)	[978,989)	[960,978)	[935,960)	< 935

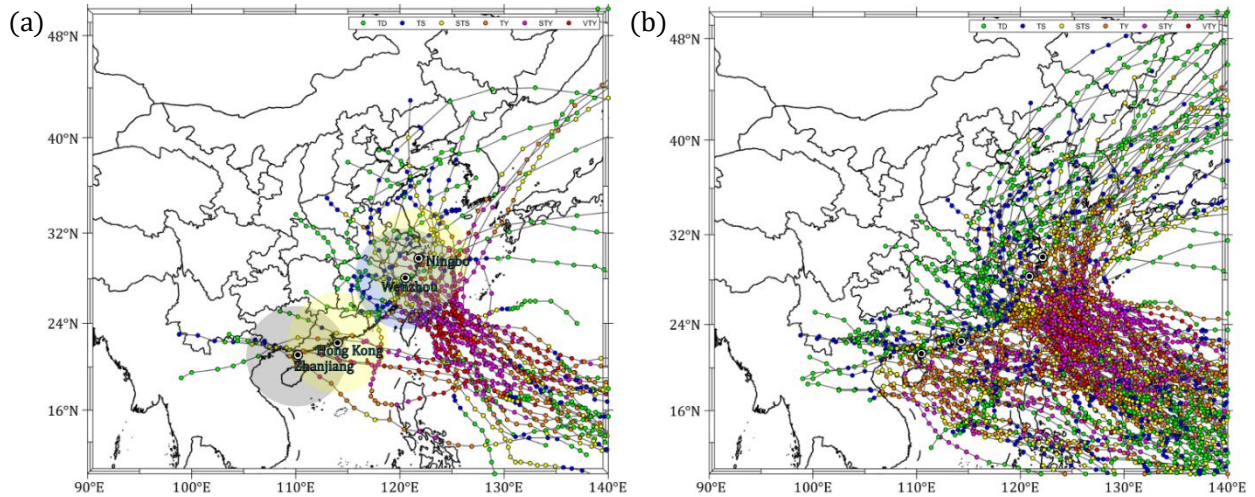


Fig. 5.19 Strong typhoon tracks affect Ningbo, Wenzhou, Hong Kong and Zhanjiang: (a) Violent typhoons; (b) Strong typhoons

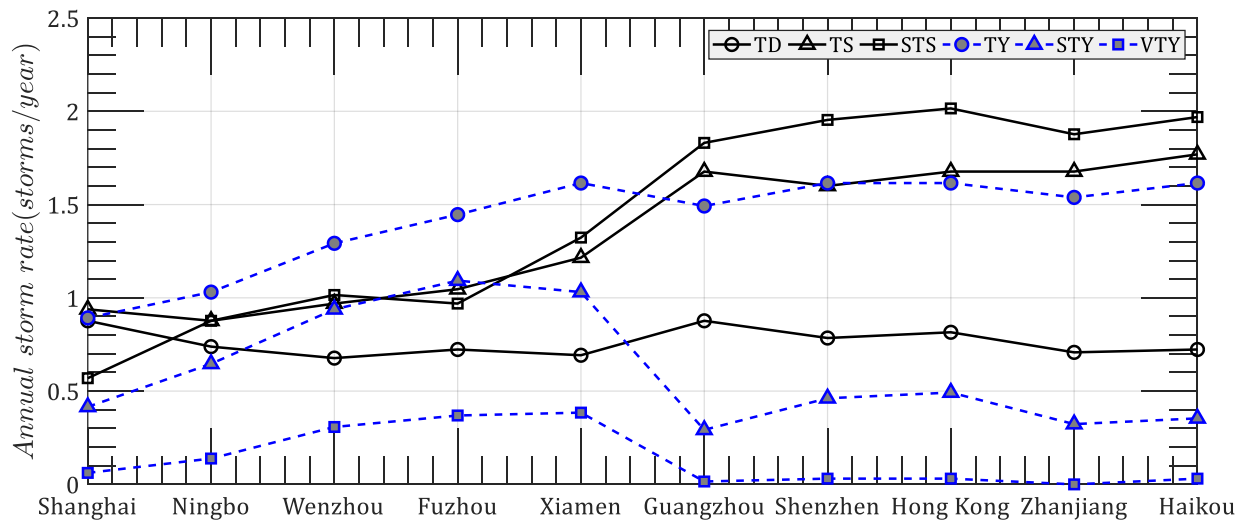


Fig. 5.20 Annual storm rates of 10 coastal cities ($R = 500$ km)

The results in Xiao et al. (2011) are higher than those in other studies or codes. There are three possible reasons for this. The first is the use of the Holland method (2008) in determining B values. This method was developed from semi-empirical relationships between gradient and surface layer as discussed by Fang et al (2018). Another reason is the use of a 1000-km-radius subregion, which would take into account many extremely violent typhoons over the distant sea before they are used for TC intensity modeling. The third one is the use of a surface roughness of 0.02 m, which is smaller than the code-specified value associated with terrain exposure B of 0.05 m.

The present wind speeds are all smaller than Li and Hong (2016), especially in Xiamen, Shenzhen, Hong Kong and Zhanjiang. Similar trend can also be observed when they are compared with Chen and Duan (2017), who used an improved full track model. Except for the potential reasons analyzed above, it is worth mentioning that Li and Hong (2016) adopted CMA track data with 2-min duration while Chen and Duan (2017) used a JTWC dataset with 1-min duration. Some errors could be introduced by the time duration gaps for different datasets.

Comparatively, the simulation results using GWR-based full track model (GER-FTM) are also listed in Table 5.3.10,000-year synthetic full tracks in Western Pacific are provided by Polamuri (2019). The parameters $R_{max,s}$ and B_s are regenerated using the present model in section 5.3.4 to be consistent with the wind field model in this study. This is because $R_{max,s}$ and B_s should be matched with a wind field model as discussed in Chapter 3. Then the design wind speed for these 10 cities are calculated using the wind field model in this study. As can be noted, the differences between the FTM and present CSM are almost within 2 m/s.

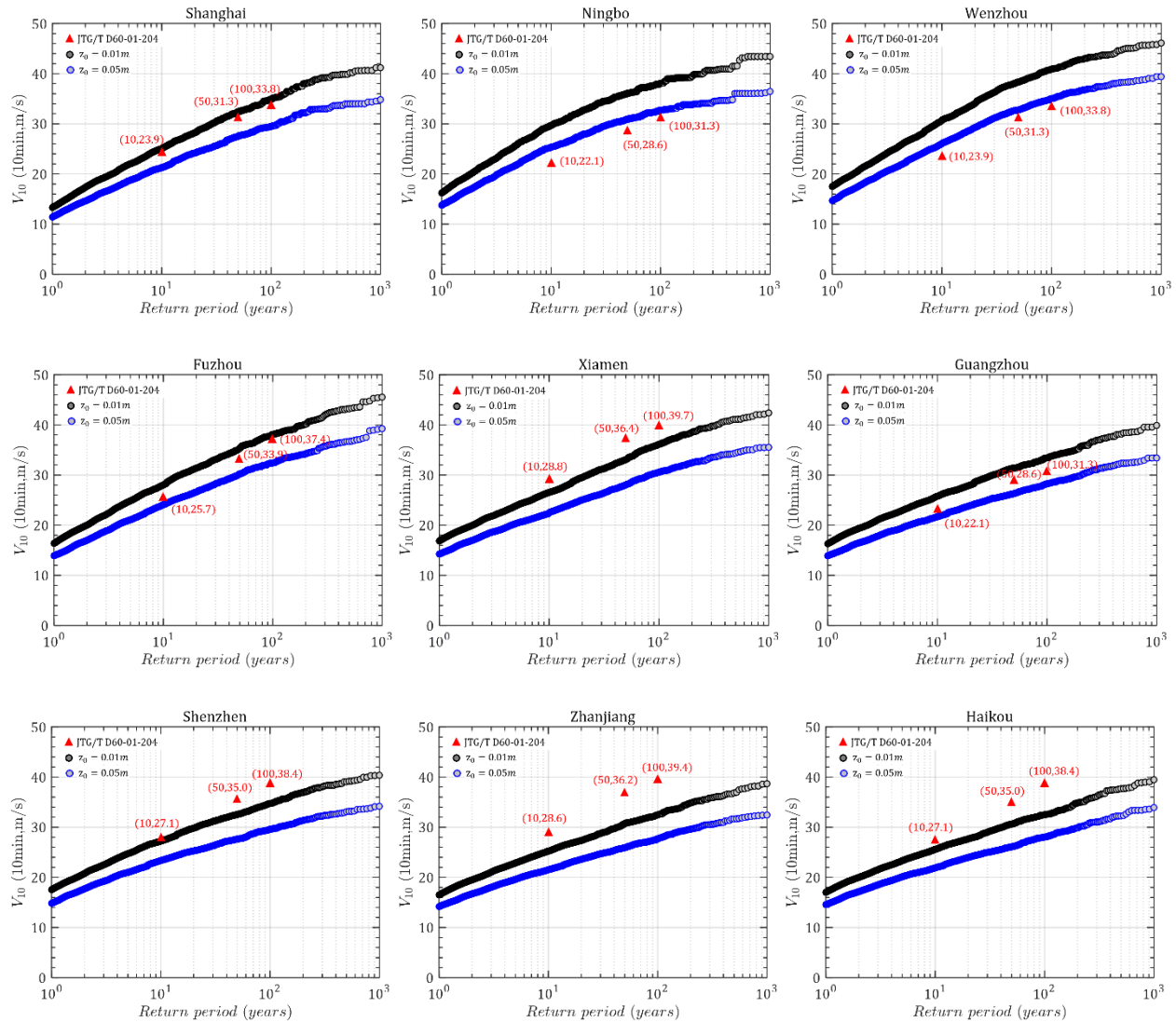


Fig. 5.21 Predicted and code-suggested typhoon design wind speed versus return period of nine coastal cities in China

Fig. 5.21 illustrates design wind speed versus return period plots (hazard curves) based on simulations together with the suggested values in Chinese codes (JTG/T D60-01-2004) for nine coastal cities. If only the $z_0 = 0.05$ m is considered, it can be seen that, consistent with previous findings, this study shows higher estimations for Ningbo and Wenzhou while it shows smaller estimations for other cities than the code. It is also found that the estimated hazard curves for Ningbo and Wenzhou have a similar trend to the code, but the design wind

speeds for other cities increase more gently with return period than the code provisions. This is closely related to the portion of TC wind samples as well as their contributions to the description of the probabilistic distribution of extreme winds in a series of largest observed annual winds as discussed above. The TC winds in Ningbo and Wenzhou could dominate the probabilistic behavior of the yearly largest wind speed while other cities have lower portions of TC winds compared to synoptic winds. However, the contributions of strong TC winds will be overused in modeling the hazard curve when they are combined with smaller synoptic winds in the yearly largest wind series. More observations on TC winds and unique descriptions of the probabilistic behavior of TC winds are necessary to model site-specific TC hazards and validate the long-term hazard predictions in this study.

5.4.3 Design wind speed map

As shown in Figs. 22-25, the design wind speed maps are developed using both full track model and present circular subregion model with respect to two terrain roughness lengths, say $z_0 = 0.01m$ and $z_0 = 0.05m$ and two return periods, say 100 years and 50 years. It can be seen that the wind speed maps obtained from FTM has smoother contours than that of subregion model. The general trends, i.e. Taiwan and coastal region between $26^\circ N$ and $32^\circ N$ of China Mainland have highest typhoon-induced design wind speeds followed by the coastal region of China Mainland between $22^\circ N$ and $24^\circ N$, are consistent between FTM and present study. The obstruction effect of Taiwan island is significant as the design wind speed suffers an apparent decrease for the coastal region of China Mainland between $24^\circ N$ and $26^\circ N$ compared with other coastal regions.

The major difference between FTM and present subregion model happens in Hainan Island with the maximum difference of design wind speed close to 6 m/s. It is not easy to define

which one is overestimation or underestimation. The full track model takes the whole Western Pacific as the simulation domain, in which the storms have more chances to reach a high intensity before making landfall. It seems that the full track model is a more convincing approach. However, there are only two Category 5 super typhoons on record in the South China Sea over past almost 70 years, say Typhoon Glenda in 1954 and Typhoon Rammasun in 2014. And only Typhoon Rammasun made landfall in Hainan Island. Moreover, as compared in Figs. F13-F14 in Appendix F, the typhoon wind field parameters between model and observations show a reasonable agreement with each other. More validations of full track model need to be conducted for these subregions in the future to provide more accurate estimates.

It is worth mentioning that the wind direction information of all simulated winds are retained and documented, which would be helpful for the structure design accounting for the directional effects. And the present height-resolving wind field model in Chapter 2 enables the calculation of wind speeds at different heights, which facilitates the development of design wind speed at any height of interest, such as the deck height of long-span bridges.

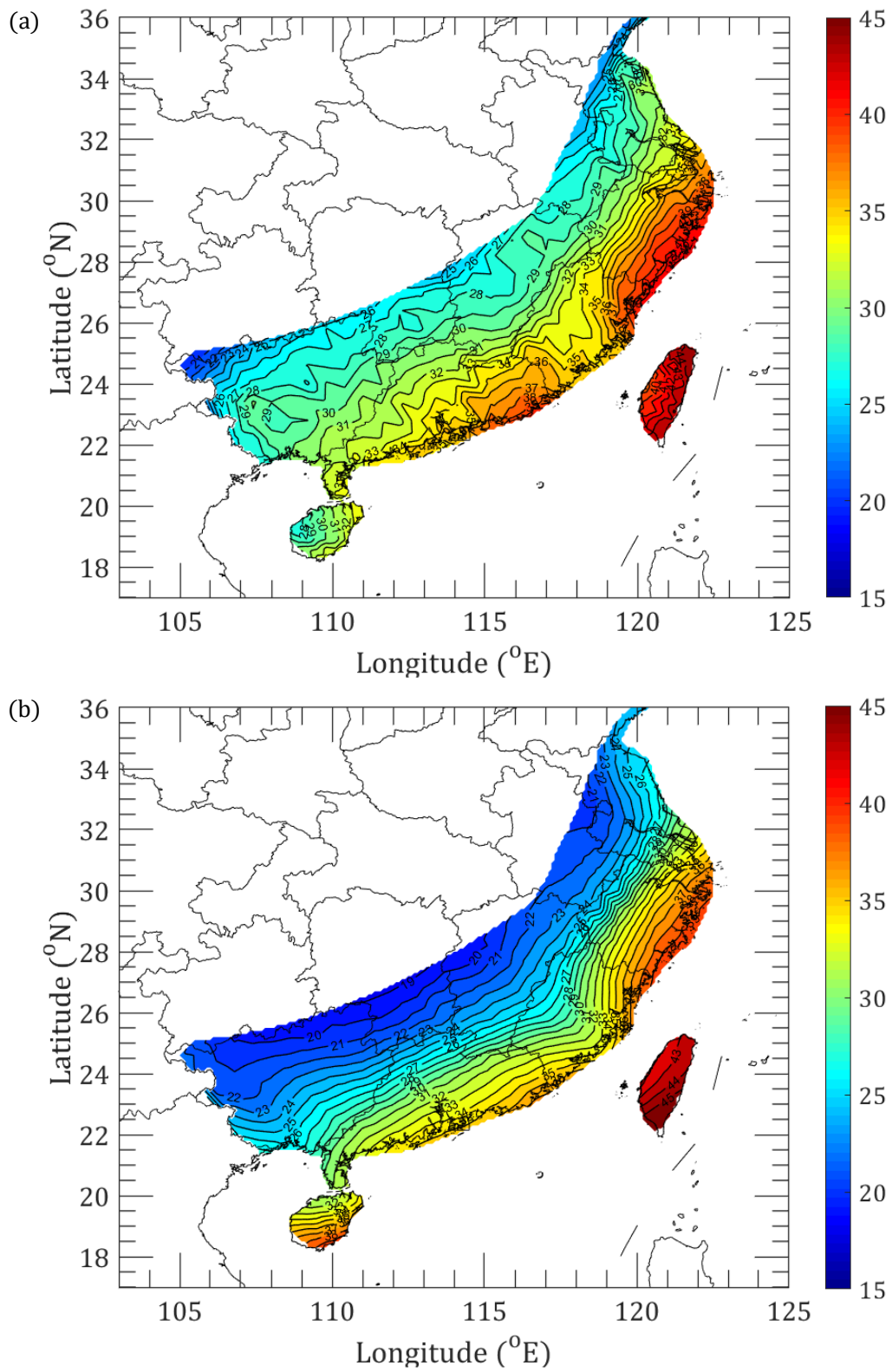


Fig. 5.22 Design wind speed map (MRI = 100 year; T = 10 min; z = 10 m, z₀ = 0.01m, m/s): (a) CSM; (b) FTM

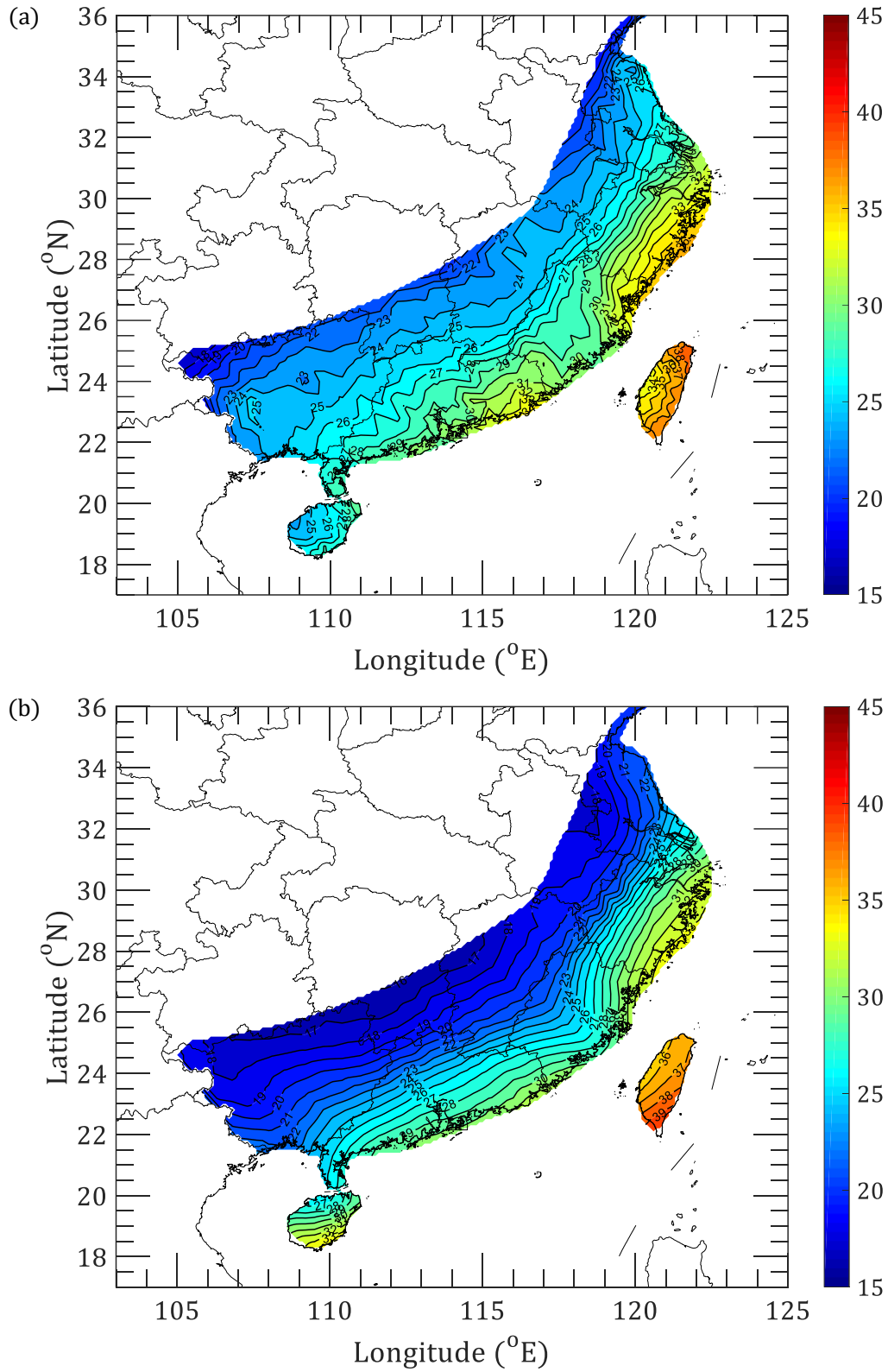


Fig. 5.23 Design wind speed map (MRI = 100 year; $T = 10$ min; $z = 10$ m, $z_0 = 0.05$ m, m/s): (a) CSM; (b) FTM

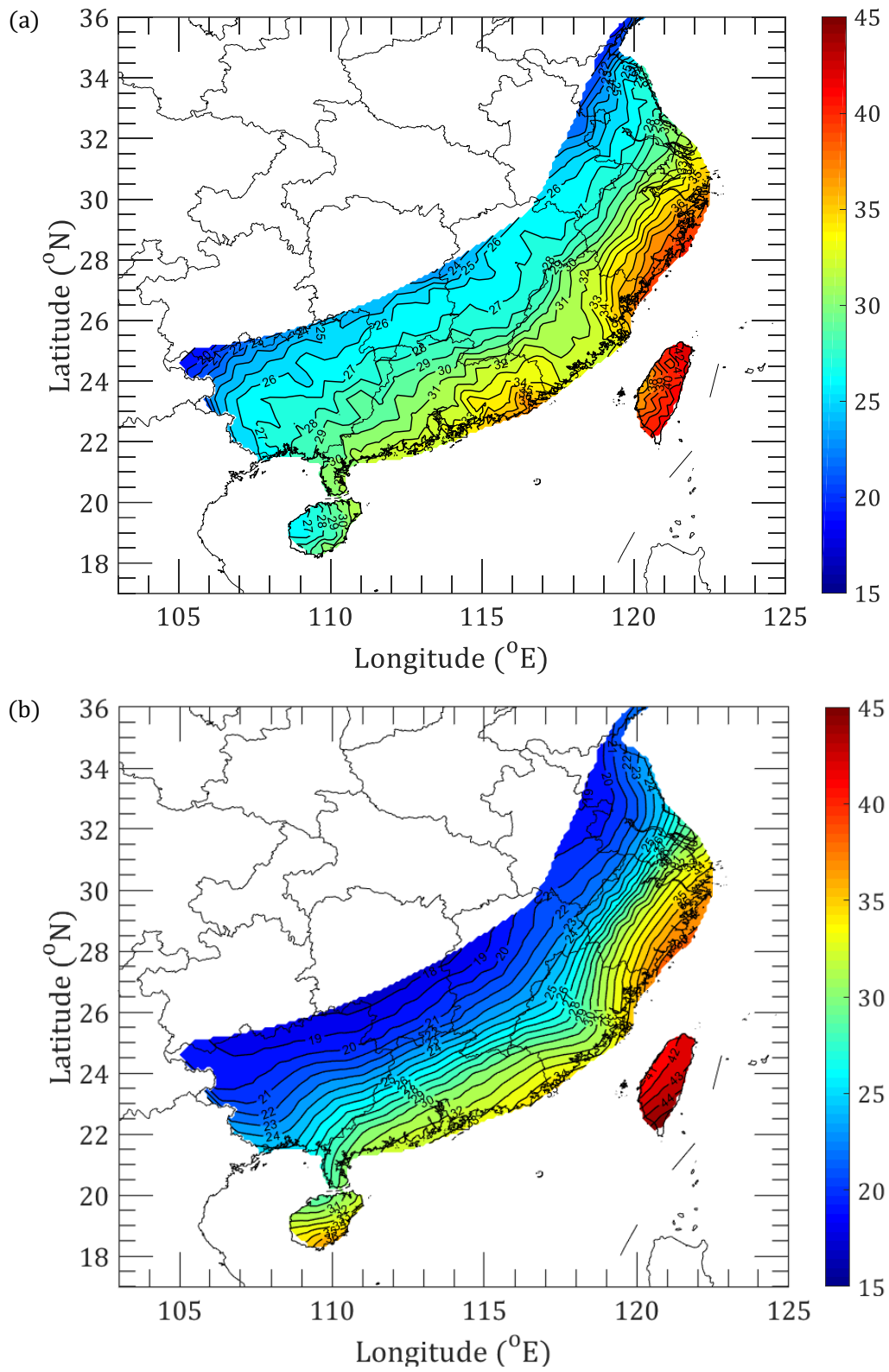


Fig. 5.24 Design wind speed map (MRI = 50 year; T = 10 min; z = 10 m, z₀ = 0.01m, m/s): (a) CSM; (b) FTM

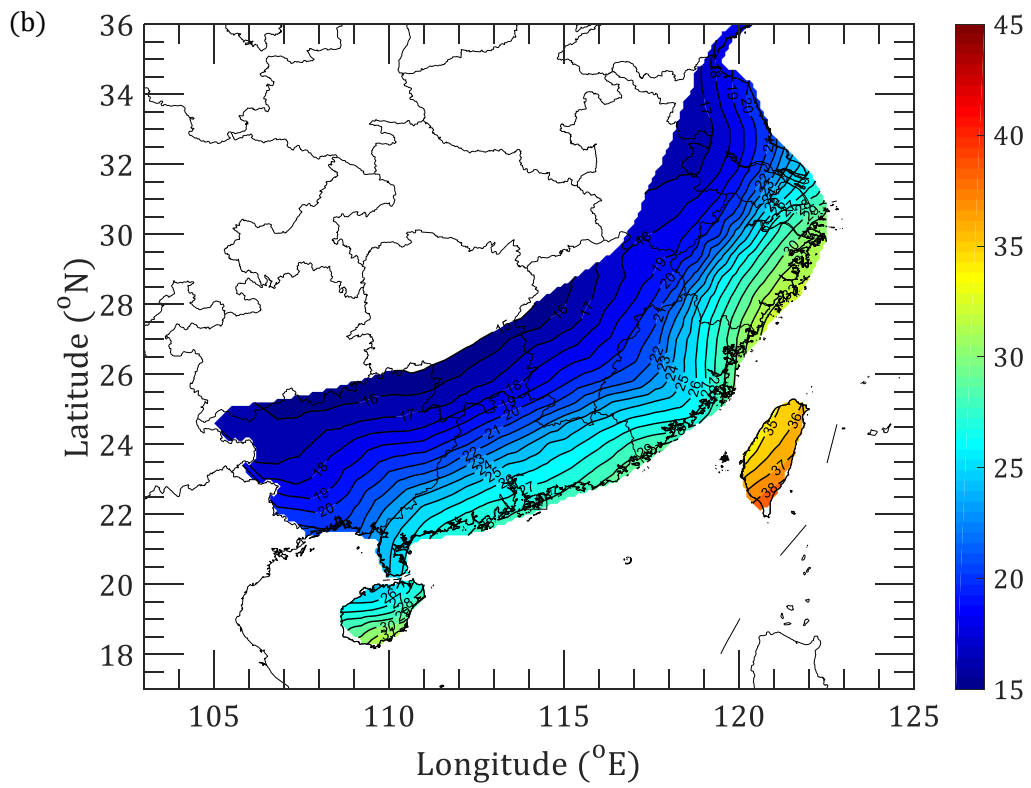
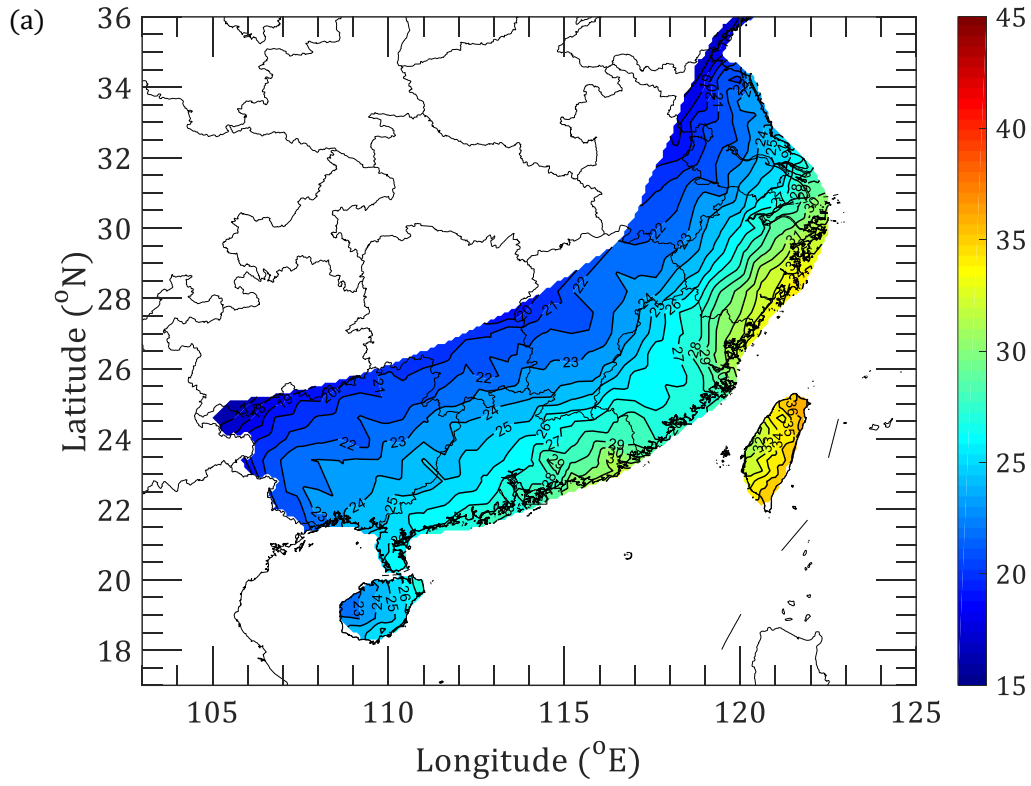


Fig. 5.25 Design wind speed map (MRI = 50 year; T = 10 min; z = 10 m, z₀ = 0.05m, m/s): (a) CSM; (b) FTM

5.5 Conclusion

The present study develops a GER-based circular subregion model for typhoon estimation in coastal region of China. The genesis model and GWR-based track forward model in terms of tracking model, intensity model and wind field parameter model were developed and validated. A series of model performance assessments were also performed. The design wind speed of ten selected coastal cities are simulated and compared with codes and other pioneering studies. It was found that the design wind speeds have remarkable differences in southern coastal cities between model and code suggestions. The design wind speed maps were also developed using both full track model and subregion model.

5.6 Reference

ASCE. Minimum Design Loads for Buildings and Other Structures (ASCE 7-16)[S]. American Society of Civil Engineers, 2017.

Batts M E, Russell L R, Simiu E. Hurricane wind speeds in the United States[J]. Journal of the Structural Division, 1980, 106(10):2001-2016.

Buildings Department, Hong Kong, Code of Practice on Wind Effects in Hong Kong 2004[S]. The Government of the Hong Kong Special Administrative Region, 2004.

Buildings Department, Hong Kong, Explanatory Materials to the Code of Practice on Wind Effects in Hong Kong 2004[S]. The Government of the Hong Kong Special Administrative Region, 2004.

Chen Y, Duan Z. A statistical dynamics track model of tropical cyclones for assessing typhoon wind hazard in the coast of southeast China[J]. Journal of Wind Engineering and Industrial Aerodynamics, 2018, 172:325-340.

Darling, R. W. R. (1991). "Estimating probabilities of hurricane wind speeds using a large-scale empirical model." *Journal of Climate*, 4(10), 1035–1046.

David D. Apsley. Numerical Modeling of Neutral and Stably Stratified Flow and Dispersion in Complex Terrain. Ph.D. Thesis, Faculty of Engineering, University of Surrey, Guildford, Surrey, United Kingdom, 1995.

Dvorak V F. Tropical cyclone intensity analysis using satellite data[J]. NOAA Tech Rept, 1984, 11.

Fang G, Zhao L, Cao S, et al. A novel analytical model for wind field simulation under typhoon boundary layer considering multi-field correlation and height-dependency[J]. *Journal of Wind Engineering and Industrial Aerodynamics*, 2018, 175:77-89.

Fang G, Zhao L, Song L, et al. Reconstruction of radial parametric pressure field near ground surface of landing typhoons in Northwest Pacific Ocean[J]. *Journal of Wind Engineering and Industrial Aerodynamics*, 2018, 183:223-234.

Fang G, Zhao L, Cao S, et al. Gust Characteristics of near-ground typhoon winds[J]. *Journal of Wind Engineering and Industrial Aerodynamics*, 2019, 188:323-337.

Federal Emergency Management Agency (FEMA). Multi-Hazard Loss Estimation Methodology. Hurricane Model, HAZUS®-MH2.1, Technical Manual. Federal Emergency Management Agency, Washington, DC. 2015

Fotheringham, A.S., Charlton, M.E., and Brunsdon, C., 1998. Geographically weighted regression: a natural evolution of the expansion method for spatial data analysis. *Environment and Planning A*, 30 (11), 1905–1927

Fotheringham, A.S., Brunsdon, C., and Charlton, M., 2002. Geographically weighted regression: the analysis of spatially varying relationships. Chichester: Wiley.

Georgiou P N. Design wind speeds in tropical cyclone-prone regions. Ph.D. Thesis, Faculty of Engineering Science, University of Western Ontario, London, Ontario, Canada, 1985.

Hadley Centre for Climate Prediction and Research (2006): Met Office HadISST 1.1 - Global sea-Ice coverage and Sea Surface Temperature (1870-2015). NCAS British Atmospheric Data Centre. <<http://catalogue.ceda.ac.uk/uuid/facafa2ae494597166217a9121a62d3c>>

Holland G J. An analytic model of the wind and pressure profiles in hurricanes[J]. Mon. Weather Rev., 108(8), 1980, 1212-1218.

Holland G J. A Revised Hurricane Pressure–Wind Model[J]. Monthly Weather Review, 2008, 136(9):3432-3445.

Holland G J, Belanger J I, Fritz A. A Revised Model for Radial Profiles of Hurricane Winds[J]. Monthly Weather Review, 2010, 138(12):4393-4401.

Huang WF, Sun JP. Prediction of typhoon design wind speed with cholesky decomposition method. Struct Design Tall Spec Build. 2018; e1480.

Iman R L, Conover W J. A distribution-free approach to inducing rank correlation among input variables[J]. 1982, 11(3):311-334.

Japan Meteorological Agency (JMA), RSMC Tokyo-Typhoon Center, Best Track Data (1951~2015). <https://www.jma.go.jp/jma/jma-eng/jma-center/rsmc-hp-public/besttrack.html>.

Keperth J D. Slab- and height-resolving models of the tropical cyclone boundary layer. Part I: Comparing the simulations[J]. Quarterly Journal of the Royal Meteorological Society, 2010, 136(652):1700-1711.

Knapp K R, Kruk M C, Levinson D H, et al. The International Best Track Archive for Climate Stewardship (IBTrACS): unifying tropical cyclone data.[J]. Bulletin of the American Meteorological Society, 2010, 91(3):363-376.

Kwok K C S, Kot S C, Ng E. Wind Code, Air Quality Standards and Air Ventilation Assessment for Hong Kong – Latest Developments, 3rd Workshop on Regional Harmonization of Wind Loading and Wind Environmental Specifications in Asia-Pacific Economies (APEC-WW 2006), New Delhi, India, 2-3 November 2006, pp. 25-38.

LeSage, J.P., 1999. The Theory and Practice of Spatial Econometrics. Department of Economics, University of Toledo.

Li S H, Hong H P. Use of historical best track data to estimate typhoon wind hazard at selected sites in China[J]. Natural Hazards, 2015, 76(2):1395-1414.

Li S H, Hong H P. Typhoon wind hazard estimation for China using an empirical track model[J]. Natural Hazards, 2016, 82(2):1009-1029.

Liu D, Pang L, Xie B. Typhoon disaster in China: prediction, prevention, and mitigation[J]. Natural Hazards, 2009, 49(3):421-436.

Liu F. Projections of future US design wind speeds due to climate change for estimating hurricane losses. Ph.D. Dissertation. Clemson, South Carolina: Clemson University; 2014.

National Standards Committee. Load code for the design of building structures, China National Standard (CNS) [S]. GB 50009-2012, National Standards Committee, Beijing, China; 2012.

Ministry of Communication of the People's Republic of China. (2004), JTG/T D60-01-2004, Wind-resistant design specification for highway bridges, China Communications Press, Beijing, China.

Polamuri Sri Harshitha, (2019). Projections of typhoon wind speeds under climate change in Asia Pacific Basin, Ph.D. Thesis, Glenn Department of Civil Engineering, Clemson University, South Carolina, United States.

Richard W. Reynolds, Viva F. Banzon, and NOAA CDR Program (2008): NOAA Optimum Interpolation 1/4 Degree Daily Sea Surface Temperature (OISST) Analysis, Version 2. NOAA National Centers for Environmental Information.

Russell L, Schueller G. Probabilistic models for Texas gulf coast hurricane occurrences. J. Petrol. Technol. 1974, 26 (26): 279–288.

Snaiki R, Wu T. Modeling tropical cyclone boundary layer: Height-resolving pressure and wind fields[J]. Journal of Wind Engineering & Industrial Aerodynamics, 2017, 170:18-27.

Song J J, Wang Y, Wu L. Trend discrepancies among three best track data sets of western North Pacific tropical cyclones[J]. Journal of Geophysical Research Atmospheres, 2010, 115(D12).

Velden C, Harper B, Wells F, et al. Supplement To: The Dvorak Tropical Cyclone Intensity Estimation Technique: A Satellite-Based Method that Has Endured for over 30 Years[J]. Bulletin of the American Meteorological Society, 2006, 87(9): S6-S9.

Vickery P J, Twisdale L.A. Prediction of Hurricane Wind Speeds in the United States[J]. Journal of Structural Engineering, 1995, 121(11):1691-1699.

Vickery P J, Skerlj P F, Steckley A C, et al. Hurricane Wind Field Model for Use in Hurricane Simulations[J]. Journal of Structural Engineering, 2000, 126(10):1203-1221.

Vickery P J, Skerlj P F, Twisdale L A. Simulation of Hurricane Risk in the U.S. Using Empirical Track Model[J]. Journal of Structural Engineering, 2000, 126(10):1222-1237.

Vickery, Peter J. Simple Empirical Models for Estimating the Increase in the Central Pressure of Tropical Cyclones after Landfall along the Coastline of the United States[J]. *Journal of Applied Meteorology*, 2005, 44(12):1807-1826.

Vickery P J, Wadhera D. Statistical Models of Holland Pressure Profile Parameter and Radius to Maximum Winds of Hurricanes from Flight-Level Pressure and H*Wind Data[J]. *Journal of Applied Meteorology and Climatology*, 2008, 47(10):2497-2517.

Vickery P J, Wadhera D, Powell M D, et al. A Hurricane Boundary Layer and Wind Field Model for Use in Engineering Applications[J]. *Journal of Applied Meteorology & Climatology*, 2009, 48(2):381-405.

Xiao Y F, Duan Z D, Xiao Y Q, et al. Typhoon wind hazard analysis for southeast China coastal regions[J]. *Structural Safety*, 2011, 33(4):286-295.

Yan Meng, Masahiro Matsui, Kazuki Hibi. An analytical model for simulation of the wind field in a typhoon boundary layer[J]. *Journal of Wind Engineering and Industrial Aerodynamics*, 1995, 56(2-3):291-310.

Ying M, Zhang W, Yu H, et al. An Overview of the China Meteorological Administration Tropical Cyclone Database[J]. *Journal of Atmospheric and Oceanic Technology*, 2014, 31(2):287-301.

Yuan J, Wang D, Wan Q, et al. A 28-year climatological analysis of size parameters for Northwestern Pacific tropical cyclones[J]. *Advances in Atmospheric Sciences*, 2007, 24(1):24-34.

Zhao L, Lu A, Zhu L, et al. Radial pressure profile of typhoon field near ground surface observed by distributed meteorologic stations[J]. *Journal of Wind Engineering and Industrial Aerodynamics*, 2013, 122:105-112.

CHAPTER 6 PROBABILISTIC FLUTTER ANALYSIS OF LONG-SPAN BRIDGES: A MONTE-CARLO SIMULATION FRAMEWORK

6.1 Background

With rapid advancements in the construction materials and techniques in recent years, there has been an upward trend in the long span bridges being proposed to cross wide canyons, rivers and straits (Xiang and Ge, 2007). However, these bridges are usually wind-sensitive as they are more flexible which results in the aerodynamic performance is the driving force as compared to the design process. Flutter instability, which will activate the violent oscillations and even result in the collapse of bridge structures, for instance, the Old Tacoma Bridge, should definitely be prevented. Accordingly, the prediction for the onset of flutter has received intensive attention over several decades by means of wind tunnel test (Scanlan, 1978; Gu et al., 2000; Diana et al., 2004), numerical simulation with computational fluid dynamics (CFD) (Larsen et al., 1997; Ge et al., 2008) as well as finite element method (FEM) (Namini et al., 1992; Ge et al., 2000; Frandsen, 2004) and theoretical solutions (Scanlan, 1978; Bartoli, 2008; Diana et al., 2010; Matsumoto et al., 2010; Wu et al., 2013). Among them, the wind tunnel is a fundamental tool for supporting the bridge aerodynamics studies and will be continuously used for a long time (Diana et al., 2015).

Conventionally, the deterministic method using some constant input parameters was commonly employed to study the flutter instability. However, all these parameters which are either estimated manually (deck width, mass, the moment of inertia, etc.) or extracted from experiments or numerical simulations inevitably involve a number of uncertainties due to some unknown information or imperfect environments (Sarkar et al., 2009a). And the flutter threshold is significantly susceptible to some parameters, which means a small perturbation

in one or few parameters would markedly influence the critical wind speed (Sarkar et al., 2009b). Accordingly, a series of pioneering studies (Ostenfeld-Rosenthal et al., 1992; Ge et al., 2000; Pourzeynali and Datta, 2002; Cheng et al., 2005) were performed in the probabilistic solution of flutter instability to achieve a fragility curve and determine the flutter failure probabilities at different reliability levels. Some commonly used reliability analysis approaches were adopted, respectively such as First Order Reliability Method (FORM) (Ge et al., 2000; Baldomir et al., 2013), response surface method (Cheng et al., 2005; Abbas and Morgenthal, 2016) or Monte Carlo simulations (Seo and Caracoglia, 2011; Argentini et al., 2014; Mannini and Bartoli, 2015).

The limitations behind most studies are that the probabilistic distributions, as well as statistical measures of input parameters, are empirically determined using some postulated values. This could cause problems when they are applied to aerodynamic parameters. For example, the flutter derivatives (FDs), which are extensively used for modeling aero-elastically unsteady self-excited force in flutter and buffeting analyses, are usually assumed to follow the normal or lognormal distribution with a manually selected standard deviation. However, the variabilities of FDs are always bridge-section-configuration-dependent and vary with wind speed due to the change of aerodynamic force (Sarkar et al., 2009a; Seo and Caracoglia, 2011, 2012; Mannini and Bartoli, 2015; Rizzo and Caracoglia, 2018). It is also found that each FD exhibits different dispersion pattern. Most importantly, the flutter limit will be greatly influenced by a small change of some FDs. Such as some widely used bluff sections in bridge girder are prone to torsional flutter instability which refers to a torsional-mode-driven motion dominated by the FD of A_2^* (Matsumoto, 1996; Seo and Caracoglia, 2011). Mannini and Bartoli (2015) found that the coefficient of variation for flutter critical

wind speed would increase from 0.8 to 5.0 (6.25-time rise for variability) when the standard deviation of normally-distributed A_2^* grows from 0.01 to 0.05. Therefore, more recent studies tried to quantify the uncertainties of FDs using inter-laboratory experimental data (Sarkar et al., 2009a; Seo and Caracoglia, 2011; Mannini and Bartoli, 2015) or multi-repetition-based data (Mannini and Bartoli, 2015; Rizzo and Caracoglia, 2018; Fabio et al., 2018; Ibuki et al., 2018).

Another benefit provided by experiment-based data is the facilitation for the consideration of inter-correlations among FDs, which were always overlooked or partially considered in most studies. Although some approximated inter-correlations between several pairs of FDs were highlighted by Scanlan et al. (1997) and Matsumoto (1996), there still remain a couple of problems to be discussed as investigated by Mannini and Bartoli (2015) that no significant correlation was observed between the pairs of FDs mentioned by Matsumoto (1996). A similar study was conducted by Ibuki et al. (2018) with the emphasis on examining the importance of correlations among FDs for the reliability analysis of bridge aerodynamic performance. It turned out that the un-correlated FDs would produce more conservative flutter wind speeds than that of correlated solutions, resulting in the unrealistic reliability index. As a result, the uncertainty quantification of FDs based on experimental results has received intensive attention and it is essentially important to facilitate the development of performance-based wind engineering as outlined by Ciampoli et al. (2011).

As shown in Fig. 6.1, the potential uncertainties of flutter analysis for long-span bridges are summarized. To achieve the fluid-structure interaction modeling between wind and bridges, the wind and bridge structures are independently simulated first. The simulation of wind, both the use of wind tunnels and numerical techniques, i.e. the Computational Fluid

Dynamics (CFD) or artificially synthetic signals are unable to well reproduce the similarity parameter for viscosity, say Reynolds number due to the scale reduction. Some other characteristics of boundary layer winds, such as the intensity, integral scale and power spectrum density of turbulence as well as the spatial correlation of winds also cannot perfectly achieved. Especially the integral scale of turbulence in the wind tunnel, it is much smaller than the real winds. The modeling of the bridge structure using finite element method (FEM) is likely much easier than that of modeling of fluid. However, some uncertainties including the element selection, element constants, element materials, and boundary conditions also contribute the variation of dynamic properties of the structure. Finally, the analysis of bridge-wind interaction can be performed using the theoretical method, wind tunnel test or CFD. The wind tunnel test and CFD are able to directly estimate the flutter critical wind speed, which is also the main technique for the preliminary analysis of flutter problem. However, they are not suitable to achieve the probabilistic solutions of flutter critical wind speeds accounting for various uncertainties. The theoretical method, which is a dynamic motion equation with a self-excited external force, coupled with wind tunnel test or CFD is customarily employed to investigate the propagation of uncertainties on the flutter onset. The wind tunnel test or CFD will provide information on the transfer functions between the wind and aerodynamic forces, i.e. flutter derivatives. Moreover, instead of conducting the expensive full-bridge aeroelastic model wind tunnel test, the 3D multimode theoretical approach has a very good performance on the prediction of flutter boundary.

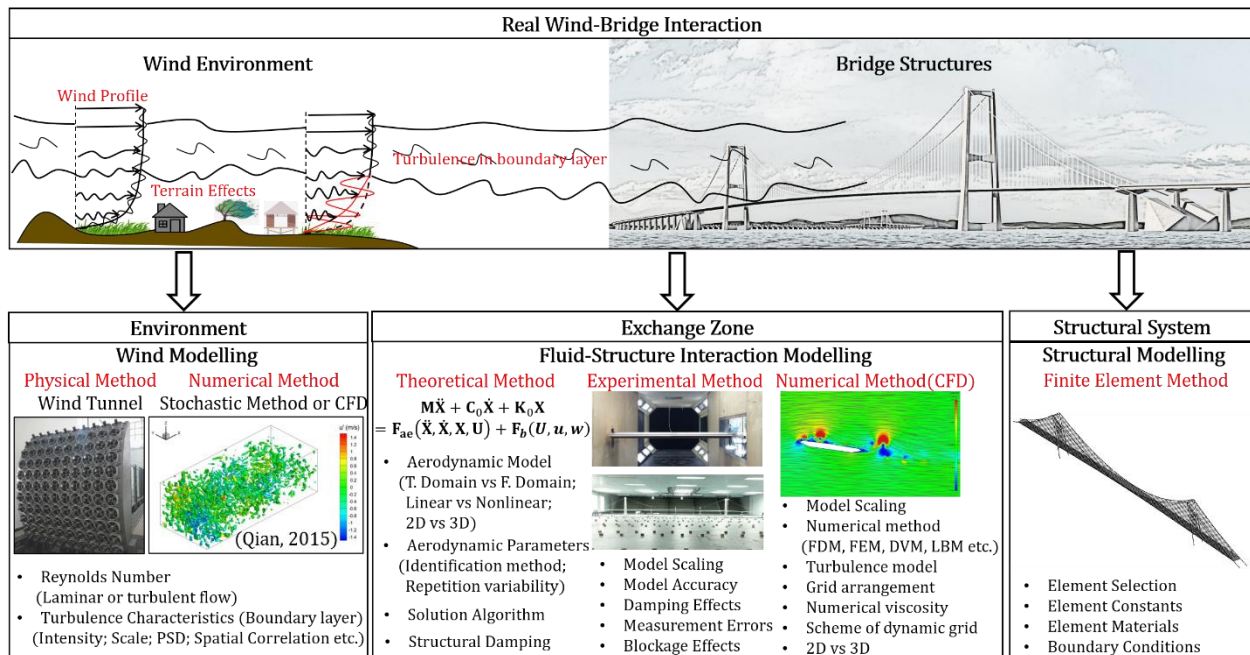


Fig. 6.1 Potential uncertainties of flutter analysis for long-span bridges

In this study, a framework for determining the probabilistic flutter solutions was developed. Four flutter analysis methods derived from the flutter-derivative-based linear model were compared and discussed. Two bridges, i.e. a 300-m span simply supported bridge and a 1385-m main span suspension bridge, and four girder sections, say an ideal thickness flat plate, a quasi-flat plate, a P-K section, and a closed-box girder section were combined to compare their flutter performance. Two categories of uncertainties, i.e. the bridge structural uncertainties in terms of natural modes and damping ratios and the aerodynamic uncertainties quantified by flutter derivatives were investigated, respectively. The stochastic finite element technique was employed to quantify the effects of randomness of mass and stiffness parameters on the variation of structural modal shapes and natural frequencies. A literature survey was conducted to achieve a statistical result of the damping ratios related to vertical and torsional modes. Repeated free vibration wind tunnel tests at each wind speed on a quasi-flat plate section model and a P-K section model were performed to

investigate the measurement errors and identification-imperfection-induced randomness of FDs. Meanwhile, a literature survey on a closed-box girder section was also performed to quantify the inter-lab- and identification-technique-induced uncertainties of FDs. Finally, a series of probabilistic solutions of flutter critical wind speed propagated from different uncertainty resources were achieved utilizing 2D step-by-step analysis and 3D multimode approach.

6.2 Models for flutter analysis

6.2.1 Bridge-wind interaction: Linear flutter theory

For a bridge deck that is immersed in the laminar incoming winds, the flutter vibration is mainly driven by the self-excited force, although the buffeting force resulting from signature turbulence would slightly contribute to the surface aerodynamic force. Physically, the self-excited force during the flutter motion can be modeled as the displacements and their first-two-order derivatives with respect to time, i.e. velocity and acceleration. Based on the linear theory, which is commonly adopted and accurate enough to estimate the flutter onset, the displacements of an oscillatory system are assumed to be tiny and follow the harmonic vibration pattern. Accordingly, the equation of motion that governs the dynamic behavior of the bridge deck under aerodynamic self-excited force can be given in the form

$$\mathbf{M}\ddot{\mathbf{X}} + \mathbf{C}_0\dot{\mathbf{X}} + \mathbf{K}_0\mathbf{X} = \mathbf{C}_{se}\dot{\mathbf{X}} + \mathbf{K}_{se}\mathbf{X} \quad (6.1)$$

in which $\mathbf{X} = \{h, p, \alpha\}^T$ represent the displacements of a three degree-of-freedom (DOF) system, h is the vertical or heaving motion (positive when downward), p is the lateral or sway motion (positive along the wind direction) and α is torsional or pitching motion (positive when nose-up), respectively, the dot denotes derivative with respect to time, i.e. $\dot{\mathbf{X}}$ and $\ddot{\mathbf{X}}$ are the speed and acceleration terms, $\mathbf{M} = \text{diag}\{m_h, m_p, I_m\}$, $\mathbf{C}_0 = \text{diag}\{c_h, c_p, c_\alpha\}$

and $\mathbf{K}_0 = \text{diag}\{k_h, k_p, k_\alpha\}$ are diagonal matrixes for generalized mass, damping, and stiffness of the structure, respectively. \mathbf{C}_{se} and \mathbf{K}_{se} are aerodynamic damping and stiffness matrixes, which are expressed as (Scanlan, 1978)

$$\mathbf{C}_{se} = \rho UB \begin{bmatrix} KH_1^* & KH_5^* & KH_2^*B \\ KP_1^* & KP_5^* & KP_2^*B \\ KA_1^* & KA_5^* & KA_2^*B \end{bmatrix} \quad (6.2)$$

$$\mathbf{K}_{se} = \rho U^2 \begin{bmatrix} K^2H_4^* & K^2H_6^* & K^2H_3^*B \\ K^2P_4^* & K^2P_6^* & K^2P_3^*B \\ K^2A_4^* & K^2A_6^* & K^2A_3^*B \end{bmatrix} \quad (6.3)$$

in which $\rho = 1.225 \text{ kg/m}^3$ is the air density, U is the mean wind speed, B is the width of the bridge deck, H_i^* , P_i^* and A_i^* ($i = 1 \sim 6$) are called flutter derivatives (FDs), which are defined as the functions of the reduced frequency and depend on the geometrical configuration of the bridge section and the wind characteristics of the incoming flow, $K = B\omega/U$ is the non-dimensional or reduced frequency. Although each FD at a given wind speed should be associated with two modal frequencies ($K_1 = B\omega_h/U$ and $K_2 = B\omega_\alpha/U$) corresponding to vertical and torsional modes as discussed by Chen and Kareem (2004) and Xu et al. (2014), an implied approximation, i.e. $H_1^*(K_1), H_4^*(K_1), A_1^*(K_1), A_4^*(K_1), H_2^*(K_2), H_3^*(K_2), A_2^*(K_2), A_3^*(K_2)$ is customarily invoked to uniquely extract all FDs using free decay vibration technique. This approximation was approved to be acceptable for modeling the self-excited forces and predicting the critical flutter velocity since the vertical vibration component associated with ω_α as well as the torsional vibration component associated with ω_h are negligible in most cases. Moreover, $H_1^*(K_2), H_4^*(K_2), A_1^*(K_2), A_4^*(K_2)$, which are technically considered to be more reasonable, have insignificant effects on flutter onset.

6.2.2 Methods for the flutter onset prediction

To solve the Eq. (6.1) to achieve the prediction of flutter onset or critical wind speed for long-span bridges to facilitate the wind-resistant design, a number of approaches have been developed in the past several decades, as summarized by Abbas et al. (2017). Generally, they consist of 2D bimodal and 3D multimodal flutter analysis methods. In 2D bimodal flutter analysis, only these selected two modes are considered. The drag force is considered to have insignificant effects on bridge aerodynamic force as well as negligible contributions to the flutter motion of streamline girder. For the sake of simplicity, the lateral DOF is usually ignored. Then, a reduced two-DOF (h and α) equations of motion for the bridge deck can be written as follows

$$\ddot{h} + 2\xi_{h0}\omega_{h0}\dot{h} + \omega_{h0}^2 h = \frac{\rho B U^2}{m_h} \left(K H_1^* \frac{\dot{h}}{U} + K H_2^* \frac{B \dot{\alpha}}{U} + K^2 H_3^* \alpha + K^2 H_4^* \frac{h}{B} \right) \quad (6.4)$$

$$\ddot{\alpha} + 2\xi_{\alpha 0}\omega_{\alpha 0}\dot{\alpha} + \omega_{\alpha 0}^2 \alpha = \frac{\rho B^2 U^2}{I_m} \left(K A_1^* \frac{\dot{h}}{U} + K A_2^* \frac{B \dot{\alpha}}{U} + K^2 A_3^* \alpha + K^2 A_4^* \frac{h}{B} \right) \quad (6.5)$$

where $\omega_{h0} = 2\pi f_{h0}$ and $\omega_{\alpha 0} = 2\pi f_{\alpha 0}$ are the circular natural frequencies of heaving and pitching modes of the bridge structure system in still air, ξ_{h0} and $\xi_{\alpha 0}$ are the mode-dependent ratios of the damping coefficients to the critical damping coefficients or damping ratios. The first fundamental symmetric heaving and pitching modes or the first fundamental antisymmetric heaving and pitch modes are employed. The solution of Eqs. (6.4)~(6.5) for the flutter limit assumes that the bridge deck starts undergoing sinusoidal vibration with the total damping ratio of the bridge-wind system approximately equal to zero and a single frequency larger than f_{h0} but smaller than $f_{\alpha 0}$. After that critical wind speed, any further increase in wind speed will result in a higher-amplitude oscillation and even an eventual

failure. Accordingly, the solutions of the vibration in heaving and pitching DOF can be assumed as

$$h = h_0 e^{i\omega t} \quad (6.6)$$

$$\alpha = \alpha_0 e^{i(\omega t + \theta)} \quad (6.7)$$

in which h_0 and α_0 are initial displacements, ω is flutter critical circular frequency, θ is the phase lag between heaving and pitching motions. Then, an iteration for frequency or damping or both is required to approximate the flutter limit because of the dependence of the flutter coefficients upon K . There are two commonly used analytical methods: the complex eigenvalue analysis (CEVA) ([Theodorsen and Garrick, 1940](#); [Simiu and Scanlan, 1996](#); [Bartoli and Mannini, 2008](#)) and the step by step analysis (SBSA) ([Matsumoto et al., 1996, 2010](#); [Yang et al., 2007](#)) or system decoupling approach (SDA) ([Xu, 2015](#)) to achieve the iteration.

Since 2D bimodal flutter analysis only takes two modes of interest into account and ignores the effects of drag force, the flutter limit could be overestimated when the contributions of higher-order modes and drag force are significant. The aeroelastic-model wind tunnel test of the Akashi Strait Bridge showed significant lateral displacement on its truss girder. And a slight lateral bending component was also observed in the flutter mode ([Miyata and Yamaguchi, 1993](#)). [Katsuchi et al. \(1998a, 1998b, 1999\)](#) and [Yamada et al. \(2006\)](#) revealed the importance of the participation of lateral mode in the flutter analysis for long-span truss-stiffened deck bridges. The inclusion of P_t^* -related aerodynamic force would considerably reduce the flutter onset wind speed, but close to the aeroelastic-model test results. Recently, a full aero-elastic model of a twin-box girder suspension bridge with main span of 5,000 m has been manufactured and investigated in Tongji University, which also found the

participation of lateral DOF during the flutter vibration (Ge et al., 2018). Moreover, the mode participation that leads to flutter of long-span bridges with spatial cable system was believed to be very complicated due to the mode shapes with strongly coupled DOFs as well as bridge deck and cables (Xie and Xiang, 1985; Yang et al., 2012). Accordingly, 3D multimodal method was developed. Xie and Xiang (1985) proposed a state-space approach to perform the multimodal flutter analysis, which only needs an input of wind speed to solve the eigenvalues without any iterative calculation (Boonyapinyo et al., 1999; Chen et al., 2000, 2001, 2002; Mishra et al., 2008). It also was widely used in the design of active control system (Wilde and Fujino, 1998; Li et al., 2015) and the flutter and buffeting analyses in time domain using rational function approximation (RFA) technique, known as Roger approximation or Karpel approximation (Wilde and Fujino, 1996; Chen et al., 2000; Guo and Ge, 2012). However, it is challenging to directly identify the coefficients of rational function for various bluff bridge decks. Often the frequency-domain flutter-derivative-based aerodynamic transfer function was employed to estimate these coefficients utilizing curve fitting (Scanlan et al., 1974; Lin and Yang, 1983; Bucher and Lin 1988; Wilde and Fujino, 1996; Boonyapinyo et al., 1999; Chen et al., 2002; Guo and Ge, 2012). The fitting algorithm and the variability of flutter derivatives would greatly affect the consequences, especially for these bluff bridge decks.

The state-of-the-art 3D flutter analysis is based on the superposition of modes and complex eigenvalue solutions of a determinant assembled with frequency-domain aerodynamic force and generalized structural modal information. It consists of multi-mode (Agar, 1989, 1991; Miyata and Yamada, 1990; Namini, 1992; Tanaka et al., 1993; Jain et al., 1996a, 1996b; Beith, 1998; Katsuchi et al., 1998; D'Asdia and Sepe, 1998; Dung et al., 1998; Hua et al., 2007) and full-order methods (Ge and Tanaka, 2000; Ding et al., 2002; Hua and Chen, 2008). The multi-

mode approach only utilizes and tracks the modes of interest at different wind speeds, whereas full-order technique incorporates the mode information of all DOFs in the FEM model, leading to an accurate analysis of flutter problem from the viewpoint of methodology (Abbas et al., 2017). In reality, if there are sufficient modes included, the prediction of flutter onset wind speed would have good precision since only a few modes are considered to contribute to the flutter instability.

6.2.3 Method comparisons of flutter solution

In order to compare the difference of these methods regarding the flutter solution, an example of a simply supported girder bridge with the section of ideal flat plate (thickness = 0) was employed. Some basic parameters of the structure are defined as: length $L = 300\text{m}$; deck width $B = 40\text{m}$; vertical bending stiffness of the deck $EI_z = 2.1 \times 10^6 \text{MPa} \cdot \text{m}^4$; lateral bending stiffness of the deck $EI_y = 1.8 \times 10^7 \text{MPa} \cdot \text{m}^4$; torsional stiffness $GI_t = 4.5 \times 10^5 \text{MPa} \cdot \text{m}^4$; unit mass $m = 2 \times 10^4 \text{kg/m}$; unit mass moment of inertia $I_m = 4.5 \times 10^6 \text{kg} \cdot \text{m}^2/\text{m}$; and air mass density $\rho = 1.225 \text{kg/m}^3$. The initial structural mechanic damping ratios are set as 0%. The self-excited aerodynamic force acting on the ideal flat plate can be solved as the Theodorsen function (Theodorsen, 1935) based on the theory of potential flow. Correspondingly, eight flutter derivatives are determined as

$$H_1^*(k) = -\frac{\pi F}{2k} \quad (6.8)$$

$$H_2^*(k) = -\frac{\pi}{8k} \left(1 + F + \frac{2G}{k}\right) \quad (6.9)$$

$$H_3^*(k) = -\frac{\pi}{4k^2} \left(F - \frac{kG}{2}\right) \quad (6.10)$$

$$H_4^*(k) = \frac{\pi}{2} \left(\frac{G}{k} + \frac{1}{2}\right) \quad (6.11)$$

$$A_1^*(k) = \frac{\pi F}{8k} \quad (6.12)$$

$$A_2^*(k) = \frac{\pi}{16k} \left(\frac{F-1}{2} + \frac{G}{k} \right) \quad (6.13)$$

$$A_3^*(k) = \frac{\pi}{16k^2} \left(F - \frac{kG}{2} + \frac{k^2}{8} \right) \quad (6.14)$$

$$A_4^*(k) = -\frac{\pi G}{8k} \quad (6.15)$$

in which $k = K/2 = b\omega/U$, F and G are the real and imaginary part of Theodorsen function, which was be approximately estimated by R. T. Jones with the form of

$$F(k) = 1 - \frac{0.165}{1 + \left(\frac{0.0455}{k}\right)^2} - \frac{0.335}{1 + \left(\frac{0.3}{k}\right)^2} \quad (6.16)$$

$$G(k) = -\frac{0.165 \times \frac{0.0455}{k}}{1 + \left(\frac{0.0455}{k}\right)^2} - \frac{0.335 \times \frac{0.3}{k}}{1 + \left(\frac{0.3}{k}\right)^2} \quad (6.17)$$

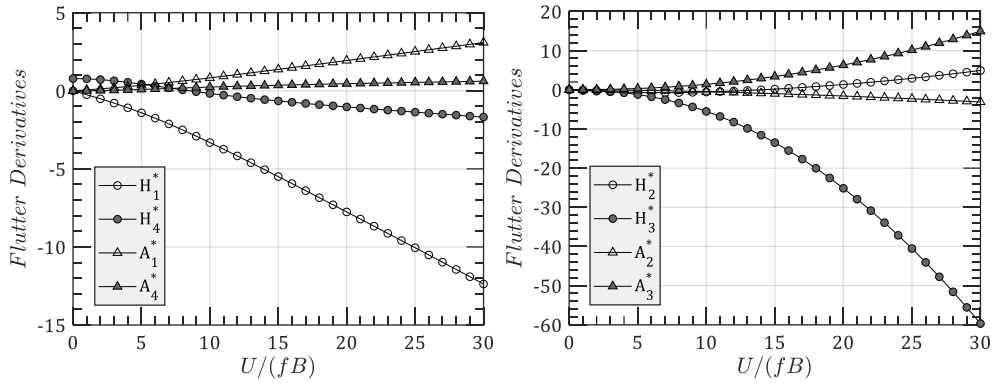


Fig. 6.2 Flutter derivatives of the ideal flat plate

Table 6.1 Flutter critical wind speed of a simply supported beam with the section of ideal flat plate

Method	U_{cr} (m/s)	ε (%)	f_{cr}	ε (%)	U_{cr}/Bf_{cr}	ε (%)
Exact solution	139.9	0.00	0.3801	0.00	9.20	0.00
CEVA	134.1	-4.15	0.3930	3.28	8.53	-7.28
SBSA	139.9	0.00	0.3792	-0.24	9.22	0.02
RFA	139.8	-0.07	0.3800	-0.03	9.20	0.00
Multimode	139.7	-0.14	0.3798	-0.08	9.20	0.00

Note: ε is the relative errors between models and the exact solution.

The flutter critical wind speeds are listed in Table 6.1. More explanations regarding the flutter analysis of this simply supported beam can be found in Appendix I. As can be seen, The SBSA, RFA and Multimode methods show a good estimation of critical wind speed and circular frequency of the flutter boundary when compared with the exact solution. The CEVA approach has a maximum error. Since the prediction result using the RFA method greatly depends on the coefficients fitting of the rational function, some undesired errors could be introduced when it was applied to various bridge decks. Accordingly, the 2D SBSA and 3D Multimode approaches would be adopted in the following probabilistic flutter analysis.

6.3 Structural parameters

6.3.1 Modal parameters

The inherent dynamic properties of a bridge structure, i.e. modal shapes and natural frequencies are usually prescribed using the finite element method (FEM). They are customarily derived from the eigenvalue analysis of Eq. (6.1) by ignoring the external force ($\mathbf{C}_{se}\dot{\mathbf{X}} + \mathbf{K}_{se}\mathbf{X}$) and damping term ($\mathbf{C}_0\dot{\mathbf{X}}$), leaving only the terms related to mass matrix \mathbf{M} and stiffness matrix \mathbf{K}_0 . In a FEM model, the lumped mass matrix for each element is given by

$$\mathbf{m}^e = \int \rho \mathbf{N}^T \mathbf{N} dV \quad (6.18)$$

in which ρ is the mass density of the element, \mathbf{N} is the shape function matrix. That is, the variability of the mass matrix can be represented by the variation of material mass density at each element. The stiffness matrix of a 3D beam element is

$$\begin{bmatrix} \frac{EA}{l} & 0 & 0 & 0 & 0 & 0 & -\frac{EA}{l} & 0 & 0 & 0 & 0 & 0 \\ 0 & \frac{12EI_z}{l^3} & 0 & 0 & 0 & \frac{6EI_z}{l^2} & 0 & -\frac{12EI_z}{l^3} & 0 & 0 & 0 & \frac{6EI_z}{l^2} \\ 0 & 0 & \frac{12EI_y}{l^3} & 0 & -\frac{6EI_y}{l^2} & 0 & 0 & 0 & -\frac{12EI_y}{l^3} & 0 & -\frac{6EI_y}{l^2} & 0 \\ 0 & 0 & 0 & \frac{GI_x}{l} & 0 & 0 & 0 & 0 & 0 & -\frac{GI_x}{l} & 0 & 0 \\ 0 & 0 & -\frac{6EI_y}{l^2} & 0 & \frac{4EI_y}{l} & 0 & 0 & 0 & \frac{6EI_y}{l^2} & 0 & \frac{2EI_y}{l} & 0 \\ 0 & \frac{6EI_z}{l^2} & 0 & 0 & 0 & \frac{4EI_z}{l} & 0 & -\frac{6EI_z}{l^2} & 0 & 0 & 0 & \frac{2EI_z}{l} \\ -\frac{EA}{l} & 0 & 0 & 0 & 0 & 0 & \frac{EA}{l} & 0 & 0 & 0 & 0 & 0 \\ 0 & -\frac{12EI_z}{l^3} & 0 & 0 & 0 & -\frac{6EI_z}{l^2} & 0 & \frac{12EI_z}{l^3} & 0 & 0 & 0 & -\frac{6EI_z}{l^2} \\ 0 & 0 & -\frac{12EI_y}{l^3} & 0 & \frac{6EI_y}{l^2} & 0 & 0 & 0 & \frac{12EI_y}{l^3} & 0 & \frac{6EI_y}{l^2} & 0 \\ 0 & 0 & 0 & -\frac{GI_x}{l} & 0 & 0 & 0 & 0 & 0 & \frac{GI_x}{l} & 0 & 0 \\ 0 & 0 & -\frac{6EI_y}{l^2} & 0 & \frac{2EI_y}{l} & 0 & 0 & 0 & \frac{6EI_y}{l^2} & 0 & \frac{4EI_y}{l} & 0 \\ 0 & \frac{6EI_z}{l^2} & 0 & 0 & 0 & \frac{2EI_z}{l} & 0 & -\frac{6EI_z}{l^2} & 0 & 0 & 0 & \frac{4EI_z}{l} \end{bmatrix} \quad (6.19)$$

There are six random variables, the modulus of elasticity E , area A , the shear modulus G and area moments of inertia about x (vertical bending along x), y (lateral bending) and z (vertical bending along z) axes, i.e. I_x, I_y, I_z . For homogeneous isotropic linear elastic materials, the following relationship holds:

$$G = \frac{E}{2(1 + \nu)} \quad (6.20)$$

in which ν is the Poisson's ratio. For simplicity, the variation of the stiffness matrix is assumed to be described by E .

For an element i in the FEM model, two coefficients of variation (CoV) are assigned to its ρ_i and E_i , respectively to depict the variability of the structure due to the defects of materials, erection errors, temperature dependence, traffic effects, etc. Conventionally, the normal and lognormal distributions were widely used to probabilistically model the mass density and modulus of elasticity (Barbato et al., 2010; Zona et al., 2010; Orton et al., 2012; Tubaldi et al., 2012; Lagaros and Nikos, 2014; Pang et al., 2014). In this study, ρ_i is assumed to follow the normal distribution while lognormal distribution is applied to E_i . The CoVs regarding three structure parts of a suspension bridge, i.e. the main girder, towers, and cables are listed in Fig. 6.2 by the survey results of other literature (Barbato et al., 2010; Zona et al., 2010; Orton et al., 2012; Tubaldi et al., 2012; Lagaros and Nikos, 2014; Pang et al., 2014). Since ρ_i and E_i are used to represent the variation of element mass and stiffness, respectively, higher CoVs would be employed than the use of only ρ_i or E_i . Moreover, an exponential decay function was adopted to account for the spatial correlation between the elements at different locations in the bridge with the form of

$$c_{i,j} = \exp\left(-a \frac{\Delta_{ij}}{L}\right) \quad (6.21)$$

in which Δ_{ij} is the distance between element i and j . L is the total length of a bridge structure component, such as the main girder, towers (pylons) and main cables, a is a decay factor. The minimum correlation occurs at $\Delta_{ij}=L$, i.e. two end elements for a certain bridge structure component with the value of $\exp(-a)$. The maximum correlation coefficient is 1 when $\Delta_{ij}=0$. The main cables for modern cable-supported bridges commonly consist of high-tensile-strength steel wires. The widely used seven-wire strands comprise wires with tensile strengths between 1770 and 1860 MPa. Typically, the nominal modulus of elasticity

for the seven-wire strand is only 6–8% lower than for the wires themselves, i.e. a typical modulus of elasticity of $E = 190GPa$ (Gimsing and Georgakis, 2012). For suspension bridges, the main cables are erected using the air-spinning method (AS) or prefabricated parallel-wire strand method (PPWS), indicating the mass and geometric parameters of the cable along its longitudinal direction almost remain unchanged. However, instead of the full correlation, the spatial correlation function with a small value of $a = 0.1$, i.e. $(c_{i,j})_{min} = 0.9$ was employed for cable elements due to the uneven distribution of materials and some inherent uncertainties. The stiffing girder is routinely erected by assembling the prefabricated deck segments. They are usually prefabricated offsite and transported into position under the main cables. The minimum spatial correlation is assumed as 0.6 ($a = 0.5$) because those deck units are predesigned and prefabricated in the same workshop. But the spatial correlations of elements should be smaller than cables since they are assembled unit by unit. And it is can also be affected by the pavements, ancillary facilities, and traffic. The bridge pylon is always cast in situ utilizing reinforced concrete. A minimum spatial correlation coefficient of 0.5 was selected, yielding $a = 0.7$.

Table 6.2 Probabilistic models for mass and stiffness parameters of the bridge structure

Parameter	PDF model	Main girder (Steel)		Cable (Steel)		Pylon (RC)	
		CoV	a	CoV	a	CoV	a
ρ (mass)	Normal	0.05	0.5	0.05	0.1	0.1	0.7
E (stiffness)	Lognormal	0.1	0.5	0.05	0.1	0.15	0.7

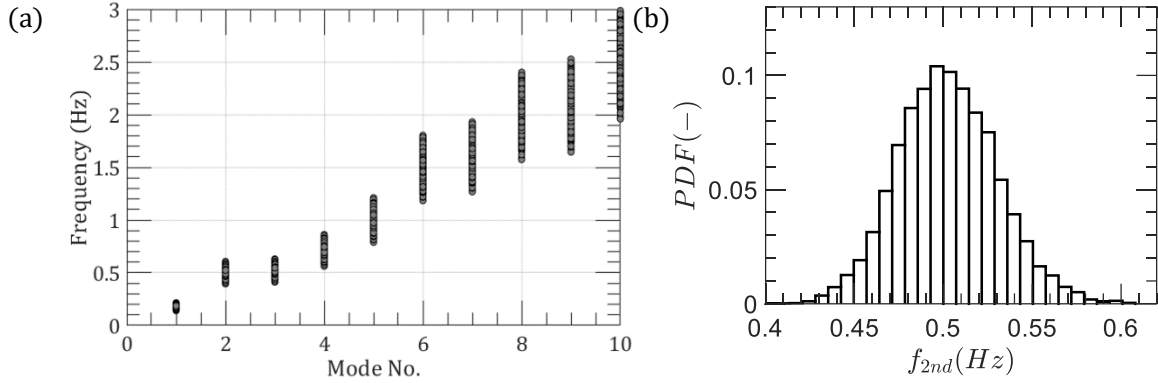


Fig. 6.3 Simulated frequencies of a simply supported beam (10,000 runs) : (a) First 10 modes; (b) 2nd mode (1st symmetric torsional mode)

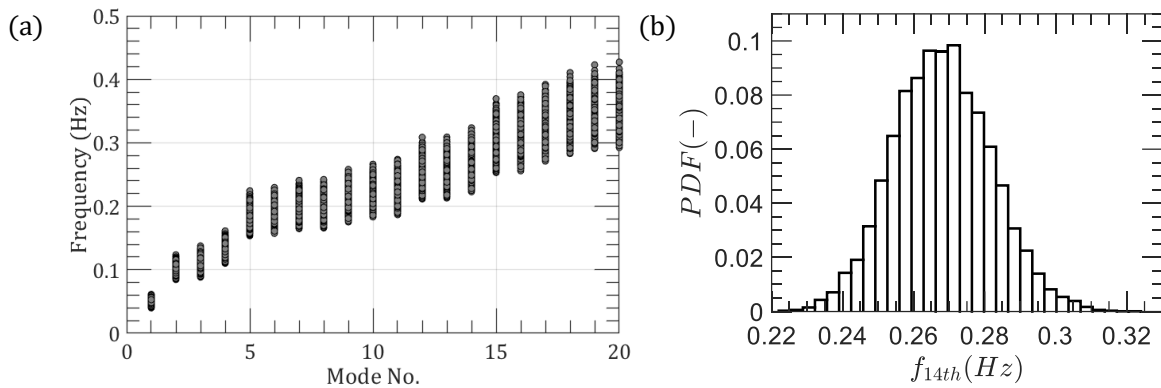


Fig. 6.4 Simulated frequencies of Jiangyin Suspension Bridge (10,000 runs): (a) First 20 modes; (b) 14th mode (1st symmetric torsional mode)

Figs. 6.3~6.4 illustrate the simulated frequencies of the simply supported beam bridge (Appendix I) and Jiangyin suspension bridge (Appendix J) by introducing the randomness of mass and stiffness parameters as mentioned before. It can be noted that the variability of frequencies associated with high-order modes shows greater dispersion than that of low-order modes. The probability densities of the frequency of the first symmetric torsional mode are also shown in Fig. 6.3 (b) and Fig. 6.4 (b). The mean is 0.5024 Hz for the torsional mode of the simply supported beam, which is close to the value of the deterministic model, i.e. 0.5029 Hz. The corresponding coefficient of variation (CoV) is 0.055. For the first symmetric torsional mode of the Jiangyin Suspension bridge, the mean and CoV are 0.2680 Hz and 0.051.

6.3.2 Damping ratios

Damping is an inherent influence within an oscillatory system to reduce or restrict the oscillations, which is quantified with a dimensionless measure, i.e. damping ratio. The variability of damping ratio for the bridge structures is usually significant. It also plays an important role on flutter issue of long-span bridges which is always driven by the negative damping ratio of the bridge-wind system. The mechanic damping matrix C_0 in Eq. (6.1) is assumed as Rayleigh damping which is formulated as the linear function of mass matrix and stiffness matrix. The damping ratios of two arbitrary modes should be predefined to determine the coefficients of this linear function (Eq. (D7)). As for the probabilistic model of bridge structural damping, Davenport and Larose (1989) suggested the lognormal probability distribution model to characterize the bridge damping ratio associated with CoV of 0.40. Kwon (2010) conducted a literature survey and collected the damping ratios of fundamental vertical and torsional modes for 8 cable-stayed bridges and 13 suspension bridges. The sample mean of 0.71% and a standard deviation of 0.42% were obtained with the CoV of 0.59. And a Weibull distribution with the parameters of (0.80, 1.83) was recommended to probabilistically model the damping ratios. A similar literature survey was performed in this study by taking account into the field-measured data of a series of cable-supported bridges (Yamaguchi and Ito, 1997; Guo et al., 2000; Fujino, 2002; Liu et al., 2013; Kim and Kim, 2017; Li et al., 2018; Kim et al., 2019). The survey results of damping ratios associated with vertical bending modes and torsional modes are summarized in Fig. 6.5. It noteworthy that some measurements were performed using the vibration data of the bridge during strong winds, the aerodynamic damping caused by the wind could result in the overestimate of the structural mechanic damping ratios (Liu et al., 2013;).The damping

ratios identified from wind-excited vibrations could reach up to 5% (Nagayama et al., 2005) or even 10% (Siringoringo and Fujino, 2008) for 1st vertical bending modes. Moreover, the damping ratios are vibration-amplitude-dependent (Nagayama et al., 2005; Liu et al., 2013; Siringoringo and Fujino, 2008), usually showing an increasing trend with the vibration amplitude. Liu's investigation (Liu et al., 2013) on Xihoumen Bridge showed that the damping ratios of 1st vertical bending mode are within the range of (0%, 2%) at relatively high wind speeds (1-hour mean wind speed > 10 m/s) after removing the effects of aerodynamic damping. It is consistent with the present study.

Two probability distribution models, i.e. the lognormal distribution and Weibull distribution were employed to fit the survey results, as shown in Fig. 6.5. The critical values for Kolmogorov–Smirnov test associated with the damping ratios of vertical mode and torsional mode are 0.11 (sample size = 147) and 0.17 (sample size = 59). As can be seen, both lognormal and Weibull distributions are acceptable candidates, but Weibull distribution is preferable. The probability density function of Weibull distribution is formulated as

$$f(x; k, \gamma) = \frac{k}{\gamma} \left(\frac{x}{\gamma}\right)^{k-1} e^{-(x/\gamma)^k}, x \geq 0 \quad (6.22)$$

In which x denotes the argument or the input of the function, k and γ are two undetermined coefficients. The distribution coefficients of Weibull distribution in Fig. 6.4 are $k = 1.034$, $\gamma = 2.219$ for the damping ratios of vertical mode and $k = 0.931$, $\gamma = 2.023$ for the damping ratios of torsional mode, respectively. Correspondingly, the CoVs of these two datasets are 0.48 and 0.53, which fall in between the Davenport's and Kwon's suggestions.

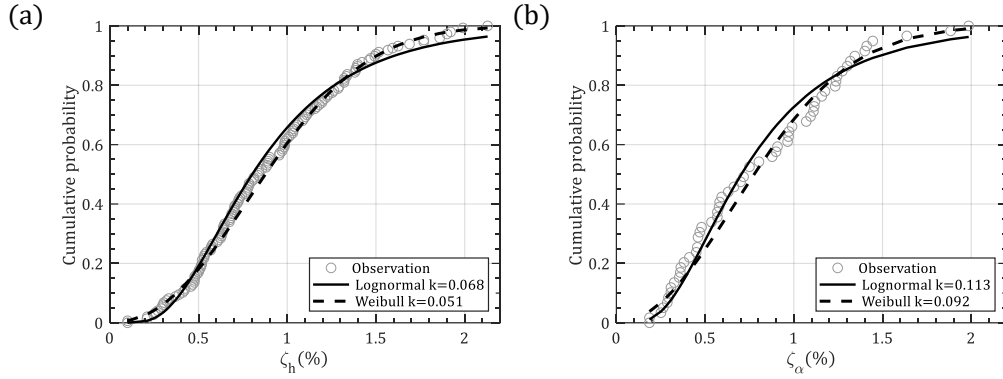


Fig. 6.5 CDF of damping ratios for cable-supported bridges: (a) Vertical bending mode; (b) Torsional mode. (k is the statistic of K-S test)

6.4 Aerodynamic parameters

The aerodynamic force or self-excited force in Eq. (6.1) is customarily expressed as the linear function of the bridge vibration state, i.e. displacement and velocity. The transfer function in terms of flutter derivatives (FDs) are usually identified using wind tunnel test or numerical simulation, say computational fluid dynamics (CFD). Generally, two kinds of approaches were employed to identify the FDs both in experiments or numerical simulations, i.e. free vibration (Sarkar et al., 1994; Sarkar et al., 2009; Ding et al., 2010; Xu et al., 2014) and forced vibration techniques (Matsumoto, 1996; Sarkar et al., 2009). The free vibration method allows the bridge deck to vibrate freely at various wind speeds while forced vibration imposes a prescribed motion on the model of interest in the airflow. Comparatively, the free vibration is easily performed due to its instrumental simplicity and operational convenience (Sarkar et al., 1994; Ding et al., 2010; Xu et al., 2014). But it is difficult to extract the FDs at high reduced wind speed because of the effects of the aerodynamic damping, especially for vertical DOF of a bridge deck model. The forced vibration test is, theoretically, able to identify the FDs in arbitrary cases, such as large reduced wind speed or turbulent winds. However, as discussed by Gao and Zhu (2016), the fluid-structure interaction between the wind and

model was not fully reproduced by the forced vibration, resulting in possible unrealities of the aerodynamic force on the bluff-body. Free vibration has close-circle feedback between the flow, aerodynamic force and motion of the model. Accordingly, the free vibration was mainly adopted in the present study for wind tunnel tests. And the forced vibration was also applied to a quasi-flat plate section using CFD simulations to validate the wind tunnel results. For free vibration technique, a series of methods have been developed in past several decades based on the free decay time histories of the bridge deck at various wind speeds, such as the Kalman filter method (Yamada et al., 1992), Ibrahim time-domain method (Sarkar et al., 1994), iterative least-squares method (Sarkar et al., 2003) and stochastic subspace identification method (Qin and Gu, 2004). A unifying least-square (ULS) method developed Gu et al. (2000) and improved by Li et al. (2003), Bartoli et al. (2009) and Ding et al. (2010) will be utilized in this study, which is referred to as the modified unifying least-square (MULS) approach. At each wind speed, the two-degree-of-freedom free decay displacements, i.e. $h(t)$ and $\alpha(t)$ can be mathematically superposed with two displacement modes as

$$h(t) = \sum_{i=h,\alpha} h_i(t) = \sum_{i=h,\alpha} A_{hi} e^{-\omega_i \zeta_i t} \cos\left(\omega_i \sqrt{1 - \zeta_i^2} t + \theta_{hi}\right) \quad (6.23)$$

$$\alpha(t) = \sum_{i=h,\alpha} \alpha_i(t) = \sum_{i=h,\alpha} A_{\alpha i} e^{-\omega_i \zeta_i t} \cos\left(\omega_i \sqrt{1 - \zeta_i^2} t + \theta_{\alpha i}\right) \quad (6.24)$$

in which A_{di} and θ_{di} ($d = h, \alpha; i = h, \alpha$) are the amplitudes and phases information for each mode, which are determined by the initial conditions, ω_i and ζ_i are the natural frequencies and damping ratios. A modified objective error function between estimated and real values was introduced as

$$J = \sum_{d=h,\alpha} w_d^2 \{e_d\}^T \{e_d\} \quad (6.25)$$

in which $\{e_d\}$ ($d = h, \alpha$) are the error vectors between estimated and real values, w_d are the weighted factors used to adjust the magnitude orders of vertical and rotational displacements, which are given by $w_h = 1/|h|_{max}$, $w_\alpha = 1/|\alpha|_{max}$. Then, twelve model parameters in Eqs. (6.23)-(6.24) can be fitted by minimizing the error term of Eq. (6.25). More details regarding this method are available in Li et al. (2003), Ding et al. (2010) and Xu et al. (2014), which are omitted herein for brevity.

As listed in Table 6.3, in this study, the wind tunnel tests of two section models, i.e. a quasi-flat plate section model (Fig. 6.6) and a Pasco-Kennewick (P-K) section model (Fig. 6.7) were conducted to investigate the experiment-induced uncertainties of FDs. And CFD simulations for the quasi-flat plate section model were also performed to validate the results of the wind tunnel tests. Usually, a quasi-flat plate model is defined as the section with the ratio of width and depth (B/D) greater than 20. Thus, a literature survey on the identifications of flutter derivatives for quasi-flat plate models was conducted (Gu et al., 2001; Gu and Qin, 2004; Boonyapinyo and Janesupasaeree, 2010; Ding et al., 2010). A similar literature survey was also performed on a closed-box girder section, as shown in Fig. 6.8. Fig. 6.6 shows the cross-sections of the quasi-flat plate model used in the present and other studies. Moreover, a similar survey was also performed on the real closed-box girder adopted by Jiangyin Bridge (Gu et al., 2000; Gu et al., 2001; Ding et al., 2001; Shao et al.,). The uncertainties from the literature survey could result from a number of sources, such as identification algorithm, turbulence of wind field, laboratory effects, etc.

Table 6.3 Arrangement of uncertainty quantification for flutter derivatives

Section	Wind tunnel test	Literature survey	CFD
Quasi-flat plate model	√	√	√
P-K section model	√		
Closed-box model		√	

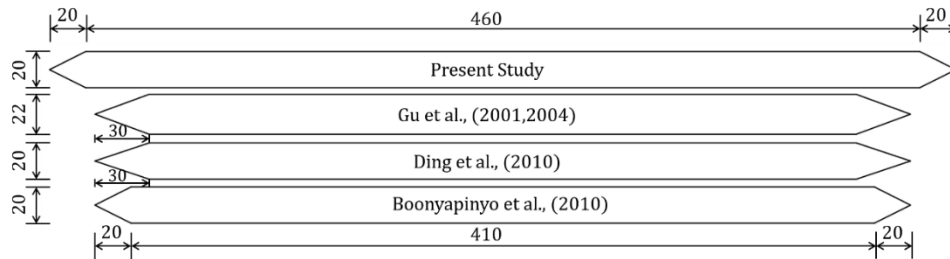


Fig. 6.6 Quasi-flat plate section models (unit: mm)

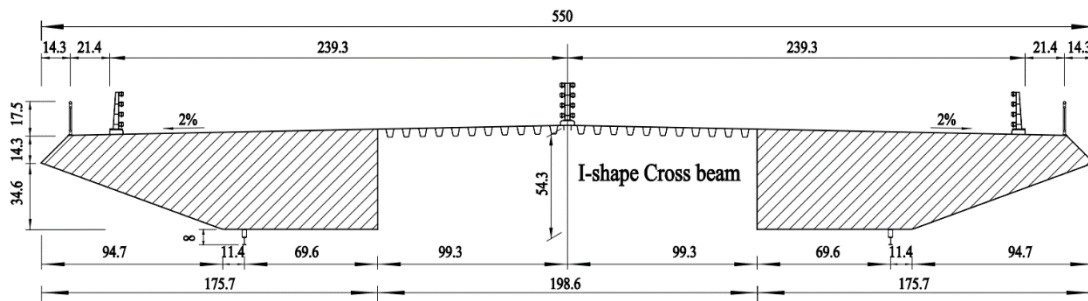


Fig. 6.7 A Pasco-Kennewick (P-K) section model (unit: mm)

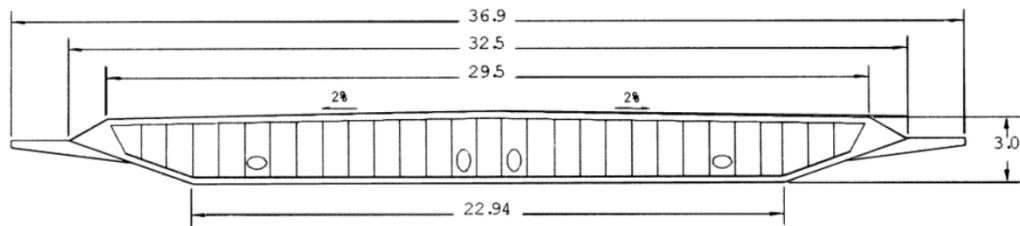


Fig. 6.8 A closed-box section model (Jiangyin bridge, unit: m, [Gu et al. \(2000\)](#))

For the quasi-flat plate section model, four oncoming wind fields with different turbulence intensities, i.e. $I_u = 1\%$, 5% , 10% , and 14% were generated using different arrangements of grids, as shown in Appendix (K). Fig. 6.9 shows the identified FDs of the present quasi-flat plate section from 20-time repetitions in four oncoming winds together with the Theodorsen function and CFD results. In CFD simulations, the forced vibration technique was adopted. Two turbulence models, say Reynolds Averaged Navier-Stokes (RANS) and Large Eddy

Simulation (LES) and two vibration amplitudes, say 3° and 5° were employed. As can be seen, the identified flutter derivatives show reasonable agreements with the Theordorsen function and CFD results. The variability of CFD results mainly attributes to the vibration amplitude and turbulence model. It can be noted that all experimentally identified FDs become more scattered with the increase of wind speeds except H_2^* , whose variability almost remains unchanged with the wind speed. The mean line with error bar plots associated with each FD subjected to different turbulence intensities is shown in Fig. (K2). The mean curves show insignificant variation with respect to turbulence intensity. However, the dispersion of FDs tends to increase remarkably at high turbulence intensity, as illustrated in Fig. (K3).

A series of pioneer studies have been performed in the effects of turbulence on bridge instability in the past several decades, but they are still not well understood. Scanlan and Lin (1978) identified the FDs of a trussed bridge deck, which was modeled with a holes-drilled U-shaped beam in grid-generated turbulence. It was found that The FDs identified form turbulent winds show a similar trend to that in the laminar flow but have slightly larger values. Huston (1986) investigated the effects of integral scale of turbulence on bridge stability, showing that the presence of large-scale upstream turbulence should exert a destabilizing influence on the aeroelastic performance of bridges. Since then, a number of wind tunnel tests were successively conducted to examine the turbulence effects of FDs for different bridge decks (Matsumoto et al., 1992; Sarkar et al., 1994; Gu et al., 2000, 2004; Hatanaka and Tanaka, 2005; Haan and Kareem, 2009). But the conclusions regarding the turbulence effects on bridge instability were not always consistent. Bucher and Lin (1988) suggested that the turbulence would decrease the coherence of self-excited force along the bridge deck, resulting a higher flutter critical win speed. In this study, the FDs extracted from

four wind fields would be analyzed from a statistical viewpoint before performing the flutter analysis.

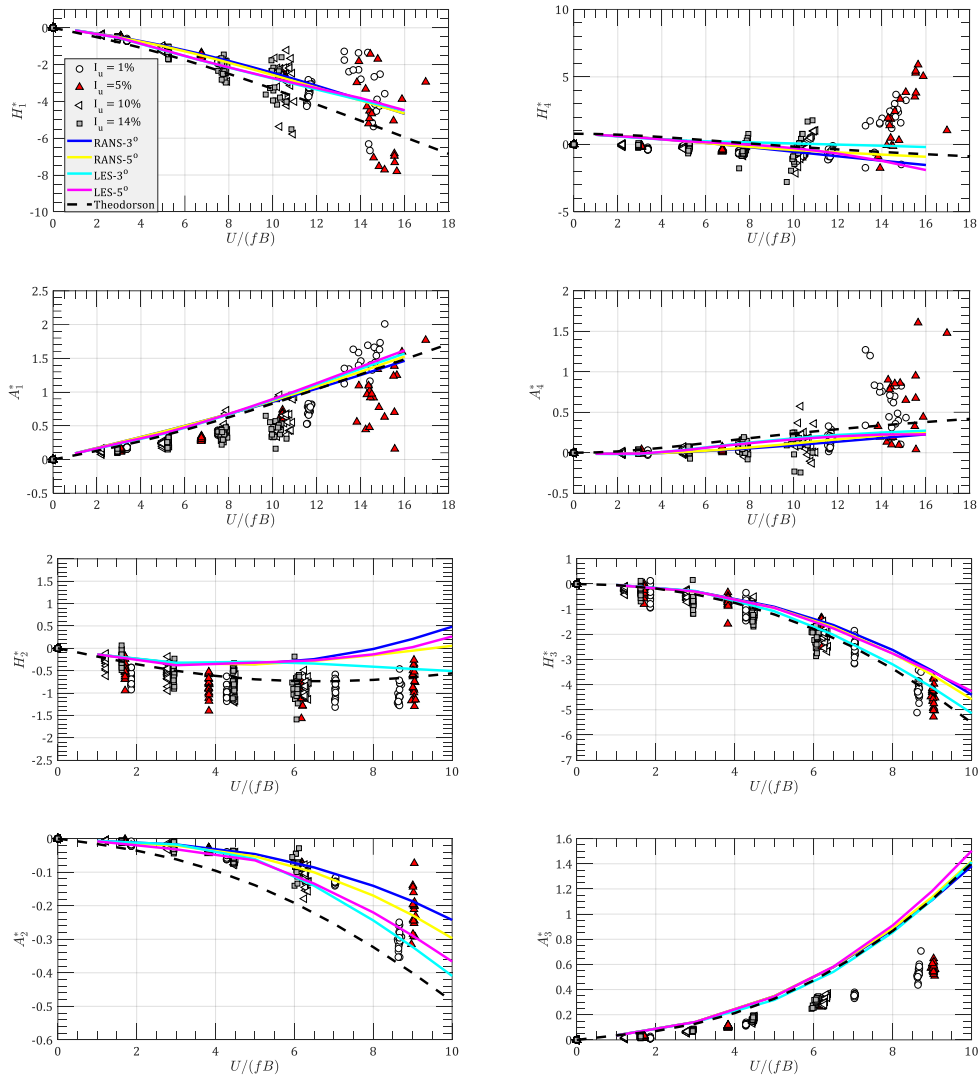


Fig. 6.9 Flutter derivatives of a quasi-flat section model

For each set of FDs associated with a turbulent wind field, the mean and standard deviation of FDs correspond to various reduced wind speeds will be determined from 20-time repetitions. To achieve this, 20 FDs at each reduced wind speed will be sorted first. Then, the interpolation is adopted to obtain the FDs at the reduced wind speed of interest. The FDs are assumed to be normally distributed at each reduced wind speed. And a correlation matrix for each turbulence case is introduced as shown in Appendix (M). The correlation matrices

are identified from the FDs of last reduced wind speed in the wind tunnel test, at which the sectional model is close to the flutter instability. The correlation matrix will be employed at all reduced wind speeds during the random simulations.

The literature survey regarding the FDs of four quasi-flat plates is shown in Appendix (N). It was found that the standard derivations of FDs calculated from these quasi-flat plates increase significantly with the reduced wind speed. It is possibly attributed to the difference in aerodynamic geometry. Although they are all categorized as quasi-flat plates, the aerodynamic forces around their surfaces show remarkable differences. It indicates the aerodynamic force of the bluff body is very sensitive to the configuration. Accordingly, to avoid introducing other uncertainties, the probabilistic flutter solutions of the quasi-flat plate will be performed only based on the experimental FDs in this study. But the dataset of FDs, such as Appendix N could be useful in the future to do some works on the generalization of the FDs with respect to deck geometry to facilitate the wind-resistant design.

The other similar experiments were also performed on the P-K section model, but only the laminar flow or 1%-turbulence wind was applied. The arrangement of the wind tunnel test is shown in the Appendix (L). Fig. 6.10 illustrates the 20-time repetition results of FDs. The variability of H_1^* , H_4^* , A_1^* and A_4^* associated with f_h will continuously increase with the wind speed while H_2^* , H_3^* show an augmentation of dispersion before becoming stable near the flutter boundary. And A_2^* and A_3^* have insignificant data scatter with the increase of reduced wind speed. It is worth noting that A_2^* is negative first and towards to zero around flutter critical wind speed which characterizes the flutter performance between the purely single DOF torsional flutter instability (A_2^* usually becomes positive before flutter is going to happen for H-section or low-aspect-ratio rectangle section) and classic two-DOF (vertical

bending and torsional motion) coupled flutter (A_2^* always remains negative and continuously decrease with wind speed for airfoil-like or streamline sections). This means the DOF coupled effect is weak for the present P-K section around the flutter threshold. As shown in Fig. L2, the standard deviations of each FD with respect to reduced wind speed are plotted. They are observed to increase with the reduced wind speed except H_2^* and H_3^* , whose variability increase first before showing drops after the reduced wind speed higher than 4. Comparatively, the standard deviations of FDs of the quasi flat plate that achieved in laminar flow, as shown in Fig. K3, are observed to continuously increase with the reduced speed. The amplitudes of standard deviations of each FD at same reduced wind speeds for these two sections show insignificant differences, except H_2^* and H_3^* of the P-K section model, which have smaller standard deviations at high reduced wind speed due to sudden drops.

Fig. 6.11 summarizes the FDs of the closed-box section model adopted by the Jiangyin Bridge from the literature survey. All of them were identified using the free vibration technique. The effects of turbulence and parameters of the sectional model, say the mass, mass moment of inertia and torsion-bending frequency ratio were considered by Gu et al., (2001). As can be seen, the scatter of FDs also appears to increase with the reduced wind speed. The H_2^* in Shao et al. (2008) will be removed due to its large deviation from most studies. The A_4^* , which was treated as insignificant to the flutter instability and ignored in the original formulas of the self-excited force (Scanlan, 1978), was not identified in Gu's studies. A_4^* provided by Ding et al. (2002) and Shao (2008) are close to zero. Accordingly, the variation of A_4^* will be neglected in this study and the results provided by Ding et al. (2002) were employed.

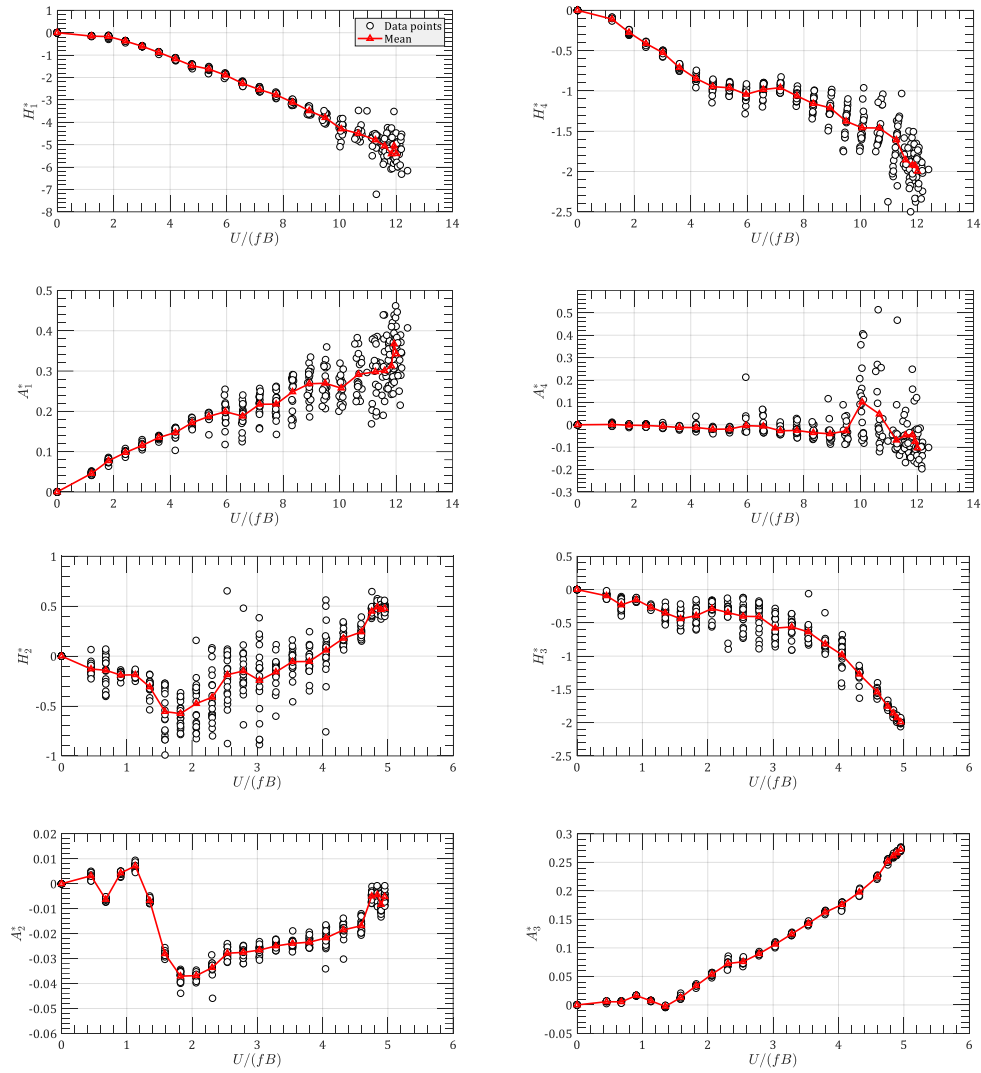


Fig. 6.10 Flutter derivatives of the P-K section model

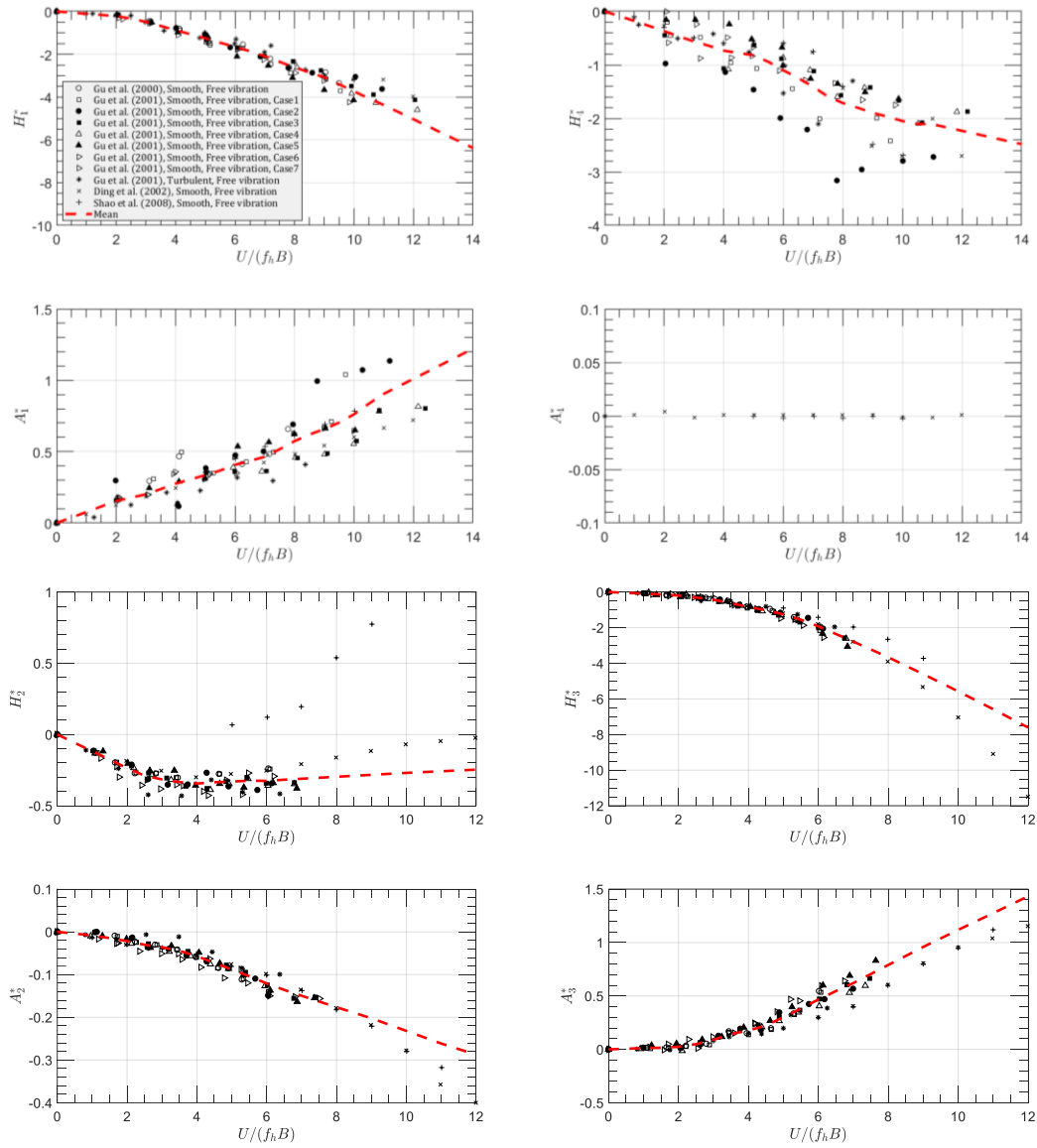


Fig. 6.11 Flutter derivatives of the closed-box section model adopted by the Jiangyin Bridge

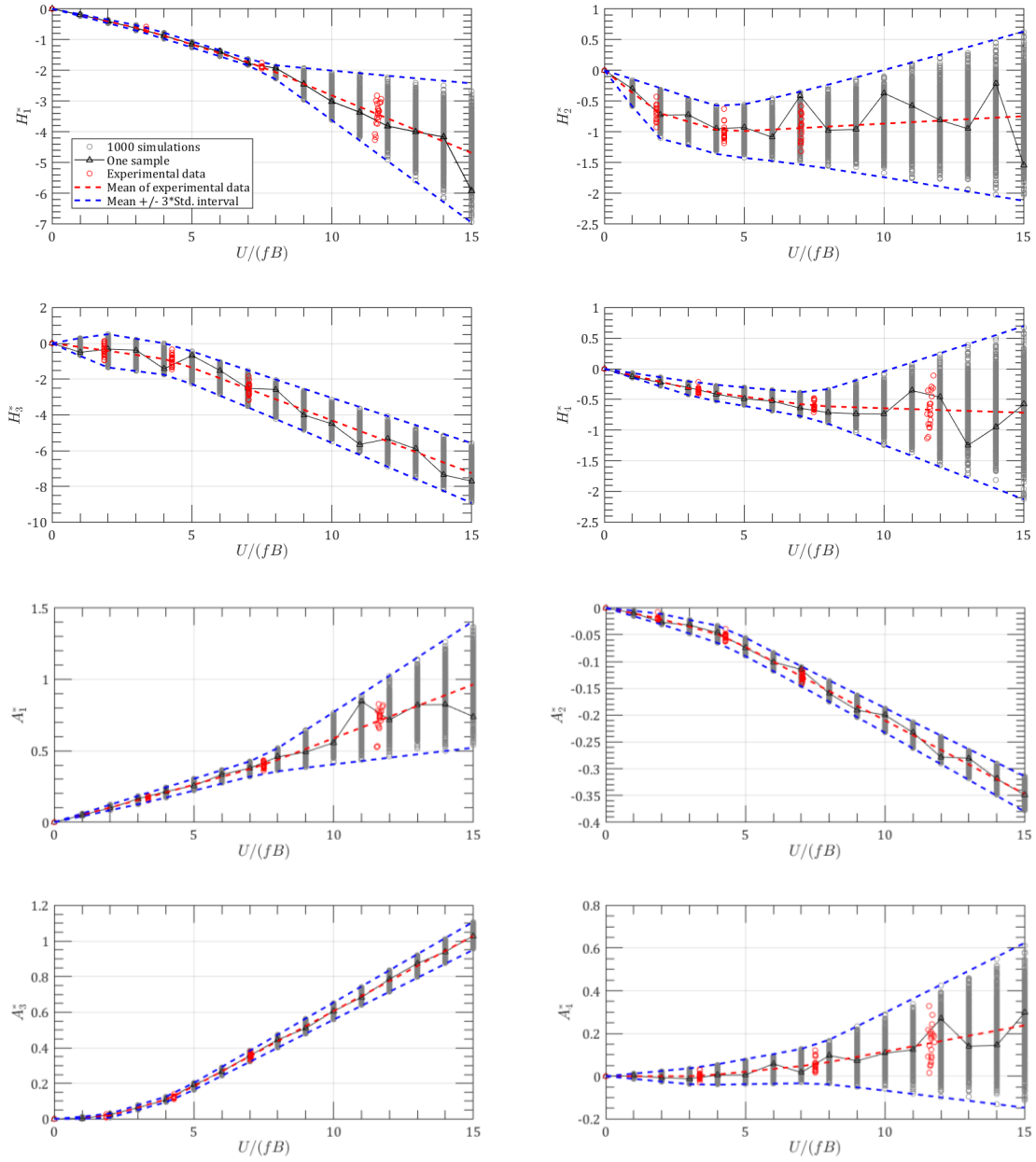


Fig. 6.12 Comparisons of simulated and experimental FDs (quasi-flat plate section model, 10% turbulence intensity)

An example of 1000 simulations for the FDs of the quasi-flat plate section model in 10% turbulent winds is shown in Fig. 6.12. To avoid any weird results of FDs, the upper and lower limits are set as the mean ± 3 times of standard deviation at each reduced wind speed. It can be seen that the simulation results show reasonable agreements with the variation pattern of experimental data. One simulated sample for each FD is also plotted. Since the FDs

obtained from wind tunnel tests are always not smooth curves, the fluctuated FDs are employed in the simulations.

Moreover, to achieve 18 FDs (Eqs. (6.1)-(6.3)) which will be utilized in 3D multimode flutter analysis, the quasi-steady approximations for another 12 FDs are adopted, as shown in Table 6.4. Correspondingly, the static coefficients for the present three girder sections (Figs. 6.4-6.6) are given in Table 6.5.

Table 6.4 Quasi-steady approximations for FDs

FDs	H_5^*	H_6^*	A_5^*	A_6^*	P_1^*	P_2^*	P_3^*	P_4^*	P_5^*	P_6^*
Quasi-steady	$\frac{1}{K}C_L$	0	$-\frac{1}{K}C_M$	0	$-\frac{1}{K}C_D$	$\frac{1}{2K}C'_D$	$\frac{1}{2K^2}C'_D$	0	$\frac{1}{2K}C'_D$	0

Table 6.5 Static coefficients for three sections

sections	C_L	C_D	C_M	C'_D
Quasi-flat plate section	0	0	0	0
P-K section	-0.054	1.186	0.017	0.032
Closed box section	-0.128	0.070	-0.007	-0.172

6.5 Probabilistic solutions

Table 6.6 listed 15 cases for comparing the probabilistic solutions of flutter critical wind speeds of two bridge structures as defined before, i.e. the simply supported beam bridge and the Jiangyin Suspension Bridge by setting different sources of uncertainties. The random input parameters including the structural modal parameters and damping ratios are given in section 6.3. The FDs of the four sections are employed, as discussed in section 6.4. The 2D SBSA and 3D multimode approaches will be adopted to achieve the probabilistic solutions of flutter critical speeds based on Monte Carlo technique, respectively. In Table 6.6, the #1 case is the deterministic solution with the flutter derivatives of the ideal flat plate section (Fig.

6.2). #2~#3 cases independently take the random structural modal parameters and random damping ratios into account. #4~#9 cases only consider the randomness of flutter derivatives and last six cases utilize all random inputs with different random models of FDs.

Table 6.6 Calculation cases for probabilistic solutions

Cases	Simply supported beam			Jiangyin suspension bridge		
	Mode	Damping	FD	Mode	Damping	FD
#1	DM	$\zeta_h = 0; \zeta_\alpha = 0$	FD1	DM	$\zeta_h = 0.5\%; \zeta_\alpha = 0.5\%$	FD1
#2	Random	$\zeta_h = 0; \zeta_\alpha = 0$	FD1	Random	$\zeta_h = 0.5\%; \zeta_\alpha = 0.5\%$	FD1
#3	DM	Random	FD1	DM	Random	FD1
#4	DM	$\zeta_h = 0; \zeta_\alpha = 0$	Random (FD2_1)	DM	$\zeta_h = 0.5\%; \zeta_\alpha = 0.5\%$	Random (FD2_1)
#5	DM	$\zeta_h = 0; \zeta_\alpha = 0$	Random (FD2_5)	DM	$\zeta_h = 0.5\%; \zeta_\alpha = 0.5\%$	Random (FD2_5)
#6	DM	$\zeta_h = 0; \zeta_\alpha = 0$	Random (FD2_10)	DM	$\zeta_h = 0.5\%; \zeta_\alpha = 0.5\%$	Random (FD2_10)
#7	DM	$\zeta_h = 0; \zeta_\alpha = 0$	Random (FD2_14)	DM	$\zeta_h = 0.5\%; \zeta_\alpha = 0.5\%$	Random (FD2_14)
#8	DM	$\zeta_h = 0; \zeta_\alpha = 0$	Random (FD3)	DM	$\zeta_h = 0.5\%; \zeta_\alpha = 0.5\%$	Random (FD3)
#9	DM	$\zeta_h = 0; \zeta_\alpha = 0$	Random (FD4)	DM	$\zeta_h = 0.5\%; \zeta_\alpha = 0.5\%$	Random (FD4)
#10	Random	Random	Random (FD2_1)	Random	Random	Random (FD2_1)
#11	Random	Random	Random (FD2_5)	Random	Random	Random (FD2_5)
#12	Random	Random	Random (FD2_10)	Random	Random	Random (FD2_10)
#13	Random	Random	Random (FD2_14)	Random	Random	Random (FD2_14)
#14	Random	Random	Random (FD3)	Random	Random	Random (FD3)
#15	Random	Random	Random (FD4)	Random	Random	Random (FD4)

Note: DM indicates the information obtained from the deterministic model; FD1, FD2, FD3, and FD4 are the flutter derivatives of the ideal flat plate section, quasi-flat plate section, PK section and closed-box section, respectively as defined in Fig. 6.6-6.8. FD2_1, FD2_5, FD2_10, FD2_14 are the flutter derivatives of the quasi-flat plate section extracted from 1%, 5%, 10% and 14% turbulent winds.

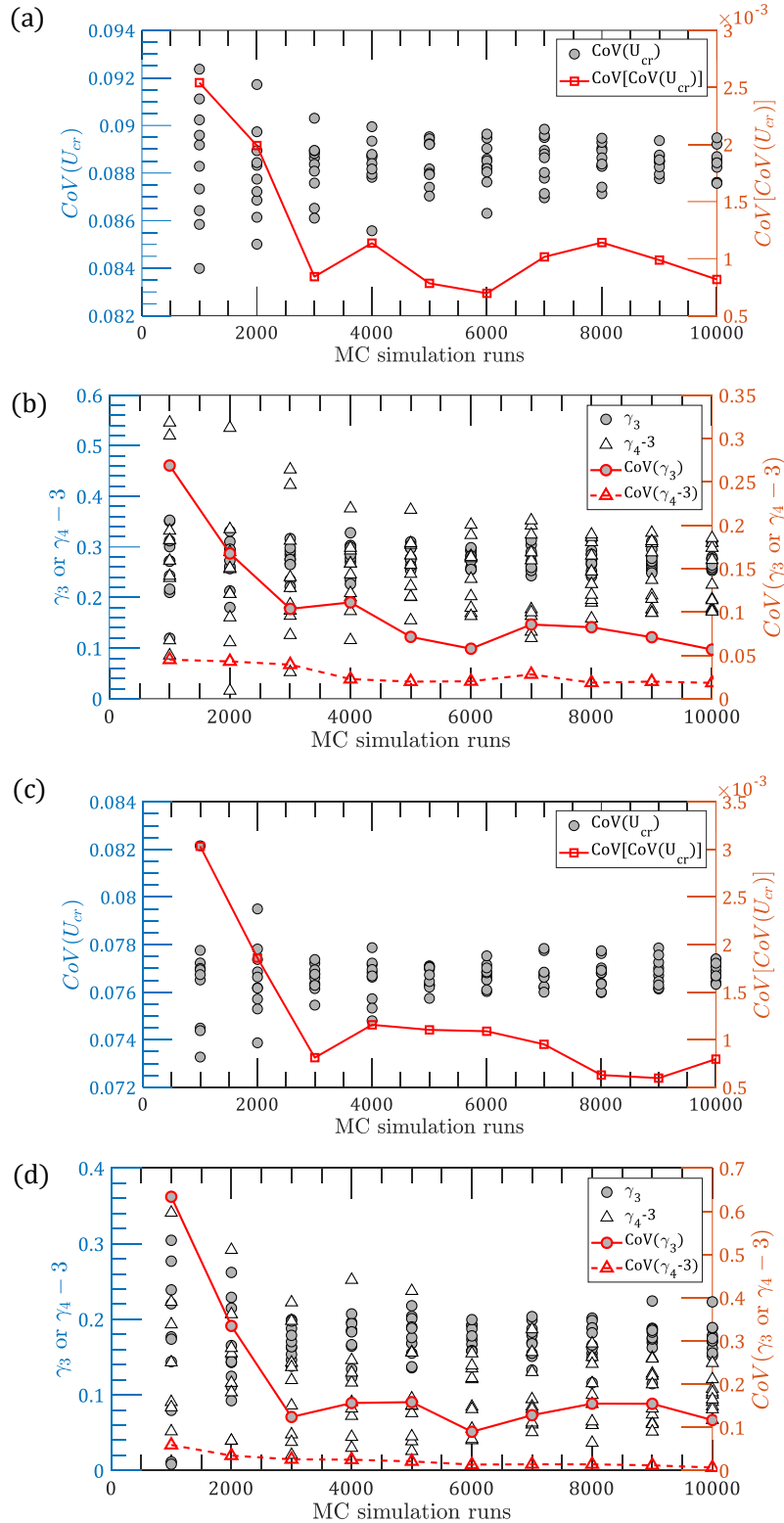


Fig. 6.13 Effects of MC simulation runs on the probabilistic solution of critical wind speed: (a) CoV for SBSA method; (b) γ_3 and γ_4 for SBSA method; (c) CoV for multimode method; (d) γ_3 and γ_4 for multimode method

Before conducting the stochastic study, an important issue that how many Monte Carlo simulations are adequate to produce a converged prediction should be prescribed. Generally, a reasonable number of MC runs is required to achieve some converged and stable statistical results of predictions, such as CDF, mean, standard deviation skewness and kurtosis. 10 repetitions for $n \times 10^3$ ($n = 1, \dots, 10$) simulations are conducted both for SBSA and multimode approaches, respectively. The scatter plots of the coefficient of variation (CoV) as well as skewness γ_3 and kurtosis γ_4 of simulated critical wind speeds for each repetition are illustrated in Fig 6.13. Their dispersions are observed to decrease and gradually converge to a constant with the increase of MC simulation numbers. Correspondingly, the variation of CoVs of these three statistics versus MC simulation numbers is also plotted. They tend to become steady when the simulation times are larger than 4×10^3 . In this study, 10^4 simulations will be adopted in this study in which case the CoVs of ten repetitions for CoV, skewness, and kurtosis of critical winds are 8.18×10^{-4} , 0.06, 0.02 for SBSA method and 7.97×10^{-4} , 0.12, 0.007 for the multimode method, respectively.

Table 6.7 listed the statistics, i.e. mean, standard deviation and coefficient of variation (CoV) of simulated solutions of flutter critical wind speed as reduced well as reduced wind speeds. Correspondingly, the empirical PDFs and CDFs of all cases are illustrated in Fig. 6.14. Several conclusions can be drawn as follows:

(1) #1~#3 cases indicate that the critical wind speeds are more sensitive to the modal parameters, say natural frequencies than damping ratios. Because of the CoV of the frequency of first symmetric torsional mode in Fig. 6.3 is about 0.055 which is much smaller than the CoV of damping ratio of torsional mode is 0.53 as shown in Fig. 6.5, but the CoV of critical wind speed of #2 case are five times of that in #3 case.

(2) #4~#7 cases indicate that the introduction of turbulence with low turbulence intensity (roughly less than 10%) is favorable to improve flutter performance. As can be seen, the mean critical wind speed has a 2% increase using SBSA method and 10% increase using multimode method when the turbulence intensity increases from 1% to 10%. However, the mean of critical wind speed suffers an unexpected drop when the turbulence intensity reaches up to 14%. A 17% and 8% decrease of mean wind speed obtained from SBSA method and multimode method, respectively can be observed. Meanwhile, the increase of turbulence intensity also contributes greater dispersions of critical wind speed.

(3) #4 and #8~#9 cases suggest the quasi-flat plate has the best flutter performance followed by the closed-box section. And the P-K section girder shows the worst flutter stability. Interestingly, the FDs of both #4 and #8 cases are obtained from repeated wind tunnel test in laminar or 1% turbulent flow, #8 case has a smaller CoV of critical wind speed than #4 case, which implies the uncertainties of FDs are section-geometry-dependent. Although FDs in #9 were collected from the literature survey for the same closed-box section, the probabilistic solutions of critical wind speeds show a significant variation, suggesting the inter-lab- and identification-technique-induced uncertainties of FDs could be very important and should be carefully studied.

(4) As expected, #10~#15 cases show a greater variability of critical wind speed when the uncertainties of all parameters are introduced. And similar trend as discussed in (2) ~ (3) can be noted.

(5) Generally, the 3D multimode method provides slightly lower predictions of critical wind speed than that of the 2D SBSA method except the #6, #12 and #7, #13 cases, which introduce turbulence effects with the turbulence intensity of 10% and 14%, respectively. The

reason is not well understood. It could be because the change of FDs allows the aerodynamic force and energy to be shared with more modes, which would benefit to reduce the energy of the mode of flutter.

(6) Multimodal distribution of critical wind speed obtained from the 2D SBSA method was found in #7 and #8 cases, which should be carefully considered in the flutter failure analysis.

Table 6.7 Statistics of probabilistic flutter solutions for the simply supported beam

Cases	Simply supported beam (B = 40 m)											
	2D SBSA						3D Multimode					
	U_{cr}			$U_{cr,R}$			U_{cr}			$U_{cr,R}$		
	μ	σ	CoV	μ	σ	CoV	μ	σ	CoV	μ	σ	CoV
#1	139.90	/	/	9.22	/	/	139.70	/	/	9.20	/	/
#2	139.93	7.01	0.05	9.22	0.22	0.02	139.38	6.94	0.05	9.18	0.22	0.02
#3	144.26	2.00	0.01	9.72	0.23	0.02	143.05	1.69	0.01	9.58	0.19	0.02
#4	142.33	10.00	0.07	7.95	0.66	0.08	139.64	6.18	0.04	7.68	0.38	0.05
#5	143.03	14.72	0.10	7.95	0.92	0.12	140.78	7.78	0.06	7.74	0.48	0.06
#6	145.14	18.20	0.13	8.19	1.23	0.15	153.67	15.83	0.10	8.69	1.04	0.12
#7	118.04	20.90	0.18	6.49	1.35	0.21	128.61	22.21	0.17	7.15	1.41	0.20
#8	79.37	1.95	0.02	4.20	0.11	0.03	72.89	1.19	0.02	3.82	0.07	0.02
#9	114.41	14.14	0.13	6.67	0.97	0.15	107.52	13.02	0.12	6.15	0.85	0.14
#10	158.14	13.93	0.09	9.00	0.82	0.09	154.81	11.80	0.08	8.66	0.65	0.07
#11	162.04	16.48	0.10	9.18	0.97	0.11	159.87	13.42	0.08	8.95	0.74	0.08
#12	160.42	20.64	0.13	9.22	1.33	0.14	169.66	17.15	0.10	9.78	1.09	0.11
#13	142.43	24.76	0.17	8.07	1.60	0.20	149.87	25.26	0.17	8.53	1.63	0.19
#14	89.10	5.75	0.06	4.80	0.23	0.05	83.33	6.48	0.08	4.45	0.31	0.07
#15	124.77	11.55	0.09	7.46	0.73	0.10	118.07	12.88	0.11	6.87	0.80	0.12

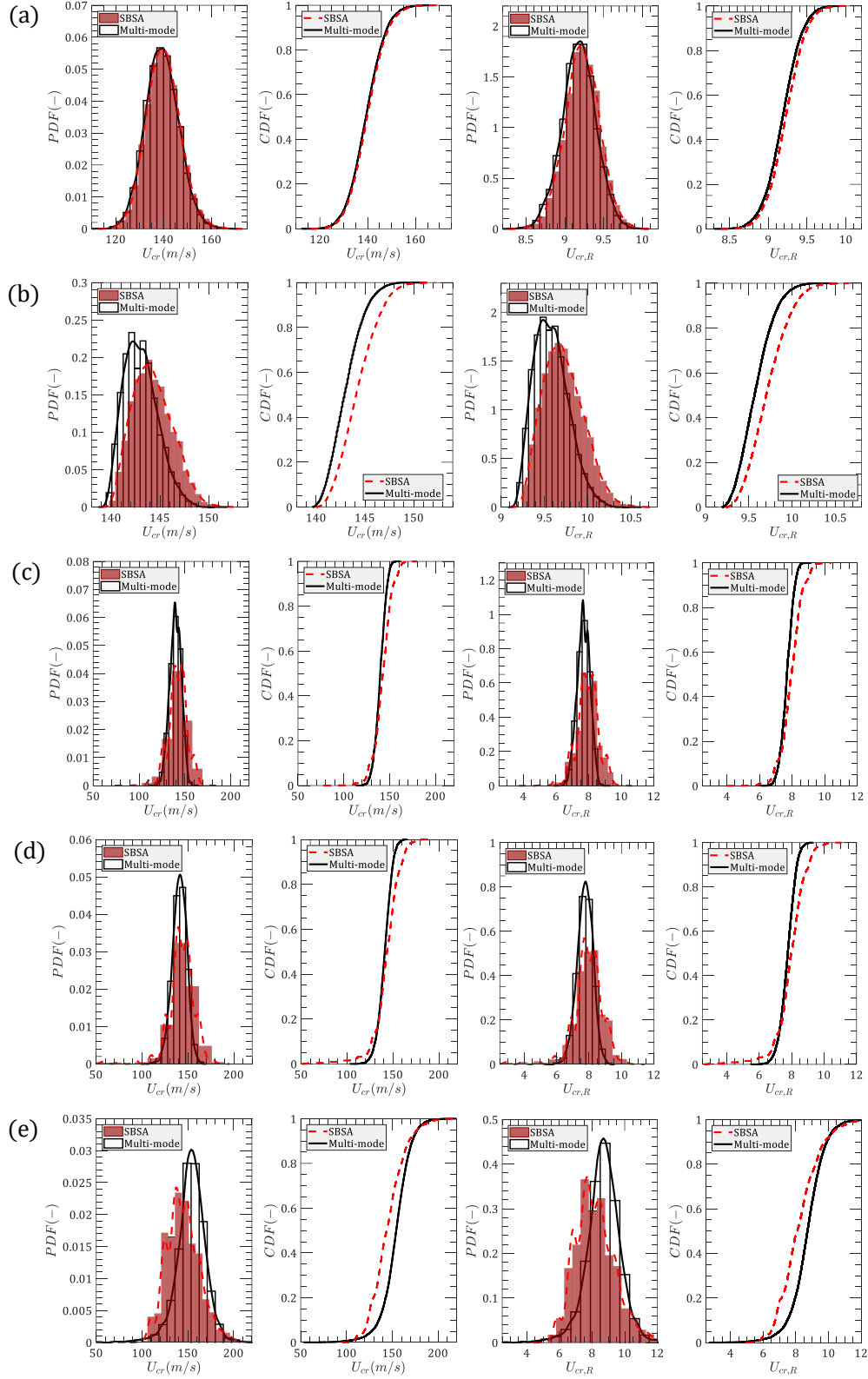


Fig. 6.14 Empirical PDFs and CDFs of probabilistic flutter solutions for the simply supported beam:

(a)~(e) Cases #2~#6

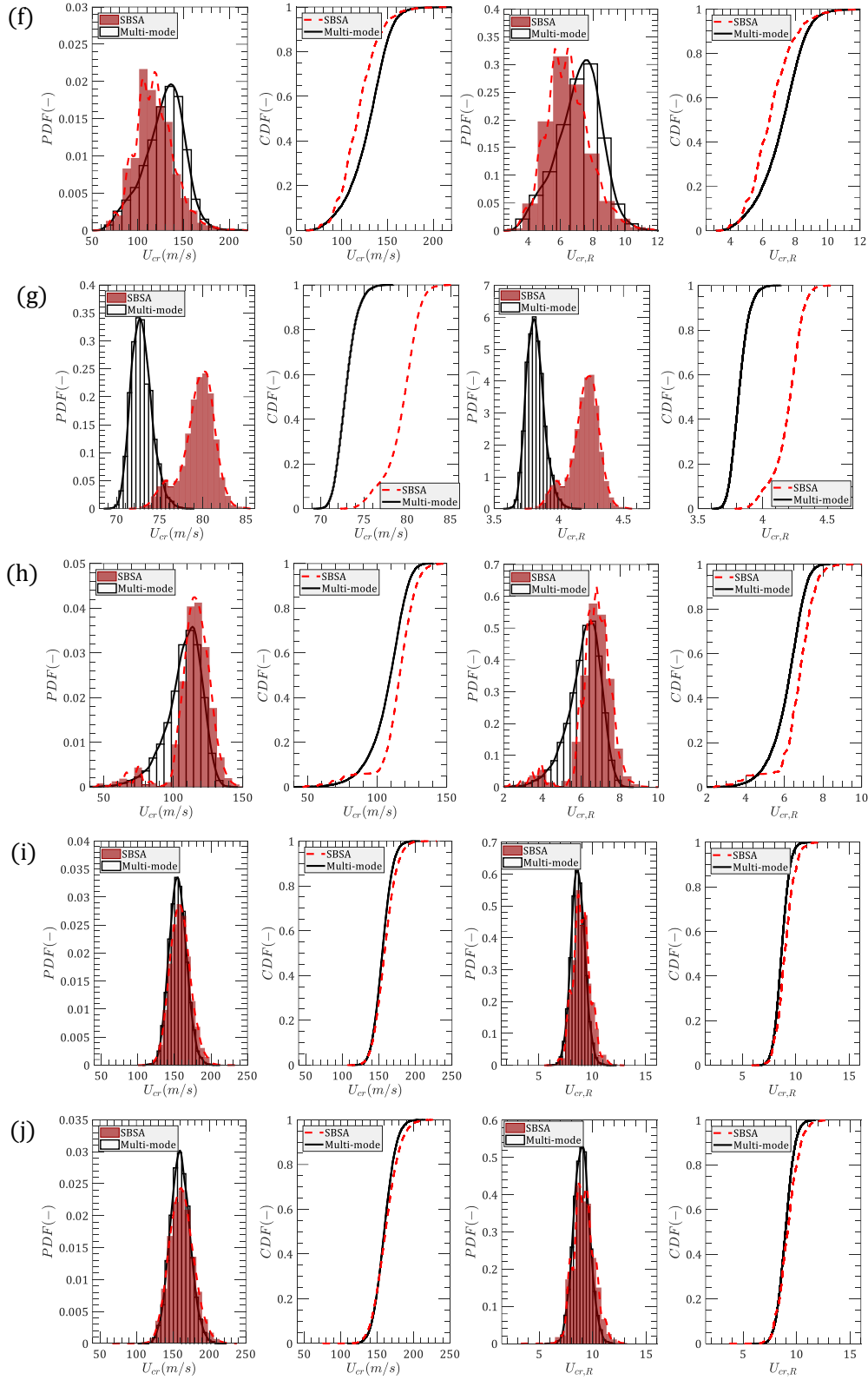


Fig. 6.14 (cont.) Empirical PDFs and CDFs of probabilistic flutter solutions for the simply supported beam: (f)~(j) Case #7~#11

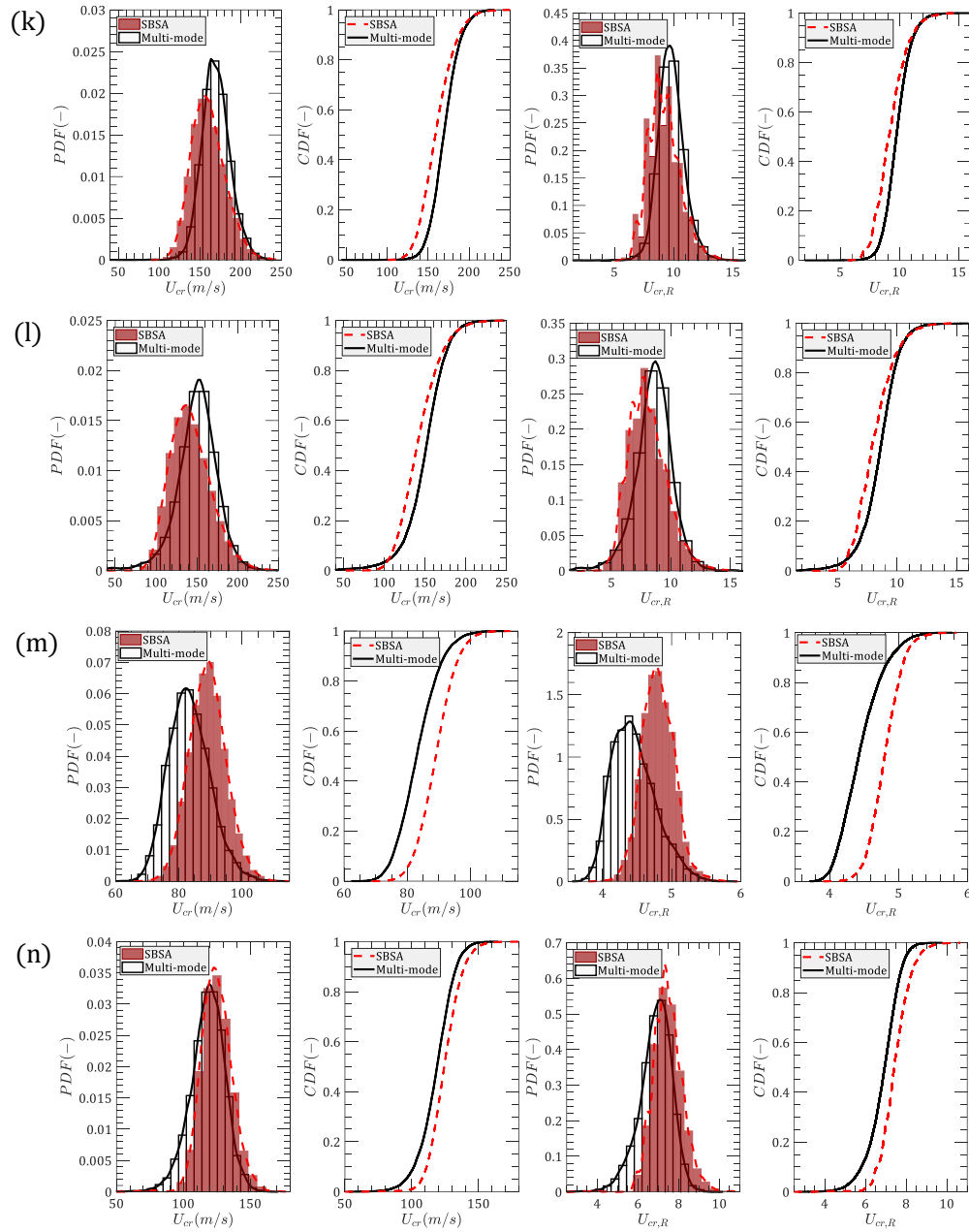


Fig. 6.14 (cont.) Empirical PDFs and CDFs of probabilistic flutter solutions for the simply supported beam: (k)~(n) Case #12~#15

Table 6.8 Statistics of probabilistic flutter solutions for the Jiangyin Suspension Bridge

Cases	Jiangyin suspension bridge (B = 36.9 m)											
	2D SBSA						3D Multimode					
	U_{cr}			$U_{cr,R}$			U_{cr}			$U_{cr,R}$		
	μ	σ	CoV	μ	σ	CoV	μ	σ	CoV	μ	σ	CoV
#1	74.05	/	/	10.06	/	/	70.70	/	/	9.01	/	/
#2	74.17	3.71	0.05	10.12	0.14	0.01	71.28	4.33	0.06	9.16	0.60	0.07
#3	74.96	0.73	0.01	10.26	0.17	0.02	72.16	1.92	0.03	9.27	0.35	0.04
#4	84.44	4.78	0.06	9.81	0.66	0.07	77.80	2.50	0.03	8.74	0.32	0.04
#5	86.03	6.09	0.07	9.91	0.82	0.08	79.83	3.08	0.04	8.97	0.39	0.04
#6	85.43	9.82	0.11	10.01	1.37	0.14	84.89	6.81	0.08	9.76	0.91	0.09
#7	74.65	12.06	0.16	8.59	1.64	0.19	74.83	10.80	0.14	8.51	1.41	0.17
#8	43.88	0.30	0.01	4.75	0.04	0.01	40.73	0.79	0.02	4.37	0.10	0.02
#9	64.54	4.41	0.07	7.81	0.63	0.08	58.42	4.99	0.09	6.76	0.65	0.10
#10	88.26	7.48	0.08	10.36	0.85	0.08	81.43	8.19	0.10	9.22	0.98	0.11
#11	90.24	8.65	0.10	10.49	1.00	0.10	83.55	8.31	0.10	9.45	0.93	0.10
#12	88.62	12.00	0.14	10.48	1.56	0.15	88.57	10.93	0.12	10.27	1.39	0.14
#13	80.21	13.92	0.17	9.35	1.83	0.20	79.01	13.71	0.17	9.08	1.74	0.19
#14	45.67	2.97	0.07	5.00	0.25	0.05	42.65	3.71	0.09	4.62	0.38	0.08
#15	66.22	5.86	0.09	8.11	0.72	0.09	61.56	7.76	0.13	7.18	0.95	0.13

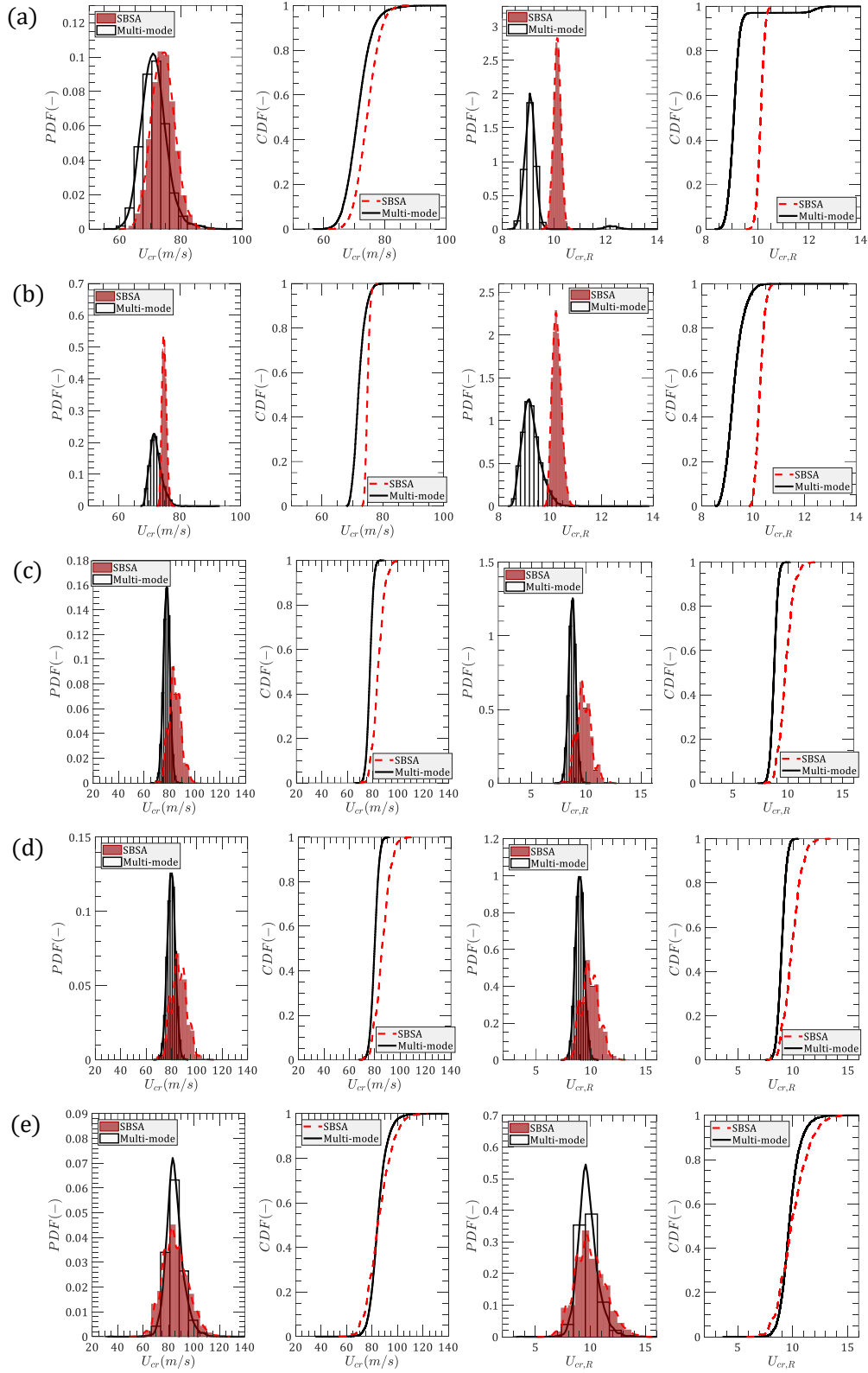


Fig. 6.15 Empirical PDFs and CDFs of probabilistic flutter solutions for the Jiangyin Suspension Bridge:

(a)~(e) Cases #2~#6

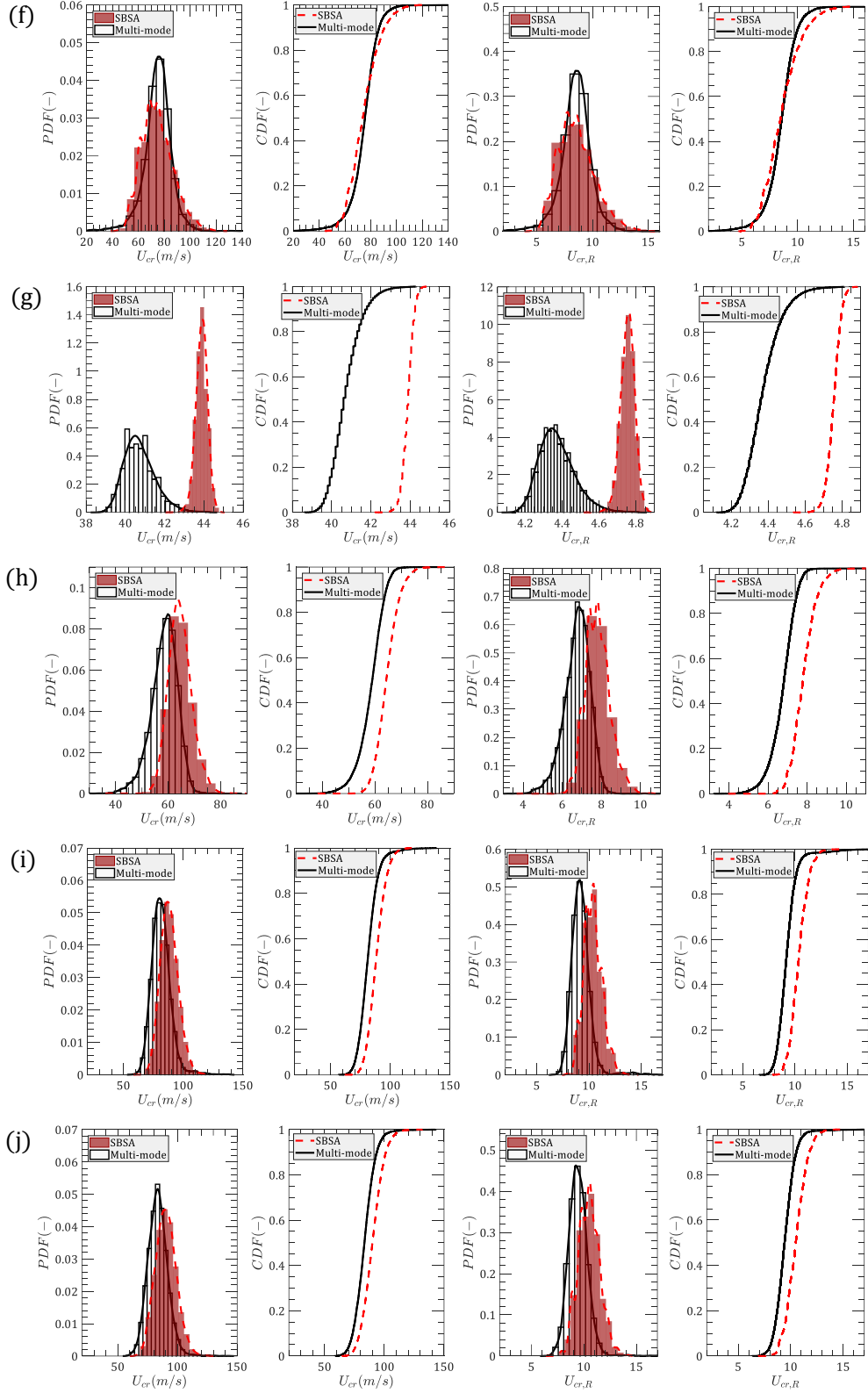


Fig. 6.15 (cont.) Empirical PDFs and CDFs of probabilistic flutter solutions for the Jiangyin Suspension Bridge: (f)~(j) Case #7~#11

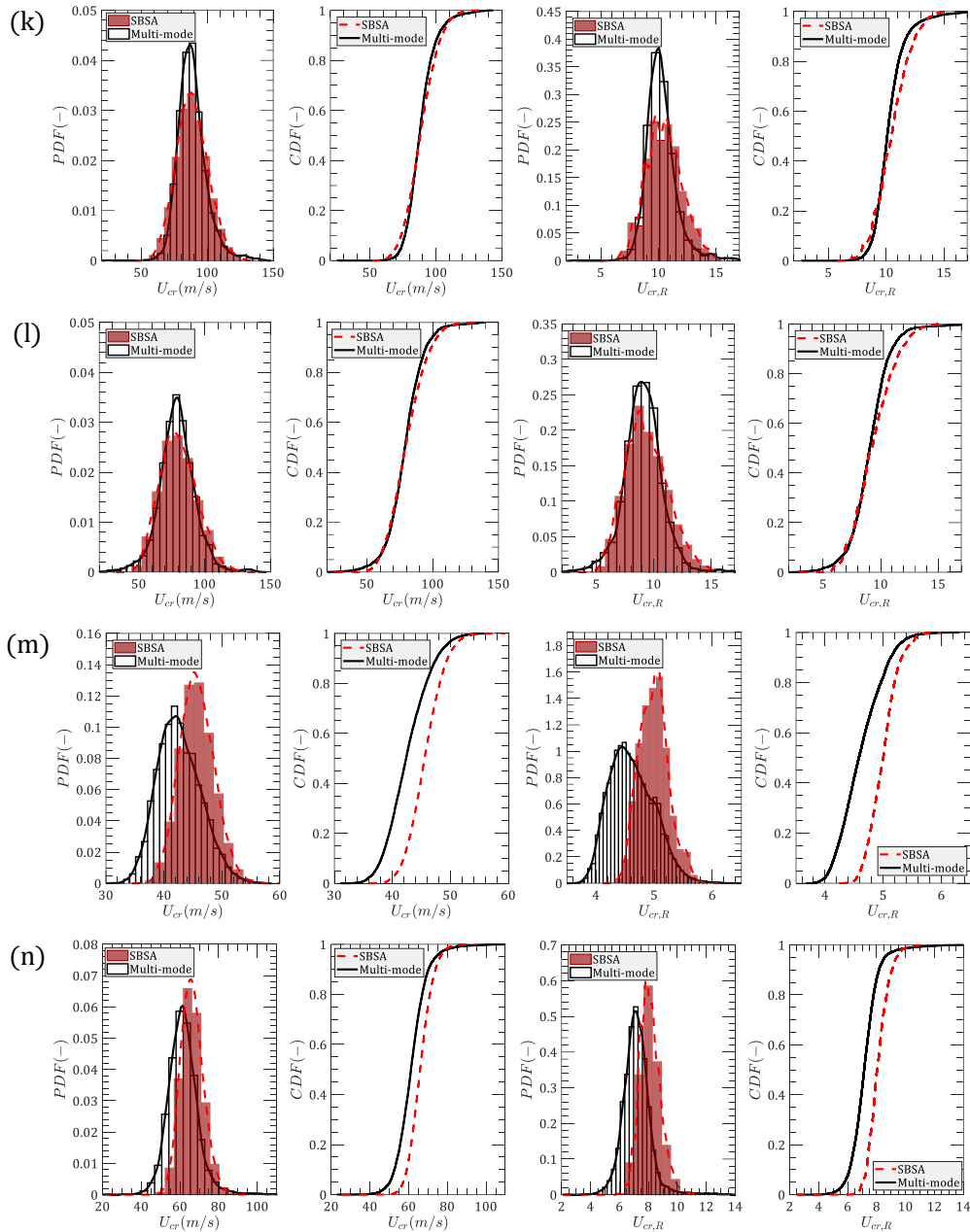


Fig. 6.15 (cont.) Empirical PDFs and CDFs of probabilistic flutter solutions for the Jiangyin Suspension Bridge: (k)~(n) Case #12~#15

Table 6.8 and Fig. 6.15 listed the results of probabilistic solutions of flutter critical wind speed for Jiangyin Suspension Bridge using various random inputs. Similar conclusions can be achieved to that of the simply supported beam bridge in Table 6.7 and Fig. 6.14. The most interesting finding is that the 14% turbulence intensity (#7 case) would decrease the mean

critical wind speed of flutter, but the mean values are very close to each other between 2D SBSA and multimode approaches, which is different from that in previous conclusions. And Fig. 6.15 (c)~(f) also show that the distributions between 2D SBSA and 3D Multimode methods gradually coincide with each other with the increase of turbulence intensity. The reasons for this phenomenon were unclear. The use of FDs related to different reduced wind speeds, the multimodal effects due to turbulence intensity and the characteristics of natural modes of the bridge structure could contribute to this result.

6.6 Conclusion

This chapter develops a framework to investigate the probabilistic solutions of flutter instability in terms of critical wind speed accounting for multiple resources of uncertainty to facilitate the development of the fragility curve of flutter issue of long-span bridges. The structural uncertainties, including the natural modes of vibration and damping ratio of the bridge structure were examined using stochastic finite element method and the literature survey results, respectively. The aerodynamic uncertainties or the variability of FDs of two sections, i.e. a quasi-flat plate section and a PK section were quantified using repeated wind tunnel tests. Meanwhile, the literature survey was performed on quasi-flat plate sections and a closed-box section to quantify the inter-lab- and identification-technique-induced uncertainties of FDs.

A series of probabilistic solutions of flutter onset for two bridges, say a simply supported beam bridge and the Jiangyin Suspension Bridge were achieved by introducing different sources of uncertainty. It was found that the turbulence would increase the dispersion of flutter critical wind speed. And large turbulence intensity, i.e. 14% could reduce the flutter

instability onset when compared with that in laminar flow from the statistical perspective. An interesting finding is that the distributions of flutter critical wind speed between 2D SBSA and 3D multimode methods gradually cross with each other with the increase of turbulence intensity.

6.7 Reference

Abbas T, Kavrakov I, Morgenthal, G, (2017). Methods for flutter stability analysis of long-span bridges: a review. *Proceedings of the Institution of Civil Engineers - Bridge Engineering*, 1-40.

Abbas T, Morgenthal G, (2016). Framework for sensitivity and uncertainty quantification in the flutter assessment of bridges. *Probabilistic Engineering Mechanics*, 43:91-105.

Agar T J A, (1989). Aerodynamic flutter analysis of suspension bridges by a modal technique. *Engineering Structures*, 11(2), 75-82.

Agar T J A, (1991). Dynamic instability of suspension bridges. *Computers & Structures*, 41(6), 1321-1328.

Argentini T, Pagani A, Rocchi D, et al., (2014). Monte Carlo analysis of total damping and flutter speed of a long span bridge: Effects of structural and aerodynamic uncertainties. *Journal of Wind Engineering and Industrial Aerodynamics*, 128:90-104.

Barbato M, Gu Q, Conte, J P, (2010). Probabilistic Push-Over Analysis of Structural and Soil-Structure Systems. *Journal of Structural Engineering*, 136(11), 1330-1341.

Baldomir A, Kusano I, Hernandez S, et al., (2013). A reliability study for the Messina Bridge with respect to flutter phenomena considering uncertainties in experimental and numerical data. *Computers & Structures*, 128:91-100.

Bartoli G, Mannini C, (2008). A simplified approach to bridge deck flutter. *Journal of Wind Engineering & Industrial Aerodynamics*, 96(2):229-256.

Bartoli G, Contri S, Mannini C, et al., (2009). Toward an Improvement in the Identification of Bridge Deck Flutter Derivatives. *Journal of Engineering Mechanics*, 135(8):771-785.

Beith, J G, (1998). A practical engineering method for the flutter analysis of long span bridges. *Journal of Wind Engineering & Industrial Aerodynamics*, 77(98), 357-366.

Boonyapinyo, V, Miyata, T, Yamada, H, (1999). Advanced aerodynamic analysis of suspension bridges by state-space approach. *Journal of Structural Engineering*, 125(12), 1357-1366.

Bucher C G, Lin Y K, (1988). Stochastic stability of bridges considering coupled modes. *Journal of Engineering Mechanics*, 114(12), 2055-2071.

Cao F, Ge Y, (2017). Air-induced nonlinear damping and added mass of vertically vibrating bridge deck section models under zero wind speed. *Journal of Wind Engineering and Industrial Aerodynamics*, 169:217-231.

Caracoglia L, Sarkar P P, Jr F L H, et al., (2009). Comparative and sensitivity study of flutter derivatives of selected bridge deck sections, Part 2: Implications on the aerodynamic stability of long-span bridges. *Engineering Structures*, 31(9):2194-2202.

Chen X, Matsumoto, M, Kareem, A, (2000). Time domain flutter and buffeting response analysis of bridges. *Journal of Engineering Mechanics*, 126(1), 7-16.

Chen X, Matsumoto, M., Kareem, A, (2000). Aerodynamic coupling effects on flutter and buffeting of bridges. *Journal of Engineering Mechanics*, 126(1), 17-26.

Chen X, Kareem, A, Matsumoto, M, (2001). Multimode coupled flutter and buffeting analysis of long span bridges. *Journal of Wind Engineering & Industrial Aerodynamics*, 89(7), 649-664.

Chen X, Kareem, A, (2002). Advances in modeling of aerodynamic forces on bridge decks. *Journal of Engineering Mechanics*, 128: 1193-1205.

Cheng J, Cai C S, Xiao R C, et al., (2005). Flutter reliability analysis of suspension bridges[J]. *Journal of Wind Engineering and Industrial Aerodynamics*, 93(10):757-775.

Chowdhury A G, Sarkar P P, (2003). A new technique for identification of eighteen flutter derivatives using a three-degree-of-freedom section model. *Engineering Structures*, 25(14):1763-1772.

Ciampoli M, Petrini F, Augusti G, (2011). Performance-Based Wind Engineering: Towards a general procedure. *Structural Safety*, 33(6):367-378.

D'Asdia, P, Sepe, V, (1998). Aeroelastic instability of long-span suspended bridges: a multi-mode approach. *Journal of Wind Engineering & Industrial Aerodynamics*, 74(2), 849-857.

Davenport G, Larose G, (1989). The structural damping of long span bridges: an interpretation of observation. *Canada-Japan Workshop on Bridge Aerodynamics*, Ottawa.

Diana G, Resta F, Zasso A, et al., (2004). Forced motion and free motion aeroelastic tests on a new concept dynamometric section model of the Messina suspension bridge. *Journal of Wind Engineering & Industrial Aerodynamics*, 92(6):441-462.

Diana G, Rocchi D, Argentini T, et al., (2010). Aerodynamic instability of a bridge deck section model: Linear and nonlinear approach to force modeling. *Journal of Wind Engineering & Industrial Aerodynamics*, 98(6):363-374.

Diana G, Rocchi D, Belloli M, (2015). Wind tunnel: a fundamental tool for long-span bridge design. *Structure and Infrastructure Engineering*, 11(4):533-555.

Ding Q, Chen A, Xiang H, (2002). Coupled flutter analysis of long-span bridges by multimode and full-order approaches. *Journal of Wind Engineering and Industrial Aerodynamics*, 90, 1981-1993.

Ding Q, Zhou Z Y, Zhu L, Xiang H, (2010). Identification of flutter derivatives of bridge decks with free vibration technique. *Journal of Wind Engineering and Industrial Aerodynamics*, 98, 911-918.

Dung N N, Miyata T, Yamada H, Minh N N, (1998). Flutter responses in long span bridges with wind induced displacement by the mode tracing method. *Journal of Wind Engineering and Industrial Aerodynamics*, 77-78, 367-379.

Fabio R, Luca C, Sergio M, (2018). Predicting the flutter speed of a pedestrian suspension bridge through examination of laboratory experimental errors. *Engineering Structures*, 172:589-613.

Frandsen J B, (2004). Numerical bridge deck studies using finite elements. Part I: flutter. *Journal of Fluids & Structures*, 19(2):171-191.

Fujino, Y. (2002). Vibration, control and monitoring of long-span bridges - recent research, developments and practice in japan. *Journal of Constructional Steel Research*, 58(1), 71-97.

Ge Y J, Tanaka H, (2000). Aerodynamic flutter analysis of cable-supported bridges by multi-mode and full-mode approaches. *Journal of Wind Engineering and Industrial Aerodynamics*, 86, 123-153.

Ge Y J, Xiang H F, Tanaka H, (2000). Application of a reliability analysis model to bridge flutter under extreme winds. *Journal of Wind Engineering & Industrial Aerodynamics*, 86(2):155-167.

Ge Y J, Xiang H F, (2008). Computational models and methods for aerodynamic flutter of long-span bridges. *Journal of Wind Engineering & Industrial Aerodynamics*, 96(10):1912-1924.

Ge Y J, Tanaka H, (2000). Aerodynamic flutter analysis of cable-supported bridges by multi-mode and full-mode approaches. *Journal of Wind Engineering and Industrial Aerodynamics*, 86: 123-153.

Ge Y, Xia J, Zhao L and Zhao S, (2018) Full Aeroelastic Model Testing for Examining Wind-Induced Vibration of a 5,000 m Spanned Suspension Bridge. *Front. Built Environ.* 4:20.

Gimsing N J, Georgakis C T, (2012). *Cable Supported Bridges: Concept and Design*, Third Edition. New York: John Wiley & Sons, Ltd.

Gu M, Zhang R, Xiang H, (2000). Identification of flutter derivatives of bridge decks. *Journal of Wind Engineering and Industrial Aerodynamics*, 84(2), 151-162.

Gu M, Zhang R, & Xiang H, (2001). Parametric study on flutter derivatives of bridge decks. *Engineering Structures*, 23(12), 1607-1613.

Gu M, & Qin X R, (2004). Direct identification of flutter derivatives and aerodynamic admittances of bridge decks. *Engineering Structures*, 26(14), 2161-2172.

Guo Z S, Chen A R, Xiang H F, (2000). Characteristics of structural damping of cable-supported bridges with long spans. *World Information on Earthquake Engineering*, 16(3), 52-57 (in Chinese).

Guo Z W, Ge Y J, (2012). A new state-space model for self-excited forces and straight forward analysis of bridge deck flutter. The Seventh International Colloquium on Bluff Body Aerodynamics and Applications (BBAA7), Shanghai, China, 480-489.

Haan Jr F L, Kareem A, 2009. Anatomy of turbulence effects on the aerodynamics of an oscillating prism. J. Eng. Mech. ASCE 135, 987–999.

Hua X G, Chen Z Q, Ni Y Q, Ko J M, (2007). Flutter analysis of long-span bridges using ANSYS. Wind and Structures An International Journal, 10(1), 61-82.

Hua X G, Chen Z Q, (2008). Full-order and multimode flutter analysis using ANSYS. Finite Elements in Analysis and Design, 44(9-10), 537-551.

Hatanaka A, Tanaka H, (2005). Effects of upstream gusting on flutter derivatives of bluff bodies. In: Proceeding of the Sixth Asia-Pacific Conference on Wind Engineering. Seoul, Korea, 491-506.

Huston D R. (1986), The effects of upstream gusting on the aeroelastic behavior of long-suspended span bridges, PhD Dissertation, Princeton University.

Ibuki K, Aitor B, Jurado José ángel, et al., (2018). The importance of correlation among flutter derivatives for the reliability based optimum design of suspension bridges[J]. Engineering Structures, 173:416-428.

Jain A, Jones N P, Scanlan R H, (1996a). Coupled aeroelastic and aerodynamic response analysis of long-span bridges. Journal of Wind Engineering & Industrial Aerodynamics, 60, 69-80.

Jain A, Jones N P, Scanlan R H, (1996b). Coupled flutter and buffeting analysis of long-span bridges. Journal of Structural Engineering, 122(7), 716-725.

Katsuchi H, Jones N P, Scanlan R H, Akiyama H, (1998a). Multi-mode flutter and buffeting analysis of the Akashi-Kaikyo bridge. *Journal of Wind Engineering & Industrial Aerodynamics*, 77–78(5), 431-441.

Katsuchi H, Jones N P, Scanlan H R, Akiyama H, (1998b). A Study of Mode Coupling in Flutter and Buffeting of the Akashi-Kaikyo Bridge, *Structural Eng./Earthquake Eng., JSCE*, 15(2), 175-190.

Katsuchi H, Jones N P, Scanlan R H, (1999). Multimode coupled flutter and buffeting analysis of the Akashi-Kaikyo bridge. *Journal of Structural Engineering*, 125(1), 60-70.

Kim S, Kim H K. (2017). Damping identification of bridges under nonstationary ambient vibration. *Engineering*, 3, 839-844.

Kim S, Jung H, Kong M J, Lee D K, An Y K, (2019). In-situ data-driven buffeting response analysis of a cable-stayed bridge. *Sensors*, 19, 3048.

Lagaros, Nikos D, (2014). Risk assessment of steel and steel-concrete composite 3d buildings considering sources of uncertainty. *Earthquakes and Structures*, 6(1), 19-43.

Larsen A, Walther J H, (1997). Aeroelastic analysis of bridge girder sections based on discrete vortex simulations. *Journal of Wind Engineering & Industrial Aerodynamics*, 67(97):253-265.

Li K, Ge Y J, Guo Z W, Zhao L, (2015). Theoretical framework of feedback aerodynamic control of flutter oscillation for long-span suspension bridges by the twin-winglet system. *Journal of Wind Engineering & Industrial Aerodynamics*, 145, 166-177.

Li Y, Liao H, Qiang S, (2003). Weighting ensemble least-square method for flutter derivatives of bridge decks. *Journal of Wind Engineering & Industrial Aerodynamics*, 91(6):713-721.

Li Z, Feng M Q, Luo L, Feng D, Xu X, (2018). Statistical analysis of modal parameters of a suspension bridge based on Bayesian spectral density approach and SHM data. *Mechanical Systems and Signal Processing*, 98, 352-367.

Lin Y K, and Yang J N, (1983). Multimode bridge response to wind excitations. *J. Eng. Mech.*, 109(2), 586–603.

Liu Y, Ge Y J, Cao F C, Zhou Y, Wang S Q. (2013). Statistics and identification of mode-dependent structural damping of cable-supported bridges. *Proceeding of the 8th Asia-Pacific Conference on Wind Engineering (APCWE-VIII)*, Chennai, India, 719-731.

Mannini C, Bartoli G, (2015). Aerodynamic uncertainty propagation in bridge flutter analysis. *Structural Safety*, 52:29-39.

Matsumoto M, Shirato H, & Hirai S. (1992). Torsional flutter mechanism of 2-D H-shaped cylinders and effect of flow turbulence. *Journal of Wind Engineering and Industrial Aerodynamics*, 41(1-3), 687-698.

Matsumoto M. (1996). Aerodynamic damping of prisms. *Journal of Wind Engineering and Industrial Aerodynamics*, 59: 159-175.

Matsumoto M, Matsumiya H, Fujiwara S, et al. (2010). New consideration on flutter properties based on step-by-step analysis. *Journal of Wind Engineering & Industrial Aerodynamics*, 98(8):429-437.

Mishra, S. S. , Kumar, K. , & Krishna, P. . (2008). Multimode flutter of long-span cable-stayed bridge based on 18 experimental aeroelastic derivatives. *Journal of Wind Engineering and Industrial Aerodynamics*, 96(1), 83-102.

Miyata, T. , & Yamada, H. . (1990). Coupled flutter estimate of a suspension bridge. *Journal of Wind Engineering & Industrial Aerodynamics*, 33(1), 341-348.

Miyata, T. , & Yamaguchi, K. . (1993). Aerodynamics of wind effects on the akashi kaikyo bridge. *Journal of Wind Engineering and Industrial Aerodynamics*, 48(2), 287-315.

Nagayama T, Abe M, Fujino Y, Ikeda K. Structural identification of a non-proportionally damped system and its application to a full-scale suspension bridge. *Journal of Structural Engineering (ASCE)* 2005;131(10):1536–45.

Namini, A. , Albrecht, P. , & Bosch, H. . (1992). Finite element - based flutter analysis of cable - suspended bridges. *Journal of Structural Engineering*, 118(6), 1509-1526.

Orton, S. L. , Kwon, O. S. , & Hazlett, T. . (2012). Statistical distribution of bridge resistance using updated material parameters. *Journal of Bridge Engineering*, 17(3), 462-469.

Ostenfeld-Rosenthal P, Madsen H O, Larsen A. Probabilistic flutter criteria for long span bridges[J]. *Journal of Wind Engineering and Industrial Aerodynamics*, 1992, 42(1):1265-1276.

Pang, Y. , Wu, X. , Shen, G. , & Yuan, W. . (2014). Seismic fragility analysis of cable-stayed bridges considering different sources of uncertainties. *Journal of Bridge Engineering*, 19(4), 04013015.

Pourzeynali S, Datta T K. Reliability analysis of suspension bridges against flutter[J]. *Journal of Sound and Vibration*, 2002, 254(1):143-162.

Qin X and Gu M. Determination of flutter derivatives by stochastic subspace identification technique, *Wind and Structures*, 2004, 7(3): 173-186.

Rizzo F, Caracoglia L. Examination of experimental errors in Scanlan derivatives of a closed-box bridge deck[J]. *Wind and Structures, An International Journal*, 2018, 26(4):2018.

Sarkar P P, Jones N P, Scanlan R H. Identification of Aeroelastic Parameters of Flexible Bridges[J]. *Journal of Engineering Mechanics*, 1994, 120(8):1718-1742.

Sarkar P P, Caracoglia L, Haan F L, et al. Comparative and sensitivity study of flutter derivatives of selected bridge deck sections, Part 1: Analysis of inter-laboratory experimental data[J]. *Engineering Structures*, 2009, 31(1):158-169.

Scanlan, R. H., Beliveau, J-G, and Budlong, K. S. (1974). Indicial aerodynamic functions for bridge decks. *J. Eng. Mech. Div.*, 100(EM4), 657-672.

Scanlan R H. The action of flexible bridges under wind, I: flutter theory. *Journal of Sound and Vibration*, 60(2): 187-199, 1978.

Scanlan, R. H., & Lin, W. H. (1978). Effects of turbulence on bridge flutter derivatives. *Journal of the Engineering Mechanics Division*, 104(4), 719-733.

Scanlan R H, Jones N P , Singh L . Inter-relations among flutter derivatives[J]. *Journal of Wind Engineering and Industrial Aerodynamics*, 1997, 69-71:829-837.

Seo D W, Caracoglia L. Estimation of torsional-flutter probability in flexible bridges considering randomness in flutter derivatives[J]. *Engineering Structures*, 2011, 33(8):2284-2296.

Seo D W, Caracoglia L. Statistical buffeting response of flexible bridges influenced by errors in aeroelastic loading estimation[J]. *Journal of Wind Engineering and Industrial Aerodynamics*, 2012, 104-106:129-140.

Shao, Y.H. (2010), Refinements on aerodynamic and aerostatic stability of super long span suspension bridges with box girder (in Chinese), PhD dissertation, Tongji University, Shanghai, China.

Simiu E and Scanlan RH (1996) *Wind Effects on Structures: Fundamentals and Applications to Design*, 3rd edn. J. Wiley and Sons, New York, NY, USA.

Siringoringo, D. M. , & Fujino, Y. . (2008). System identification of suspension bridge from ambient vibration response. *Engineering Structures*, 30(2), 462-477.

Tanaka, H., Yamamura, N., and Shiraishi, N. (1993). Multi-mode flutter analysis and two and three dimensional model tests on bridges with non-analogous modal shapes. *J. Struct. Mech. and Earthquake Engrg.*, Tokyo, Japan, 10(2), 35-46.

T. Theodorsen, *General Theory of Aerodynamic Instability and the Mechanism of Flutter*, Technical Report No. 496, National Advisory Committee for Aeronautics, 1935.

T. Theodorsen and I. E. Garrick, *Mechanism of Flutter: A Theoretical and Experimental Investigation of the Flutter Problem*, Report 685 (NACA, 1940).

Tubaldi, E. , Barbato, M. , & Dall'Asta, A. (2012). Influence of model parameter uncertainty on seismic transverse response and vulnerability of steel–concrete composite bridges with dual load path. *Journal of Structural Engineering*, 138(3), 363-374.

V. Boonyapinyo, T. Janesupasaeree, Data-driven stochastic subspace identification of flutter derivatives of bridge decks, *Journal of Wind Engineering and Industrial Aerodynamics* 98 (2010) 784–799.

Wilde, K. , & Fujino, Y. . (1998). Aerodynamic control of bridge deck flutter by active surfaces. *Journal of Engineering Mechanics*, 124(7), 718-727.

Wu T, Kareem A. Bridge aerodynamics and aeroelasticity: A comparison of modeling schemes[J]. *Journal of Fluids & Structures*, 2013, 43(7):347-370.

Xiang H, Ge Y. Aerodynamic challenges in span length of suspension bridges[J]. *Frontiers of Architecture & Civil Engineering in China*, 2007, 1(2):153-162.

Xie, J., and Xiang, H. (1985). “State-space method for 3-D flutter analysis of bridge structures.” *Proc., Asia Pacific Symp. on Wind Engrg.*, India, 269–276.

Xu F, Zhu L, Ge X, et al. Some new insights into the identification of bridge deck flutter derivatives[J]. *Engineering Structures*, 2014, 75(8):418-428.

Xu, F., Y. . (2015). System decoupling approach for 3-dof bridge flutter analysis. *Journal of Structural Engineering*, 141(7), 04014168.

Yamada H, Miyata T, Ichikawa H. Measurement of Aerodynamic Coefficients by System identification methods[J]. *Journal of Wind Engineering. & Industrial Aerodynamics*, 1992, 42(1-3):1255-1263.

Yamaguchi, H. , & Ito, M. . (1997). Mode-dependence of structural damping in cable-stayed bridges. *Journal of Wind Engineering & Industrial Aerodynamics*, 72(1), 289-300.

Yang D C, Ge Y J, Xiang H F. (2012). Influence of local vibrations of cables on flutter behaviors of cable-stayed bridges. *The Seventh International Colloquium on Bluff Body Aerodynamics and Applications (BBAA7)*, Shanghai, China, 1365-1370.

Yang Y X, Ge Y J, Xiang H F. Investigation on flutter mechanism of long-span bridges with 2d-3DOF method. *Wind and Structures*, 10(5): 421-435, 2007.

Zhang M, Xu F. Nonlinear vibration characteristics of bridge deck section models in still air[J]. *Journal of Bridge Engineering*, 2018, 23(9): 04018059.

Zona, A. , Barbato, M. , Andrea Dall'Asta, & Dezi, L. . (2010). Probabilistic analysis for design assessment of continuous steel-concrete composite girders. *Journal of Constructional Steel Research*, 66(7), 897-905.

CHAPTER 7 FLUTTER FRAGILITY ANALYSIS OF LONG-SPAN BRIDGES SUBJECTED TO TYPHOON WINDS

7.1 Background

The aerodynamic flutter instability problem of long-span bridges has received intensive attention since the collapse of 853.4 m-main-span Old Tacoma suspension bridge in 1940. As a divergent motion that would lead to catastrophic failure of the bridge, flutter is always the top priority issue during the wind-resistant design process. Recently, the advanced high-strength materials, progressive technologies of construction and continuous improvements of design theory have allowed the main spans of bridges to be longer than 2 km or even reach 5 km to cross wide canyons, rivers and straits ([Brancaleoni and Diana, 1993](#); [Xiang and Ge, 2007](#)). The risks of flutter instability for such extremely slender and flexible structures should be carefully evaluated.

Many coastal regions around the world are expected to construct long-span bridges to link the islands and different economic zones for supporting the development of the local economy. Some of them are exposed to the threats of strong winds caused by typhoon storms. Such as the Western Pacific Basin is the most active typhoon basin globally with 30 typhoons on average every year, accounting for nearly one-third of annual tropical cyclones around the world. As shown in Fig. 7.1, southeast coast of China is a typhoon-prone region, which is also featured with a high density of long-span bridges. Three long-span cable-stayed bridges with the main span longer than 1000 m in China, i.e. the Hutong Bridge in Shanghai (main span of 1092 m), the Sutong Bridge in Jiangsu Province (main span of 1088 m), the Stonecutters Bridge in Hong Kong (main span of 1018 m) are all located in the typhoon-prone region. Meanwhile, there are at least three completed or under-construction

suspension bridges with the main span longer than 1500 m at risk of strong typhoon winds, say the Xihoumen Bridge in Zhejiang Province (main span of 1650 m), the Humen 2nd Bridge (main span of 1688 m) and the Lingdingyang Bridge of Shenzhong Link Project (main span of 1666 m). Moreover, the proposal of an extra-long-span suspension bridge with the main span of 5000 m was developed and investigated by [Xiang and Ge \(2007\)](#). Accordingly, it is great of importance to study of typhoon risks on long-span bridges, especially their flutter instability issue.

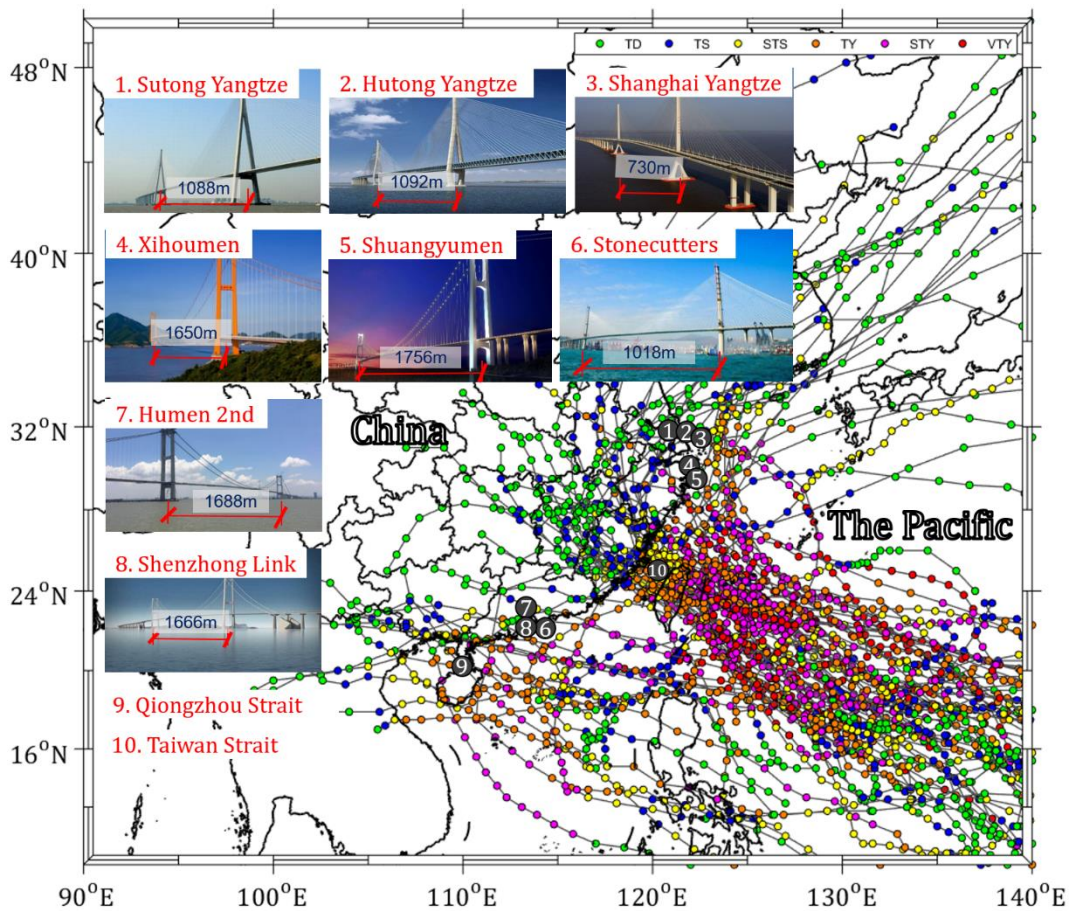


Fig. 7.1 Threats of strong typhoons on long-span bridges along coastal regions of China

The flutter risk assessment of long-span bridges subjected to typhoon winds requires the probabilistic models of flutter capacity of bridges and wind hazards in terms of wind speed.

In this study, the Lingdingyang suspension bridge with the main span of 1666 m (Fig. 7.2)

which will connect Shenzhen and Zhongshan on the Pearl River Delta (location 8 in Fig 7.1, 113.7454°E, 22.4852°N), was employed as an example. The flutter capacity of this bridge was achieved using the method proposed in Chapter 6. And the typhoon wind hazards will be analyzed utilizing the approach developed in Chapter 5.

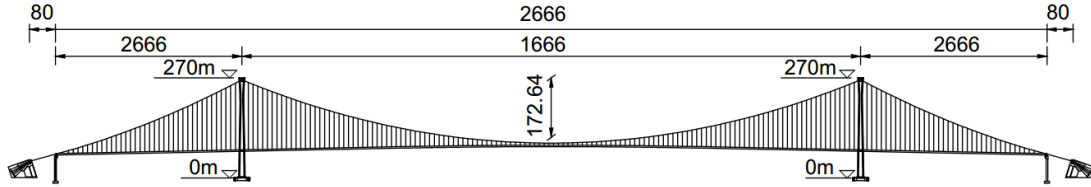


Fig. 7.2 Layout of the Lingdingyang suspension bridge

7.2 Linear flutter model

The self-excited force of a bridge deck that immersed in laminar oncoming winds was customarily modeled as the function of the mean wind speed U and a state-space representation of the vibration, i.e. displacements and velocities. At flutter onset, the motion of the bridge deck is assumed to be tiny and follow the harmonic vibration pattern. Then, the self-excited forces can be formulated as (Scanlan, 1978)

$$L_h = \frac{1}{2} \rho U^2 (2B) \left(KH_1^* \frac{\dot{h}}{U} + KH_2^* \frac{B\dot{\alpha}}{U} + K^2 H_3^* \alpha + K^2 H_4^* \frac{h}{B} + KH_5^* \frac{\dot{p}}{U} + K^2 H_6^* \frac{p}{B} \right) \quad (7.1)$$

$$D_p = \frac{1}{2} \rho U^2 (2B) \left(KP_1^* \frac{\dot{h}}{U} + KP_2^* \frac{B\dot{\alpha}}{U} + K^2 P_3^* \alpha + K^2 P_4^* \frac{h}{B} + KP_5^* \frac{\dot{p}}{U} + K^2 P_6^* \frac{p}{B} \right) \quad (7.2)$$

$$M_\alpha = \frac{1}{2} \rho U^2 (2B^2) \left(KA_1^* \frac{\dot{h}}{U} + KA_2^* \frac{B\dot{\alpha}}{U} + K^2 A_3^* \alpha + K^2 A_4^* \frac{h}{B} + KA_5^* \frac{\dot{p}}{U} + K^2 A_6^* \frac{p}{B} \right) \quad (7.3)$$

in which L_h , D_p and M_α are lift force, drag force and pitching moment, respectively, ρ is the air density, B is the width of the bridge deck, H_i^* , P_i^* and A_i^* ($i = 1 \sim 6$) are flutter derivatives (FDs), which are defined as the functions of the reduced frequency and depend on the geometrical configuration of the bridge section and the wind characteristics of the incoming

flow, $K = B\omega/U$ is the non-dimensional or reduced frequency, where ω is the circular frequency of the oscillation, h is the vertical or heaving motion (positive when downward), p is the lateral or sway motion (positive along the wind direction) and α is torsional or pitching motion (positive when nose-up), respectively, the dot denotes derivative with respect to time.

The techniques for the extraction of flutter derivatives can be generally grouped into two categories, i.e. free vibration and forced vibration tests. Commonly, the coupled free vibration method is the preference to extract the bridge FDs due to its instrumental simplicity and operational convenience (Sarkar et al., 1994; Ding et al., 2010; Xu et al., 2014). Meanwhile, a number of methods have been developed in past several decades using free vibration technique by generating the free decay time histories of the bridge deck at various wind speeds, such as the Kalman filter method (Yamada et al., 1992), Ibrahim time-domain method (Sarkar et al., 1994), iterative least-squares method (Chowdhury and Sarkar, 2003) and stochastic subspace identification method (Qin and Gu, 2004). A unifying least-square (ULS) method developed Gu et al. (2000) and improved by Li et al. (2003), Bartoli et al. (2009) and Ding et al. (2010) will be utilized in this study, which is referred to as the modified unifying least-square (MULS) approach. For a two-degree-of-freedom (DOF) (i.e. h and α) sectional model, the governing equation of free decay motion for the deck model after an initial excitation is

$$\ddot{\mathbf{X}} + \mathbf{C}^{ef}\dot{\mathbf{X}} + \mathbf{K}^{ef}\mathbf{X} = \mathbf{0} \quad (7.4)$$

in which $\mathbf{X} = [h \ \alpha]^T$ a displacement vector,

$$\mathbf{C}^{ef} = \begin{bmatrix} 2\xi_{h0}\omega_{h0} - \frac{\rho B^2 \omega H_1^*(K)}{m} & -\frac{\rho B^3 \omega H_2^*(K)}{m} \\ -\frac{\rho B^3 \omega A_1^*(K)}{I} & 2\xi_{\alpha 0}\omega_{\alpha 0} - \frac{\rho B^4 \omega A_2^*(K)}{I} \end{bmatrix} \quad (7.6)$$

$$\mathbf{K}^{ef} = \begin{bmatrix} \omega_{h0}^2 - \frac{\rho B^2 \omega^2 H_4^*(K)}{m} & -\frac{\rho B^3 \omega^2 H_3^*(K)}{m} \\ -\frac{\rho B^3 \omega^2 A_4^*(K)}{I} & \omega_{\alpha 0}^2 - \frac{\rho B^4 \omega^2 A_3^*(K)}{I} \end{bmatrix} \quad (7.7)$$

where ξ_{h0} and $\xi_{\alpha 0}$ are the mechanical damping ratios of the sectional model system at zero wind associated with vertical bending and torsional modes, ω_{h0} and $\omega_{\alpha 0}$ are the corresponding circular frequencies, these four parameters can be determined by fitting the free decay response of the bridge sectional model system in still air, m and I are mass and moment of inertia per unit length of the bridge deck model. \mathbf{C}^{ef} and \mathbf{K}^{ef} are extracted by fitting the free decay response in the DOFs of h and α with two mode-coupled motion equations with the form of

$$h(t) = \sum_{i=h,\alpha} h_i(t) = \sum_{i=h,\alpha} A_{hi} e^{-\omega_i \zeta_i t} \cos\left(\omega_i \sqrt{1 - \zeta_i^2} t + \theta_{hi}\right) \quad (7.8)$$

$$\alpha(t) = \sum_{i=h,\alpha} \alpha_i(t) = \sum_{i=h,\alpha} A_{\alpha i} e^{-\omega_i \zeta_i t} \cos\left(\omega_i \sqrt{1 - \zeta_i^2} t + \theta_{\alpha i}\right) \quad (7.9)$$

in which A_{di} and θ_{di} ($d = h, \alpha$; $i = h, \alpha$) are the amplitudes and phases information for each mode, which are determined by the initial conditions, ω_i and ζ_i are the natural frequencies and damping ratios. The FDs can then be readily identified from \mathbf{C}^{ef} and \mathbf{K}^{ef} . More details regarding this method are available in Li et al. (2003), Ding et al. (2010) and Xu et al. (2014), which are omitted herein for brevity.

The above method can also be applied to three DOFs to achieve all 18 FDs in Eqs. (7.1)-(7.3).

In this study, the quasi-steady approximations were employed, as listed in Table 6.4. The

static coefficients are obtained from the force balance test. $C_L = -0.0810$, $C_D = 1.2440$, $C_M = 0.0100$, $C'_D = -0.0005$

Flutter threshold is defined as the critical wind at which the net damping of the structure and air system is approximately equal to zero and the structure will be undergoing simple harmonic motion, after that, any further increase of wind speed will result in a higher-amplitude oscillation and even an eventual failure. And the derivative-based linear flutter theory as expressed in Eqs. (7.1)-(7.3) is accurate and reliable enough to predict the flutter critical wind speed since most nonlinear aerodynamics (usually modeled as the second- or higher-order displacement or velocity) related to large amplitudes are applied for post-flutter analysis. Moreover, it is a widely accepted theory not only for its simplicity but for its physical meaning of FDs. The solution of flutter critical wind speed is usually a double iteration procedure with respect to wind speed and system frequency based on Eqs. (7.1)-(7.3). It can be solved in 2 DOFs, i.e. h and α using two modes of interest or in 3 DOFs by introducing lateral DOF, say p utilizing multiple modes. There are two main approaches commonly adopted for the 2D bimodal flutter analysis, i.e. complex eigenvalue analysis (CEVA) ([Theodorsen and Garrick, 1940](#); [Simiu and Scanlan, 1996](#); [Bartoli and Mannini, 2008](#)) and the step by step analysis (SBSA) ([Matsumoto et al., 1996, 2010](#); [Yang et al., 2007](#)) or system decoupling approach (SDA) ([Xu, 2015](#)). The CEVA method would examine the system frequency and damping ratio relationship at the flutter threshold, which is unable to investigate the variation of system damping ratio and frequency with wind speeds and fails to reveal the potential mechanics of flutter by using the derivatives. Comparatively, the SBSA technique is more advantageous for such limitations and it enables the interpretation of the role of FDs on flutter instability and stabilization with an excitation and feedback interaction

process. The 3D multi-mode method is considered to be a more efficient and accurate technique for determining the flutter critical wind speed. However, it requires more computation resources and time. In this study, both 2D SBSA approach and multimode method were employed.

7.3 Structural and aerodynamic randomness

According to the dynamic equation of motion coupled with the self-excited forces of Eqs. (7.1)-(7.3), the source of uncertainties regarding the bridge flutter instability are generally grouped into two categories. One of them is the mechanical characteristics of the bridge system in terms of modal and damping information. The other is the aerodynamic parameters or flutter derivatives.

7.3.1 Structural randomness

The randomness of bridge modal shapes and natural frequencies can be determined using the stochastic finite element method (SFEM). A finite element model of the bridge was first developed (Fig. 7.3). Then the material density and modulus of elasticity constants of each element would be randomly generated to account for the potential variations of mass and stiffness of the bridge structures. The material density is assumed to follow the normal distribution while lognormal distribution is applied to the modulus of elasticity. The coefficients of variation (CoV) of material density for the main girder, main cable and pylon are set as 0.05, 0.05 and 0.1 while the CoVs for the modulus of elasticity are set as 0.1, 0.05 and 0.15, respectively. Meanwhile, a distance-dependent exponential decay function $c_{i,j} = \exp(-a\Delta_{ij}/L)$, in which Δ_{ij} is the distance between element i and j , L is the total length of a bridge structure component, a is a decay factor. a is determined by considering the variation of materials and the effects of the construction procedure of modern suspension bridges. The

values of 0.5, 0.1 and 0.7 are assigned to a , respectively to describe spatial correlations of main girder, main cable, and pylon. Fig 7.4 (a) illustrates the variation of frequencies of the first 20 modes from 10,000 simulations after applying aforementioned random structural parameters. As can be noted, the scatters of frequency values tend to increase with the mode number. The probability density distribution is plotted in Fig. 7.4 (b), with the first four-order moments, i.e. mean, standard deviation, skewness, and kurtosis of 0.227, 0.012, 0.099, 2.97. The mean is equal to the frequency value obtained by the deterministic model. The skewness and kurtosis are close to 0 and 3, respectively, suggesting that the result of random frequencies approximately follows the normal distribution.

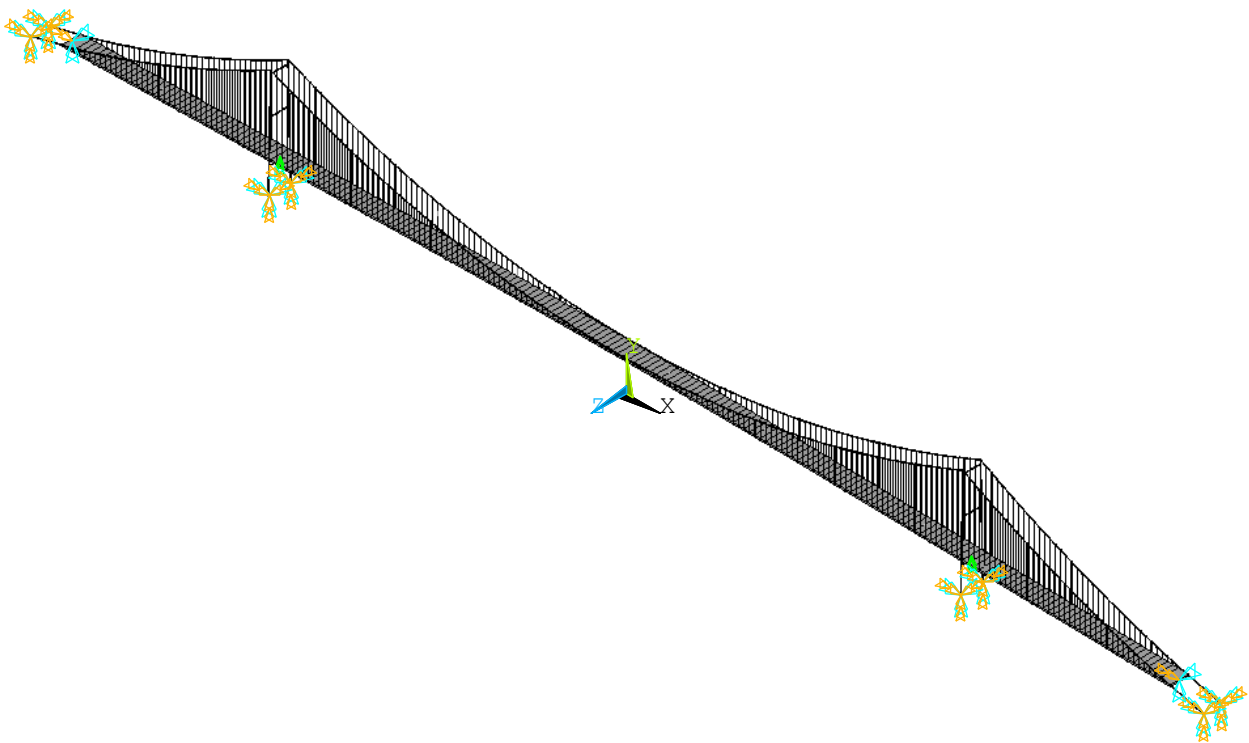


Fig. 7.3 The finite element model of the Lingdingyang Suspension Bridge

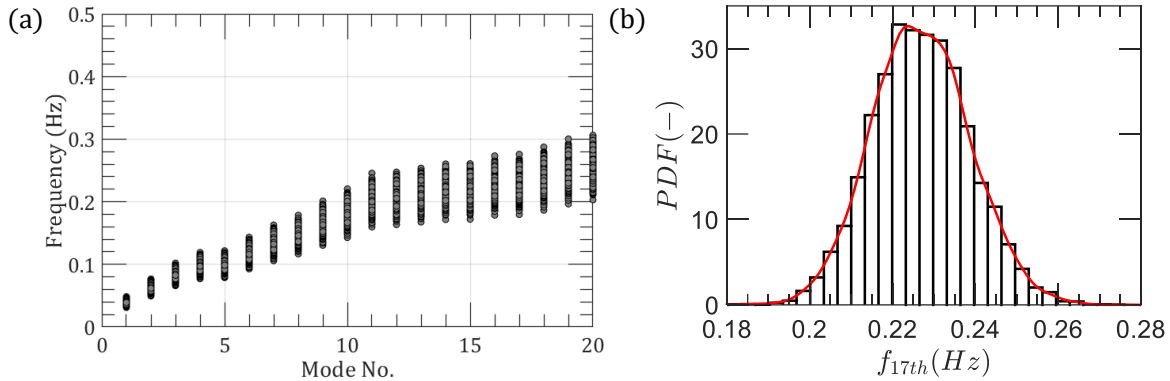


Fig. 7.4 Simulated frequencies of Lingdingyang Suspension Bridge (10,000 runs): (a) First 20 modes; (b) 14th mode (1st symmetric torsional mode)

The mechanical damping ratios of the bridge structures are prescribed during the flutter analysis. For 2D bimodal flutter analysis, the damping ratios of first symmetric vertical bending and torsional modes or first antisymmetric vertical bending and torsional modes are utilized. For the 3D multimode method, the mechanic damping matrix is assumed as Rayleigh damping which is formulated as the linear function of mass matrix and stiffness matrix. The damping ratios of two arbitrary modes should be predefined to determine the coefficients of this linear function. Normally, these two arbitrary modes are also selected as the first symmetric vertical bending and torsional modes or first antisymmetric vertical bending and torsional modes. A literature survey was performed in this study by taking account into the field-measured data of a series of cable-supported bridges (Yamaguchi and Ito, 1997; Guo et al., 2000; Fujino, 2002; Liu et al., 2013; Kim and Kim, 2017; Li et al., 2018; Kim et al., 2019). As shown in Fig. 7.5, the damping ratios obtained from field measurements are grouped into that of vertical bending modes and torsional modes. The lognormal and Weibull probabilistic distribution functions are applied to model their cumulative probability curves. As can be seen, the Weibull distribution is preferable to both of damping

ratios with smaller Kolmogorov–Smirnov test statistics, which will also be employed in this study.

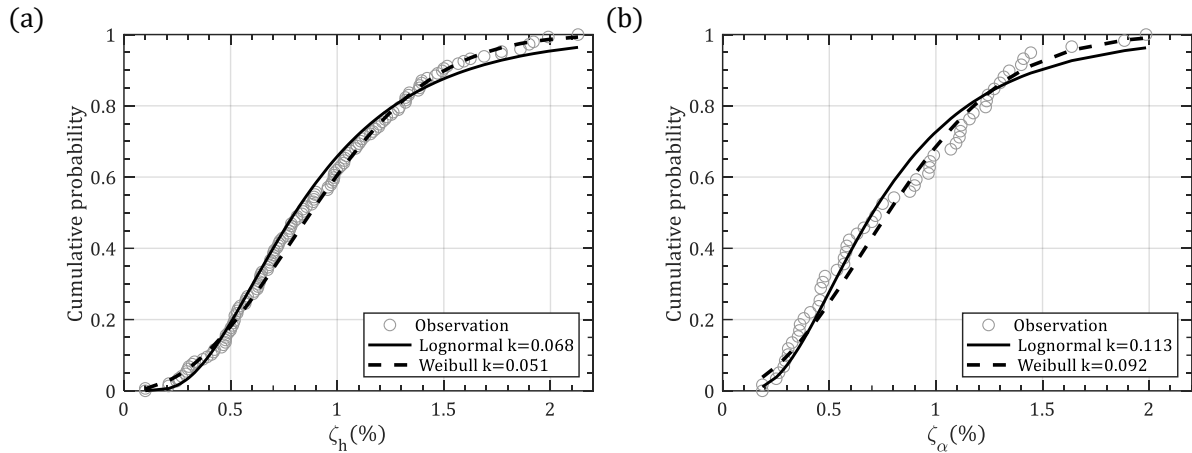


Fig. 7.5 CDF of damping ratios for cable-supported bridges: (a) Vertical bending mode; (b) Torsional mode. (k is the statistic of K-S test)

7.3.2 Aerodynamic randomness

The linear self-excited aerodynamic force in Eqs. (7.1)-(7.3) are modeled with a transfer function in the frequency domain, i.e. FDs. The aerodynamic uncertainties mainly attributed to the randomness of FDs obtained from physical experiments or numerical simulations. A sectional model wind tunnel test of the present bridge was performed to quantify the experiment- and identification-induced errors of the FDs.

(1) Experimental setup

Based on the design information of the main navigation channel bridge of Shenzhen-Zhongshan Link, i.e. the Lingdingyang suspension Bridge with the main span of 1666 meters, a rigid sectional model with the reduced scale ratio of 1:80 was designed with the cross-section as shown in Fig. 7.6. The model was firmly assembled with a rigid inner steel frame and several wood panels to ensure that the model has enough stiffness with the fundamental

frequency larger than about 25 Hz. All handrails and ancillary structures were manufactured with CNC engraving machines to strictly guarantee the dimensions of the model. The model is 1.74 m in length, 0.6215 m in width and 0.05 m in depth to achieve a reasonable length-over-width ratio. Table 7.1 lists the major design parameters of the sectional model. The fundamental frequencies (f_h and f_α) are estimated from the dynamically equivalent mass and moment of inertia of the spring-suspended model system. It is noteworthy that the real frequencies and damping ratios of the model extracted from the free decay vibration signals are not constants, which would fluctuate within a certain range due to the effects of some mechanical nonlinearities (Gao and Zhu, 2015; Cao and Ge, 2017) and other randomness. This is also one of the reasons to quantitatively figure out the uncertainties of these parameters as well as their effects on the flutter performance of the bridge.

All tests of the sectional model were conducted in the TJ-1 boundary layer wind tunnel of Tongji University, China, which is an open-jet wind tunnel with 1.8 m in width and 1.8 m in depth (Fig. 7.7). The total length for the test section is 12.0 m. The wind speed is continuously adjustable from 1.0 to 30 m/s with the inhomogeneity of the wind speed less than 1.0 % and turbulence intensity less than 1.0 %, respectively. The inherent attack and yaw angles of incoming winds are both within $\pm 0.5^\circ$. The model was elastically suspended by eight springs between two wind tunnel sidewalls. If the blockage limit is set as 3%, the amplitude limitation of the torsional vibration is about 5° . The sway motion of the model in the wind direction was restrained via two steel cables. Four Panasonic HL-C235CE-W laser displacement transducers with the measurement range of ± 200 mm were mounted to capture the vibration signals. A Pitot probe was mounted at one of the side walls to measure the wind speed. A thin but high-strength string was fixed off-axis at the midspan position on

the bottom surface of the model to excite the free vibration with two degrees of freedom (DOFs), i.e., vertical bending and torsion. It can also be a defense of the sudden divergence vibration due to the flutter.

Table 7.1 Design parameters of the sectional model

H (m)	B (m)	m (kg/m)	I (kg·m ² /m)	f_h (Hz)	f_α (Hz)	ε (-)	ζ_h (%)	ζ_α (%)
0.05	0.6215	6.731	0.234	2.700	6.208	2.30	0.500	0.500

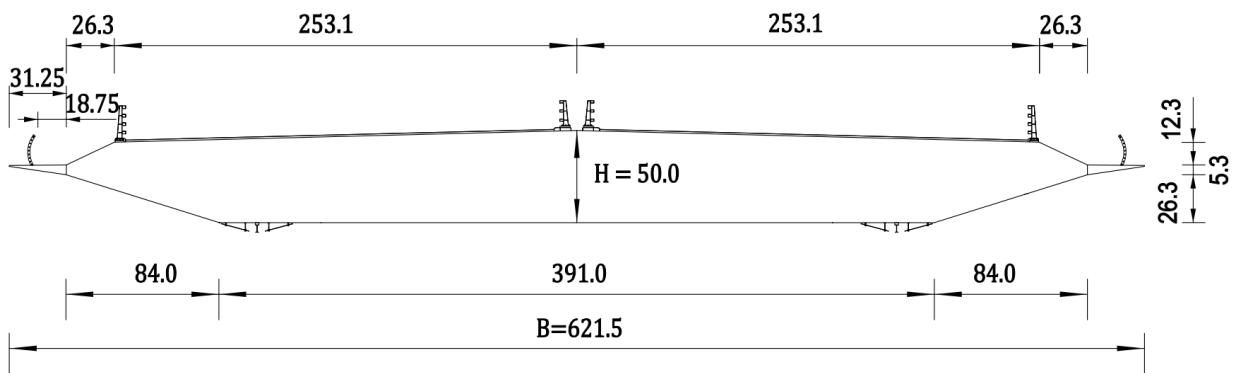


Fig. 7.6 Cross-section of the sectional model (Unit: mm)

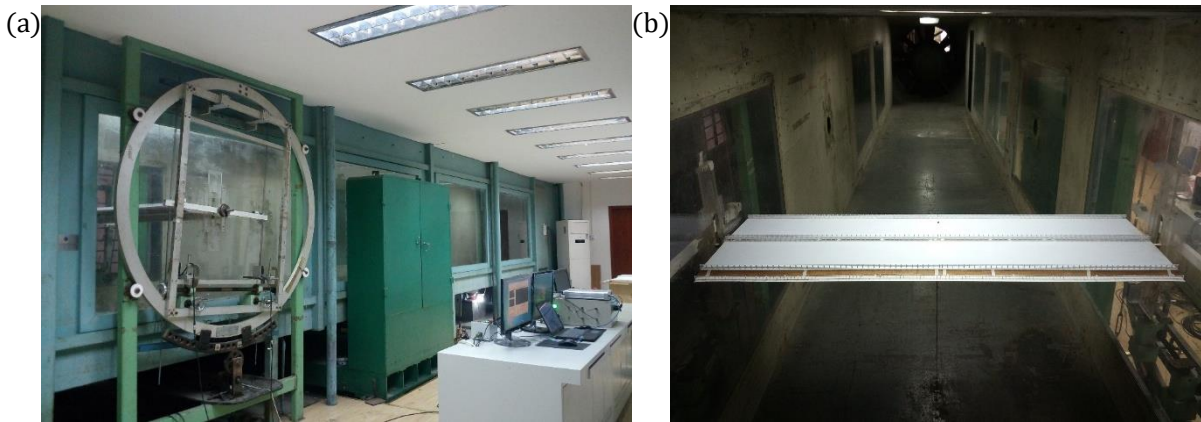


Fig. 7.7 Wind tunnel test: (a) The TJ-1 open-jet wind tunnel; (b) Sectional model

(2) Extraction of flutter derivatives

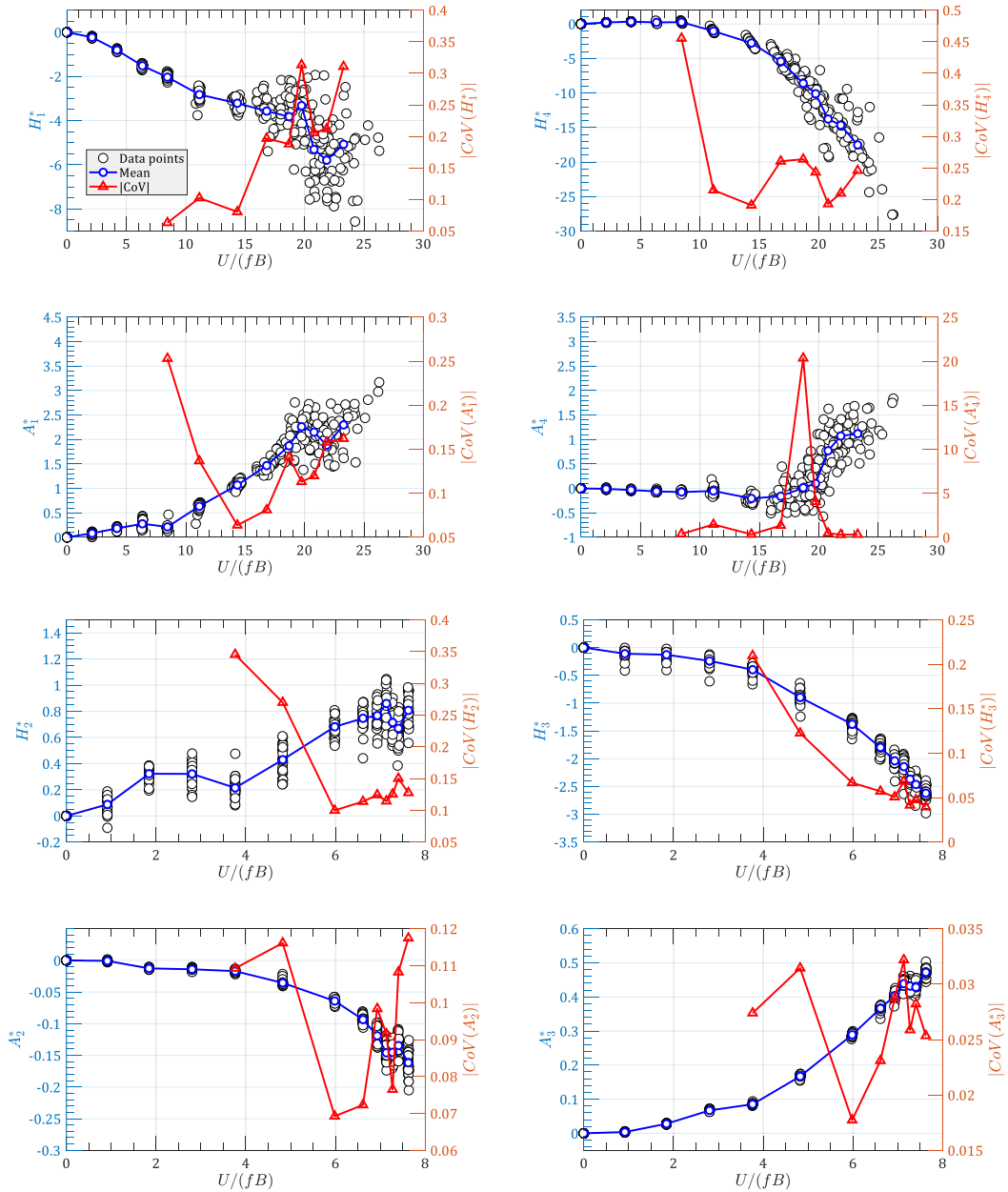


Fig. 7.8 Flutter derivatives from 30-time repeated tests

To quantify the experiment- and identification-induced uncertainties of FDs, the free decay vibration test of the section model was repeated for 30 times at each wind speed. Fig. 7.8 illustrates the FDs obtained from 30 repetitions. The scatters of the data points for all FDs are observed to increase with reduced wind speed, except H_2^* and H_3^* . The absolute values of

coefficient of variation (CoV) from 5th experimental wind speed to the last wind speed also plotted in Fig. 7.8. The CoVs at first four wind speeds are ignored since the mean values of FDs are relatively low which could result in high CoVs. And the variations of FDs at the wind speed that is close to the flutter boundary is always our concern. It can be noted that the CoV of H_1^* shows an apparent increase with reduced wind speed while CoVs of A_1^* and A_2^* witness a decrease first before a rise occurs at high reduced wind speed. Comparatively, CoVs of H_2^* , H_3^* and H_4^* decrease first and almost remain unchanged near the flutter boundary of the sectional model. The mean of A_4^* is close to zero which leads to an extreme peak at the reduced wind speed of about 18.5 but shows no obvious change at high wind speeds. A_3^* has the smallest CoVs, showing a relatively strong fluctuation.

As discussed by Scanlan et al. (1997) for the theoretical solutions of an ideal plate, some approximate relations between FDs were concluded for high reduced wind speeds as $A_1^* \cong -KA_3^*$, $A_4^* \cong -KA_3^*$, $H_1^* \cong KH_3^*$. Furthermore, Matsumoto (1996) introduced one more mutual dependence equation as $H_4^* \cong -KH_2^*$ and verified them using forced vibration technique coupled with surface pressure measurements for various aspect-ratio prisms. This means some inter-correlations between FDs should be carefully concerned. And it is also plausible since eight FDs are simultaneously estimated using Eqs. (7.8)~(7.9). As illustrated in Fig. 7.9, the variation of correlation coefficients ρ with wind speed between different pairs of FDs were calculated. Since the free vibration technique applies different frequencies, i.e. the frequencies associated with vertical bending and torsional modes to H_1^* , H_4^* , A_1^* , A_4^* and H_2^* , H_3^* , A_2^* , A_3^* , the independent variables or reduced wind speeds related to these two sets of FDs are not equal to each other, as shown in Fig. 7.8-Fig. 7.9. Accordingly, the correlations between these two sets of FDs are ignored. Moreover, the major concern of

their correlations is near the flutter boundary. Hence, the correlation matrix at last reduced wind speed, as shown in Eq. 7.10 will be employed to randomly simulate the FDs. It noteworthy that the correlation coefficients between FDs appear to be convergent near the flutter onset., especially between H_1^* and A_1^* , H_1^* and A_4^* , H_4^* and A_4^* , H_2^* and H_3^* , H_2^* and A_2^* , H_2^* and A_3^* and H_3^* and A_2^* . That means the use of the correlation matrix near the flutter boundary could provide enough confidence to consider the correlations between FDs.

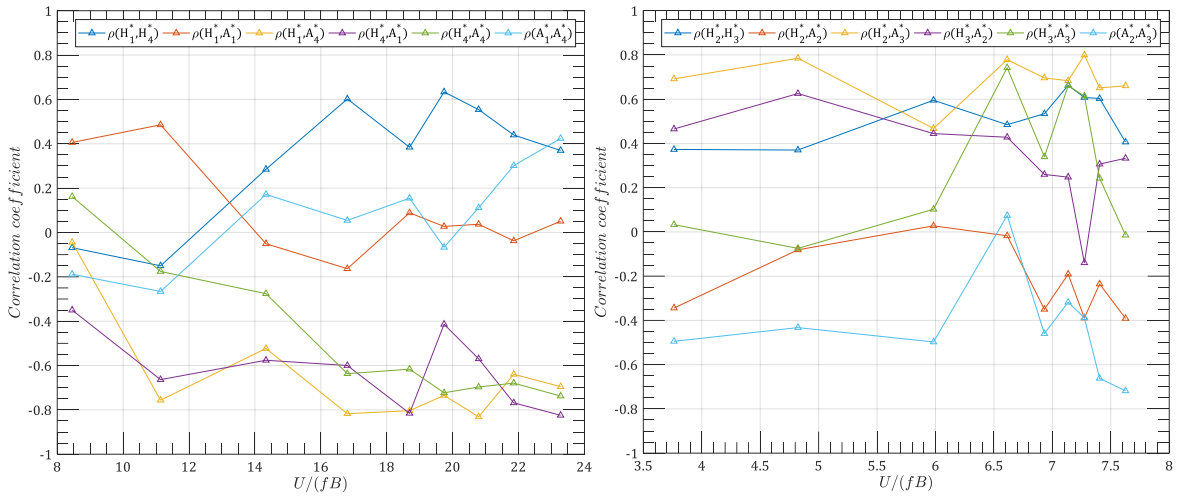


Fig. 7.9 Correlation coefficients between flutter derivatives

	H_1^*	H_4^*	A_1^*	A_4^*	H_2^*	H_3^*	A_2^*	A_3^*	
H_1^*	1.00	0.37	0.05	-0.70	0.00	0.00	0.00	0.00	(7.10)
H_4^*	0.37	1.00	-0.82	-0.74	0.00	0.00	0.00	0.00	
A_1^*	0.05	-0.82	1.00	0.42	0.00	0.00	0.00	0.00	
A_4^*	-0.70	-0.74	0.42	1.00	0.00	0.00	0.00	0.00	
H_2^*	0.00	0.00	0.00	0.00	1.00	0.41	-0.39	0.66	
H_3^*	0.00	0.00	0.00	0.00	0.41	1.00	0.33	-0.01	
A_2^*	0.00	0.00	0.00	0.00	-0.39	0.33	1.00	-0.72	
A_3^*	0.00	0.00	0.00	0.00	0.66	-0.01	-0.72	1.00	

Fig. 7.10 compares 1000 simulations of FDs with these obtained from wind tunnel tests. At each reduced wind speed, simulated FDs are limited to mean ± 3 times of standard deviation of wind tunnel results. As can be seen, almost all experimental data are covered by simulations, except several weird data points.

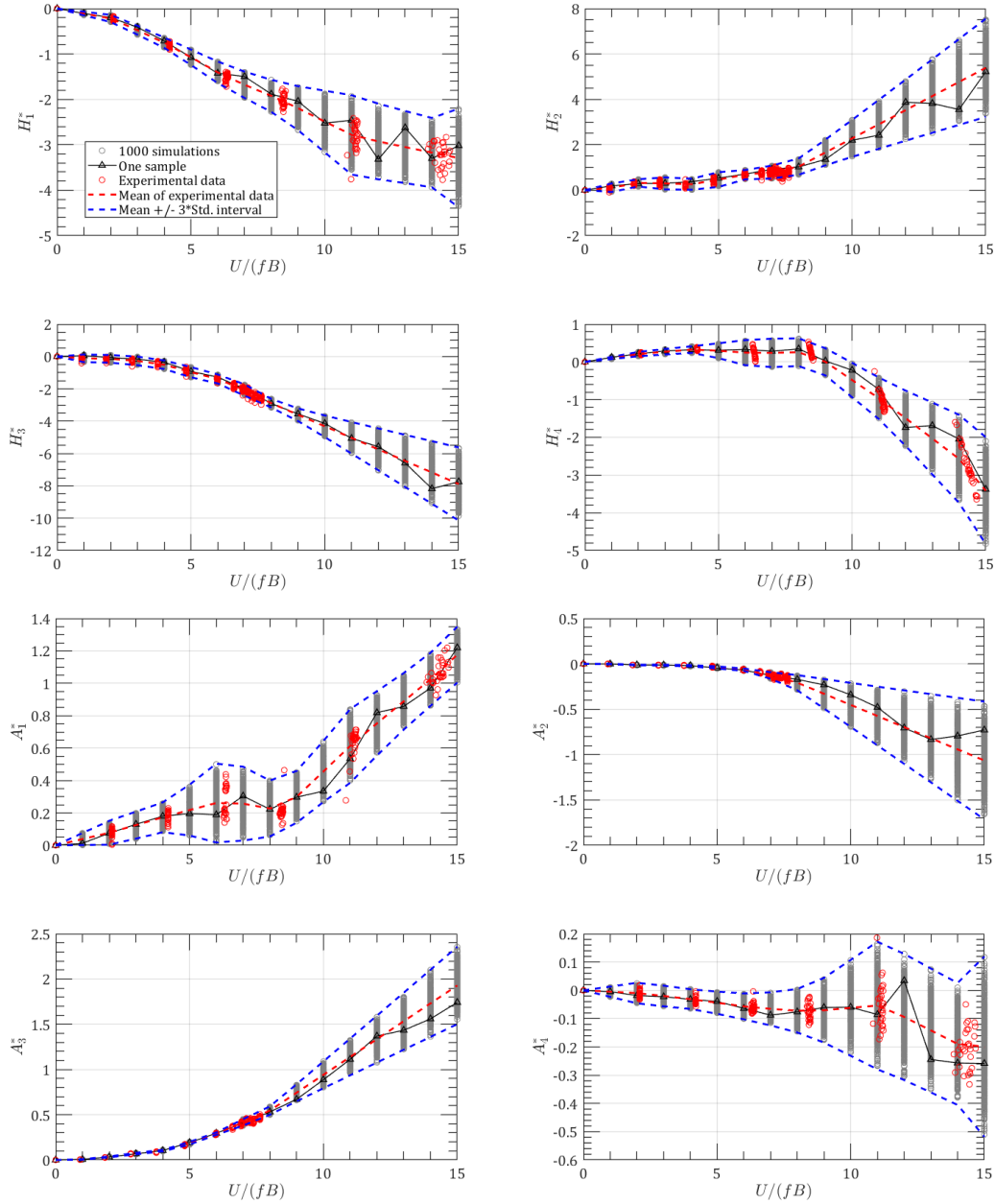


Fig. 7.10 Comparisons of simulated and experimental FDs (1000 runs)

7.4 Fragility curve of flutter instability

The probabilistic solutions of flutter critical wind speed are achieved by taking the randomness of structural parameters and aerodynamic parameters into account as discussed above. Table 7.3 listed the probabilistic solutions of two different cases using SBSA and multimode methods. #1 case introduces both the uncertainties of structural and

aerodynamic parameters. Since the FDs for the present bridge section were identified in laminar flow, the scatter pattern of FDs due to the influence of turbulence was unavailable. As discussed in Chapter 6, the increase of turbulence intensity would enlarge the dispersion of the FDs, but the mean values of FDs have insignificant variation. #2 case in Table 7.3 utilized a 1.5-time increased standard deviation of FDs to examine the effects of higher dispersion of FDs on the flutter performance of the present bridge deck.

The probabilistic flutter solutions are listed in Table 7.2 and plotted in Fig. 7.11. As can be seen, the critical wind speed V_{cr} obtained by SBSA are generally smaller than that of multimode solutions but have a slightly greater standard deviation. Interestingly, the standard deviation of reduced wind speeds calculated from SBSA is more than twice that of multimode results. The increase of the standard deviation of FDs slightly enlarges the dispersion of the flutter critical wind speeds both for SBSA and multimode methods. A small possibility with the critical wind speed about 60 m/s was achieved by the SBSA method, but it does not happen in the multimode analysis.

Table 7.2 Statistics of probabilistic flutter solutions

Case	FDs	2D SBSA						3D Multimode					
		V_{cr}			$V_{cr,R}$			V_{cr}			$V_{cr,R}$		
		μ	σ	CoV	μ	σ	CoV	μ	σ	CoV	μ	σ	CoV
#1	σ_{exp}	95.97	5.49	0.06	13.31	0.93	0.07	99.01	5.29	0.05	12.92	0.40	0.03
#2	$1.5\sigma_{exp}$	95.27	6.41	0.07	12.99	1.29	0.10	98.98	5.55	0.06	12.92	0.49	0.04

Note: σ_{exp} is the standard deviation of FDs obtained from 30-time repeated tests (Fig. 7.8).

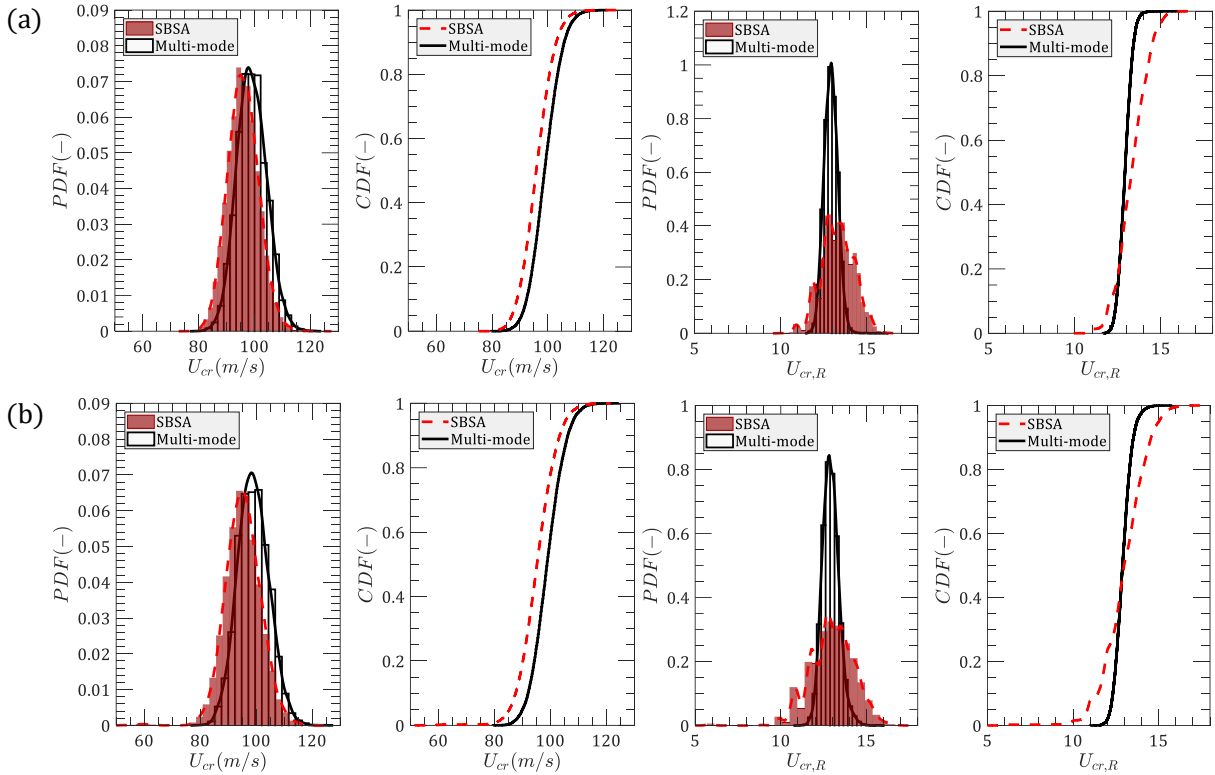


Fig. 7.11 Empirically probabilistic distribution of flutter critical wind speed: (a) σ_{exp} of FDs; (b) $1.5\sigma_{exp}$ of FDs;

7.5 Hazard curves of typhoon wind

7.5.1 10-min mean wind hazard curves

The site-specific subregion method as discussed in Chapter 5 was adopted to develop the wind hazard curve in the bridge site. As shown in Fig 7.12, 15-year simulated tracks are compared with observed real tracks from the year 2001 to 2015 within the circular region with a radius of 500 km. The genesis of all simulated storms is imposed around the circular boundary, which is concentrated on the southeast semi-circular arc, showing a reasonable agreement with real tracks. Several strong typhoons can also be noted for over-sea storms. Fig. 7.13 compares the empirical probability density function between real and 10000-year simulated parameters within the circular domain. Generally, the distributions of simulated parameters are consistent with real observations. More performance assessments of the

subregion model have been well discussed in Chapter 5, which will be omitted here for brevity.

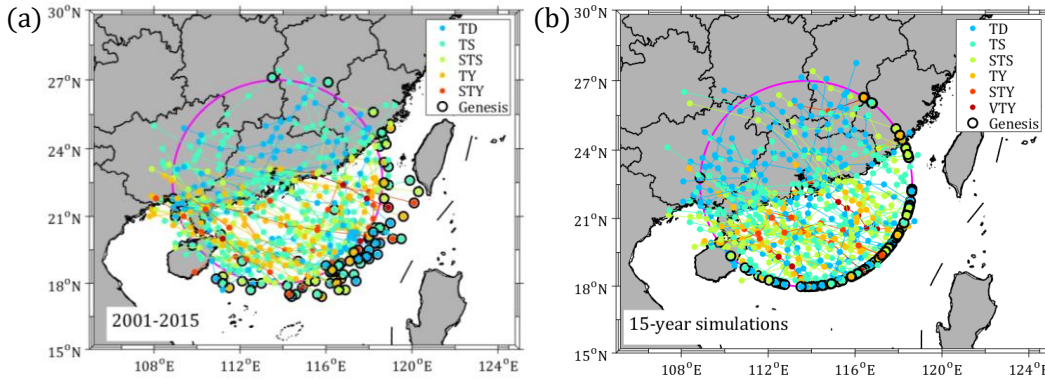


Fig. 7.12 Comparison between real and simulated 15-year storms around the bridge site: (a) Real observation from 2001 to 2015; (b) 15-year simulations

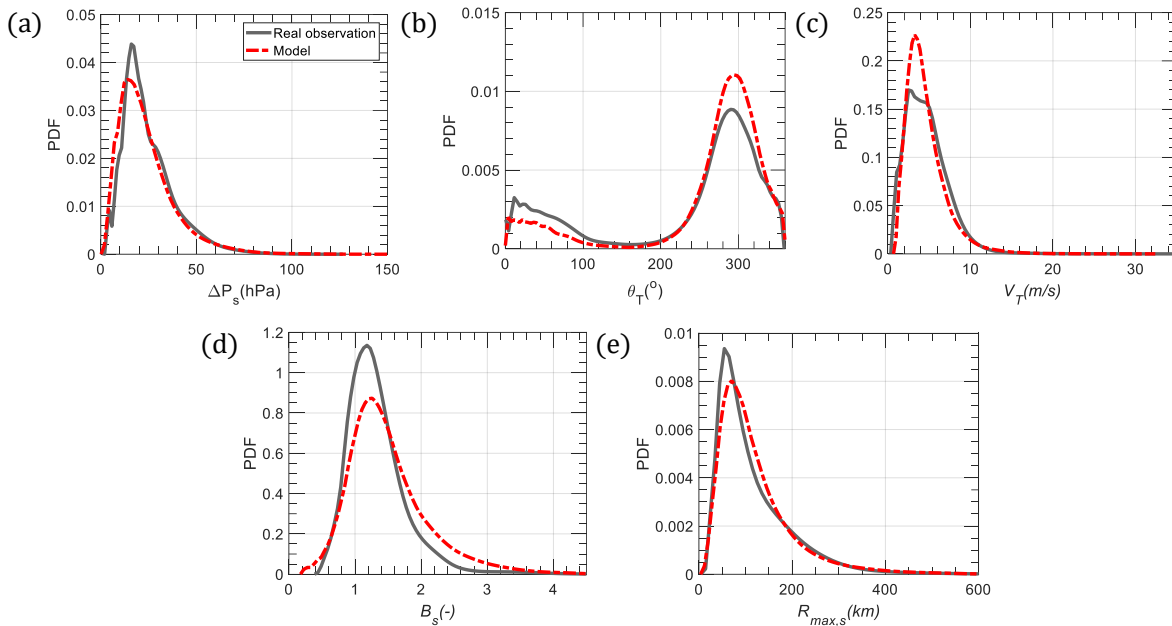


Fig. 7.13 Comparison of empirical PDFs for real and simulated parameters within the circular subregion centered in bridge site (10,000-year simulations): (a) Central pressure deficit ΔP_s ; (b) Heading direction θ_T ; (c) Forward speed V_T ; (d) Radius to maximum winds $R_{max,s}$; (e) Pressure shape parameter B_s

Fig. 7.14 illustrates the design wind speed or the demand wind speed (V_d) curves with respect to return period at height of bridge deck, say $z = 91.5$ m. The similar curves obtained from the full track model are also plotted for comparison. Since the long-span bridge in this

study is over open water with the nearest distance to the land larger than 5 km, two underlying roughness lengths $z_0 = 0.01$ m and $z_0 = 0.0002$ m are employed. $z_0 = 0.01$ m is the suggested roughness length by Chinese codes (JTG/T D60-01-2004; GB 50009-2012) for open water exposure. $z_0 = 0.0002$ m is the suggested value for the open sea with fetch at least 5 km recommended by MODIS (Table 3.1). In reality, the surface roughness length of over-water condition is a function of wind speed as the effects of wind-driven waves. If the Eqs. (3.26)-(3.28) is adopted, the maximum $z_0 \approx 0.0034$ m. Accordingly, the real z_0 should fall in the range of [0.0002 m, 0.01 m] for high wind conditions. It can be seen in Fig. 7.14 that the design wind speeds obtained from FTM are consistent with CSM for short return periods, i.e. less than 100 years. However, the design wind speeds of FTM for longer return periods are significantly underestimated when compared with CSM. This is because FTM only utilizes 10,000-year simulations while CSM uses 100,000-year random generated samples. Hence, the predictions achieved by CSM will be employed to construct the typhoon wind hazard curves of the bridge site.

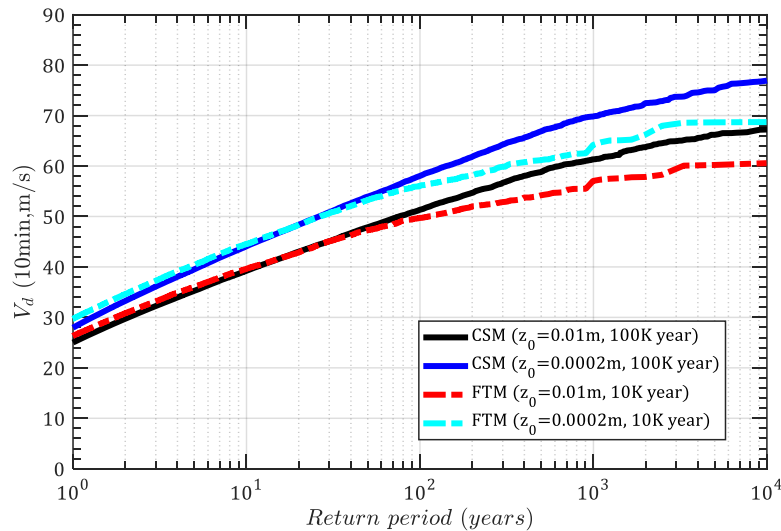


Fig. 7.14 Predicted typhoon design wind speed versus return period of the bridge site at height of bridge deck ($z = 91.5$ m, CSM: circular subregion model, FTM: full track model)

As discussed in Chapter 5, the Poisson distribution is used to model the occurrence probability $P_T(n)$ of n typhoons over the time period T if we assume the number of storms occurring in a given season is independent of any other season. Then, the probability that the extreme wind speed v_i is larger than a certain wind speed V within a time period T can be determined as

$$P_T(v_i > V) = 1 - \sum_{n=0}^{\infty} P(v_i \leq V|n)P_T(n) = 1 - \exp\left(-\frac{N}{Y}T\right) \quad (7.11)$$

in which $P(v_i \leq V|n)$ is the probability that the peak wind speed v_i of a given TC is less than or equal to V , N is the total number of TCs that each of them has a peak wind v_i larger than V , and Y is total simulation years. If $T = 1$, $P_T(v_i > V)$ is the annual probability of exceeding a given wind speed V or the probability of a wind speed v_i exceeding V in any given year. Generally, $P_T(v_i > V)$ represents the probability of a wind speed v_i exceeding V in any given T years. As shown in Fig. 7.15, the curves of the probability of exceedance at any given T years for the bridge site are plotted. As expected, the probability of exceedance of a specific wind speed event increase with T .

Although sometimes, the yaw or skew winds related to the bridge deck could pose more unfavorable flutter wind speed than that of perpendicular winds (Zhu et al., 2002a, b, 2013; Huang et al., 2012), the perpendicular wind was found to be the most unfavorable for the suspension bridge in this study by the full-bridge aeroelastic model wind tunnel test (Zhao et al., 2019). Hence, the directions of maximum wind for 100,000-year simulated storms are shown in Fig. 7.16. As can be seen, the maximum wind in the bridge site most likely blows from the direction sector of (101.25°,123.75°) or ESE followed by the sectors of (78.75°, 101.25°) or E and (56.25°, 78.75°) or ENE. The results should be reasonable since most

tracks head toward the northwestern direction (Fig. 7.12) and the maximum wind of each storm most likely occurs at the closest location to the site of interest. The northwestern semi-circular region has a similar chance to be attacked by the maximum wind of each storm. The left rear quadrant has the smallest probability of experiencing the maximum winds. The bridge orientation is about 65° clockwise from due north.

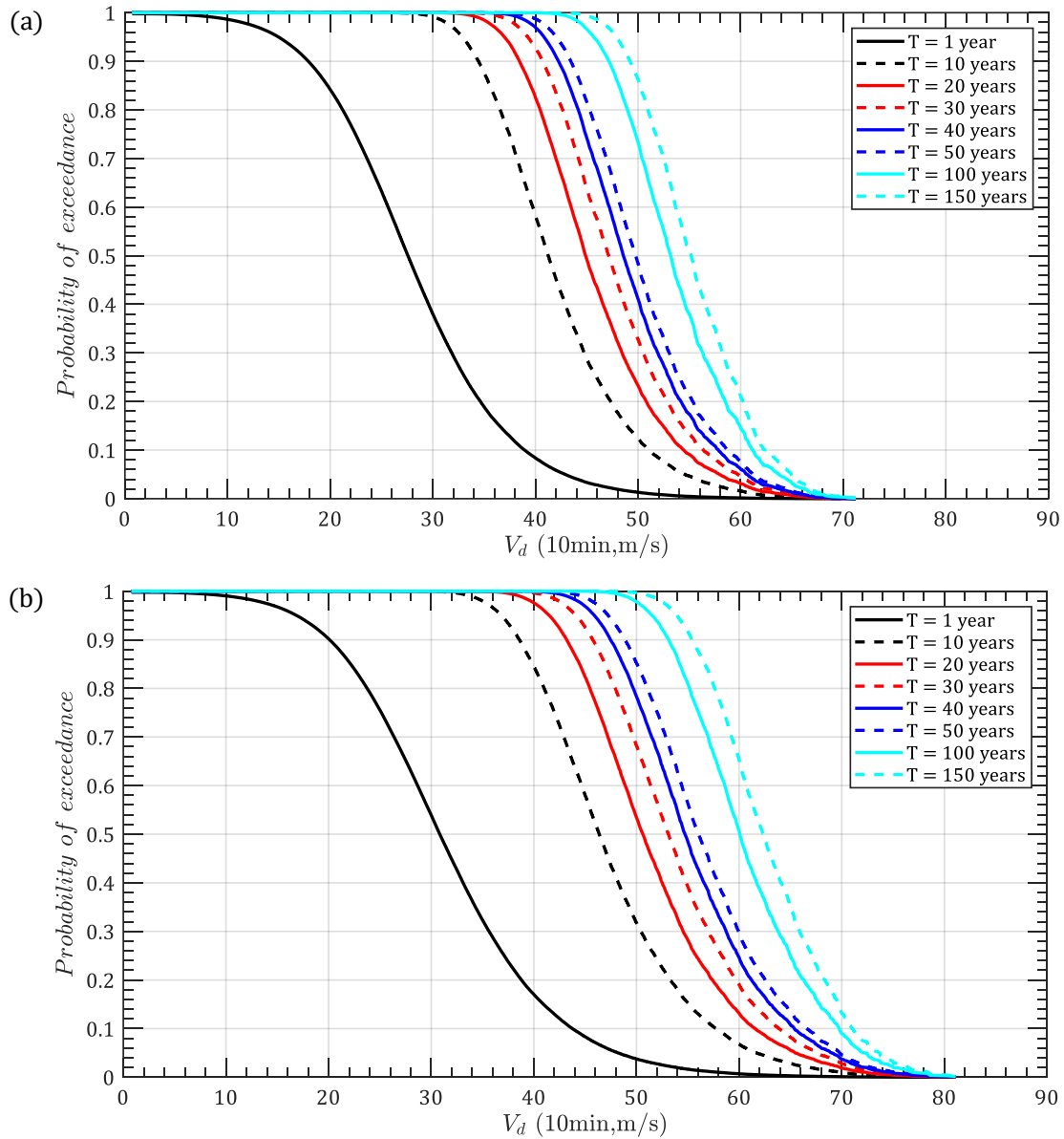


Fig. 7.15 Probability of exceedance at any given T years of maximum typhoon winds ($z = 91.5$ m): (a) $z_0 = 0.01$ m; (b) $z_0 = 0.0002$ m

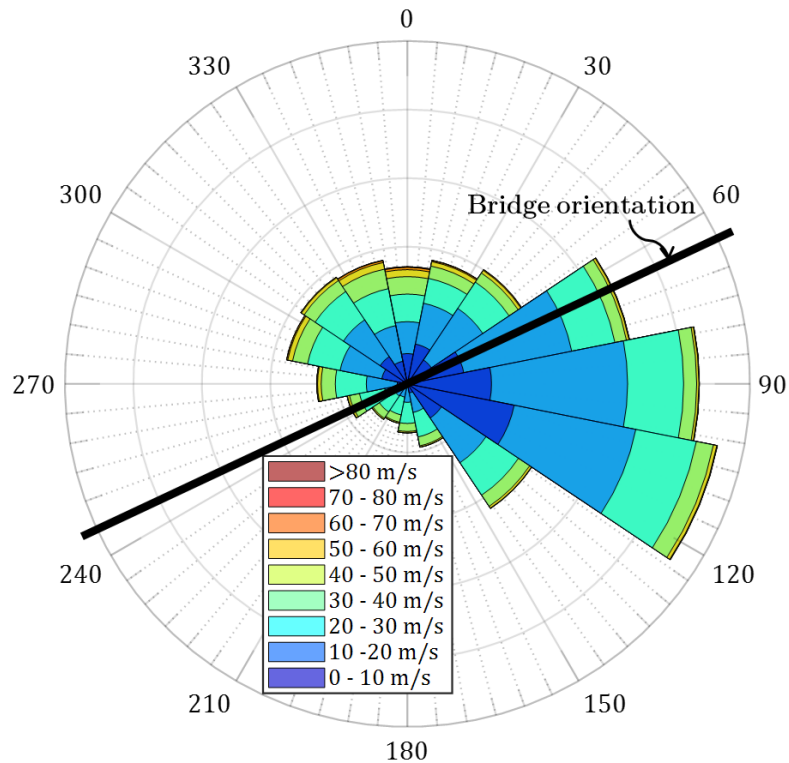


Fig. 7.16 Wind rose of maximum wind for 100,000-year simulated storms ($z = 91.5$ m, $z_0 = 0.0002$ m)

Correspondingly, the curves of the probability of exceedance are constructed with respect to the maximum winds that are perpendicular to the bridge deck. Instead of simply decomposing the maximum winds in Fig. 7.16 into the perpendicular direction to the bridge orientation, which could underestimate the maximum perpendicular winds, the perpendicular winds at every time steps of each storm would be calculated before determining the largest perpendicular wind. Then these largest perpendicular winds of every storm were employed to develop the curves of the probability of exceedance. As shown in Fig. 7.17, the probability of exceedance for each wind speed is slightly smaller than that shown in Fig. 7.15.

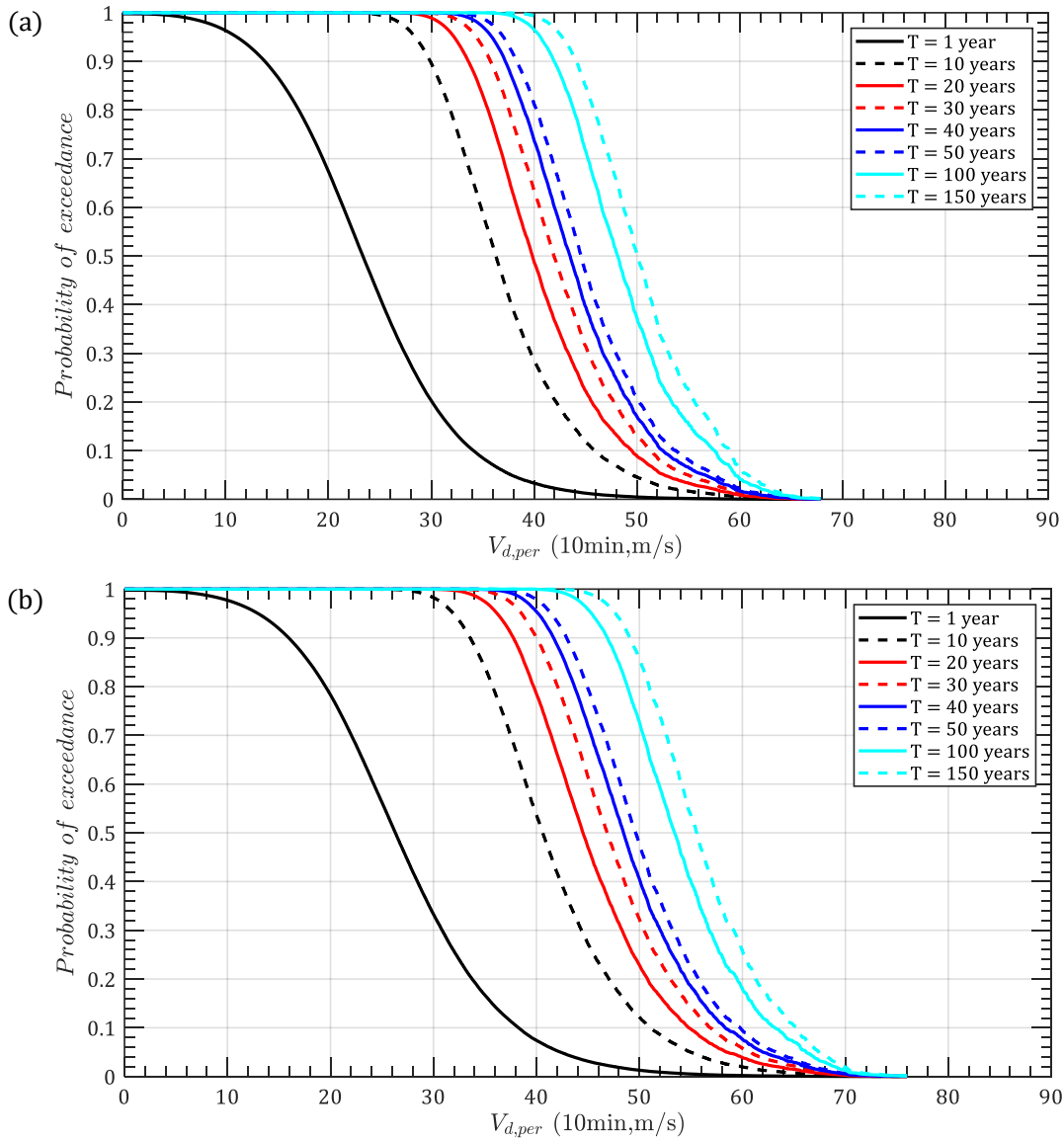


Fig. 7.17 Probability of exceedance at any given T years of maximum typhoon winds that are perpendicular to the bridge deck ($z = 91.5$ m): (a) $z_0 = 0.01$ m; (b) $z_0 = 0.0002$ m

7.5.2 Gust factor

As discussed in Chapter 4, the gust factor (conversion factor from 10 min wind speed) of wind speed, which is a conversion factor from 10-min mean wind speed to 3-s gust wind speed suffers a significant variation due to non-Gaussian effects. Ge et al. (2000) assumed the gust factor follows a normal distribution with the code-suggested mean and standard deviation of 0.07 times of mean value, which was followed by Cheng et al. (2005). In this

study, the probabilistic solution of the gust factor developed in Chapter 4 was utilized. Due to the wind data at height of bridge deck are not available, the distribution parameters of skewness and kurtosis of 10-m typhoon winds (Li et al. 2015) in Table 4.1 were adopted, i.e. normal distribution for skewness with mean and standard deviation of -0.28 and 0.3, lognormal distribution for kurtosis with the logarithmic mean and standard deviation of 1.11 and 0.20. A correlation coefficient of -0.3 between skewness and kurtosis was used. As shown in Fig. 7.18, the empirical probability density functions of gust factor with gust directions of 3 s and 1 min at height of the bridge deck ($z = 91.5$ m) are obtained using 10,000 Monte Carlo simulations.

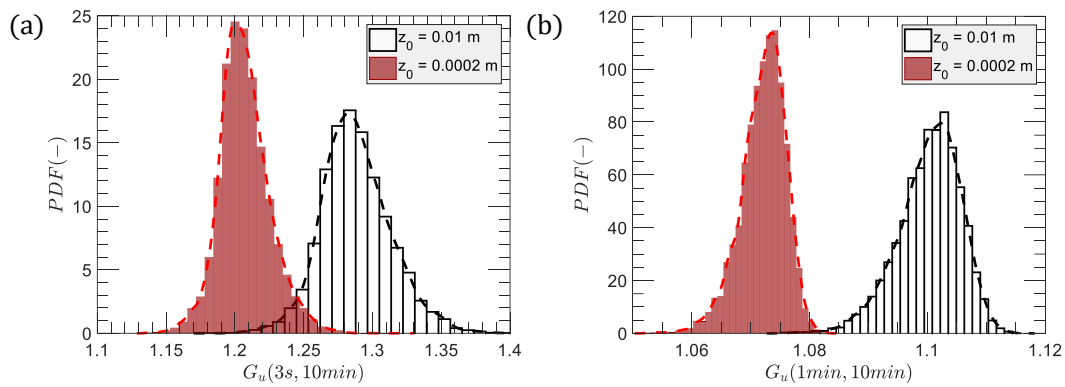


Fig. 7.18 Empirical probability density functions of gust factor (10,000 simulations, $z = 91.5$ m): (a) Gust duration $\tau = 3$ s; (b) Gust duration $\tau = 1$ min

7.6 Flutter failure probability

The flutter failure occurs when the real wind speed reaches or exceeds the critical wind speed of the bridge. Accordingly, the limit state function of bridge flutter issue can be expressed as

$$Z = V_{cr} - G_u \cdot V_d \quad (7.12)$$

in which V_{cr} and $G_u \cdot V_d$ are obtained from sections 7.4 and 7.5, respectively. A correlation

coefficient of -0.5 will be introduced between G_u and V_d based on the correlation analyses in Fig. 4.4. The failure probability P_f of the flutter instability is defined as the probability of

$$P_f = P(Z < 0) \quad (7.13)$$

The failure probability P_f can also be alternatively represented as a reliability index β with the form of

$$P_f = \Phi(-\beta) \quad (7.14)$$

in which Φ is the PDF of the standard normal distribution.

To determine the failure probability, the Monte Carlo simulation technique was adopted in this study. The inverse transform sampling based on the CDF of each parameter in Eq. (7.12) was employed to generate random samples. For each case, 10^8 samples were generated. As shown in Table 7.3~7.10, the failure probability with respect to different combinations of flutter fragility curves and typhoon wind hazard curves were calculated. Several findings can be concluded as:

- (1) The largest failure probability occurs at the combination of the fragility curves obtained from SBSA solutions using $1.5\sigma_{exp}$ for FDs and all winds that do not consider the effects wind direction when $z_0 = 0.0002 m$ and gust duration is 3 s. In this case, the flutter failure probabilities correspond to T = 100 years and 150 years are 1.5×10^{-2} and 2.2×10^{-2} .
- (2) For the same gust duration, the flutter failure probabilities associated with $z_0 = 0.0002 m$ is higher than that with $z_0 = 0.01 m$. For the same z_0 , The use of different gust durations would result in significant differences in failure probability.
- (3) The increase of uncertainties of FDs would result in obvious greater failure probabilities using the SBSA solutions. But the results based on multimode-deduced fragility curves are insignificant when $1.5\sigma_{exp}$ was applied to FDs.

(4) The increase of uncertainties of FDs would result in obvious greater failure probabilities using the SBSA solutions. But the results based on multimode-deduced fragility curves are insignificant when $1.5\sigma_{exp}$ was applied to FDs. This can also be understood from the difference of fragility curves shown in Fig. 7.11.

(5) If only the wind components that are perpendicular to the bridge orientation were considered, the flutter failure probability would be significantly decreased.

Table 7.3 Flutter failure probability (Fragility curves: SBSA solutions using σ_{exp} for FDs; Wind hazard curves: all winds no considerations of wind direction)

T (year)	$z_0 = 0.01 \text{ m}$						$z_0 = 0.0002 \text{ m}$					
	$\tau = 3s$		$\tau = 1min$		$\tau = 10min$		$\tau = 3s$		$\tau = 1min$		$\tau = 10min$	
	P_f	β	P_f	β	P_f	β	P_f	β	P_f	β	P_f	β
1	6.9×10^{-6}	4.3	$< 10^{-7}$	> 5.2	$< 10^{-7}$	> 5.2	6.9×10^{-5}	3.8	3.6×10^{-6}	4.5	$< 10^{-7}$	> 5.2
10	7.2×10^{-5}	3.8	$< 10^{-7}$	> 5.2	$< 10^{-7}$	> 5.2	7.3×10^{-5}	3.2	1.6×10^{-5}	4.2	6.8×10^{-7}	4.8
50	4.2×10^{-4}	3.3	1.6×10^{-7}	5.1	$< 10^{-7}$	> 5.2	4.0×10^{-3}	2.7	9.6×10^{-5}	3.7	4.2×10^{-6}	4.5
100	9.3×10^{-4}	3.1	2.0×10^{-7}	5.1	$< 10^{-7}$	> 5.2	8.4×10^{-3}	2.4	1.9×10^{-4}	3.6	6.6×10^{-6}	4.4
150	1.4×10^{-3}	3.0	3.4×10^{-7}	5.0	$< 10^{-7}$	> 5.2	1.3×10^{-2}	2.2	3.0×10^{-4}	3.4	8.6×10^{-6}	4.3

Note: $\tau = 10 \text{ min}$ indicates no gust factor was considered.

Table 7.4 Flutter failure probability (Fragility curves: SBSA solutions using σ_{exp} for FDs; Wind hazard curves: only wind components that are perpendicular to the bridge orientation)

T (year)	$z_0 = 0.01 \text{ m}$						$z_0 = 0.0002 \text{ m}$					
	$\tau = 3s$		$\tau = 1min$		$\tau = 10min$		$\tau = 3s$		$\tau = 1min$		$\tau = 10min$	
	P_f	β	P_f	β	P_f	β	P_f	β	P_f	β	P_f	β
1	5.2×10^{-7}	4.9	$< 10^{-7}$	> 5.2	$< 10^{-7}$	> 5.2	3.0×10^{-6}	4.5	$< 10^{-7}$	> 5.2	$< 10^{-7}$	> 5.2
10	6.5×10^{-6}	4.4	$< 10^{-7}$	> 5.2	$< 10^{-7}$	> 5.2	4.9×10^{-5}	3.9	6.4×10^{-7}	4.8	$< 10^{-7}$	> 5.2
50	3.8×10^{-5}	4.0	$< 10^{-7}$	> 5.2	$< 10^{-7}$	> 5.2	2.6×10^{-4}	3.5	3.0×10^{-6}	4.5	$< 10^{-7}$	> 5.2
100	8.2×10^{-5}	3.8	$< 10^{-7}$	> 5.2	$< 10^{-7}$	> 5.2	5.7×10^{-4}	3.3	5.1×10^{-6}	4.4	$< 10^{-7}$	> 5.2
150	1.4×10^{-4}	3.6	$< 10^{-7}$	> 5.2	$< 10^{-7}$	> 5.2	8.6×10^{-4}	3.1	8.3×10^{-6}	4.3	1.4×10^{-7}	5.1

Table 7.5 Flutter failure probability (Fragility curves: SBSA solutions using $1.5\sigma_{exp}$ for FDs; Wind hazard curves: all winds no considerations of wind direction)

T (year)	$z_0 = 0.01 m$						$z_0 = 0.0002 m$					
	$\tau = 3s$		$\tau = 1min$		$\tau = 10min$		$\tau = 3s$		$\tau = 1min$		$\tau = 10min$	
	P_f	β	P_f	β	P_f	β	P_f	β	P_f	β	P_f	β
1	8.9×10^{-4}	3.8	1.8×10^{-5}	4.1	6.2×10^{-6}	4.4	2.2×10^{-4}	3.5	5.8×10^{-5}	3.9	2.9×10^{-5}	4.0
10	8.6×10^{-4}	3.1	1.8×10^{-4}	3.6	6.3×10^{-5}	3.8	2.1×10^{-3}	2.9	4.9×10^{-4}	3.3	2.5×10^{-4}	3.5
50	3.0×10^{-3}	2.8	7.8×10^{-4}	3.2	2.9×10^{-4}	3.4	8.5×10^{-3}	2.4	1.8×10^{-3}	2.9	9.9×10^{-4}	3.1
100	4.6×10^{-3}	2.6	1.3×10^{-3}	3.0	5.1×10^{-4}	3.3	1.5×10^{-2}	2.2	2.7×10^{-3}	2.8	1.6×10^{-3}	3.0
150	5.8×10^{-3}	2.5	1.6×10^{-3}	2.9	7.2×10^{-4}	3.2	2.2×10^{-2}	2.0	3.3×10^{-3}	2.7	1.9×10^{-3}	2.9

Table 7.6 Flutter failure probability (Fragility curves: SBSA solutions using $1.5\sigma_{exp}$ for FDs; Wind hazard curves: only wind components that are perpendicular to the bridge orientation)

T (year)	$z_0 = 0.01 m$						$z_0 = 0.0002 m$					
	$\tau = 3s$		$\tau = 1min$		$\tau = 10min$		$\tau = 3s$		$\tau = 1min$		$\tau = 10min$	
	P_f	β	P_f	β	P_f	β	P_f	β	P_f	β	P_f	β
1	2.9×10^{-5}	4.0	7.4×10^{-6}	4.3	2.8×10^{-6}	4.5	3.8×10^{-5}	4.0	1.1×10^{-5}	4.2	6.0×10^{-6}	4.4
10	3.0×10^{-4}	3.4	6.4×10^{-5}	3.8	1.8×10^{-5}	4.1	5.1×10^{-4}	3.3	1.5×10^{-4}	3.6	7.6×10^{-5}	3.8
50	1.3×10^{-3}	3.0	3.0×10^{-4}	3.4	1.0×10^{-4}	3.7	2.0×10^{-3}	2.9	6.4×10^{-4}	3.2	3.4×10^{-4}	3.4
100	2.1×10^{-3}	2.9	5.6×10^{-4}	3.3	2.0×10^{-4}	3.5	3.4×10^{-3}	2.7	1.1×10^{-3}	3.1	6.2×10^{-4}	3.2
150	2.6×10^{-3}	2.8	8.0×10^{-4}	3.2	2.8×10^{-4}	3.4	4.3×10^{-3}	2.6	1.5×10^{-3}	3.0	8.4×10^{-4}	3.1

Table 7.7 Flutter failure probability (Fragility curves: multimode solutions using σ_{exp} for FDs; Wind hazard curves: all winds no considerations of wind direction)

T (year)	$z_0 = 0.01 m$						$z_0 = 0.0002 m$					
	$\tau = 3s$		$\tau = 1min$		$\tau = 10min$		$\tau = 3s$		$\tau = 1min$		$\tau = 10min$	
	P_f	β	P_f	β	P_f	β	P_f	β	P_f	β	P_f	β
1	7.8×10^{-7}	4.8	$< 10^{-7}$	> 5.2	$< 10^{-7}$	> 5.2	1.4×10^{-5}	4.2	3.4×10^{-7}	5.0	$< 10^{-7}$	> 5.2
10	1.2×10^{-5}	4.2	$< 10^{-7}$	> 5.2	$< 10^{-7}$	> 5.2	2.5×10^{-4}	3.5	3.1×10^{-6}	4.5	$< 10^{-7}$	> 5.2
50	9.0×10^{-5}	3.7	$< 10^{-7}$	> 5.2	$< 10^{-7}$	> 5.2	1.4×10^{-3}	3.0	1.5×10^{-5}	4.2	5.8×10^{-7}	4.9
100	1.9×10^{-4}	3.6	$< 10^{-7}$	> 5.2	$< 10^{-7}$	> 5.2	2.9×10^{-3}	2.8	3.3×10^{-5}	4.0	7.4×10^{-7}	4.8
150	3.1×10^{-4}	3.4	$< 10^{-7}$	> 5.2	$< 10^{-7}$	> 5.2	4.5×10^{-3}	2.6	4.6×10^{-5}	3.9	8.2×10^{-7}	4.8

Table 7.8 Flutter failure probability (Fragility curves: multimode solutions using σ_{exp} for FDs; Wind hazard curves: only wind components that are perpendicular to the bridge orientation)

T (year)	$z_0 = 0.01 \text{ m}$						$z_0 = 0.0002 \text{ m}$					
	$\tau = 3s$		$\tau = 1min$		$\tau = 10min$		$\tau = 3s$		$\tau = 1min$		$\tau = 10min$	
	P_f	β	P_f	β	P_f	β	P_f	β	P_f	β	P_f	β
1	$< 10^{-7}$	>5.2	$< 10^{-7}$	>5.2	$< 10^{-7}$	>5.2	8.0×10^{-7}	4.8	$< 10^{-7}$	>5.2	$< 10^{-7}$	>5.2
10	1.0×10^{-6}	4.8	$< 10^{-7}$	>5.2	$< 10^{-7}$	>5.2	1.3×10^{-5}	4.2	$< 10^{-7}$	>5.2	$< 10^{-7}$	>5.2
50	5.3×10^{-5}	4.4	$< 10^{-7}$	>5.2	$< 10^{-7}$	>5.2	6.4×10^{-5}	3.8	3.4×10^{-7}	5.0	$< 10^{-7}$	>5.2
100	1.3×10^{-5}	4.2	$< 10^{-7}$	>5.2	$< 10^{-7}$	>5.2	1.4×10^{-4}	3.6	5.4×10^{-7}	4.9	$< 10^{-7}$	>5.2
150	2.0×10^{-5}	4.1	$< 10^{-7}$	>5.2	$< 10^{-7}$	>5.2	2.1×10^{-4}	3.5	8.2×10^{-7}	4.8	$< 10^{-7}$	>5.2

Table 7.9 Flutter failure probability (Fragility curves: multimode solutions using $1.5\sigma_{exp}$ for FDs; Wind hazard curves: all winds no considerations of wind direction)

T (year)	$z_0 = 0.01 \text{ m}$						$z_0 = 0.0002 \text{ m}$					
	$\tau = 3s$		$\tau = 1min$		$\tau = 10min$		$\tau = 3s$		$\tau = 1min$		$\tau = 10min$	
	P_f	β	P_f	β	P_f	β	P_f	β	P_f	β	P_f	β
1	1.5×10^{-6}	4.7	$< 10^{-7}$	>5.2	$< 10^{-7}$	>5.2	1.7×10^{-5}	4.1	3.4×10^{-7}	5.0	$< 10^{-7}$	>5.2
10	1.7×10^{-5}	4.2	$< 10^{-7}$	>5.2	$< 10^{-7}$	>5.2	2.8×10^{-4}	3.5	4.2×10^{-6}	4.5	1.0×10^{-7}	5.2
50	1.0×10^{-4}	3.7	$< 10^{-7}$	>5.2	$< 10^{-7}$	>5.2	1.6×10^{-3}	3.0	1.9×10^{-5}	4.1	4.2×10^{-7}	4.9
100	2.3×10^{-4}	3.5	$< 10^{-7}$	>5.2	$< 10^{-7}$	>5.2	3.4×10^{-3}	2.7	4.3×10^{-5}	3.9	1.1×10^{-6}	4.7
150	3.7×10^{-4}	3.4	$< 10^{-7}$	>5.2	$< 10^{-7}$	>5.2	5.2×10^{-3}	2.5	6.5×10^{-5}	3.8	1.7×10^{-6}	4.6

Table 7.10 Flutter failure probability (Fragility curves: multimode solutions using $1.5\sigma_{exp}$ for FDs; Wind hazard curves: only wind components that are perpendicular to the bridge orientation)

T (year)	$z_0 = 0.01 \text{ m}$						$z_0 = 0.0002 \text{ m}$					
	$\tau = 3s$		$\tau = 1min$		$\tau = 10min$		$\tau = 3s$		$\tau = 1min$		$\tau = 10min$	
	P_f	β	P_f	β	P_f	β	P_f	β	P_f	β	P_f	β
1	1.2×10^{-7}	5.2	$< 10^{-7}$	>5.2	$< 10^{-7}$	>5.2	1.2×10^{-6}	4.7	$< 10^{-7}$	>5.2	$< 10^{-7}$	>5.2
10	1.0×10^{-6}	4.7	$< 10^{-7}$	>5.2	$< 10^{-7}$	>5.2	1.3×10^{-5}	4.2	1.0×10^{-7}	5.2	$< 10^{-7}$	>5.2
50	7.4×10^{-6}	4.3	$< 10^{-7}$	>5.2	$< 10^{-7}$	>5.2	7.8×10^{-5}	3.8	2.2×10^{-7}	5.1	$< 10^{-7}$	>5.2
100	1.6×10^{-5}	4.2	$< 10^{-7}$	>5.2	$< 10^{-7}$	>5.2	1.7×10^{-4}	3.6	5.4×10^{-7}	4.9	$< 10^{-7}$	>5.2
150	2.7×10^{-5}	4.0	$< 10^{-7}$	>5.2	$< 10^{-7}$	>5.2	2.7×10^{-4}	3.5	1.2×10^{-6}	4.7	$< 10^{-7}$	>5.2

Table 7.11 Target reliability (Annual probability of failure, P_f) and associated reliability indices (β) for load conditions that do not include earthquake, tsunami, or extraordinary events (ASCE/SEI, 2016)

Basis	Risk Category							
	I		II		III		IV	
	P_f	β	P_f	β	P_f	β	P_f	β
Failure that is not sudden and does not lead to widespread progression of damage	1.25 $\times 10^{-4}$	2.5	3.0 $\times 10^{-5}$	3.0	1.25 $\times 10^{-5}$	3.25	5.0 $\times 10^{-6}$	3.5
Failure that is either sudden or leads to widespread progression of damage	3.0 $\times 10^{-5}$	3.0	5.0 $\times 10^{-6}$	3.5	2.0 $\times 10^{-6}$	3.75	7.0 $\times 10^{-7}$	4.0
Failure that is sudden and results in widespread progression of damage	5.0 $\times 10^{-6}$	3.5	7.0 $\times 10^{-7}$	4.0	2.5 $\times 10^{-7}$	4.25	1.0 $\times 10^{-7}$	4.5

Note: P_f = annualized probability of failure; β = reliability index for a 50-year reference period.

Table 7.11 listed the annual probability of failure, P_f and associated reliability indices, β in 50-year service period for the load conditions that do not include earthquake, tsunami, or extraordinary events provided by ASCE/SEI 7-16 (2016). Given that the failure of a long-bridge due to flutter is a sudden event that would result in the collapse of the structure and a substantial economic impact. Accordingly, the target failure reliability related to risk category IV, i.e. annual probability of failure $P_f = 1.0 \times 10^{-7}$ and reliability indices in 50 years $\beta = 4.5$ should be selected. If only the flutter failure probabilities in Table 7.8, which utilize the multimode solutions of flutter critical wind speed and the wind components that are perpendicular to the bridge orientation is compared, all annual probabilities of failure are less than 1.0×10^{-7} except when $z_0 = 0.0002 \text{ m}$ and $\tau = 3 \text{ s}$ with the $P_f = 8.0 \times 10^{-7}$. As for the reliability indices in $T = 50$ years, the modelled β associated with $\tau = 3 \text{ s}$ for both $z_0 = 0.01 \text{ m}$ and $z_0 = 0.0002 \text{ m}$ cases are smaller than 4.5. However, the gust duration $\tau = 3 \text{ s}$ could be too short to excite the flutter of the bridges. The gust duration $\tau = 60 \text{ s}$ or 1 min should be preferable. Consequently, we have sufficient evidence to conclude that the

Lindingyang suspension bridge meets the reliability requirement for the flutter-resistant design subjected to typhoon winds.

7.7 Conclusion

This chapter is an application of the outputs obtained from previous chapters. The risk assessments of a long-span suspension bridge subjected to typhoon winds were conducted. The flutter fragility curves of the present bridge in terms of critical wind speed were developed by taking the uncertainties of structural parameters and aerodynamic parameters into account. The typhoon wind hazard curves as the probability of occurrence in any years of interest were developed in the bridge site using the GWR-based subregion circular method. The gust factor effects on wind speed were also introduced to formulate the limit state function of flutter failure. A series of the failure probabilities with respect to different combinations of flutter fragility curves and typhoon wind hazard curves were developed utilizing Monte Carlo simulation technique.

7.8 Reference

- ASCE/SEI. (2016). Minimum design loads and associated criteria for buildings and other structures. ASCE/SEI 7-16, Reston, VA.
- Bartoli G, Mannini C, (2008). A simplified approach to bridge deck flutter. *Journal of Wind Engineering & Industrial Aerodynamics*, 96(2):229-256.
- Bartoli G, Contri S, Mannini C, et al., (2009). Toward an Improvement in the Identification of Bridge Deck Flutter Derivatives. *Journal of Engineering Mechanics*, 135(8):771-785.

Brancaleoni, F. Diana G. (1993). The aerodynamic design of the Messina Straits Bridge. *Journal of Wind Engineering & Industrial Aerodynamics*, 48, 395-409.

Cao F, Ge Y, (2017). Air-induced nonlinear damping and added mass of vertically vibrating bridge deck section models under zero wind speed. *Journal of Wind Engineering and Industrial Aerodynamics*, 169:217-231.

Cheng J, Cai C S, Xiao R C, Chen S R. (2005). Flutter reliability analysis of suspension bridges, *Journal of Wind Engineering & Industrial Aerodynamics*. 93(10):757–775.

Chen, X. , Matsumoto, M. , & Kareem, A. . (2000). Aerodynamic coupling effects on flutter and buffeting of bridges. *Journal of Engineering Mechanics*, 126(1), 17-26.

Chowdhury A G, Sarkar P P, (2003). A new technique for identification of eighteen flutter derivatives using a three-degree-of-freedom section model. *Engineering Structures*, 25(14):1763-1772.

Ding Q, Zhou Z Y, Zhu L, Xiang H, (2010). Identification of flutter derivatives of bridge decks with free vibration technique. *Journal of Wind Engineering and Industrial Aerodynamics*, 98, 911-918.

Fujino, Y. (2002). Vibration, control and monitoring of long-span bridges - recent research, developments and practice in japan. *Journal of Constructional Steel Research*, 58(1), 71-97.

Gao, G, Zhu, L, Han, W, & Li, J. Nonlinear post-flutter behavior and self-excited force model of a twin-side-girder bridge deck[J]. *Journal of Wind Engineering and Industrial Aerodynamics*, 2018, 177, 227-241.

Ge Y J, Xiang H F, Tanaka H. (2000). Application of a reliability analysis model to bridge flutter under extreme winds, *Journal of Wind Engineering & Industrial Aerodynamics*. 86: 155–167.

Gu M, Zhang R, Xiang H, (2000). Identification of flutter derivatives of bridge decks. *Journal of Wind Engineering and Industrial Aerodynamics*, 84(2), 151-162.

Guo Z S, Chen A R, Xiang H F, (2000). Characteristics of structural damping of cable-supported bridges with long spans. *World Information on Earthquake Engineering*, 16(3), 52-57 (in Chinese).

Huang M H, Lin Y Y, Weng M X, (2012). Flutter and buffeting analysis of bridges subjected to skew wind. *Journal of Applied Science and Engineering*, 15(4), 401-413.

Kim S, Kim H K. (2017). Damping identification of bridges under nonstationary ambient vibration. *Engineering*, 3, 839-844.

Kim S, Jung H, Kong M J, Lee D K, An Y K, (2019). In-situ data-driven buffeting response analysis of a cable-stayed bridge. *Sensors*, 19, 3048.

Li L, Kareem A, Xiao Y, et al. A comparative study of field measurements of the turbulence characteristics of typhoon and hurricane winds[J]. *Journal of Wind Engineering & Industrial Aerodynamics*, 2015, 140:49-66.

Li Y, Liao H, Qiang S, (2003). Weighting ensemble least-square method for flutter derivatives of bridge decks. *Journal of Wind Engineering & Industrial Aerodynamics*, 91(6):713-721.

Li Z, Feng M Q, Luo L, Feng D, Xu X, (2018). Statistical analysis of modal parameters of a suspension bridge based on Bayesian spectral density approach and SHM data. *Mechanical Systems and Signal Processing*, 98, 352-367.

Liu Y, Ge Y J, Cao F C, Zhou Y, Wang S Q. (2013). Statistics and identification of mode-dependent structural damping of cable-supported bridges. *Proceeding of the 8th Asia-Pacific Conference on Wind Engineering (APCWE-VIII)*, Chennai, India, 719-731.

Matsumoto M. (1996). Aerodynamic damping of prisms. *Journal of Wind Engineering and Industrial Aerodynamics*, 59: 159-175.

Matsumoto M, Matsumiya H, Fujiwara S, et al. (2010). New consideration on flutter properties based on step-by-step analysis. *Journal of Wind Engineering & Industrial Aerodynamics*, 98(8):429-437.

Ministry of Communication of the People's Republic of China. (2004), JTG/T D60-01-2004, Wind-resistant design specification for highway bridges, China Communications Press, Beijing, China.

National Standards Committee. Load code for the design of building structures, China National Standard (CNS) [S]. GB 50009-2012, National Standards Committee, Beijing, China; 2012.

Qin X and Gu M. Determination of flutter derivatives by stochastic subspace identification technique, *Wind and Structures*, 2004, 7(3): 173-186.

Sarkar P P, Jones N P, Scanlan R H. Identification of Aeroelastic Parameters of Flexible Bridges[J]. *Journal of Engineering Mechanics*, 1994, 120(8):1718-1742.

Scanlan R H. The action of flexible bridges under wind, I: flutter theory. *Journal of Sound and Vibration*, 60(2): 187-199, 1978.

Scanlan R H, Jones N P, Singh L . Inter-relations among flutter derivatives[J]. *Journal of Wind Engineering and Industrial Aerodynamics*, 1997, 69-71:829-837.

Simiu E and Scanlan RH (1996) *Wind Effects on Structures: Fundamentals and Applications to Design*, 3rd edn. J. Wiley and Sons, New York, NY, USA.

T. Theodorsen and I. E. Garrick, *Mechanism of Flutter: A Theoretical and Experimental Investigation of the Flutter Problem*, Report 685 (NACA, 1940).

Xiang H, Ge Y. Aerodynamic challenges in span length of suspension bridges[J]. *Frontiers of Architecture & Civil Engineering in China*, 2007, 1(2):153-162.

Xu F, Zhu L, Ge X, et al. Some new insights into the identification of bridge deck flutter derivatives[J]. *Engineering Structures*, 2014, 75(8):418-428.

Xu, F., Y. . (2015). System decoupling approach for 3-DOF bridge flutter analysis. *Journal of Structural Engineering*, 141(7), 04014168.

Xu, Y.-L. *Wind Effects on Cable-Supported Bridges*. John Wiley & Sons Singapore Pte. Ltd., 2013.

Yamaguchi, H. , & Ito, M. . (1997). Mode-dependence of structural damping in cable-stayed bridges. *Journal of Wind Engineering & Industrial Aerodynamics*, 72(1), 289-300.

Yang Y X, Ge Y J, Xiang H F. Investigation on flutter mechanism of long-span bridges with 2d-3DOF method. *Wind and Structures*, 10(5): 421-435, 2007.

Zhao L, Wang Q, Song S Y, Chen W L, Wu M Y, Liao H L, Ge Y J. (2019). Investigation on Wind-resistance Performance of Lingdingyang Bridge with Main-span 1666m in Shen-Zhong Link. *China Journal of Highway and Transport* (In Chinese, Accepted).

Zhu L D, Xu Y L, Xiang H F, (2002a). Tsing Ma bridge deck under skew winds—Part I: Aerodynamic coefficients. *Journal of Wind Engineering & Industrial Aerodynamics*, 90 (7), 781–805.

Zhu L D, Xu Y L, Xiang H F, (2002b). Tsing Ma bridge deck under skew winds—Part II: Flutter derivatives. *Journal of Wind Engineering & Industrial Aerodynamics*, 90 (7), 807–837.

Zhu L D, Xu Y L, Guo Z, Chang G Z, Tan X. (2013). Yaw wind effect on flutter instability of four typical bridge decks. *Wind and Structures: An International Journal*, 17(3), 317-343.

CHAPTER 8 CONCLUSIONS AND RECOMMENDATIONS

8.1 Conclusions and summary

In order to investigate the typhoon wind hazards and their potential threats on long-span bridges along coastal regions of China, a systematic typhoon simulation algorithm was developed to generate more than 10,000-year synthetic typhoon tracks and perform the flutter risk assessment on long-span bridges. Major contributions of this study are summarized as follows:

(1) A semi-analytical height-resolving typhoon boundary layer model was developed which allows the estimation of typhoon wind speeds at any heights of interest. Meanwhile, the physical basis behind the present wind field model is able to help us better understand the inner structure of typhoon storms.

(2) The wind fields of historical typhoon storms are reconstructed by optimally fitting two wind field parameters, i.e. $R_{max,s}$ and B_s using JMA best track dataset coupled with the present wind field model. The dataset of $R_{max,s}$ and B_s allows the development of recursive models to account for the autocorrelations of parameters between different time steps, which can be site-specific and can be applied to both sub-region typhoon simulations and full track simulations. The extraction of $R_{max,s}$ and B_s for each typhoon event also facilitates the reconstruction of wind hazard footprints. The directional upstream terrain effects on wind speed in terms of an equivalent roughness length z_0 and topographic speed-up factor K_t were investigated. The wind hazard footprints for over-water, roughness only and roughness and topography combined conditions of 184 observed landed or offshore typhoon-scale storms are generated and archived for risk assessment.

(3) The non-stationary and non-Gaussian characteristics of near-ground typhoon winds were carefully examined using observed data. A non-Gaussian PSD- and moment-based translation model was developed to estimate the peak factor as well as the gust factor of strong typhoon winds. It was found that a large portion of gust factors would be underestimated if the non-Gaussian effects were ignored by comparing with the non-Gaussian solutions.

(4) A GER-based circular subregion model, in terms of the genesis model and track forward model, was developed to facilitate the typhoon wind estimation. This model can be applied to any site of interest to perform a rapid prediction of typhoon wind hazards. The design wind speed maps in the southeastern typhoon-prone region of China were also developed. The dataset of typhoon wind design wind speeds with respect to various return periods, two surface roughness lengths and different wind directions could be of great help for the future typhoon-resistant design of building and bridge structures.

(5) A framework for determining the probabilistic solutions of flutter critical wind speeds of long-span bridges was developed. Two major sources of uncertainty, i.e. the structural parameters in terms of the natural modal information and damping ratios and the aerodynamic parameters or flutter derivatives were examined and discussed. The uncertainty of each parameter was quantified using a literature survey or repeated wind tunnel test data. A series of probabilistic studies of flutter critical wind speed were performed based on three sections, FDs obtained from four turbulent winds as well as two bridge structural systems using 2D SBSA and multimode methods.

(6) A case study of typhoon wind risks on a long-span suspension bridge. The flutter failure probabilities of this bridge with respect to different combinations of flutter fragility curves

and typhoon wind hard curves were calculated using the Monte Carlo technique. To author's knowledge, this study is the first time to systematically perform the flutter risk assessments of long-span bridges subjected to typhoon winds.

8.2 Recommendations for future study

To improve and expand the current study, several topics can be continued for future research as follows:

(1) To validate and improve the accuracy of the present typhoon wind speed design maps using real observation typhoon wind data. As mentioned before, the design wind speeds in current codes of China for the typhoon-prone regions were developed based on the probability distribution of several-decade real wind data. On the one hand, some very strong typhoon winds were always failed to be captured since the damage of observation devices and sensors. On the other hand, the use of extreme distribution based on typhoon and non-typhoon winds could result in some ridiculous predictions as discussed before. Accordingly, the current code suggestions cannot provide enough confidence to prove our predictions are accurate or not. More real data, especially typhoon wind data would help to perform the future validation work.

(2) To conduct cross-validations using multi-agency best track datasets. As discussed in Chapter 5, the inconsistency of best track dataset in terms of storm intensity and time-averaged duration of parameters would result in significant differences if different datasets were employed. The comparison of criteria for the development of best track dataset from different agencies would be of great help to provide more accurate predictions of typhoon wind hazards.

(3) To figure out the turbulence effects on FDs from the statistical perspective. It was found that high turbulence intensity could reduce the flutter critical wind speed of long-span bridges. And typhoon winds are usually featured with high turbulence intensity. As can be noted in Chapter 6, the distributions of flutter critical wind speed between 2D SBSA and 3D multimode methods gradually cross with each other with the increase of turbulence intensity. More wind tunnel tests of different section models can be performed in the future. It would be great of interest to ascertain this phenomenon utilizing both statistical and physical methods.

APPENDIX A. COEFFICIENTS OF TRACKING MODEL

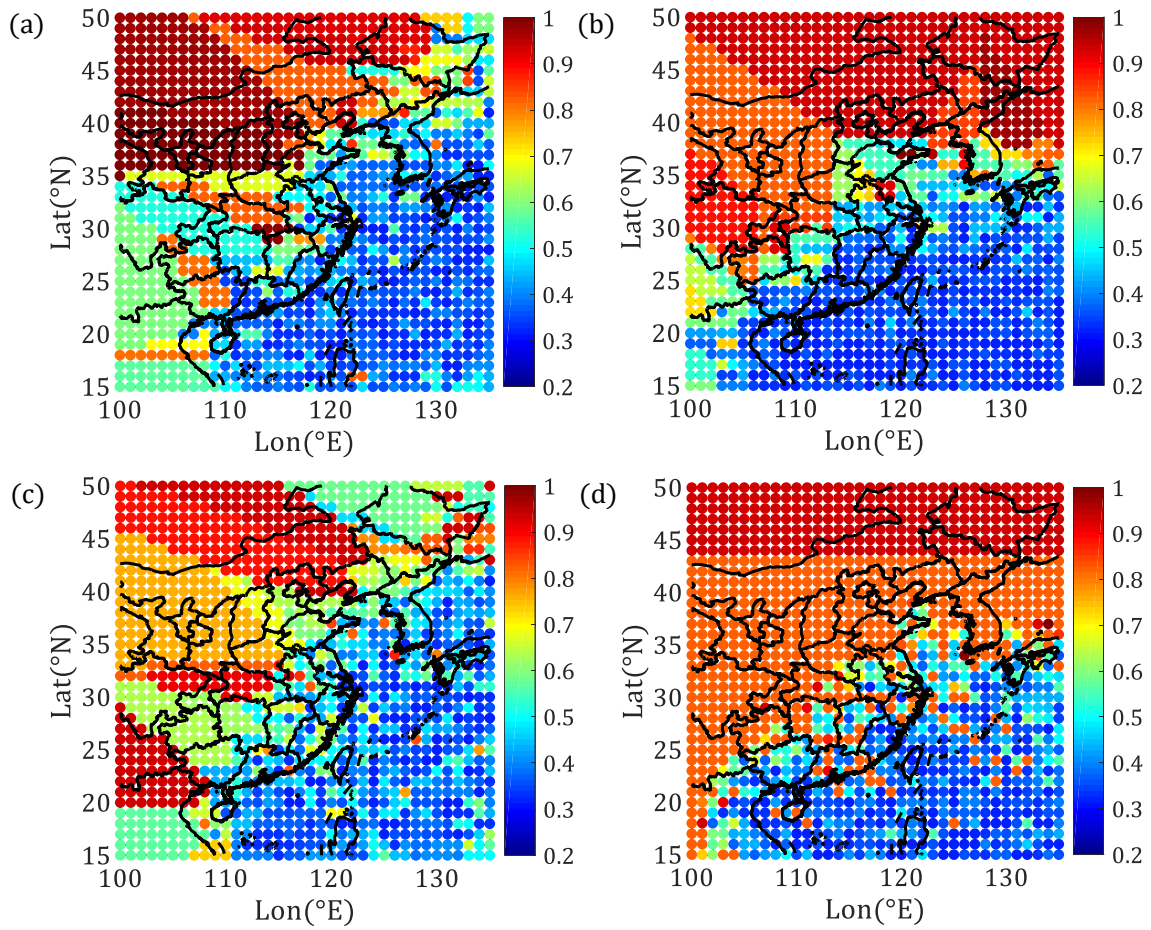


Fig. A1 The optimal bandwidths for tracking model: (a) V_T for easterly headed storms; (b) V_T for westerly headed storms; (c) θ_T for easterly headed storms; (d) θ_T for westerly headed storms

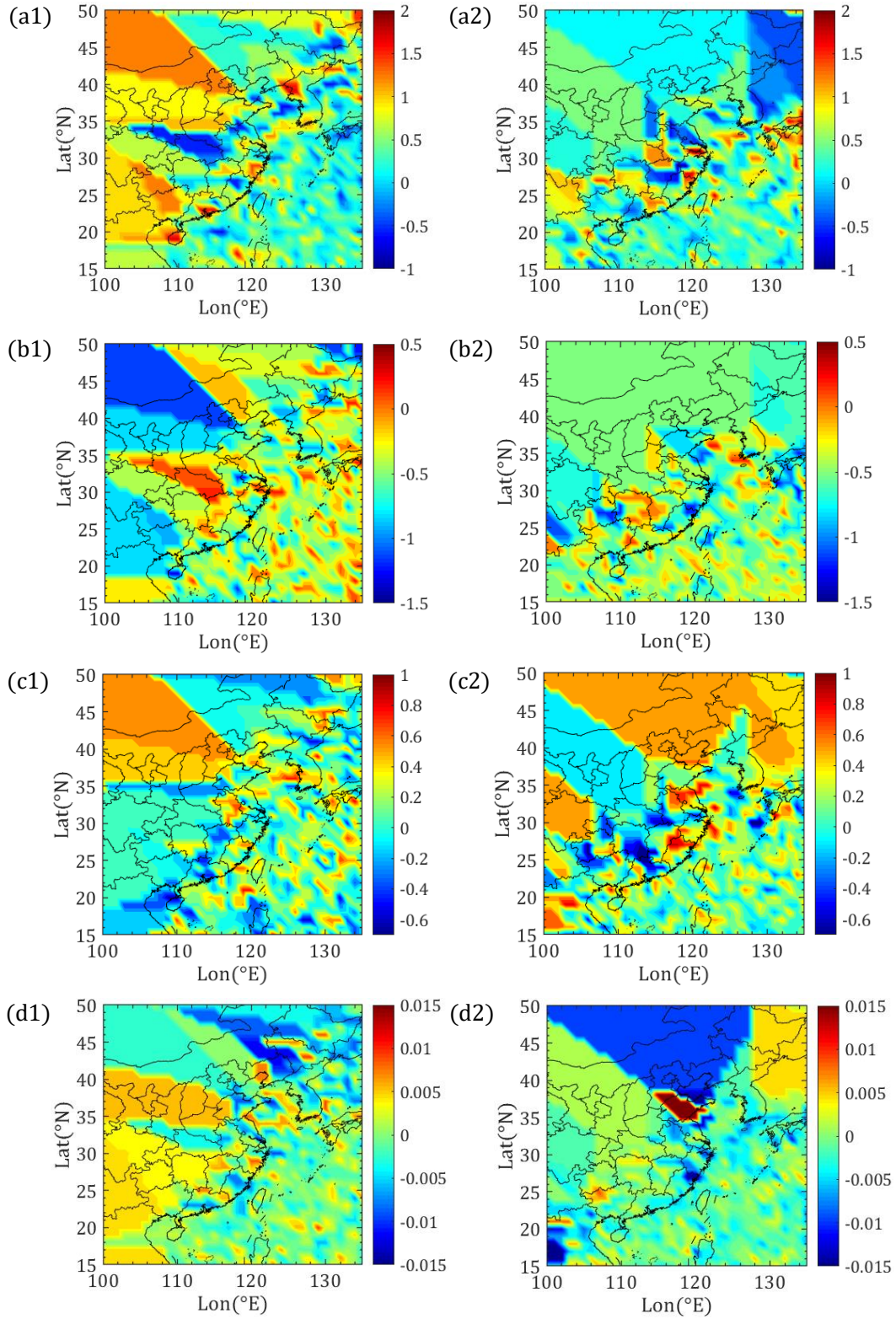


Fig. A2 Contour plots of coefficients for forward speed model: (a)~(d) $v_1 \sim v_4$; left column corresponds to easterly headed storms, right column corresponds to westerly headed storms

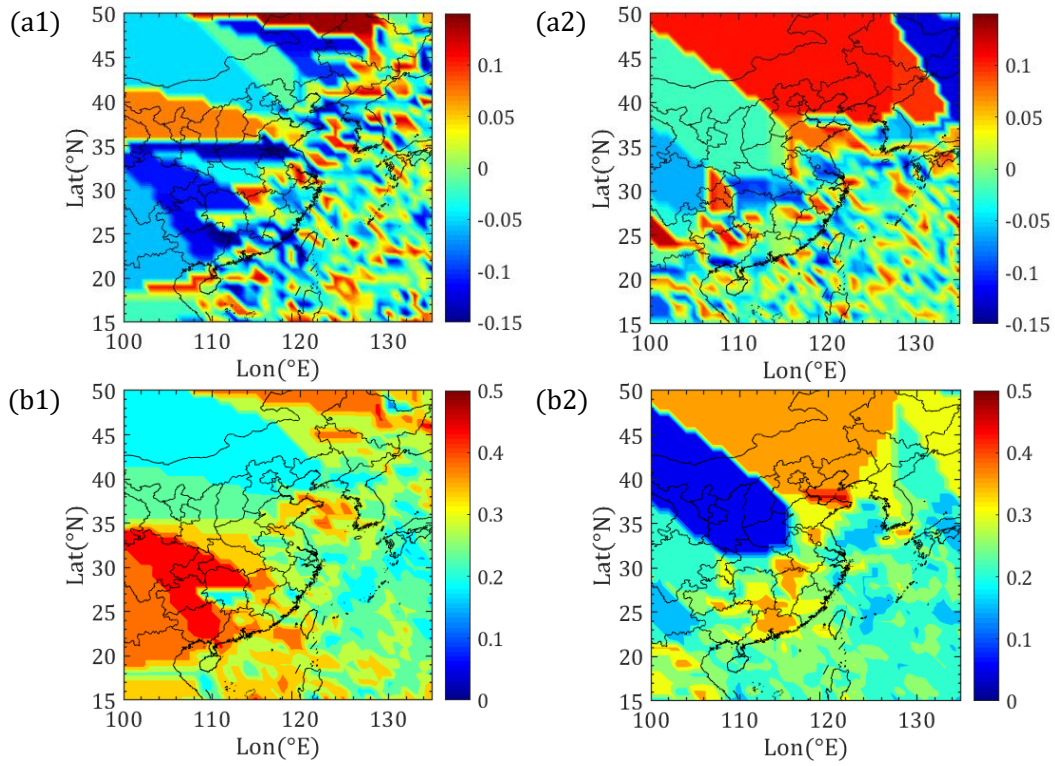


Fig. A3 Contour plots of error term for forward speed model: (a) error mean; (b) error standard deviation; the left column corresponds to easterly headed storms, right column corresponds to westerly headed storms

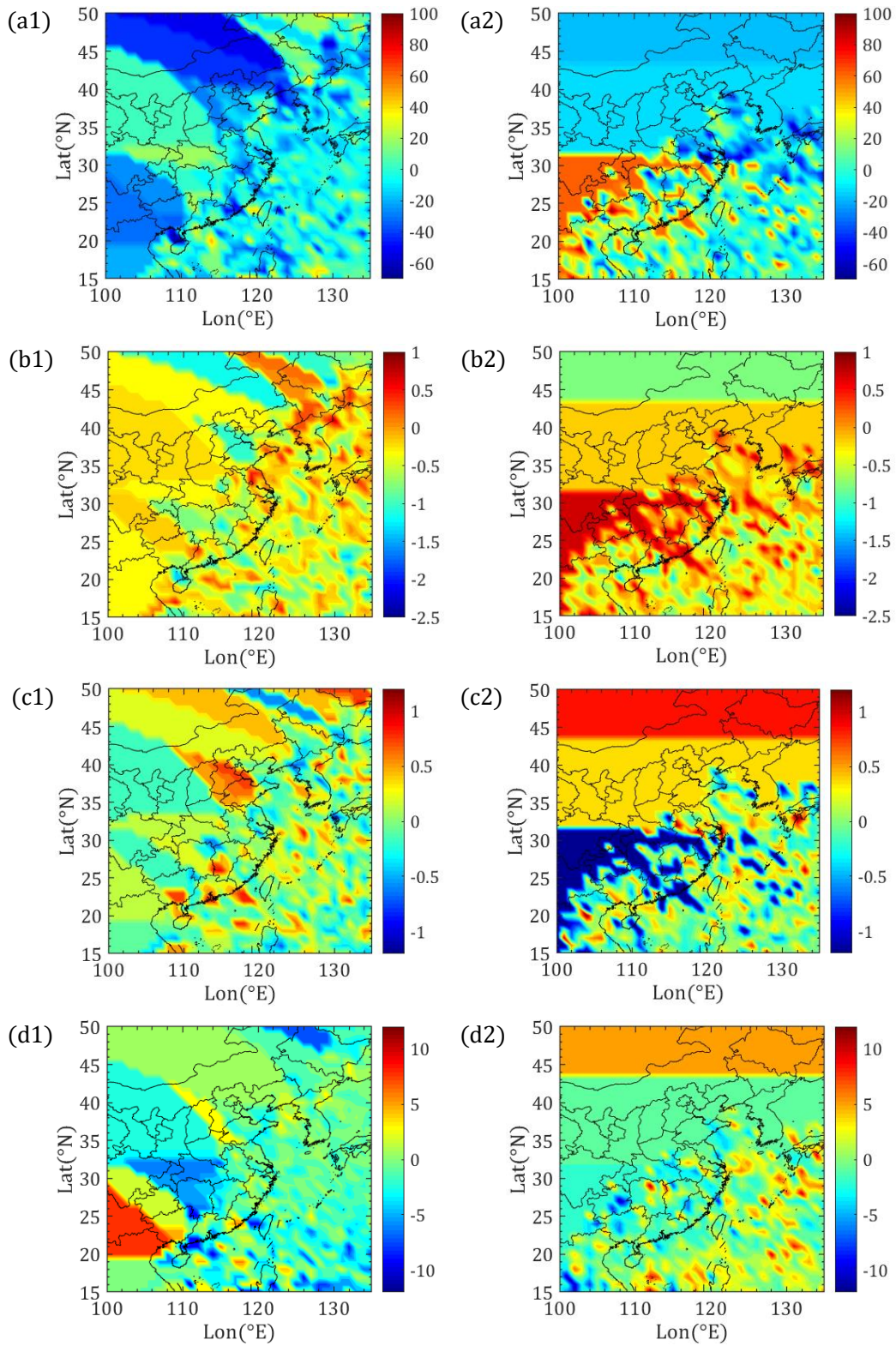


Fig. A4 Contour plots of coefficients for heading direction model: (a)~(d) $h_1 \sim h_4$; left column corresponds to easterly headed storms, right column corresponds to westerly headed storms

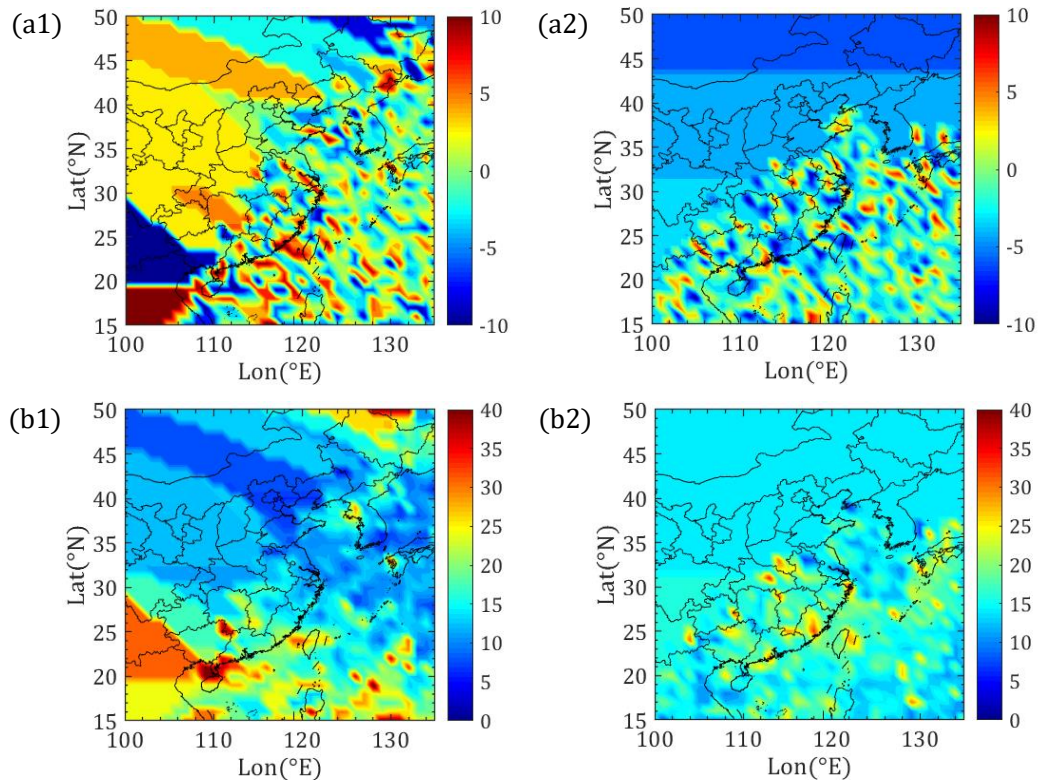


Fig. A5 Contour plots of error term for heading direction model: (a) error mean; (b) error standard deviation; the left column corresponds to easterly headed storms, right column corresponds to westerly headed storms

APPENDIX B. PERFORMANCE ASSESSMENT OF THE TRACKING MODEL

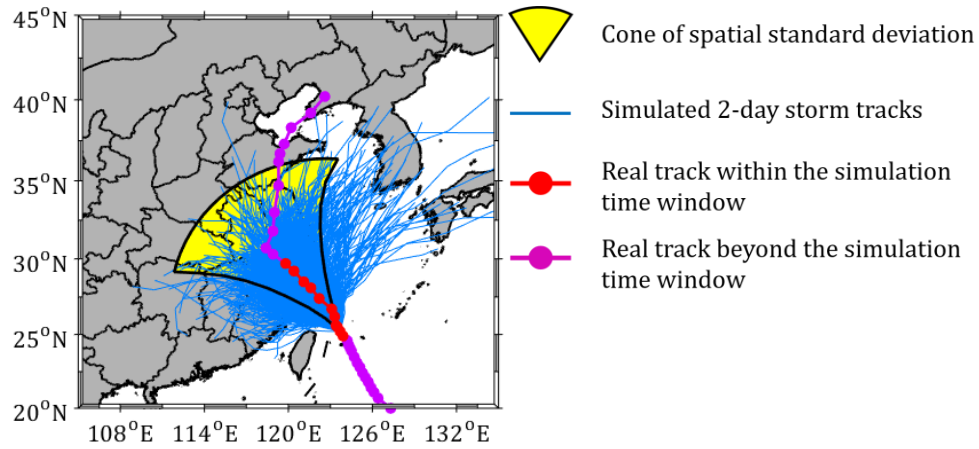


Fig. B1 Typhoon Matsa: 2-day simulation from 2005-08-04 15:00 UTC

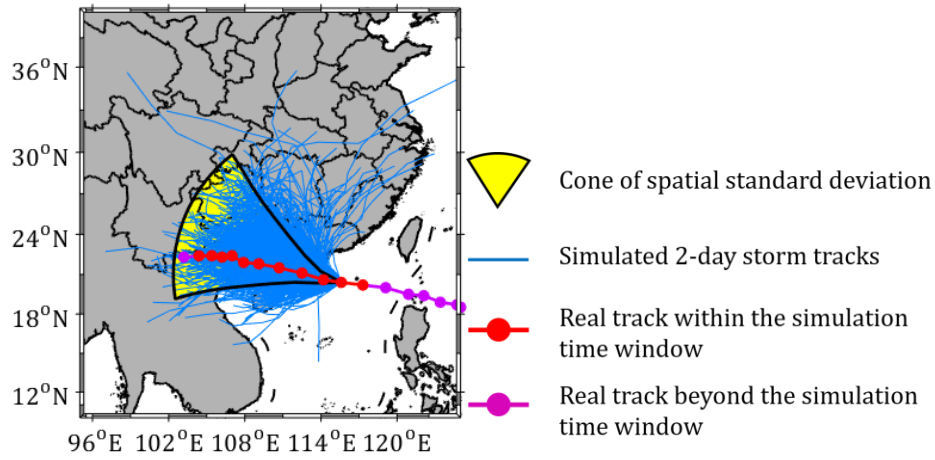


Fig. B2 Typhoon Hagupit: 2-day simulation from 2008-09-23 00:00 UTC

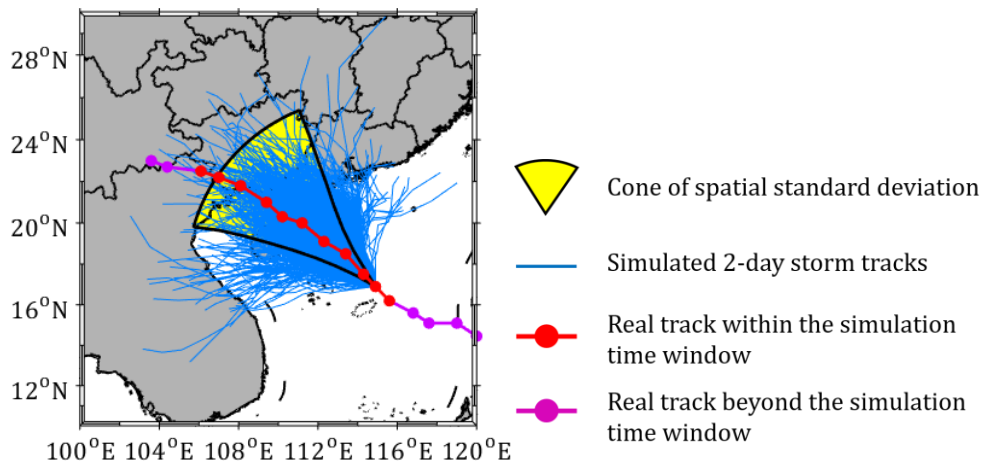


Fig. B3 Typhoon Rammasun: 2-day simulation from 2014-07-17 00:00 UTC

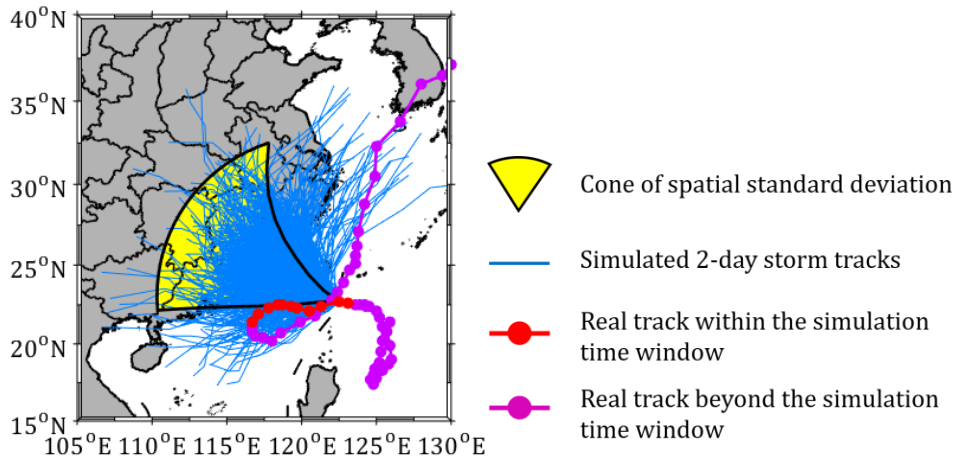


Fig. B4 Typhoon Tembin: 2-day simulation from 2012-08-23 06:00 UTC

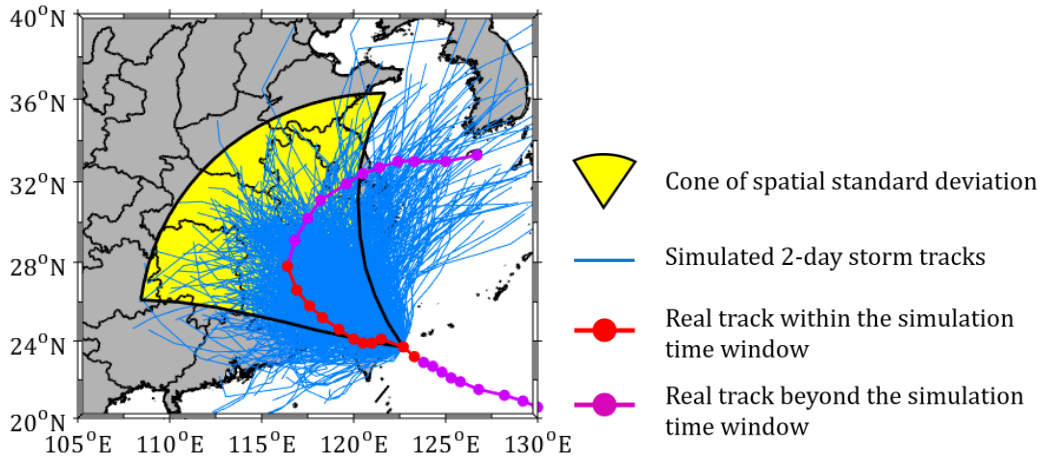


Fig. B5 Typhoon Soudelor: 2-day simulation from 2015-08-07 15:00 UTC

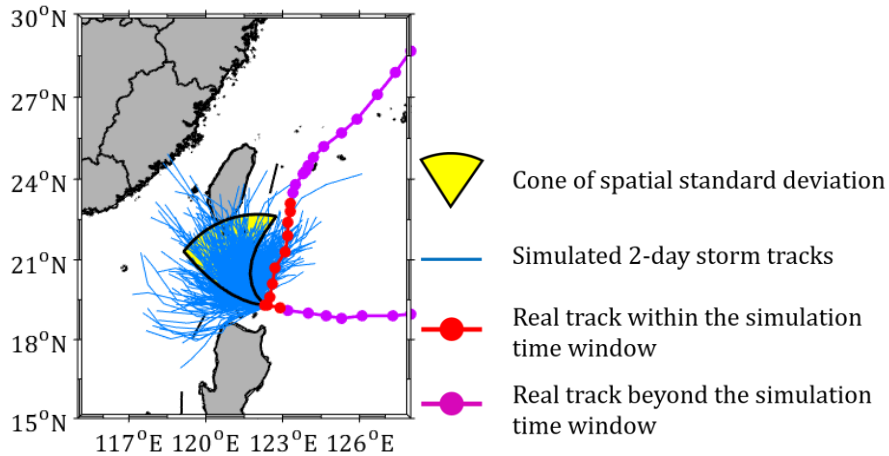


Fig. B6 Typhoon Goni: 2-day simulation from 2015-08-21 00:00 UTC

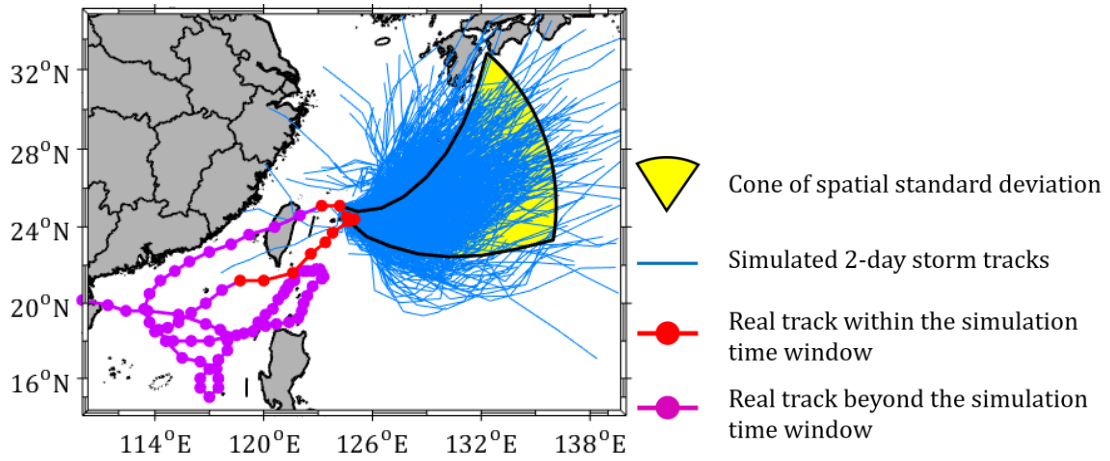


Fig. B7 Typhoon Wayne: 2-day simulation from 1986-08-22 12:00 UTC

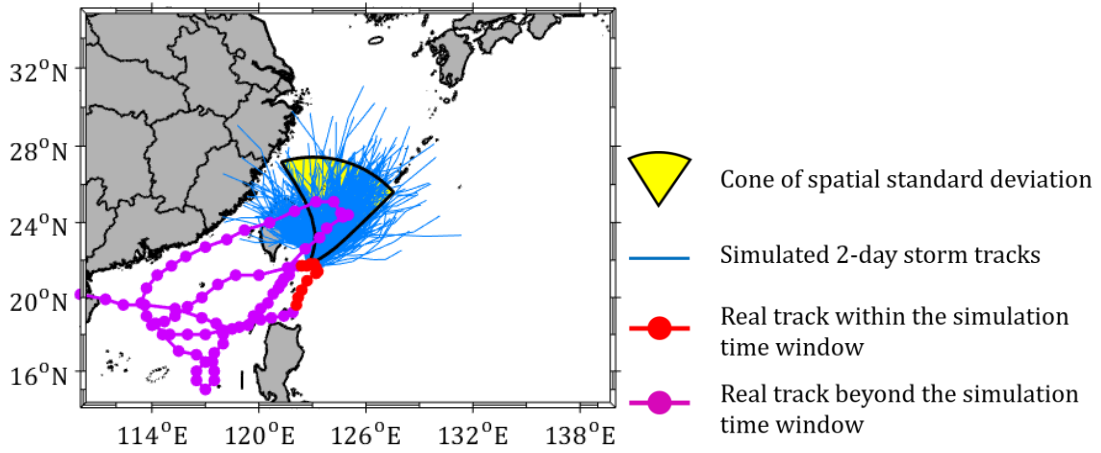


Fig. B8 Typhoon Wayne: 2-day simulation from 1986-08-30 12:00 UTC

APPENDIX C. COEFFICIENTS OF INTENSITY MODEL

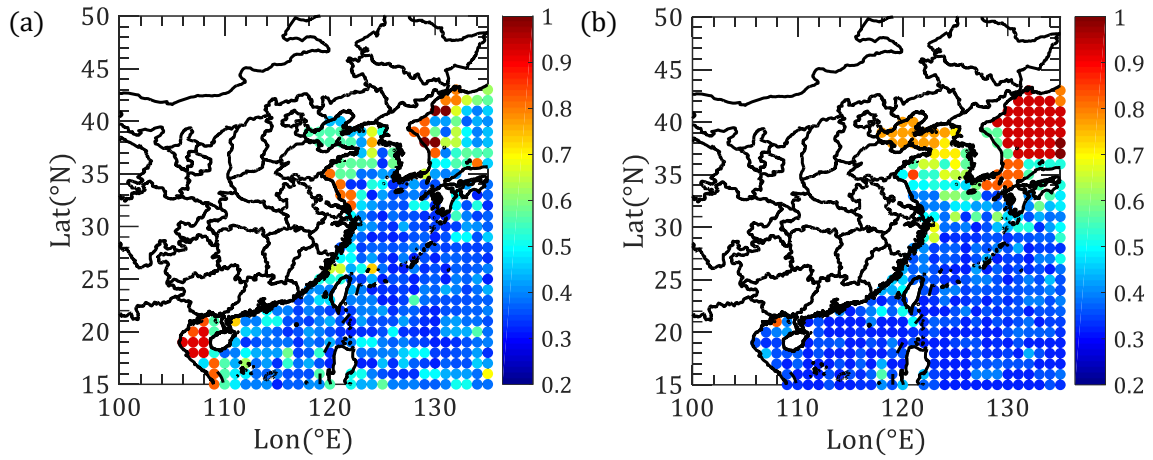


Fig. C1 The optimal bandwidths for intensity model: (a) Easterly headed storms; (b) Westerly headed storms;

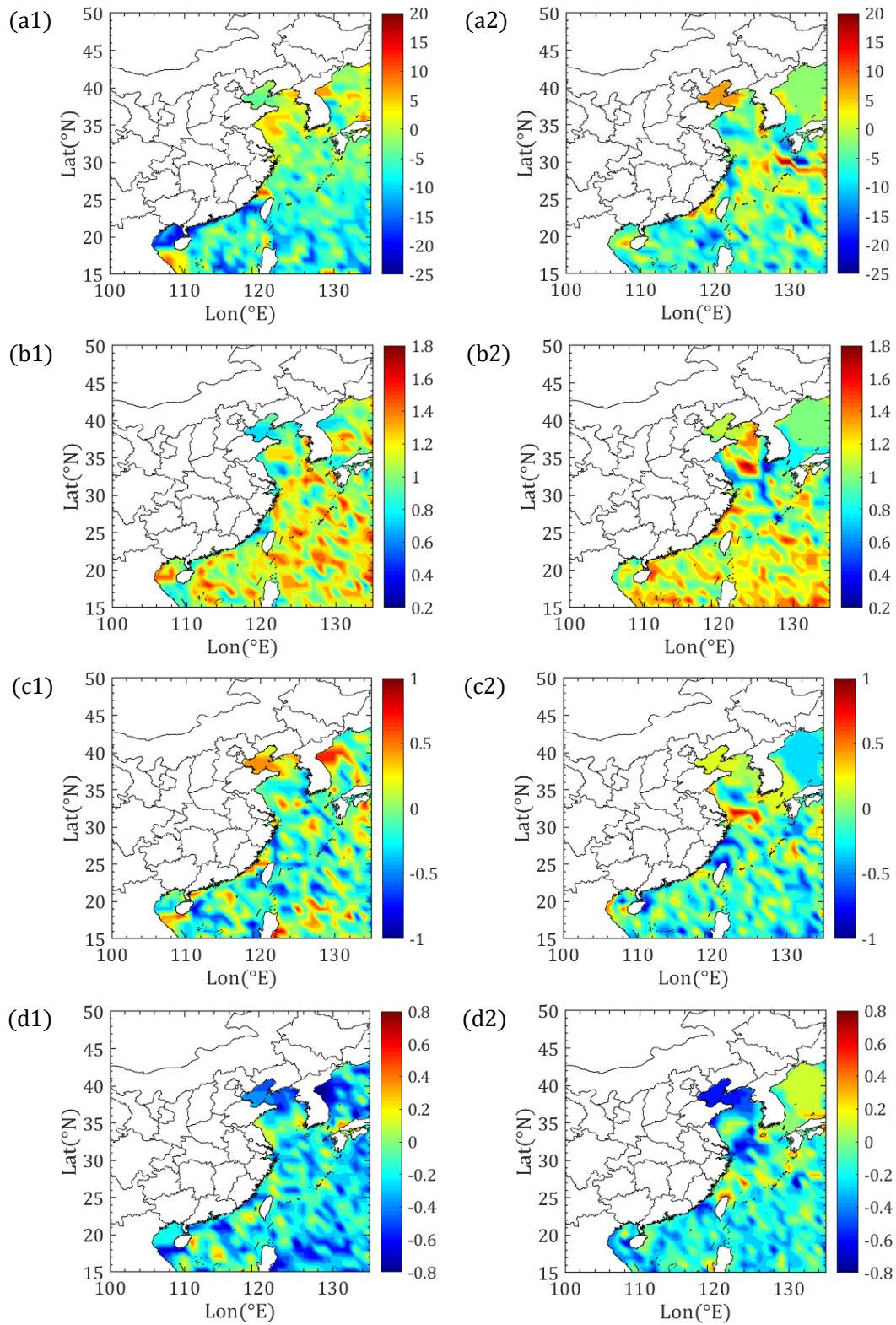


Fig. C2 Contour plots of coefficients for relative intensity model: (a)~(d) $a_1 \sim a_4$; left column corresponds to easterly headed storms, right column corresponds to westerly headed storms

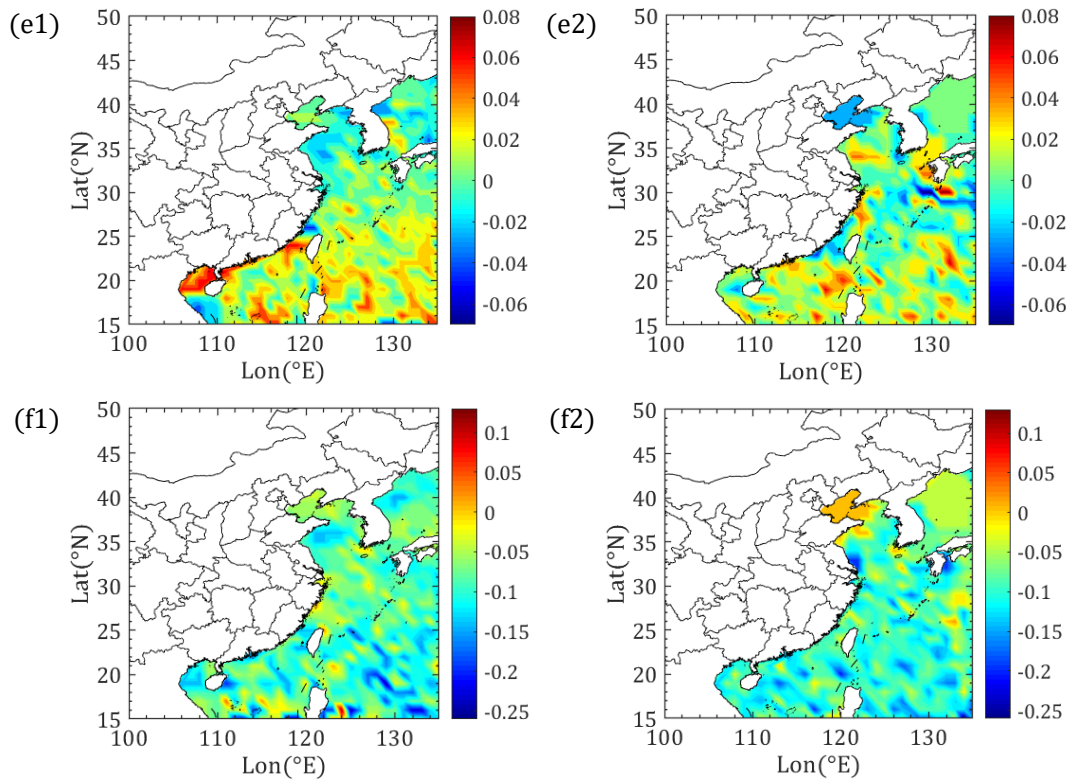


Fig. C2 (cont.) Contour plots of coefficients for relative intensity model: (e)~(f) $a_5 \sim a_6$; left column corresponds to easterly headed storms, right column corresponds to westerly headed storms

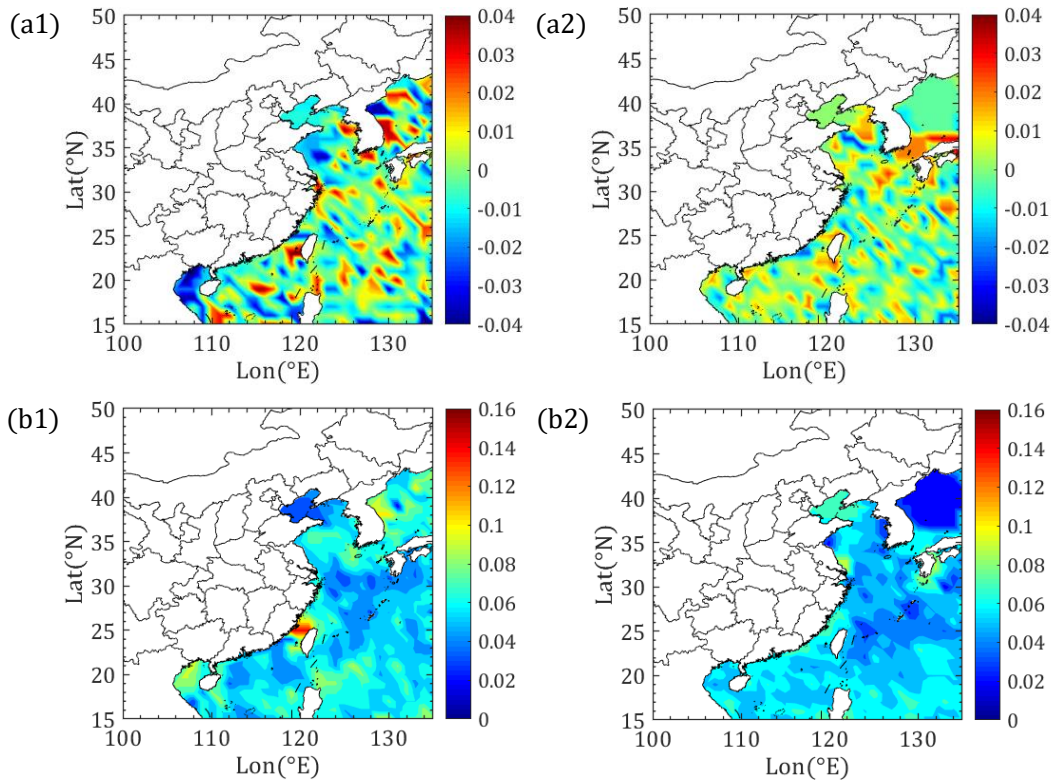


Fig. C3 Contour plots of error term for relative intensity model: (a) error mean; (b) error standard deviation; left column corresponds to easterly headed storms, right column corresponds to westerly headed storms

APPENDIX D. COEFFICIENTS OF $R_{MAX,S}$ AND B_S MODEL

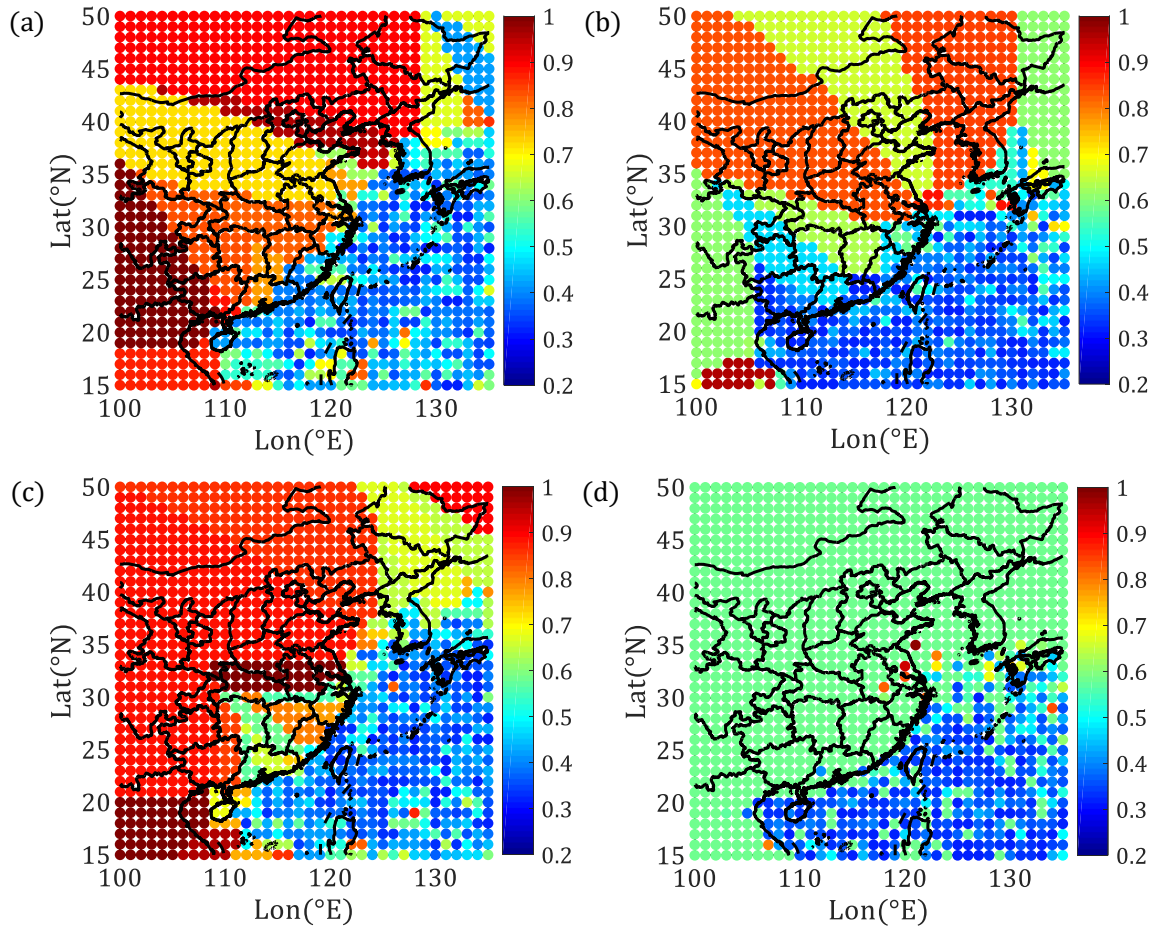


Fig. D1 The optimal bandwidths for $R_{max,s}$ and B_s models: (a) $R_{max,s}$ for easterly headed storms; (b) $R_{max,s}$ for westerly headed storms; (c) B_s for easterly headed storms; (d) B_s for westerly headed storms

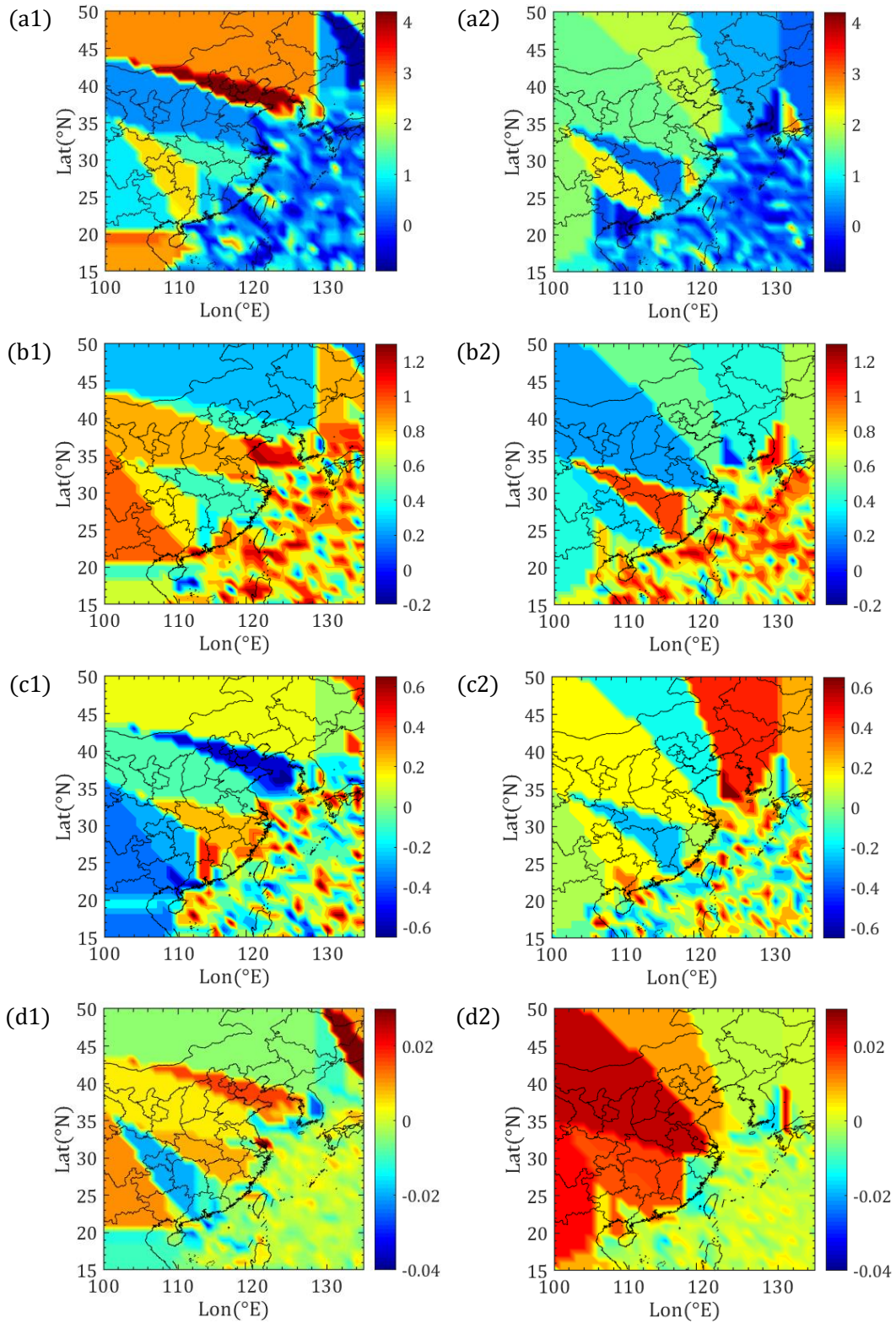


Fig. D2 Contour plots of coefficients for $R_{max,s}$ model: (a)~(d) $r_1 \sim r_4$; left column corresponds to easterly headed storms, right column corresponds to westerly headed storms

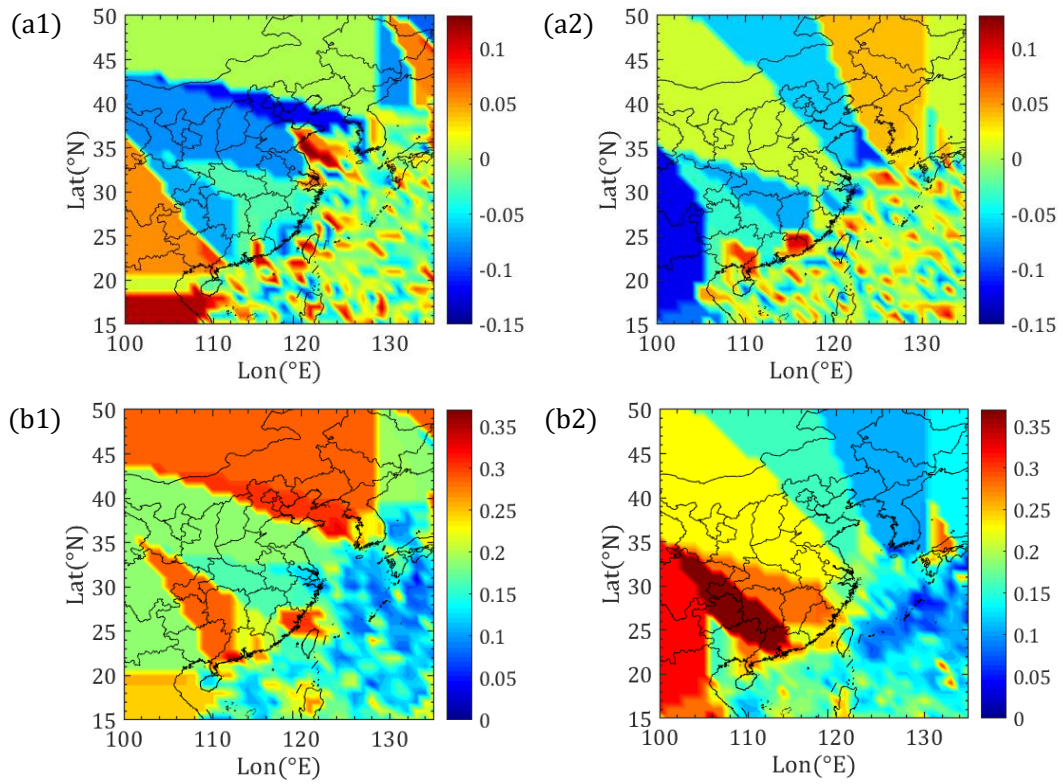


Fig. D3 Contour plots of error term for $R_{max,s}$ model: (a) error mean; (b) error standard deviation; left column corresponds to easterly headed storms, right column corresponds to westerly headed storms

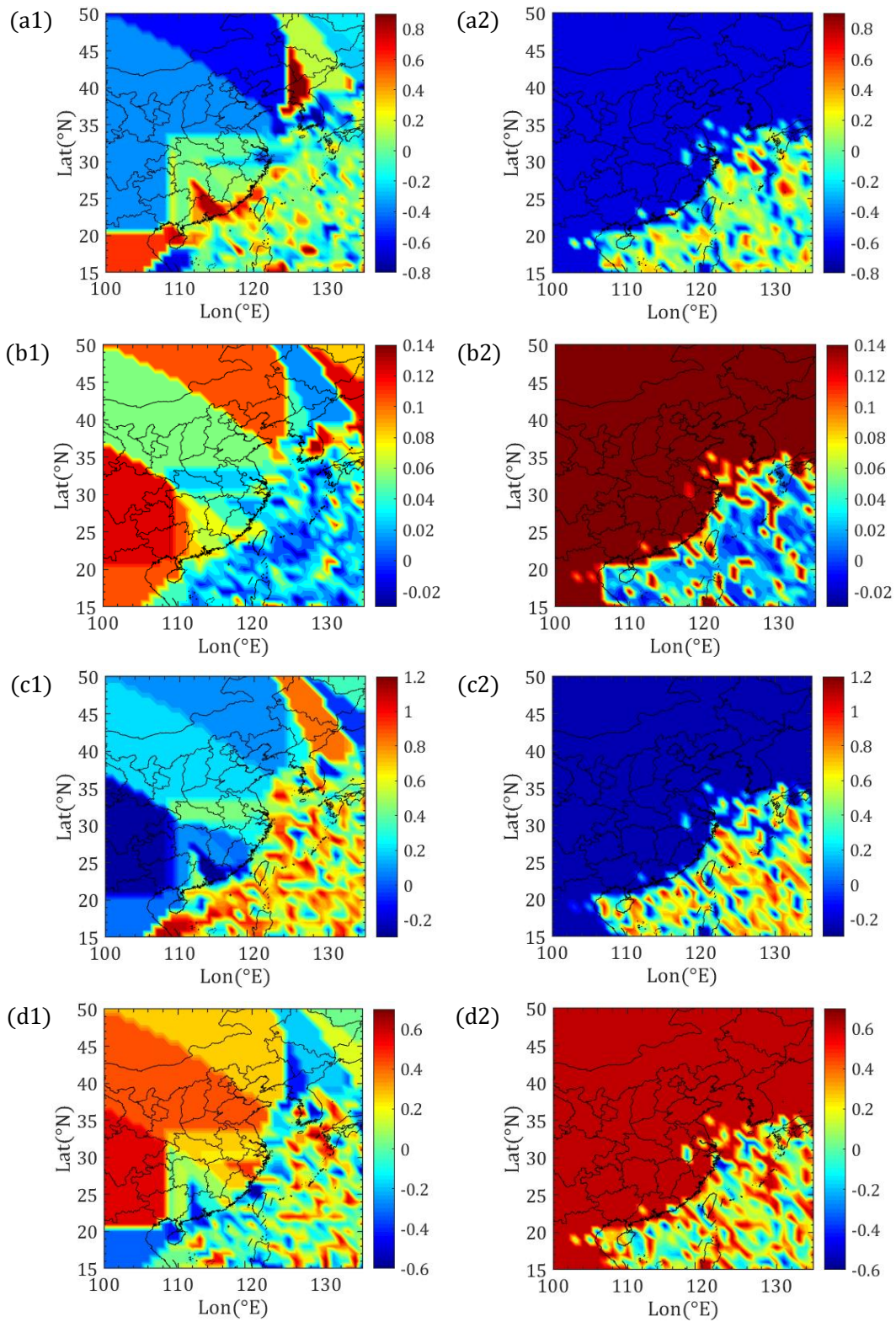


Fig. D4 Contour plots of coefficients for B_S model: (a)~(d) $b_1 \sim b_4$; left column corresponds to easterly headed storms, right column corresponds to westerly headed storms

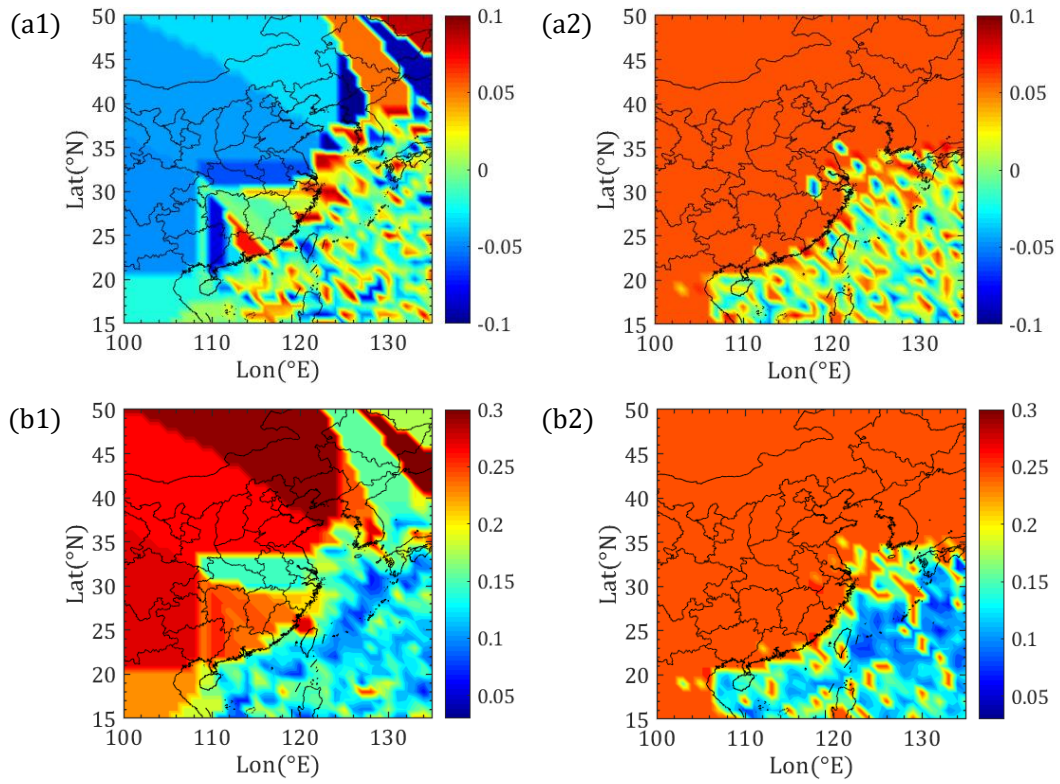


Fig. D5 Contour plots of error term for B_s model: (a) error mean; (b) error standard deviation; left column corresponds to easterly headed storms, right column corresponds to westerly headed storms

APPENDIX E. PERFORMANCE ASSESSMENT OF SUBREGION MODEL:
TIME HISTORIES OF PARAMETERS

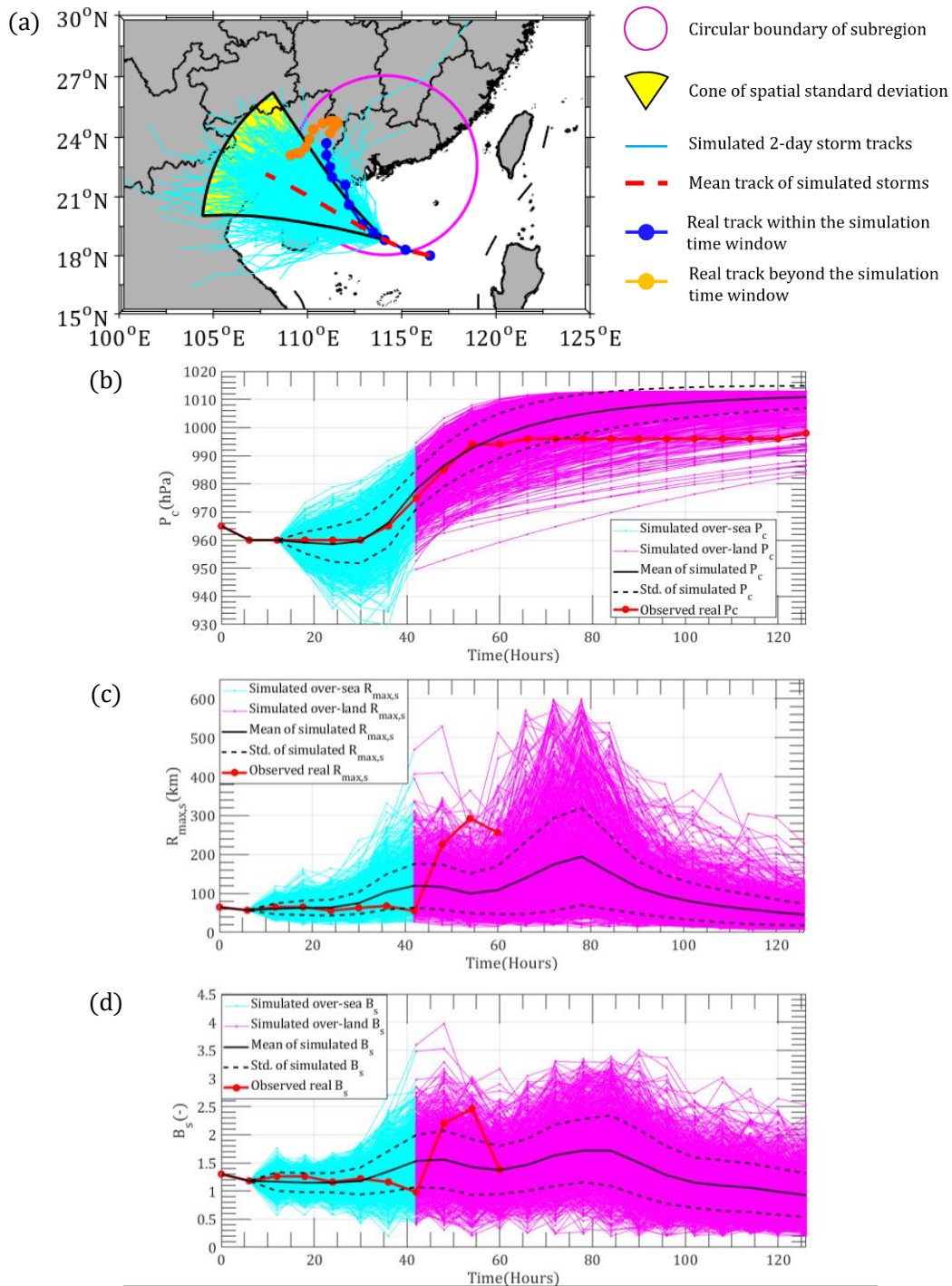


Fig. E1 Typhoon Utor: simulation from 2013-08-12 18:00 UTC: (a) 2-Day track simulation; (b) central pressure; (c) $R_{max,s}$; (d) B_s

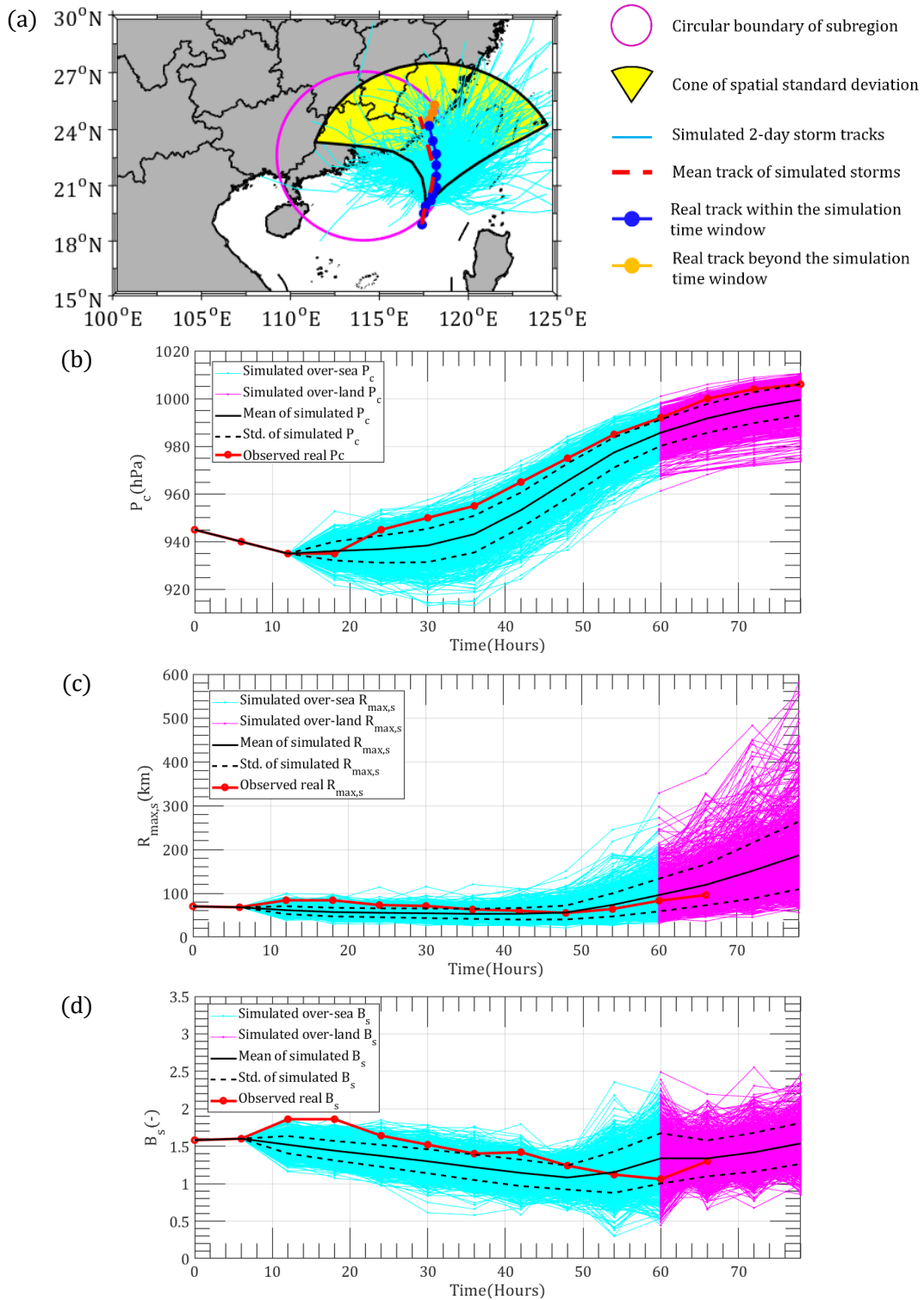


Fig. E2 Typhoon Megi: simulation from 2010-10-20 18:00 UTC: (a) 2-Day track simulation; (b) central pressure; (c) $R_{max,s}$; (d) B_s

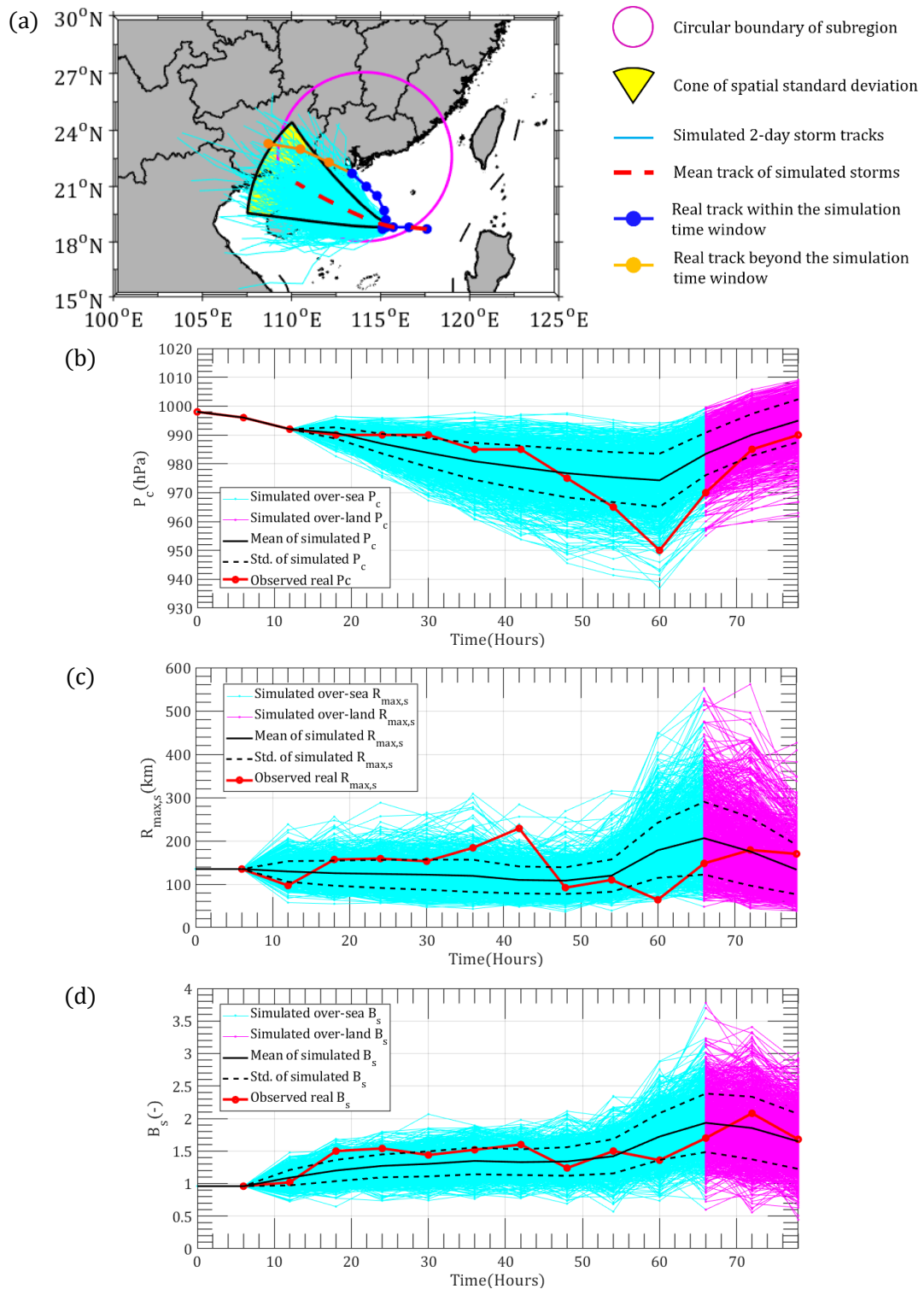


Fig. E3 Typhoon Vicente: simulation from 2012-07-21 06:00 UTC: (a) 2-Day track simulation; (b) central pressure; (c) $R_{max,s}$; (d) B_s

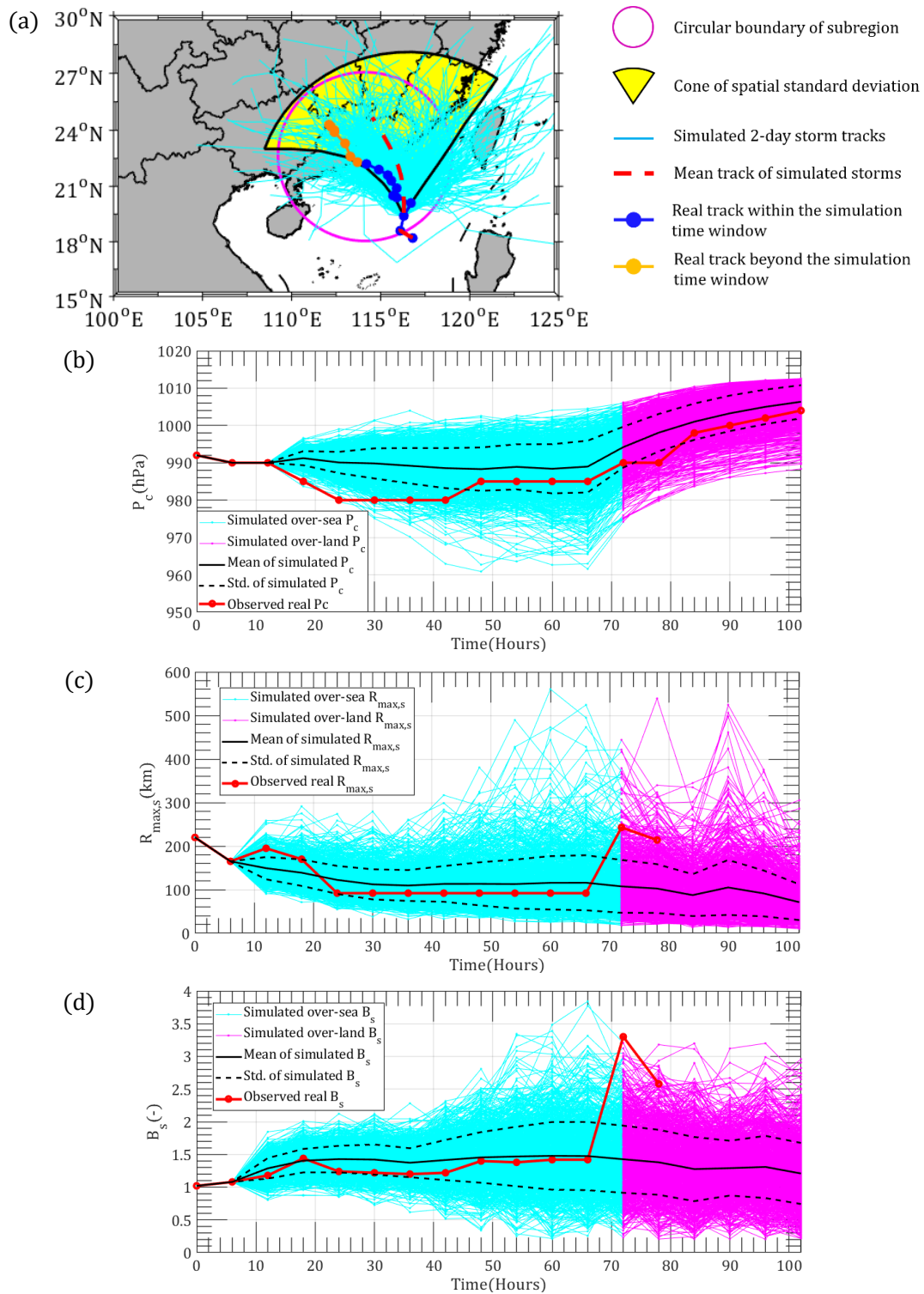


Fig. E4 Typhoon York: simulation from 1999-09-13 12:00 UTC: (a) 2-Day track simulation; (b) central pressure; (c) $R_{max,s}$; (d) B_s

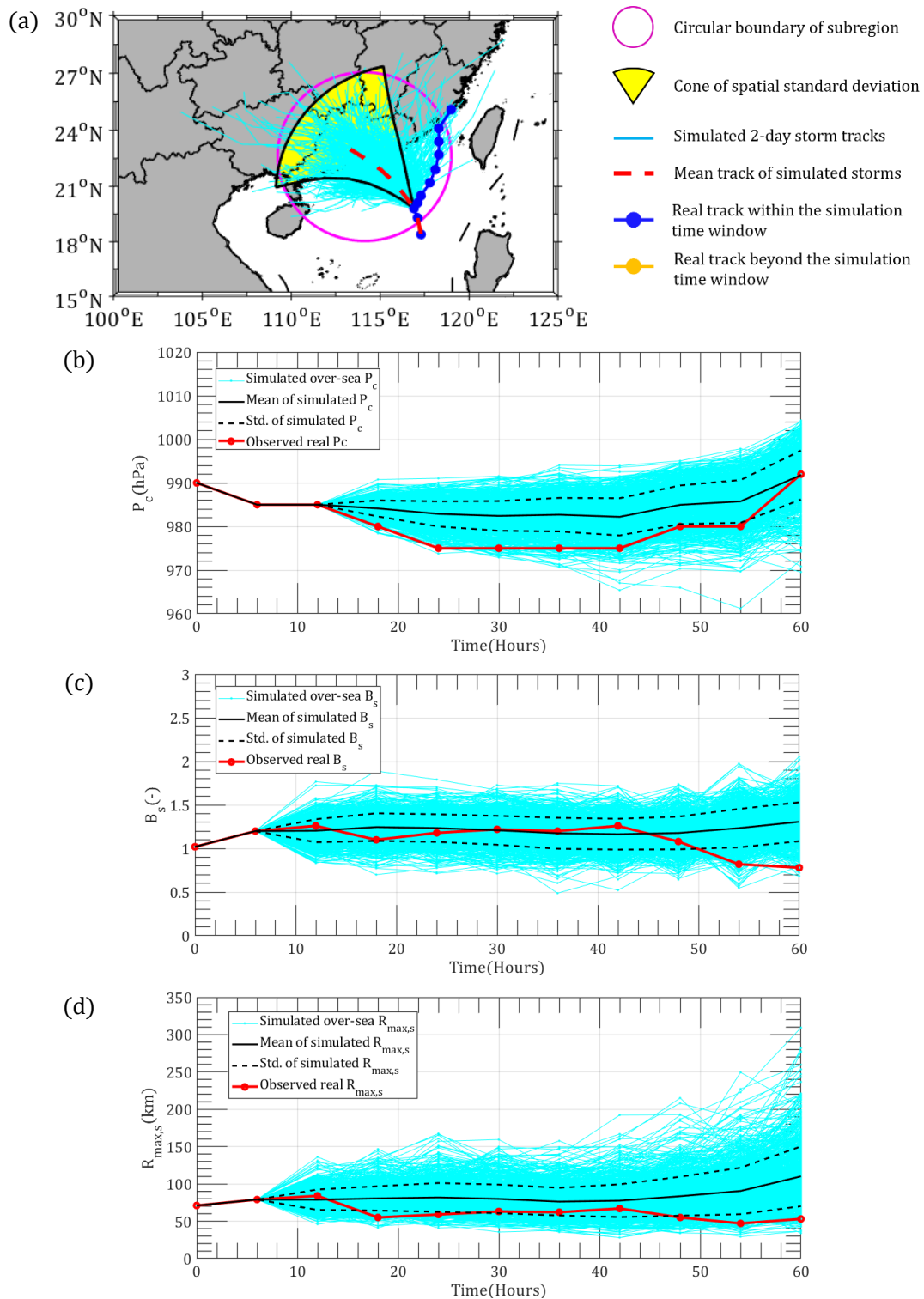


Fig. E5 Typhoon Linfa: simulation from 2009-06-19 06:00 UTC: (a) 2-Day track simulation; (b) central pressure; (c) $R_{max,s}$; (d) B_s

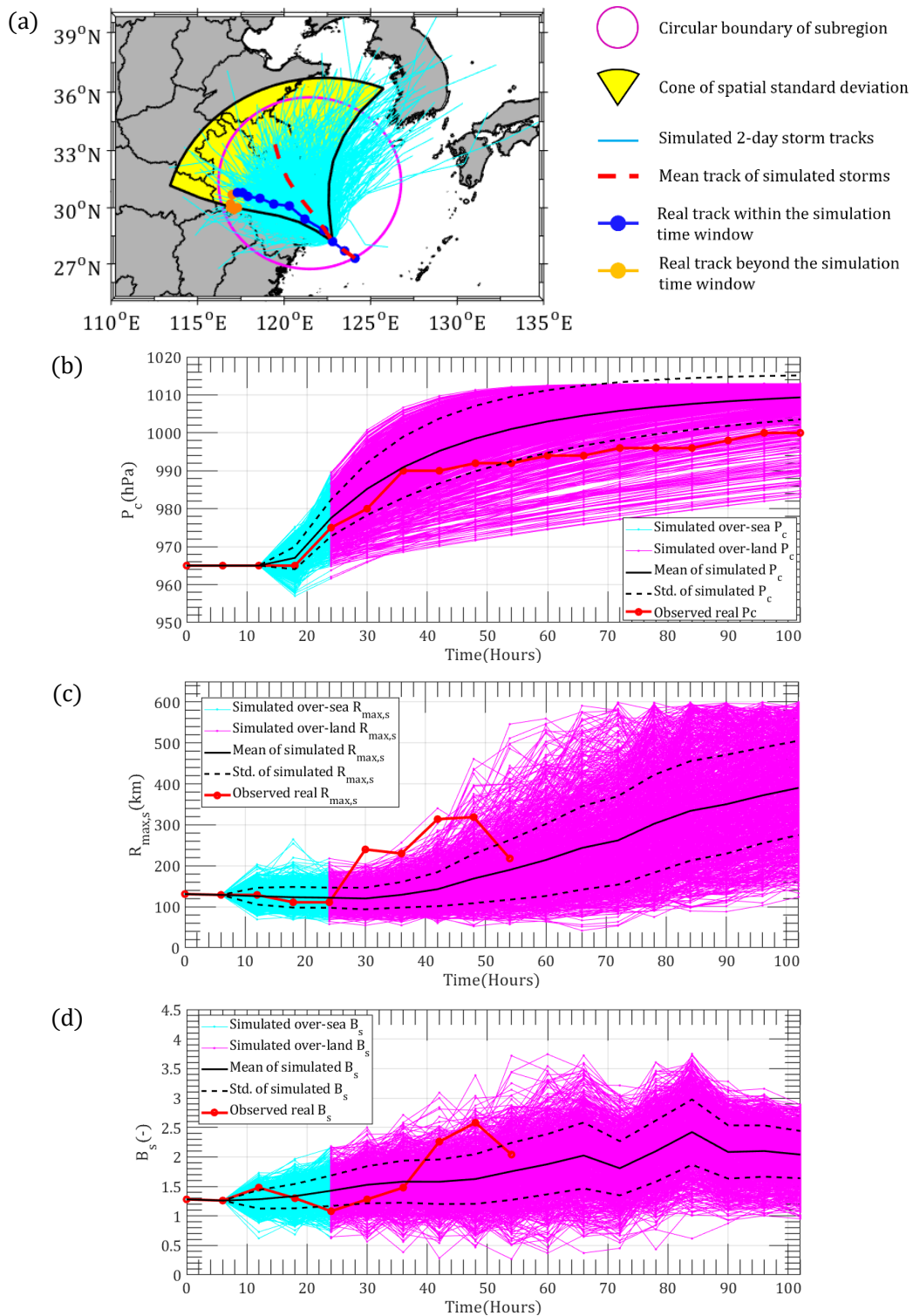


Fig. E6 Typhoon Haikui: simulation from 2012-08-07 00:00 UTC: (a) 2-Day track simulation; (b) central pressure; (c) $R_{max,s}$; (d) B_s

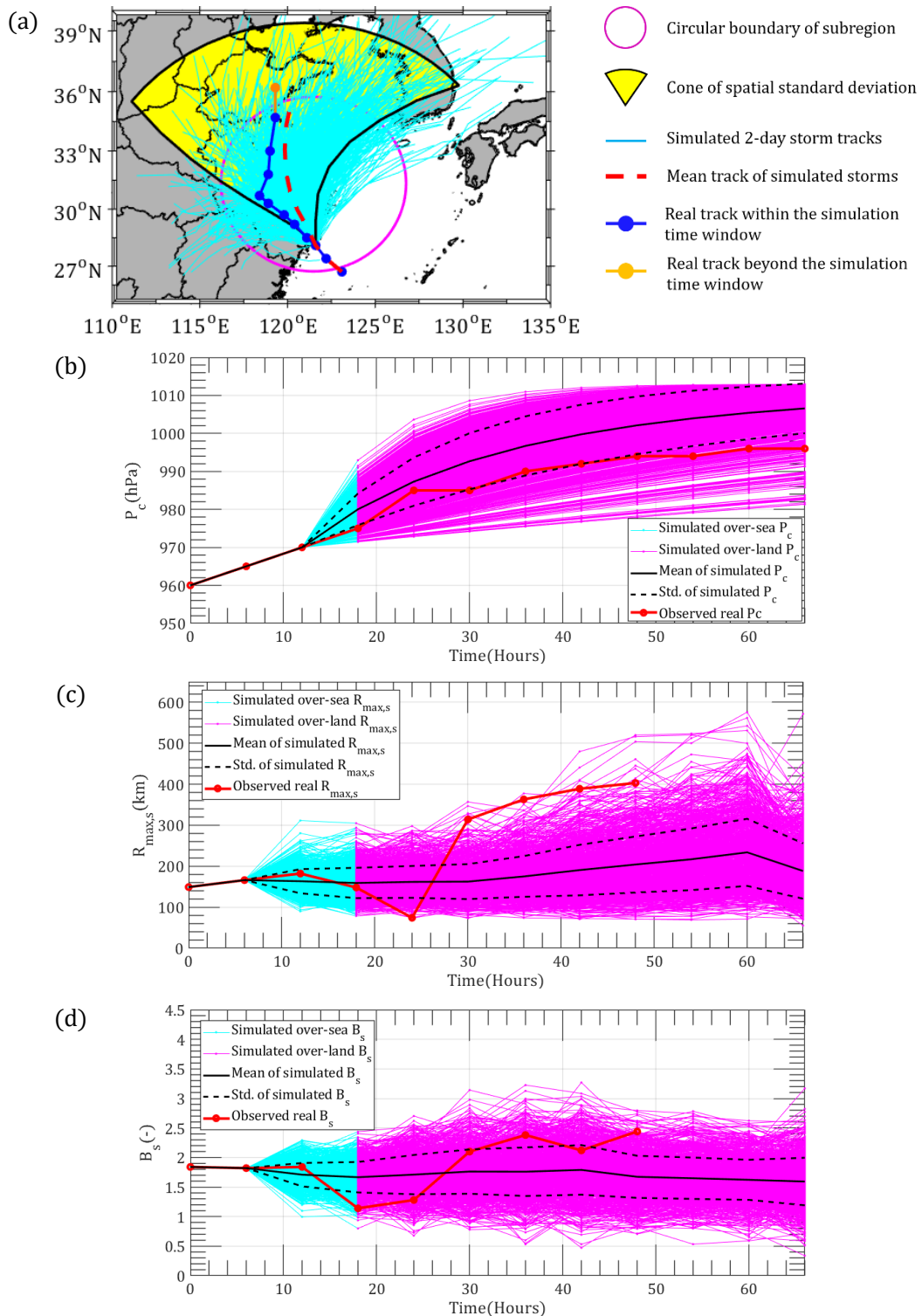


Fig. E7 Typhoon Matsa: simulation from 2005-08-05 06:00 UTC: (a) 2-Day track simulation; (b) central pressure; (c) $R_{max,s}$; (d) B_s

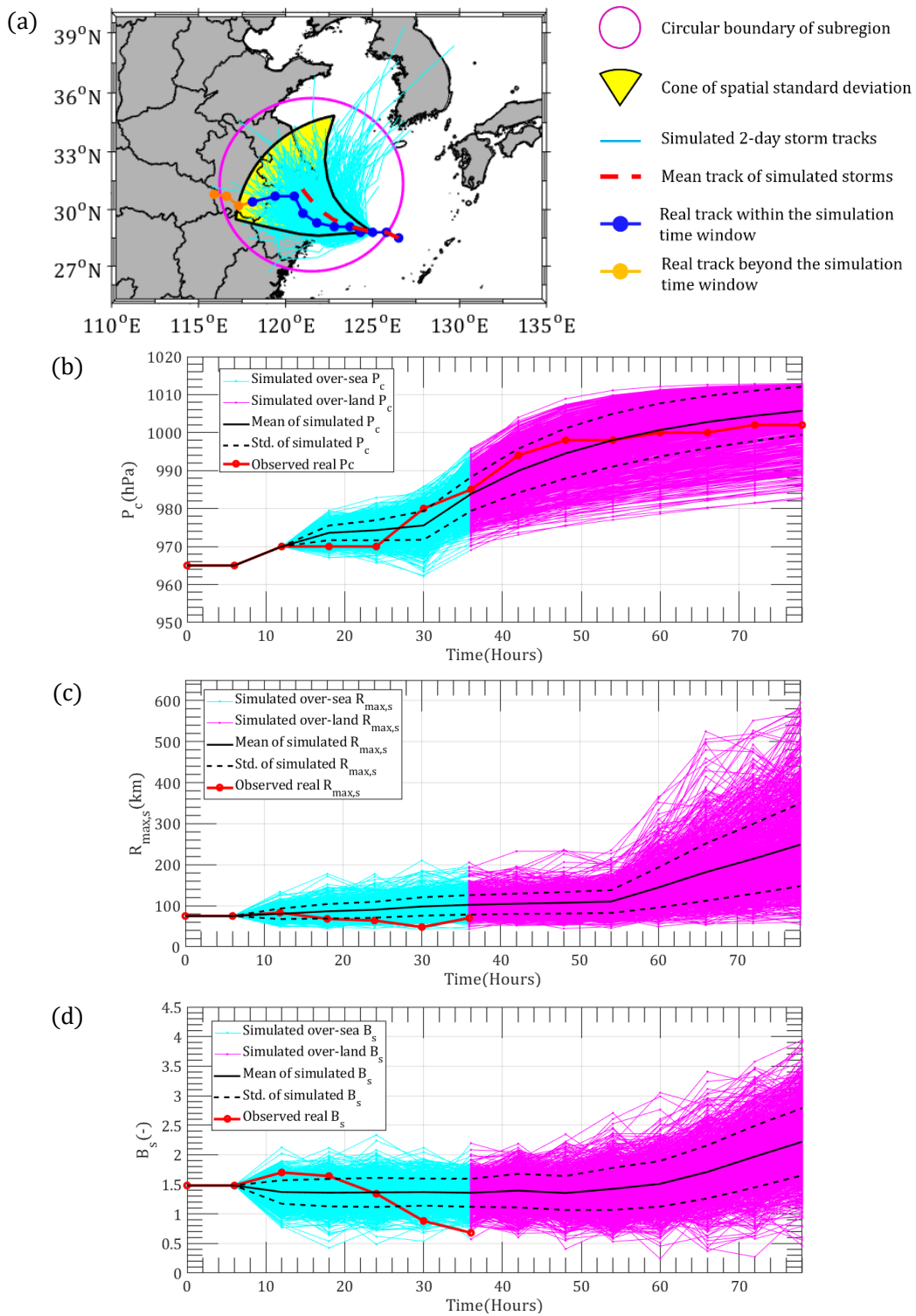


Fig. E8 Typhoon Jelawat: simulation from 2000-08-09 00:00 UTC: (a) 2-Day track simulation; (b) central pressure; (c) $R_{max,s}$; (d) B_s

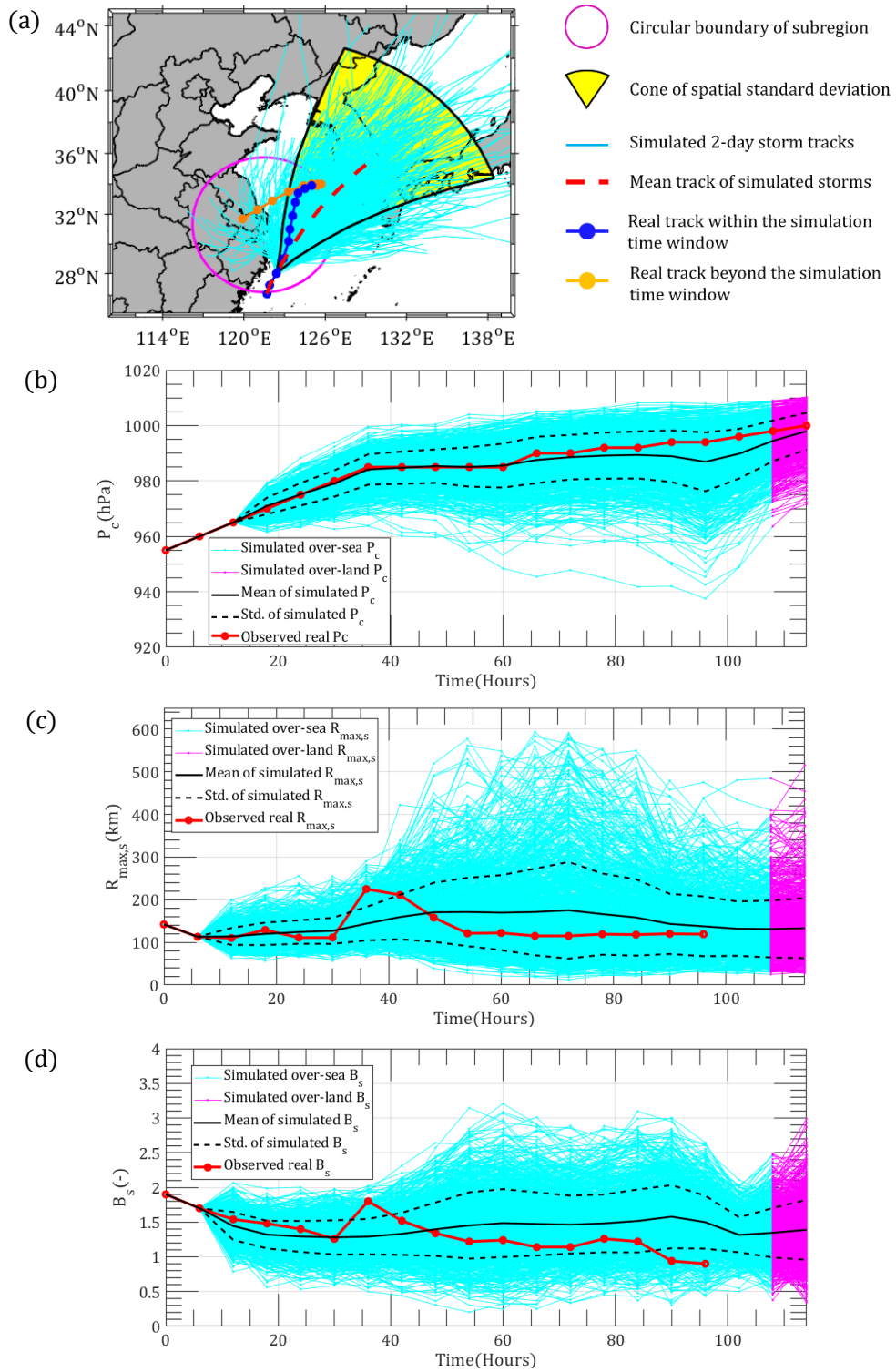


Fig. E9 Typhoon Doug: simulation from 1994-08-08 06:00 UTC: (a) 2-Day track simulation; (b) central pressure; (c) $R_{max,s}$; (d) B_s

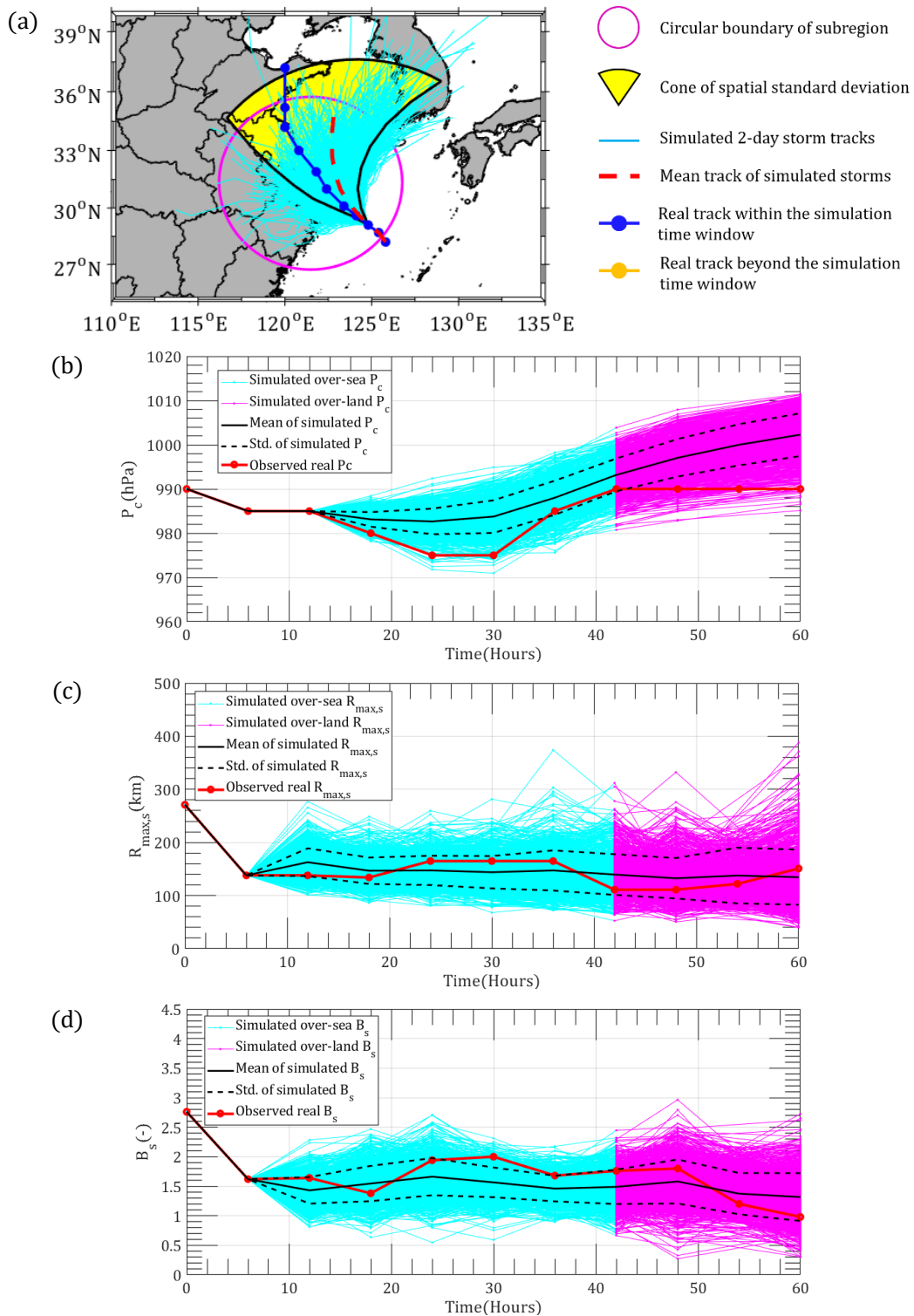


Fig. E10 Typhoon Mamie: simulation from 1985-08-16 18:00 UTC: (a) 2-Day track simulation; (b) central pressure; (c) $R_{max,s}$; (d) B_s

APPENDIX F. PERFORMANCE ASSESSMENT OF SUBREGION MODEL: PDFS OF PARAMETERS

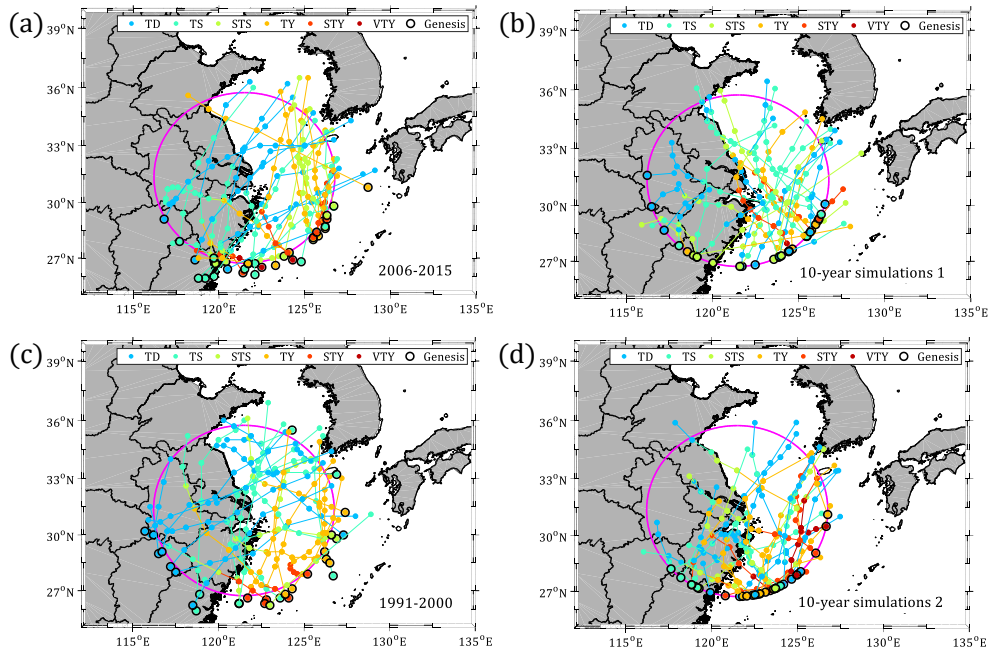


Fig. F1 Comparison between real and simulated storms around Shanghai (121.483°E, 31.233°N): (a) Real tracks from 2006 to 2015; (b) Simulated 10-year storms 1; (c) Real tracks from 1991 to 2000; (d) Simulated 10-year storms 2

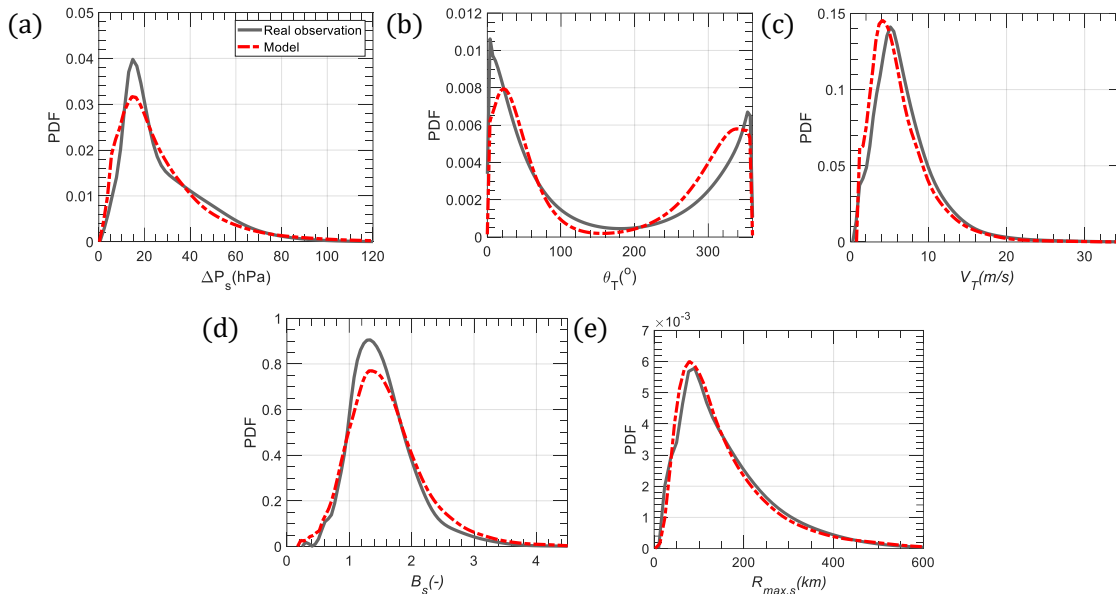


Fig. F2 Comparison of PDF for real and simulated parameters within the circular subregion centered in Shanghai (10,000-year simulations): (a) Central pressure deficit ΔP_s ; (b) Heading direction θ_T ; (c) Forward speed V_T ; (d) Radius to maximum winds $R_{max,s}$; (e) Pressure shape parameter B_s

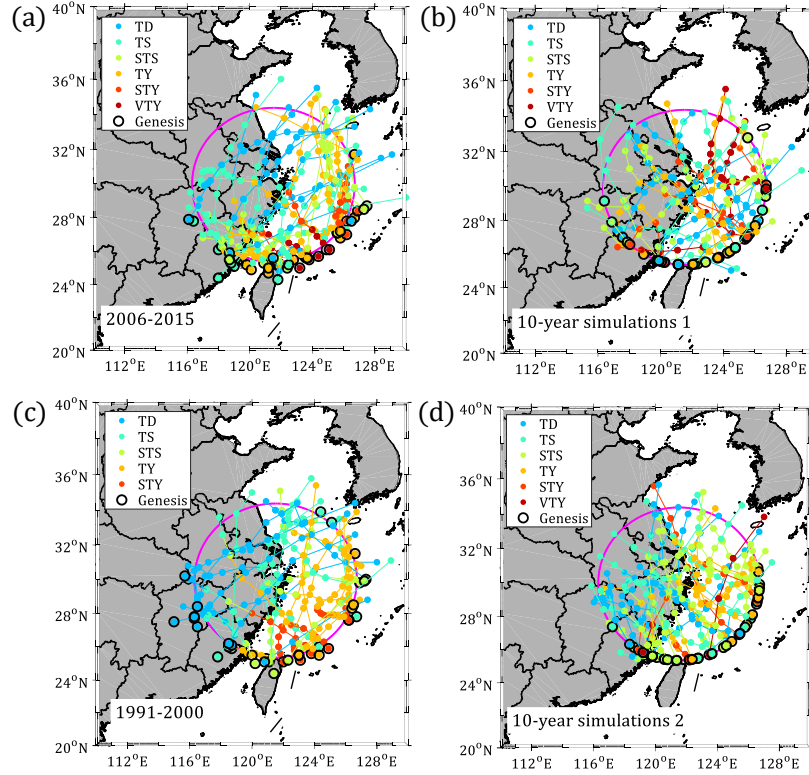


Fig. F3 Comparison between real and simulated storms around Ningbo (121.517°E , 29.867°N): (a) Real tracks from 2006 to 2015; (b) Simulated 10-year storms 1; (c) Real tracks from 1991 to 2000; (d) Simulated 10-year storms 2

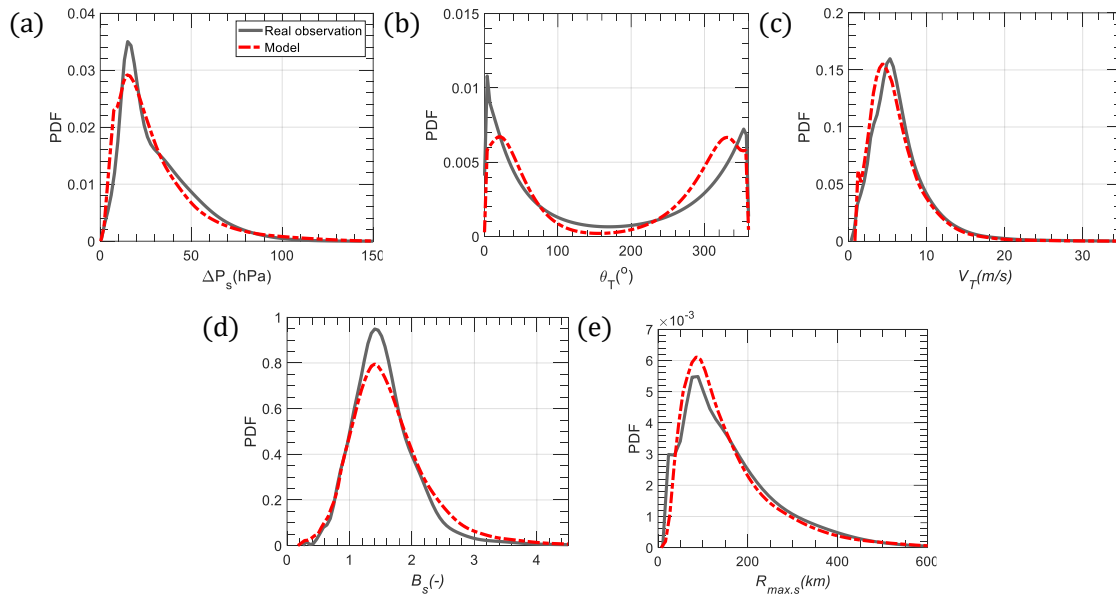


Fig. F4 Comparison of PDF for real and simulated parameters within the circular subregion centered in Ningbo (10,000-year simulations): (a) Central pressure deficit ΔP_s ; (b) Heading direction θ_T ; (c) Forward speed V_T ; (d) Radius to maximum winds $R_{max,s}$; (e) Pressure shape parameter B_s

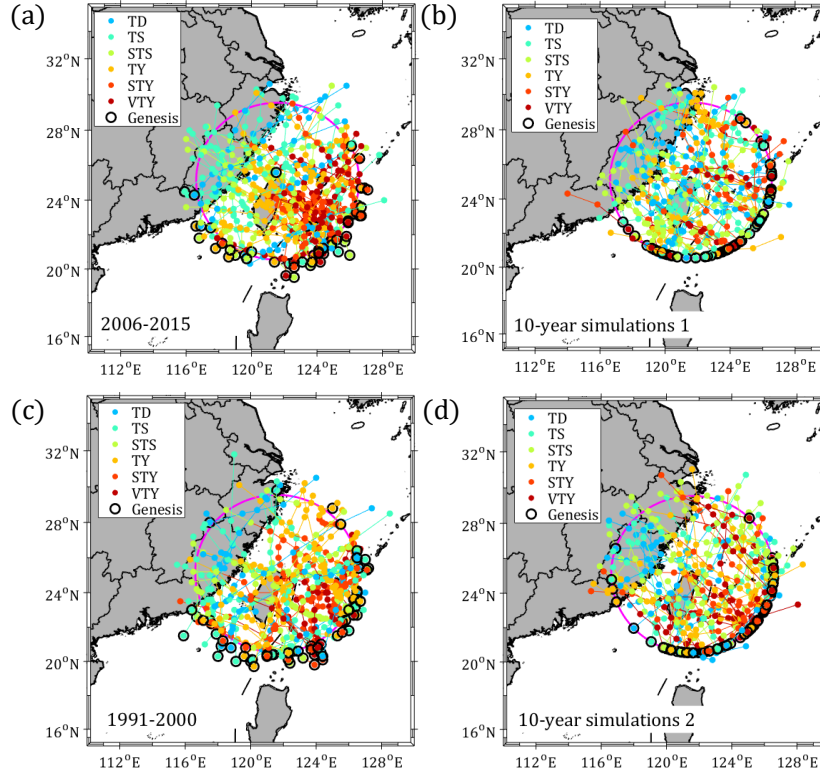


Fig. F5 Comparison between real and simulated storms around Taipei (121.593°E, 25.041°N): (a) Real tracks from 2006 to 2015; (b) Simulated 10-year storms 1; (c) Real tracks from 1991 to 2000; (d) Simulated 10-year storms 2

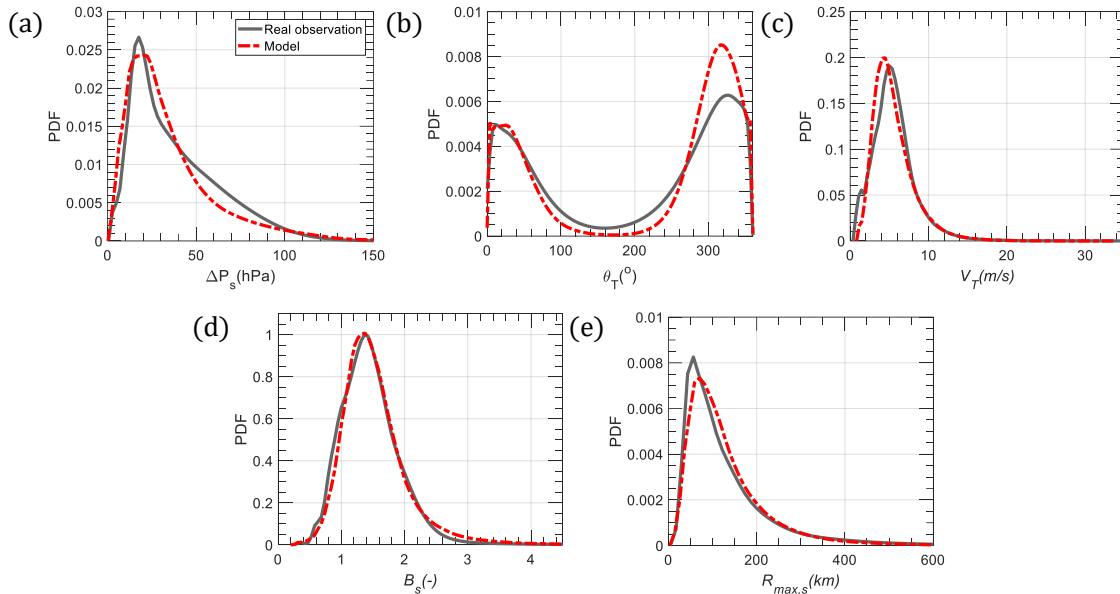


Fig. F6 Comparison of PDF for real and simulated parameters within the circular subregion centered in Taipei (10,000-year simulations): (a) Central pressure deficit ΔP_s ; (b) Heading direction θ_T ; (c) Forward speed V_T ; (d) Radius to maximum winds $R_{max,s}$; (e) Pressure shape parameter B_s

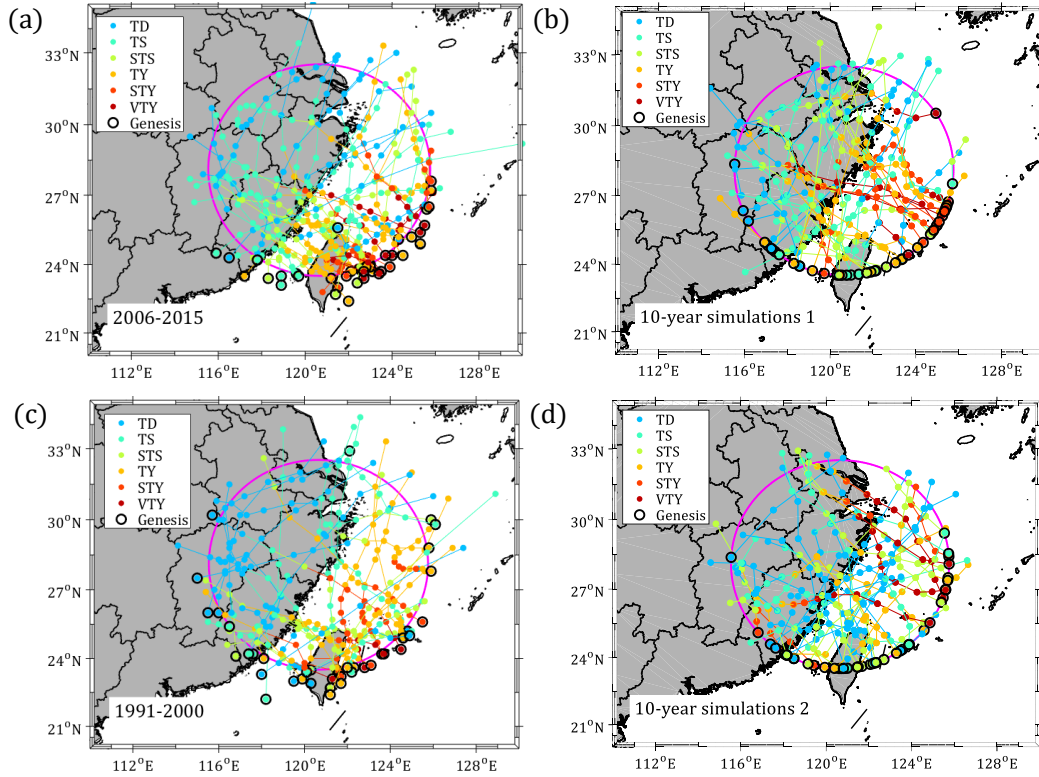


Fig. F7 Comparison between real and simulated storms around Wenzhou (120.650°E, 28.017°N): (a) Real tracks from 2006 to 2015; (b) Simulated 10-year storms 1; (c) Real tracks from 1991 to 2000; (d) Simulated 10-year storms 2

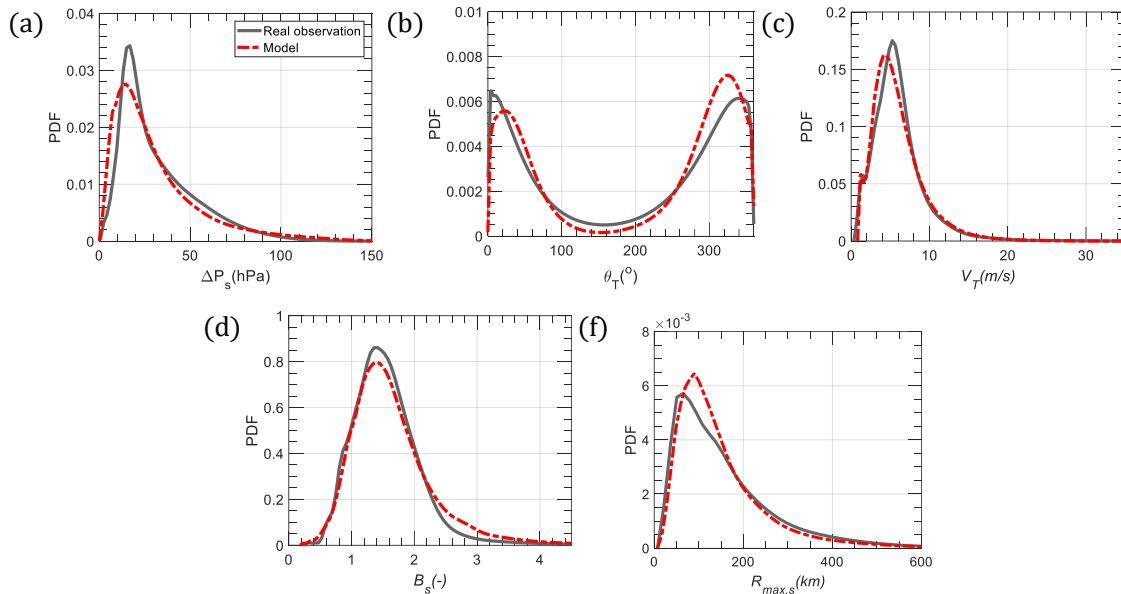


Fig. F8 Comparison of PDF for real and simulated parameters within the circular subregion centered in Wenzhou (10,000-year simulations): (a) Central pressure deficit ΔP_s ; (b) Heading direction θ_T ; (c) Forward speed V_T ; (d) Radius to maximum winds $R_{max,s}$; (e) Pressure shape parameter B_s

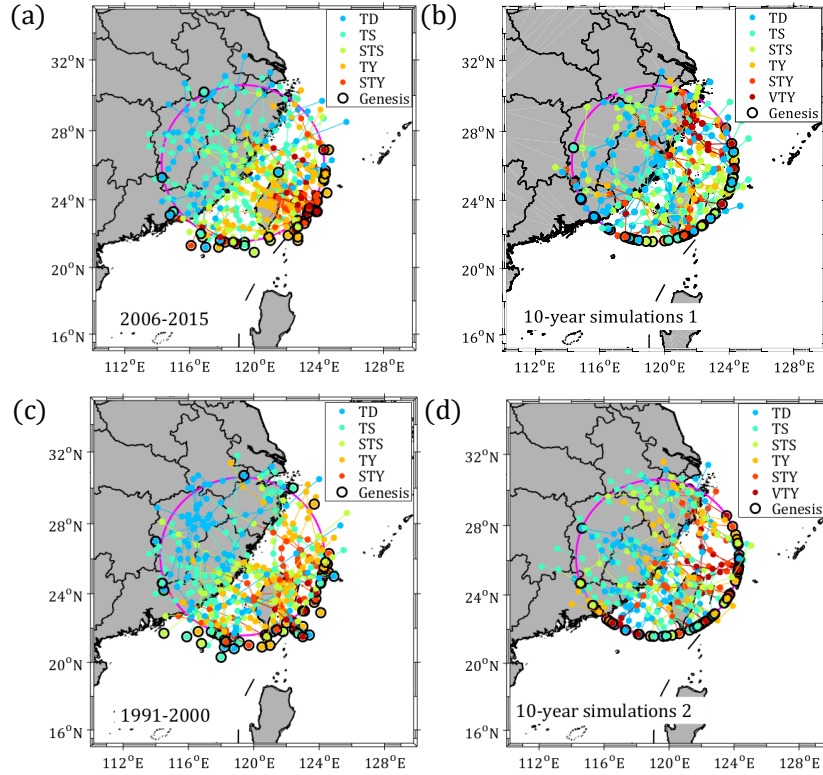


Fig. F9 Comparison between real and simulated storms around Fuzhou (119.300°E , 26.083°N): (a) Real tracks from 2006 to 2015; (b) Simulated 10-year storms 1; (c) Real tracks from 1991 to 2000; (d) Simulated 10-year storms 2

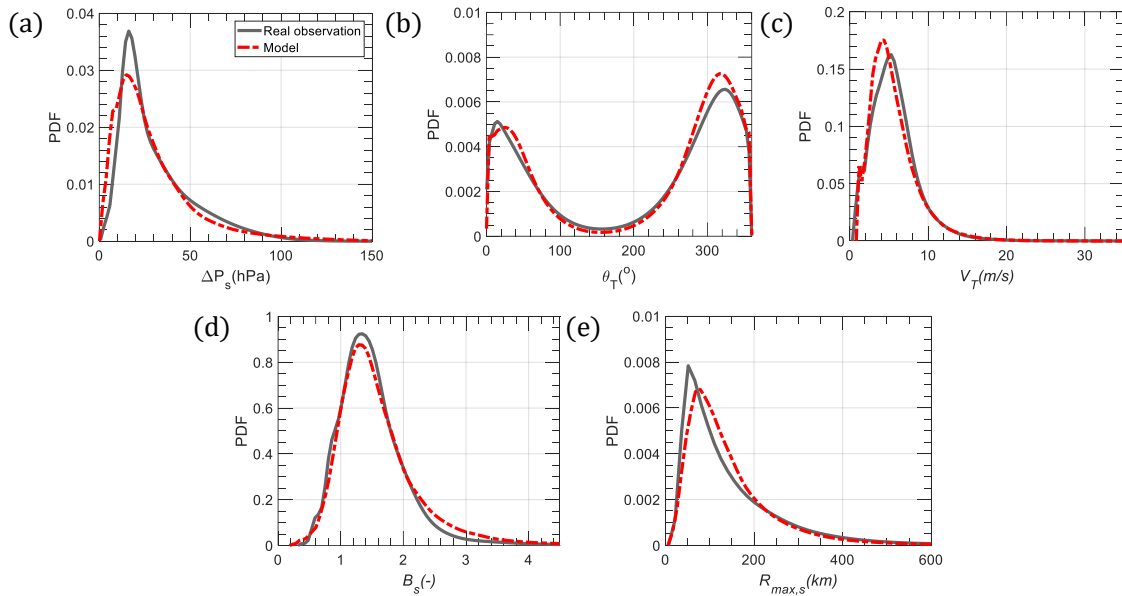


Fig. F10 Comparison of PDF for real and simulated parameters within the circular subregion centered in Fuzhou (10,000-year simulations): (a) Central pressure deficit ΔP_s ; (b) Heading direction θ_T ; (c) Forward speed V_T ; (d) Radius to maximum winds $R_{max,s}$; (e) Pressure shape parameter B_s

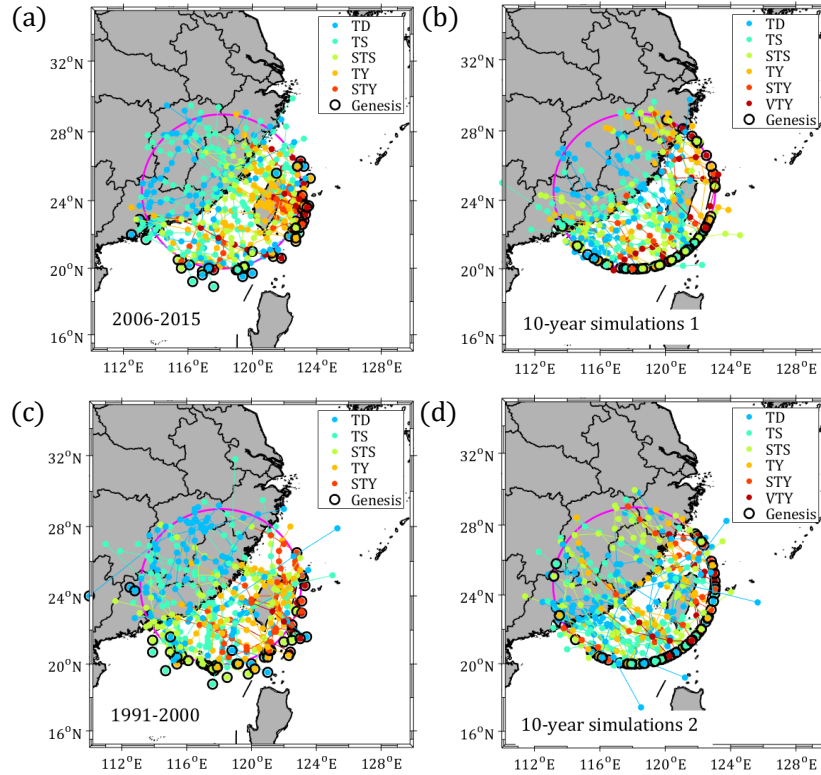


Fig. F11 Comparison between real and simulated storms around Xiamen (118.100°E, 24.483°N): (a) Real tracks from 2006 to 2015; (b) Simulated 10-year storms 1; (c) Real tracks from 1991 to 2000; (d) Simulated 10-year storms 2

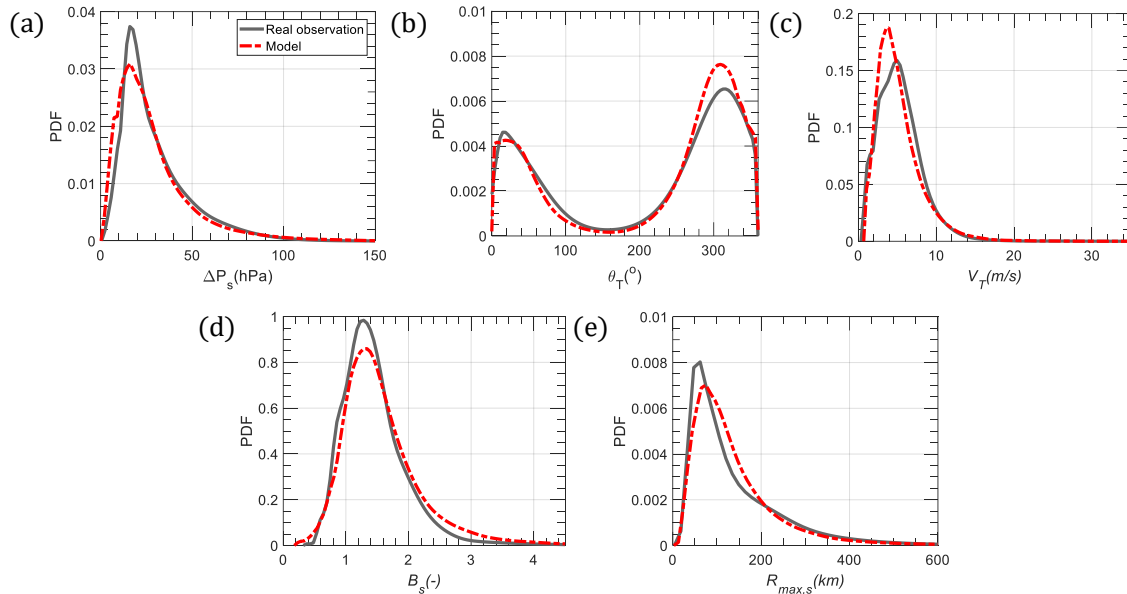


Fig. F12 Comparison of PDF for real and simulated parameters within the circular subregion centered in Xiamen (10,000-year simulations): (a) Central pressure deficit ΔP_s ; (b) Heading direction θ_T ; (c) Forward speed V_T ; (d) Radius to maximum winds $R_{max,s}$; (e) Pressure shape parameter B_s

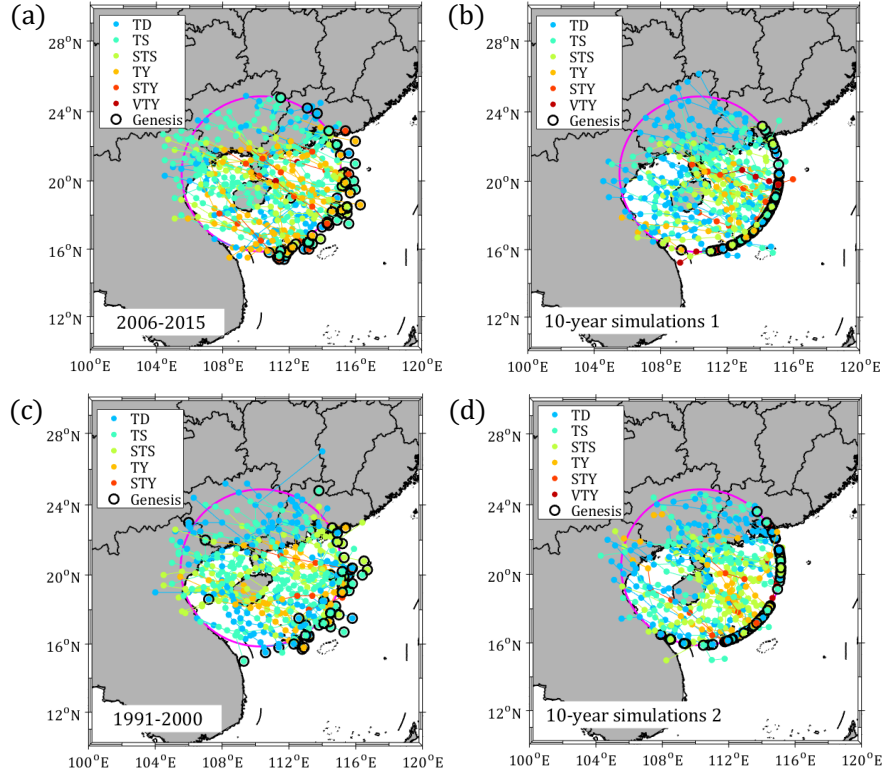


Fig. F13 Comparison between real and simulated storms around Haikou (110.333°E, 20.367°N): (a) Real tracks from 2006 to 2015; (b) Simulated 10-year storms 1; (c) Real tracks from 1991 to 2000; (d) Simulated 10-year storms 2

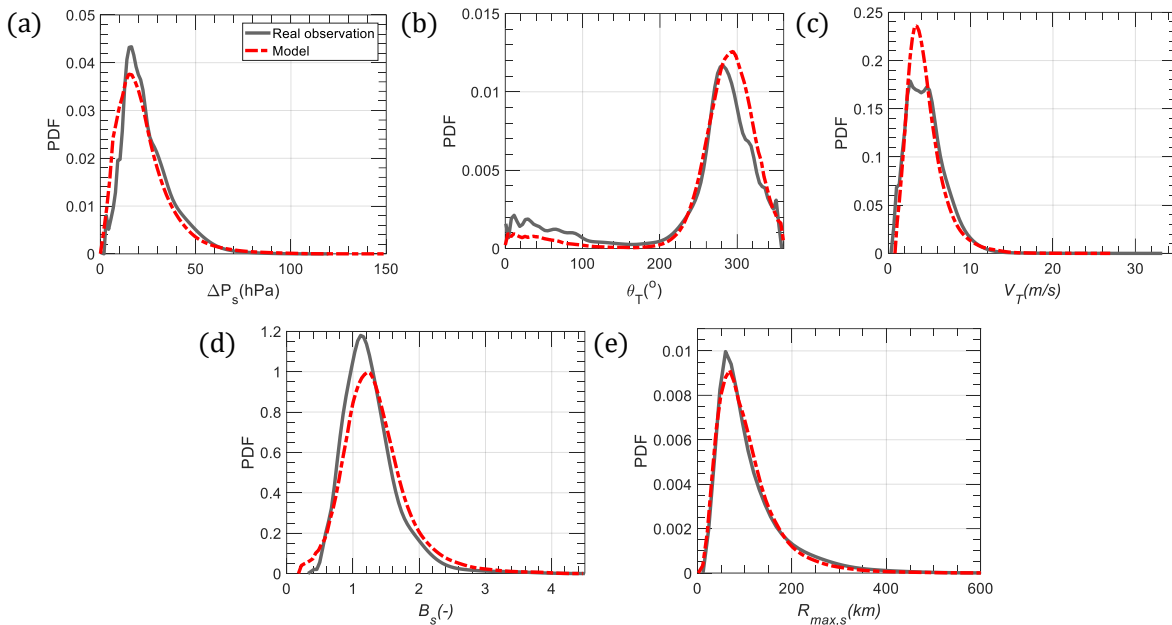


Fig. F14 Comparison of PDF for real and simulated parameters within the circular subregion centered in Haikou (10,000-year simulations): (a) Central pressure deficit ΔP_s ; (b) Heading direction θ_T ; (c) Forward speed V_T ; (d) Radius to maximum winds $R_{max,s}$; (e) Pressure shape parameter B_s

APPENDIX G. CDFs OF GENESIS PARAMETERS OF NINE COASTAL CITIES

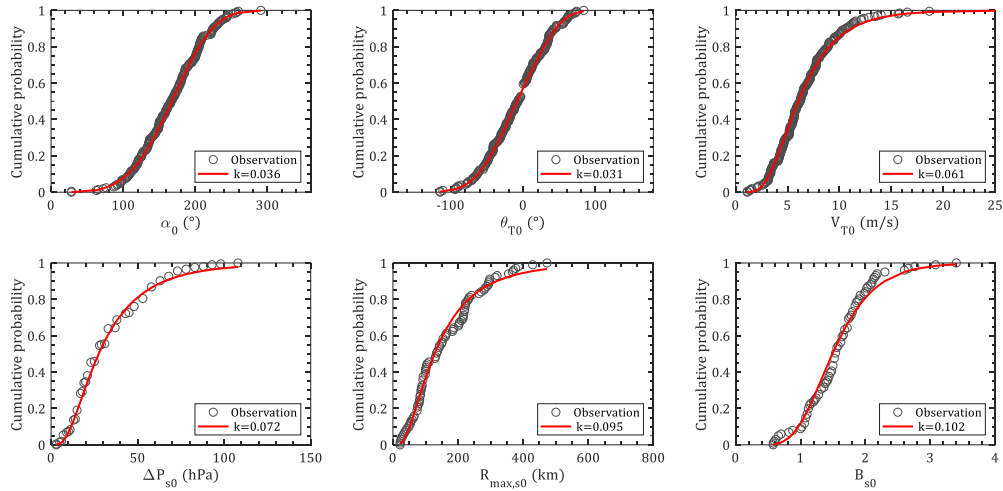


Fig. G1 CDFs of genesis parameters for Shanghai: (a) α_0 ; (b) ΔP_0 ; (c) θ_{T0} ; (d) V_{T0} ; (e) $R_{max,s0}$; (f) B_{s0}

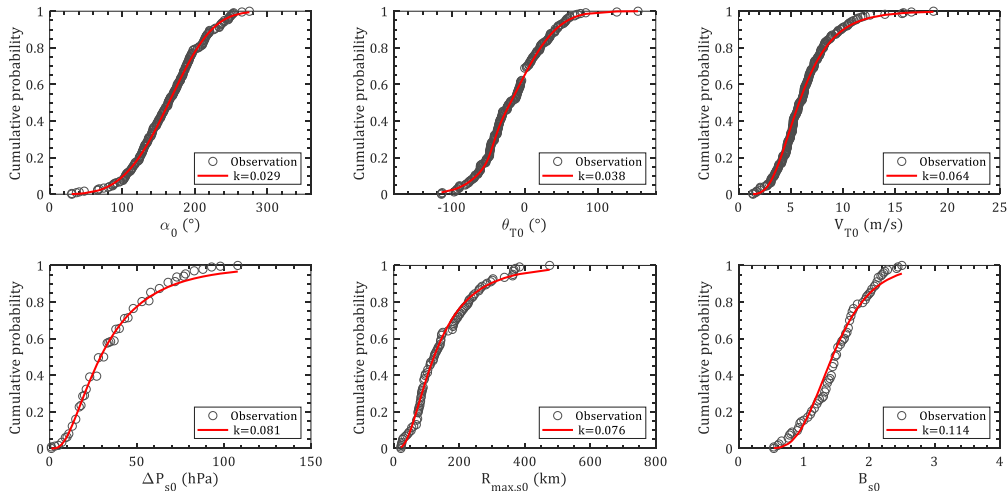


Fig. G2 CDFs of genesis parameters for Ningbo: (a) α_0 ; (b) ΔP_0 ; (c) θ_{T0} ; (d) V_{T0} ; (e) $R_{max,s0}$; (f) B_{s0}

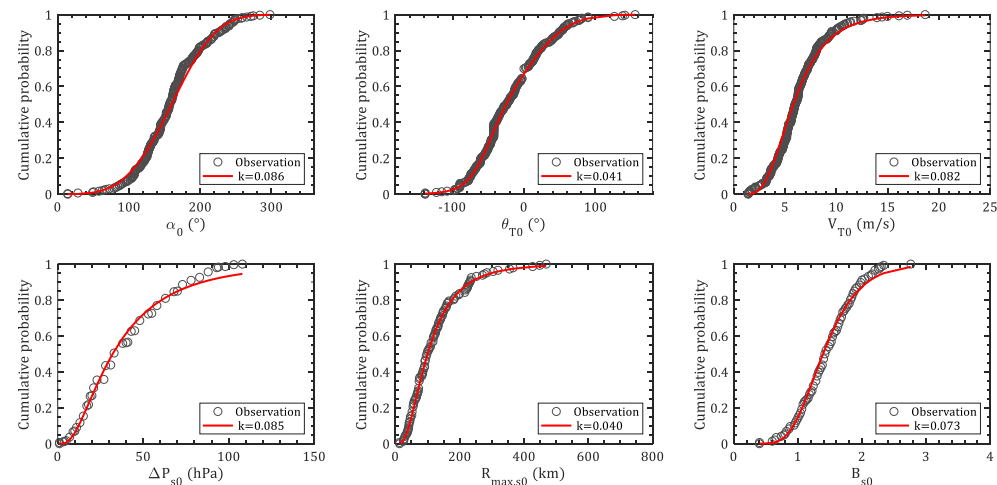


Fig. G3 CDFs of genesis parameters for Wenzhou: (a) α_0 ; (b) ΔP_0 ; (c) θ_{T0} ; (d) V_{T0} ; (e) $R_{max,s0}$; (f) B_{s0}

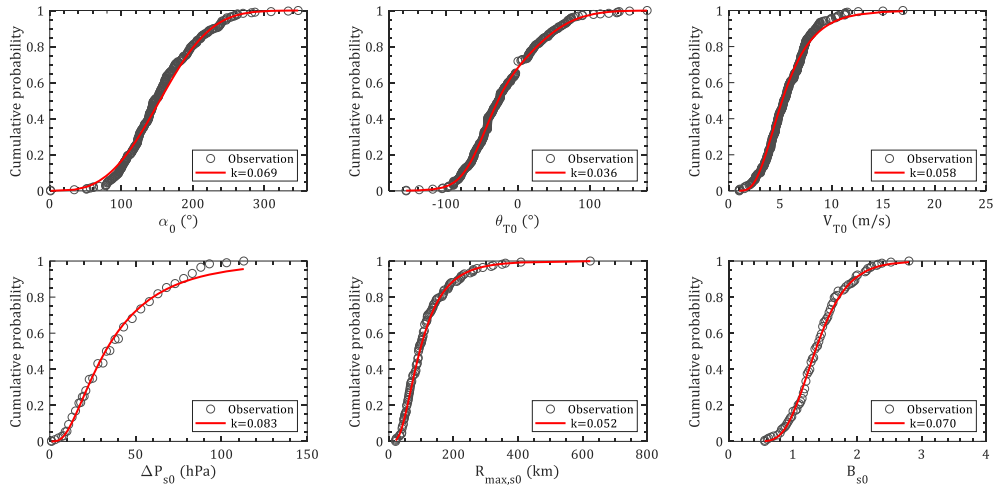


Fig. G4 CDFs of genesis parameters for Fuzhou: (a) α_0 ; (b) ΔP_0 ; (c) θ_{T0} ; (d) V_{T0} ; (e) $R_{max,s0}$; (f) B_{s0}

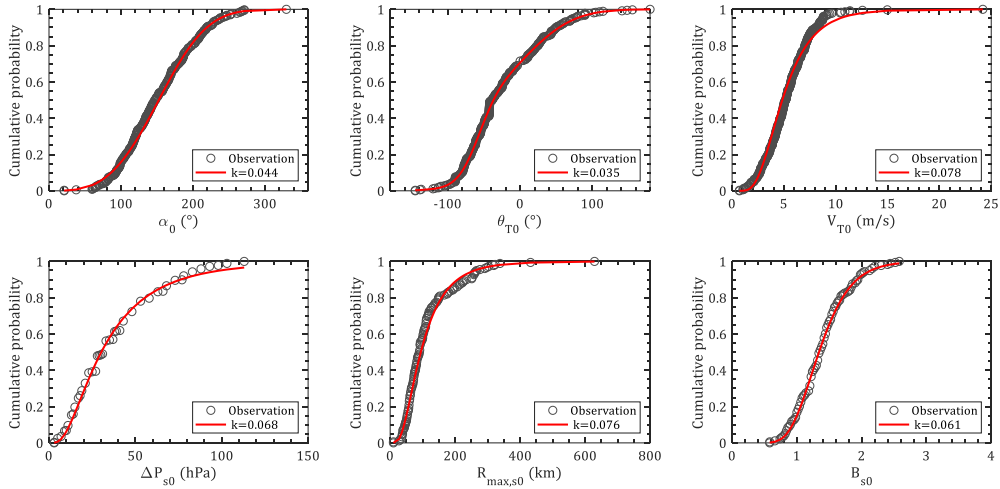


Fig. G5 CDFs of genesis parameters for Xiamen: (a) α_0 ; (b) ΔP_0 ; (c) θ_{T0} ; (d) V_{T0} ; (e) $R_{max,s0}$; (f) B_{s0}

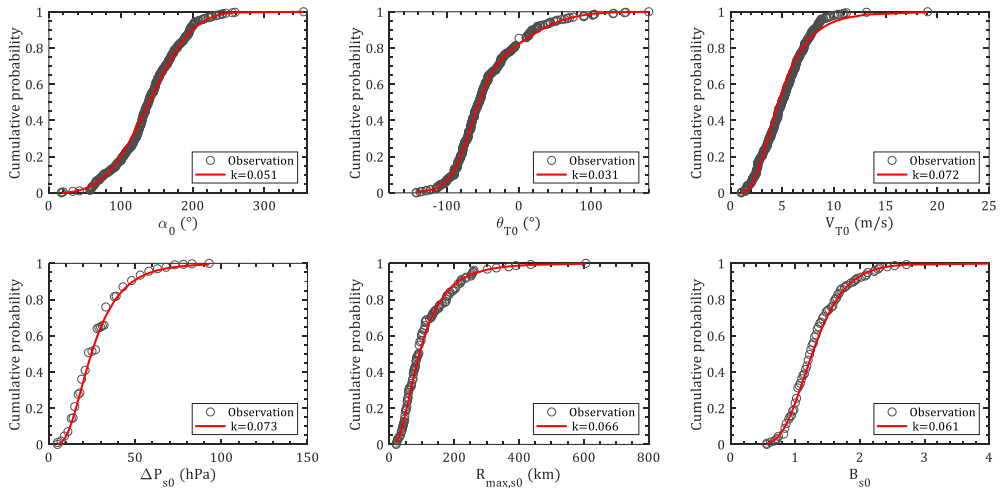


Fig. G6 CDFs of genesis parameters for Guangzhou: (a) α_0 ; (b) ΔP_0 ; (c) θ_{T0} ; (d) V_{T0} ; (e) $R_{max,s0}$; (f) B_{s0}

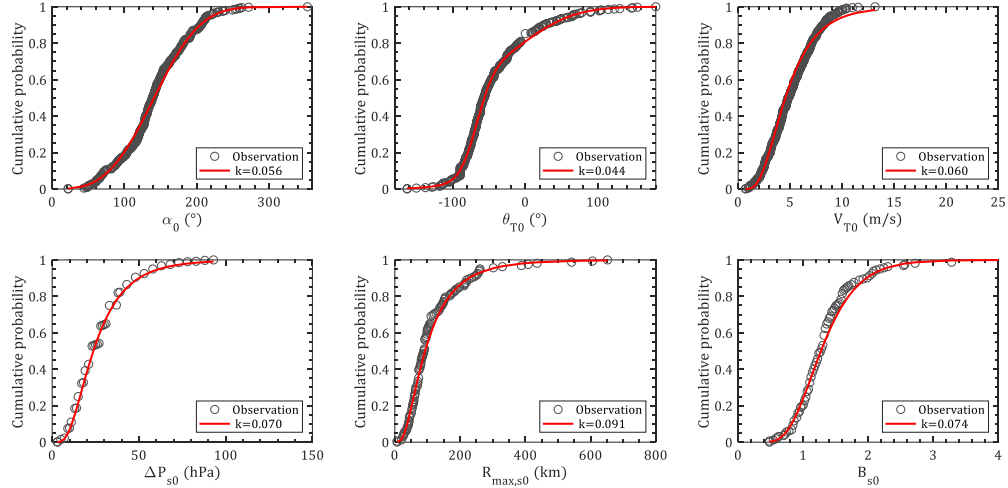


Fig. G7 CDFs of genesis parameters for Shenzhen: (a) α_0 ; (b) ΔP_{s0} ; (c) θ_{T0} ; (d) V_{T0} ; (e) $R_{max,s0}$; (f) B_{s0}

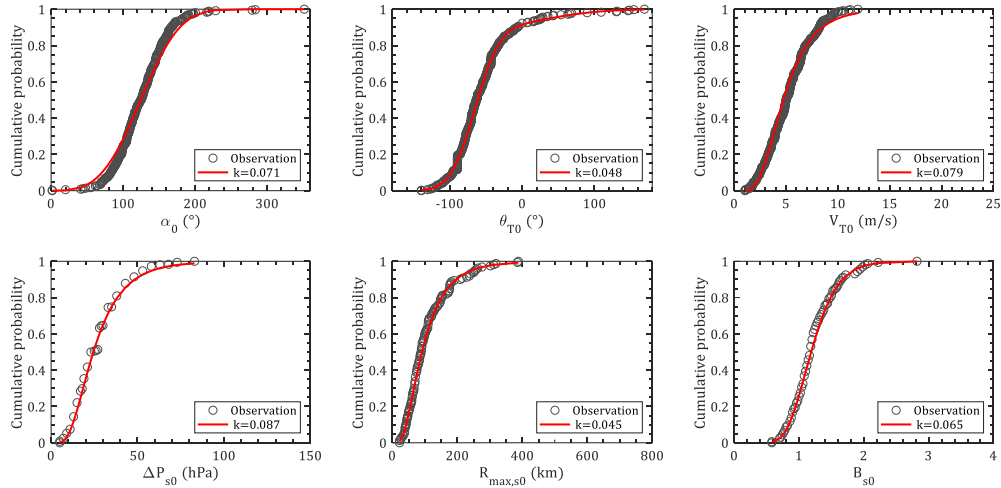


Fig. G8 CDFs of genesis parameters for Zhanjiang: (a) α_0 ; (b) ΔP_{s0} ; (c) θ_{T0} ; (d) V_{T0} ; (e) $R_{max,s0}$; (f) B_{s0}

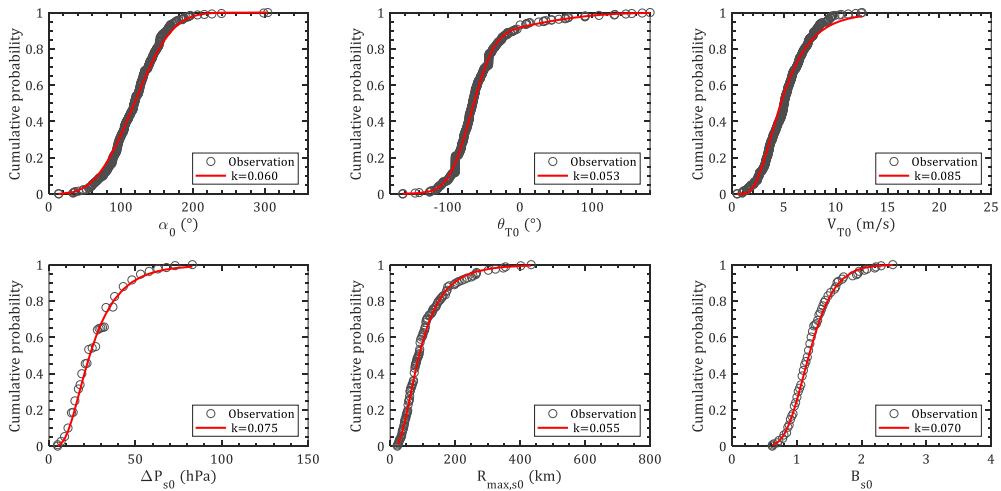


Fig. G9 CDFs of genesis parameters for Haikou: (a) α_0 ; (b) ΔP_{s0} ; (c) θ_{T0} ; (d) V_{T0} ; (e) $R_{max,s0}$; (f) B_{s0}

APPENDIX H. FLUTTER ANALYSIS MODELS

H.1 2D complex eigenvalue analysis (CEVA) or semi-inverse method

By introducing a non-dimensional time term $s = Ut/B$, Eqs. (6.4)~(6.5) can be implicitly expressed as non-wind-speed formulas in the form of

$$\frac{h''}{B} + 2\xi_{h0}K_{h0}\frac{h'}{B} + K_{h0}^2\frac{h}{B} = \frac{\rho B^2}{m_h} \left(KH_1^*\frac{h'}{B} + KH_2^*\alpha' + K^2H_3^*\alpha + K^2H_4^*\frac{h}{B} \right) \quad (H1)$$

$$\alpha'' + 2\xi_{\alpha 0}K_{\alpha 0}\alpha' + K_{\alpha 0}^2\alpha = \frac{\rho B^4}{I_m} \left(KA_1^*\frac{h'}{B} + KA_2^*\alpha' + K^2A_3^*\alpha + K^2A_4^*\frac{h}{B} \right) \quad (H2)$$

in which $h' = \dot{h}B/U$, $\alpha' = \dot{\alpha}B/U$, $K_{h0} = B\omega_{h0}/U$, $K_{\alpha 0} = B\omega_{\alpha 0}/U$. At flutter boundary, the vertical and torsional displacements can be assumed as

$$\frac{h}{B} = \frac{h_0}{B} e^{i\omega t} = \frac{h_0}{B} e^{iKs} \quad (H3)$$

$$\alpha = \alpha_0 e^{i(\omega t + \theta)} = \alpha_0 e^{iKs} \quad (H4)$$

Then, Eqs. (H1)~(H2) can be rearranged as

$$\begin{bmatrix} -X^2 + 2i\xi_{h0}X + 1 - \frac{X^2}{\gamma_m} (iH_1^* + H_4^*) & -\frac{X^2}{\gamma_m} (iH_2^* + H_3^*) \\ -\frac{X^2}{\gamma_I} (iA_1^* + A_4^*) & -X^2 + 2i\xi_{\alpha 0}\gamma_\omega X + \gamma_\omega^2 - \frac{X^2}{\gamma_I} (iA_2^* + A_3^*) \end{bmatrix} \begin{Bmatrix} \frac{h_0}{B} \\ \alpha_0 \end{Bmatrix} = \begin{Bmatrix} 0 \\ 0 \end{Bmatrix} \quad (H5)$$

Setting the determinant of the coefficient matrix of Eq.(H5) equal to zero and re-writing it as a function of $X = \omega/\omega_{h0}$, which leads to a four-degree complex formula. Then, two characteristic equations will be obtained by separating the determinant equation in real and imaginary parts as

$$R_4X^4 + R_3X^3 + R_2X^2 + R_1X + \gamma_\omega^2 = 0 \quad (H6)$$

$$I_3X^3 + I_2X^2 + I_1X + (2\xi_{h0}\gamma_\omega^2 + 2\xi_{\alpha 0}\gamma_\omega) = 0 \quad (H7)$$

in which the coefficients are formulated as

$$R_1 = 0 \quad (H8)$$

$$R_2 = -\gamma_\omega^2 - 4\xi_{\alpha 0}\xi_{h0}\gamma_\omega - 1 - \frac{A_3^*}{\gamma_I} - \gamma_\omega^2 \frac{H_4^*}{\gamma_m} \quad (\text{H9})$$

$$R_3 = 2\xi_{\alpha 0}\gamma_\omega \frac{H_1^*}{\gamma_m} + 2\xi_{h0} \frac{A_2^*}{\gamma_I} \quad (\text{H10})$$

$$R_4 = 1 + \frac{H_4^*}{\gamma_m} + \frac{A_3^*}{\gamma_I} + \frac{A_1^*H_2^* - A_2^*H_1^* + A_3^*H_4^* - A_4^*H_3^*}{\gamma_m\gamma_I} \quad (\text{H11})$$

$$I_1 = -\frac{A_2^*}{\gamma_I} - \gamma_\omega^2 \frac{H_1^*}{\gamma_m} \quad (\text{H12})$$

$$I_2 = -2\xi_{\alpha 0}\gamma_\omega - 2\xi_{h0} - 2\xi_{\alpha 0}\gamma_\omega \frac{H_4^*}{\gamma_m} - 2\xi_{h0} \frac{A_3^*}{\gamma_I} \quad (\text{H13})$$

$$I_3 = \frac{H_1^*}{\gamma_m} + \frac{A_2^*}{\gamma_I} + \frac{A_2^*H_4^* + A_3^*H_1^* - A_1^*H_3^* - A_4^*H_2^*}{\gamma_m\gamma_I} \quad (\text{H14})$$

$$\gamma_\omega = \frac{\omega_{\alpha 0}}{\omega_{h0}} \quad (\text{H15})$$

$$\gamma_m = \frac{m}{\rho B^2} \quad (\text{H16})$$

$$\gamma_I = \frac{I_m}{\rho B^4} \quad (\text{H17})$$

Eqs. (H6) and (H7) are then successively solved using different assumed values of K , resulting in two curves of $X(K)$. The flutter onset occurs at the intersection of two plots (K_c, X_c) with the critical frequency of $f_{h0}X_c$ and wind speed of $B\omega_{h0}X_c/K_c$.

H.2 2D bimodal step by step analysis (SBSA) or system decoupling approach (SDA)

The motion equation of Eq. (6.4) can be rewritten as

$$\ddot{h} + 2\xi'_h \omega \dot{h} + \omega_h'^2 h = \frac{\rho B^3}{m_h} (\omega H_2^* \dot{\alpha} + \omega^2 H_3^* \alpha) \quad (\text{H18})$$

In which

$$2\xi'_h \omega = 2\xi_{h0} \omega_{h0} - \frac{\rho B^2}{m_h} \omega H_1^* \quad (\text{H19})$$

$$\omega_h'^2 = \omega_{h0}^2 - \frac{\rho B^2}{m_h} \omega^2 H_4^* \quad (\text{H20})$$

Eq. (H18) can be solved as

$$h = \frac{\rho B^3}{m_h} \Omega_{h\alpha} \alpha_0 \left[H_2^* e^{i(\omega_\alpha t + \frac{\pi}{2} - \theta_{h\alpha})} + H_3^* e^{i(\omega_\alpha t - \theta_{h\alpha})} \right] \quad (\text{H21})$$

in which $\theta_{h\alpha}$ is the phase lag of heaving response from the torsional response. For long-span bridges, ω_α is usually greater than ω_h , which results in $\frac{\pi}{2} < \theta_{h\alpha} < \pi$

$$\Omega_{h\alpha} = \frac{\omega_\alpha^2}{\sqrt{(\omega_h'^2 - \omega_\alpha^2)^2 + (2\xi'_h \omega_\alpha^2)^2}} \quad (\text{H22})$$

$$\theta_{h\alpha} = \arctan \frac{2\xi'_h \omega_\alpha^2}{\omega_h'^2 - \omega_\alpha^2} + \pi \quad (\text{H23})$$

Eq. (6.5) will be decoupled as a motion equation associated with the torsional DOF

$$\begin{aligned} & \ddot{\alpha} \\ & + \left\{ 2\xi_{\alpha 0} \omega_{\alpha 0} - \frac{\rho B^4}{I_m} \omega_\alpha A_2^* \right. \\ & \left. - \frac{\rho^2 B^6}{I_m \cdot m_h} \Omega_{h\alpha} \omega_\alpha (A_4^* H_2^* \cos \theta_{h\alpha} - A_4^* H_3^* \sin \theta_{h\alpha} + A_1^* H_2^* \sin \theta_{h\alpha} + A_1^* H_3^* \cos \theta_{h\alpha}) \right\} \dot{\alpha} \\ & + \left\{ \omega_{\alpha 0}^2 - \frac{\rho B^4 \omega_\alpha^2 A_3^*}{I_m} - \frac{\rho^2 B^6}{I_m \cdot m_h} \Omega_{h\alpha} \omega_\alpha^2 (A_4^* H_2^* \sin \theta_{h\alpha} + A_4^* H_3^* \cos \theta_{h\alpha} - A_1^* H_2^* \cos \theta_{h\alpha} + A_1^* H_3^* \sin \theta_{h\alpha}) \right\} \alpha \\ & = 0 \end{aligned} \quad (\text{H24})$$

Accordingly, the frequency and damping ratio of torsional DOF can be calculated by

$$\omega_\alpha = \omega_{\alpha 0} / \left\{ 1 + \frac{\rho B^4 A_3^*}{I_m} + \frac{\rho^2 B^6}{I_m \cdot m_h} \Omega_{h\alpha} [(A_4^* H_2^* + A_1^* H_3^*) \sin \theta_{h\alpha} + (A_4^* H_3^* - A_1^* H_2^*) \cos \theta_{h\alpha}] \right\}^{1/2} \quad (\text{H25})$$

$$\xi_\alpha = \frac{\xi_{\alpha 0} \omega_{\alpha 0}}{\omega_\alpha} - \frac{\rho B^4 A_2^*}{2I_m} - \frac{\rho^2 B^6}{2I_m \cdot m_h} \Omega_{h\alpha} [(A_1^* H_2^* - A_4^* H_3^*) \sin \theta_{h\alpha} + (A_4^* H_2^* + A_1^* H_3^*) \cos \theta_{h\alpha}] \quad (\text{H26})$$

Similarly, the frequency and damping ratio of heaving DOF can be calculated by

$$\omega_h = \omega_{h 0} / \left\{ 1 + \frac{\rho B^2 H_4^*}{m_h} + \frac{\rho^2 B^6}{I_m \cdot m_h} \Omega_{\alpha h} [(H_2^* A_4^* + H_3^* A_1^*) \sin \theta_{\alpha h} + (H_3^* A_4^* - H_2^* A_1^*) \cos \theta_{\alpha h}] \right\}^{1/2} \quad (\text{H27})$$

$$\xi_h = \frac{\xi_{h 0} \omega_{h 0}}{\omega_h} - \frac{\rho B^2 H_1^*}{2m_h} - \frac{\rho^2 B^6}{2I_m \cdot m_h} \Omega_{\alpha h} [(H_2^* A_1^* - H_3^* A_4^*) \sin \theta_{\alpha h} + (H_2^* A_4^* + H_3^* A_1^*) \cos \theta_{\alpha h}] \quad (\text{H28})$$

in which

$$\Omega_{\alpha h} = \frac{\omega_h^2}{\sqrt{(\omega_\alpha'^2 - \omega_h^2)^2 + (2\xi_\alpha' \omega_h^2)^2}} \quad (\text{H29})$$

$$\theta_{\alpha h} = \arctan \frac{2\xi_\alpha' \omega_h^2}{\omega_\alpha'^2 - \omega_h^2} + \pi \quad (\text{H30})$$

four parameters associated two DOFs, i.e. ω_α , ω_h , ξ_α and ξ_h can be progressively solved using Eqs. (H25) - (H28) with the increase of wind speed. The flutter onset is defined as the wind speed at which $\xi_\alpha = 0$.

H.3 Rational-function-approximation (RFA) -based state space method

The aerodynamic force (the right side of the Eq. (6.1)) can be transferred to the time domain using Laplace transformation. In the Laplace domain, the aerodynamic force is expressed as

$$\mathbf{F}_{se} = \rho U^2 \mathbf{b}^T \mathbf{Q} \mathbf{b} \tilde{\mathbf{X}} \quad (\text{H31})$$

in which

$$\mathbf{b} = \begin{bmatrix} 1 & 0 & 0 \\ 0 & 1 & 0 \\ 0 & 0 & B \end{bmatrix} \quad (\text{H32})$$

$$\mathbf{Q} = \begin{bmatrix} K^2 H_4^* + \lambda K H_1^* & K^2 H_6^* + \lambda K H_5^* & K^2 H_3^* + \lambda K H_2^* \\ K^2 P_4^* + \lambda K P_1^* & K^2 P_6^* + \lambda K P_5^* & K^2 P_3^* + \lambda K P_2^* \\ K^2 A_4^* + \lambda K A_1^* & K^2 A_6^* + \lambda K A_5^* & K^2 A_3^* + \lambda K A_2^* \end{bmatrix} \quad (\text{H33})$$

$$\lambda = \frac{sB}{U} \quad (\text{H34})$$

$$s = (-\zeta + i)\omega \quad (\text{H35})$$

$$\tilde{\mathbf{X}} = [\tilde{h} \quad \tilde{p} \quad \tilde{\alpha}]^T \quad (\text{H36})$$

Because the flutter derivatives obtained from wind tunnel test or CFD are scattered points, the inverse Laplace transformation cannot be directly applied to $\tilde{\mathbf{F}}_{se}$ to achieve the aerodynamic force in the time domain. Alternatively, the frequency response function \mathbf{Q} is fitted with a rational function approximation (Roger approximation) with the form of

$$\mathbf{Q} \approx \mathbf{A}_1 + \mathbf{A}_2 \lambda + \mathbf{A}_3 \lambda^2 + \sum_{l=1}^m \frac{\mathbf{A}_{l+3} \lambda}{\lambda + d_l} \quad (\text{H37})$$

in which matrices \mathbf{A}_i ($i = 1, 2, 3, \dots, l + 3$) and d_l ($d_l \geq 0$, $l = 1, 2, \dots, m$) are frequency-independent coefficients, \mathbf{A}_1 and \mathbf{A}_2 are static-aerodynamics and aerodynamic damping, respectively, \mathbf{A}_3 is the additional aerodynamic mass due to the wind loads and is generally negligible. The rational partial fractions (last part of Eq. (H37)) serve as the memory effects of self-excited forces on the motion of the structure or unsteady characteristics of the self-excited forces. It represents the aerodynamic forces lag the velocity components with

approximated time delays of d_l (Chen et al., 2000). Then, the aerodynamic force in the time domain will be achieved by performing inverse Laplace transformation on Eq. (H31) as

$$\mathbf{F}_{se} = \rho U^2 \left(\mathbf{b}^T \mathbf{A}_1 \mathbf{b} \mathbf{X} + \frac{B}{U} \mathbf{b}^T \mathbf{A}_2 \mathbf{b} \dot{\mathbf{X}} + \frac{B^2}{U^2} \mathbf{b}^T \mathbf{A}_3 \mathbf{b} \ddot{\mathbf{X}} + \sum_{l=1}^m \Delta_l \right) \quad (\text{H38})$$

in which

$$\Delta_l = L^{-1}(\tilde{\Delta}_l) \quad (\text{H39})$$

$$\tilde{\Delta}_l = \frac{\mathbf{b}^T \mathbf{A}_{l+3} \mathbf{b} \lambda}{\lambda + d_l} \tilde{\mathbf{X}} \quad (\text{H40})$$

$$\dot{\Delta}_l = \mathbf{b}^T \mathbf{A}_{l+3} \mathbf{b} \dot{\mathbf{X}} - \frac{d_l U}{B} \cdot \Delta_l \quad (\text{H41})$$

Then, the equation of motion can be expressed as

$$\ddot{\mathbf{X}} + \bar{\mathbf{M}}^{-1} \bar{\mathbf{C}} \dot{\mathbf{X}} + \bar{\mathbf{M}}^{-1} \bar{\mathbf{K}} \mathbf{X} = \rho U^2 \bar{\mathbf{M}}^{-1} \sum_{l=1}^m \Delta_l \quad (\text{H42})$$

in which

$$\bar{\mathbf{M}} = \mathbf{M} - \rho B^2 \mathbf{b}^T \mathbf{A}_3 \mathbf{b} \quad (\text{H43})$$

$$\bar{\mathbf{C}} = \mathbf{C}_0 - \rho U B \mathbf{b}^T \mathbf{A}_2 \mathbf{b} \quad (\text{H44})$$

$$\bar{\mathbf{K}} = \mathbf{K}_0 - \rho U^2 \mathbf{b}^T \mathbf{A}_1 \mathbf{b} \quad (\text{H45})$$

Eq. (C12) can be rewritten as the state-space representation with the form of

$$\dot{\mathbf{X}}_R = \mathbf{S} \mathbf{X}_R \quad (\text{H46})$$

in which

$$\mathbf{X}_R = \left\{ \begin{array}{c} \mathbf{X} \\ \dot{\mathbf{X}} \\ \Delta_1 \\ \vdots \\ \Delta_m \end{array} \right\} \quad (\text{H47})$$

$$\mathbf{S} = \begin{bmatrix} \mathbf{0} & \mathbf{I} & \mathbf{0} & \dots & \mathbf{0} \\ -\bar{\mathbf{M}}^{-1}\bar{\mathbf{K}} & \bar{\mathbf{M}}^{-1}\bar{\mathbf{C}} & \rho U^2 \bar{\mathbf{M}}^{-1} & \dots & \rho U^2 \bar{\mathbf{M}}^{-1} \\ \mathbf{0} & \mathbf{b}^T \mathbf{A}_4 \mathbf{b} & -\frac{d_1 U}{B} \mathbf{I} & \mathbf{0} & \mathbf{0} \\ \vdots & \vdots & \vdots & \vdots & \vdots \\ \mathbf{0} & \mathbf{b}^T \mathbf{A}_m \mathbf{b} & \mathbf{0} & \dots & -\frac{d_m U}{B} \mathbf{I} \end{bmatrix} \quad (\text{H48})$$

By solving the eigenvalues of Eq. (H46), say $\det(\mathbf{S}) = 0$, the critical wind speed, and critical frequency can be determined.

H.4 3D multimodal method

Flutter is always characterized by the single-mode non-damping harmonic vibration. If the circular frequency is assumed as ω , Eq. (6.1) can be rearranged in the complex frequency domain as

$$\mathbf{M}\ddot{\mathbf{X}} + \mathbf{C}_0\dot{\mathbf{X}} + \mathbf{K}_0\mathbf{X} = \mathbf{F}_{se} = \omega^2\mathbf{A}_{sd}\mathbf{X} \quad (\text{H49})$$

in which \mathbf{A}_{sd} consists of aerodynamic stiffness and damping terms with the form of

$$\mathbf{A}_{sd} = \rho B^2 \begin{bmatrix} iH_1^* + H_4^* & iH_5^* + H_6^* & B(iH_2^* + H_3^*) \\ iP_1^* + P_4^* & iP_5^* + P_6^* & B(iP_2^* + P_3^*) \\ B(iA_1^* + A_4^*) & B(iA_5^* + A_6^*) & B^2(iA_2^* + A_3^*) \end{bmatrix} \quad (\text{H50})$$

in which i is the unit imaginary number. In the frequency domain, the displacement matrix \mathbf{X} can be expanded as the sum of first N modes as

$$\mathbf{X} = \mathbf{\Phi}\mathbf{q} \quad (\text{H51})$$

in which $\mathbf{\Phi}$ is the mode shape matrix, \mathbf{q} is the modal coordinate. $\mathbf{\Phi}$ can be obtained from modal analysis using the finite element model and normalized by mass matrix, then Eq. (H49) can be rearranged in terms of modal coordinates as

$$\ddot{\mathbf{q}} + \tilde{\mathbf{C}}_0\dot{\mathbf{q}} + \tilde{\mathbf{K}}_0\mathbf{q} = \omega^2\tilde{\mathbf{A}}_{sd}\mathbf{q} \quad (\text{H52})$$

in which

$$\tilde{\mathbf{C}}_0 = \mathbf{\Phi}^T\mathbf{C}_0\mathbf{\Phi} = \begin{bmatrix} 2\zeta_1\omega_1 & \cdots & 0 \\ \vdots & \ddots & \vdots \\ 0 & \cdots & 2\zeta_N\omega_N \end{bmatrix} \quad (\text{H53})$$

$$\tilde{\mathbf{K}}_0 = \mathbf{\Phi}^T\mathbf{K}_0\mathbf{\Phi} = \begin{bmatrix} \omega_1^2 & \cdots & 0 \\ \vdots & \ddots & \vdots \\ 0 & \cdots & \omega_N^2 \end{bmatrix} \quad (\text{H54})$$

In which ζ_n and ω_n ($n = 1, 2, \dots, N$) are modal damping ratios and circular frequencies. The damping matrix is expressed as the linear sum of mass matrix and stiffness matrix as, i.e. Rayleigh damping

$$\mathbf{C}_0 = \alpha \mathbf{M} + \beta \mathbf{K}_0 \quad (\text{H55})$$

If the damping ratios of two modes are prescribed, α and β can be derived as

$$\begin{Bmatrix} \alpha \\ \beta \end{Bmatrix} = \frac{2\omega_m\omega_n}{\omega_m^2 - \omega_n^2} \begin{bmatrix} \omega_n & -\omega_m \\ -1/\omega_n & 1/\omega_m \end{bmatrix} \begin{Bmatrix} \zeta_m \\ \zeta_n \end{Bmatrix} \quad (\text{H56})$$

This yield

$$\tilde{\mathbf{C}}_0 = \Phi^T \mathbf{C}_0 \Phi = \alpha \mathbf{I} + \beta \Phi^T \mathbf{K}_0 \Phi = \alpha \mathbf{I} + \beta \tilde{\mathbf{K}}_0 \quad (\text{H57})$$

At flutter boundary, \mathbf{q} can be expressed as

$$\mathbf{q} = \mathbf{q}_0 e^{\lambda t} \quad (\text{H58})$$

Then, Eq. (H52) is rewritten as

$$[\lambda^2(\mathbf{I} + \tilde{\mathbf{A}}_{sd}) + \lambda \tilde{\mathbf{C}}_0 + \tilde{\mathbf{K}}_0] \mathbf{q}_0 e^{\lambda t} = \mathbf{0} \quad (\text{H59})$$

Or the state-space representation with the form of

$$\dot{\mathbf{Y}} = \begin{bmatrix} \mathbf{0} & \mathbf{I} \\ -(\mathbf{I} + \tilde{\mathbf{A}}_{sd})^{-1} \tilde{\mathbf{K}}_0 & -(\mathbf{I} + \tilde{\mathbf{A}}_{sd})^{-1} \tilde{\mathbf{C}}_0 \end{bmatrix} \mathbf{Y} = \mathbf{A} \mathbf{Y} \quad (\text{H60})$$

In which

$$\mathbf{Y} = \begin{Bmatrix} \mathbf{q} \\ \dot{\mathbf{q}} \end{Bmatrix} \quad (\text{H61})$$

\mathbf{A} is a complex matrix with an order of $2N \times 2N$.

At each wind speed, the reduced wind speed defined by every frequency will be calculated as $U/f_j B$. The flutter derivatives with respect to each reduced wind speed will be extracted to assemble the aerodynamic matrix \mathbf{A}_{sd} . Then the $2N$ conjugate eigenvalues and eigenvectors of \mathbf{A} can be solved as

$$\lambda_n = (-\zeta_n \pm i)\omega_n \quad (\text{H62})$$

$$\mathbf{q} = \mathbf{a} \pm \mathbf{b}i \quad (\text{H63})$$

in which N eigenvalues with positive imaginary part represent the frequency and damping ratio of the system, correspondingly, the upper half of \mathbf{q} related to the displacement in the state vector \mathbf{Y} stands for the generalized coordinate for each complex mode of the system.

The amplitude and phase of each mode is expressed as

$$|q_n| = \sqrt{a_n^2 \pm b_n^2} \quad (\text{H64})$$

$$|\varphi_n| = \arctan \frac{b_n}{a_n} \quad (\text{H65})$$

Energy ratio for each mode during the flutter is

$$e_i = \frac{E_i}{E} = \frac{1/2 \omega_{cr}^2 |q_n|^2}{\sum 1/2 \omega_{cr}^2 |q_n|^2} = \frac{|q_n|^2}{\sum |q_n|^2} \quad (\text{H66})$$

in which ω_{cr} is the circular frequency of flutter vibration.

The flutter critical wind speed is determined when one of ζ_n reaches zero. In the FEM model, the positive direction is defined by the Cartesian coordinate system (right-handed coordinates). However, the vertical displacement (h) and lift force (L_h) in Scanlan's aerodynamic model are defined to be positive when downward. For each element, the distributed aerodynamic force is treated as the equivalent nodal force. At both ends (i, j) of an element, the self-excited force related to six DOFs ($x, y, z, \alpha, \beta, \gamma$) is

$$\mathbf{A}_{sdi} = \mathbf{A}_{sdj} = \frac{l}{2} \rho B^2 \begin{bmatrix} 0 & 0 & 0 & 0 & 0 & 0 \\ 0 & iH_1^* + H_4^* & -iH_5^* - H_6^* & -B(iH_2^* + H_3^*) & 0 & 0 \\ 0 & -iP_5^* - P_6^* & iP_1^* + P_4^* & B(iP_2^* + P_3^*) & 0 & 0 \\ 0 & -B(iA_1^* + A_4^*) & (iA_5^* + A_6^*) & B^2(iA_2^* + A_3^*) & 0 & 0 \\ 0 & 0 & 0 & 0 & 0 & 0 \\ 0 & 0 & 0 & 0 & 0 & 0 \end{bmatrix} \quad (\text{H67})$$

in which l is the length of the element.

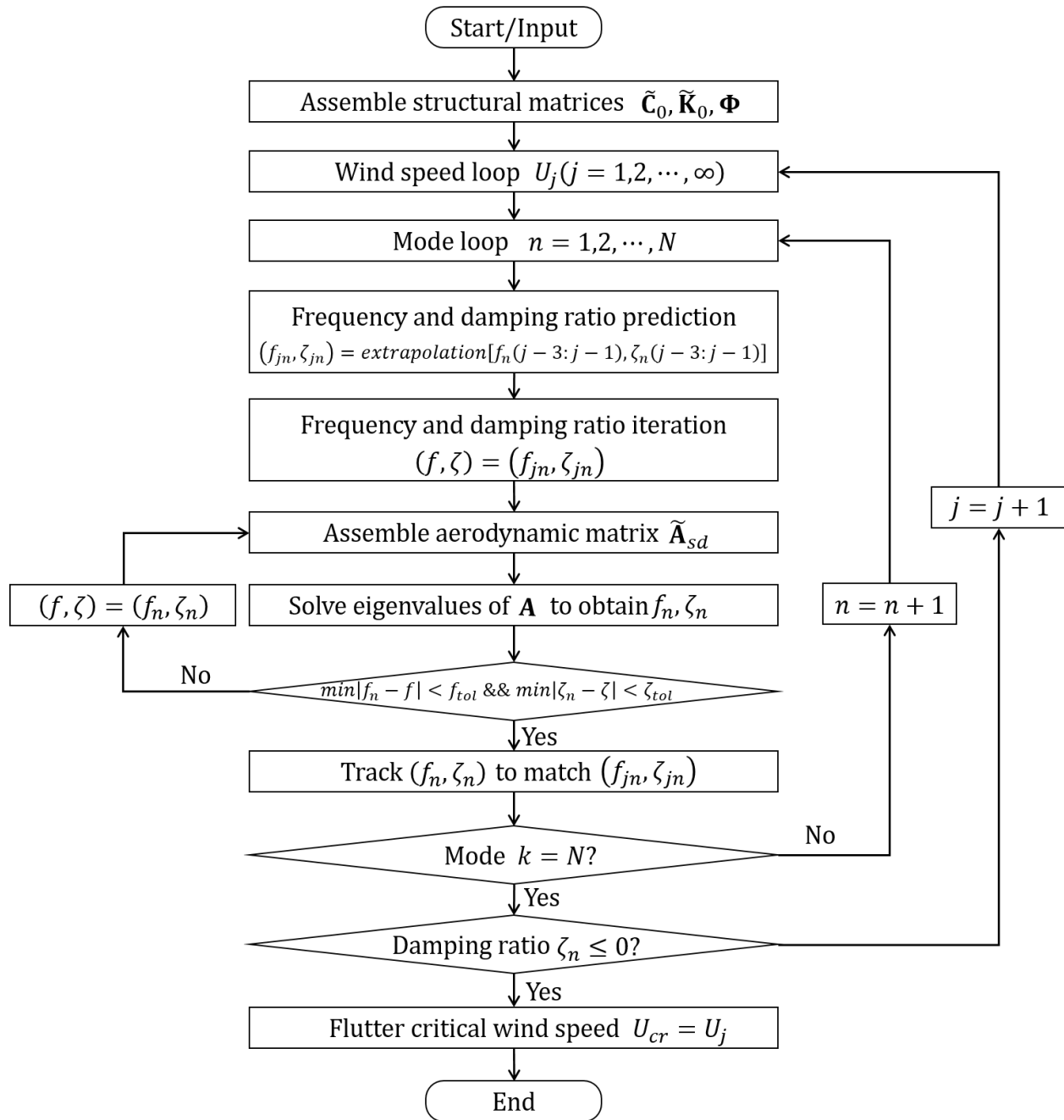


Fig. H1 The flowchart of multimode flutter analysis

APPENDIX I. FLUTTER ANALYSIS OF A SIMPLY SUPPORTED BEAM WITH AN IDEAL PLATE FLATE SECTION

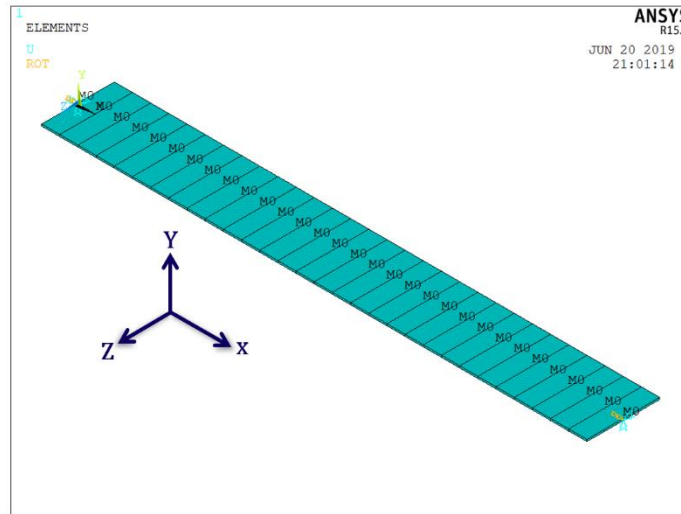


Fig. I1 FEM model of a simply supported beam

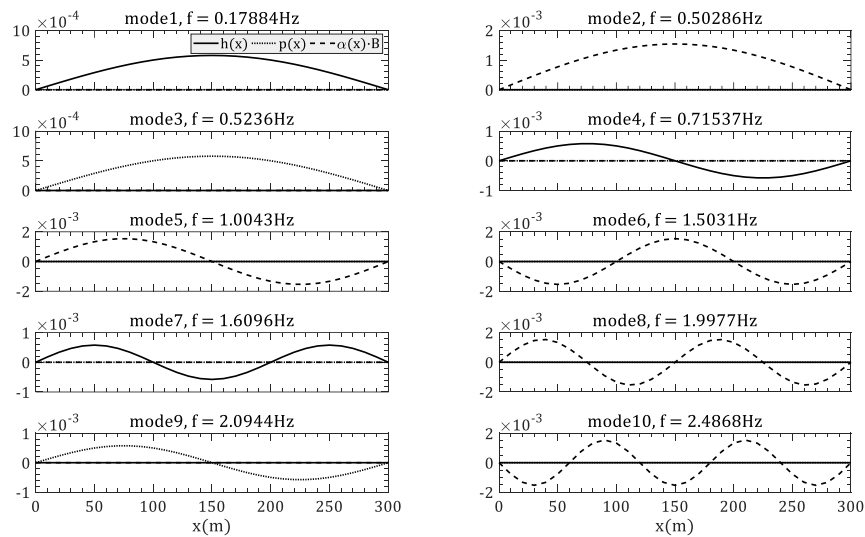


Fig. I2 Frequencies and mode shapes of the first ten modes

(I1) CEVA method

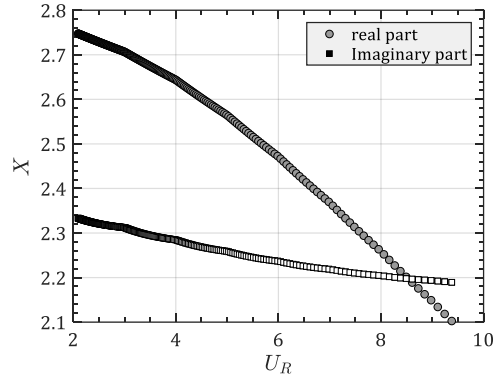


Fig. 13 Flutter solution using CEVA

(I2) SBSA method

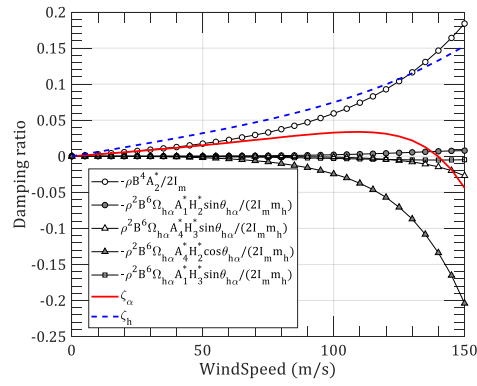


Fig. 14 Flutter solution using SBSA

(I3) RFA-based state space method

For RFA-based state space method, the coefficients \mathbf{A}_i ($i = 1, 2, 3, \dots, l + 3$) were fitted by taking into account two order memory effects, i.e. $l = 2$. The fitting algorithm of Roger's function proposed by Guo and Ge (2012) was adopted using the prescribed flutter derivatives. The results for the ideal flat plate are shown as

$$\mathbf{A}_1 = \begin{bmatrix} -6.678 \times 10^{-5} & -6.283 \\ 6.549 \times 10^{-7} & 1.5794 \end{bmatrix} \quad (I1)$$

$$\mathbf{A}_2 = \begin{bmatrix} -3.142 & -2.356 \\ 0.785 & -0.203 \end{bmatrix} \quad (12)$$

$$\mathbf{A}_3 = \begin{bmatrix} -1.571 & 1.414 \times 10^{-5} \\ 1.174 \times 10^{-5} & -0.040 \end{bmatrix} \quad (13)$$

$$\mathbf{A}_4 = \begin{bmatrix} -1.263 & 1.789 \\ 0.316 & -0.436 \end{bmatrix} \quad (14)$$

$$\mathbf{A}_5 = \begin{bmatrix} -0.094 & 1.013 \\ 0.024 & -0.264 \end{bmatrix} \quad (15)$$

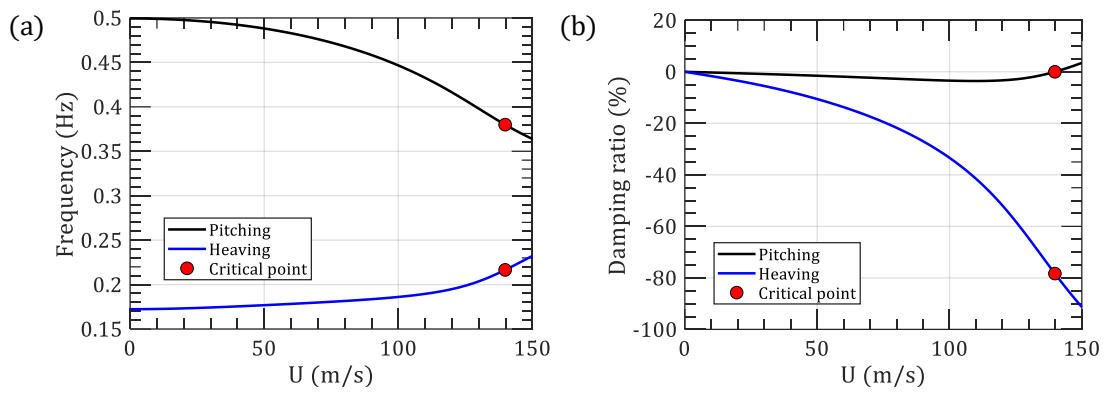


Fig. 15 Flutter solution using Roger-function-based state space method: (a) Frequency vs. wind speed; (b) Damping ratio vs. wind speed

(I4) Multi-mode method

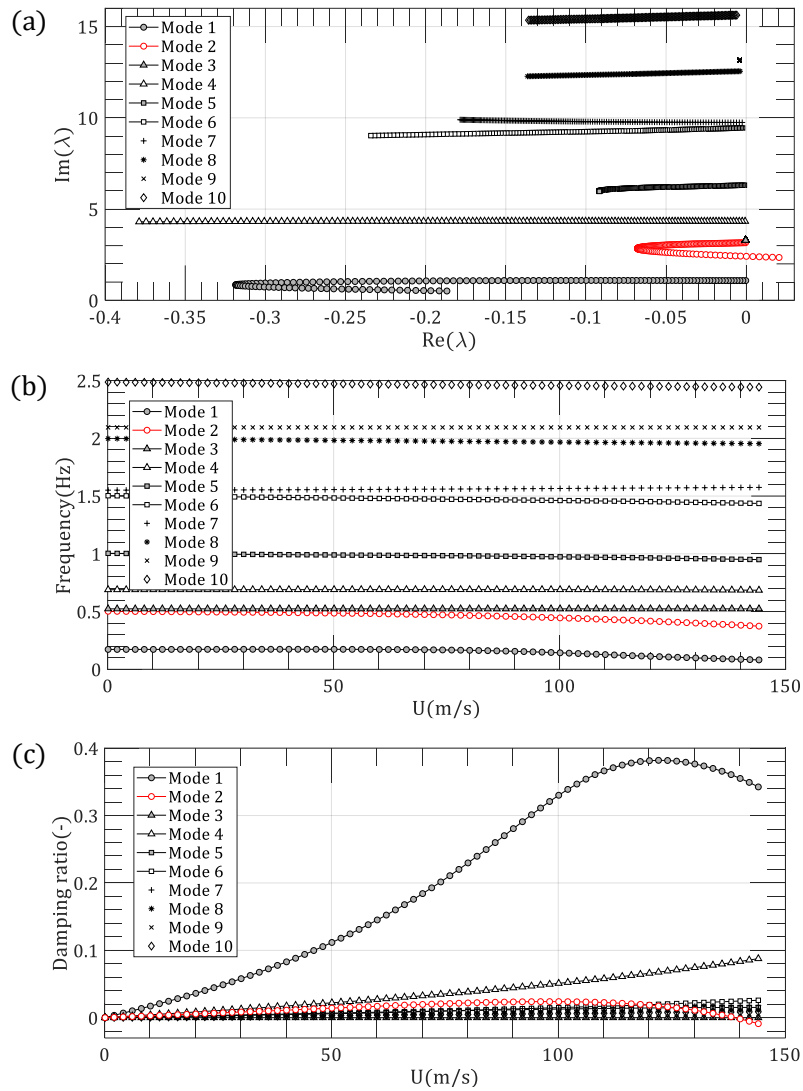


Fig. I6 Flutter solution using multi-mode method: (a) Real part vs. imaginary part of eigen values; (b) Frequency vs. wind speed; (c) Damping ratio vs. wind speed

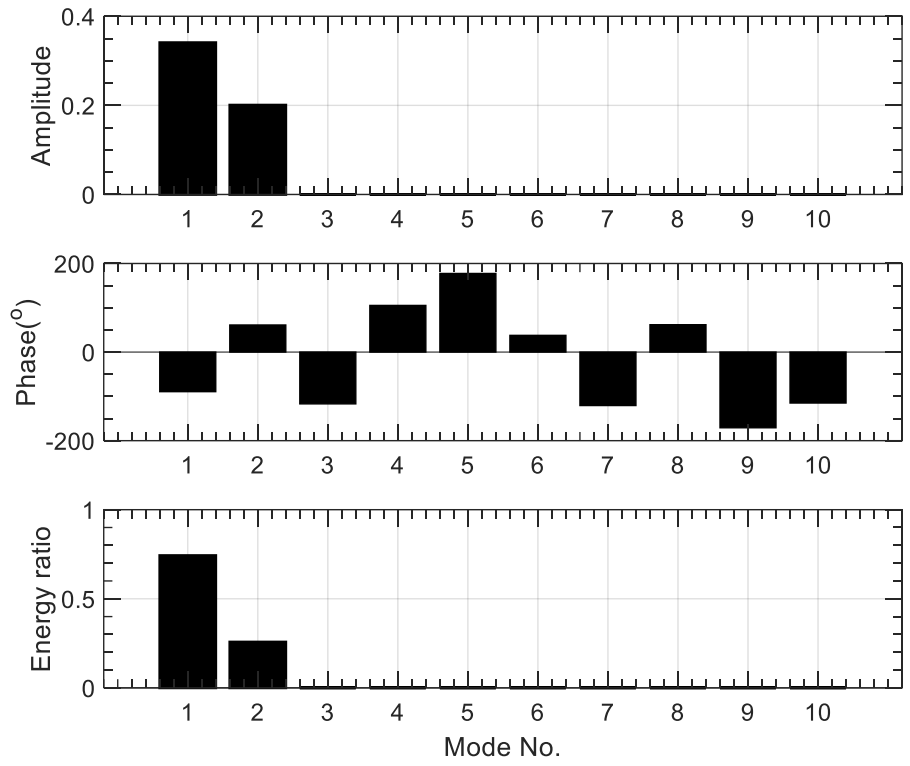


Fig. I7 Flutter motion in terms of the structural modal participation ($U = 139.7$ m/s)

**APPENDIX J. FLUTTER ANALYSIS OF JIANGYIN SUSPENSION BRIDGE
WITH AN IDEAL FLAT PLATE SECTION GIRDER**

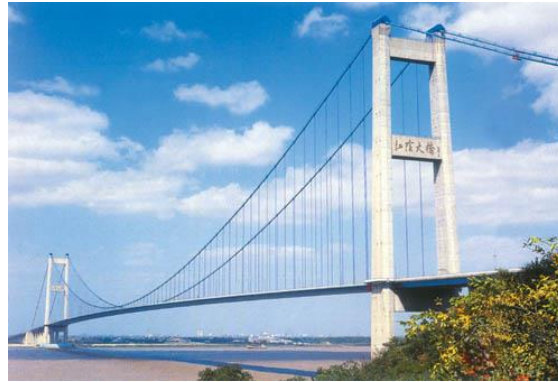


Fig. J1 Jiangyin suspension bridge (<http://highestbridges.com/wiki/index.php?title=File:Jiangyin.jpg>)

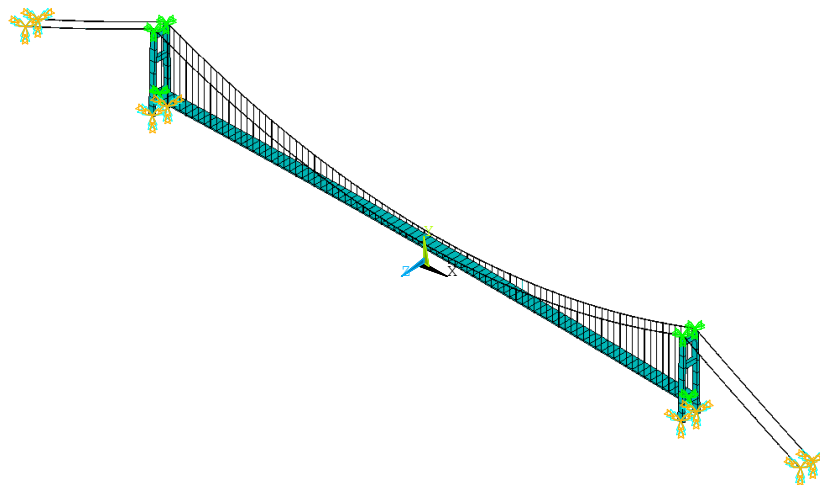


Fig. J2 ANSYS FEM model of Jiangyin suspension bridge

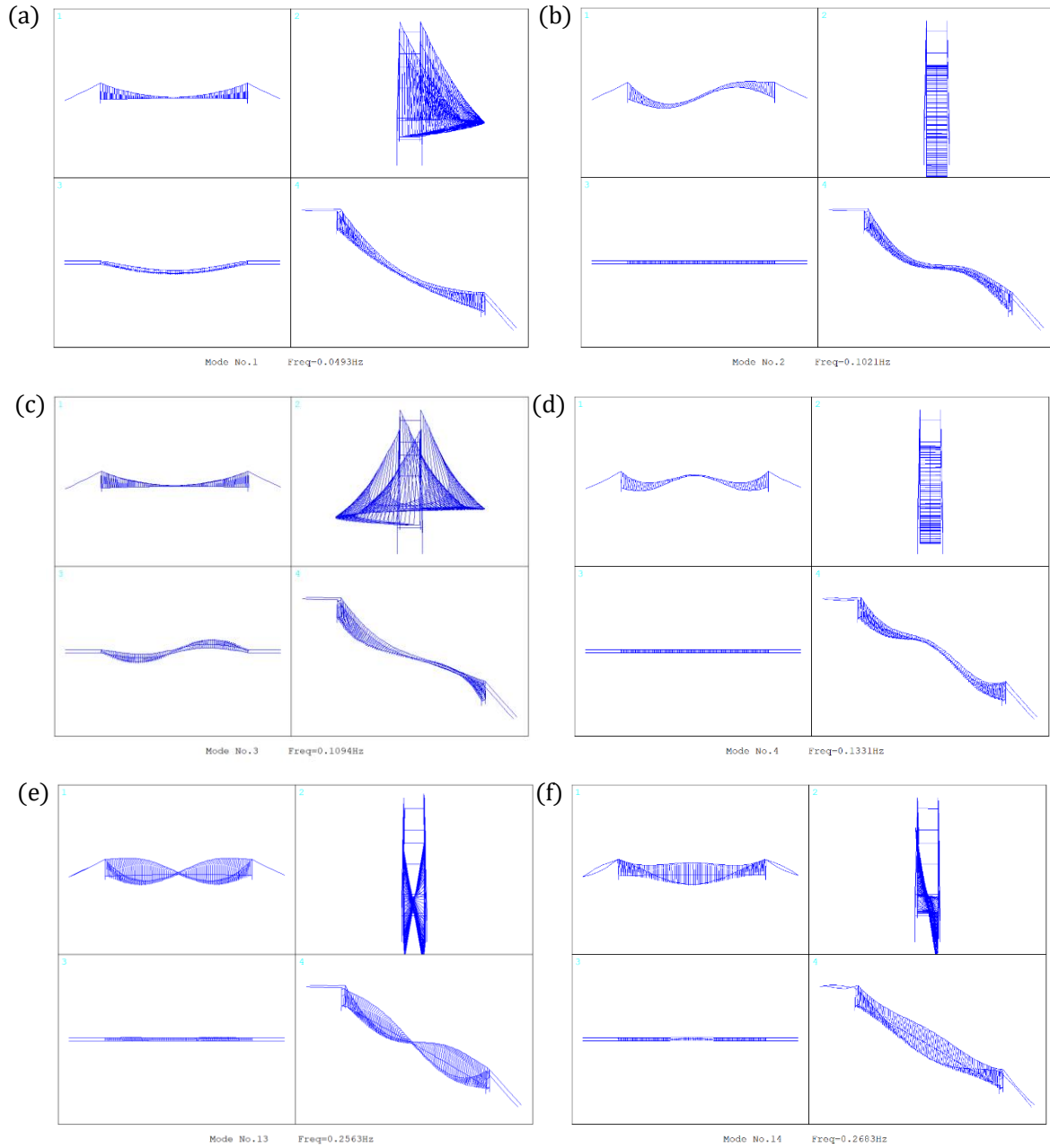


Fig. J3 Mode shapes of first two fundamental modes: (a) Symmetric lateral bending; (b) Antisymmetric vertical bending; (c) Antisymmetric lateral bending; (d) Symmetric vertical bending; (e) Antisymmetric torsion; (f) Symmetric torsion;

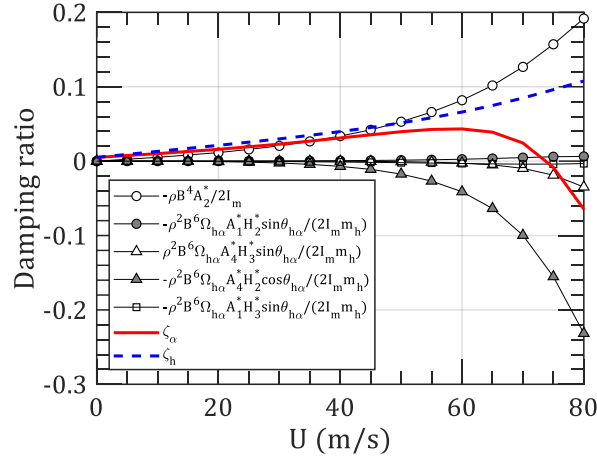


Fig. J4 Flutter solution using SBSA

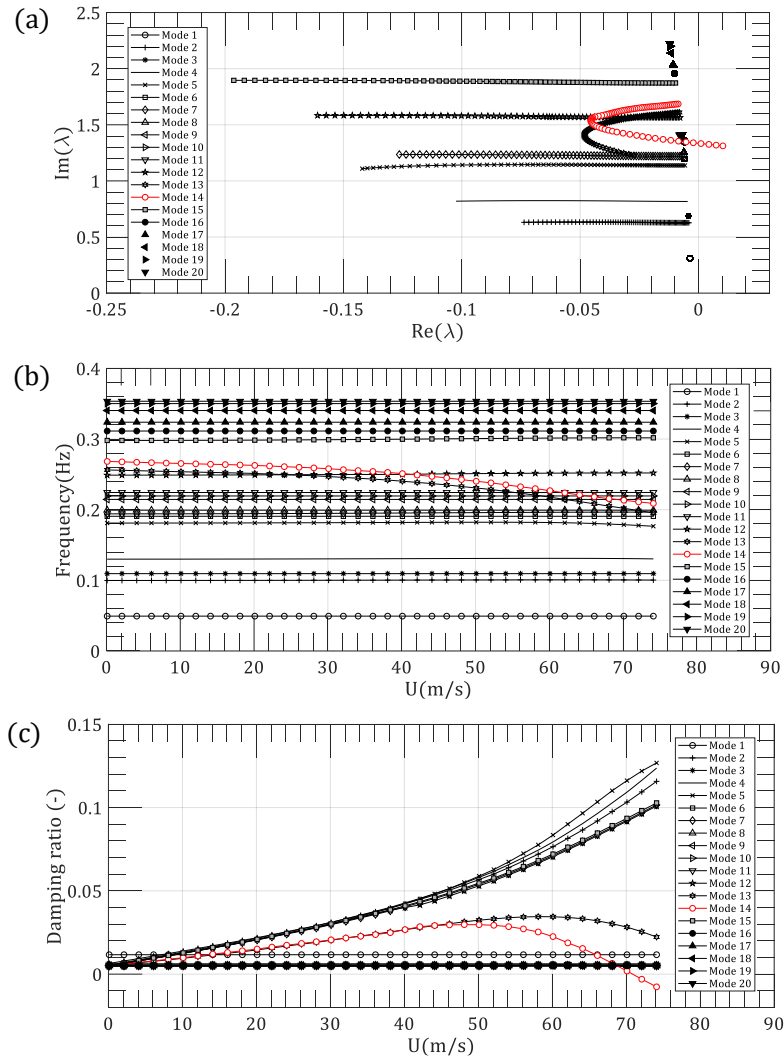


Fig. J5 Flutter solution using the multi-mode method: (a) Real part vs. imaginary part of eigenvalues; (b) Frequency vs. wind speed; (c) Damping ratio vs. wind speed

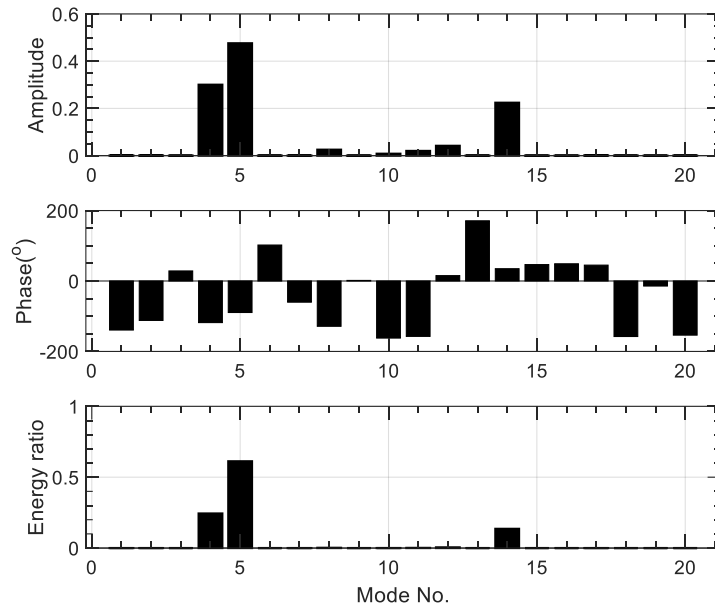


Fig. J6 Flutter motion in terms of the structural modal participation ($U = 70.9$ m/s)

APPENDIX K. WIND TUNNEL TEST OF A QUASI-FLAT PLATE MODEL

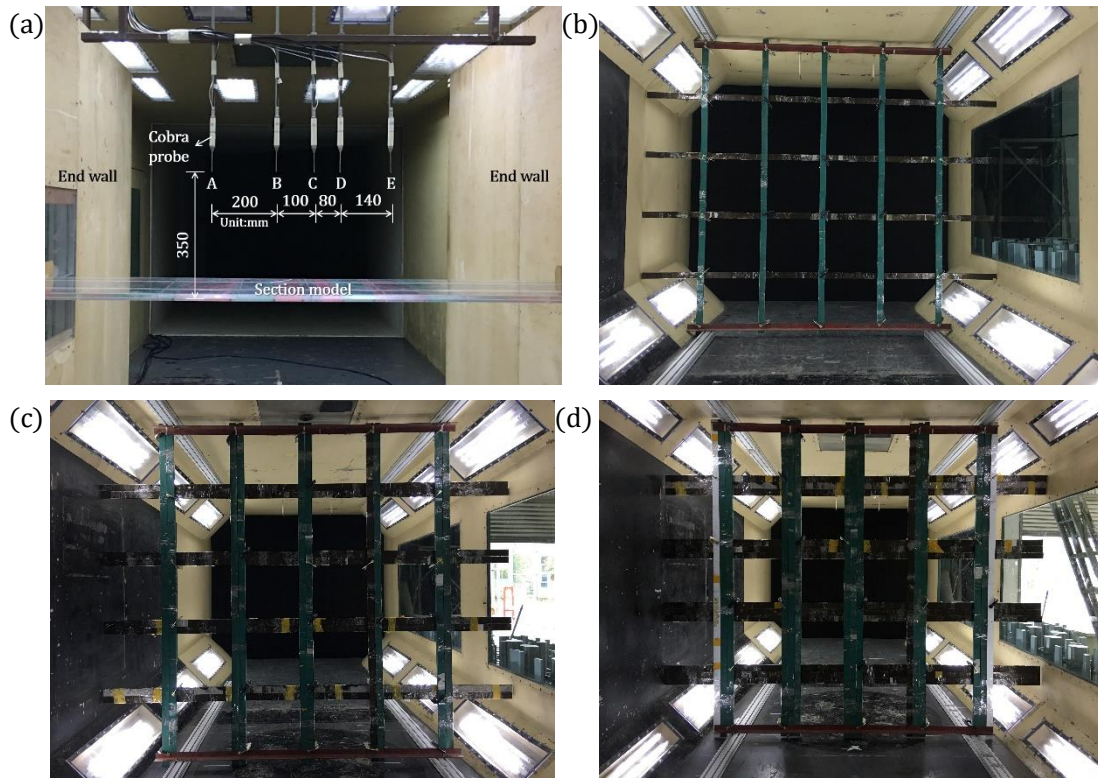


Fig. K1 Wind tunnel test of a quasi-flat plate: (a) Sectional model and Cobra probe; (b) Grid I ($I_u = 5\%$); (c) Grid II ($I_u = 10\%$); (d) Grid III ($I_u = 14\%$)

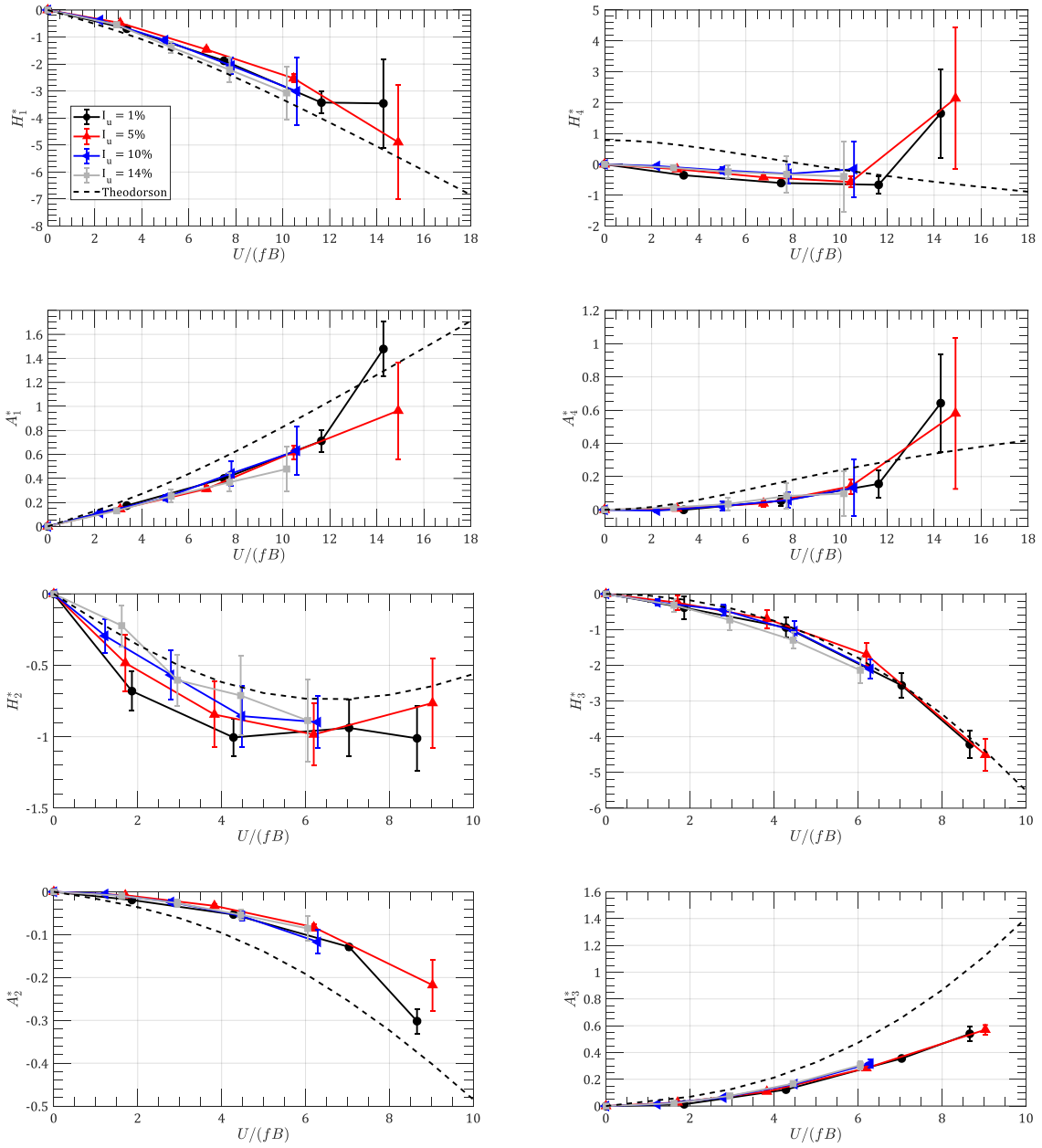


Fig. K2 Mean and standard deviations for flutter derivatives of the quasi-flat section model

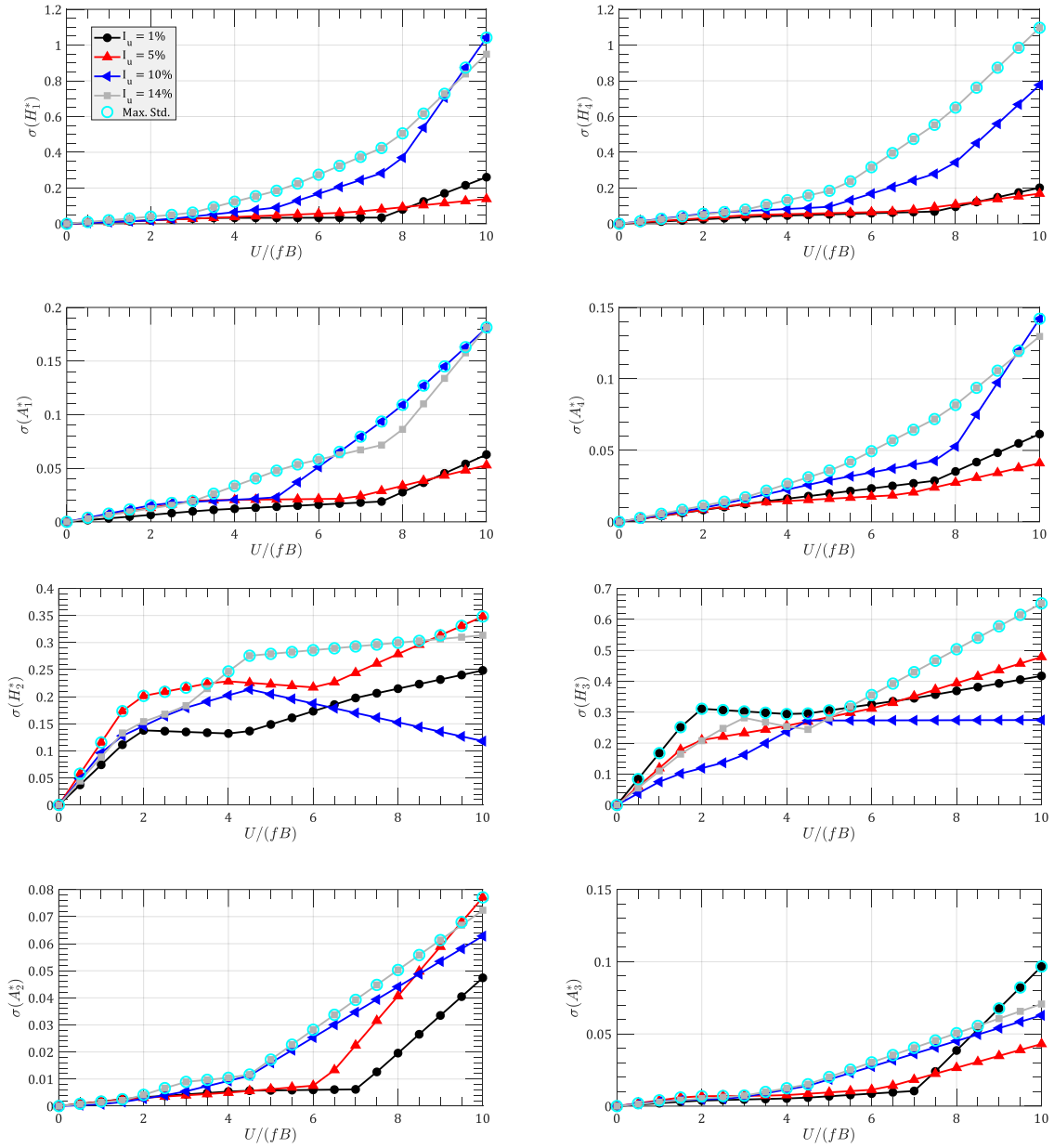


Fig. K3 Standard deviations for flutter derivatives of the quasi-flat section model

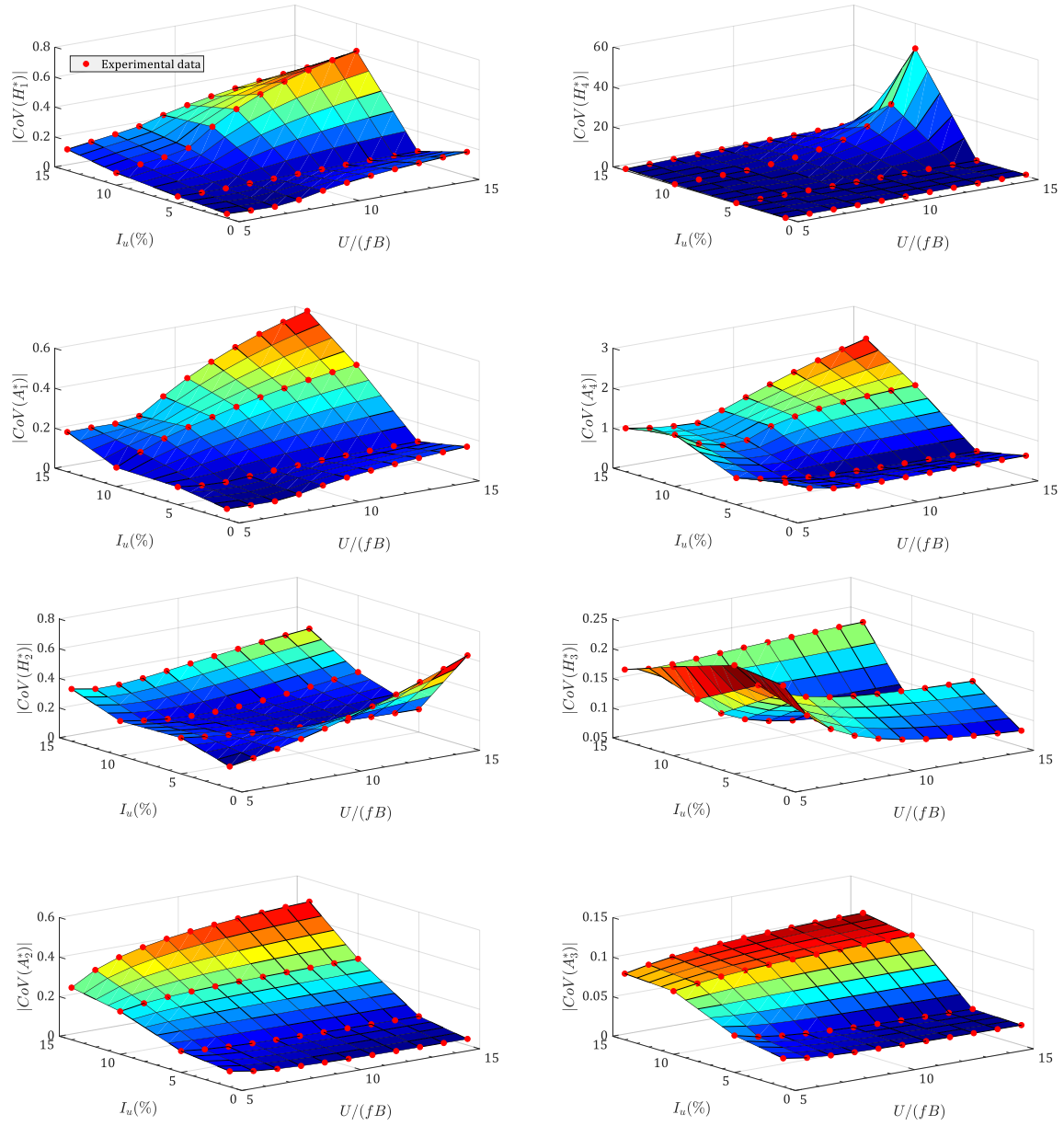


Fig. K4 Surface plots of the coefficient of variation of flutter derivatives for the quasi-flat section model

APPENDIX L. WIND TUNNEL TEST OF A PK SECTION MODEL

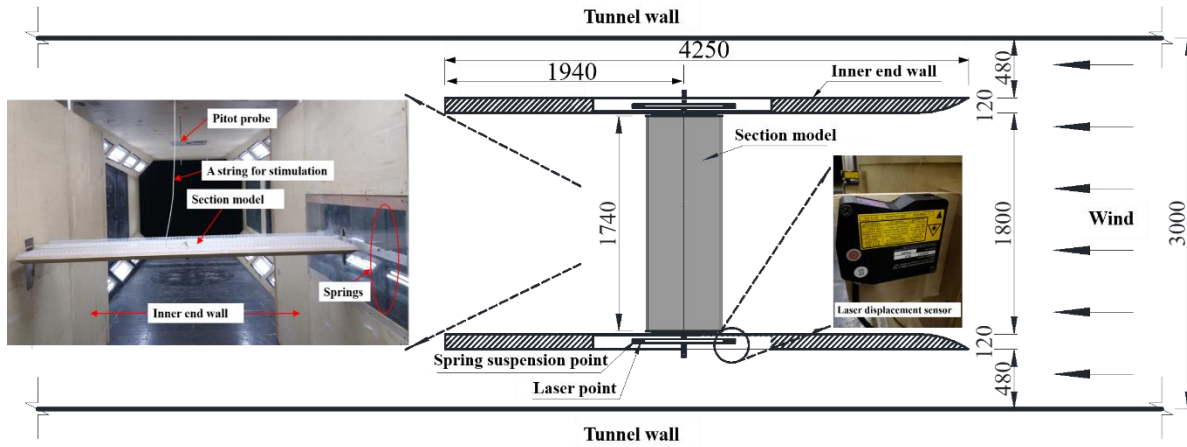


Fig. L1 Wind tunnel setup of a PK section model

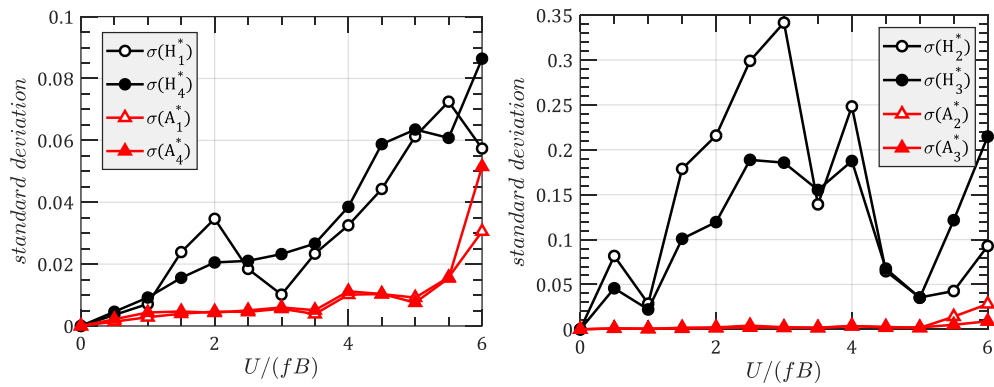


Fig. L2 Standard deviations of flutter derivatives of the P-K section model

APPENDIX M. CORRELATION COEFFICIENT MATRIX OF FLUTTER DERIVATIVES

(M1) The quasi-flat plate model: turbulence intensity $I_u = 1\%$

$$\begin{array}{c}
 H_1^* \\
 H_4^* \\
 A_1^* \\
 A_4^* \\
 H_2^* \\
 H_3^* \\
 A_2^* \\
 A_3^*
 \end{array}
 \begin{bmatrix}
 H_1^* & H_4^* & A_1^* & A_4^* & H_2^* & H_3^* & A_2^* & A_3^* \\
 1.00 & -0.54 & -0.34 & 0.22 & 0.00 & 0.00 & 0.00 & 0.00 \\
 -0.54 & 1.00 & 0.05 & -0.02 & 0.00 & 0.00 & 0.00 & 0.00 \\
 -0.34 & 0.05 & 1.00 & -0.25 & 0.00 & 0.00 & 0.00 & 0.00 \\
 0.22 & -0.02 & 0.25 & 1.00 & 0.00 & 0.00 & 0.00 & 0.00 \\
 0.00 & 0.00 & 0.00 & 0.00 & 1.00 & 0.01 & 0.59 & 0.36 \\
 0.00 & 0.00 & 0.00 & 0.00 & 0.01 & 1.00 & 0.10 & 0.45 \\
 0.00 & 0.00 & 0.00 & 0.00 & 0.59 & 0.10 & 1.00 & 0.13 \\
 0.00 & 0.00 & 0.00 & 0.00 & 0.36 & 0.45 & 0.13 & 1.00
 \end{bmatrix}
 \quad (M1)$$

(M2) The quasi-flat plate model: turbulence intensity $I_u = 5\%$

$$\begin{array}{c}
 H_1^* \\
 H_4^* \\
 A_1^* \\
 A_4^* \\
 H_2^* \\
 H_3^* \\
 A_2^* \\
 A_3^*
 \end{array}
 \begin{bmatrix}
 H_1^* & H_4^* & A_1^* & A_4^* & H_2^* & H_3^* & A_2^* & A_3^* \\
 1.00 & -0.77 & 0.27 & -0.43 & 0.00 & 0.00 & 0.00 & 0.00 \\
 -0.77 & 1.00 & 0.15 & 0.49 & 0.00 & 0.00 & 0.00 & 0.00 \\
 0.27 & 0.05 & 1.00 & 0.48 & 0.00 & 0.00 & 0.00 & 0.00 \\
 -0.43 & 0.49 & 0.48 & 1.00 & 0.00 & 0.00 & 0.00 & 0.00 \\
 0.00 & 0.00 & 0.00 & 0.00 & 1.00 & -0.53 & 0.39 & -0.39 \\
 0.00 & 0.00 & 0.00 & 0.00 & -0.53 & 1.00 & 0.05 & 0.69 \\
 0.00 & 0.00 & 0.00 & 0.00 & 0.39 & 0.05 & 1.00 & 0.07 \\
 0.00 & 0.00 & 0.00 & 0.00 & -0.39 & 0.69 & 0.07 & 1.00
 \end{bmatrix}
 \quad (M2)$$

(M3) The quasi-flat plate model: turbulence intensity $I_u = 10\%$

$$\begin{array}{c}
 H_1^* \\
 H_4^* \\
 A_1^* \\
 A_4^* \\
 H_2^* \\
 H_3^* \\
 A_2^* \\
 A_3^*
 \end{array}
 \begin{bmatrix}
 H_1^* & H_4^* & A_1^* & A_4^* & H_2^* & H_3^* & A_2^* & A_3^* \\
 1.00 & -0.18 & -0.26 & -0.76 & 0.00 & 0.00 & 0.00 & 0.00 \\
 -0.18 & 1.00 & 0.60 & 0.24 & 0.00 & 0.00 & 0.00 & 0.00 \\
 -0.26 & 0.60 & 1.00 & 0.48 & 0.00 & 0.00 & 0.00 & 0.00 \\
 -0.76 & 0.24 & 0.48 & 1.00 & 0.00 & 0.00 & 0.00 & 0.00 \\
 0.00 & 0.00 & 0.00 & 0.00 & 1.00 & -0.32 & -0.52 & -0.43 \\
 0.00 & 0.00 & 0.00 & 0.00 & -0.32 & 1.00 & 0.80 & -0.37 \\
 0.00 & 0.00 & 0.00 & 0.00 & -0.52 & 0.80 & 1.00 & -0.25 \\
 0.00 & 0.00 & 0.00 & 0.00 & -0.43 & -0.37 & -0.25 & 1.00
 \end{bmatrix}
 \quad (M3)$$

(M4) The quasi-flat plate model: turbulence intensity $I_u = 14\%$

$$\begin{array}{c}
 H_1^* \\
 H_4^* \\
 A_1^* \\
 A_4^* \\
 H_2^* \\
 H_3^* \\
 A_2^* \\
 A_3^*
 \end{array}
 \left[\begin{array}{cccccccc}
 H_1^* & H_4^* & A_1^* & A_4^* & H_2^* & H_3^* & A_2^* & A_3^* \\
 1.00 & -0.28 & -0.35 & -0.22 & 0.00 & 0.00 & 0.00 & 0.00 \\
 -0.28 & 1.00 & 0.71 & -0.62 & 0.00 & 0.00 & 0.00 & 0.00 \\
 -0.35 & 0.71 & 1.00 & -0.29 & 0.00 & 0.00 & 0.00 & 0.00 \\
 -0.22 & -0.62 & -0.29 & 1.00 & 0.00 & 0.00 & 0.00 & 0.00 \\
 0.00 & 0.00 & 0.00 & 0.00 & 1.00 & -0.27 & -0.26 & -0.19 \\
 0.00 & 0.00 & 0.00 & 0.00 & -0.27 & 1.00 & 0.26 & -0.50 \\
 0.00 & 0.00 & 0.00 & 0.00 & -0.26 & 0.26 & 1.00 & -0.42 \\
 0.00 & 0.00 & 0.00 & 0.00 & -0.19 & -0.50 & -0.42 & 1.00
 \end{array} \right] \quad (M4)$$

(M5) The PK section model

$$\begin{array}{c}
 H_1^* \\
 H_4^* \\
 A_1^* \\
 A_4^* \\
 H_2^* \\
 H_3^* \\
 A_2^* \\
 A_3^*
 \end{array}
 \left[\begin{array}{cccccccc}
 H_1^* & H_4^* & A_1^* & A_4^* & H_2^* & H_3^* & A_2^* & A_3^* \\
 1.00 & -0.13 & 0.33 & -0.69 & 0.00 & 0.00 & 0.00 & 0.00 \\
 -0.13 & 1.00 & 0.11 & -0.23 & 0.00 & 0.00 & 0.00 & 0.00 \\
 0.33 & 0.11 & 1.00 & -0.65 & 0.00 & 0.00 & 0.00 & 0.00 \\
 -0.69 & -0.23 & -0.65 & 1.00 & 0.00 & 0.00 & 0.00 & 0.00 \\
 0.00 & 0.00 & 0.00 & 0.00 & 1.00 & 0.34 & 0.17 & -0.46 \\
 0.00 & 0.00 & 0.00 & 0.00 & 0.34 & 1.00 & 0.00 & -0.56 \\
 0.00 & 0.00 & 0.00 & 0.00 & 0.17 & 0.00 & 1.00 & 0.19 \\
 0.00 & 0.00 & 0.00 & 0.00 & -0.46 & -0.56 & 0.19 & 1.00
 \end{array} \right] \quad (M5)$$

APPENDIX N. LITERATURE SURVEY RESULTS OF FLUTTER DERIVATIVES OF QUASI-FLAT PLATE SECTIONS

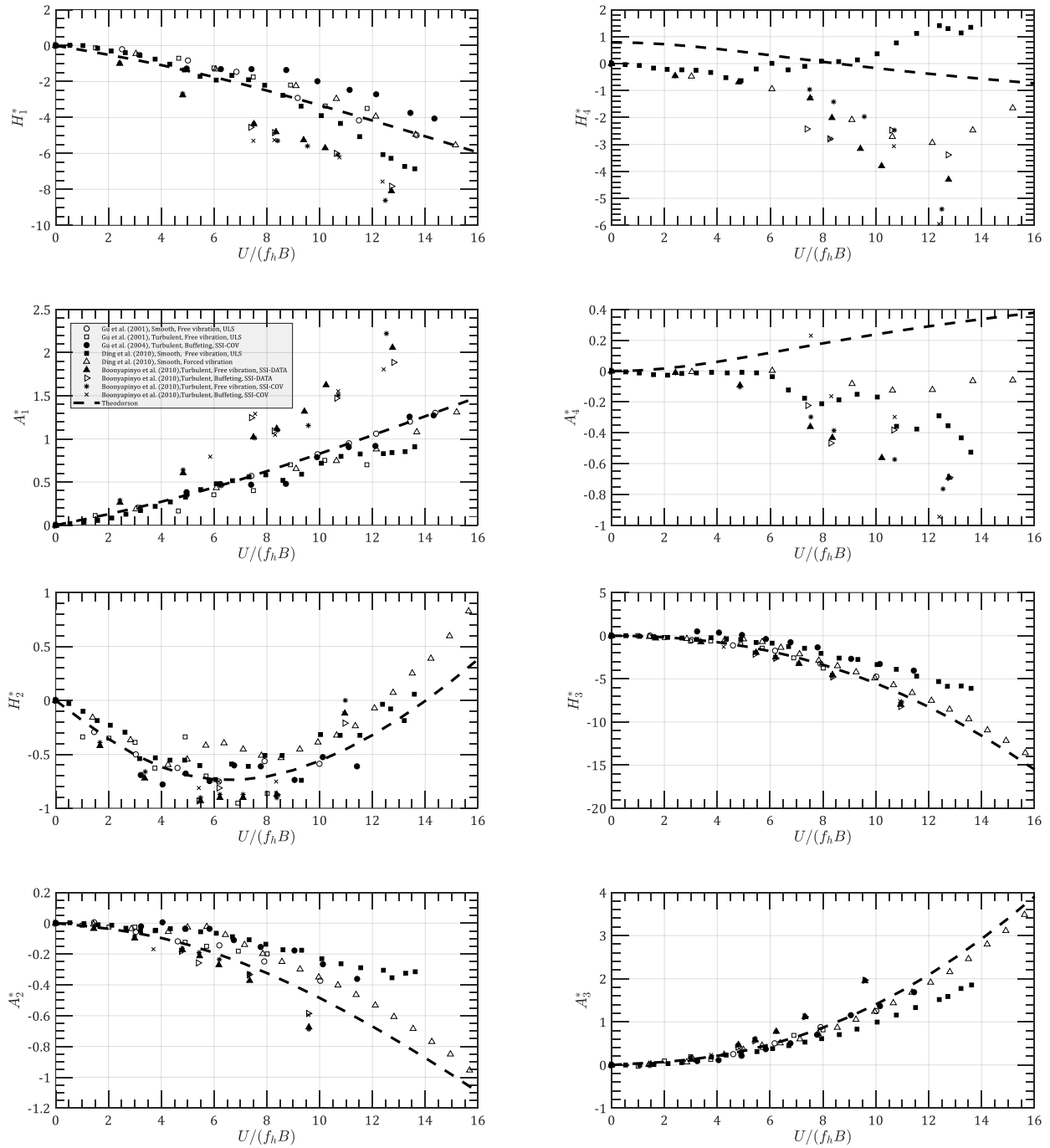


Fig. N1 Flutter derivatives of quasi-flat plates

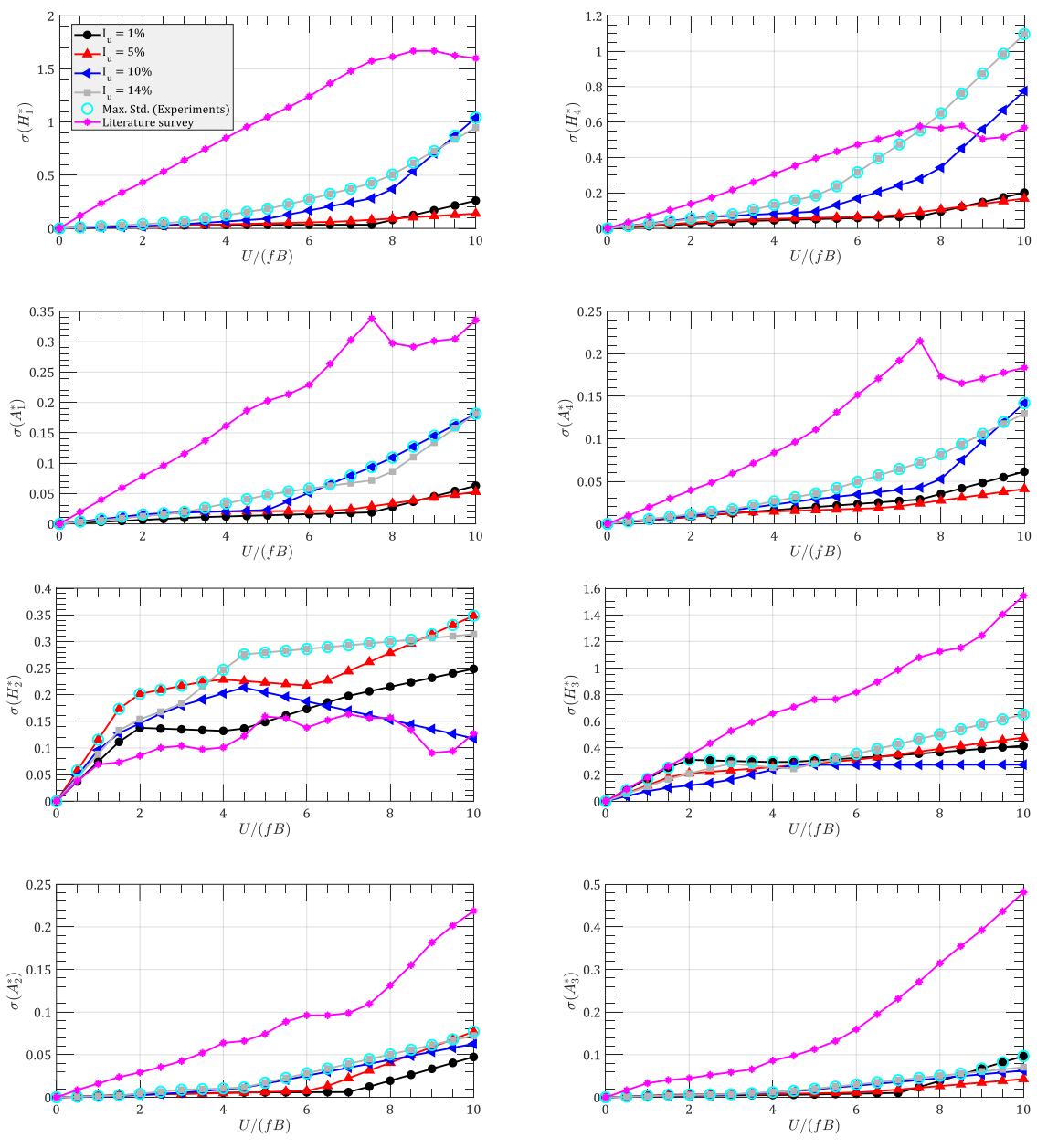


Fig. N2 Comparison of standard deviations of flutter derivatives for quasi-flat plates between the literature survey and present study

CURRICULUM VITAE

Name: Genshen Fang (方根深)

Education: Southeast University
Nanjing, Jiangsu, China
Bachelor of Engineering (Civil Engineering)
09/2010-06/2014

Tongji University
Shanghai, China
Ph.D. Candidate (Civil Engineering)
09/2014-present

Clemson University
Clemson, SC, Unites States
Ph.D. Candidate (Civil Engineering)
01/2018-present

Publications:

Journal papers

[1] **G. S. Fang**, J. Q. Wang, S. Li and S. B. Zhang. Dynamic characteristics analysis of partial-interaction composite continuous beams, *Steel & Composite Structures*, 2016, 21(1):195-216.

[2] **G. S. Fang**, L. Zhao, S. Y. Cao, Y. J. Ge and W. C. Pang. A Novel Analytical Model for Wind Field Simulation under Typhoon Boundary Layer Considering Multi-Field Parameters Correlation, *Journal of Wind Engineering and Industrial Aerodynamics*, 2018, 175:77-89.

[3] **G. S. Fang**, L. Zhao, L. L. Song, X. D. Liang, L. D. Zhu, S. Y. Cao and Y. J. Ge. Reconstruction of radial parametric pressure field near ground surface of landing typhoons in northwest Pacific Ocean, *Journal of Wind Engineering & Industrial Aerodynamics*, 2018, 183:223-234.

[4] **G. S. Fang**, L. Zhao, S. Y. Cao, Y. J. Ge and K. Li. Gust characteristics of near-ground typhoon winds, *Journal of Wind Engineering & Industrial Aerodynamics*, 2019, 188:323-337.

[5] **G. S. Fang**, Y. X. Yang, Y. J. Ge and Z. Y. Zhou. Vortex-induced Vibration Performance and Countermeasures of Semi-open Separated Twin-box Deck, *China Civil Engineering Journal*, 2017, 50(3):74-82. (in Chinese)

[6] **G. S. Fang**, L. Zhao, X. D. Liang, L. L. Song, L. D. Zhu and Y. J. Ge. The Applicability of Typhoon Field Parameters in Engineering Model for South Coastal Region of China: A Case Study on a Strong Typhoon Hagupit 0814, *Journal of Building Structures*, 2018,39(2):106-113. (In Chinese)

[7] **G. S. Fang**, Y. X. Yang, and Y. J. Ge. Flutter performance of PK section girders for long-span bridges, *Journal of Vibration and Shock*, 2018, 37(9):25-31. (In Chinese)

[8] **G. S. Fang**, L. Zhao, L.L. Song and Y. J. Ge. Investigation of design wind environment in Shanghai using an engineering-based typhoon wind model considering correlation among field parameters, *Journal of Building Structures*, 2019, 40(7): 13-22. (In Chinese)

[9] L. Zhao, X. N. Yang, **G. S. Fang**, W. Cui, L. L. Song and Y. J. Ge. Observation-based study for the evolution of vertical wind profiles in the boundary layer during super typhoon Mangkhut, *Acta Aerodynamica Sinica*, Changsha, 2019, 37(1): 43-54. (In Chinese)

[10] **G. S. Fang**, L. Zhao, X. Chen, J. X. Cao, S. Y. Cao and Y. J. Ge. Normal and Typhoon Wind Loadings on a Large Cooling Tower: A Comparative Study, *Journal of Fluid and Structures*, 2019. (Under Review)

[11] **G. S. Fang**, J. X. Cao, Y. X. Yang, L. Zhao and Y. J. Ge. Experimental Uncertainty Quantification of Flutter Derivatives for a P-K Section Girder and Its Application on Probabilistic Flutter Analysis, *Journal of Bridge Engineering*, ASCE, 2019. (Under Review)

Conference Proceedings

[1] **G. S. Fang**, L. Zhao, and Y. J. Ge. Calibration of Typhoon Engineering Model based on Field Observation and Its Application for Typical Sites, *the 2016 World Congress on Advances in Civil, Environmental, and Materials Research (ACEM16)*, Jeju, Korea, 2016.09.

[2] **G. S. Fang**, L. Zhao, S. Y. Cao and Y. J. Ge. Typhoon Wind Field considering the Probabilistic Correlation among Field Parameters: Modelling and Validation, *9th Asia-Pacific Conference on Wind Engineering*, Auckland, New Zealand, 2017.12.

[3] **G. S. Fang**, W. C. Pang, L. Zhao, S.Y. Cao and Y. J. Ge. Gust factor of near-ground typhoon winds: a nonstationary and non-Gaussian perspective, *5th American Association for Wind Engineering Workshop*, Miami, Florida, 2018.08.

[4] **G. S. Fang**, W. Pang, L. Zhao, S. Y. Cao and Y. J. Ge. Toward a Refined Estimation of Typhoon Wind Hazards: Parametric Modelling and Upstream Terrain Effects, *the 15th International Conference on Wind Engineering*, Beijing, China, 2019.09.

[5] **G. S. Fang**, L. Zhao, S. Y. Cao and Y. J. Ge. An Analytical Model for Typhoon Wind Field considering Multi-Field Parameters Correlation, *the 18th National Conference on Structural Wind Engineering and the 4th National Forum on Wind Engineering for Graduate Students*, Changsha, China, 2017.08. (in Chinese)

[6] **G. S. Fang**, C. Hong and Y. J. Ge. The effects of incoming turbulence on critical wind speed of flutter for long-span bridges with close steel box girder, *the 17th National Conference on Structural Wind Engineering and the 3rd National Forum on Wind Engineering for Graduate Students*, Wuhan, China, 2015.08. (in Chinese)

[7] X. N. Yang, L. Zhao, L. L. Song, **G. S. Fang** and Y. J. Ge. Stochastic Simulation of Tropical Cyclone Tracks and Its Engineering Applications, *the 18th National Conference on Structural Wind Engineering and the 4th National Forum on Wind Engineering for Graduate Students*, Changsha, China, 2017.08. (in Chinese)